

J Last et al

Raising the JET Toroidal Field to 4 Tesla

“This document contains JET information in a form not yet suitable for publication. The report has been prepared primarily for discussion and information within the JET Project and the Associations. It must not be quoted in publications or in Abstract Journals. External distribution requires approval from the Publications Officer, JET Joint Undertaking, Abingdon, Oxon, OX14 3EA, UK”.

Raising the JET Toroidal Field to 4 Tesla

E Bertolini, M Buzio¹, A Kaye, J R Last, P Miele¹,
P Noll, S Papastergiou², V Riccardo³, G Sannazzaro⁴,
M Sjöholm¹, R Walton⁵.

JET Joint Undertaking, Abingdon, Oxfordshire, OX14 3EA, UK.

¹CERN, Geneva, Switzerland.

²ENEA, Frascati, Italy.

³UKAEA, Culham, UK.

⁴ITER, Garching, Germany.

⁵EC, Brussels, Belgium.

Raising the JET Toroidal Field to 4 Tesla

A feasibility study relating to torus components

*E. Bertolini, M. Buzio¹, A. Kaye, J.R. Last, P. Miele¹, P. Noll, S. Papastergiou²,
V. Riccardo³, G. Sannazzaro⁴, M. Sjolholm¹, R. Walton⁵*

29 November 1999

1. *CERN, Geneva*
2. *ENEA, Frascati*
3. *UKAEA, Culham*
4. *ITER, Garching*
5. *EC, Brussels*

Contents

1. Introduction	
3	
2. TF coils and Mechanical Structure	
5	
2.1. Description	5
2.2. Analysis	6
2.3. Machine Operation Data	20
2.4. Tests	22
2.5. Assessment of analysis and test results	30
2.6. Summary for TF coil	33
3. P1 coils	
34	
3.1. Description	34
3.2. Forces and stresses	35
3.3. Allowables	35
3.4. Analysis	35
3.5. Summary for P1 coil	38
4. Vacuum Vessel	
39	
4.1. Description	39
4.2. Analysis	41
4.3. Tests of vacuum vessel materials	52
4.4. Summary for vacuum vessel	55
5. Conclusions	
56	
6. Acknowledgements	
58	
7. JET publications relating to 4T study	
59	
8. List of Tables	
60	
9. List of Figures	
61	
10. List of Appendices	
63	

1. Introduction

The TF coils were originally designed for operation at 3.45 T. Margins in the original design suggested that a higher field might be possible. A simple scaling up of the stresses in the copper showed reasonable stresses. Operation at 4 T appeared to offer substantial advances in plasma performance so in mid 1995 a detailed feasibility study was started. Upgrade of the power supplies was also studied and is reported elsewhere^[1].

JET was conceived by the original designers with a high degree of built in flexibility. Among other aspects, it is the only tokamak in the world, designed in eight octants, each one including a section of the vacuum vessel, four toroidal coils and the corresponding section of the mechanical structure. This choice allowed nine complete octants to be procured, i.e. to provide a spare section of the vacuum vessel, of the mechanical structure and four spare toroidal coils.

In addition, the central solenoid was designed in eight pancakes and two spares were also procured. These were used to upgrade the ohmic heating system, when JET was modified to increase the plasma current from 4.8 MA to 7.0 MA in limiter configuration and from 3.0 to 5.0 MA in X-point configuration (without divertor) in 1987-88.

The 32 TF coils heat up adiabatically during the pulse and were originally water cooled in between pulses. As in other major tokamaks, water leaks developed. In JET these leaks occurred in three of the TF coils leading eventually to interturn short-circuits.

Because:

- four spare coils were available (plus a prototype coil)
- the machine was designed in 8 sections (octants) and
- there were no individual coil casings,

it was possible to replace these coils relatively quickly. In addition the coolant was changed to an insulating organic fluid to avoid the recurrence of short-circuits. This measure was considered adequate, because even the faulty coils were found to be fully sound mechanically.

When the decision was taken, in July 1995, to embark in a comprehensive study to upgrade the toroidal field from 3.4 to 4.0 T, a detailed plan for both experimental work and computer modelling was set up.

The experimental work included:

- shear tests on samples taken from one of the (electrically) faulty coils, to repeat the tests on synthetic samples performed as part of the qualification of the manufacturing process for the coils,
- stiffness tests comparing a new coil with a second (electrically) faulty coil that operated in the machine for several years.

These types of tests have shown that the coils are even better than would have been expected from the tests performed during manufacture and have proved that there has been no deterioration in the mechanical capability of the coils. The results obtained in this way are unique because:

- extensive tests on used coils have not been done before,
- they cannot be repeated because today there are no tokamaks in the world with TF spare coils available, and
- no other tokamaks have modular construction to facilitate coil replacement in the same way as JET.

The study is divided into three main sections corresponding to the three main components in JET affected by the toroidal field;

1. the TF coils, where forces increase in proportion to the toroidal field squared,
2. the P1 coils, where the external pressure increases in proportion to the toroidal field squared and
3. the vacuum vessel, where the toroidal field affects behaviour of the vessel during disruptions.

Most attention was focussed on the TF coils, which had previously been studied in 1989 in connection with the upgrade of plasma current from 5 MA to 7MA and again in a reliability study in 1994. High stress regions identified in previous studies were investigated further and other features were studied in greater detail than had been attempted earlier. Tests were made on coils that had been removed from the machine and many new analyses were made.

A simple analysis of the P1 coil, extended an earlier detailed study to include 4 Tesla operation. The P1 coils were considered in less detail than the TF coils, because all primary stresses are compressive, which reduces the likelihood of crack formation and improves the shear properties of insulation and the P1 coils can be replaced by existing spares, if damaged.

The vacuum vessel only experiences large forces during disruptions. The plasma moves vertically or tilts and exerts forces on the vessel. Two types of vessel displacement were considered: rolling motion due to symmetrical vertical plasma displacement and sideways displacements due to asymmetrical plasma movement. An increase in toroidal field can lead to increased forces on the vacuum vessel. Extrapolated worst case events were considered using several new finite element and lumped parameter models and acceptable operational limits were defined.

2. TF coils and Mechanical Structure

21. Description

The JET TF magnet comprises 32 “D” shaped coils originally designed to produce a field of 3.45 T at 2.9 m. radius. The coils use liquid cooled copper conductors and epoxy resin impregnated glass fibre insulation.

Each coil consists of two pancakes with 12 turns. Each conductor incorporates two parallel cooling channels symmetrically located in the cross section and all turns are cooled in parallel.

As the coils are “D” shaped, the toroidal field causes only tensile stresses in the conductor. Each toroidal coil is subject to a net inward force, which is reacted along the straight section by the inner poloidal coils (P1). Both the tension in the toroidal coils and the inward force on the inner poloidal coils are proportional to B^2 (where B is the toroidal field).

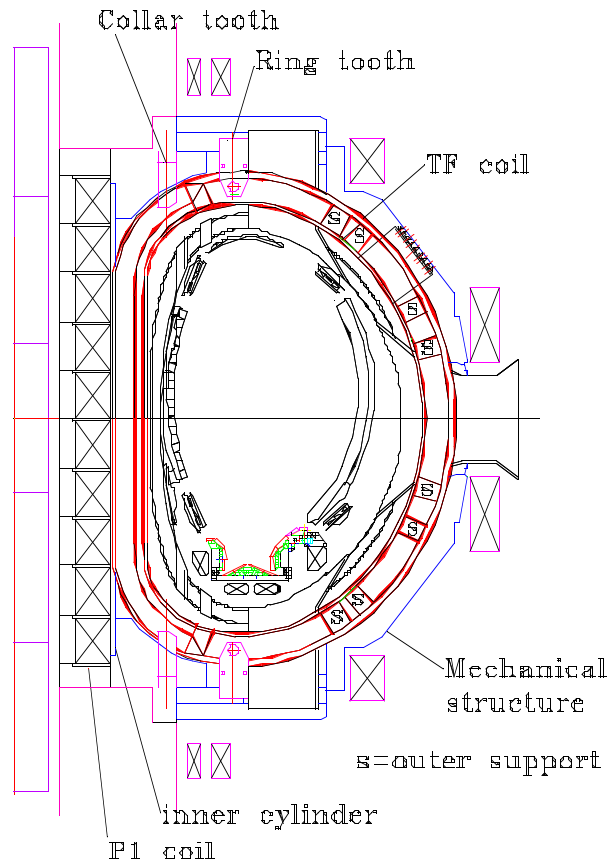


Figure 1. Cross section through the JET machine showing toroidal and poloidal coils

The poloidal field causes out of plane forces on the TF coils, which increase linearly with B. Taken together these forces represent a torsional force applied to the whole TF coil set. These forces are reacted by the mechanical structure (Figure 2), which consists of inner cylinder, upper and lower ring and collar and outer shell. The interface between the structure and coil is made by the fluted inner cylinder along the straight nose section, by collar and ring teeth at top and bottom and by wedges in the outer shell casting.

Torsional forces are resisted by the outer shell, which is the stiff part of the mechanical structure. The outer shell is made of austenitic nodular iron castings, which are split into 8 octants. Each shell octant is split into upper and lower castings. The inter octant joints are made by special adjustable inter octant keys. The rings and collars transmit forces from the inner cylinder to the outer shell and also contain the ring and collar teeth. The inner cylinder is made from 8 stainless steel sectors doweled to the collars at top and bottom.

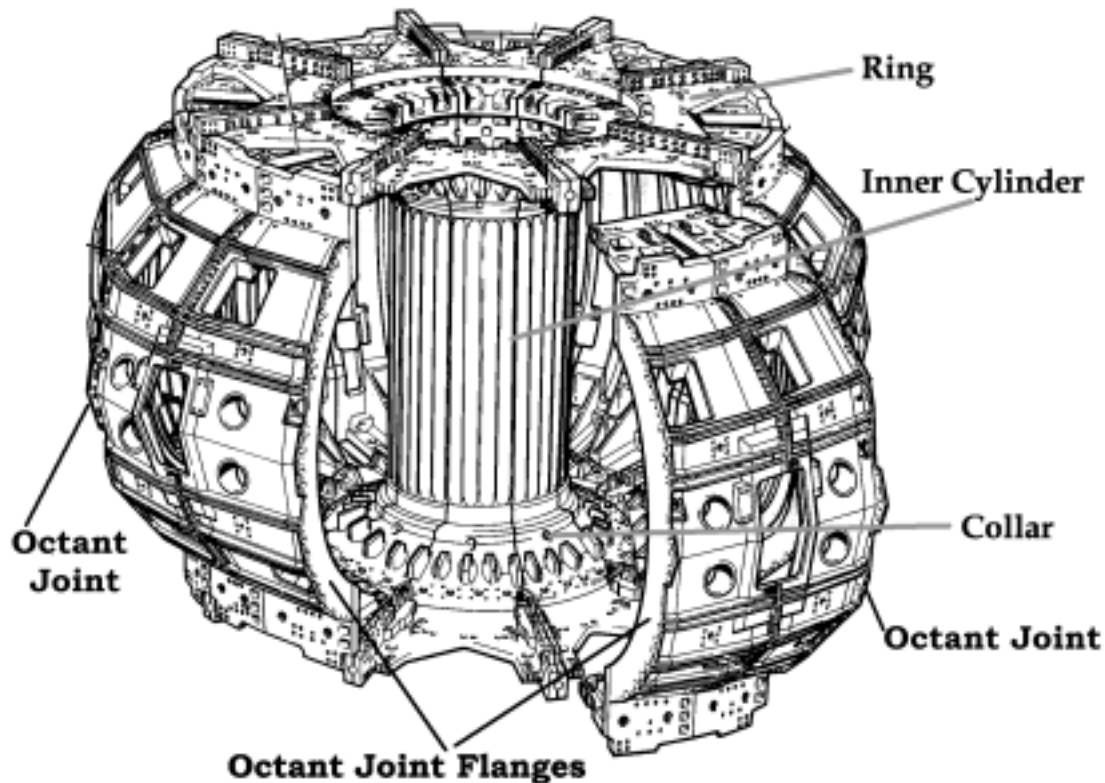


Figure 2. Mechanical structure which supports TF coil torsional forces

2.2. Analysis

2.2.1. Definition of 4 Tesla toroidal field

The toroidal field is given by

$$B_t = \frac{\mu_0 I_t N_{tot}}{2\pi R}$$

where I_t is the coil conductor or power supply current,

N_{tot} is the total number of turns on all coils ($24 \times 32 = 768$) and

R is the radius at which the field is required.

The original maximum operating current was 67 kA, which gave a field of 3.45 T at 2.98 m. radius. The "4 T" operating current is defined as **78 kA** and this gives a field of **4 T** at **3.00 m.** radius.

Calculations of 4 T stress in this report are based on a current of 78 kA, except some thermal calculations where 80 kA has been used. In this case the $\int_t^2 dt$ is important, not the maximum current.

2.2.2. Tension in TF coil

Field for idealised TF coil

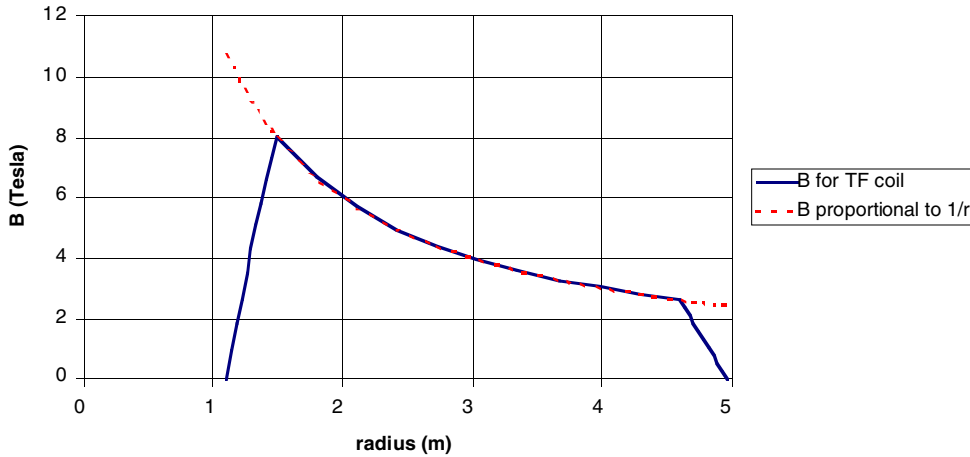


Figure 3. Toroidal field vs. radius in median plane. The field varies as $1/R$

The TF coils are designed to be free of bending moments and the magnetic forces are contained by a constant tension in the coil conductors. The total force acting on the coils is found by integrating the magnetic pressure over the median plane enclosed by the coils. The tension in one coil is given by

$$T = \frac{\mu_0 I^2 N_c N_t^2}{8\pi} \ln \frac{R_2}{R_1}$$

where R_1 = effective inner leg radius = 1.373 m.,

R_2 = effective outer leg radius = 4.733 m,

N_c = number of coils = 32,

N_t = number of turns per coil = 24,

I_t = coil conductor or power supply current

Note that R_1 and R_2 are moved inward from the coil geometric centre line.

The membrane stress in the coils is given by (Tension)/(cross-sectional area of the copper conductors). Values at 67 and 78 kA are as follows.

Current Amperes	Tension in each coil MN	Membrane stress in inner reduced section MPa	Membrane stress in outer full section MPa
67000	5.12	83	57
78000	6.94	113	77

An FE calculation gave a tension of 7 MN (compared with 6.94 analytically) at 78 kA. Errors in the analytical formula are due to the discrete nature of the TF coils so that the effective radius of the outer leg is not clear.

2.2.3. General method

The coils are subject to electromagnetic forces due to the toroidal and poloidal fields, which are described in detail in Appendix A

In-plane loads on the TF coils are due to the current in the coils themselves. The distributed force ($d\mathbf{F}/ds=\mathbf{I}_{TF}\times\mathbf{B}_{TOR}$) is normal to the coil, lies in its plane and is up-down symmetric. This load scales with I_{TF}^2 and its distribution (depending upon the toroidal magnetic field) is independent of the plasma configuration.

Out-of-plane loads are due to poloidal fields caused by the plasma and the poloidal field coils. The distributed force ($d\mathbf{F}/ds=\mathbf{I}_{TF}\times\mathbf{B}_{POL}$) is normal to the coil and to its plane. This load scales linearly with I_{TF} and, for a given plasma configuration, linearly with plasma current. Its distribution depends upon the whole magnetic configuration of the pulse. This is calculated using a plasma equilibrium program (MaxFEA) which gives as output the poloidal magnetic field normal to the TF coil. This field is then scaled into a distributed out of plane force and used as an input for mechanical finite element models.

A typical force and stress calculation is given below.

First the normal magnetic field is calculated using MaxFEA (Figure 4).

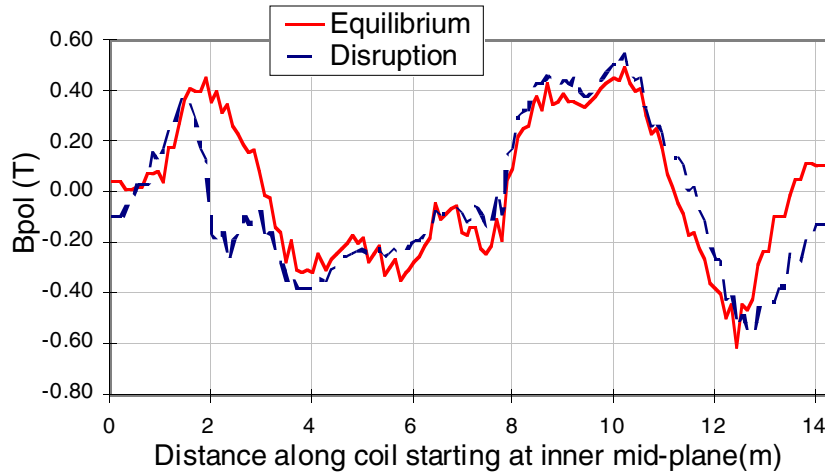


Figure 4. Normal magnetic field along TF coil periphery; example shows 6 MA plasma

The normal magnetic field together with the toroidal current generates out of plane forces which are used in an FE model. Figure 5 and Figure 6 show stresses calculated using the ABAQUS beam model.

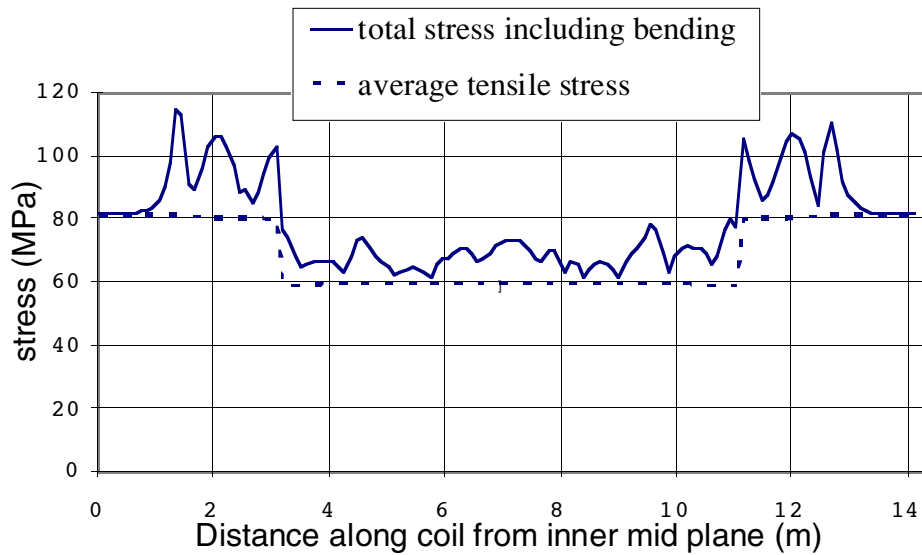


Figure 5. Tensile stresses in the TF coil conductor; example - 6 MA plasma at 4T

The tensile force in the coil is constant so the average tensile stress only changes at changes in coil cross-section. The total tensile stress includes bending stress. There are small in-plane bending stresses due to deviations from the perfect theoretical shape but most of the bending is due to out of plane forces. It also depends on the support positions. Similarly the shear stress is composed of in-plane and out-of-plane shear and torsional shear.

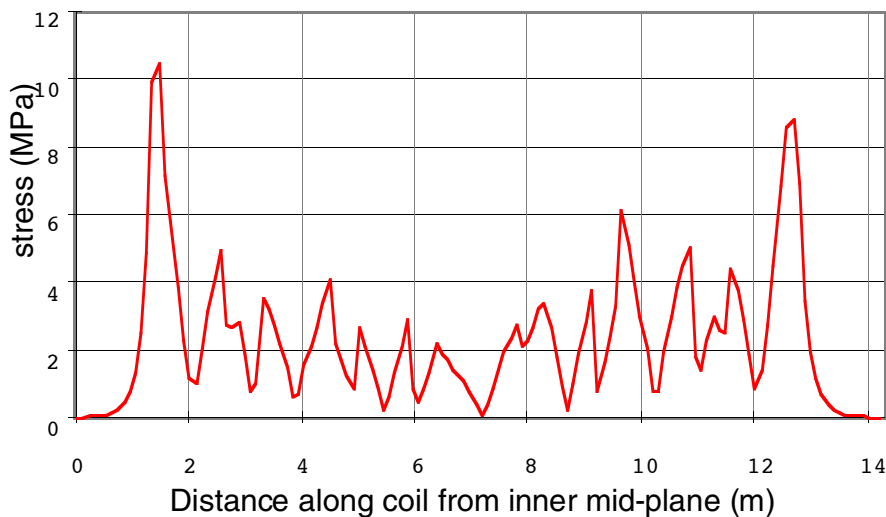


Figure 6. Shear stress in the TF coil insulation; example - 6 MA plasma at 4T

The FE model also gives the reaction forces. The two reaction forces of greatest concern are the Ring Tooth and Collar Tooth.

Thermal loads are caused by the Joule effect, which increases the coils' temperature during the pulse. The temperature rise is proportional to $\int^2(t)dt$. Maximum thermal stress usually occurs at the end of the pulse when temperatures are highest but

maximum total stress is usually at the end of the current flat top, when stresses due to both thermal and electro-magnetic effects are high.

2.2.4. Stress Analysis of coils

In plane and ex plane magnetic forces are used as input to FE models of the coil for stress analysis. Five main models have been used.

a) Beam model. A model of a TF coil with in-plane and out of plane supports using beam elements with average properties for the coil cross section. It calculates tensile, bending and shear stresses due to the magnetic loads. As the beam elements have properties averaged over the cross section, stresses produced by the model have to be scaled to give stress in the copper conductors. The model is useful for quick analysis of plasma scenarios but local stress concentrations can not be modelled. More details are given in Appendix B.

b) Hybrid model. A detailed brick model of the coil collar region coupled to beam elements for the rest of the coil. More details are given in Appendix C.

c) Simple brick model. A simple brick model of the whole coil with rectangular coil cross section used for studies of the effect of insulation modulus on coil stiffness. More details are given in Appendix B.

d) Improved brick model. A more complex brick model with correct representation of the coil cross section used for accurate overall stress calculation and validation of the beam model. More details are given in Appendix B.

e) Model of coil connection region. A 3D brick model of the coil connection region. The tapered coil tails and inter-pancake joint are modelled in detail, the rest of the coil coarsely. Sub models have also been used (2D of the whole region, 3D of tail tip, 2D coolant inlet/outlet) for particular detailed studies. More details are given in Appendix D and Appendix E.

2.2.4.1. Beam model

The model is consists of 136 beam elements with cross sectional properties, based on the coil materials and dimensions (Appendix B).

Its boundary conditions reproduce those of a coils fitted in the machine:

- in plane gap supports and out of plane supports along the inner vertical leg
- out of plane supports (usually pins, but spring can be employed as well) at the Ring Teeth and MS outer supports
- offset out of plane support at the Collar Teeth
- pre-loaded in plane springs at the Push Pull Jacks
- the vertical support is moved from below the coil to the mid-plane for simplicity

The loads are:

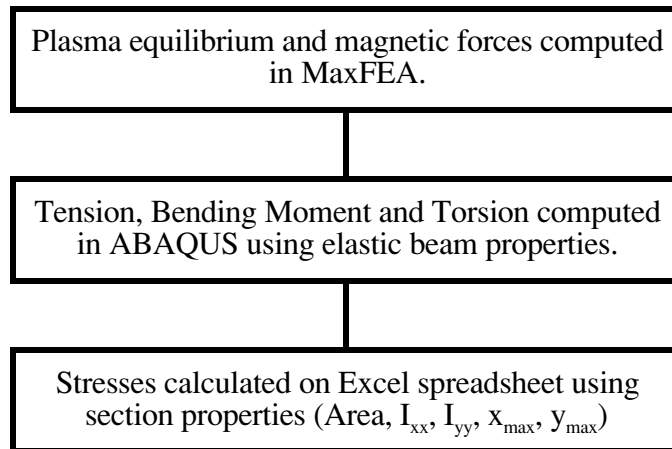
- in plane loads (proportional to the square of the TF current, computed for a reference 1 A TF current)
- out of plane loads (scaling the poloidal field normal to the coil, computed with MaxFEA, with the TF current)

The model is used to assess plasma scenarios both in equilibrium and in disruption. It produces out of plane support reactions, section forces and torques, which can be used to compute stresses according to the beam theory. The model is unable to predict local stress concentration.

The quantities of interest computed with the aid of this model are:

- out of plane reaction forces at the collar and ring
- membrane and bending stresses in the copper
- inter-pancake shear stress in the insulation

The procedure for analysing plasma scenarios is summarised in the diagram below.



2.2.4.2 Simple brick model

The simple brick model (Figure 7) was developed to investigate the effects of the shear modulus of the epoxy/glass insulation on the global coil deflections (Appendix B). This exercise is not possible using the beam model, since there the Poisson ratio has to be smaller than 0.5, limiting the insulation G to be larger than 4 GPa.

The model is made with 136x4x4 brick elements: each beam of the beam model constitutes a slice of the brick model, each slice is divided in 4x4 elements. Convergence has been checked by comparison with 136x3x3 and 136x5x5 models, which gave about the same displacements for the same load cases.

The model was used to reproduce force/deflection tests made on used and unused coils. It was hoped to determine the insulation shear modulus from these tests. Unfortunately uncertainties on both the tests and the model accuracy are too large to come to a conclusive answer. The insulation shear modulus was determined by separate tests on small samples of insulation.

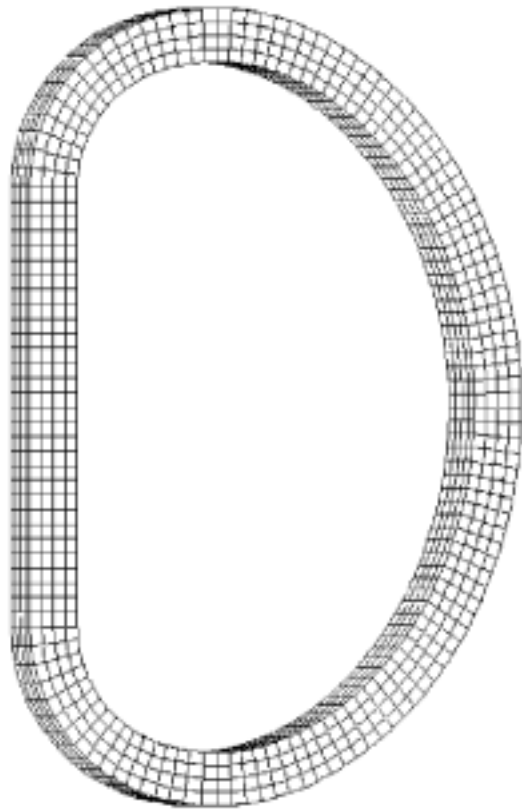


Figure 7. Simple Brick model

2.2.4.3. Polygonal cross section brick model

This model was designed to overcome the limitations of the beam model in analysing coil stresses for plasma scenarios (Appendix B). The outer perimeter of the copper conductors is modelled exactly and the inter-pancake insulation is modelled explicitly. Properties of the rest of the model are adjusted to reflect the ratio of copper to insulation.

Features of the three whole coil models are compared in Table I.

Table I. Comparison of whole coil models			
Feature	Beam model	Simple brick model	Polygonal cross section brick model
Size	136 beam elements (1D)	136x4x4 bricks (quadratic)	136x5x7 bricks (quadratic)
Time per run	40 sec	~10 min	20 min
Boundary conditions			
Interface to curved inner cylinder	not modelled.	not modelled.	Correctly modelled with compression at nose and allowing sliding of nose in groove.
Boundary conditions at supports	assumed to be at centre of beam (except at collar)		Correctly modelled as compression only on the out-of-plane face
Stress in copper			
Stress in sharply curved regions of the coil	May be inaccurate as simple beam theory applies when cross-sectional dimensions \ll radius	Bricks may improve stress calculation but not really small enough	Stress distribution should be accurate with 5x7 quadratic bricks
Stress at outer surface of coil	Maxima can be found by correct post processing	Not accurate because outer surface is not modelled	Should be correct when scaled to allow for non copper area
Shear			
In plane shear deformation	Can not be correctly modelled due to Poisson's Ratio limitations.	Bricks allow free setting of parameters	Bricks allow free setting of parameters
Inter pancake shear	Shear in different planes not combined correctly	Modelled with limited accuracy	Inter pancake insulation modelled explicitly
Inter-turn shear (such as at the collar)	Not modelled	Modelled very roughly. Hybrid model still needed for accuracy.	Modelled roughly. Hybrid model still needed for accuracy.
Other effects			
Distribution of magnetic force	On centre line	Uniform	In plane forces distributed accurately, out of plane forces distributed uniformly across section
Compression effects in the nose of the coil	Not modelled at all	Modelled with limited accuracy	Modelled correctly. Modifies distribution of longitudinal tension by Poisson's ratio effects.

In summary the polygonal cross-section brick model attempts to model the whole coil as accurately as possible within the limitations of our computer memory. A typical displaced mesh for this model is shown in Figure 8.

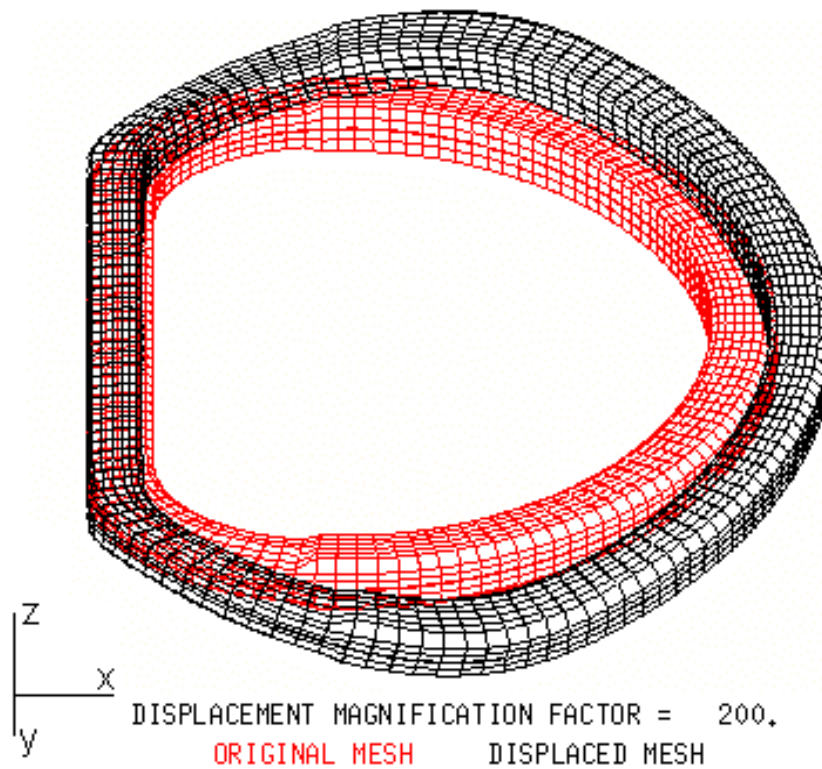


Figure 8. Polygonal cross section brick model showing displaced mesh under VDE (see 4.2.1) loading conditions

2.2.4.4. Hybrid model of collar region

This combines the properties of overall and local models (Appendix D). Most of the coil is modelled coarsely with beam elements, while regions of interest are modelled in detail with 3D brick elements (Figure 9). The detailed region is equivalent to local models with fixed boundary conditions studied previously and the coarsely meshed region provides accurate boundary conditions for the detailed region.

A calculation made in 1988, using average properties for a copper and insulation mixture, showed that 50 tonnes collar tooth force corresponds to 17 MPa peak or 15 MPa average stress in the coil. This calculation has been repeated using the more detailed hybrid model, where the insulation is modelled explicitly.

The calculation shows that the shear stress in the insulation is a function of the shear modulus of the insulation (Figure 10). The maximum shear stress varies between 9 MPa if $G = 1.2$ GPa and 12 MPa if $G = 4$ GPa. Note that even with the higher value of G the maximum shear stress is less than the previous value found with a simpler model and that at higher temperatures G will reduce. The reduced G will lead to lower stresses, which will compensate for the reduced strength at higher temperature.

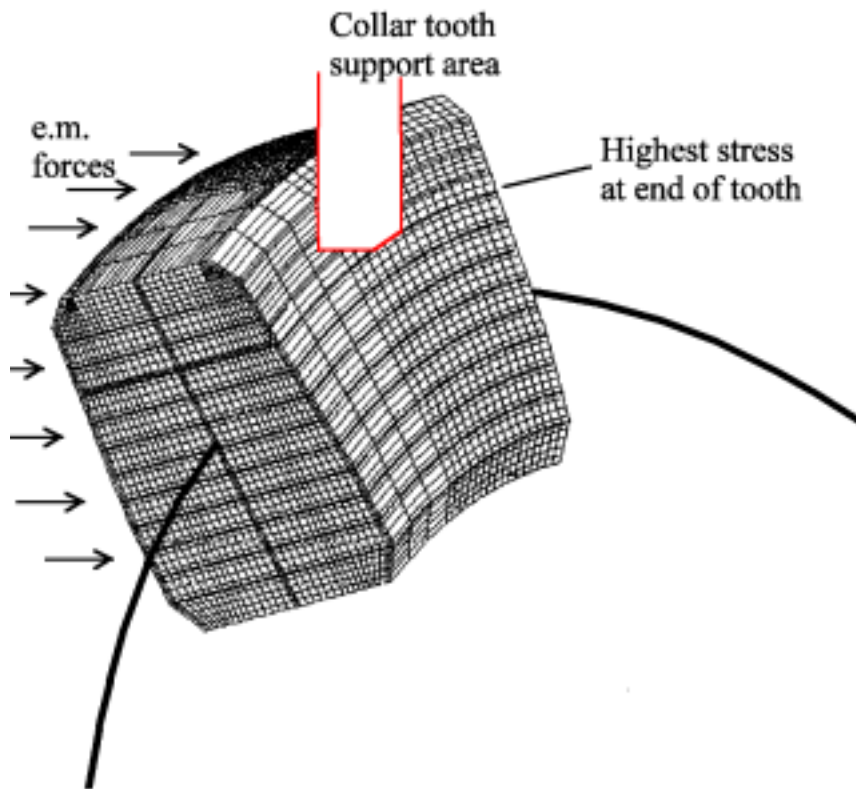


Figure 9. Hybrid model using brick and beam elements. A small part of the coil near the collar tooth is modelled in detail.

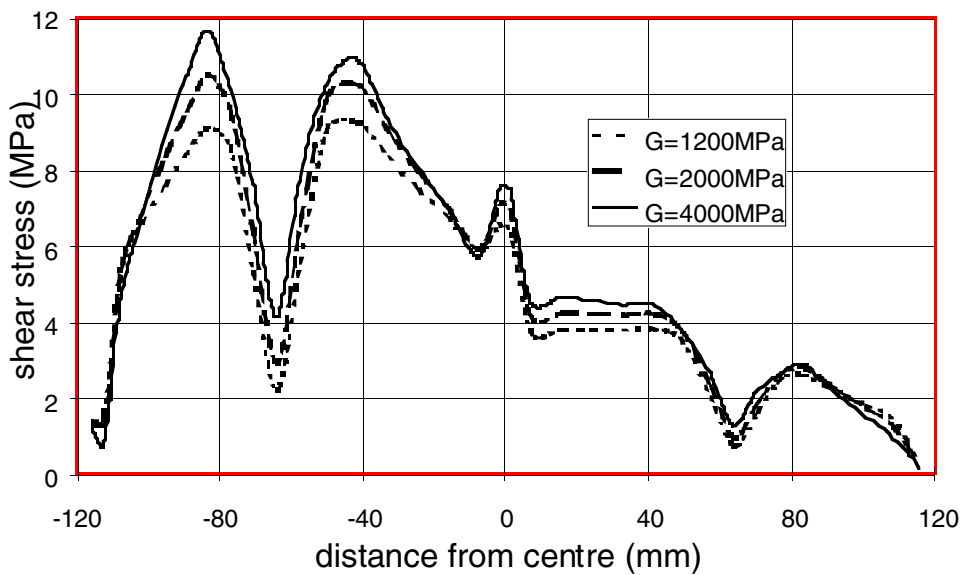


Figure 10. Shear stress in inter-turn coil insulation at collar tooth end for three values of shear modulus

2.2.4.5. Model of connection and tail region

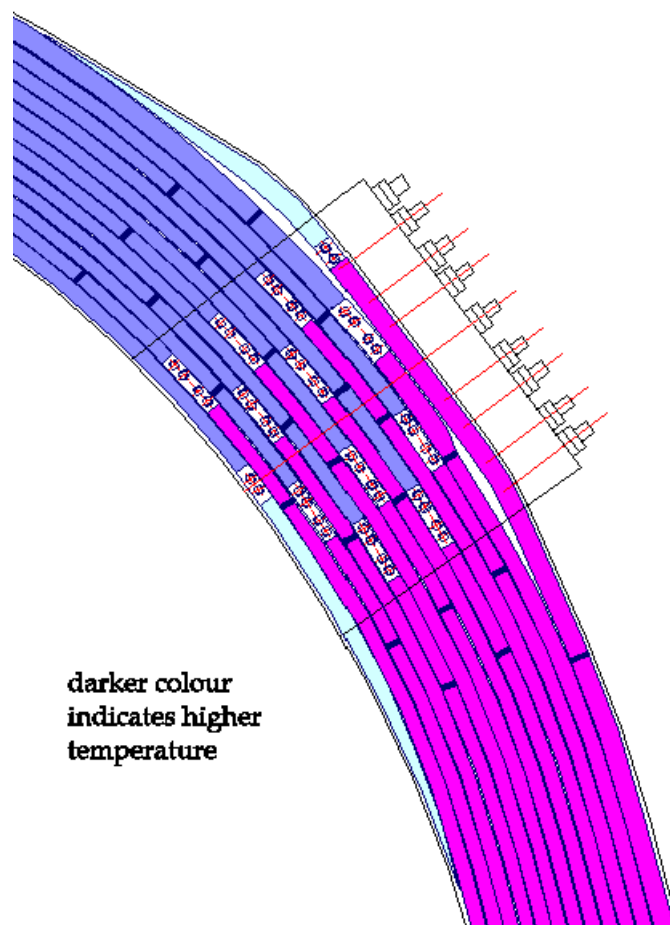


Figure 11. Coil connection region showing position of coolant connections, position of brazed joints and tapered tails

The coil current enters through an electrical terminal at the outside of one pancake and spirals inward to the inside of the pancake (Figure 11). It then crosses to the other pancake and spirals out to the other electrical terminal. The coolant however only makes one turn. It enters and leaves the conductor at adjacent points through specially made conductors incorporating coolant connections.

The coil connection region therefore includes:

- electrical terminals on the outside of the coil
- inter-pancake joint on the inside of the coil
- tapered coil tails at inside and outside of coil intended to react tensile stresses
- coolant inlet and outlet connections
- brazed joints between main conductor and special conductor with coolant connections

These features cause problems as described below.

1. Tensile stresses in the conductors are offset at the inter-pancake joint. This would tend to make the inter-pancake connection piece rotate. This rotation is resisted by tapered tails, which form part of the inter-pancake connection piece. However these tails have stress concentrations due to the conductor tensile stresses, differential temperatures and end effects. These problems are addressed by a 3D brick model of the coil connection region (Figure 12 and Appendix E). The tapered coil tails and inter-pancake joint are modelled in detail, the rest of the coil coarsely. Similar stresses occur at the outer tapered tails.
2. The adjacent coolant inlet and outlet points cause high longitudinal temperature gradients. As the coolant connection points are staggered, temperatures in adjacent conductors are different leading to inter-turn shear stresses. These stresses have been evaluated using a 2D model of the inlet/outlet region.
3. The brazed joints do not affect the analysis as the brazed joint material will have the same cyclic modulus of elasticity and the bulk of the copper. The brazed joints do have lower strength than the hard copper so allowable stresses in this region are lower.

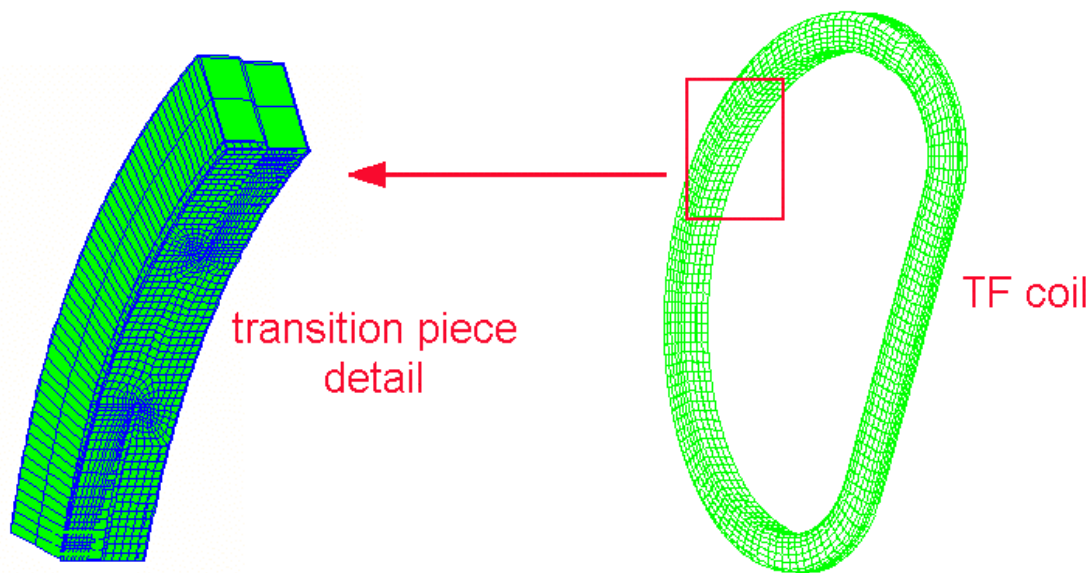


Figure 12. Model of inter-pancake joint and tails

Calculations using the model shown in Figure 12 and sub-models show that the highest stresses in the insulation occur at the tip of the tapered tails (see Figure 13). In addition to shear stresses there are high tensile stresses perpendicular to the copper surface at the tail tip. Fracture mechanics considerations indicate that a Mode I crack might start at the tail tip and continue as a Mode II crack in the inter-turn insulation. However crack energy calculations indicate that the crack growth rate should be slow.

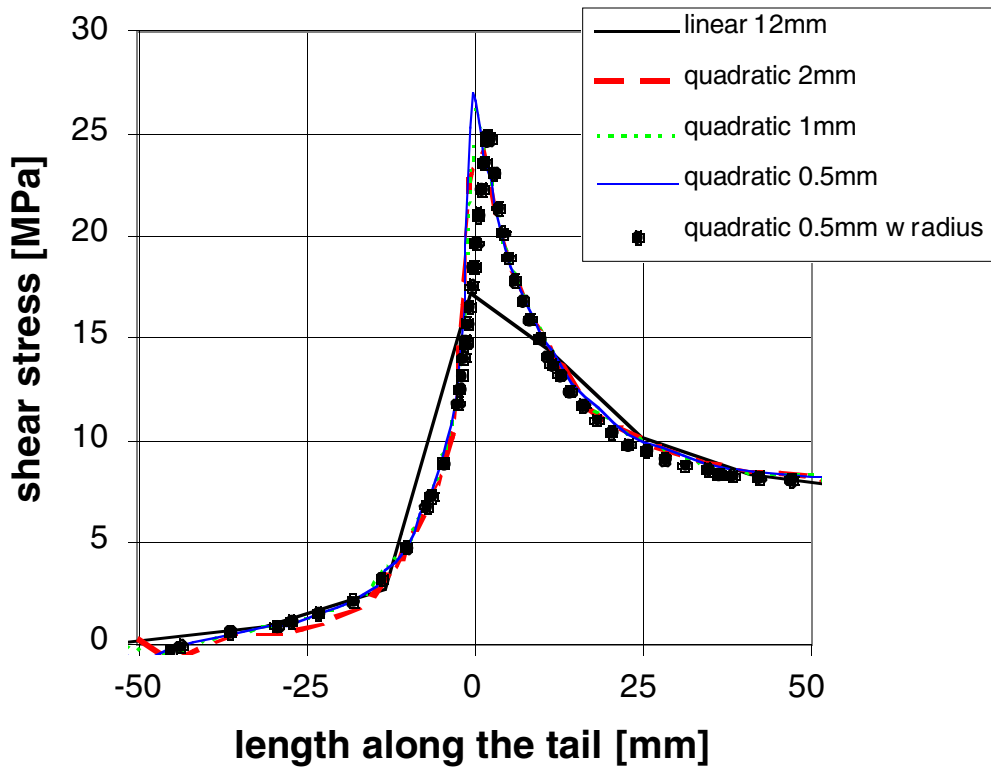


Figure 13. Shear stress at tip of coil tail. The different curves show the effect of FE element size.

2.2.5. Thermal Analysis

The coil is heated by current during the pulse. The cooling system runs continuously but has little effect during the pulse. After the pulse the coil cools from the inlet end first. As the coolant only makes a single turn and all turns are cooled in parallel, temperature gradients across the coil cross-section are avoided. Thermal analysis is described in detail in Appendix F.

Cooling analysis calculates the temperature distribution through the coil both during and after the pulse. This distribution is required for analysis of thermal stresses. Several analysis models have been used and are described in Table II.

Table II. Thermal models				
Dimension of model	Type	Portion of coil considered	Advantage	Used for
2 D	finite element (JET programme.)	1 turn	shows longitudinal & perpendicular temperature distribution.	JET design modifications (e.g. change to Freon)
1 D	solves differential equations (JET programme)	up to 4 turns + tails	flexible	temp grad at connection region coil tails
3 D	finite element (Abaqus)	1 turn	accurate potentially good interface to stress calculation.	checking 1 D model

2.2.6. Mechanical Structure

The basic structure (shell, ring and collar) is adequately strong to resist all foreseen machine torques. A point of interest is the flexibility of the structure for out-of-plane loads as this strongly affects the reaction forces and stresses in the TF coils. This has been analysed using an FE model (see Appendix H).

The outer parts of the coil lie in grooves in the outer shell so forces are directly transmitted to the structure. However the ring and collar teeth protrude from the main structure and are more highly stressed. Stresses in the ring and collar teeth are considered in detail in Appendix I and allowable forces derived.

2.2.7. Inter Octant Joints

The out of plane forces on the toroidal coils are resisted by the mechanical structure. The total effect of these forces is to apply a torque to the upper half of the structure, which is resisted by an equal and opposite torque applied to the lower half of the structure. This torque causes shear stresses in the structure and shear forces at the octant joints of the structure. Octant joints are described in more detail in Appendix J.

The shear at the octant joints is resisted by a series of keys (Figure 14). The keys are circular and contain adjustment wedges. The key and wedge assembly is held in compression by the octant joint bolts. The bolts play no direct role in resisting the shear but are important in holding the key in compression and also carry a proportion of loads normal to the octant joint.

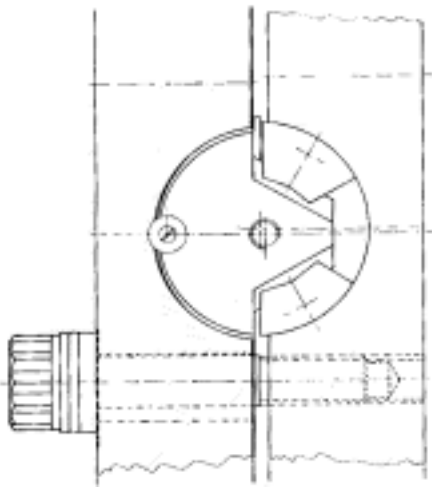


Figure 14. Octant joint key showing wedges and octant joint bolt (1 of 2 per key)

The bolts were accurately tightened when the machine was initially assembled and again in 1990 when an octant was removed. Recent checks have shown that the bolt tension is reducing. Extrapolation of trends suggests that 70% of original tension will be reached around January 2001.

New allowable shear forces for 70% bolt tension have been established at;

- 350 kN per key for repetitive operation and
- 560 kN per key for occasional events.

These forces will not be exceeded by any foreseen plasmas. The machine is therefore safe for operation until 2001 but it is recommended that the bolts should be fully checked and tightened in the years 2000 or 2001. Some bolts are accessible and some need coils P3 and P4 to be moved. To avoid stress concentrations, all of the bolts must be tightened at the same time. This means that coils P3 and P4 have to be moved for the bolts to be tightened. The total time required to carry out this work is about 6 months.

23. Machine Operation Data

Measurements made on the TF coils during operation using installed instrumentation enable the performance of the coils to be monitored. The measurements listed in Table III are recorded for every pulse.

Table III. TF coil instrumentation	
Transducer	Function
currents and voltages	monitors operation of coil and power supply
flux loops	measure the poloidal magnetic flux crossing the coil
ampere turns	Rogowski coils measure the ampere-turns in each coil, used for protection
coil voltages	compares voltages between coils, used for fault detection
dew-point and ambient temperatures.	Checks humidity and temperature of torus hall air to avoid condensation
coolant temperatures: 32 Coils and busbars	outlet temperature from each coil shows that cooling flows are balanced and gives indication of copper temperature

epoxy insulation temperatures: measured at 5 positions on 8 coils	shows the effect of vacuum vessel on coil surface temperature
mid plane radial displacements on 16 coils	shows expansion of coil due to magnetic force and temperature rise
vertical displacements at top and bottom of 32 coils	shows vertical expansion and displacement of coil
push pull jacks at top and bottom on 32 coils	checks operation of push pull jacks, which maintain coil in contact with inner cylinder
displacement of mechanical structure	measures vertical, radial and tangential displacement of mechanical structure relative to a fixed reference

Data collected during JET pulses can be analysed to assess how much of the machine life has been consumed (see Appendix K). Statistics collected for pulses between 1984 and 1998 show that the 36,000 pulses were distributed in current level as shown in Figure 15.

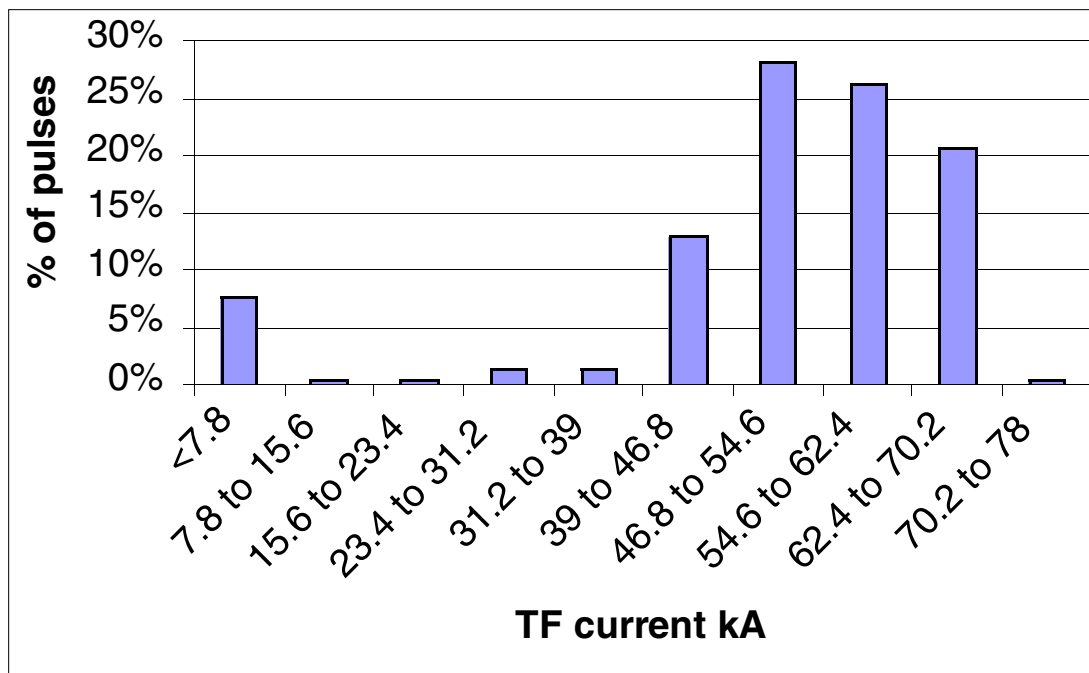


Figure 15. Distribution of TF coil pulses with respect to current level showing for example that 21% of pulses were at ~67 kA, the old maximum current

An equivalence between pulses at different current levels can be determined using fatigue data. Table IV shows the effective number of pulses made at levels equivalent to 4T operation.

Parameter	Maximum level at 4T	Equivalent number of pulses made 1990 to 1998
Tensile stress in copper	170 MPa	5000

conductor		
Shear stress in insulation at coil tail	25 MPa	130
Machine torque (1990 to 1998)	Equivalent to 5 MA, 4 T equilibrium	5,400

Other measurements can be used to check on correct operation of components (see Appendix L). For example;

- the radial expansion of the coil (at outer mid plane and push pull jacks) has been shown to be proportional to I_{tf}^2 and $\int I_{tf}^2 dt$,
- the deformation of octant joints is proportional to the TF coil torque and
- TF coil flux loop measurements have been correlated with equilibrium calculations.

2.4. Tests

2.4.1. Mechanical tests on prototype coil in 1988.

Two types of test were made in 1988.

The first test 1 simulated the typical magnetic loading of the coil in the region of the collar support. Static forces up to 1430 kN and cyclic forces up to 1250 kN (10,000 cycles) were applied at the collar support with no detectable effect. These forces are double the present allowable force of 650 kN.

Test 2 examined the behaviour of the coil at the entry into the flute of the inner cylinder. Forces up to 940 kN were applied giving an inter-pancake shear stress of 27 MPa and an inter-turn shear stress of 52 MPa. The inter-turn shear stress was accompanied by a perpendicular compressive stress of 25 MPa simulating the magnetic pressure against the inner cylinder.

Recent calculations have confirmed that stress concentrations such as those occurring at the collar teeth are mainly determined by the locally applied force rather than the remote boundary conditions. These tests were therefore valid tests of the coils under local operational stress conditions and show large margins of safety in the collar region.

2.4.2. Tests on used and unused coils in 1996/97

The object was to compare the mechanical stiffness of used and unused coils to see if coils had been affected by operation. An unused spare coil was compared with a coil that had been used on the machine for 7 years. These tests are described in Appendix M.

The coils were subjected to in-plane and out-of-plane bending. Stresses and deflection calculations for all proposed tests were made to determine the forces required to give suitable stress levels (i.e. significant but not excessive).

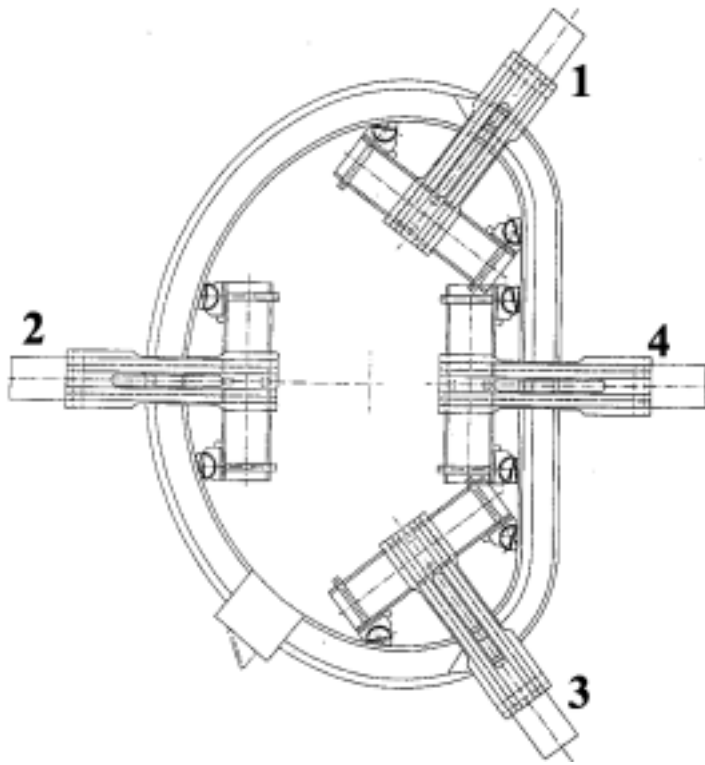


Figure 16. Positions of testing machine. The machine applies a central load, which is reacted on either side.

In plane test positions are shown in (Figure 16). The tests showed that the used coil had stiffness within 8% of the unused coil. As the used and unused coils had similar stiffness, it was concluded that coils in the machine have not been adversely affected by operation.

2.4.3. Tests on coil insulation

A coil that had been removed from the JET machine, due to an inter-turn fault, was cut up and used for tests. These tests are described in Appendix O and Appendix P. Cross sectional slices were cut from this coil and examined in the following ways

- micrographic examination of the insulation
- shear strength tests
- measure shear modulus of elasticity

2.4.3.1. Inspection

The micrographic analysis included taking samples at different positions in the cross-section of the coil and comparison between the straight and curved regions. Void content and glass-resin content were measured by calcination of samples. The average void content was 0.66% with no significant difference between the straight and curved regions. This complies with quality standards for good impregnation, which require less than 1% voids. The average glass content was 64%, which is acceptable. No correlation was found between void content and strength.

Although the volumetric void content was small and had no effect on strength, the inter-turn insulation was found to contain a plane of weakness at its centre. This was due to a layer of pre-impregnated glass epoxy, which was inserted during winding to avoid

damage to the dry glass tape. The pre-impregnated tape prevented perfect vacuum impregnation and left a plane of small voids at the centre of the inter-turn insulation. After breaking shear samples the total surface area of defects was measured and correlated with strength.

2.4.3.2. Static shear strength

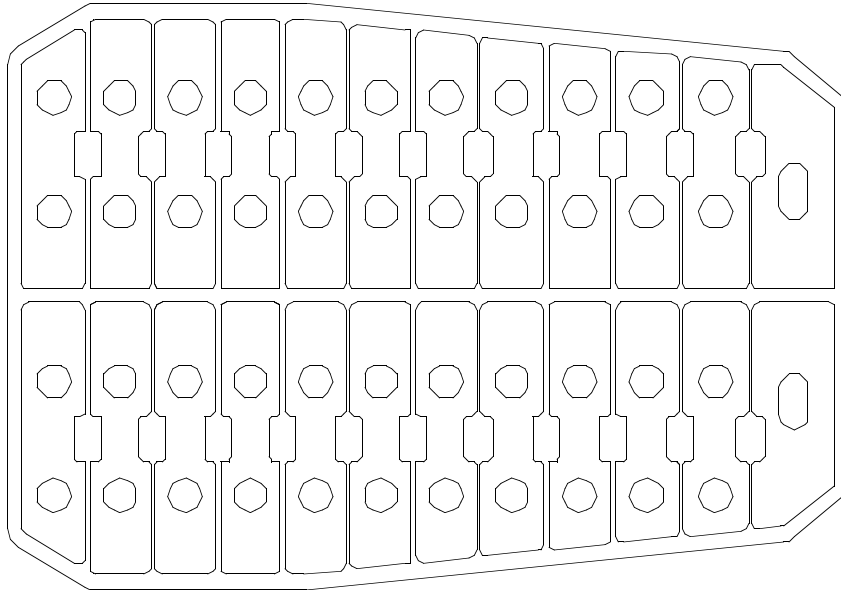


Figure 17. Typical cross-section of TF coil.

Three types of mechanical test samples were cut from the slices as shown in (Figure 18).

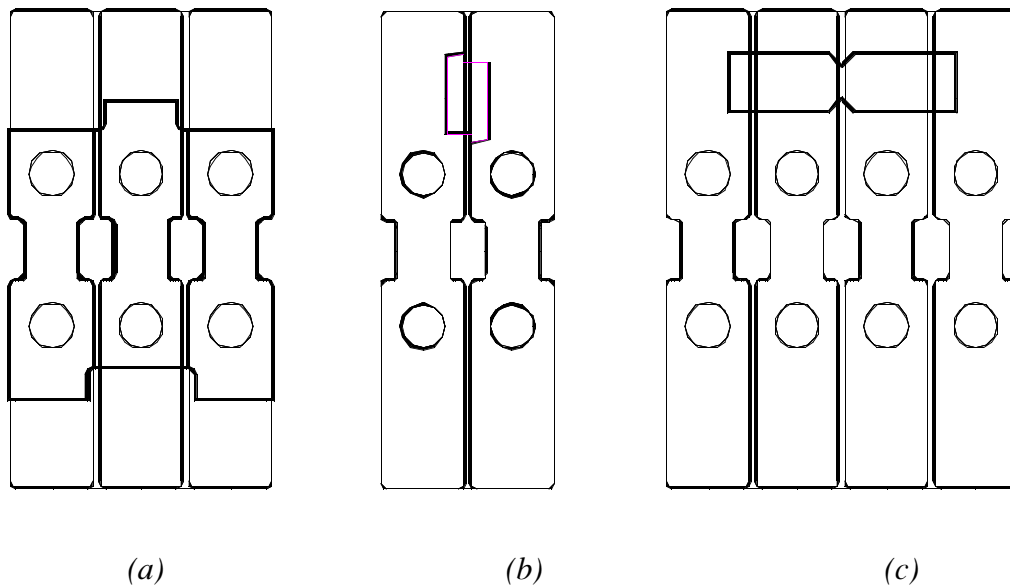


Figure 18. Showing how test samples are cut from coil conductors; (a) double shear sample, (b) small single shear sample, (c) Iosipescu sample

Advantages and disadvantages of the three sample types are listed in Table V.

Table V. Shear test sample types

EM forces and plasma scenarios

V. Riccardo
26 October 1999

Contents

1.	Operational loads.....	1
2.	Out-of-plane loads and reactions.....	2
3.	In-plane loads	3

1. Operational loads

During a pulse JET TF coils are subject to different loads:

Electromechanical In-Plane Loads The distributed force $d\mathbf{F}/ds = \mathbf{I}_{TF} \times \mathbf{B}_{TOR}$ is normal to the coil, lying in its plane and up-down symmetric. This load scales with I_{TF}^2 and its distribution (depending upon the toroidal magnetic field) is known independently from the plasma configuration.

Electromechanical Out-of-Plane Loads The distributed force $d\mathbf{F}/ds = \mathbf{I}_{TF} \times \mathbf{B}_{POL}$ is normal to the coil and to its plane. This load scales linearly with and I_{TF} is somewhat increasing with the plasma current; its distribution, though depends upon the whole magnetic configuration of the pulse and, as such, is harder to evaluate.

Thermal Loads Due to the Joule effect, the coils' temperature increases during the pulse depending on $\int I^2(t) dt$. The largest stresses in the coils are caused by temperature gradients (freon inlet-outlet, tip of the tails). These loads depend only on the TF current waveform.

The only loads depending on the plasma scenarios are the out-of-plane ones. Two are the regions of greatest concern, from the point of view of the out-of-plane loads: the Ring Tooth and Collar Tooth. The main difficulty in estimating the EM forces in these region is to work out the distribution of the component of the poloidal magnetic field normal to the coil. This evaluation can be done with reasonable accuracy off-line with MAXFEA or another finite element electromagnetic code and on-line with far less

accuracy with the set of 10 TF flux loops fitted on coils 6/4 and 2/4, which provide information on the average value of the normal field within each of them. The analytical route to the EM force computation is the following: first the configuration (equilibrium or disruption) has to be run with MAXFEA to get the poloidal magnetic field normal to the TF coil, then this field is scaled into a distributed out of plane force and used as an input for a beam model.

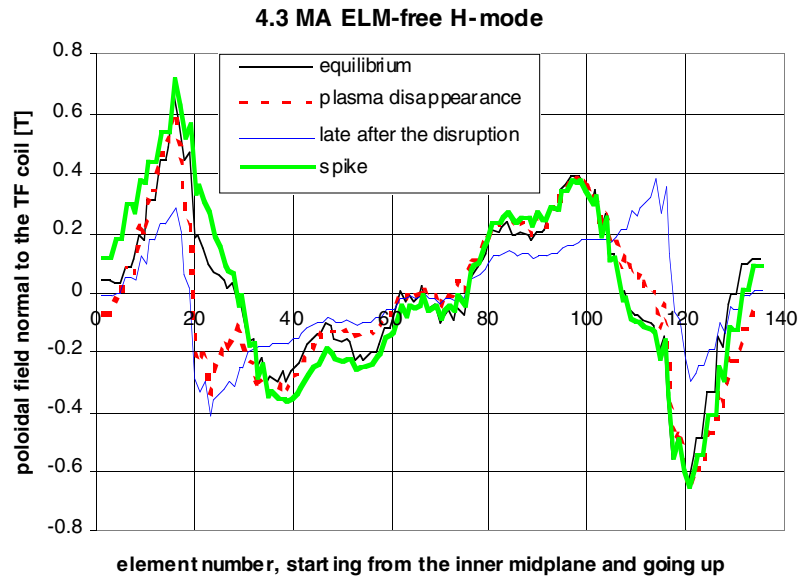


Fig. 1 Poloidal field normal to the TF coil along its centre line.

2. Out-of-plane loads and reactions

The shape of the poloidal field normal to the TF coils depends on the scenario and changes significantly during disruption. In figure 1 four typical snapshots of the poloidal field are plotted for the ELM-free H-mode scenario (4.3 MA and 4 T). This figure clearly shows how the field reverse four times along the TF coil trace: in the top and bottom sections of the inner and outer leg it is pushing in opposite directions, in addition it also reverses more or less at the ring tooth location (both top and bottom). The element numbers corresponding to the ring teeth are 32 and 105, those corresponding to the collar teeth are 26 and 111. The shape of the normal component of the poloidal field is similar in equilibrium and during a VDE: in both cases the plasma is present, although at different locations, and the out-of-plane forces reverses at a radius close to the one of the ring supports. The main difference between an equilibrium and a VDE-spike distribution is that the latter has a more pronounced and wider peak. When the plasma is not present the normal field reverses at a smaller radius, so that the direction of the force is the same at the collar and the ring.

Typical values for the forces on the collar and ring teeth are the following:

Configuration Description	Plasma Current [MA]	Toroidal Field [T]	Top Ring Tooth [kN]	Top Collar Tooth [kN]	Bottom Collar Tooth [kN]	Bottom Ring Tooth [kN]
MkIIa-OS	3.5	3.2	68	-347	385	-168
MkIIa-oldHI	3.8	3.4	364	-222	150	-460
MkIIa-triaHI	2.5	2.5	297	-153	116	-328
MkIIa-ELMyH	4.7	3.27	246	-330	286	-366

MkI-ELMyH	5.9	3.4	295	-486	404	-471
ITER- ρ^* scaling	4	4	520	-232	160	-660
high ICRH coupling	5	4	506	-481	400	-616
hypotetic 6MA	6	4	577	-478	426	-701
<i>Force limits in operation (low field)</i>		<3.4	560	420	420	560
<i>Force limits in operation (high field)</i>		>3.4	560	350	350	560

3. In-plane loads

When using the beam model to (App. B) to compute the TF coil stress distribution, the in-plane hoop load has to be uniform on the TF cross-section. Instead when the brick model (App. B) is used the actual shape of the load on the cross-section can be prescribed. This has been compute using a Biot-Savart integration routine.

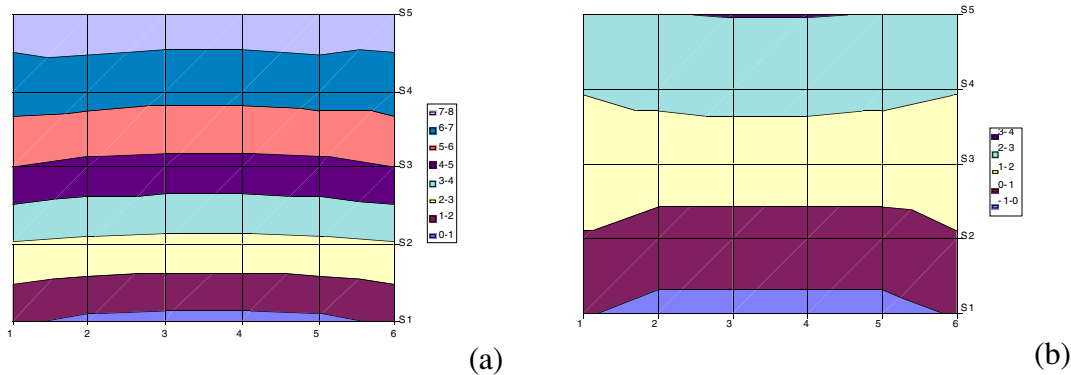
The toroidal field, and hence the in-plane force, can be computed on the single element of the brick model using a simple Biot Savart integration code. The field computation is in itself simple and reliable (not very efficient from the CPU point of view), while great care and trouble has been taken to describe accurately the geometry of the current (a filament on the central axis of each element) and the position of the points (the middle points of each element) where the field has to be computed.

The magnetic field has also radial and vertical components in each section (which are equal and opposite on the two out of plane sides of the section and produce no net force or torque but only compression of the section). The out-of-plane compressive load can have a second order effect on the detailed stress distribution, including compression of the inter-pancake insulation.

Note that the forces computed in this way can be stored and scaled to any required field value.

The toroidal field at the inner midplane (a), outer midplane (b), top ring (c) and bottom ring (d) sections is plotted in Fig. 2 using its values at the centre-point of the element (therefore the drop at the edge cannot be seen).

The radial field at the inner midplane (a) and at the outer midplane (b) is plotted in Fig. 3 (the radial field is close to zero at the top and bottom ring sections). The vertical field at the top ring (c) and at the bottom ring (d) is plotted in Fig. 3 (the vertical field is zero at the inner and outer midplane sections). Fig. 3 shows how the in plane field close in the section feels the presence of the current. This is a local effect which sums up with the global toroidal field produced by the set of coils.



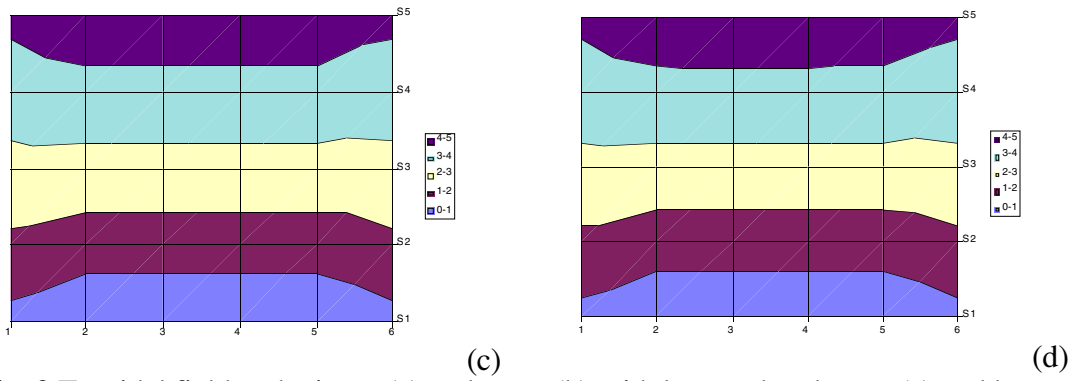


Fig. 2 Toroidal field at the inner (a) and outer (b) midplane and at the top (c) and bottom ring (d) in the coil cross section.

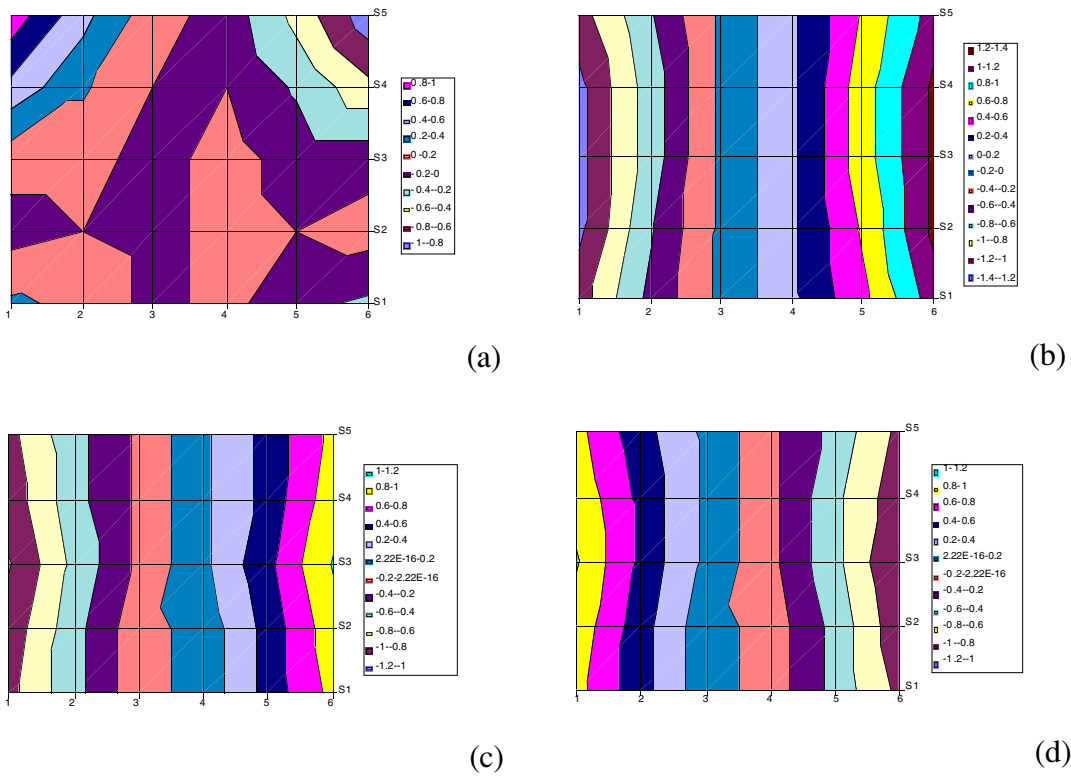


Fig. 3 Radial field at the inner (a) and outer (b) midplane and vertical field at the top ring (c) and bottom ring (d) in the coil cross section.

The contour plot of the modulus of the field produced by the TF coils at the midplane around and inside the coil is reported in Fig. 4. The conductors, to smooth the field inside the coil, has been replaced by 12 row, each made of 25 filaments. The centre point of each filament is representative of the same area (i.e. the coil section is divided in 300 quadrilaterals of the same area).

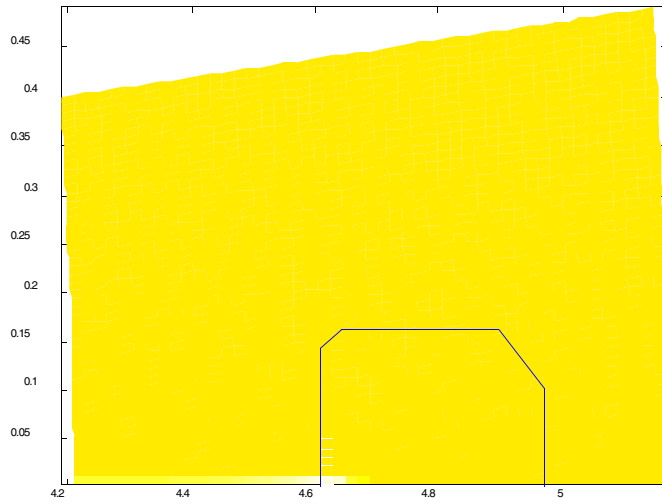


Fig. 4 TFcoil field around and inside the outer midplane leg.

The slice-total radial and vertical load computed with the BSI routine and with MaxFEA 3D are very similar (Fig. 5 and 6) as it is the average hoop linear force (Fig. 7). However, if the uniform hoop load is applied on a solid model the turnXturn hoop load is rather different (Fig. 8), with the inward turns in higher compression than the outward ones (the hoop linear force even reverses along the section).

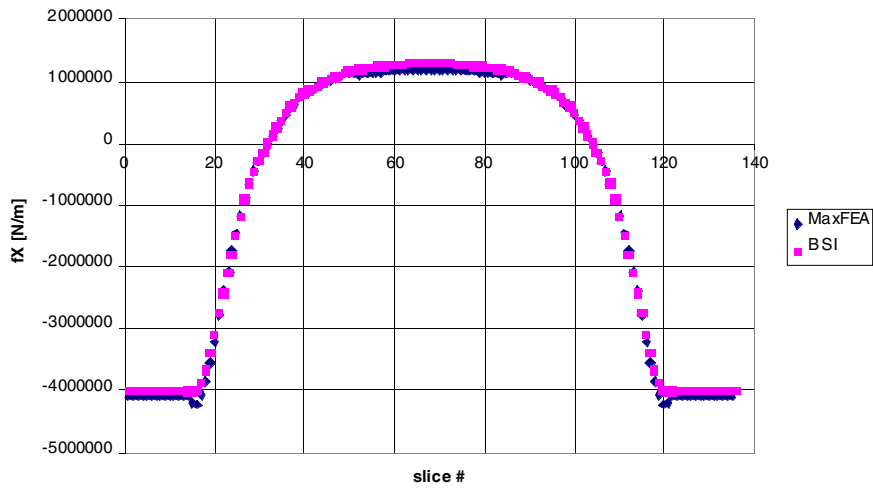


Fig. 5 Radial in-plane load (on the full slice)

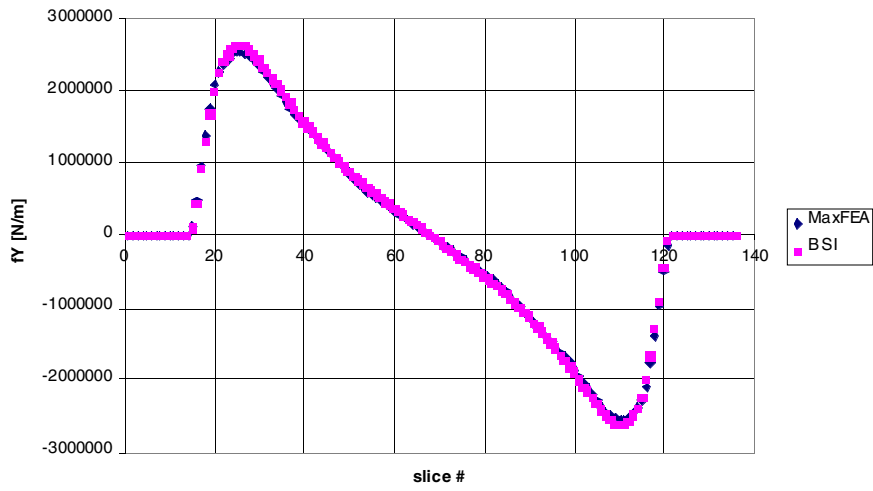


Fig. 6 Vertical in-plane load (on the full slice)

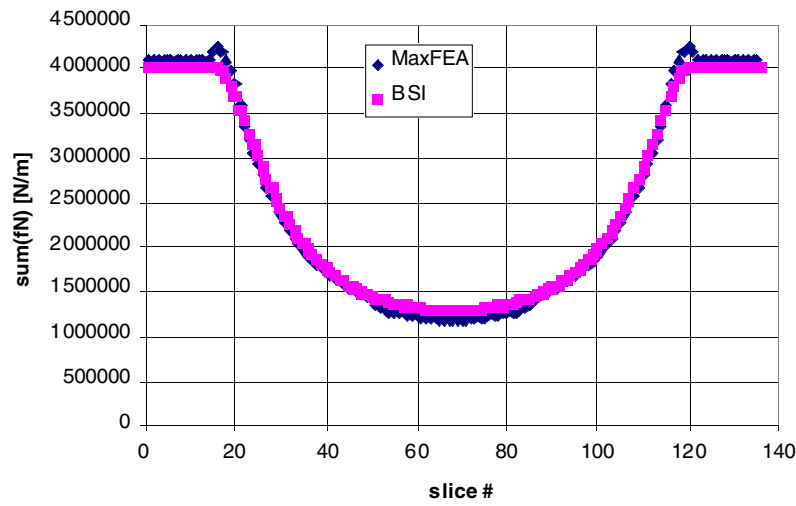


Fig. 7 Normal in-plane load (on the full slice)

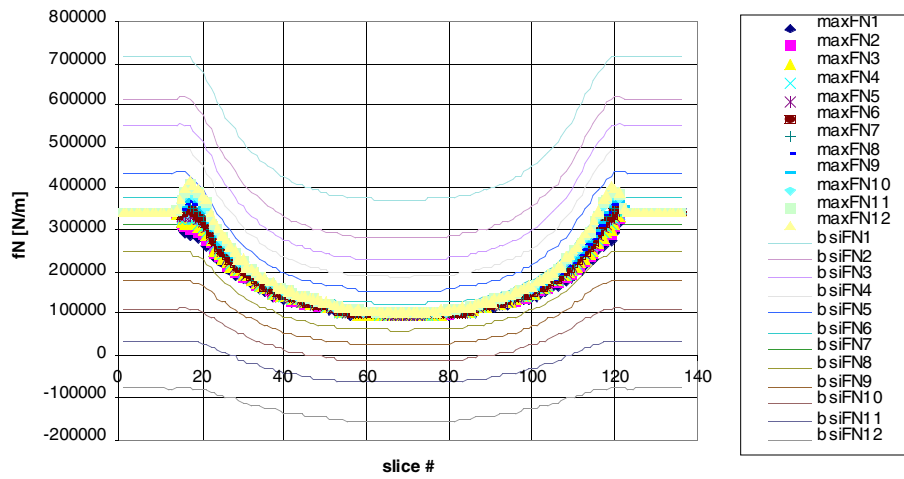


Fig. 8 Normal in-plane load (turn per turn)

Beam & Brick Models

V. Riccardo

26 October 1999

Contents

1. Beam Model.....	1
2. Brick Model for Noell's tests	7
3. Brick Model for scenario assessment	12
3.1. Model description.....	12
3.2. Model boundary conditions.....	15
3.3. Model results.....	18

1. Beam Model

The model is made by 136 beams (Fig. 1). The material used is uniform, with smeared properties ($E=98$ GPa and $\nu=0.48$) coming from the actual coil materials (copper and epoxy, the latter taken with $G=4$ GPa in order to have a Poisson ration smaller than 0.5 as required to use beams).

Its boundary conditions reproduce as much as possible those of a coils fitted in the machine:

- in plane gap supports and out of plane supports along the inner vertical leg
- out of plane supports (usually pins, but spring can be employed as well) at the Ring Teeth and MS outer supports
- offset out of plane support at the Collar Teeth
- pre-loaded in plane springs at the Push Pull Jacks
- the vertical support is moved from below the coil to the mid-plane for simplicity

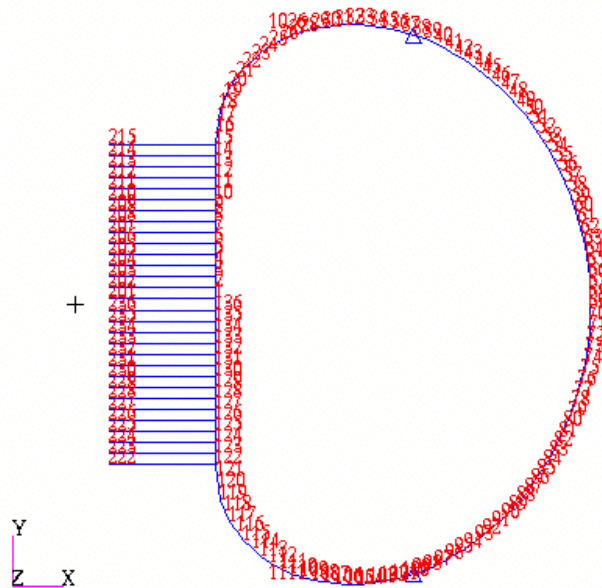


Fig. 1 1Beam model elements and supports

The loads are:

- in plane loads (proportional to the square of the TF current, computed for a reference 1 A TF current)
- out of plane loads (scaling the poloidal field normal to the coil, computed with MAXFEA, with the TF current)

The model is used to assess plasma scenarios both in equilibrium and in disruption. It produces out of plane support reactions, section forces and torques, which can be used to compute stresses according to the beam theory. The model is unable to predict local stress concentration.

The quantities of interest computed with the aid of this model are:

- out of plane reaction forces at the supports, in particular collar and ring
- forces and torques along and about the principal element directions (1: axial, 2: in-plane, 3: out-of-plane, see figure 2)

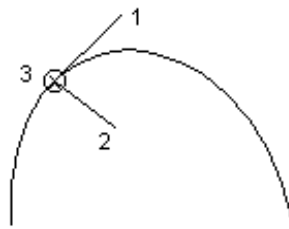
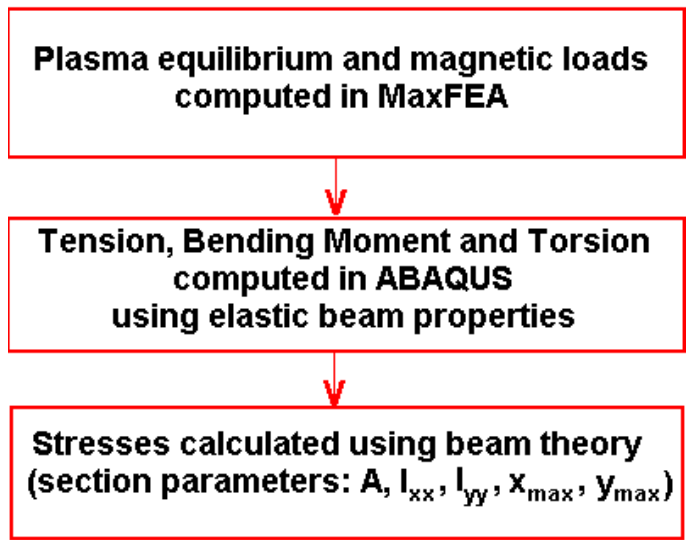


Fig. 2 principal directions in the beam model



From the forces and torques along and about the principal element directions the pancake and inter-pancake stresses can be estimated using the beam theory. The total stress is given by

$$\sigma = \frac{T}{A} + \frac{y M_{xx}}{I_{xx}} + \frac{x M_{yy}}{I_{yy}}$$

In a rectangular cross-section the maximum total stress will always occur in one of the 4 corners:

$$\sigma_{max} = \left| \frac{T}{A} \right| + \left| \frac{y M_{xx}}{I_{xx}} \right| + \left| \frac{x M_{yy}}{I_{yy}} \right|$$

However the TF coil have octagonal (and decagonal) cross-sections (fig. 3). So the corner of maximum stress of the rectangle is removed. Which corner of the octagon is maximum depends on the ratio of the in-plane bending to the out-of -plane banding stress so it is simplest to calculate all 8 and take the maximum.

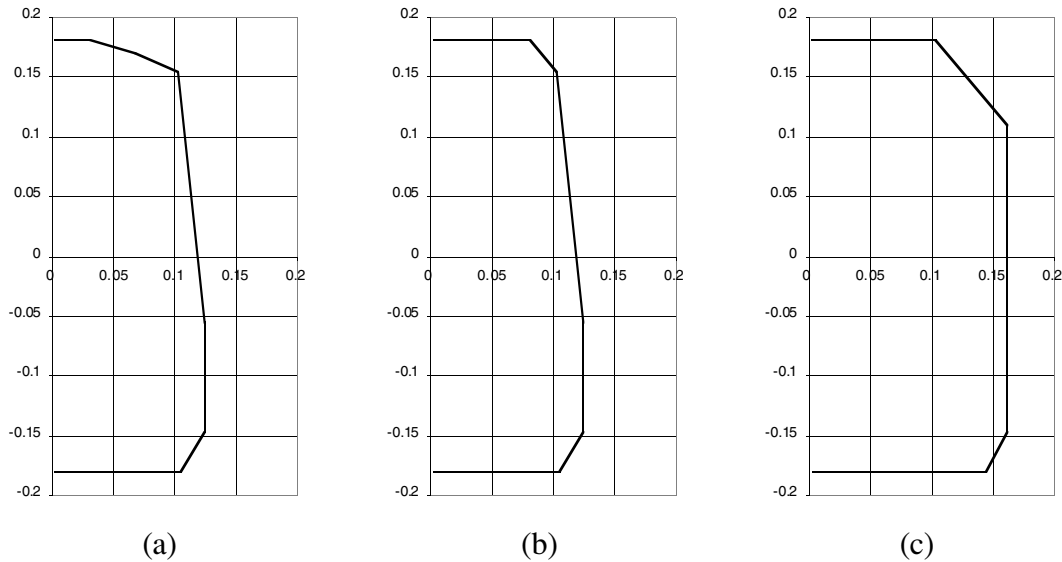


Fig. 3 Reference TF coil cross sections: (a) straight, (b) curved and (c) outer

The stresses along the conductor for the VDE-spike of the ELM-free H-mode 4.3 MA 4 T scenario are reported in Fig. 4-7.

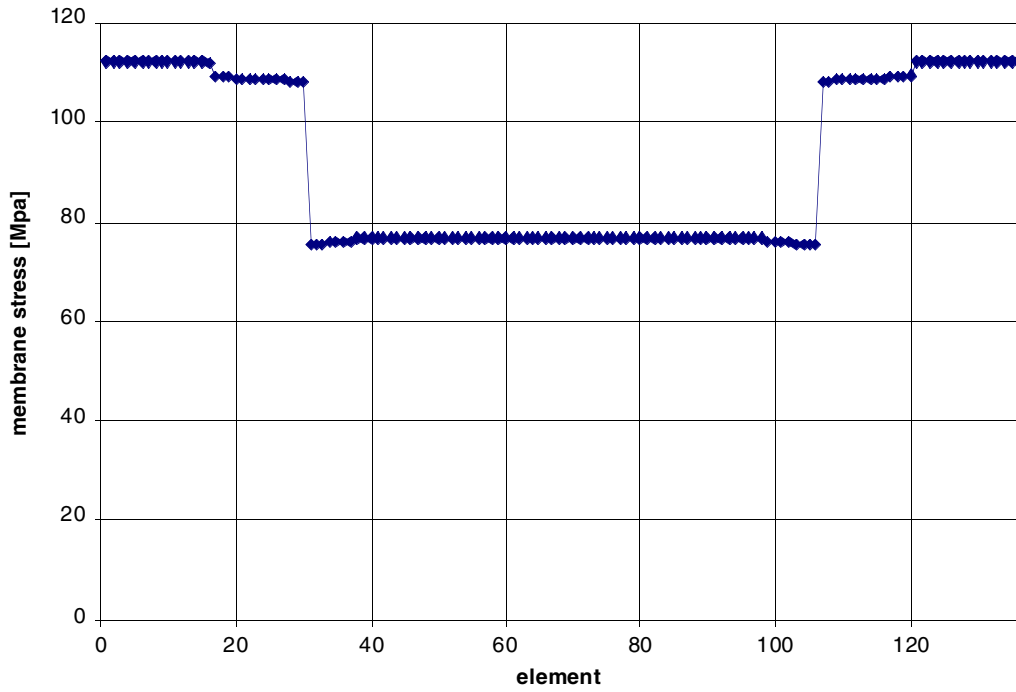


Fig. 4 Membrane axial stress in the copper

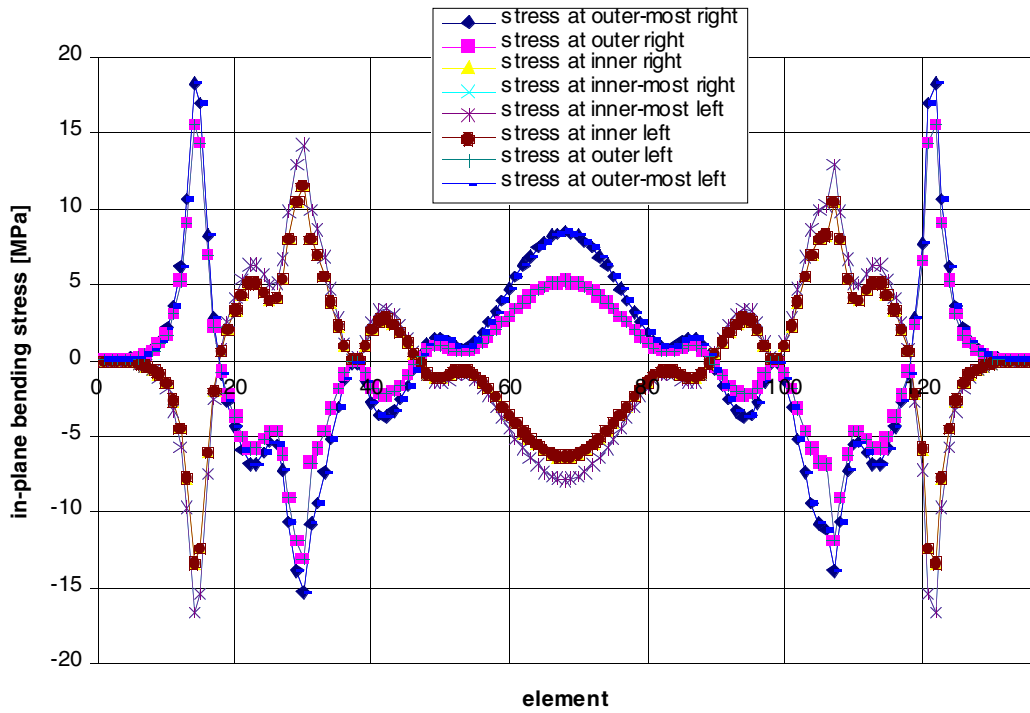


Fig. 5 In-plane bending axial stress in the copper

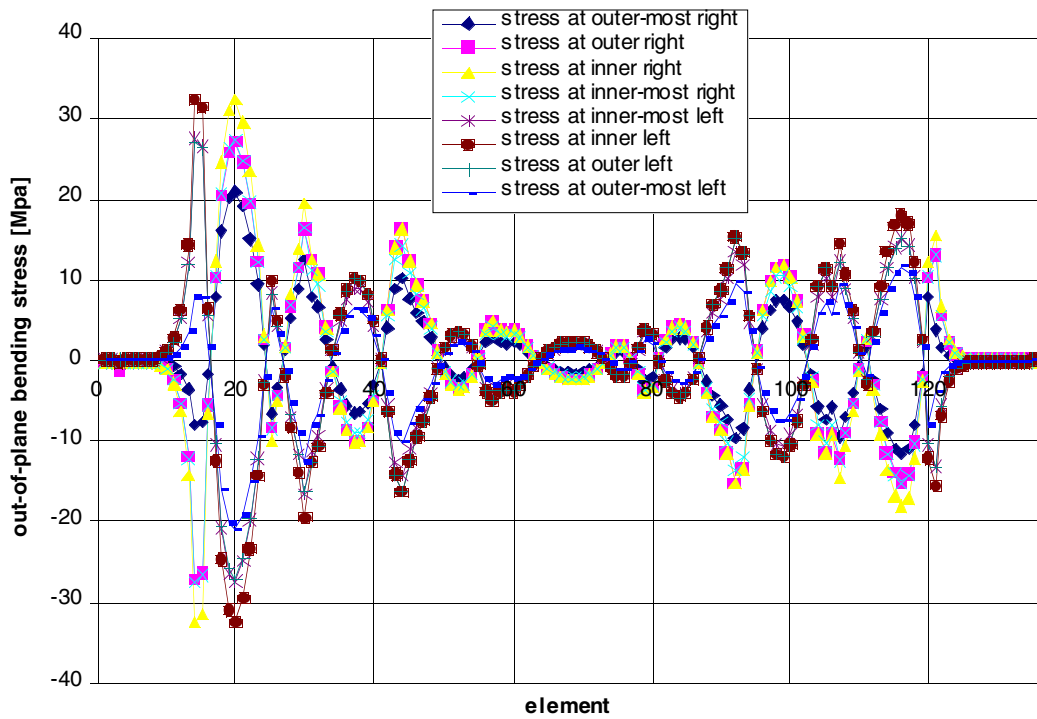


Fig. 6 Out-of-plane bending axial stress in the copper

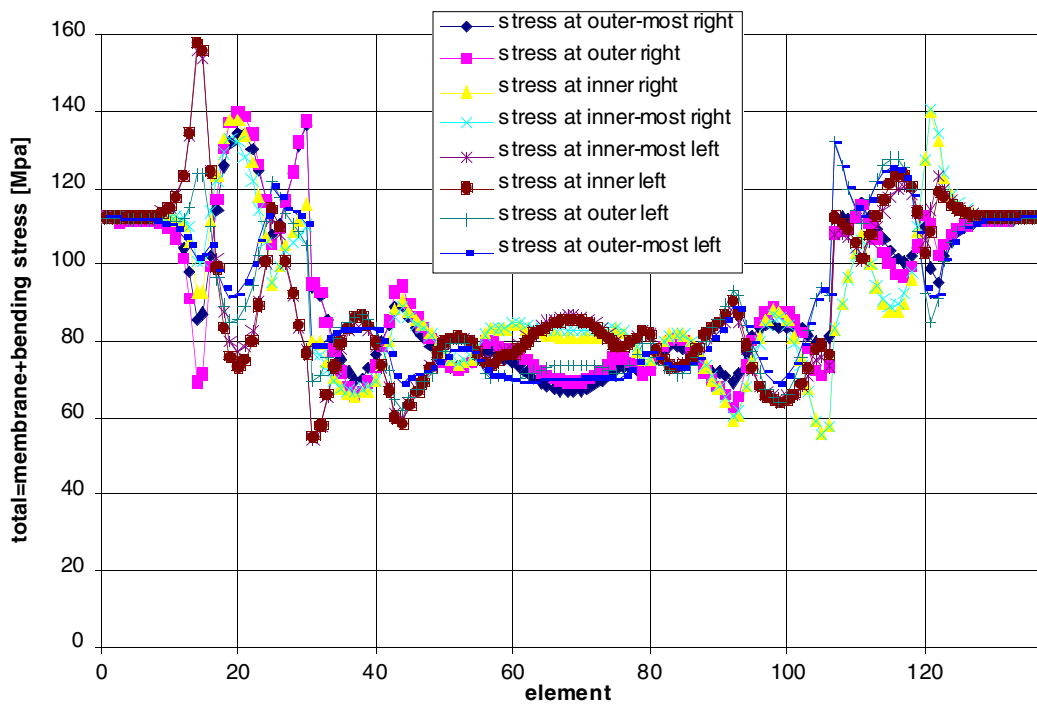


Fig. 7 Total axial stress in the copper: membrane + in-plane bending + out-of-plane bending

The beam model is easy to handle and therefore suitable to investigate the effect of scenario dependent loads. The copper stresses for all the out-of-plane loadings of the three 4.0 T GB scenario proposed in May '98 (ELMy H-mode at 5 MA, the ELM-free H-mode at 4.3 MA and the Optimised Shear at 4 MA are listed in Table 1 and 2). Each scenario has at least an equilibrium, a fast plasma disappearance, a late-after-the-disruption and a VDE calculation. The scenario with the highest nose stresses is the

VDE of the ELM-free H-mode. The one with the highest brazed joints stresses is the VDE spike of the ELMy H-mode, and its value is 83.4 MPa. Overall it is not a huge difference and both of them occur in an unlikely scenario. In contrast there is a strong dependence of the support reaction forces on the out-of-plane load distribution (Table 3).

	outer-most right	outer right	inner right	inner-most right	inner-most left	inner left	outer left	outer-most left
ELMy-eq	78.7	80.9	82.4	82.0	82.3	82.7	81.2	78.8
ELMy-beta0	75.7	76.0	77.9	78.2	78.2	77.9	76.0	75.7
ELMy-dis	79.2	81.7	83.2	82.8	82.3	82.7	81.2	78.8
ELMy-late	78.1	80.0	81.5	81.3	80.8	80.9	79.3	77.6
ELMy-spike	79.3	81.9	83.4	82.9	82.6	83.1	81.6	79.1
ELMfree-eq	77.8	79.6	81.1	80.9	80.5	80.7	79.1	77.5
ELMfree-dis	78.3	80.4	81.9	81.6	80.7	80.8	79.3	77.6
ELMfree-late	77.8	79.6	81.2	81.0	80.5	80.6	79.0	77.4
ELMfree-spike	78.4	80.5	82.0	81.7	80.8	81.0	79.5	77.8
OS-eq	78.2	80.1	81.6	81.4	81.4	81.7	80.2	78.2
OS-lowbeta	77.9	79.7	81.2	80.9	81.0	81.3	79.8	77.9
OS-beta0	77.6	79.2	80.7	80.5	80.6	80.8	79.3	77.6
OS-dis	78.7	80.9	82.4	82.0	81.5	81.9	80.3	78.3
OS-late	77.7	79.4	81.0	80.8	80.4	80.5	78.8	77.3
OS-spike	78.7	81.0	82.6	82.2	81.8	82.2	80.7	78.5
max	79.3	81.9	83.4	82.9	82.6	83.1	81.6	79.1
mean	78.1	80.1	81.6	81.3	81.0	81.3	79.7	77.9
std	0.9	1.4	1.3	1.1	1.1	1.3	1.3	0.8
max @ Brazed Joints [MPa]	83.4							

Table 1 Brazed joints membrane+bending stresses in the 8 corners (MPa)

	outer-most right	outer right	inner right	inner-most right	inner-most left	inner left	outer left	outer-most left
ELMy-eq	131.2	131.1	140.9	141.3	145.8	145.8	132.4	131.7
ELMy-beta0	123.6	121.3	125.4	128.6	128.6	125.4	121.3	123.6
ELMy-dis	129.4	128.8	135.5	136.7	129.5	126.5	129.4	129.4
ELMy-late	126.2	128.2	133.1	134.7	134.5	132.9	130.6	128.1
ELMy-spike	136.0	141.2	141.6	141.9	153.5	154.8	132.7	131.7
ELMfree-eq	133.4	134.0	139.3	139.9	149.5	150.1	132.3	131.6
ELMfree-dis	131.4	131.3	134.5	135.9	134.8	132.7	129.3	129.3
ELMfree-late	128.7	131.4	131.4	133.2	135.6	134.2	131.6	128.8
ELMfree-spike	136.2	139.6	139.8	140.4	156.0	157.8	132.2	131.6
OS-eq	130.7	130.5	137.5	138.4	144.5	144.2	130.6	130.3
OS-lowbeta	130.8	130.6	139.0	139.7	145.7	145.6	131.0	130.6
OS-beta0	130.9	130.7	140.7	141.1	146.9	147.1	131.5	131.0
OS-dis	129.4	128.8	133.0	134.6	131.2	128.5	128.2	128.5
OS-late	125.2	126.9	131.8	133.7	133.8	132.0	128.7	126.5
OS-spike	133.0	134.0	137.8	138.7	149.5	150.2	130.5	130.3
max	136.2	141.2	141.6	141.9	156.0	157.8	132.7	131.7
mean	130.4	131.2	136.1	137.3	141.3	140.5	130.2	129.5
std	3.6	4.8	4.5	3.8	9.1	10.7	2.8	2.2
max @ nose [MPa]	157.8							

Table 2 Nose membrane+bending stresses in the 8 corners (MPa)

	top collar	bottom collar	top ring	bottom ring
ELMy-e q	-298	332	297	-389
ELMy-dis	1511	163	464	-477
ELMy-late	334	-262	406	-358
ELMy-spike	-450	334	489	-375
ELMfre e-eq	-277	250	443	-498
ELMfre e-dis	125	101	569	-560
ELMfre e-late	351	-320	443	-396
ELMfre e-spike	-427	272	675	-477
OS-eq	-222	245	313	-364
OS-lowbeta	-263	287	282	-326
OS-beta0	-307	333	245	-286
OS-dis	136	110	456	-439
OS-late	291	-234	367	-327
OS-spike	-405	270	549	-337

Table 3 Out-of-plane reaction forces at the collar and ring supports (kN)

2. Brick Model for Noell's tests

A first brick model with coarse representation of the shape of the cross-section (Fig. 8) has been developed to investigate the effects of the shear modulus of the insulation on the global coil deflections. This exercise is not possible using the beam model, since there the Poisson ratio has to be smaller than 0.5, limiting the insulation G to be larger than 4 GPa. The hybrid model could not be used to this end because only in a section the Copper and the epoxy are discriminated.

The brick model was meant to reproduce Noell's tests, but the uncertainties on both the tests and the model accuracy are too large to come to a conclusive answer. It could replace the beam model for the scenario assessment if there were the need to use a smaller insulation shear modulus. This model is good for global behaviour, bad for local stress.

The model is made with 136X4X4 brick elements: each beam of the beam model constitutes a slice of the brick model, each slice is divided in 4X4 elements. Convergence has been checked by comparison with 136X3X3 and 136X5X5 models, which gave about the same displacements for the same load cases.

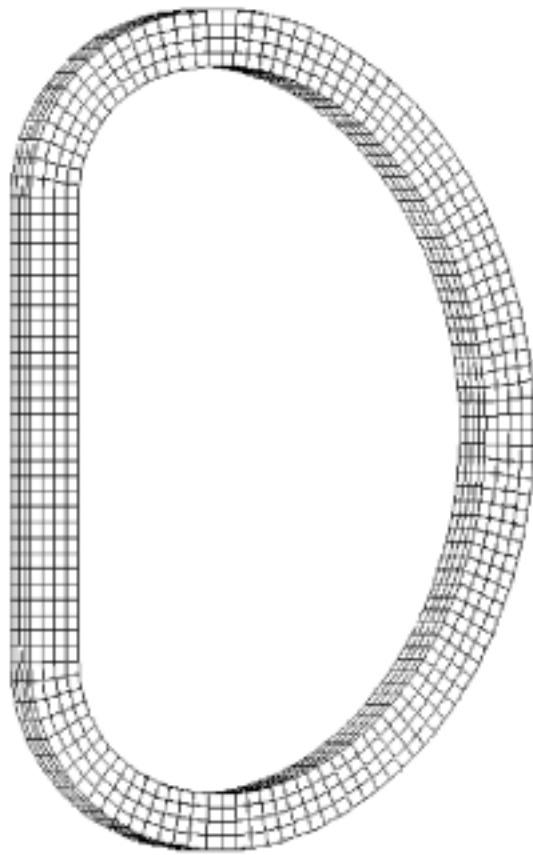


Fig. 8 Brick model

The material elastic properties of the TF coil elements are reported in the tables 4.

Young's modulus	E_C	128	GPa
Poisson's ratio	ν_C	0.34	#
Shear modulus	G_C	48	GPa

Table 4a Copper elastic properties

Young's modulus	E_E	3	GPa
Poisson's ratio	ν_E	0.38	#
Shear modulus	G_E	1	GPa

Table 4b Epoxy elastic properties (room temperature)

Young's modulus	E_F	73	GPa
Poisson's ratio	ν_F	0.22	#
Shear modulus	G_F	30	GPa

Table 4c Fibre elastic properties

The composite properties have been worked out with the method of mixtures starting from a schematic representation of a typical cube of material as shown in Fig. 9. Please note that the elastic properties in the lamination plane do not depend on the direction, since each lamination is made by a layer of woven cloth containing fibres in both directions. The properties in the lamination plane are subscribed with P and those in the transverse plane with T.

$$E_{Ix} = E_{Iy} = E_{IP} = \beta \lambda E_F + (1-\beta)E_E + \frac{\beta(1-\lambda)}{\frac{\lambda}{E_F} + \frac{1-\lambda}{E_E}}$$

$$E_{Iz} = E_{IT} = (1-\lambda)^2 E_E + \frac{\lambda(2-\lambda)}{\frac{\beta}{E_F} + \frac{1-\beta}{E_E}}$$

$$G_{Ixy} = G_{IP} = (1-\beta)G_E + \beta(\lambda G_F + (1-\lambda)G_E)$$

$$G_{Ixz} = G_{Iyz} = G_{IT} = \frac{1}{\frac{1-\beta}{G_E} + \frac{\beta}{\lambda G_F + \frac{1-\lambda}{\frac{\lambda}{E_F} + \frac{1-\lambda}{E_E}}}}$$

$$v_{IP} = v_{IT} = v_E v_E + v_F v_F$$

where λ and β are as defined in Fig. 9 and the fraction of fibre and epoxy volume is

$$v_F = \beta \lambda(2-\lambda)$$

$$v_E = 1 - v_F$$

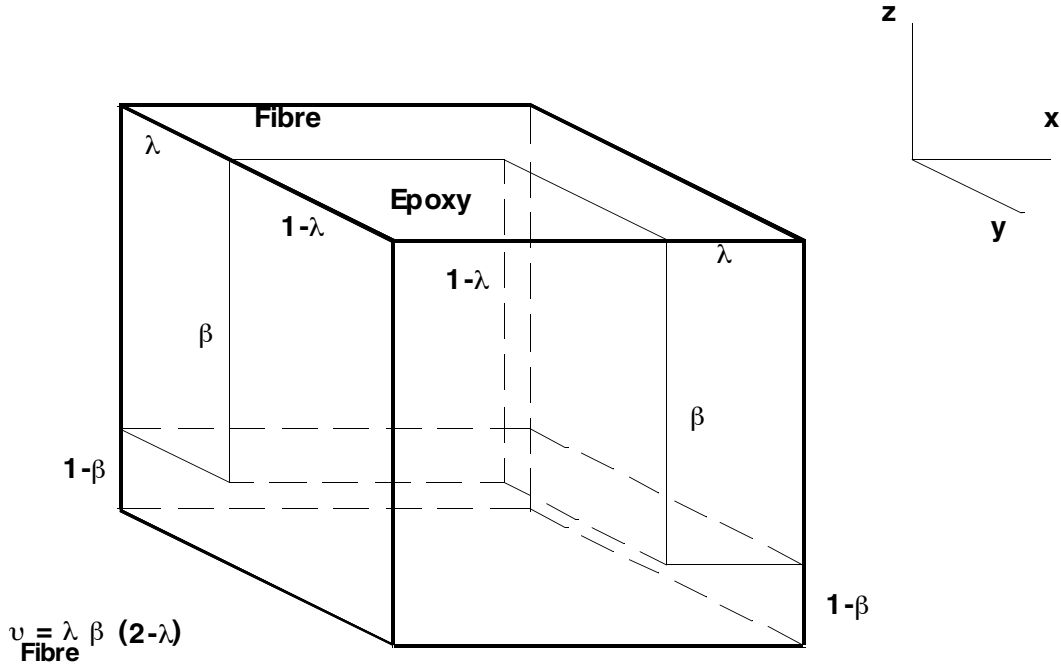


Fig. 9 The reference cube for the insulation composite

The non-isotropic properties for a smeared-property (homogeneous) material to be used in a global coil model can be evaluated by forcing the equivalence between the elastic coefficients of the real structure and the model in the various directions as can be calculated with the so-called rule of the mixtures. Since the coil has three planes of symmetry the material can be considered orthotropic. So the elastic properties, in general, could be expressed by 9 independent elastic constants; in this case they are constrained by the geometry chosen.

$$E_1 = E_{IP}\lambda_{I2} + E_{aux1}\lambda_{C2} \quad \frac{1}{E_{aux1}} = \frac{\lambda_{C1}}{0.7E_C} + \frac{\lambda_{I1}}{E_{IT}}$$

$$E_2 = E_{IP}\lambda_{I1} + E_{aux2}\lambda_{C1} \quad \frac{1}{E_{aux1}} = \frac{\lambda_{C2}}{0.8E_C} + \frac{\lambda_{I2}}{E_{IT}}$$

$$E_3 = E_{IP}\alpha_{CX} + E_C\alpha_{IX}$$

$$v_{12} = \lambda_{I1}v_I + \lambda_{C1}v_C$$

$$v_{13} = \lambda_{I1}v_I + \lambda_{C1}v_C$$

$$v_{23} = \lambda_{I2}v_I + \lambda_{C2}v_C$$

$$\frac{1}{G_{13}} = \frac{\lambda_{C1}}{G_C} + \frac{\lambda_{I1}}{G_{IP}}$$

$$G_{23} = G_{12}$$

The material properties are reported in Table 5 have been computed assuming

$$\alpha_{CX} = 0.65$$

$$\alpha_{IX} = 0.35$$

$$\lambda_{I1} = 0.085$$

$$\lambda_{C1} = 0.915$$

$$\lambda_{I2} = 0.09$$

$$\lambda_{C2} = 0.91$$

and arbitrarily varying the combination of λ (0.4 / 0.45) and β (0.8 / 0.85) in order to keep a fibre fraction close to the expected one. The values presented are relevant for room temperature as the model was built mainly to provide a numerical comparison with Noell full coil tests.

λ	0.45	0.40	0.40	0.45	#
β	0.80	0.80	0.85	0.85	#
$v_F(\lambda, \beta)$	0.56	0.51	0.54	0.59	#
$v_E(\lambda, \beta)$	0.44	0.49	0.46	0.41	#
E_{IP}	29.2	26.3	27.8	30.8	GPa
v_{IP}	0.291	0.298	0.293	0.285	#
G_{IP}	11.4	10.3	10.9	12.1	GPa
E_{IT}	9.9	9.3	11.5	12.2	GPa
v_{IT}	0.291	0.298	0.293	0.285	#
G_{IT}	3.9	3.8	4.6	4.8	GPa
E_1	51.0	49.4	54.1	55.8	GPa
E_2	53.4	51.6	57.0	58.9	GPa
E_3	93.4	92.4	92.9	94.0	GPa
v_1	0.336	0.336	0.336	0.335	#
v_2	0.336	0.336	0.336	0.335	#
v_3	0.336	0.336	0.336	0.335	#
G_{I2}	23.8	23.5	26.1	26.5	GPa
G_{I3}	37.7	36.6	37.2	38.3	GPa
G_{23}	23.8	23.5	26.1	26.5	GPa

Table 5 Reliable values for the inter-turn insulation are around 4 GPa (at room temperature)

The dependence of the G_{IT} on the geometrical properties has been investigated (Fig. 10) together with the geometrical constraints coming from Frascati tests to set limits to the possible G_{IT} values independently from the comparison with Noell tests.

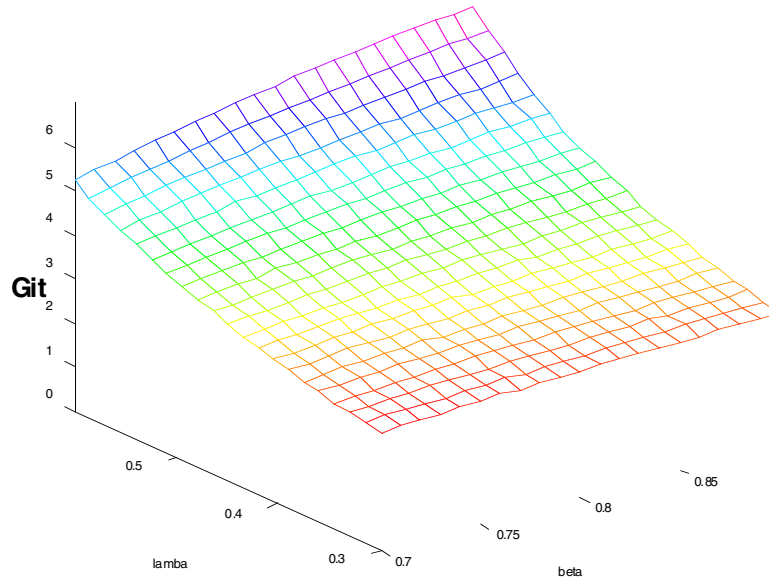


Fig. 10 G_{IT} is sensible to λ and less to β .

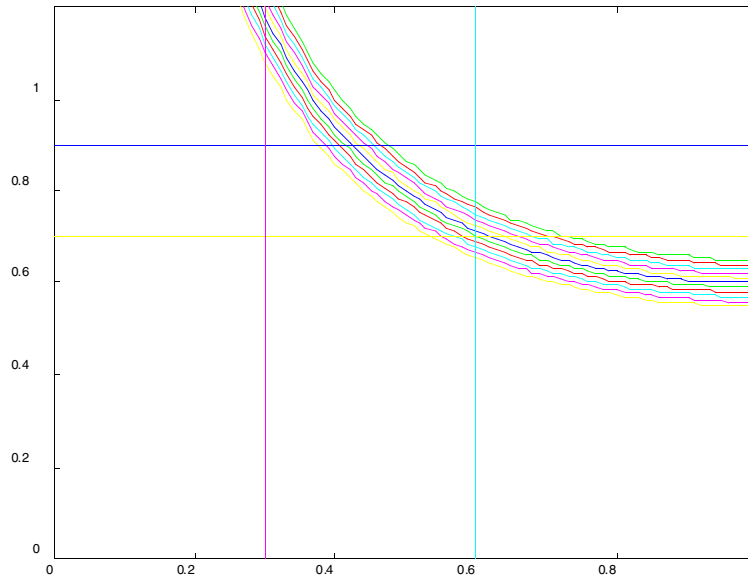


Fig. 11 Constraints in choosing the reference cube parameters

If the fraction of volume of fibre is fixed (measured 60% in Frascati), λ and β are linked and have to be less than 1 (in Fig. 11 also the suggested bracket for λ and β is plotted). Iso- v_F and iso- G_{IT} (Fig. 12) show how the G_{IT} value is limited because of the geometrical and material constraints.

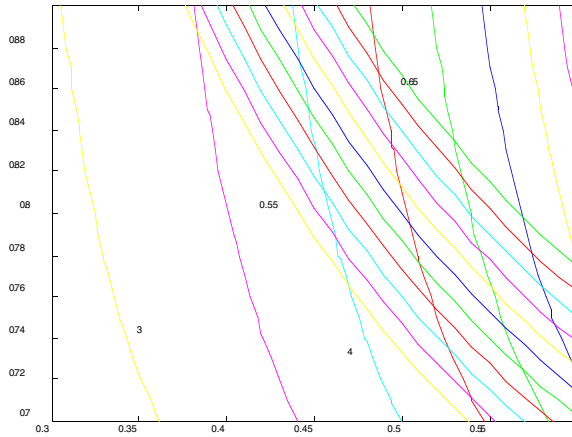


Fig. 12 Iso- G_{II} curves overlapped by iso- v_F curves in the λ - β of reference

The ABAQUS brick model results are compared with Noell measurements in Table 6 (for a force of **500 kN**, all displacements are in **mm**). The changes in G do not produce significant changes in the coil deflection to be compared with Noell's tests.

	G=4000MPa with $\lambda=0.46$ and $\beta=0.81$	G=3000MPa with $\lambda=0.35$ and $\beta=0.74$	G=2000MPa with $\lambda=0.3$ and $\beta=0.56$	NOELL
(in plane) inner mid-plane	0.41	0.43	0.45	0.53
(in plane) outer mid-plane	0.29	0.30	0.31	0.36
(in plane) collar	1.36	1.42	1.42	1.62
(out of plane) collar	0.97	1.02	1.03	1.04

Table 6 Comparison with Noell using also incorrect β

3. Brick Model for scenario assessment

3.1. Model description

The TF coil can be divided in regions of different cross section: the straight, the curved and the outer. The accurate perimeter of these three cross sections has been taken from JET drawings. The geometry actually used in the model is as close as possible to the original with minor simplification for the straight-leg cross section.

The inter-pancake has been modelled separately from the pancake. The ground wrap is not included.

There is still a pancake packing factor, as the pancake includes the inter-turn insulation, the keys and the cooling channels. The pancake-only packing factor has to be taken into account when the output stresses are post-processed.

The coil is divided in 136 slices (as there are 136 beam elements in the beam model, this is the simplest way to be able to apply the same loadings to the two models and later on to compare results coming from the two models). Each slice is divided into 35 elements (30 of which make up the two pancakes and 5 the inter-pancake). The elements are 20-node quadratic bricks (C3D20 in ABAQUS). The mesh of the model is plotted in Fig. 13.

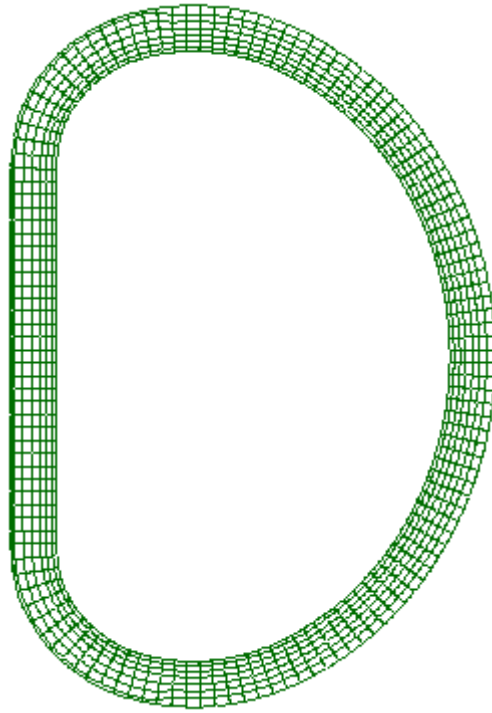
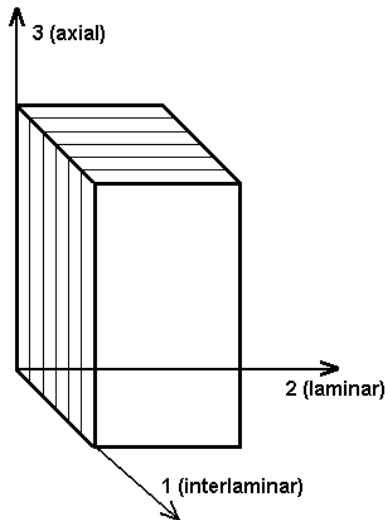


Fig. 13 Mesh of the new 3D brick model of the full TF coil

The insulation and copper material properties used are:

	E [GPa]	G [GPa]	ν [#]
copper	120	46	0.3
insulation	10.4	4.0	0.3

The coil is divided in inter-pancake (modelled with isotropic insulation) and pancake (assumed as a unidirectional packing of turn and insulation); 3 is the winding direction and 2 is the out of plane direction.



The pancake properties to be input in the FE model are then estimated assuming that the length ratio of copper (λ_{Cu}) and insulation (λ_{IT}) to the total length is proportional to the area ratio (pancake packing factor) of copper (α_{Cu}) and insulation (α_{IT}) to the total area of the pancake):

$$\lambda_{Cu} = \alpha_{Cu} = \frac{\text{area copper}}{\text{total pancake area}}$$

$$\lambda_{IT} = \alpha_{IT} = \frac{\text{area insulation}}{\text{total pancake area}}$$

The sum of F_{Cu} and F_{IT} is less than 1. Because a fraction of the pancake area is occupied by cooling channels which do not play an active role in the load shearing.

The Young modulus in the inter-laminar direction (copper and insulation in series) is

$$E_1 = \frac{1}{\frac{\lambda_{Cu}}{E_{Cu}} + \frac{\lambda_{IT}}{E_{IT}}}$$

The Young modulus in the laminar and axial direction is given by the parallel of copper and insulation and it is

$$E_2 = E_3 = \alpha_{Cu}E_{Cu} + \alpha_{IT}E_{IT}$$

In plane the copper and the insulation work in shear as a series, consequently

$$G_{12} = G_{13} = \frac{1}{\frac{\lambda_{Cu}}{G_{Cu}} + \frac{\lambda_{IT}}{G_{IT}}}$$

Out of plane the copper and the insulation work in shear as a parallel, so

$$G_{23} = \alpha_{Cu}G_{Cu} + \alpha_{IT}G_{IT}$$

The in plane Poisson ratio is given by the series of copper and insulation

$$\nu_{12} = \nu_{13} = \alpha_{Cu}\nu_{Cu} + \alpha_{IT}\nu_{IT}$$

while the out of plane Poisson ratio is set to produce orthotropic strain

$$\nu_{23} = \frac{E_1\nu_{12}}{E_3}$$

The numerical values of these material properties are summarised in Table 7. The last row of this table is the correction coefficient: the inverse of the global pancake packing factor: (total pancake area) / (copper area); this is the coefficient by which the tensile stresses computed with this model in the direction of winding have to be multiplied to obtain the real stresses.

The in-plane load can be prescribed either as uniform on the cross-section or with their actual shape.

The TF coil current is almost uniform in the cross section, assuming the change of the poloidal field normal to the coil is small across the section the out of plane force acting on the coil slices is uniform in each slice. Therefore the out of plane load used for each beam of the beam model can be uniformly distributed to the elements of the corresponding slice.

	Straight	curved	outer
A_{tot} [mm ²]	80124	81269	110899
A_{copper} [mm ²]	62284	63599	91039
A_{it} [mm ²]	9487	9317	11057
F_{copper} [#]	0.777	0.783	0.821
F_{it} [#]	0.118	0.115	0.100
E_1 [GPa]	56.0	57.0	60.9
E_2 [GPa]	94.5	95.1	99.5
E_3 [GPa]	94.5	95.1	99.5
G_{12} [GPa]	21.5	21.9	23.4
G_{13} [GPa]	21.5	21.9	23.4
G_{23} [GPa]	36.4	36.6	38.3
ν_{12} [#]	0.335	0.334	0.326
ν_{13} [#]	0.335	0.334	0.326
ν_{23} [#]	0.198	0.200	0.199
correction coefficient	<i>1.28643</i>	<i>1.277835</i>	<i>1.218148</i>

Table 7 Material properties used in the brick model, where directions 1 and 2 lie in the cross section (with 1 in-plane and 2 out of plane) and the direction 3 follows the winding.

3.2. Model boundary conditions

The coil has been constrained as in the JET-assembly (Fig. 14 shows the TF coil with the supports) except for the vertical supports, which have been moved from the bottom end to the mid plane (as it is done for the beam model). The coil is supported both radially and out of plane at the inner cylinder (with constraints that make it slide along its outside surface). The push-pull jacks provide an additional radial constraint in the outer part of the coil and they are pre-loaded with 69 kN (each for top and bottom) and have a spring constant of 2.34 MN/m. The out of plane supports are at collar, ring and four pairs on the outer MS shell. The collar support is modelled differently than on the beam model as the brick model allows for a partial support of the cross section approximately of the size and in the location of the real one.

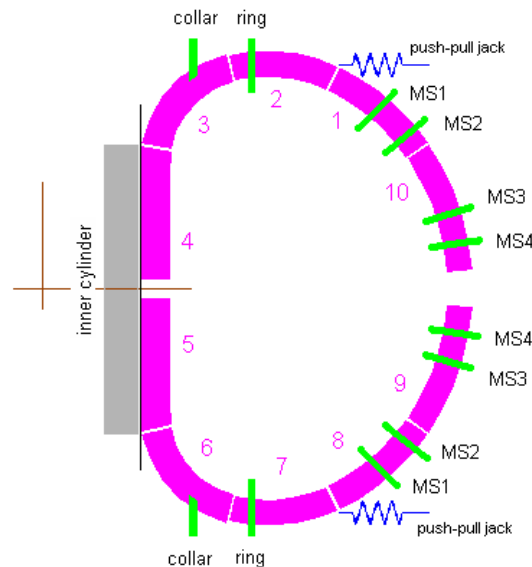


Fig. 14 TF coil with modelled supports

The brick model gives the opportunity of modelling the boundary conditions at the inner cylinder and on the MS in a more realistic way: the nose of the coil can be modelled as sliding inside the fluted column support at the inner cylinder and unidirectional springs can be placed on both sides of the MS supports with gaps so that only the side in

compression react the load (this is not possible in the beam model where the supports act on the centre-line of the coil). The analysis of the out-of-plane supports' displacement on the copper and inter-pancake stresses can be performed both explicitly and synthetically. The latter analysis is of particular interest because it allows the beam results to be interpreted in a more general way: given the out-of-plane reaction forces from the beam model it is possible to compute the support displacements and from these to adjust the TF coil stresses and displacements accounting for the effect of the out-of-plane deformation.

To get the **synthetic-approach** matrix linking support displacements to support forces and additional stresses the coil is not loaded with any magnetic load, it is supported as in the machine (inner cylinder, collar, ring and MS supports). One support at a time is displaced, by 1 mm. For the inner cylinder two runs have been done, one with the nose rigidly shifted by 1 mm and one with the nose tilted in the y,z plane (being y the out-of-plane and z the vertical direction) with the top and the bottom displaced by +1 mm and -1 mm respectively. After each run the support reaction forces and the relevant stresses are collected. These are used to get a coil stiffness matrix (qualitatively shown in Fig. 15, please note the symmetry: displacement of the j support makes the same on the i support as the displacement of the i support makes on the j support). During operation the supports move to react a force due to the magnetic load, which is partially taken by the coil's own displacement:

$$F_j^p = -\sum_i k_{ij} d_i + k_j^{MS} d_j$$

where the suffix p indicates quantities due to the magnetic loading and MS to the MS-model results. The unknown are the support displacements, which can be computed knowing the supports' stiffness. These have been taken from G. Sannazzaro MS-model as listed in Table 8. Once the displacements are computed any stress can be estimated as

$$\sigma(u) = \sigma^p(u) + \sum_i d_i \sigma_i(u)$$

where u is a dummy variable running along the coil and the σ_i are the additional stresses due to the support displacements, saved in the single-displacement runs.

	MN/m
collar	500
ring	500
ms1	670
ms2	630
ms3	1500
ms4	2000
cyl(tilt)	2060
cyl(shift)	8000

Table 8 MS supports' stiffness

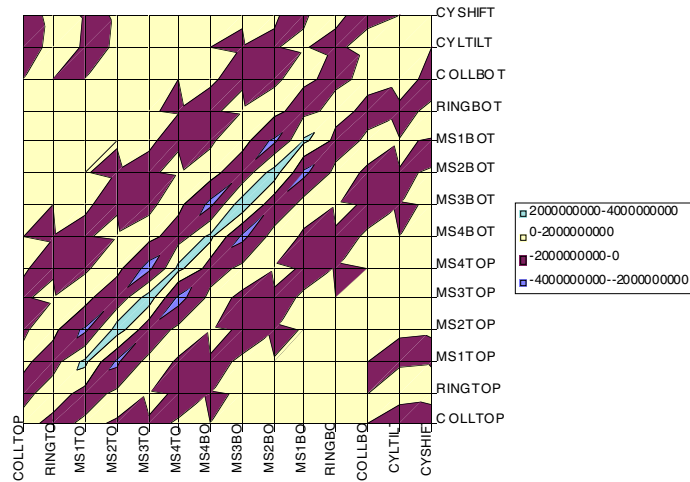


Fig. 15 Force/displacement matrix

For the reference scenario (the ELM-free H-mode at the VDE-spike) the copper stresses with and without the effects of the support displacement are reported in Table 9. A summary of the effect of the supports' displacements is given in the following subsection, the aim of this subsection is to validate the synthetic approach. Comparing the out-of-plane displacement estimated using the synthetic approach (and assuming the inner cylinder is infinitely stiff) with those computed moving the MS-supports by the amount required according to the computed supports' out-of-plane force is a practical test to validate the synthetic approach and feel confident in using it to account for compliance at the inner cylinder. The out-of-plane displacement (in the case of an infinitely stiff inner cylinder) is plotted in Fig. 16 for a compliant, a moved and a fixed set of MS supports; the out-of-plane displacements computed with (the plasma load and) the moved MS supports has to be reproduced exactly by the synthetic (fixed+supports' displacement effect) displacement. This is not equal to the out-of-plane displacement computed when springs are placed at the MS-supports as the synthetic approach does not account for the compression/deformation of the coil cross section.

external (l)	external (r)	internal (l)	internal (r)	
121.0	117.3	146.9	149.8	inner
78.2	82.0	97.9	98.2	outer
73.9	74.2	87.6	88.1	brazed joints

without the additional stresses due to the support displacements

external (l)	external (r)	internal (l)	internal (r)	
128.1	122.7	149.6	154.4	inner
89.6	88.5	113.3	112.1	outer
70.8	73.2	84.0	86.9	brazed joints

with the additional stresses due to the support displacements

Table 9 membrane+bending stresses with and without effect of support displacements

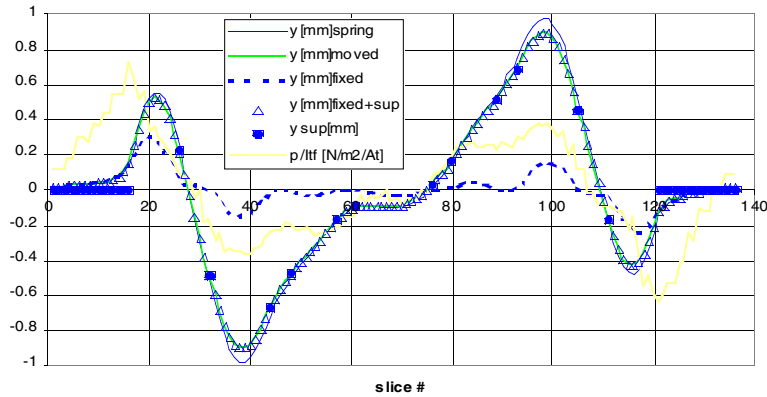


Fig. 16 Support displacements (y_{sup}), coil displacement from the FE calculation (y_{spring} : MS springs; y_{moved} : MS displaced pins; y_{fixed} : MS pins), synthetic displacement ($y_{fixed+sup}$: to be compared with y_{moved}) and out-plane load (p/Itf).

3.3. Model results

To ease the comparison of the preciously reported results of the beam model in Fig. 17 the glossary for the corner elements and corner points is shown.

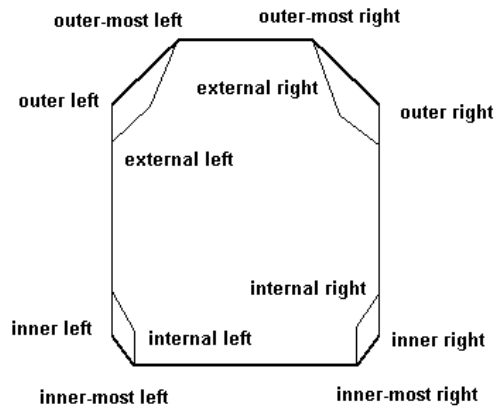
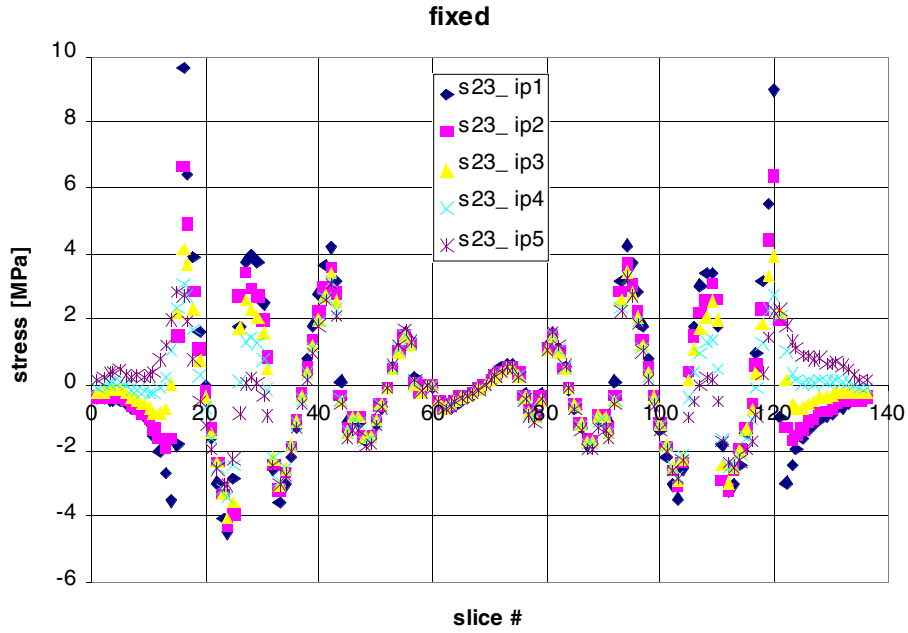
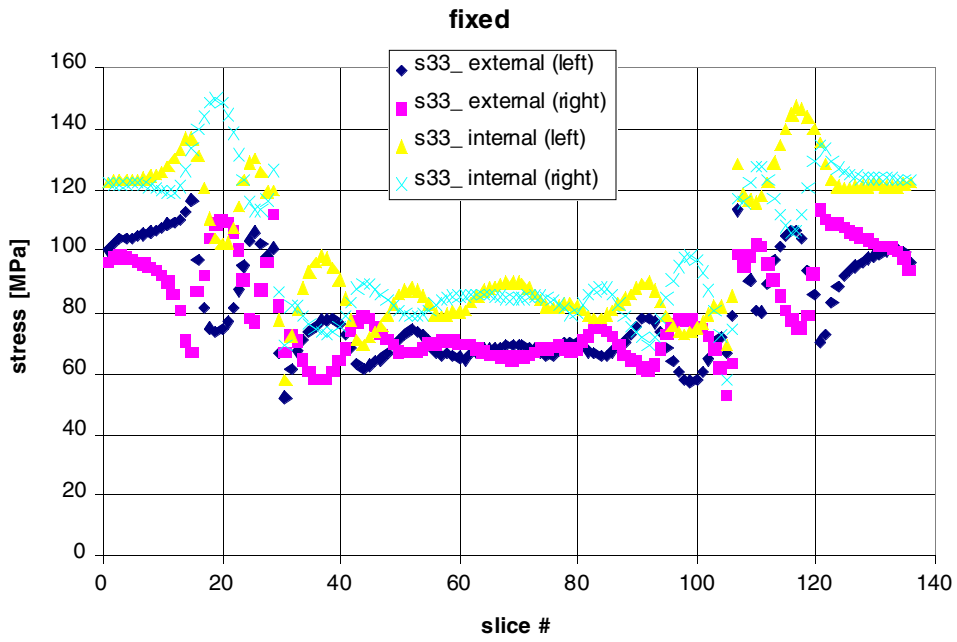


Fig. 17 Corner elements (brick model) and points (beam model post-processing)

In the following (fig. 18 to fig. 19) the copper axial stresses, the inter-pancake out-of-plane shear stresses are reported (the reference scenario is the ELM-free H-mode at the VDE-spike) in the two significant cases: all supports fixed with uniform in-plane load on the cross-section (fig. 18, almost as with the beam model) and MS-springs and sliding in groove linked to collar with shaped in-plane load (fig. 19, the simulation closer to the actual loads and boundary conditions). In addition in Fig. 20 the displacements in 6 different possible combinations of in-plane load distributions and boundary conditions are reported. For the same 6 case the out-of-plane forces are plotted in Fig. 21 and listed in Table 10. As far as the out-of-plane forces are concerned the in-plane load distribution is not relevant. Only for the out-of-plane forces also the results of the beam model have been listed.

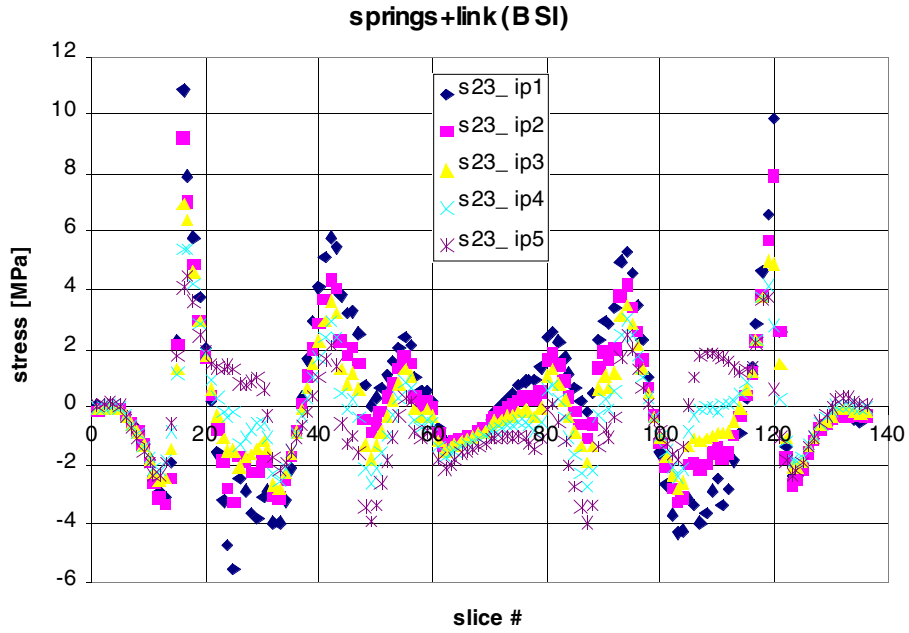
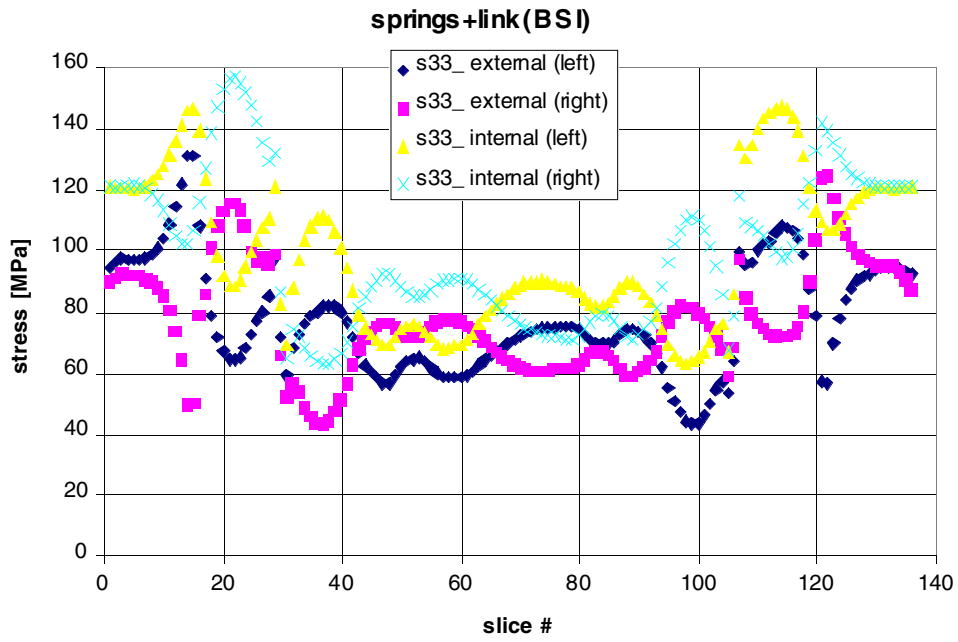


all values in the tables are in MPa

external (l)	external (r)	internal (l)	internal (r)	
116.3	113.2	146.8	149.5	inner
78.3	82.1	98.1	98.4	outer
73.9	74.2	87.6	88.1	brazed joints

	section 1	section 2	section 3	section 4	section 5
top	9.7	6.7	4.1	3.2	3.1
bottom	9.0	6.4	3.9	3.3	3.3

Fig. 18 All out-of-plane support fixed (sliding inner cylinder), uniform in-plane load

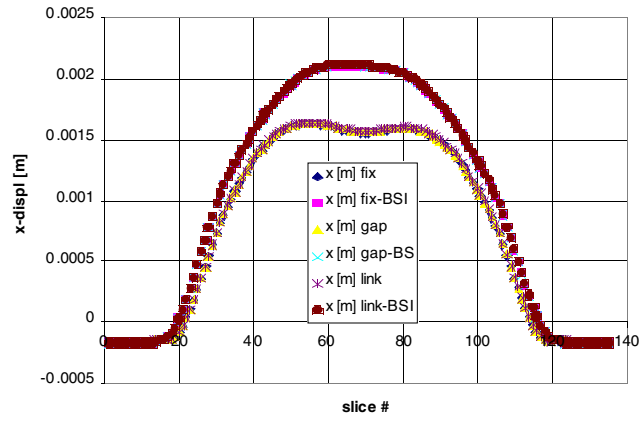


all values in the tables are in MPa

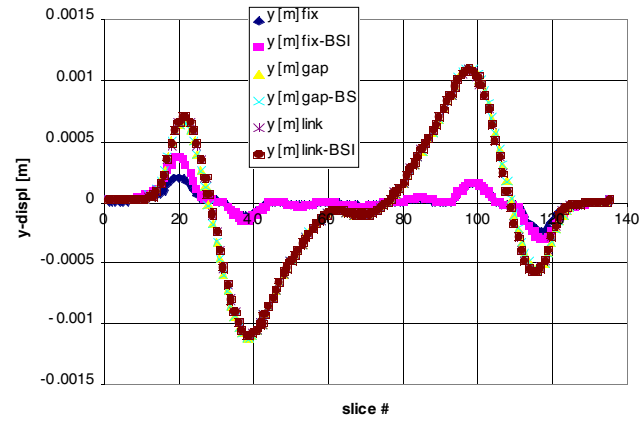
external (l)	external (r)	internal (l)	internal (r)	
130.8	124.1	146.9	156.4	inner
81.8	81.9	111.3	111.2	outer
73.0	75.0	85.4	90.6	brazed joints

	section 1	section 2	section 3	section 4	section 5
top	10.8	9.2	7.0	5.4	4.5
bottom	9.9	7.9	5.0	4.2	3.8

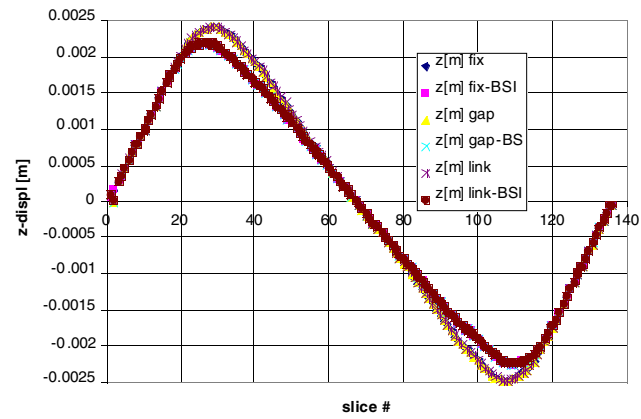
Fig. 19 MS-springs and sliding in groove linked to collar, shaped in-plane load



(a)



(b)



(c)

Fig. 20 TF coil displacements: (a) radial, (b) out-of-plane and (c) vertical
 fix: all out-of-plane supports fixed; gap: MS+inner-cylinder as unilateral compressive
 springs; link: MS+inner-cylinder as unilateral compressive springs with end of the
 inner-cylinder linked to the collar support; BSI: shaped in-plane load

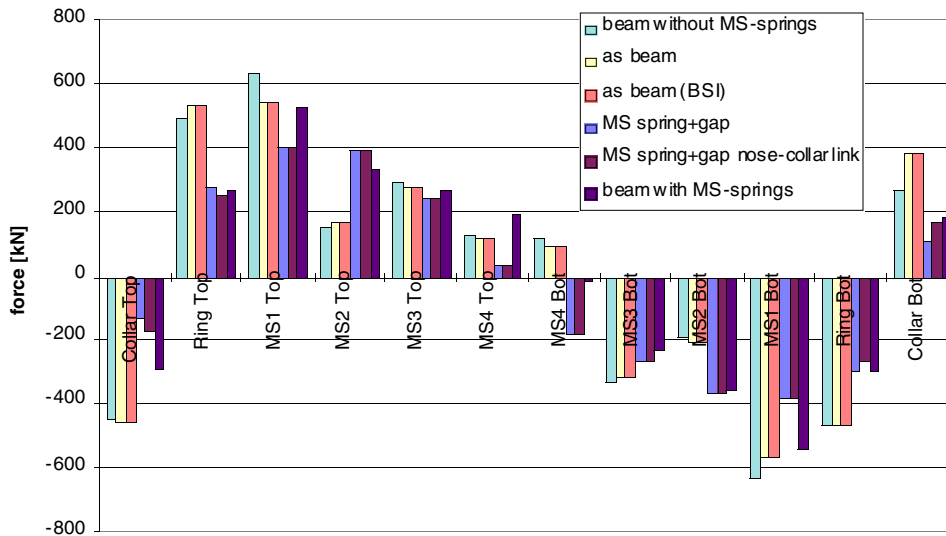


Fig. 21 Out-of-plane reaction force at the MS supports for the same scenario and different out-of-plane boundary conditions.

	MS spring+gap	MS spring+gap nose-collar link	as beam	beam without MS- springs	beam with MS- springs	as beam (BSI)
Collar Top	-135	-176	-458	-447	-291	-459
Ring Top	281	254	535	498	266	535
MS1 Top	397	396	546	630	524	546
MS2 Top	392	394	167	153	339	167
MS3 Top	243	245	274	296	267	274
MS4 Top	36	37	122	128	194	122
MS4 Bot	-184	-184	87	119	-16	87
MS3 Bot	-262	-264	-318	-333	-228	-318
MS2 Bot	-366	-367	-201	-190	-357	-201
MS1 Bot	-384	-383	-567	-634	-538	-567
Ring Bot	-297	-268	-463	-471	-300	-463
Collar Bot	113	163	384	268	189	384

Table 10 Out-of-plane reaction force at the MS supports for the same scenario and different out-of-plane boundary conditions(all values in kN)

In the following there are the FE results on a inner leg cross-section (reduced, hence with higher stresses) for a in-plane uniform load only:

- contour plots: stresses extrapolated from the integration points to the element nodes (PF not included, in Pa)
- listing of the average element stresses divided by the pancake packing factor (PF included, in MPa)

The in-plane compression (Fig. 22) peaks against the inner-cylinder support, the axial tension (Fig. 24) is highest on the opposite side of the cross-section, therefore the von Mises (Fig. 28) and the tresca (Fig. 29) are almost constant. This is also because the axial tension and the support compression are the main stresses in this case, as the load is only in-plane: the out-of-plane tensile stress (Fig. 23) is close to zero as the out-of-plane shear stresses (Fig. 25 and 26) are too.

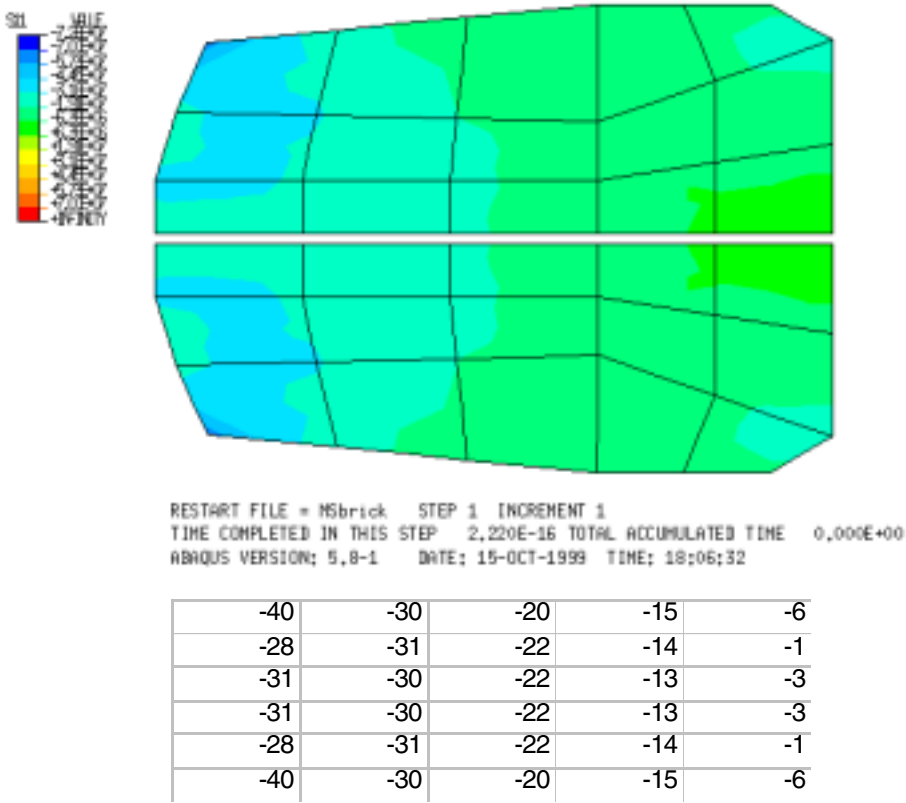


Fig. 22 S11: on the cross-section plane, in-plane tensile stress

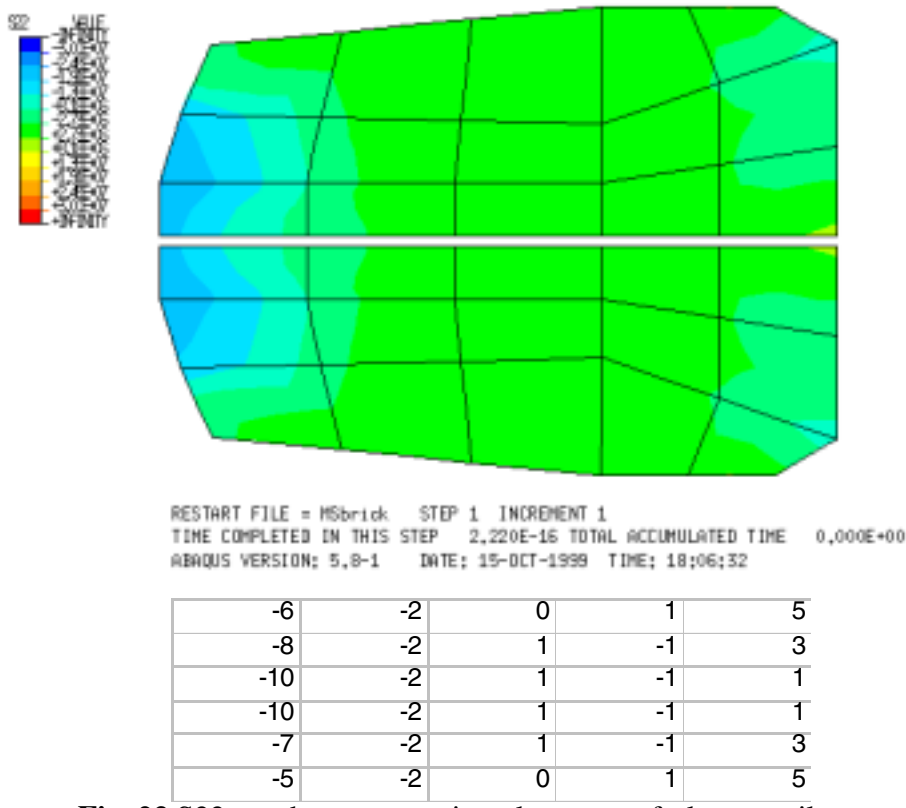
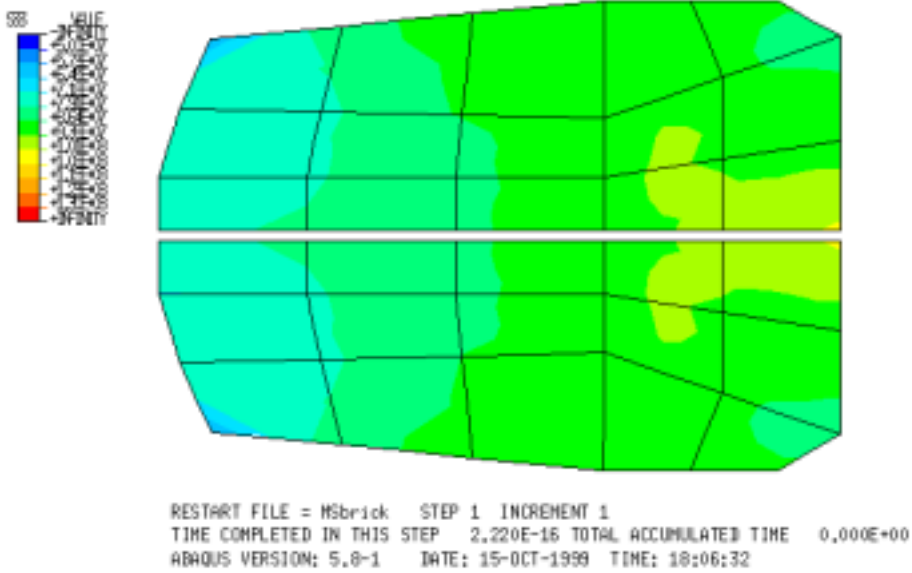
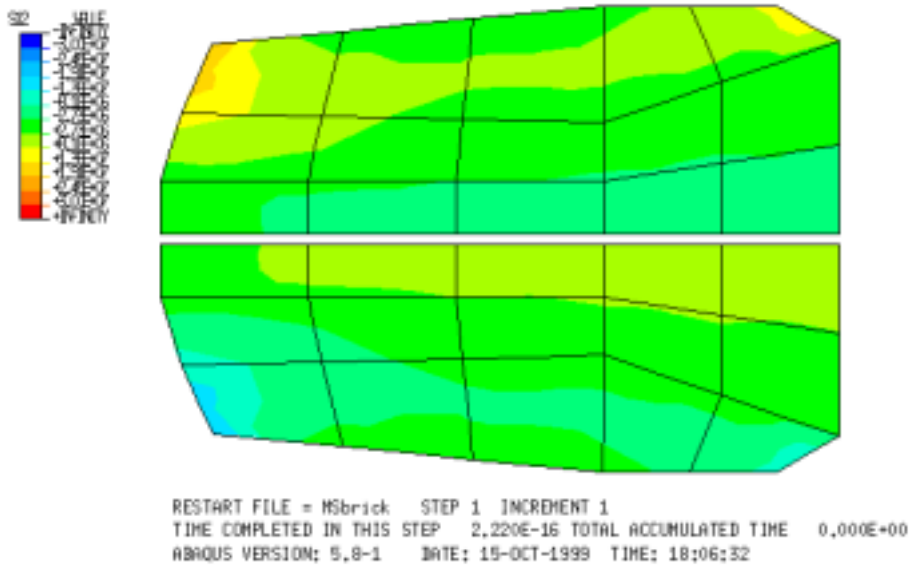


Fig. 23 S22: on the cross-section plane, out-of-plane tensile stress



100	107	114	118	123
106	107	114	118	126
104	107	113	119	124
104	107	113	119	125
106	107	114	118	126
100	107	114	118	124

Fig. 24 S33: along the winding direction tensile stress



-4.2	0.9	1.0	0.8	0.9
-4.5	-0.8	0.5	0.3	-0.5
-1.6	-1.8	-1.2	-0.5	0.0
1.8	1.9	1.3	0.5	0.0
4.6	0.9	-0.5	-0.3	0.5
4.2	-0.9	-1.0	-0.8	-0.9

Fig. 25 S12: in-plane shear stress

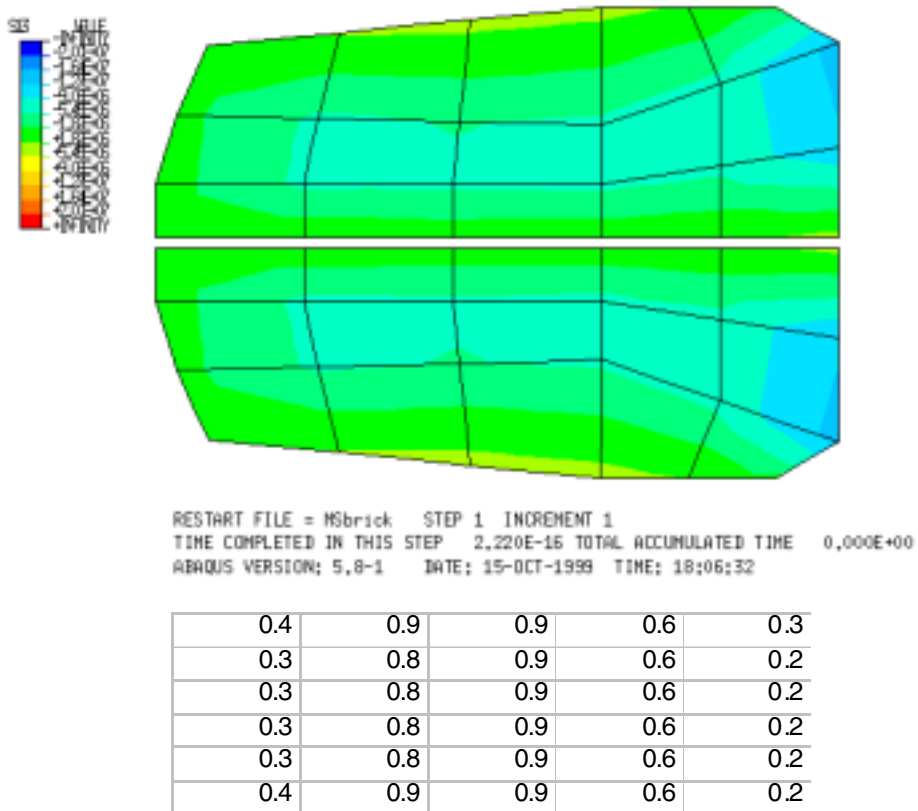


Fig. 26 S13: inter-turn shear stress

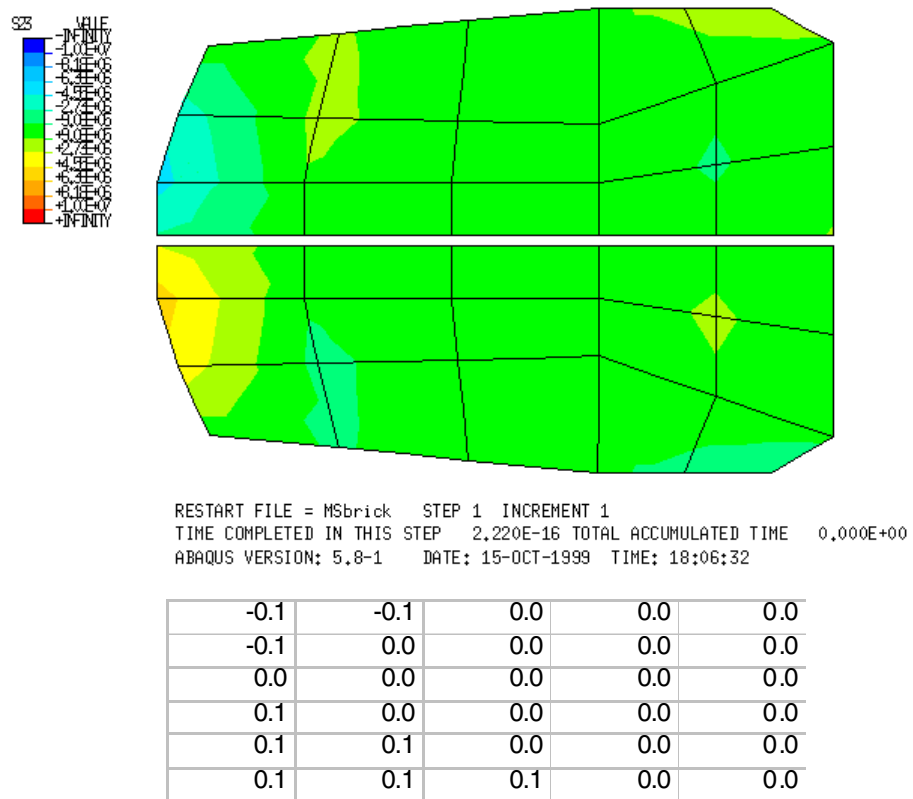
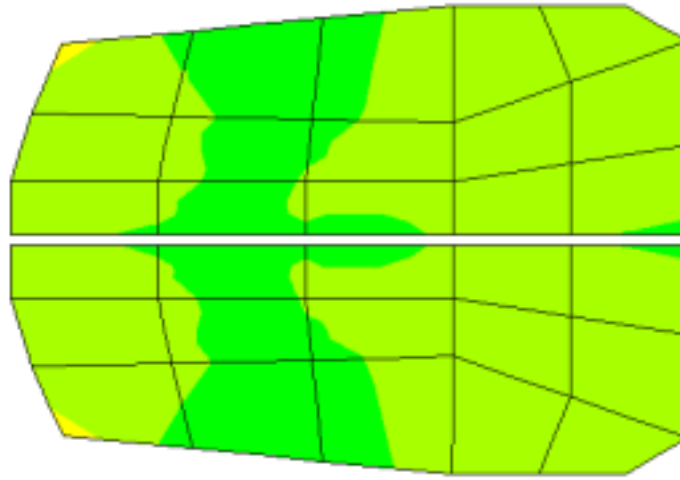
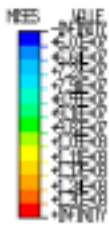


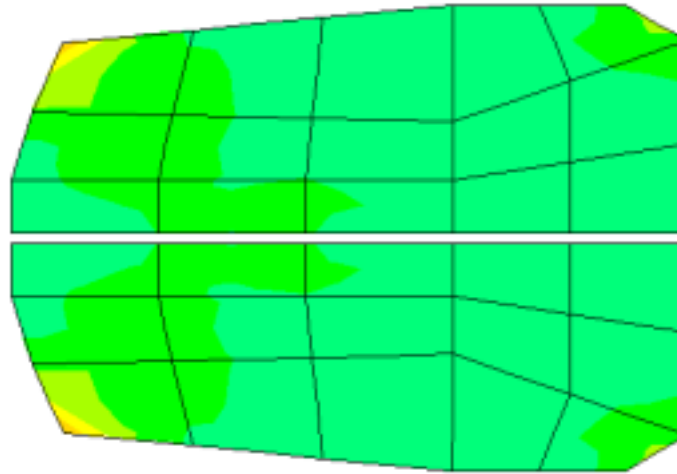
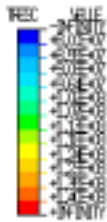
Fig. 27 S23: inter-pancake shear stress



RESTART FILE = MSbrick STEP 1 INCREMENT 1
 TIME COMPLETED IN THIS STEP 2.220E-16 TOTAL ACCUMULATED TIME 0.000E+00
 ABAQUS VERSION: 5.8-1 DATE: 15-OCT-1999 TIME: 18:06:32

127	126	126	126	125
126	126	126	126	125
126	126	126	126	125
126	126	126	126	126
126	126	126	126	125
127	126	126	126	125

Fig. 28 von Mises



RESTART FILE = MSbrick STEP 1 INCREMENT 1
 TIME COMPLETED IN THIS STEP 2.220E-16 TOTAL ACCUMULATED TIME 0.000E+00
 ABAQUS VERSION: 5.8-1 DATE: 15-OCT-1999 TIME: 18:06:32

141	138	135	133	130
135	138	135	132	127
135	137	135	132	128
135	137	136	132	128
136	138	135	132	127
141	138	135	133	130

Fig. 29 tresca

Hybrid Model of Collar Region

Paola Miele

10 November 1999

Contents

1.	Introduction	1
2.	Models	2
3.	Analysis	2
4.	Results	3
	4.1. Comparison with the Different Models.....	5
	4.2. Confidence.....	6
	4.3. Sensitivity with G.....	6
5.	Key Efficiency And Delamination Effects	6
6.	Conclusions	7

1. Introduction.

The JET toroidal field magnet system comprises 32 D-shaped coils originally designed to produce a field of 3.45 T at 2.96 m radius. Water-cooled and lately freon-cooled copper conductors and glass fibres-epoxy resin insulation are the main components of the coils. Interactions between the toroidal and poloidal magnetic fields and the current flowing in the coils create in-plane and out-of-plane forces distributed along the coils. In-plane forces are mainly reacted along the central straight section of the coils by the inner cylinder and out-of-plane forces by the inner cylinder grooves and the mechanical structure supports around the curved outer part of the coils. Among these the collar tooth support area constitutes the most critical point due to the offset of the load [1]. In order to allow for upgrading the JET toroidal field to 4 Tesla new detailed analysis of the TF coils has been carried out and extra safety margin has been found. Sensitivity analysis of the shear stress in the insulation with the shear modulus of elasticity G was carried out and the actual G value was substantiated through measurements with Iosipescu method. Moreover key efficiency and crack propagation analysis show a trend of a crack non-propagation effect.

2. Models.

A beam model of the TF coil is being used to investigate the averaged stress in the section under operational load.

The most critical point is the collar tooth support position due to the offset of the reaction force.

In order to investigate the level of peak shear stress in the insulation in the area of interest, more detailed models which represent the single components of the section are required.

The 3D straight partial model is a preliminary model of a section of the coil 800 mm long, fully restrained at both ends, which is straight instead of bent for simplicity of construction and which represents the copper and the insulation in detail with their own mechanical properties.

It is a preliminary model which was aimed to investigate the level of shear stress in the insulation itself, since all previous models were coarse models with smeared properties on the section.

Nevertheless the straightness of the model and the assumed boundary conditions do not represent the coil in its whole.

Therefore an hybrid model was developed. This comprises a 3D detailed model of the area of interest and a beam model of the remaining coil, so as to model the whole coil.

This 3D curved model with the correct material properties should predict accurately peak stresses, without depending on boundary conditions.

3. Analysis.

In order to investigate the level of peak shear stresses in the insulation the section of the coil has to be modelled with its single components, namely the copper conductors and the glass-resin insulation.

Due to hardware limitations there are difficulties to represent the whole length of the coil that way. Therefore an artifice has been used and explicit modelling of copper and insulation has been done at the region with the highest stress distribution, while coarser modelling represents the remaining coil.

An hybrid model of the TF coil has been created. This comprises a 3D detailed model 600 mm long of the collar tooth area and a beam model of the remaining coil, so as to model the whole coil, Fig. 1.

Both the sections at the interface 3D brick - beam elements have been modelled with rigid elements, to simulate continuity of the section. These elements connect the central node of the section, correspondent with the beam node, with the other nodes of the section. In this way these nodes are forced to remain in a plane and the mechanical actions may be transferred from the beam to the 3D model.

The 3D detailed model with brick elements comprises the single components of the section, namely the copper conductors and the glass - resin insulation, with their material properties.

The coarse model with beam elements represents the material with properties averaged in the section.

The pad at the collar tooth area has been modelled with rigid elements to maintain plane the correspondent surface.

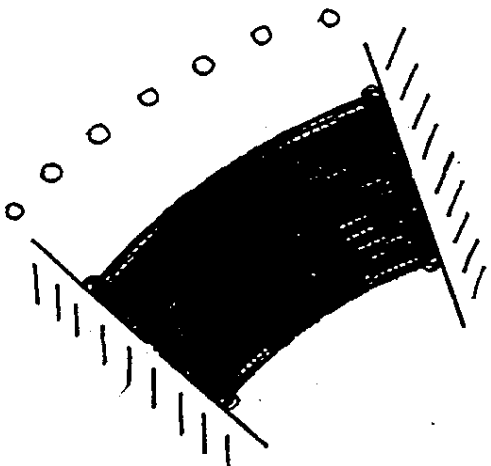
In plane supports by the inner cylinder and out of plane supports by the mechanical structure have been imposed at the different positions along the coil, Fig. 2 [2]. Distributed load has been applied on the copper turn bricks of the 3D model [N/m^3] and on the beams of the beam model [N/m], as for operational scenario with the highest impact on the collar tooth (Pulse 26805). This load is calculated with the magnetic field configuration produced by MAXFEA Code.

Both out of plane forces and in plane forces have been applied; the former are responsible for the high peak shear stress at the third interturn layer in correspondence of the collar tooth position.

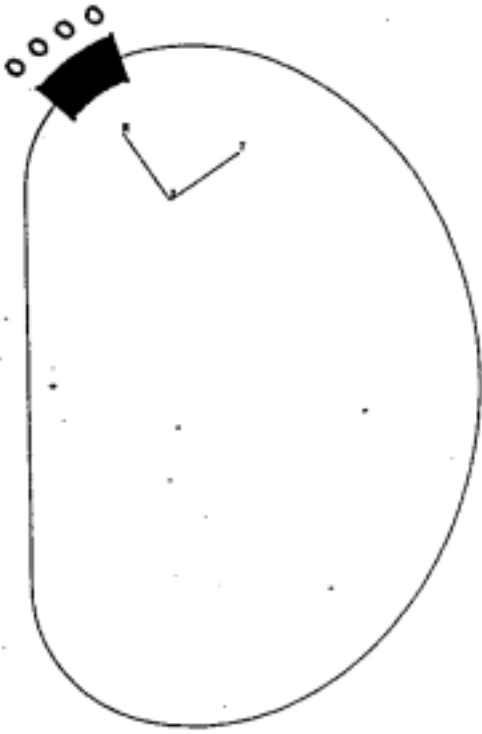
4. Results.

Different simulations have been done with different assumptions on the load distribution and the boundary conditions.

The following analyses were performed.

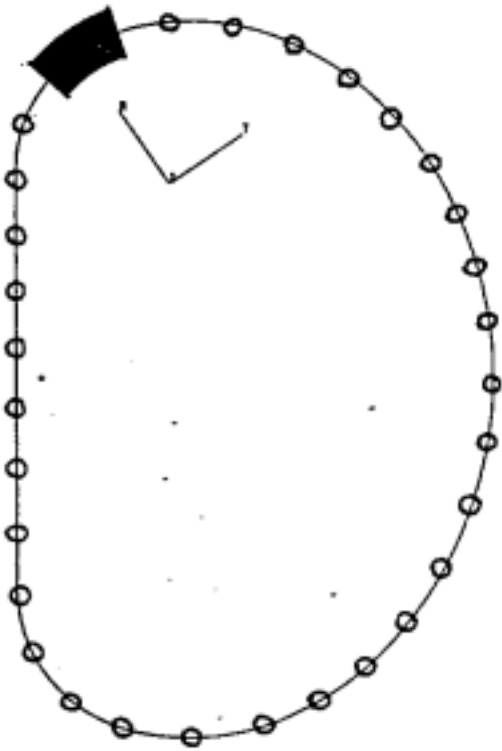
1 	<ul style="list-style-type: none">• 3D curved model at the collar tooth area only, fully restrained at both ends• Constant out of plane forces distributed on the copper turns, corresponding to a reaction force at the collar tooth of 50T
---	---

2

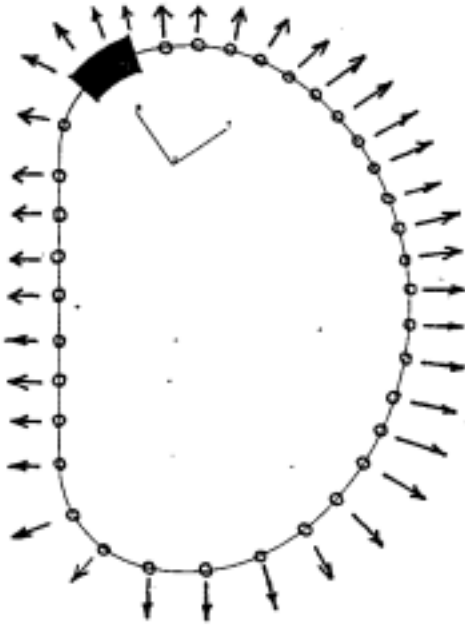


- Hybrid model
- Constant out of plane forces distributed on the copper turns in the 3D model only, corresponding to a reaction force at the collar tooth of 50T

3



- Hybrid Model
- Out of plane forces only distributed on the copper turns and along the beam elements, as for the scenario with the highest impact on the collar tooth (pulse 26805)



- Hybrid Model
- Out of plane and in plane forces distributed on the copper turns and on the beam elements, as for the scenario with the highest impact on the collar tooth (pulse 26805)

The result is independent of the assumptions as long as the reaction force at the collar tooth is the same, which implies that boundary conditions and load distribution far away from the area of interest do not affect the result.

The peak shear stress at the third interturn is $\tau = 12$ MPa for a correspondent reaction force at the collar tooth $F = 570$ kN and $G = 4000$ MPa, Fig. 4, while it is $\tau = 10$ MPa for $F = 520$ kN and $G = 1200$ MPa.

Fig. 5 shows the distribution of the shear stress in the interpancake insulation in correspondence of the collar tooth area. A peak shear stress $\tau=9$ MPa is acting in the section of the coil in correspondence of the collar tooth, where the out of plane forces are the highest.

4.1. Comparison with the Different Models.

Comparison with previous analysis proves consistency of the results.

Table 1 shows the peak shear stress at the third interturn.

A slightly lower stress has been found out with the hybrid model, but the percentage increase of the shear stress with G is the same for the 2 different models. The same happens for smeared properties.

It must be emphasised that the peak shear stress decreases down by 15% from the straight to the hybrid model.

This may be due to the curvature of the fibres, which contributes to distribute more evenly the stress in the insulation, because of the higher contribution by the copper and the different sharing of torsion and pure shear stress.

Table 2 shows the maximum shear stress at the interpancake.

A conservative approach has been used in the beam model to calculate the maximum shear stress in the section, combining the different contributions given by pure shear and torsion. This, together with the higher $G = 4000$ MPa, explain the higher stress obtained.

Peak Shear Stress at the third interturn layer [MPa]

MODEL	G = 1200 MPa	G = 4000 MPa	Smearred Properties
Hybrid Model	10.	12.	14.
3D Straight Model	12.	15.	17.
Beam Model	Max shear stress in the section of the coil: 9.5		

4.2. Confidence.

- Sensitivity analysis at the interface 3D brick - beam elements: the shear stress at the collar tooth position is not affected by the rigid elements used to model the interface.
- Sensitivity analysis with the number of elements through the thickness of the insulation gives the same result.
- The same percentage increase of the shear stress with G has been found out for both the hybrid and the straight partial 3D models. The same happens for the smeared properties.
- Different simulations with different assumptions on the load distribution and the boundary conditions give about the same value of the peak shear stress at the insulation as long as the collar tooth reaction force remains the same: this implies that boundary conditions and load distribution far away from the area of interest do not affect the result.
- Different models give results that are comparable, Table 1.

4.3. Sensitivity with G.

Sensitivity analysis of the shear stress with the shear modulus of elasticity of the insulation G has been carried out. Fig. 5 shows the trend of the shear stress across the third interturn for different values of G. The decrease of the stress in correspondence of the keys confirms the key efficiency [1]. Fig. 6 shows the dependence of the peak shear stress with G: even in the worst assumption of G = 4000 MPa the peak shear stress is still within the allowable $\tau_{\text{amm}} = 15$ MPa.

For a range of G = 1200 ÷ 4000 MPa the shear stress in the insulation increases up by 25%. The correspondent peak tensile stress in the copper decreases by about 5%. The comparison with the beam model shows good correspondence between the results which is a basis for the model validation, Table 1.

Since the shear stress in the insulation is strongly affected by G, it is of the utmost interest to measure this parameter. Since cylindrical samples for standard measurement of shear properties could not be machined out of the available material of the coil, the Iosipescu method for the measurement of G on rectangular samples was implemented [3]. This is a standard method for G measurement in glass - resin fibres, designed to produce pure shear load. Measurements performed at different temperatures give G = 1200÷4000 MPa for a range T = 90 ÷ 20°C, Fig.6. This is the range of the coil operating temperatures and the range of G values used for the analysis [4].

5. Key Efficiency And Delamination Effects

Delamination effects in case of initiation of a crack in the insulation - copper interface at the third interturn have been investigated, by introducing a crack of variable width on the whole length of the third interturn. Key efficiency has also been investigated through comparison of the results with a modified model where all the keys have been removed

and replaced by copper. The keys only affects the distribution of the shear stress across the interturn and contribute to decrease the level of the peak shear stress only in case of delamination.

Furthermore a crack of variable length has been introduced to investigate evolution and crack growth effects. Fig. 7 shows the distribution of the shear stress along the third interturn and Fig. 8 across the same interturn. Fig. 7 gives evidence of the fact that at the tip of the crack the peak shear stress decreases with the length.

6. Conclusions

- The peak shear stress at the third interturn insulation is $\tau = 12$ MPa for a correspondent reaction force at the collar tooth $F = 570$ KN and $G = 4000$ MPa and it is $\tau = 10$ MPa for $F = 520$ KN and $G = 1200$ MPa, which is within our admissible $\tau_{adm} = 16$ MPa .
- The peak shear stress decreases down by 15% from the straight model to the curved model of the coil, this giving an extra safety margin with respect to previous analysis. This may be due to the curvature of the fibres, which could contribute to distribute evenly the stress on the insulation.
- The peak shear stress is strictly related to the reaction force a the collar tooth and boundary conditions and load distribution far away from the area of interest do not affect the result.
- The same percentage increase of the shear stress with G has been found for both the hybrid and the straight partial 3D models. The same happens for the smeared properties.
- The key plays a role only in case of delamination.
- There is a tendency of a crack non-propagation effect.

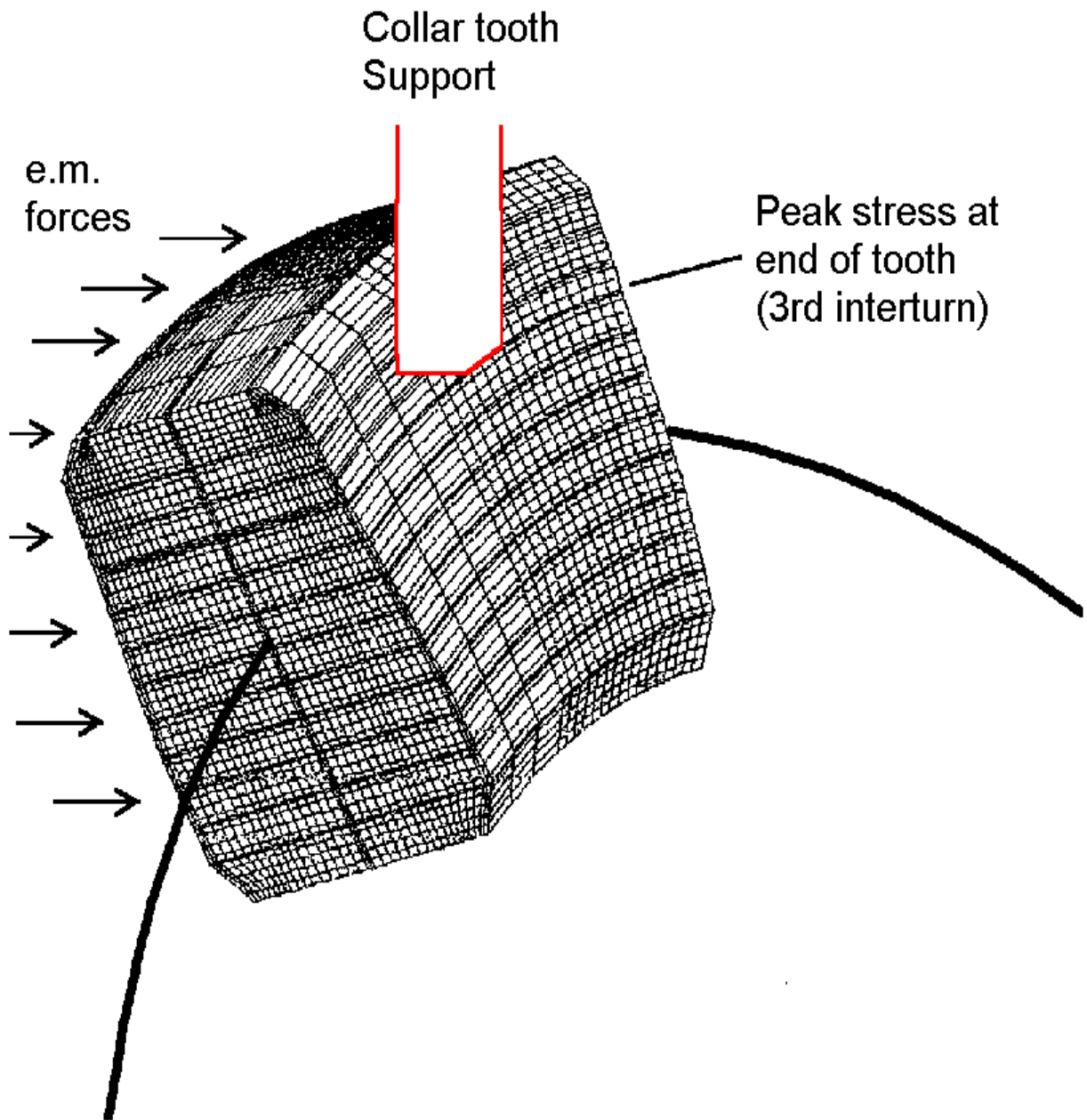


Fig.1: Collar Tooth Support Area

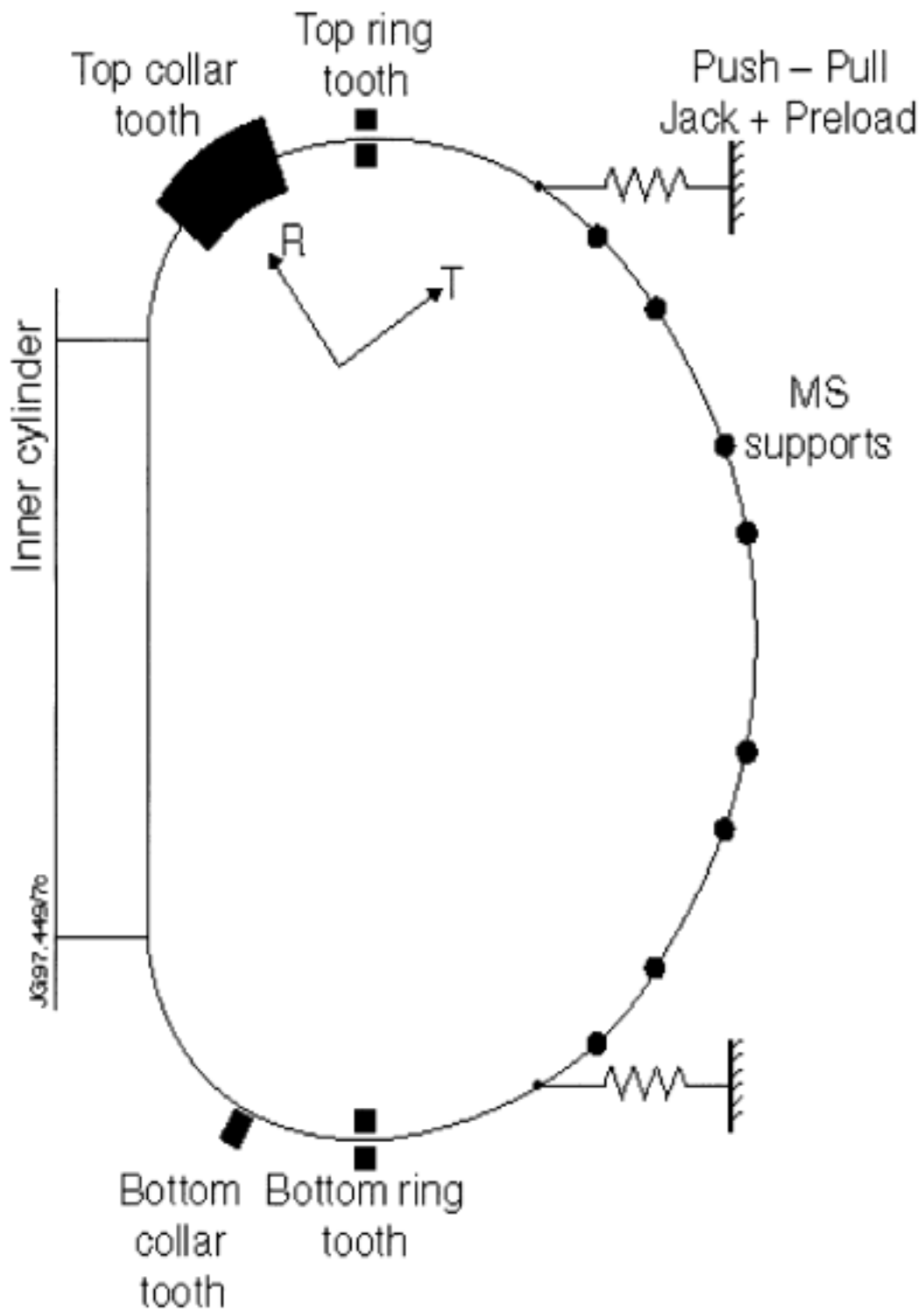


Fig. 2: Hybrid Model of a TF Coil

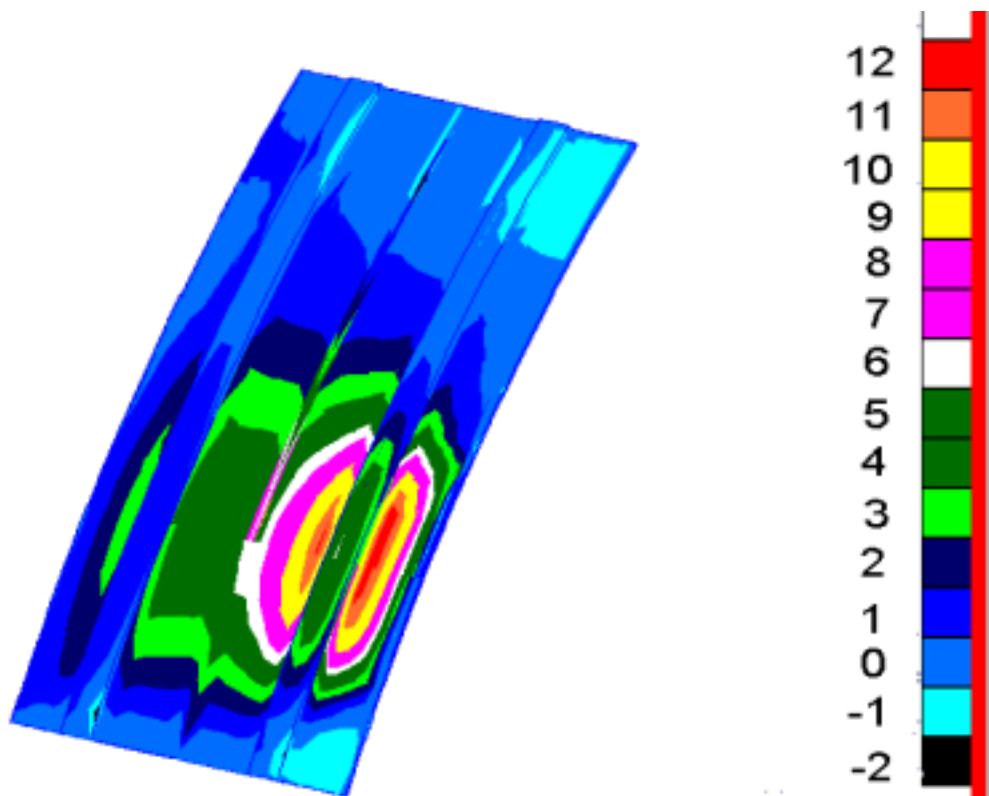


Fig. 3: Shear Stress in the 3rd interturn layer

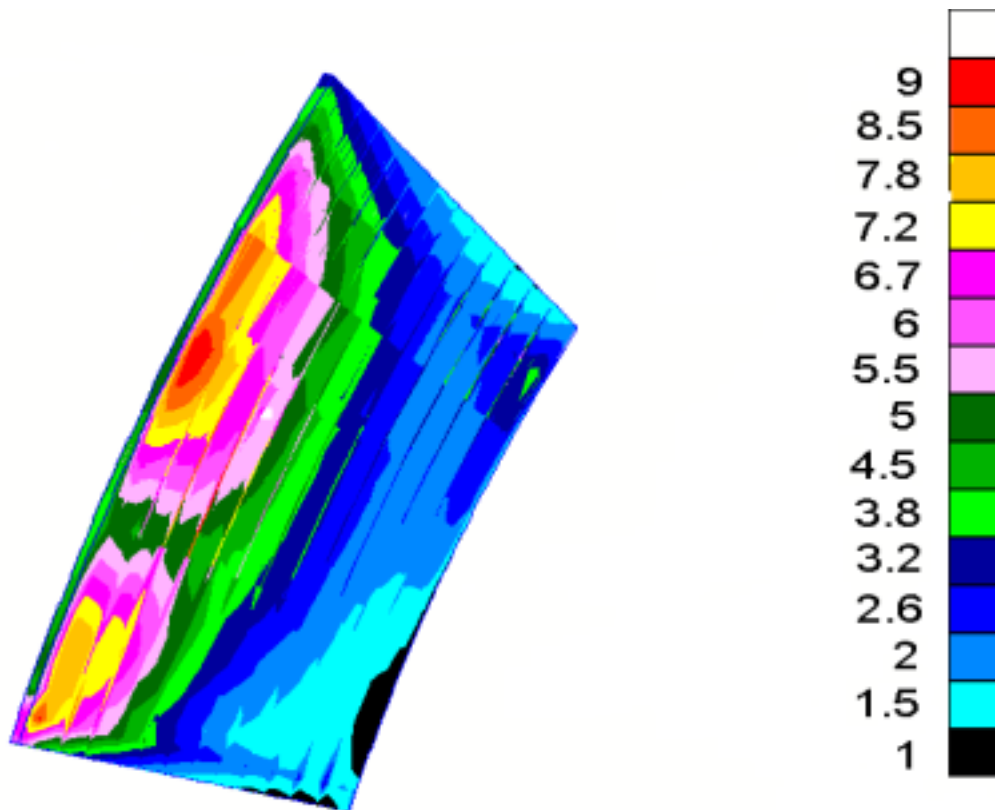


Fig. 4: Shear Stress in the Interpancake

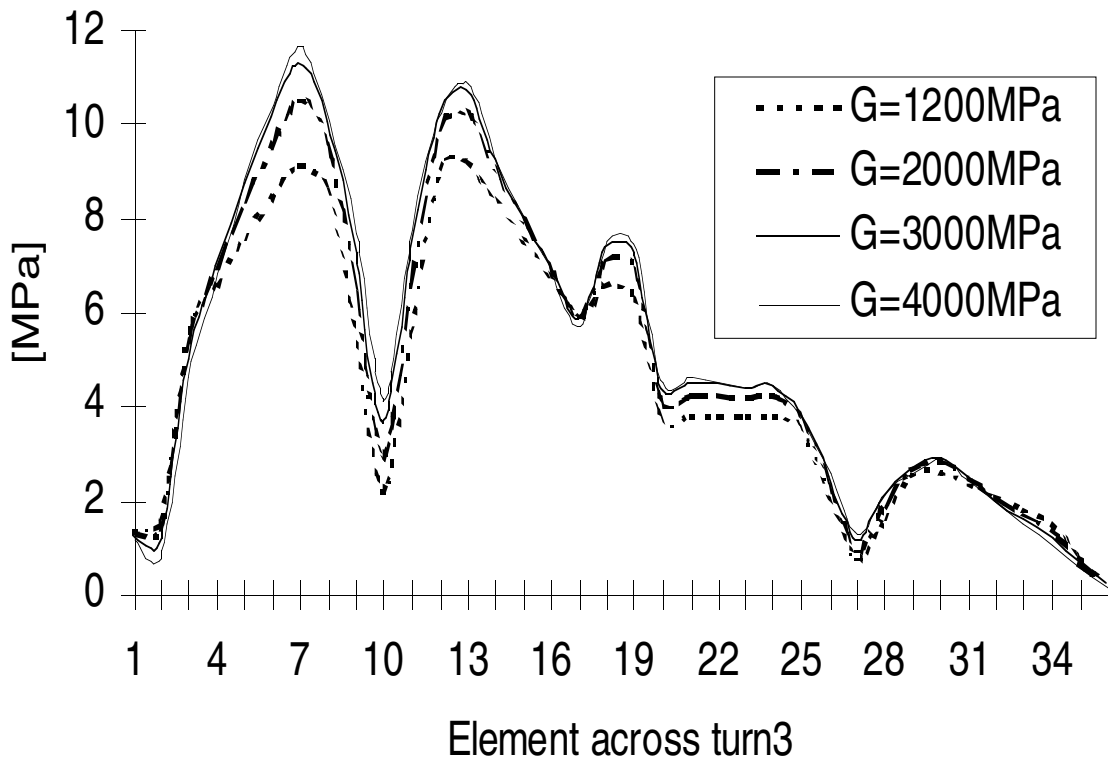


Fig. 5: Sensitivity of the Shear Stress with G

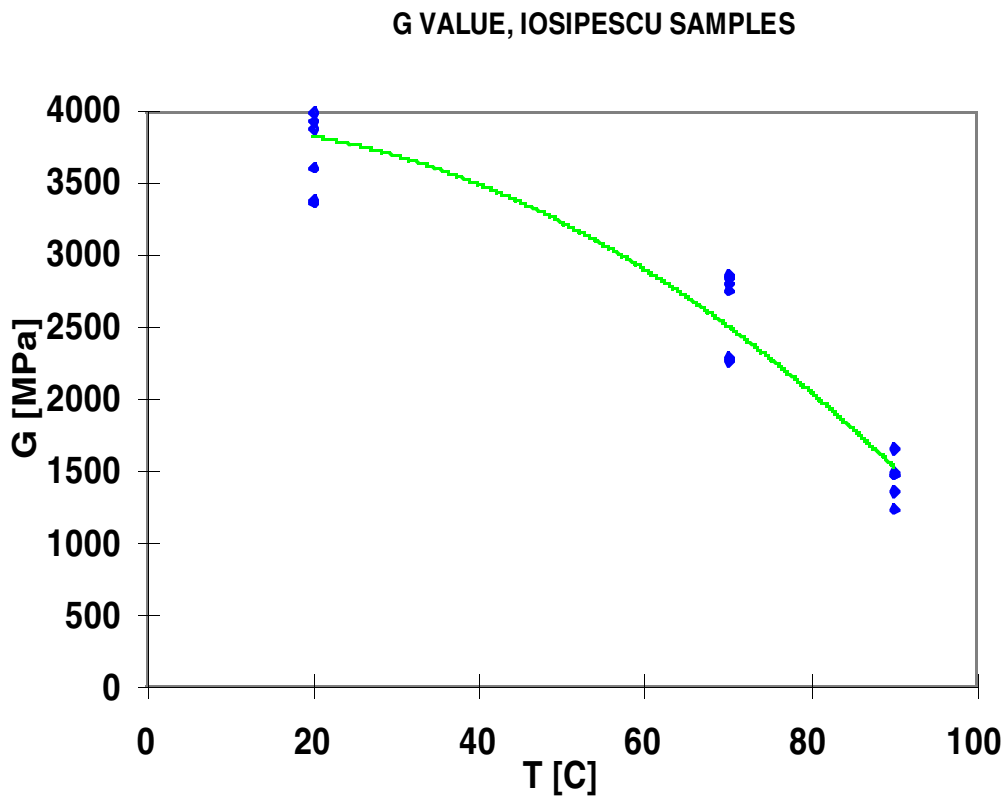


Fig. 6: Sensitivity of G with Temperature

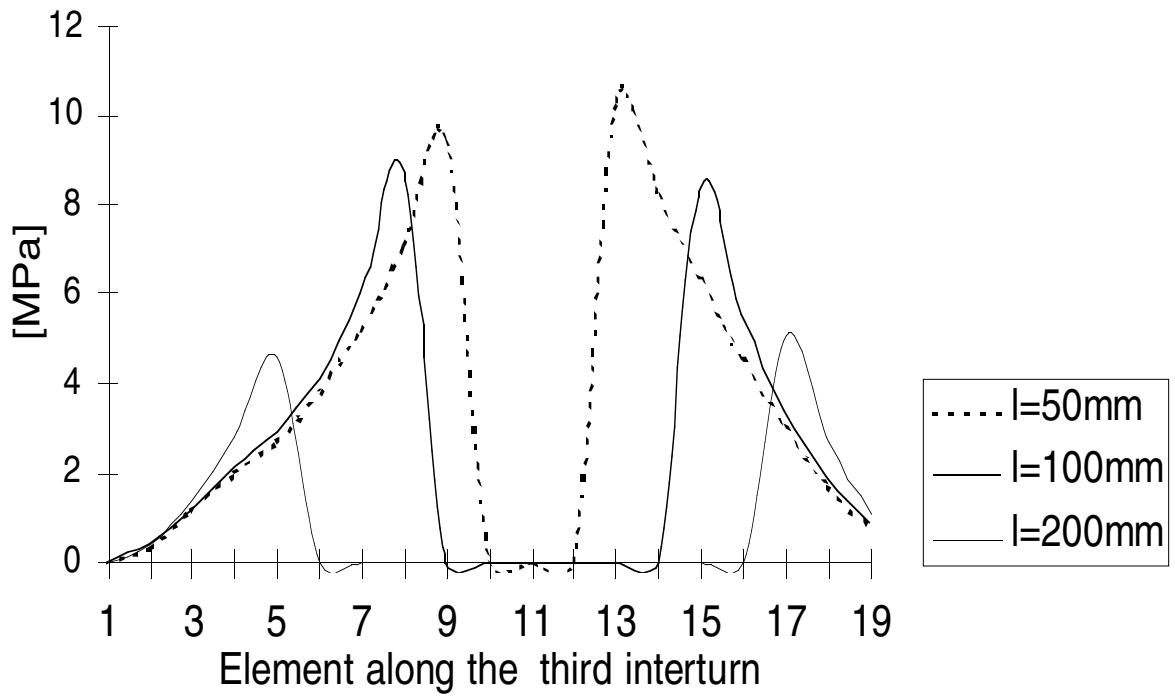


Fig. 7: Shear Stress along turn3

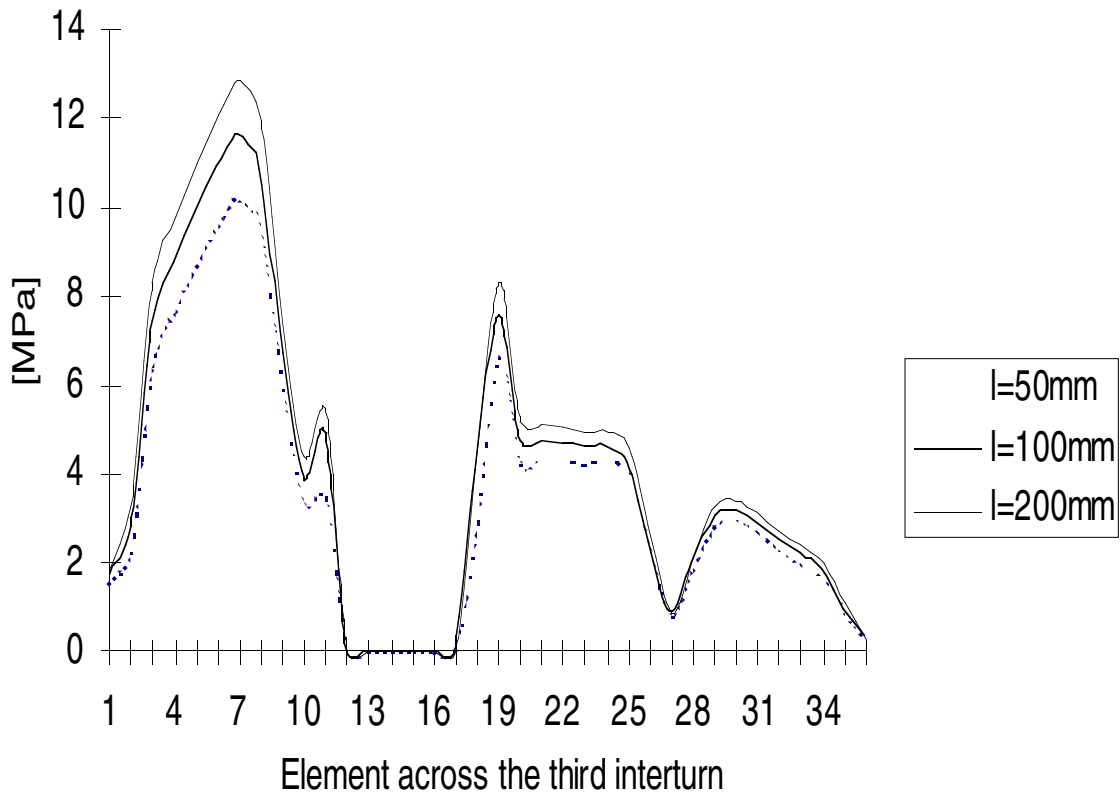


Fig. 8: Shear Stress across turn3

Model of connection and tail region

M. Sjöholm
11 November 1999

Contents

1.	Introduction.....	2
2.	Background.....	3
	2.1. Load.....	3
	2.2. Introductory hand calculations	5
	2.3. FE Model.....	9
	2.4. Boundary Conditions and Load	13
	2.5. Results	13
	2.6. Scaling to 4T.....	18
3.	Thermal analysis	19
	3.1. Thermal analysis	19
	3.2. Stress analysis.....	20
	3.3. FE model.....	20
	3.4. Results	23
	3.5. Thicker insulation at the tail.....	23
4.	References & Lists.....	24
	4.1. Reference	24
	4.2. List of Figures.....	24
	4.3. List of Tables	24

1. Introduction

The raised stresses found in and around the inter-pancake transition piece (see Figure 1-1 and Figure 1-2) have been carefully investigated, first in a thesis for the degree of Master of Science and later with extensive thermal analysis included. The calculations were mainly made with FEM, but they were backed up with hand calculations where possible. The analysis was executed in a stepwise manner starting with simplified plane models to find the general behaviour of the structure under load and incorporating increasing levels of detail. In this appendix, only the final model will be presented, preceding models and analysis have been presented elsewhere [1].

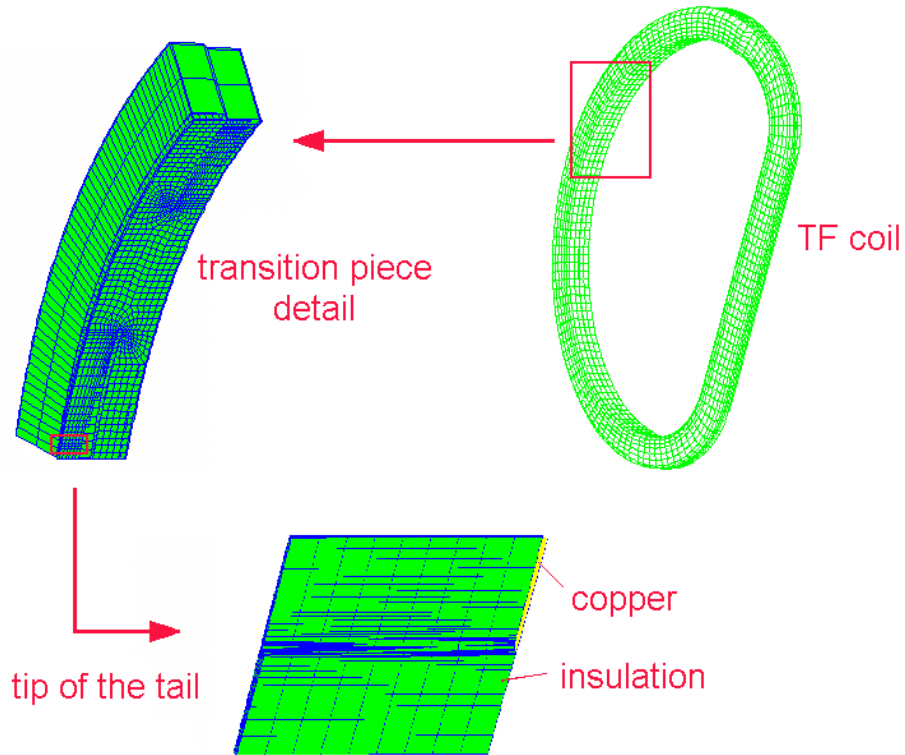


Figure 1-1. Cut-out of a TF-coil at the connection region, transition piece shown.

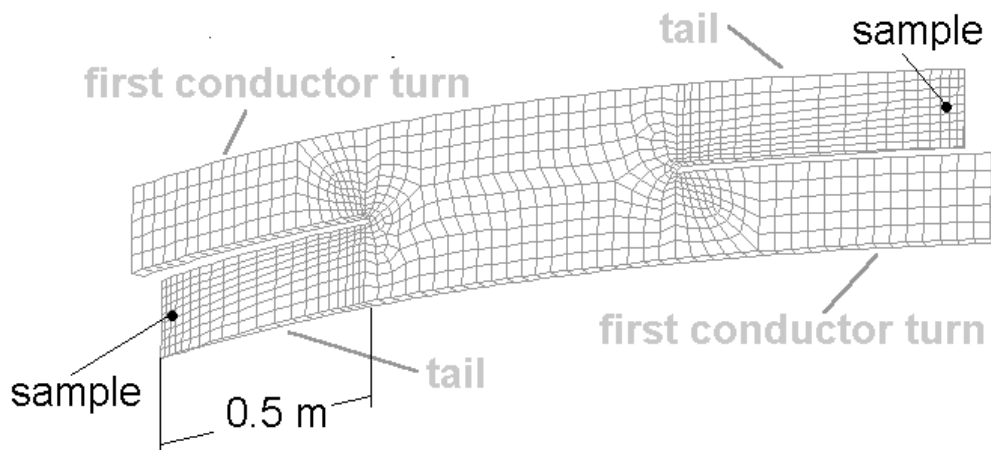


Figure 1-2. Inter-pancake transition piece

2. Background

When the curved TF-coil is loaded by magnetic force, the conductors in the coil will be subject to tension. At the transition piece, where the conductor crosses over between the pancakes, a bending moment will occur. The main part of this bending moment will be reacted via a tensile force from the two tails. The tails are not part of the continuous conductor carrying current but taper down from 28mm to 3mm at the end some 500mm from the transition plate. This means that the tensile force from the plate will be reacted by shear stress in the insulation between the tail and the adjacent conductor (see Figure 2-1).

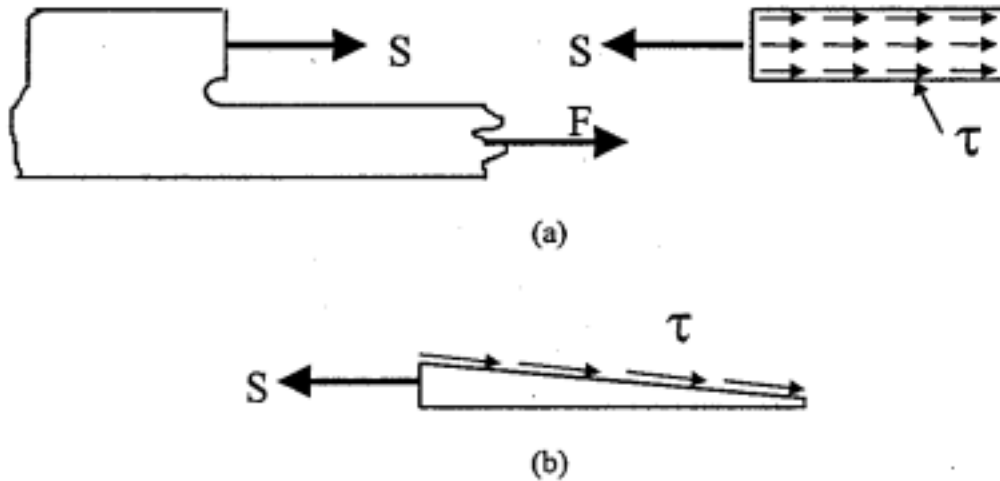


Figure 2-1. (a) Simplified transition piece. (b) Tail seen from the side.

The critical regions of stress have been identified as the radius between the tail and the conductor where they connect to the plate, but raised stresses in the insulation have been found also at the end of the tail.

2.1. Load

The tensile force in the TF-coil conductors is given by the interaction between the toroidal field and the current running through the coils. The D-shape of the coil has been chosen so that the varying magnetic field give mainly hoop stress.

The value of the perpendicular magnetic body-force B_r at a certain position in the coil is determined through calculating the *magnetic flux density* (magnetic field) B at that location and multiplying it with the *current density* J in the copper conductor.

The magnetic field varies with the distance to the centre of the torus as shown in Figure 2-2, and it is assumed that the field decreases linearly through the thickness of the coil to become zero at its outer edge (Figure 2-2).

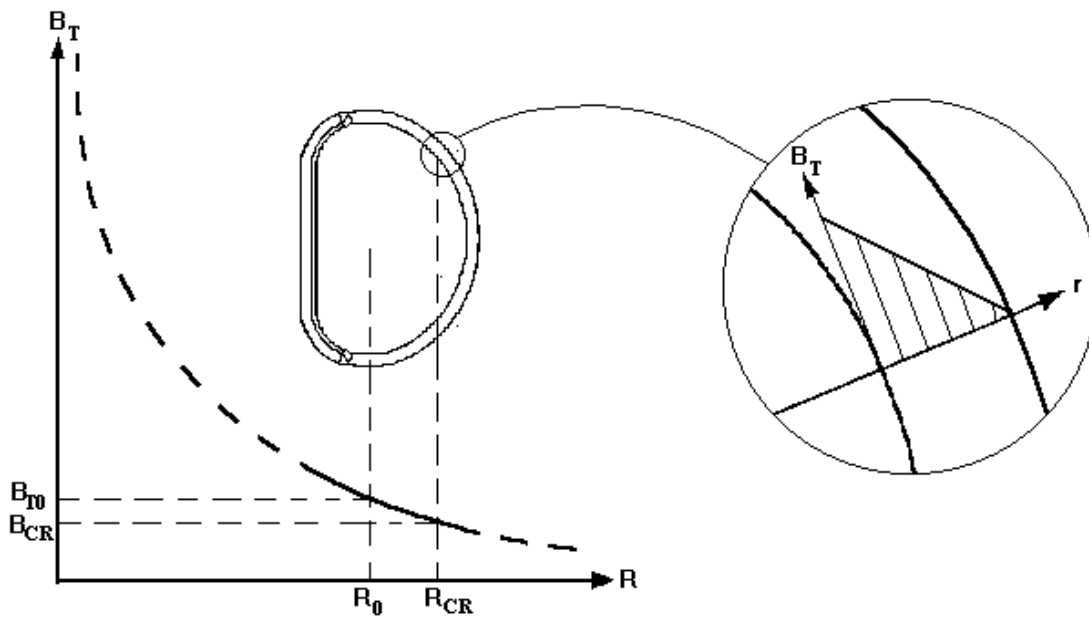


Figure 2-2. Variation of load on the TF-coils.

This assumption has been compared to results from calculations of the magnetic flux density made with a program developed for calculating magnetic fields using integration of Biot-Savart's law. A plot of the magnetic field through the thickness of the coil calculated with the BISON code is shown in Figure 2-3.

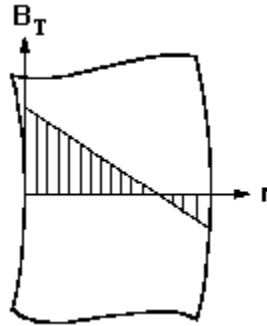


Figure 2-3. Magnetic field through the thickness of the TF-coil, calculated by Biot Savart integration.

The plot in Figure 2-3 shows that the field decreases linearly through the coil, as assumed, but instead of decreasing to zero at the outer edge as assumed in the calculations, it passes below zero and gives a field in the reverse direction at the outer part of the coil cross-section. The reason for this is believed to be *ripple effects* due to the discrete nature of the coil arrangement. Since the direction of field at the outer part is reversed, the radial force is also reversed and produces an inward force that counteracts the outward force on the inner part of the coil. The integrated outward force over the cross-section of the coil is therefore lower in reality than assumed in these calculations, making the assumption slightly pessimistic.

The outward radial force per unit volume of the conductor, B_r , is calculated as

$$B_r = J_{cond} B_T \tag{Equation 1}$$

where J_{cond} is the current density in the conductor and B_T is the toroidal magnetic field. The toroidal magnetic field B_T at a distance R from the centre of the torus is given by

$$B_T = B_{T0} \frac{R_0}{R} \quad \text{Equation 2}$$

where B_{T0} is the magnetic field at the major radius R_0 , referred to as the reference field and reference radius respectively. The field is produced by the current running through the conductors and since the parameter of interest is the magnetic field the current can be expressed as a function of magnetic field by the *Circuital law*. This gives the current in the conductor to

$$B_T = \frac{\mu_{TF} * 32 * 24}{2\pi R} = \frac{384\mu_{TF}}{\pi R} \quad \text{Equation 3}$$

where μ_{TF} denotes the permeability in air. $2\pi R$ is the path inside the torus, encircling the current in the straight inner part of the coils. The term $32*24$ in the denominator comes from the 32 TF-coils consisting of 24 conductors each. Equation 3 and Equation 2 in Equation 1 gives the radial magnetic body force caused by the interaction between the magnetic field and the coil current to

$$B_r = \frac{\pi(R_0 B_{T0})^2}{384 \mu_{cond} R} \quad \text{Equation 4}$$

where A_{cond} is the cross-sectional area of a conductor. It can be noted from Equation 4 that an increase in magnetic field will give a squared increase in body force. Equation 4 is the expression for the body force on the inner periphery of the coils where the force is fully developed. Since the magnetic field decreases when going outwards through the thickness of the coil, the expression must be adjusted for this variation as well. It has already been shown that the assumption that the force decreases linearly through the thickness of the coil is valid. The use of this assumption gives an expression on the form:

$$B_r = \frac{\pi(R_0 B_{T0})^2}{384 \mu_{cond} R} \left(1 - \frac{t}{T}\right) \quad \text{Equation 5}$$

where t is a co-ordinate in the normal outward direction of the coil starting from zero at the inner periphery of the coil. T in Equation 5 is the coil thickness in the normal direction. The result is a body-force on the coil that varies not only with the distance to the centre of the torus but also through the thickness of the coil.

2.2 Introductory hand calculations

Tensile stress in conductors

With the above-derived body-force it is possible to determine the hoop stress in the coil. The average radius to the centre-line of the coil in the transition sector is

$r_{mean,avg} = 2620.735$ mm. Comparing the thickness of the coil to its radius determines whether use of thin-wall theory is accepted. The ratio of mean radius to thickness is

$$\frac{r_{centre-line,avg}}{t} = \frac{2620.735}{358} \approx 7.3$$

Equation 6

As the use of thin-walled theory is recommended only for ratios of at least 10, thick-walled theory will be used to calculate the stress distribution through the thickness of the coil.

Treating the coil as a thick-walled cylinder makes it possible to derive an expression for the hoop stress in the coil in the inner conductor. Formulas for thick-walled cylinders subject to internal pressure or rotational acceleration are readily available in textbooks but for the variation of body force in this special case an expression needs to be derived. From a small element of a thick-walled cylinder - as pictured in an equilibrium equation can be set up.

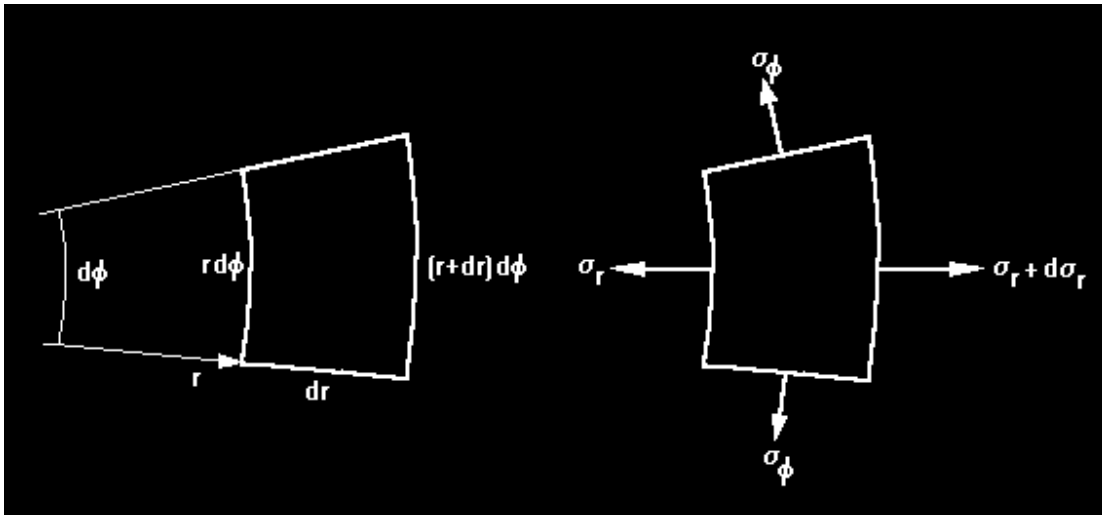


Figure 2-4. Stresses on a small element of a thick-walled cylinder.

Equilibrium gives

$$\sigma_r r d\phi + 2\sigma_\phi dr \sin\left(\frac{d\phi}{2}\right) - (\sigma_r + d\sigma_r)(r + dr)d\phi = B_r \frac{r + (r + dr)}{2} dr d\phi$$

Equation 7

where B_r is the radially acting body-force from the magnetic load. Letting $d\phi \rightarrow 0$ and $dr \rightarrow 0$ gives

$$\sigma_r + r \frac{d\sigma_r}{dr} - \sigma_\phi = -rB_r$$

Equation 8

Compatibility and the constitutive equations according to Hooke's generalised law for linearly elastic material together with the expression for B_r , as written in Equation 5 yields

$$r^2 \frac{d^2 \sigma_r}{dr^2} + 3r \frac{d\sigma_r}{dr} - (3 + \nu)kr^2 + (2 + \nu)mr = 0 \quad \text{Equation 9}$$

This is an Euler type differential equation which has the solution

$$\sigma_r = C_1 + C_2 r^{-2} + \frac{3 + \nu}{8} kr^2 - \frac{2 + \nu}{3} mr \quad \text{Equation 10}$$

The two constants C_1 and C_2 are determined with boundary conditions, which in this case are zero radial stress at the edges. Using values of radius and magnetic field at the inner edge of the coil, averaged over the connection region, gives expressions for the stresses in a circular coil with constant magnetic force. This is the condition which the coils were made to produce (giving mainly tensile stresses) which makes the simplification seem valid.

Equation 10 assumes a solid cross-section of the coil with the whole cross-section being subject to the magnetic force, but in reality the coil is built up by layers of insulation and copper. The insulation does not conduct any current and is thereby not subject to any force which means that the total force acting on the layered cross-section is less than the one given by the obtained expression. Scaling the stress with the ratio of copper area of the cross-section to total area gives an approximation of the real stress distributions, shown in figure 2-5.

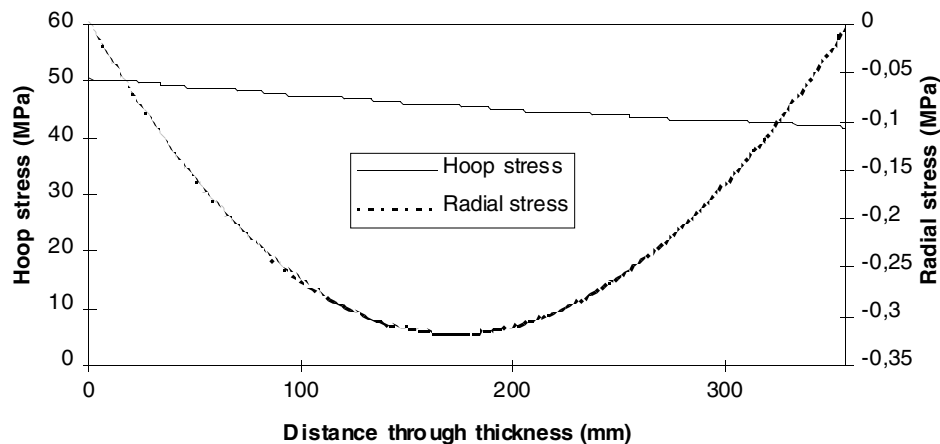


Figure 2-5. Stresses in coil, scaled analytical expression for a magnetic field of $BT_0=3.45 \text{ T}$. Note that the radial component is compressive.

It can be seen in figure 2-5 that the tensile stress in the innermost conductor is approx. 50MPa. Multiplying this stress with a Stress Concentration Factor for the radius where the conductor joins the plate we get a stress of

$$\sigma_{SCF} = SCF * \sigma_{cond} = 2.8 * 50 = 140 \text{ MPa}$$

Shear stress in insulation

Calculating the average shear stress over the area of the tails using the symbols in Figure 2-1 with $F=50\text{MPa}\cdot A_{cond}$ from the paragraph above gives $\tau_{avg}=2.7\text{MPa}$. In the real case a uniform level of stress is not obtained, the stress peaks at the ends. This can be shown analytically by solving the system of differential equations for the stresses. Note that the calculations are only valid for a tail with uniform thickness.

To find the distribution of shear stress at the edge of the tails (uniform thickness considered), a situation according to Figure 2-6 is obtained.

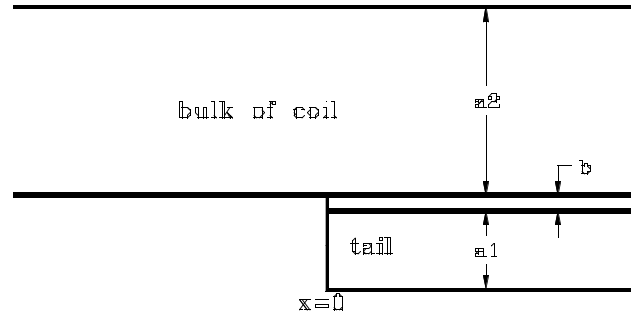
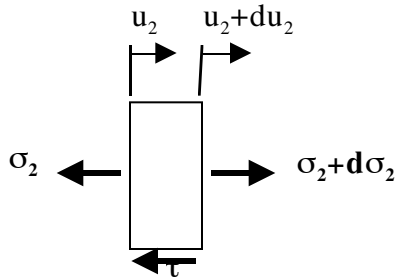


Figure 2-6. Detail over tail end (tail of uniform thickness).

Assuming a uniform shear through the insulation thickness b gives for a small piece (length dx) of the conductor:



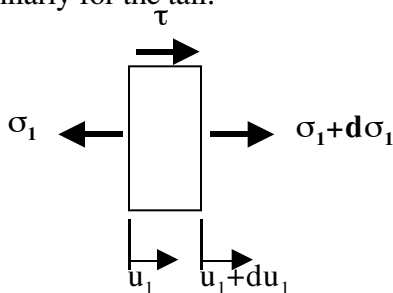
A force equilibrium gives:

$$\diamond \quad \sigma_2 a_2 + d\sigma_2 a_2 - \sigma_2 a_2 - \tau dx = 0 \quad ? \quad \tau = a_2 \frac{d\sigma_2}{dx} \quad \text{Equation 11}$$

Compatibility gives

$$\epsilon_2 = \frac{du_2}{dx} \quad ? \quad \sigma_2 = E \frac{du_2}{dx} \quad \text{Equation 12}$$

Similarly for the tail:



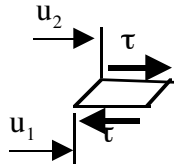
Force equilibrium:

$$\diamond \sigma_1 a_1 + d\sigma_1 a_1 - \sigma_1 a_1 + \tau dx = 0 \quad ? \quad \tau = -a_1 \frac{d\sigma_1}{dx} \quad \text{Equation 13}$$

Compatibility gives:

$$\epsilon_1 = \frac{du_1}{dx} \quad ? \quad \sigma_1 = E \frac{du_1}{dx} \quad \text{Equation 14}$$

For a small piece of the insulation, the following situation is obtained:



Compatibility gives:

$$\gamma = \frac{u_2 - u_1}{b} \quad ? \quad \tau = G \frac{u_2 - u_1}{b} \quad \text{Equation 15}$$

Combining the above equations gives:

$$\frac{d^2}{dx^2}(u_2 - u_1) - \frac{2G}{Eb} \left[\frac{1}{a_1} + \frac{1}{a_2} \right] (u_2 - u_1) = 0$$

This is a differential equation with the solution:

$$u_2 - u_1 = C_1 e^{\frac{x}{L}} + C_2 e^{-\frac{x}{L}} \quad \text{where } L = \sqrt{\frac{Eb}{2G \left[\frac{1}{a_1} + \frac{1}{a_2} \right]}}$$

Assuming that the shear angle, and thereby $u_1 - u_2$, will be constant when x is large (away from the end) gives $C_1 = 0$. The other boundary conditions are that $\sigma_2 = \sigma_0$ for $x=0$ and $\sigma_2 = \sigma_0 / (1 + a_1/a_2)$ for $x \rightarrow \infty$. σ_0 is the tension in the coil conductors. With $E=120\text{GPa}$, $G=1\text{GPa}$, $a_1=3\text{mm}$, $a_2=336\text{mm}$, $b=2\text{mm}$ and $\sigma_0=50\text{MPa}$ gives:

$$\tau = 5.7 e^{-\frac{x}{L}} \quad \text{where } L \approx 27\text{mm}$$

Thus we would expect a peak shear stress of **5.7 MPa** in the insulation at the end of the tail and a peak stress of approx. **140 MPa** in the copper at the radius where the conductor joins the plate.

2.3. FE Model

The final FE model covers approx. 2 m of the coil at the transition region. The innermost copper and insulation layer have been explicitly modelled whereas solid blocks represent the rest of the turns, one block for each pancake. The innermost layers were modelled as

densely as practically possible and the two solid blocks were coarser. The connection between the differing mesh sizes was accommodated by the “Tied Contact” command in ABAQUS.

The transition piece and adjacent insulation were meshed with eight-node linear brick elements (ABAQUS C3D8), using only one element through the thickness since no bending in this direction was expected. The mesh was concentrated to the corner radius and at the end of the tails. The overall mesh density was rather coarse, a total of 1996 elements, in order to check the model behaviour and the computing time before making further refinements. Since the insulation was meshed with the same mesh pattern as the transition piece, quite high aspect ratios were obtained due to the relatively thin insulation layer. Separate shear tests were made on elements of this type, size and shape and they showed that elements used for modelling the insulation behave well in shear even with high aspect ratios if the stress/displacement gradient is low. The model of the transition piece and attached insulation can be found in Figure 2-7 and Figure 2-8 below.

The curved beam with smeared properties (simulation the layered structure of copper/insulation) was modelled with quadratic 20-node brick elements with two elements through the thickness. The inter-pancake insulation was explicitly modelled. The model with smeared beam can be seen in Figure 2-9.

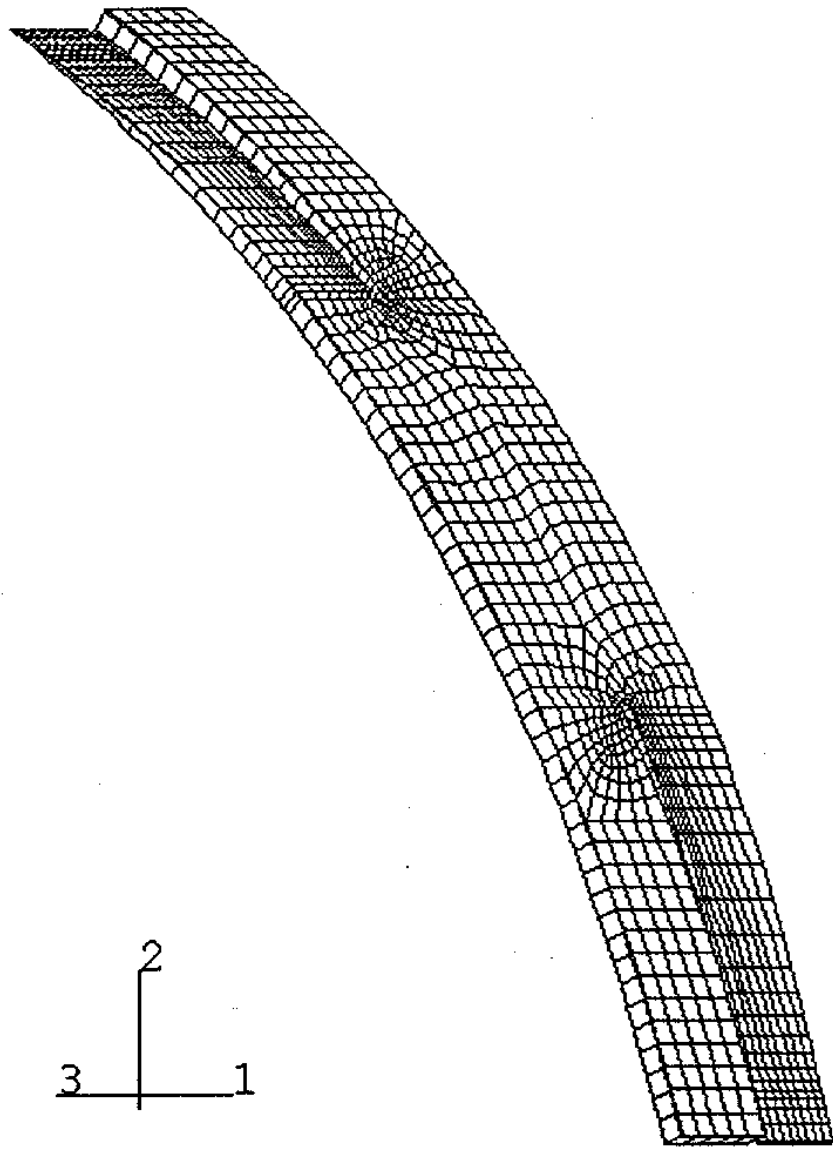


Figure 2-7. Geometry and mesh pattern of FEM6.

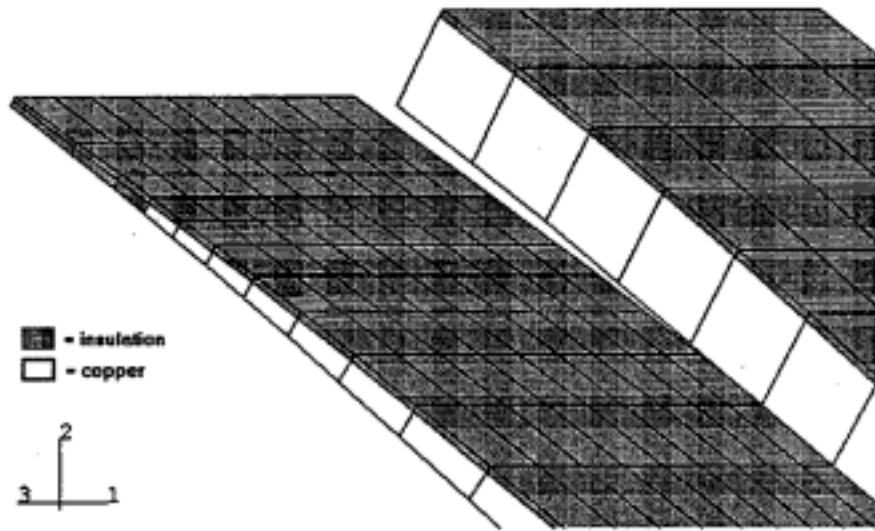


Figure 2-8. Detail of the tail end of FEM6

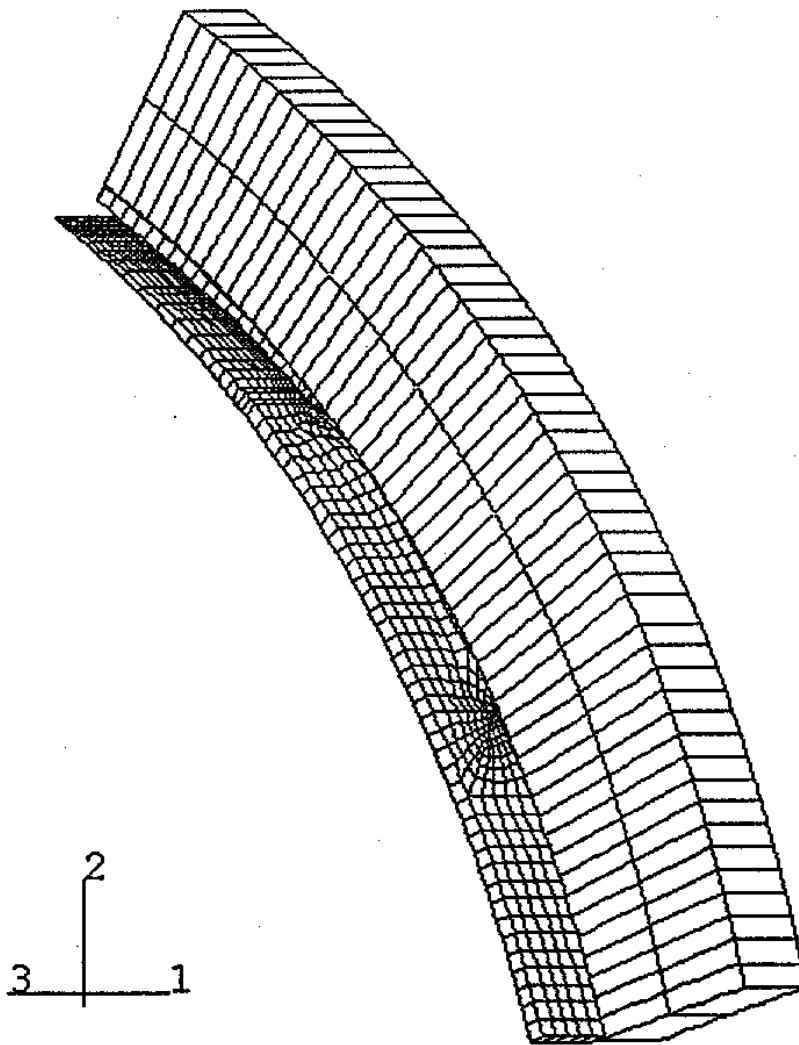


Figure 2-9. FEM6 with one of the smeared beams removed for the sake of clarity.

24. Boundary Conditions and Load

The ends of the model were constrained to radial displacement only, in co-ordinate systems corresponding to the position in the real coil, as shown in Figure 2-10.

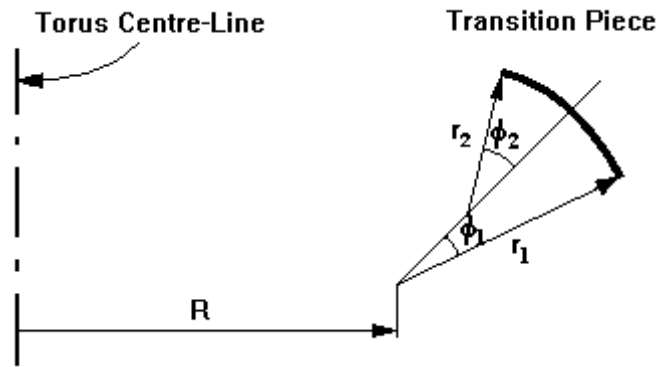


Figure 2-10. Transition piece in relative to Torus centre line

The expression for the magnetic load, depending on the position in the coil, was used directly in the FE model through the subroutine DLOAD (ABAQUS) that enables user specified varying body force. The force pushes the model radially outwards, and as the ends are constrained only to move radially the model is put under tension in the longitudinal direction. Of course only the parts that carry current - the conductors and the plate, not the tails - are subject to the magnetic load.

25. Results

The total number of user-defined elements was 2208 but the software generates internal elements for the contact command connecting faces with differing mesh patterns, so the total number of elements was 6384. The total number of variables (degrees of freedom plus any Lagrange multiplier variables) was 20256 and the allocated workspace was 103 Mb. The total CPU time was only 215 seconds, but the total running time on the network was about 40 minutes.

The displaced shape of the transition piece is shown in Figure 2-9.

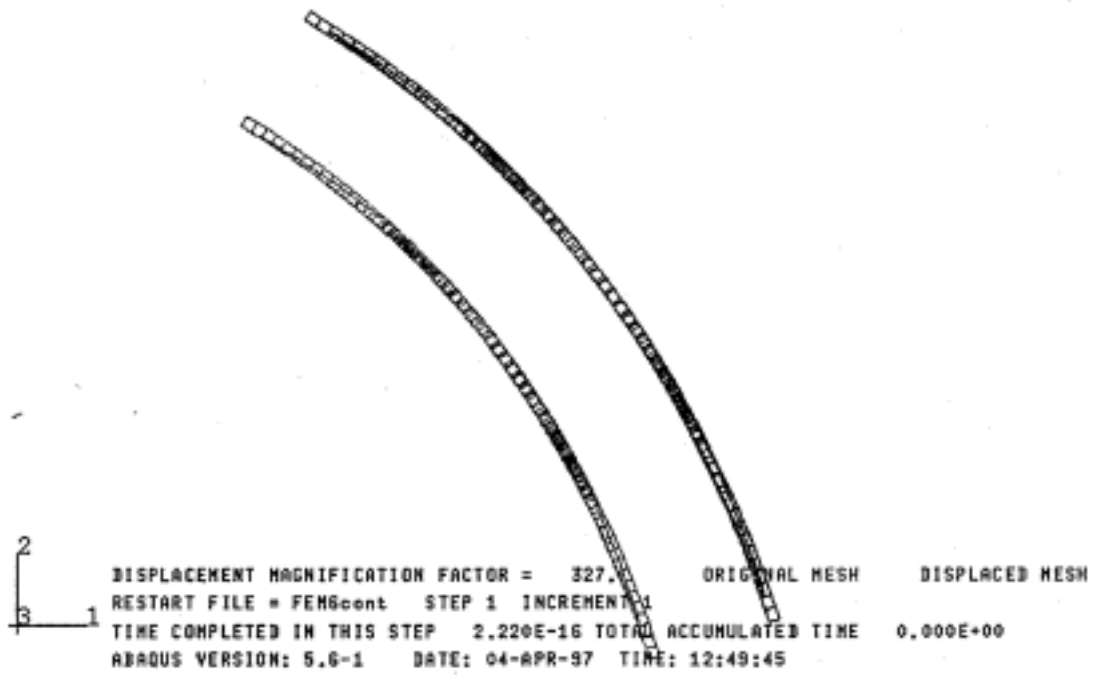


Figure 2-11. Deformed shape of curved model supported by a curved beam (FEM6).

Copper

The tensile stress in the smeared beam is more or less uniformly distributed through the thickness, indicating that the in-plane bending stress is small. A contour plot of the von Mises equivalent stress in the innermost layer at the conductor-plate-tail joint can be found in Figure 2-12.

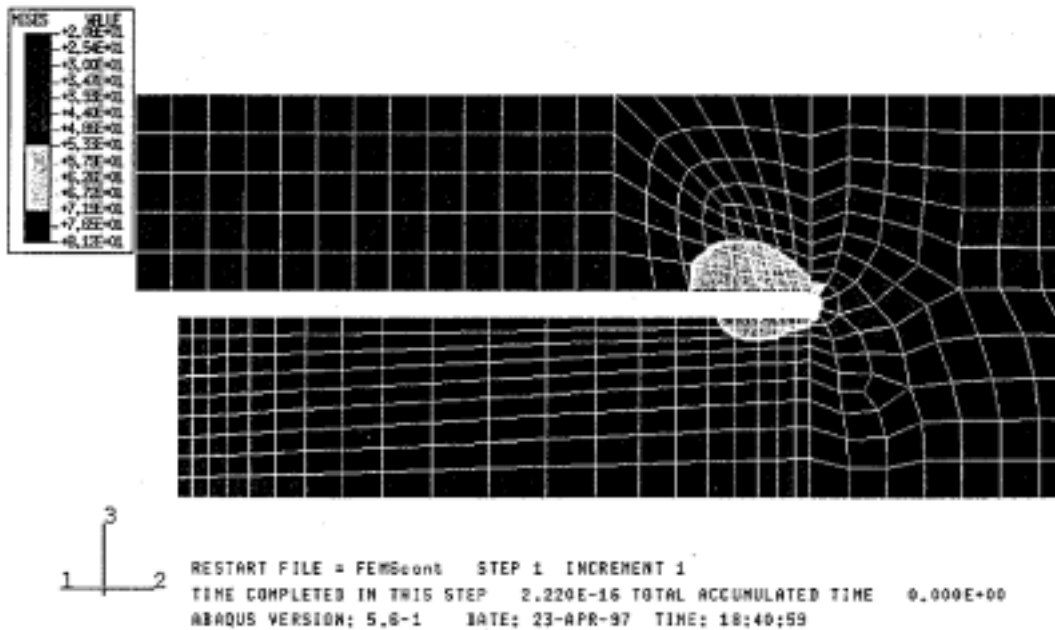


Figure 2-12. Von Mises equivalent stress in the copper (FEM6).

The stress in the conductors, away from the corners, shows uniform values agreeing well with the membrane stresses calculated with simpler models, the stress being about $\sigma_{\text{Hoop, inner turn}} = 50$ MPa.

The maximum stress in the copper was, as expected, found at the radius in the corner between the conductor and the plate. The maximum value was $\sigma_{\text{max}} = 75$ MPa, although the mesh of the model is believed not to be fine enough for the results to be converged. A detailed picture of the von Mises equivalent stress in the corner is shown in Figure 2-13. It shows some inter-element discontinuities where the maximum value is found, an indication that the mesh needs to be refined.

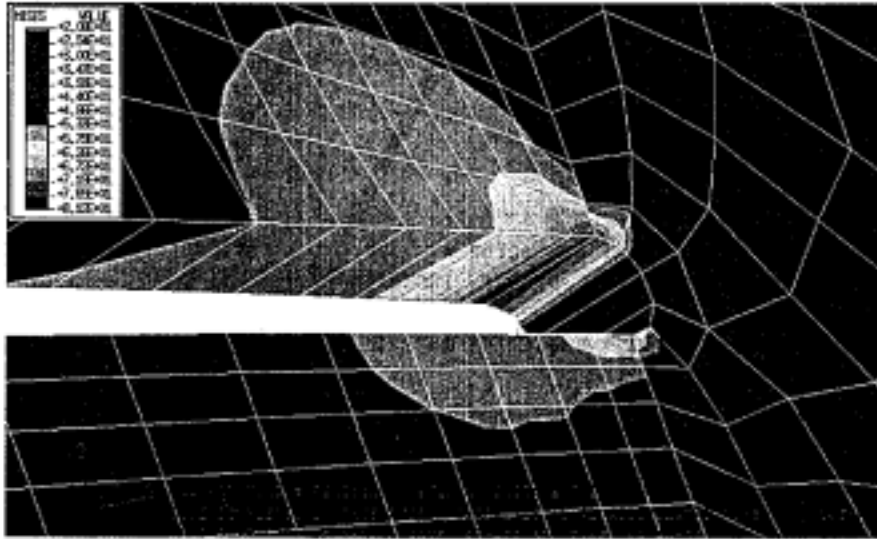


Figure 2-13. Von Mises equivalent stress in the corner of the transition piece (FEM6).

Insulation

Figure 2-14 shows the shear stress in the insulation at the same position.

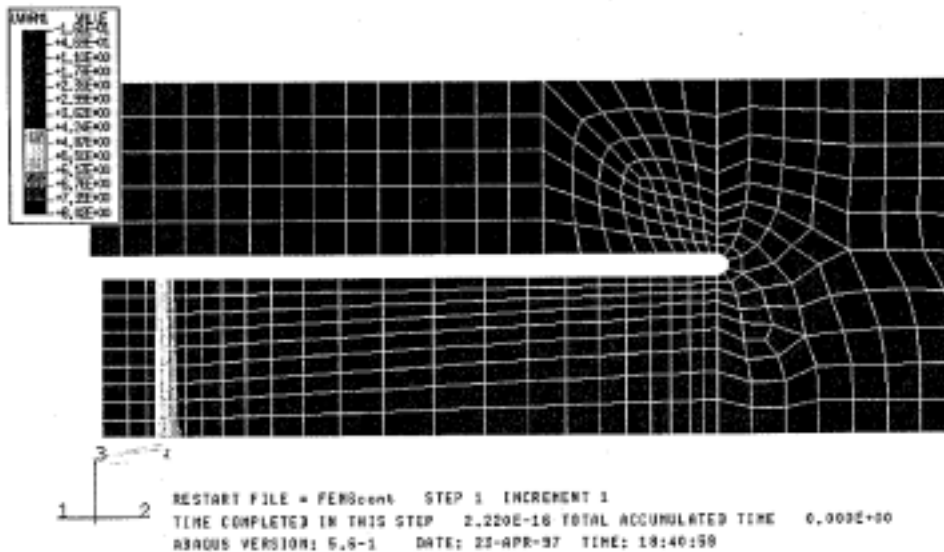


Figure 2-14. Shear stress in insulation (FEM6).

The bulk of shear is found in the insulation attached to the tails with a peak at the end. The value of longitudinal shear stress along a path from the end of the tail through the transition piece and the conductor (see Figure 2-15) shows a fairly uniform shear stress along the tail with a peak at the end and only very low values on the plate and conductor.

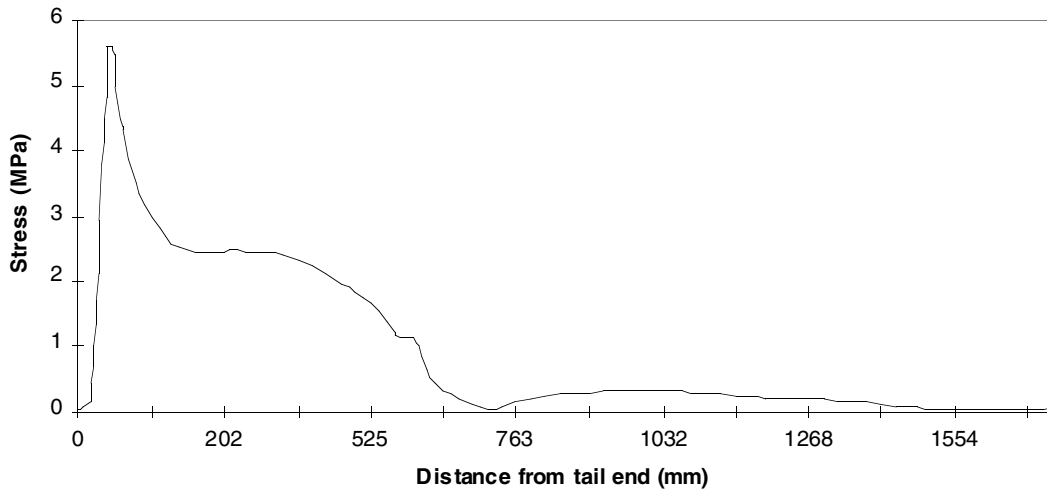


Figure 2-15. Shear stress in insulation along a path from the end of the tail to the conductor (FEM6, $B_{T0}=3.4T$).

The peak stress in the corner is not believed to be fully converged, refinement of the mesh is needed (see coming paragraphs).

The peak shear stress in the insulation is perhaps not fully converged either but the insulation is considerably softer than the copper and does not show a peak as sharp as that in the copper. The value of peak shear conforms quite well to what previous models have shown; the plane models showed a peak stress of $\sigma_{max}=5.1$ MPa (see chapter 5.1.4.2).

Result summary

A summary of the stresses obtained in FEM6 can be found in table 2-1 below.

Table 2-1. Maximum stresses obtained in FEM6.	
	Stress (MPa)
Hoop stress in innermost conductor	49.9
Peak stress in corner	75.0
Peak shear stress at tail end	5.9

The hoop stress in the conductor conforms well with the anticipated ($\sigma=50$ MPa), a fact that adds reliability to the geometry of the model and the choice of boundary conditions.

The max. stresses are peak stresses and they are not believed to be converged with this initial mesh, refinement of the mesh is needed (see next paragraph).

Sub-model of corner region (FEM7)

The highest stress gradient in this problem is concentrated to the corner and the tail end, but the tail end is assumed not to be a problem because the insulation is much more

compliant than the copper and therefore not so sensitive to peak stresses. Refinement of the FE mesh was therefore, at this stage, concentrated to the corner area.

Sub-modelling technique was used to create a detailed local mesh that uses the displacement results from the main model as boundary conditions at its perimeter. The procedure is valid since the local behaviour in the corner does not change the global behaviour of the structure when the mesh is locally refined.

The mesh of the sub-model can be seen in Figure 2-16, note that the insulation layer now continues over the radius. This has been done in order to better monitor the shear stresses in the insulation, and reduce the influence of edge effects due to the modelling.

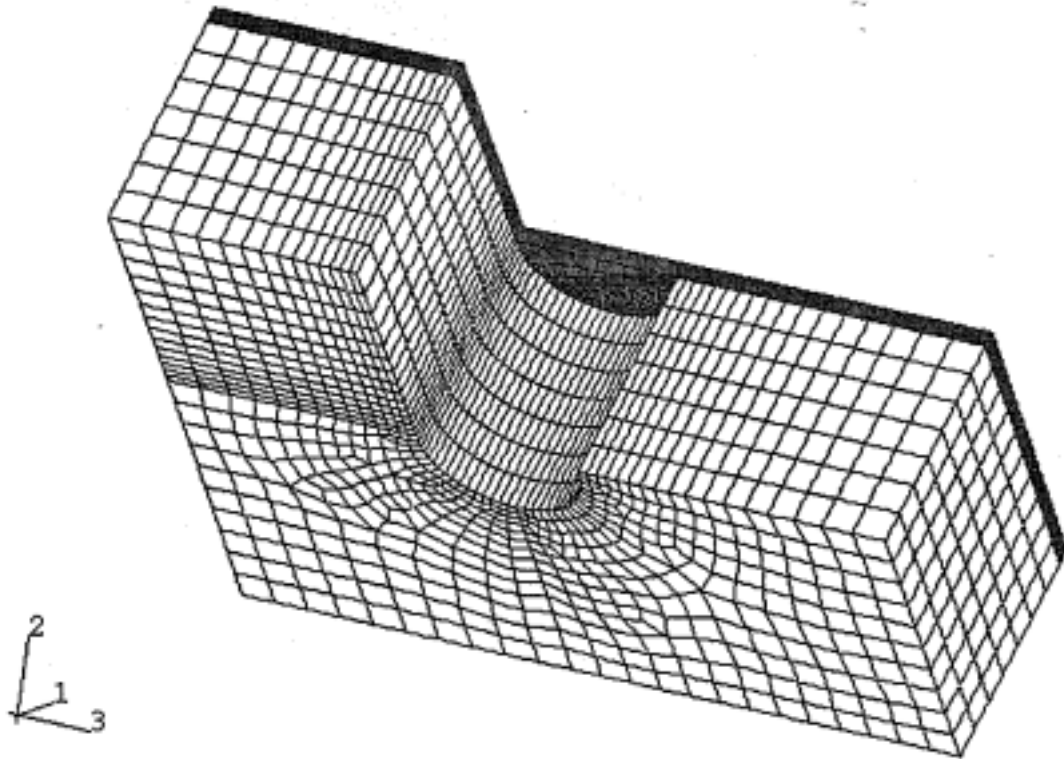


Figure 2-16. Mesh pattern of sub-model over corner (FEM7).

Results from sub-model (FEM7)

The maximum stresses in the copper and insulation can be found in table 2-2.

Table 2-2. Stress results from sub-model (FEM7).	
	Maximum stress (MPa)
In copper	104.6
In insulation	5.04

It can be noted that the shear stress in the insulation is not far from what was given at the tail ends in FEM6 ($\sigma_{\max}=5.9$ MPa). A check of the shear stress in the corner of FEM6 showed a value of $\sigma_{\text{corner}}=4.4$ MPa, meaning that the local mesh refinement gave an increase in shear stress of about 14%. The step in mesh refinement is too large to give an adequate judgement of whether this value has converged or not.

The peak stress in the copper increased 40% compared to the previous mesh (FEM6). This can be expected, since there is a stress concentration in the corner and the coarse mesh of one row of linear elements with an edge length of about 6 mm is refined considerably when improved in one step to seven rows of quadratic elements with an edge length of 1 mm. It cannot be recommended from a FE technical point of view to use such a large step in mesh refinement, convergence should preferably be monitored by making smaller refinements and checking how the results change. However, in this model the meshing of the structure is very time consuming and time was limited, so further refinements and convergence control were not attempted.

2.6. Scaling to 4T

Calculations up to here were made

- for a field of 3.45T, the stresses need to be scaled to 4T
- with $G_{\text{insulation}}=1\text{GPa}$, which needs to be changed to 4GPa
- ignoring the copper packing factor effect, which means that the stresses have to be scaled up by 15%

These factors are corrected in the following tables.

All stresses in MPa	Stress in the copper		Shear stress in the insulation	
	membrane σ_{membrane}	maximum $\sigma_{\text{Von Mises}}$	at end of tail τ_{max}	in corner τ_{max}
$G_{\text{insulation}}=1000\text{ MPa}$	76.5	116	9.2	6.8
$G_{\text{insulation}}=4000\text{ MPa}$	75.4	112	11.1	17.2

All stresses in MPa.	Maximum stress	
	in copper σ_{max}	in insulation τ_{max}
$G_{\text{insulation}}=1000\text{ MPa}$	162	7.8
$G_{\text{insulation}}=4000\text{ MPa}$	158	17.4

3. Thermal analysis

Added to the mechanical load on the TF-coils, there is a thermal component due to the Ohmic heating of the copper when the current flows through it. The areas of large thermal stresses are; around the coolant inlets and outlets, between the hot conductor and the cold tail. To study the latter, a thermal analysis of the FE model was performed.

To the existing FE model was added ground insulation and insulation in all hollows of the coil, between tail and conductor at the radius for example. The analysis was performed in two steps:

1. Thermal analysis, steady state and transient to find the temperature distribution in the structure at different times.
2. Stress analysis using the temperature profile from the thermal analysis and the magnetic load as before.

3.1. Thermal analysis

The thermal analysis was performed in two steps, one steady state to get the temperature between the pulses and one transient during the pulse.

The first step was done simulating the coolant flowing in the coil and thereby keeping all conductors at 10°C. Hot air was circulating around the coil on the outside, providing (forced) convection heating through the ground insulation.

The second, transient, step was implemented through specifying a temperature/time curve for the conductors. This curve has been derived earlier (Appendix F) and is believed to give the correct conductor temperature in time during the pulse.

Since the magnetic field is applied as a piecewise linear function – linear ramp up, constant flat-top and linear ramp down – the maximum combination of stresses occur when the temperature is as high as possible when the magnetic field is still at full value. This occurs at the end of the flat-top of the current pulse. At this time, the thermal analysis is stopped and the results are saved for use in the stress calculation. A plot of the temperature versus time is found in Figure 3-1 below.

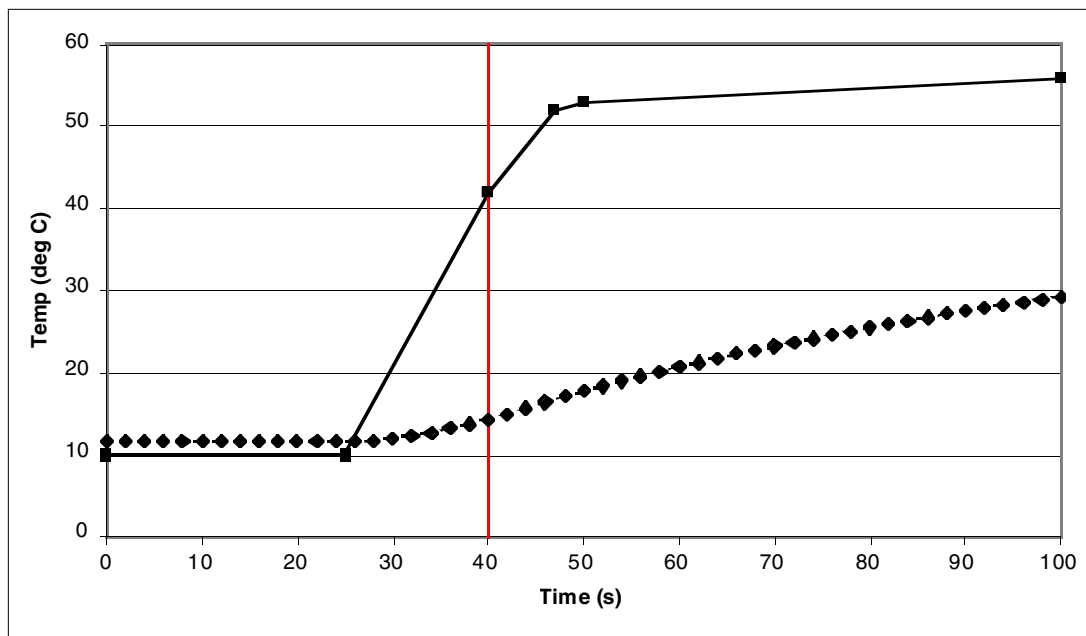


Figure 3-1. Temperature vs. time in tail and adjacent conductor. The temperature distribution is saved for stress analysis at t=40s (end of current flat-top) marked in red.

The temperature in the conductor at t=40s is 42°C and in the tail 14°C so the differential is approx. 28°C.

3.2. Stress analysis

Hand calculation

Using the same formulae as is in paragraph 2.2, with an added expression for the thermal strain, the peak stress can be found in the same way as before. The magnetic contribution is the same but to this we have to add the thermal stress, see Table 3-1 below for details.

Table 3-1. Hand calculated peak shear stresses at the tail-end.	
	Stress (MPa)
Magnetic stress	15
Thermal stress	13
Combined	28

3.3. FE model

The temperature profile from the thermal analysis at the end of the flat top was used together with the distributed body-force as before and the stresses were calculated automatically. The initial model showed very high peak stresses at the tail-end, see Figure 3-2 and Figure 3-3 below.

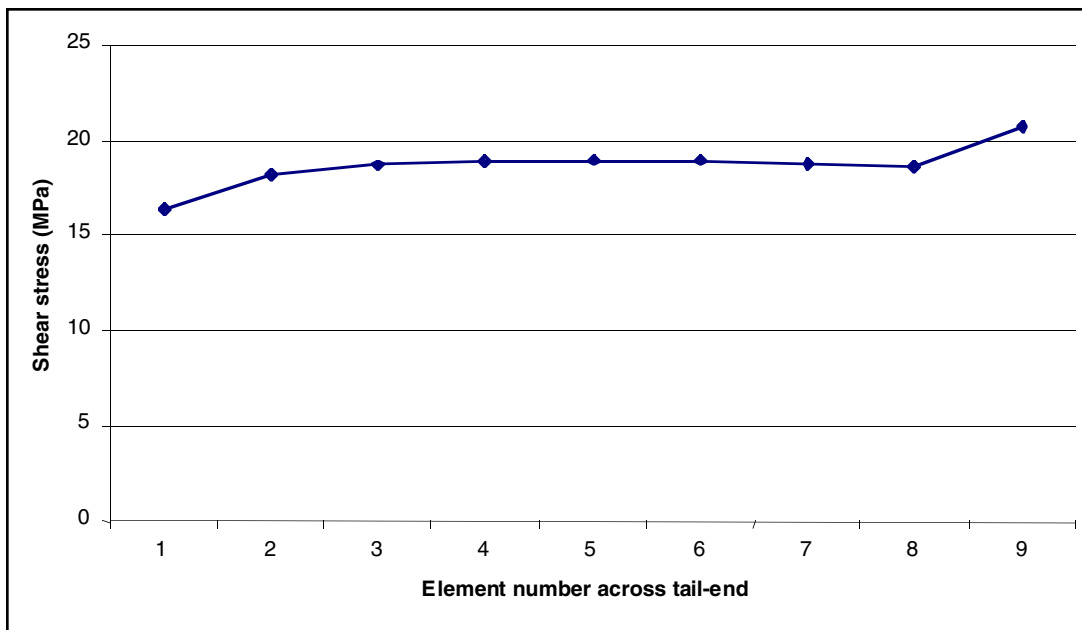


Figure 3-2. Shear stress across tail-end in FEM6, $B_{T0}=4T$ and $I^2t=12e10 A^2s$.

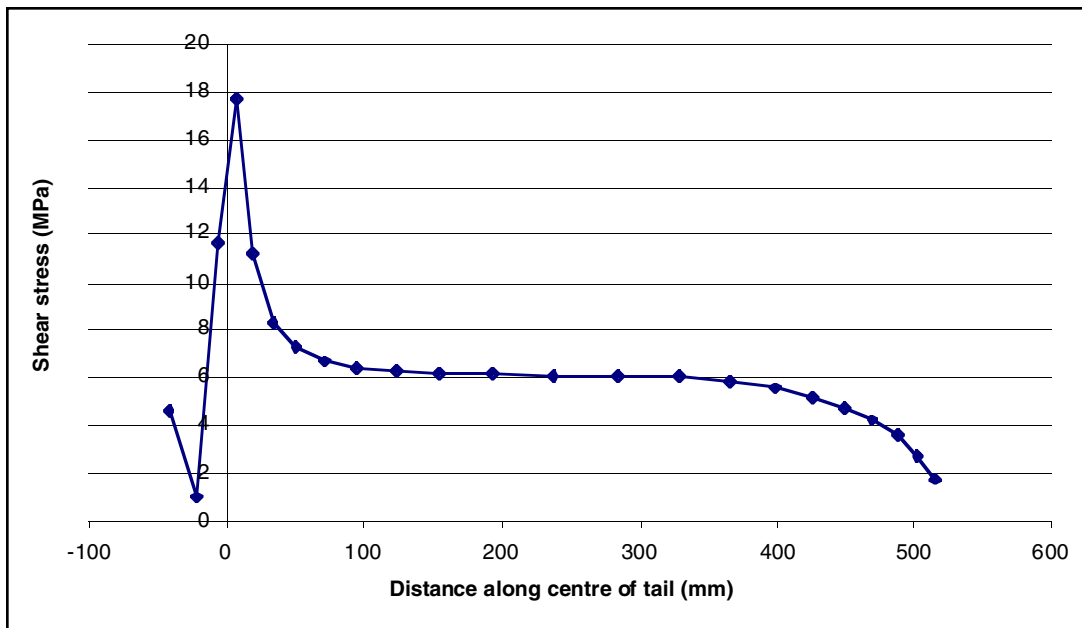


Figure 3-3. Shear stress along centre of tail in FEM6, $B_{T0}=4T$ and $I^2t=12e10 A^2s$.

The peak stress is clearly not well modelled, a refinement of the mesh is necessary. For this reason a sub-model over the tail-end was made. It is shown in Figure 3-4 below.

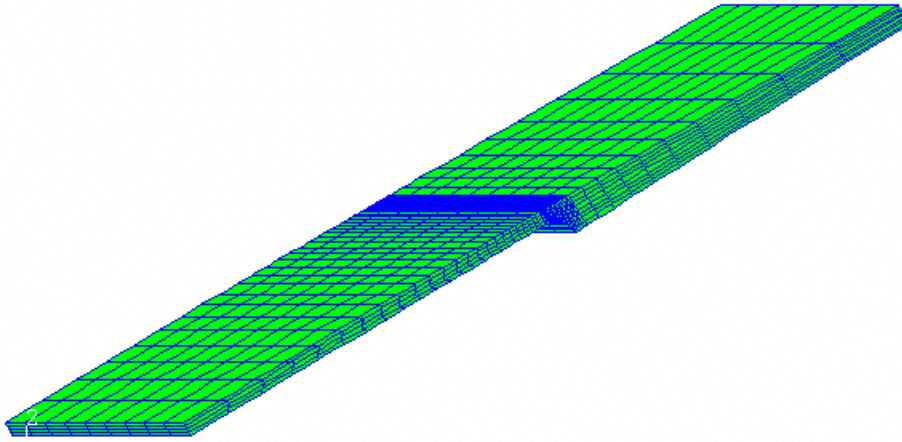


Figure 3-4. Sub-model over tail-end. Only the insulation is shown. The main body of the coil is above the insulation and the tail below fits into the indentation of the insulation.

The sub-model was meshed with consecutively finer meshes and the last mesh also included the smooth radius at the tail-end. A figure of the stresses along the centre of the tail for the different meshes is found in Figure 3-5.

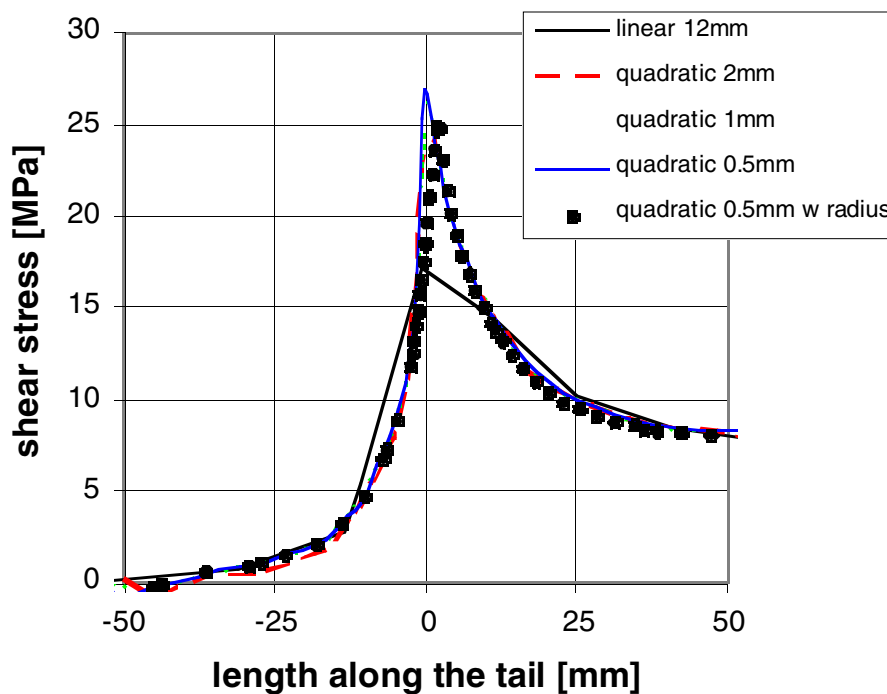


Figure 3-5. Shear stress along centre of tail for different meshes in sub-model over tail-end.

3.4. Results

The added thermal strain on the tail gives high combined shear stresses. The analysis of a 78kA pulse with a total I^2t of $112e9 \text{ A}^2\text{s}$ gave the stress in the middle of the insulation of 25 MPa, close to the 28MPa predicted with hand calculation.

3.5. Thicker insulation at the tail

The drawing of the TF-coils states that the inter-turn insulation thickness at the tail-end is 3mm, not 2mm as was used in the calculations. It is however impossible to see in this drawing how the thickness varies over the length of the tail: Does it taper out over the whole tail length? Does it taper out only close to the tip?

Both cases would reduce the calculated shear stresses in the insulation, but by varying amounts. The least reduction would be seen with a thickness tapering from 2mm at the root of the tail to 3mm at the tip. The largest reduction would be seen with the thickness tapering out only where the stresses start to go up, i.e. some small distance from the tip. Some FE calculations were made on these two cases, the last case with a tapering distance of 50mm.

Table 3-2. Stress reductions according to tapering length.

	Max. int. pt. shear stress (MPa)
2mm insulation (original calculation)	31.0
3mm tapering over whole tail length (525mm)	25.4
3mm tapering over last 50mm	24.3

The reductions in max stresses is 18% and 22% respectively, figures that compare well with the analytically derived $1/\sqrt{b}$ (b is the constant insulation thickness over the tail) dependency on stress from the analysis in paragraph 2.2:

$$reduction = \frac{2}{3} - \frac{\sqrt{2}}{\sqrt{3}} * 100\% = 18\%$$

To achieve larger reductions in peak stress, one would need to taper the thickness over an even shorter length, comparable to the characteristic length of the solution to the differential calculations for the stresses (~15mm, see paragraph 2.2). This is however not likely to be the case in the coil.

4. References & Lists

4.1. Reference

Mikael Sjöholm, Stress Analysis of Magnetic Field Coil in the Joint European Torus, October 1997, Thesis for the Degree of Master of Science, Division of Solid Mechanics, Chalmers University of Technology

4.2. List of Figures

Figure 1-1. Cut-out of a TF-coil at the connection region, transition piece shown.	2
Figure 1-2. Inter-pancake transition piece	2
Figure 2-1. (a) Simplified transition piece. (b) Tail seen from the side.	3
Figure 2-2. Variation of load on the TF-coils.	4
Figure 2-3. Magnetic field through the thickness of the TF-coil, calculated by Biot Savart integration.	4
Figure 2-4. Stresses on a small element of a thick-walled cylinder.	6
Figure 2-5. Stresses in coil, scaled analytical expression for a magnetic field of $B_{T0}=3.45$ T. Note that the radial component is compressive.	7
Figure 2-6. Detail over tail end (tail of uniform thickness).	8
Figure 2-7. Geometry and mesh pattern of FEM6.	11
Figure 2-8. Detail of the tail end of FEM6	12
Figure 2-9. FEM6 with one of the smeared beams removed for the sake of clarity.	12
Figure 2-10. Transition piece in relative to Torus centre line	13
Figure 2-11. Deformed shape of curved model supported by a curved beam (FEM6).	14
Figure 2-12. Von Mises equivalent stress in the copper (FEM6).	14
Figure 2-13. Von Mises equivalent stress in the corner of the transition piece (FEM6).	15
Figure 2-14. Shear stress in insulation (FEM6).	15
Figure 2-15. Shear stress in insulation along a path from the end of the tail to the conductor (FEM6, $B_{T0}=3.4$ T).	16
Figure 2-16. Mesh pattern of sub-model over corner (FEM7).	17
Figure 3-1. Temperature vs. time in tail and adjacent conductor. The temperature distribution is saved for stress analysis at $t=40$ s (end of current flat-top) marked in red.	20
Figure 3-2. Shear stress across tail-end in FEM6, $B_{T0}=4$ T and $I^2t=12e10$ A ² s.	21
Figure 3-3. Shear stress along centre of tail in FEM6, $B_{T0}=4$ T and $I^2t=12e10$ A ² s.	21
Figure 3-4. Sub-model over tail-end. Only the insulation is shown. The main body of the coil is above the insulation and the tail below fits into the indentation of the insulation.	22
Figure 3-5. Shear stress along centre of tail for different meshes in sub-model over tail-end.	22

4.3. List of Tables

Table 2-1. Maximum stresses obtained in FEM6.	16
---	----

Table 2-2. Stress results from sub-model (FEM7).	17
Table 2-3. Stress results from FEM6, $B_{T0}=4.0$ T.	18
Table 2-4. Stress results from sub-model (FEM7), $B_{T0}=4.0$ T.	18
Table 3-1. Hand calculated peak shear stresses at the tail-end.	20
Table 3-2. Stress reductions according to tapering length.	23

Stresses and Cracks at the TF Coil Tails

V. Riccardo
26 October 1999

Contents

1. Introduction.....	1
2. Cracks at the tip of the tail.....	2
2.1. FE models with cracks.....	6
2.2. Effect of a small delamination on stress fields.....	9
3. Large delaminations.....	12

1. Introduction

This note describes further work on the model of the coil connection region introduced in Appendix D.

Stresses at the tail tips are calculated using a sub model, small cracks are introduced and the fracture energy calculated.

Large cracks extending over several metres are also studied and it is shown that friction will eventually stop the crack.

2. Cracks at the tip of the tail

In Fig. #1a and #1b the radial stress (S11) is plotted on a -25/+25 MPa scale for the 2D tail and the 3D tail-submodel respectively. Both models show a peak on the top of the tip of about 25 MPa and an increased tension towards the sharp end of the of the tail (more pronounced in the 2D model). In addition the radial field goes approximately to zero on the free surface of the ground wrap (as it should).

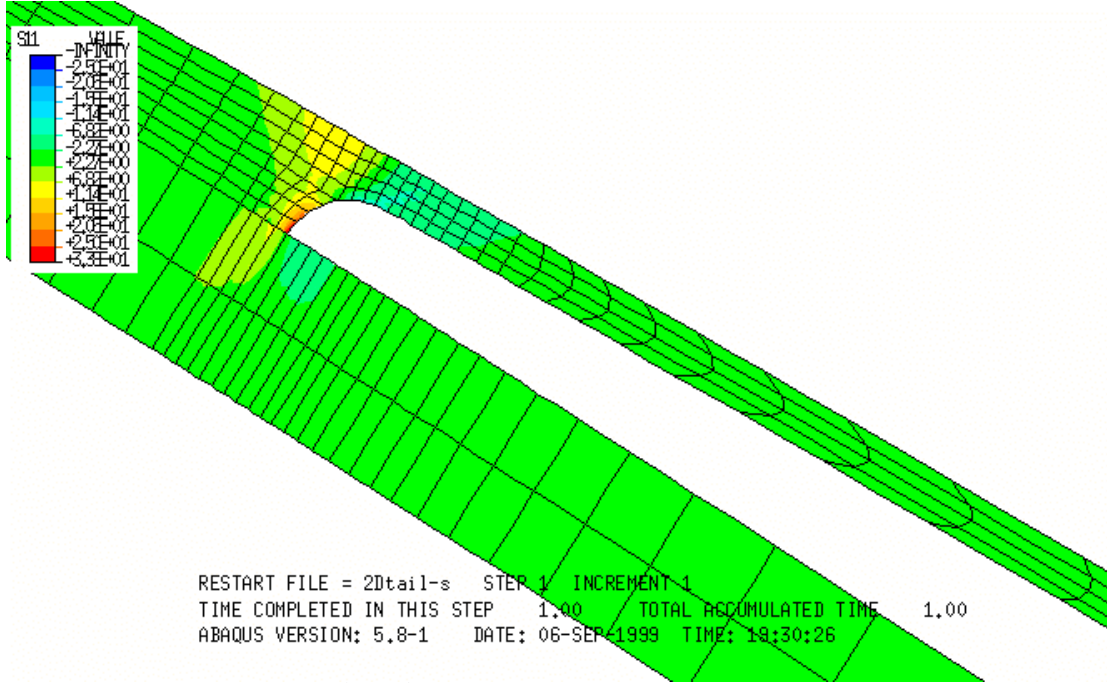


Fig. #1a Radial tensile stress (2Dtail)

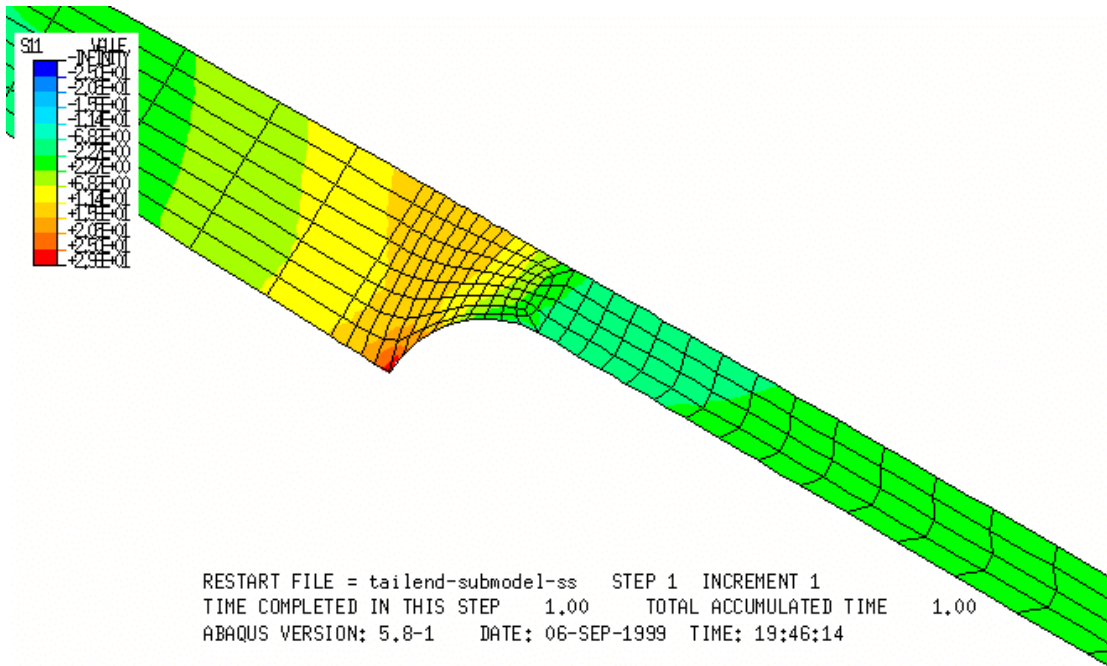


Fig. #1b Radial tensile stress (tail-submodel)

The axial stress (S22) is plotted in Fig. #2a and #2b for the 2D tail and the 3D tail-submodel respectively on a -40/+40 MPa scale. Both models show a peak at the curved end of the tail (about 30 MPa).

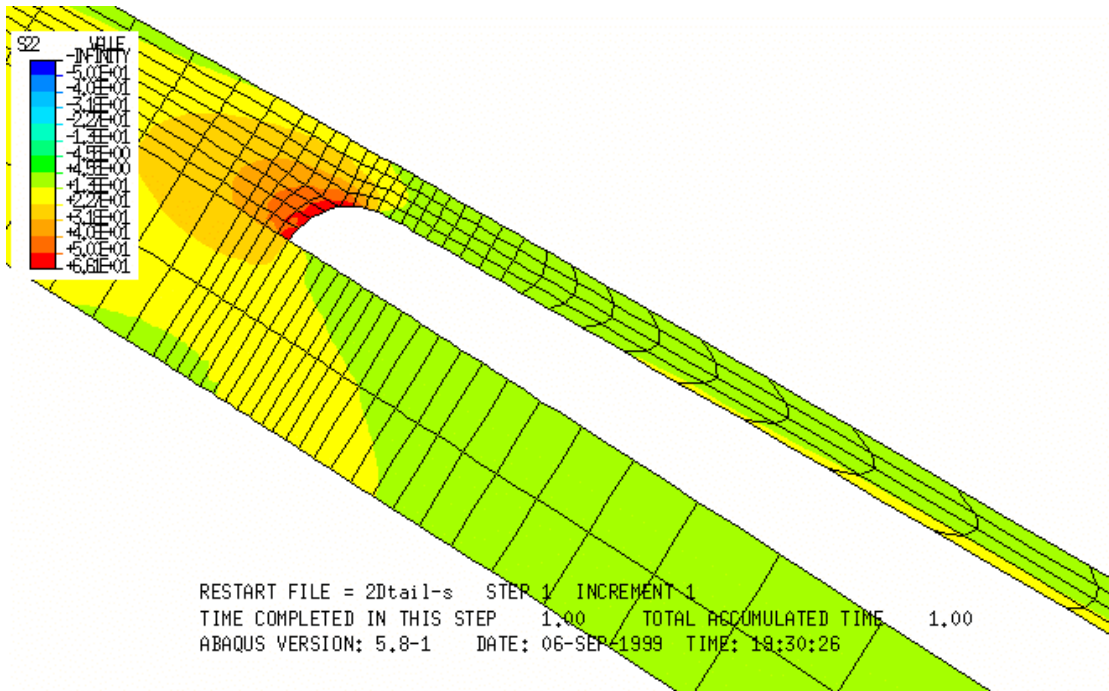


Fig. #2a Axial tensile stress (2Dtail)

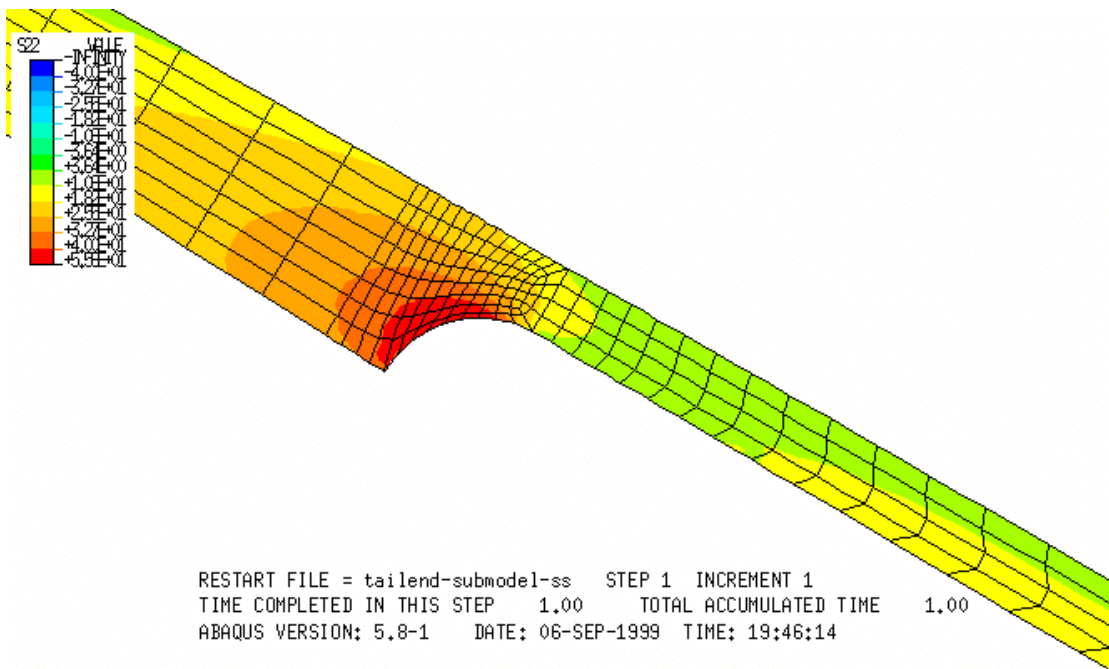


Fig. #2b Axial tensile stress (tail-submodel)

Fig. #3a and #3b shows the shear stress (-30/30 MPa scale): both models have about 30 MPa at the junction between the curved end and the straight of the tail).

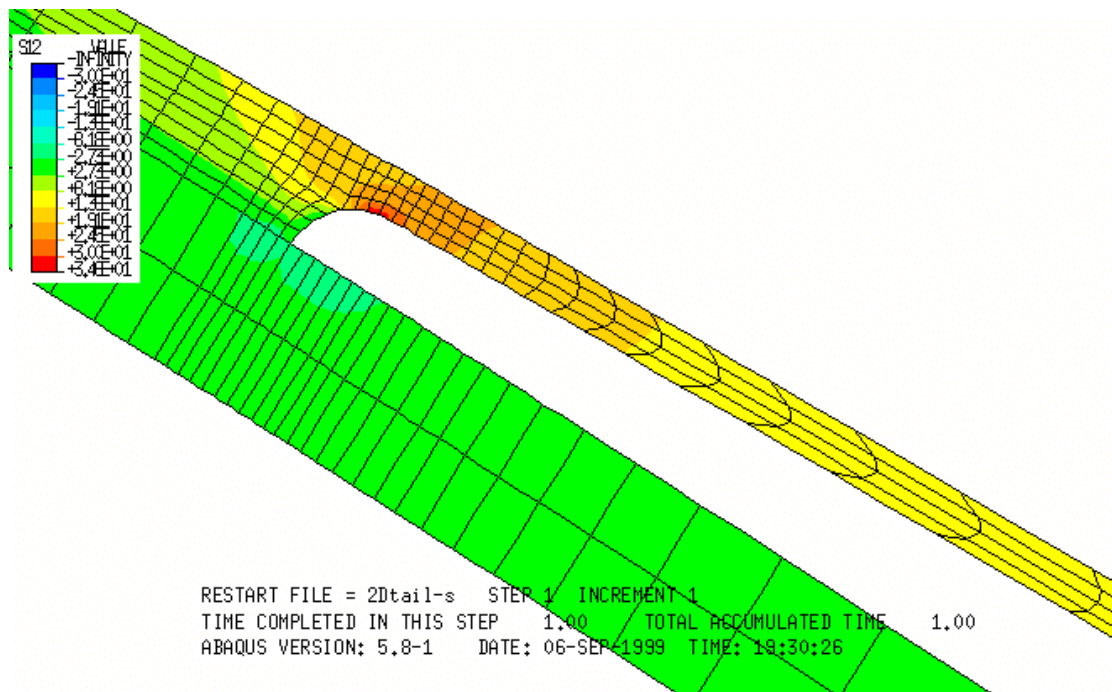


Fig. #3a Shear stress (2Dtail)

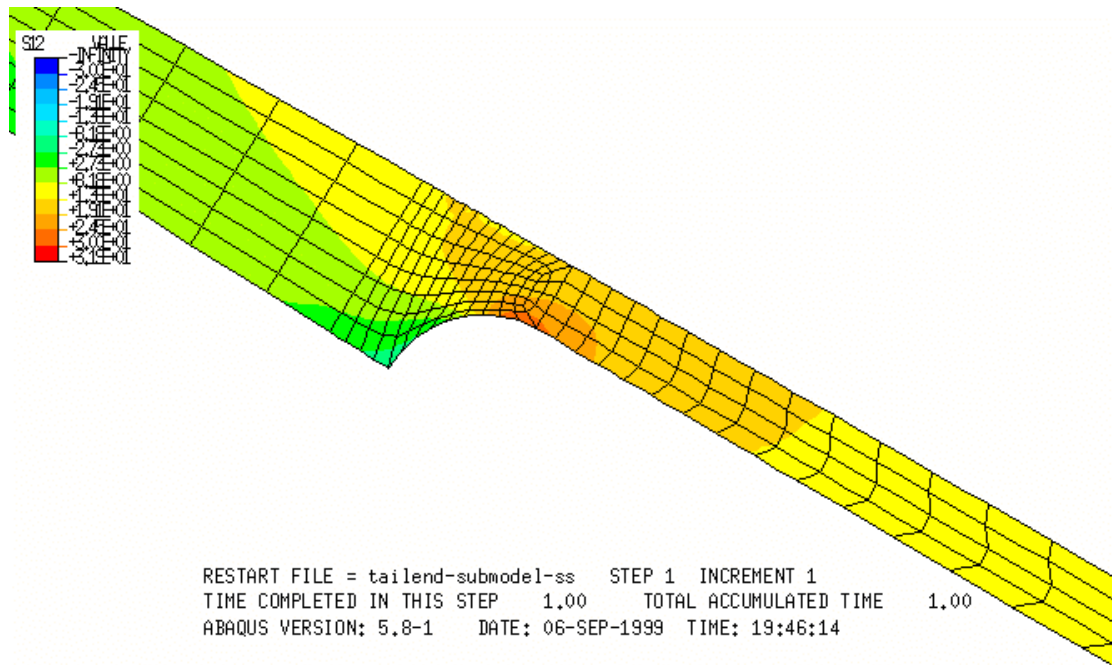


Fig. #3b Shear stress (tail-submodel)

Von Mises stresses are plotted in Fig. #4a and #4b (on a 0/50 MPa scale) and these show how the stress field is dominated by the shear at the tip of the tail.

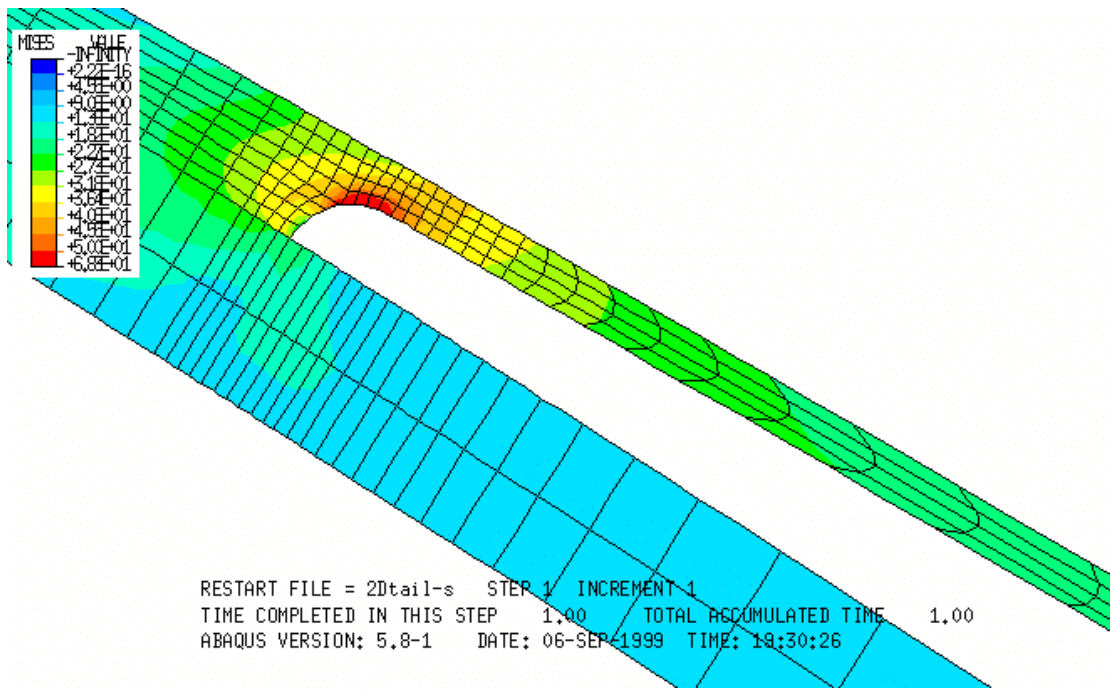


Fig. #4a Von Mises stress (2Dtail)

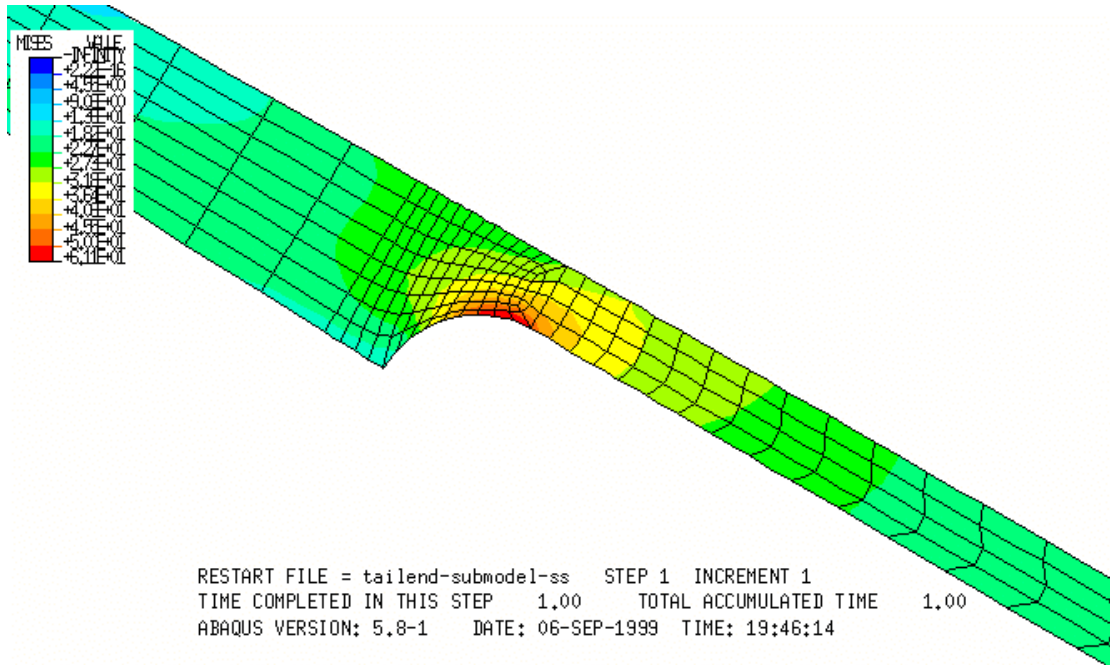


Fig. #4b Von Mises stress (tail-submodel)

In addition Fig. #5 show a deformed plot of the 2Dtail model, which a huge magnification factor to highlight the region in tension and those in compression: the leading mechanism is a shrinking away of the tail which tries to carry the insulation with it, causing therefore tension at the tip

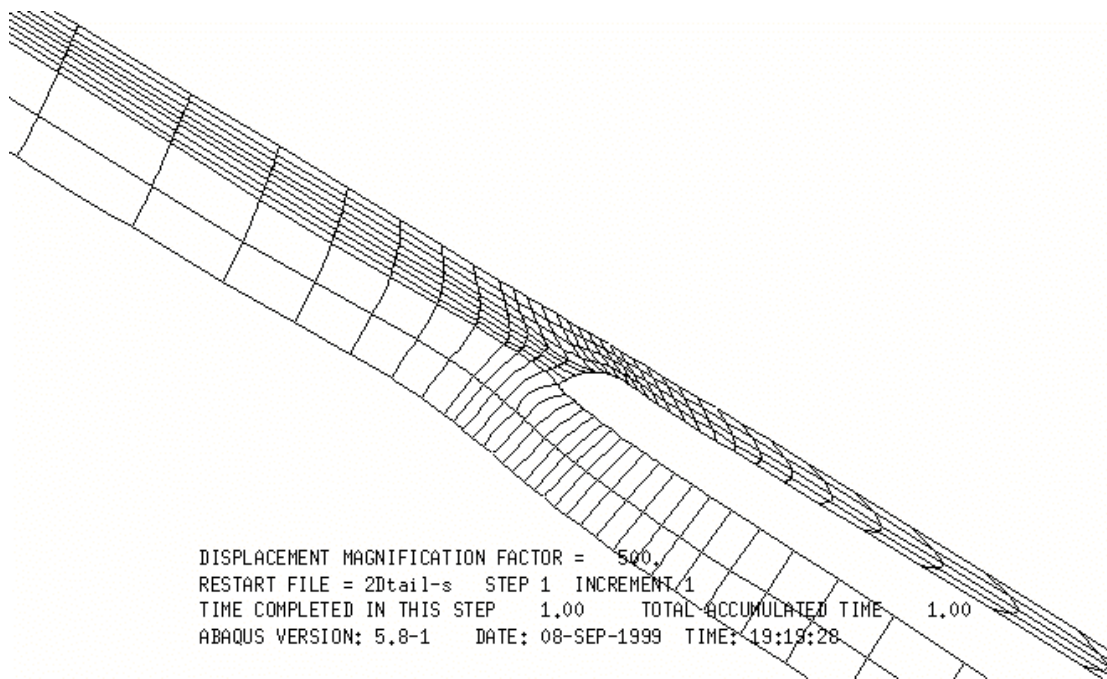


Fig. 5 Displaced 2Dtail

It is then understood that:

1. The crack will start where the tension perpendicular to the copper surface is maximum: this tensile stress is high on a wider region than the relatively lower shear stress. The von Mises stress is not very relevant because the coil insulation has particular planes of weakness (on bondings) and the tension at the tip is on one of those.
2. This will be a mode I crack.
3. Therefore it would be worth modelling a crack in this region (preferably on the copper/insulation interface: the J integral calculates crack energy so, if the theory is right, it should be independent of material boundaries).
4. It's unlikely that this mode I crack will grow to become a mode II crack at the centre of the inter-turn insulation. Rather it might follow the surface of the copper. This because the TF insulation is certainly not isotropic (once the crack is on a plane between glass wraps it stays there: cracks should not propagate across glass fibres).

21. FE models with cracks

From the analysis of the tail region, it appears that if a crack has to start, the most likely position is where the tension perpendicular to the rounded interface copper/insulation. This will start as a mode I crack. This mode I crack probably will not grow to become a mode II crack at the centre of the inter-turn insulation, but it will rather follow the surface of the copper (because the TF insulation is certainly not isotropic and cracks should not propagate across glass fibres), which is known to be a weak point from the tests on the used TF-coil samples.

Therefore a crack on the interface has been modelled and the results (stresses and J-integrals) of this analysis compared with those of the same basic model but with a crack inside the inter-turn insulation. In this model two cracks are present (one at the time is open) and they have the same length (1.5 mm).

Stresses are increased sensibly by the presence of the crack. The J values (table #1) of less than 200 N/m does not seem enough to produce the fracture energy needed for crack propagation in mode II, at least according to NPL data (2400 N/m) on glass-fibre+resin composites similar to ours and to the data on a glass fibre (Owen Corning) + epoxy (Araldite, Giba Geigy) with 7.7% strain for failure in tension (also this seems similar to ours) in Rikards et al. in Eng. Fract. Mech. 1998 (1700±500 N/m). However, at least in Rikards et al., the released energy is close to the one needed to start a crack in mode I (227±52 N/m).

<i>Average J values for path 2-4 left [N/m]</i>		
Inside insulation 1.5 mm	91	92
On copper/insulation interface 1.5 mm	160	195

Table #1 J values for two crack positions at the tip of the tail

The evaluation of J value on a mixed material region can raise suspects, but this is an energy and as such independent of the material properties but dependent on the stress field. In addition, in literature (Carlsson and Aksoy, Int. Jour. Of Fract. 1991) it has been shown that the J value for inter-ply and interface cracks is dependent only on the stress field and (Sundaraman and Davidson, Eng. Fract. Mech. 1998) mixed domain are used to analyse interfacial toughness.

The stress patterns away from the crack regions are not affected by the change in the geometry (smaller mixed-type elements) while close to the closed singularities some stress concentration is present. The model has been run with both cracks closed and with a crack open at a time. The stress patterns at the location of the closed crack are again not affected by the opening of the other crack and are similar to those in the both-closed simulation. Stresses increase locally at the crack tips of the open crack (as expected). The deformed plot for the two cases are in Fig. #6 and Fig. #7.

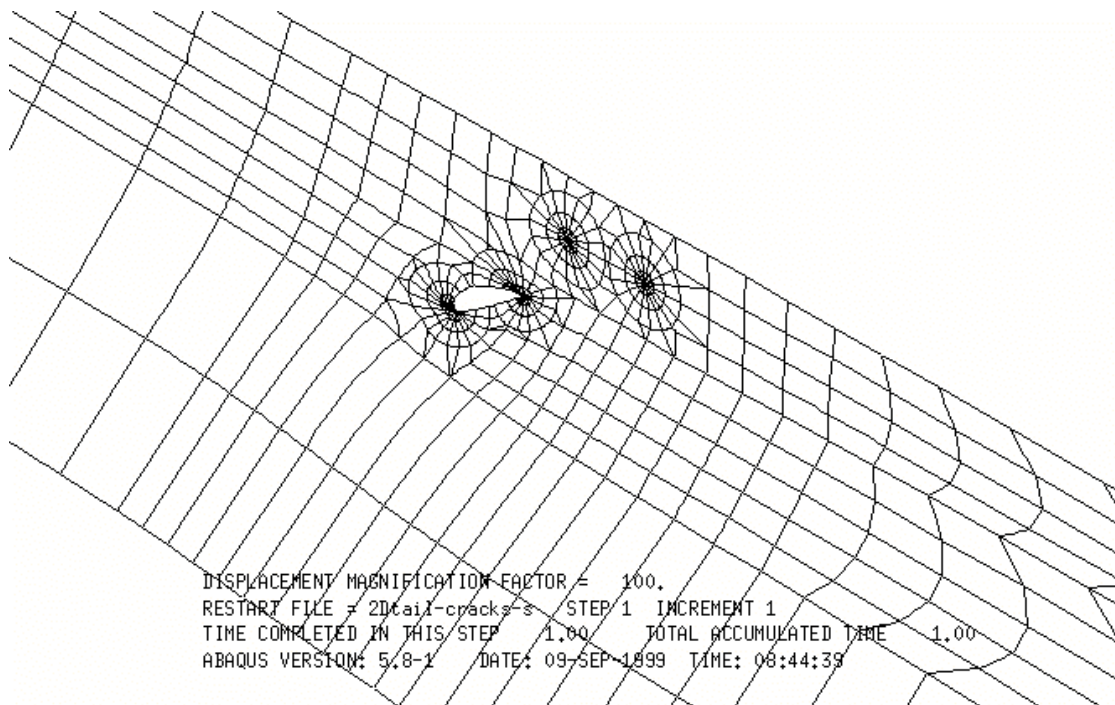


Fig. #6 Deformed mesh (interface crack - mode I)

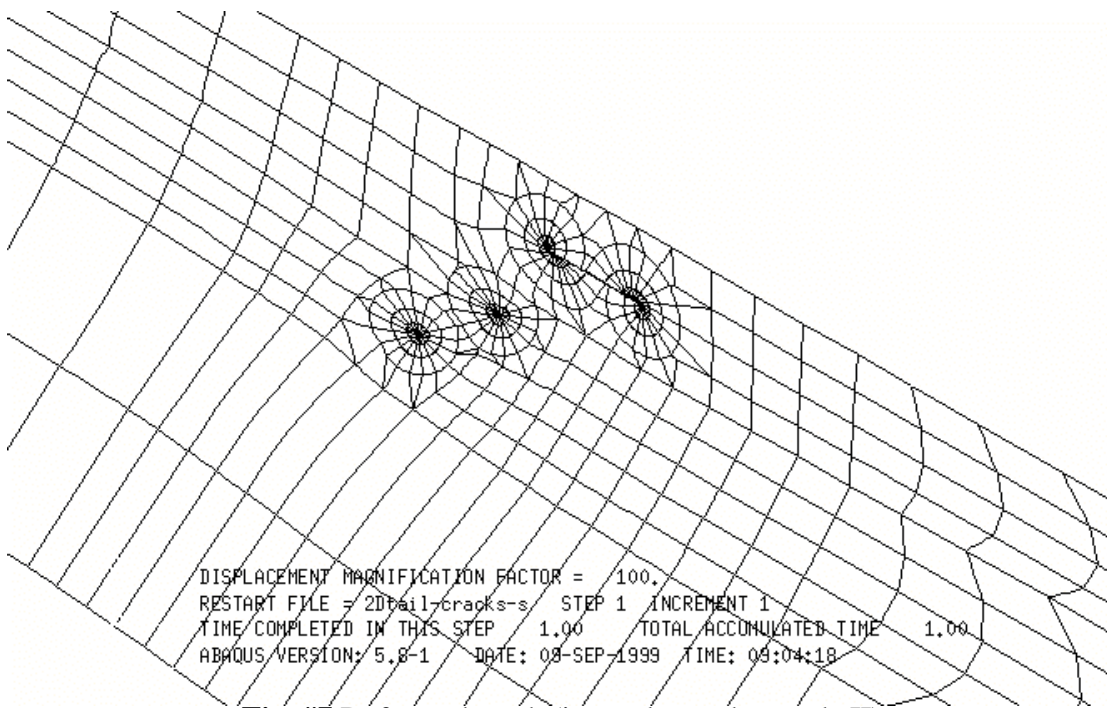


Fig. #7 Deformed mesh (inter-ply crack - mode II)

As the most likely mechanism of failure is a mode I crack starting in the high tension region on the bonding between the copper and the insulation at the tip of the tail, a small delamination has then been modelled. This starts at the junction with the ground wrap and ends in the peak shear region (long enough to have the element average peak shear equal to 40 MPa at the “right” tip).

The deformed mesh is plotted in Fig. #8. The shear stress is plotted in Fig. #9.

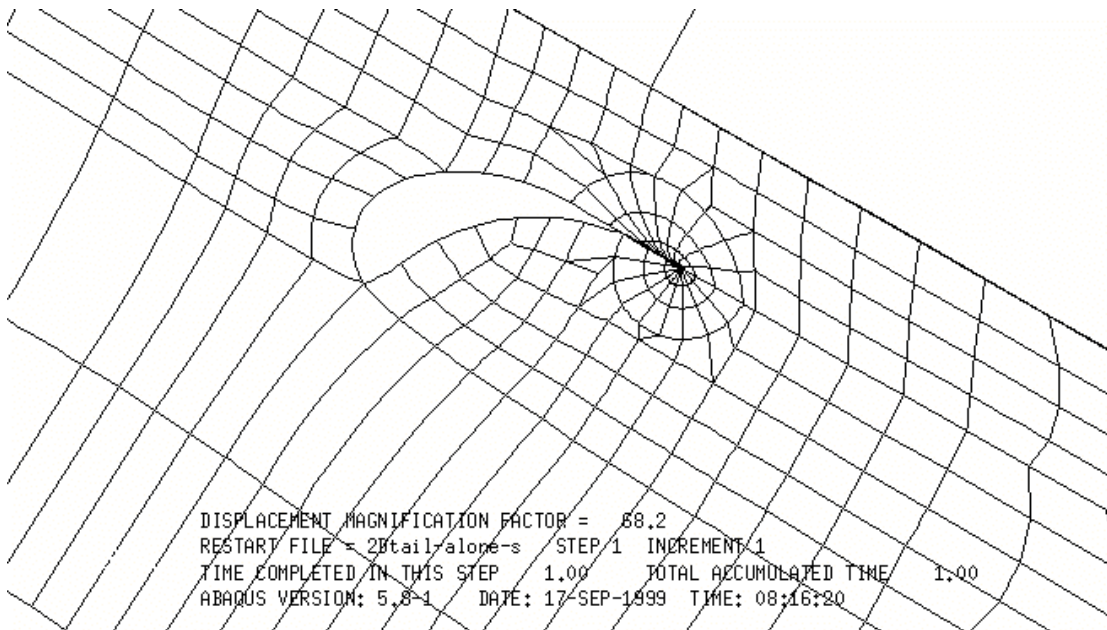


Fig. #8 Deformed mesh with delamination and J-integral region

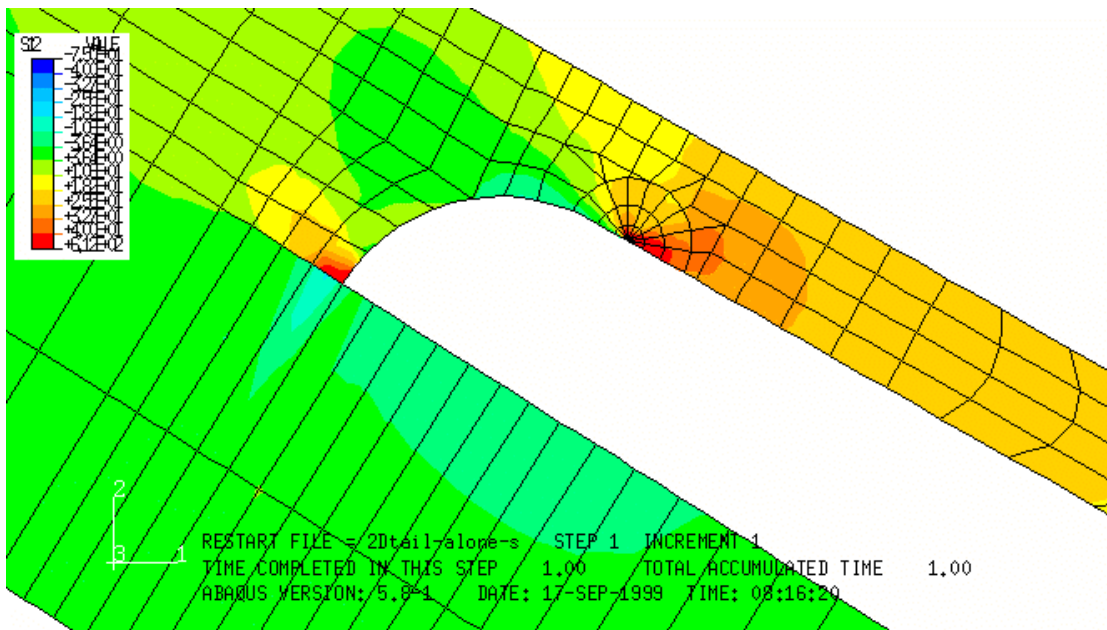


Fig. #9 Shear stress after tip delamination

At this point the crack is mainly a mode II. The value of the J-integral is 372 N/m, i.e. $\sim 1/6$ of the critical value for a mode II crack in a 50+50 glass-fibre+epoxy woven insulation (~ 2400 N/m). In the VAMAS round-robin NPL report on mode II growth rate tests, measurements done on an insulation not too different from the one of the JET TF coils: Vetrotex moulded VERESTER woven glass-fibre in a Ciba-Geigy araldite epoxy matrix, LY 556 resin, HY 916 hardener and DY 070 accelerator, with $k_I=0.54$ point towards a rate of $\sim 10^{-4}$ mm/cycle when the J value is about 1/4 of its critical value (as it appears to be in the case of the TF tail tip). Therefore, once the crack has quickly gone through the mode I propagation region, it will slowly grow along the copper/insulation interface above the tail in a mixed mode, probably dominated by mode II as the tension across the crack remains small even after the delamination has occurred.

2.2. Effect of a small delamination on stress fields

A small delamination has been added in several stages starting from the junction with the ground wrap. Along the tip of the tail 15 elements (one more every run, as labelled in Fig. #10) have been detached and the stresses (as element averages) collected on the insulation elements facing the tail tip.

Resulting tension and shear stresses are plotted in Fig. #11, #12, #13 and #14. The delamination of the first elements does not produce an increase in the shear stress on the top face of the tail, but only an increase in the tension across the bonding between the tail and the insulation in the winding direction, up to 85 MPa. After most of the end face of the tail has been detached also the shear increases. This stress reaches a maximum of ~ 40 MPa then starts to decrease again. The von Mises stress is initially dominated by the shear stress, but when the delamination is substantial it is dominated by the tension.

An analysis of a larger delamination, to assess whether the shear stress goes on decreasing when the crack grows, has not been carried out: the element size on the tail from this point onwards increases so the computed reduction in stress could be misinterpreted as the actual one. If necessary, this computation could be done after the relevant region has been remeshed.

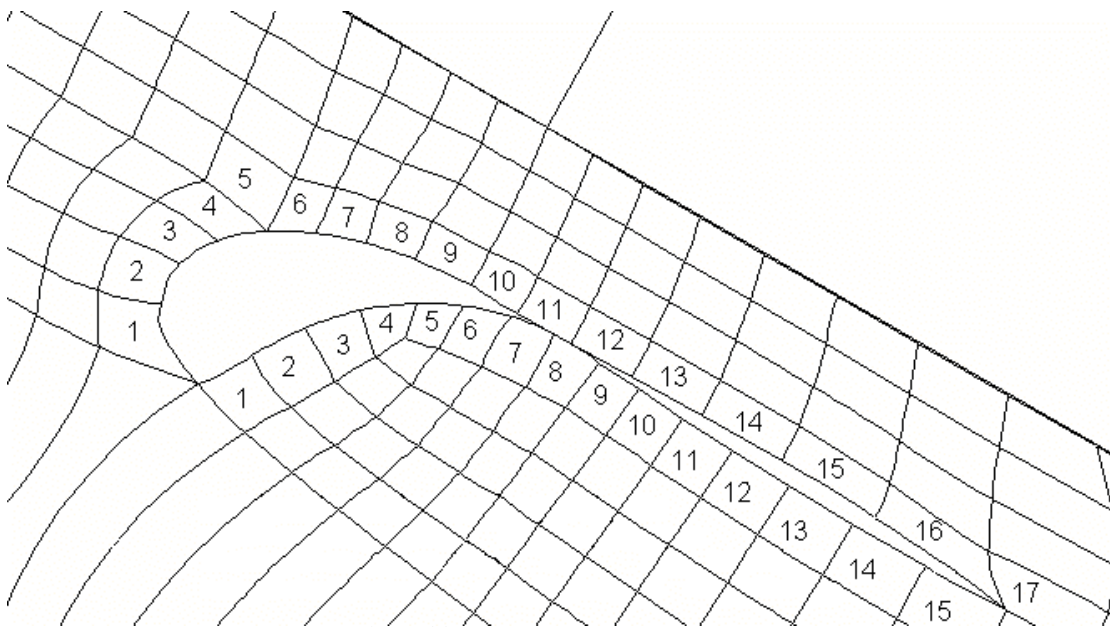


Fig. #10 15-element delamination

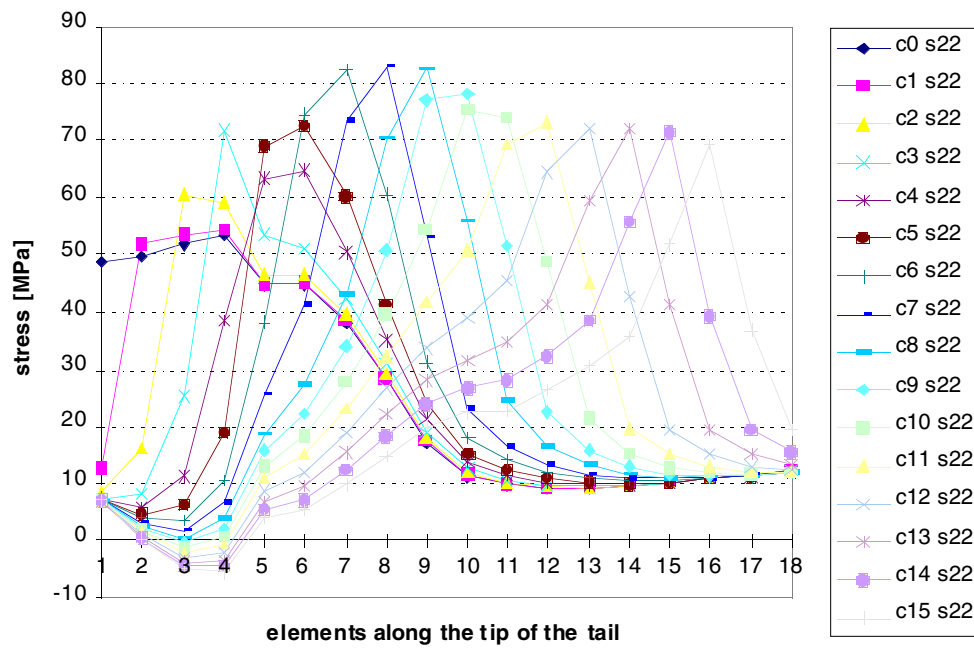


Fig. #11 Tension along the winding direction (axial) in the insulation

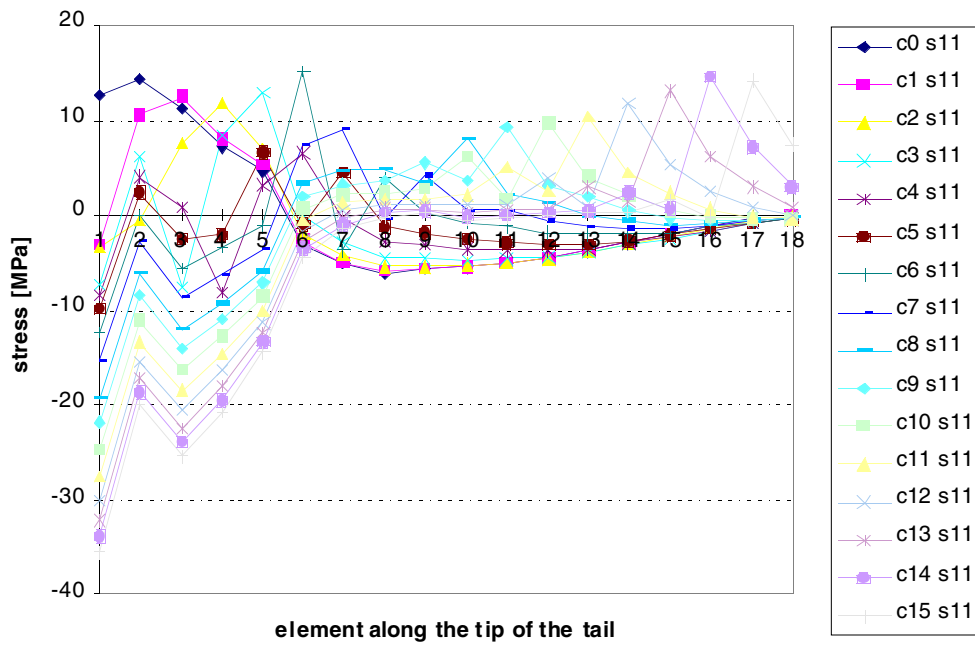


Fig. #12 Tension across the winding direction (radial) in the insulation

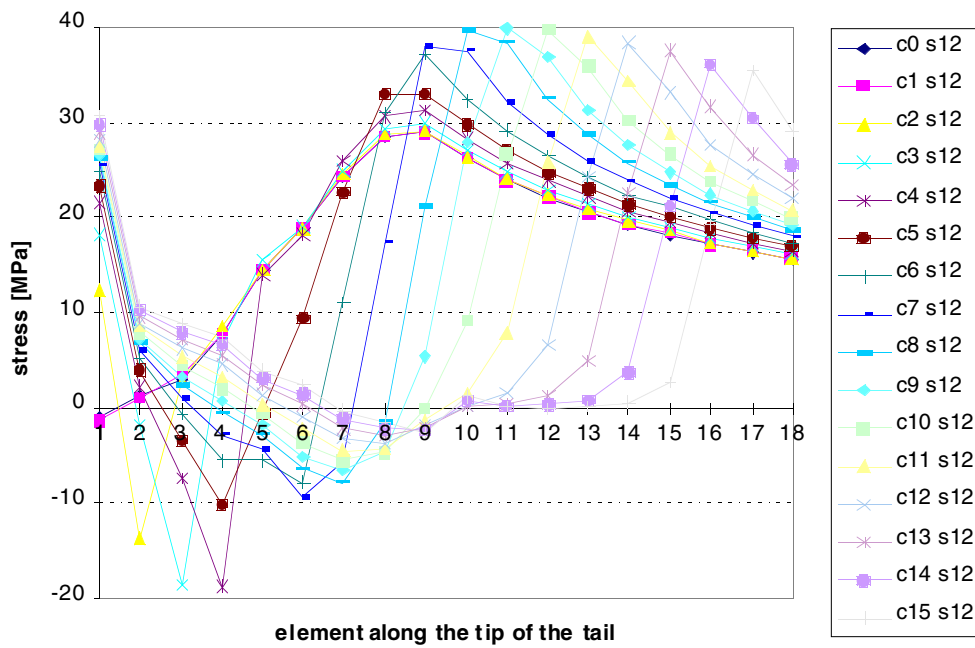


Fig. #13 Shear stress in the insulation

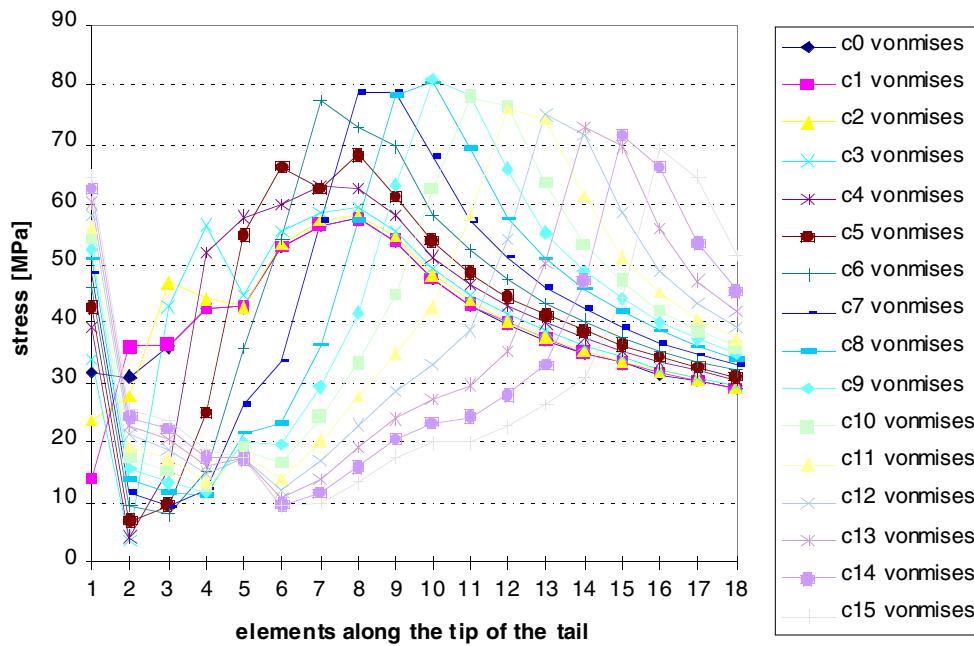


Fig. #14 von Mises stress in the insulation

3. Large delaminations

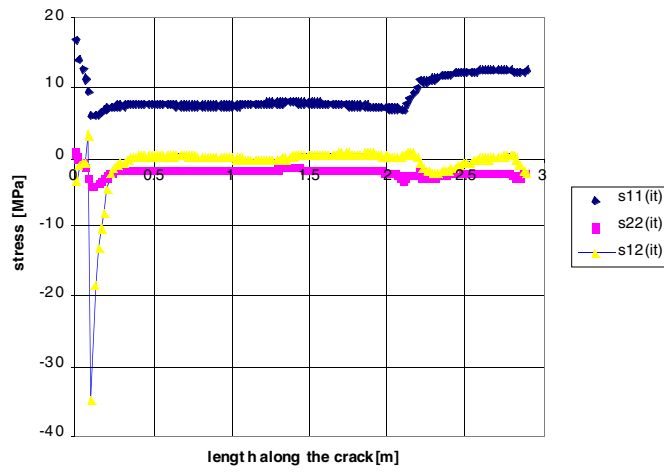
A 2D/1-pancake model of the coil has been used to investigate the possible delamination of the innermost turn following a fully developed tail crack.

The coil model is made of 12 turns and 11 inter-turns. The total width of the cross section is 362 mm, of these 11x 2 mm is taken by the insulation (isotropic with $E=10.4$ GPa and $\nu=0.3$) and the rest by the copper (isotropic with $E=106$ GPa and $\nu=0.35$). The coil is divided into 136 slices, and each slice is split in the winding direction into 5 layers: therefore the total number of elements is 23 (1 row) X 5 (rows per slice) X 136 (slices).

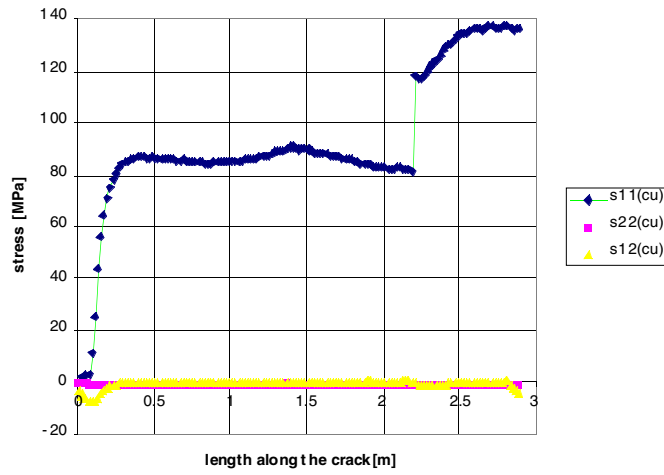
The coil is loaded (magnetic load only, as the temperature difference is present only in the tail region) and supported (inner cylinder and push-pull jacks) only in-plane. The magnetic load is shaped: higher on the inside, lower on the outside. To introduce the delamination, the magnetic load is kept unchanged, but the innermost turn is cut at the joggle location (removing one element) and detached on one side of it. The friction between the first turn and the rest of the coil is simulated by an equivalent shear force.

The model has been run for 4 delamination lengths: 1, 6, 11 and 14 (where, with this friction coefficient a crack going towards the high field region stops) slices.

For each simulation the 1st turn and the 1st inter-turn stresses in the relevant region are plotted in Fig. #15,#17,#19,#21, in Fig. #16,#18,#20,#22 the copper axial stress in the full coil is plotted to show how it is perturbed the presence of the crack, while in Fig. #23 the shear in the inter-turn is collected for different crack lengths. Where the crack stops depends mainly on the friction coefficient, but the non-propagation trend is clear.



(a)



(b)

Fig. #15 (a) 1st inter-turn stresses; (b) 1st turn stresses (102 mm long delamination)

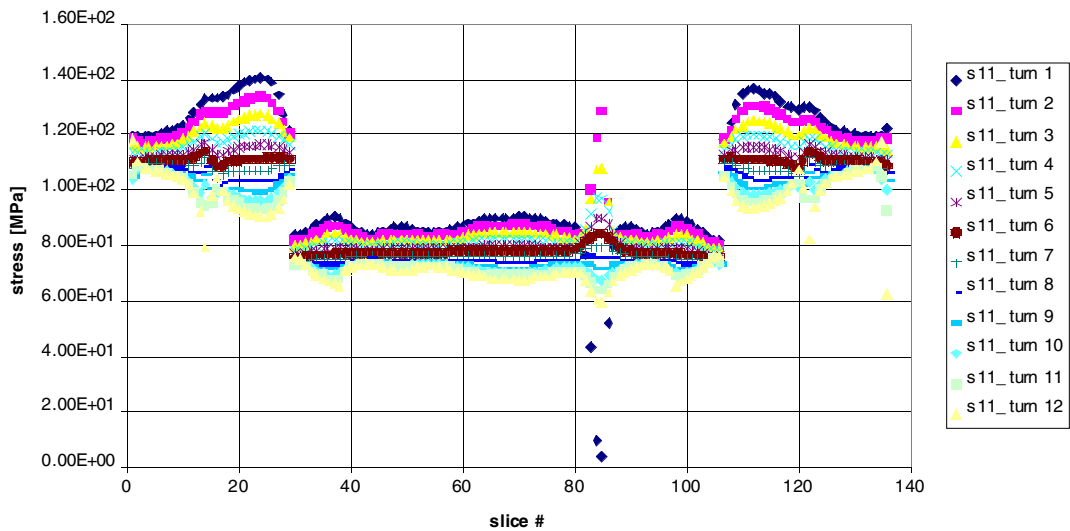
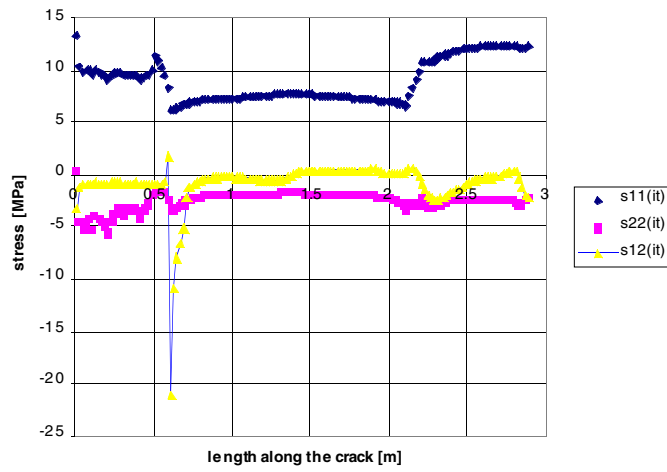
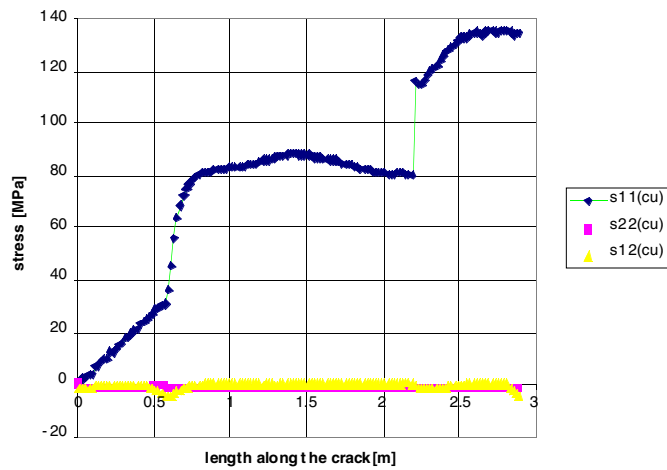


Fig. #16 Slice average copper axial stresses (102 mm long delamination)



(a)



(b)

Fig. #17 (a) 1st inter-turn stresses; (b) 1st turn stresses (612 mm long delamination)

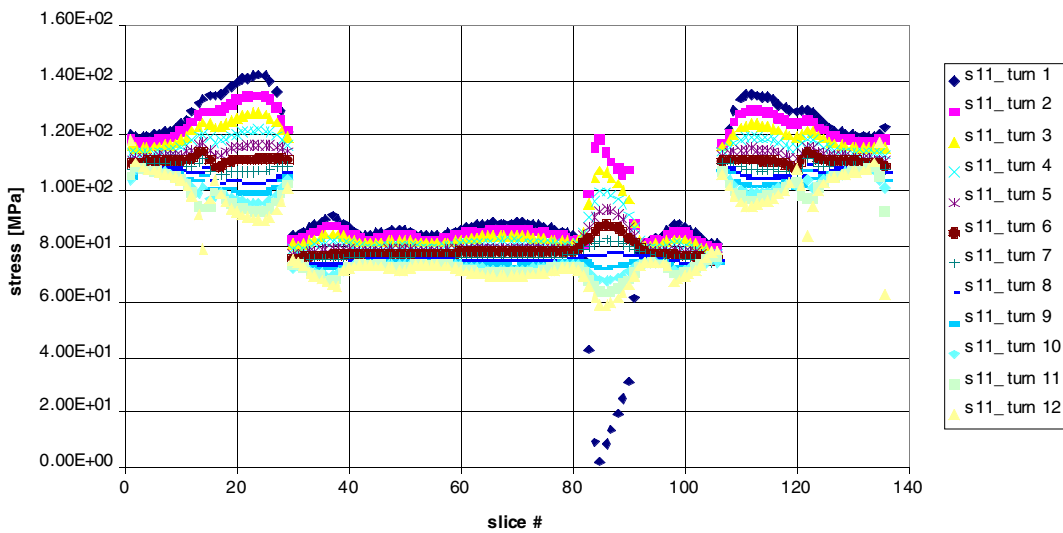
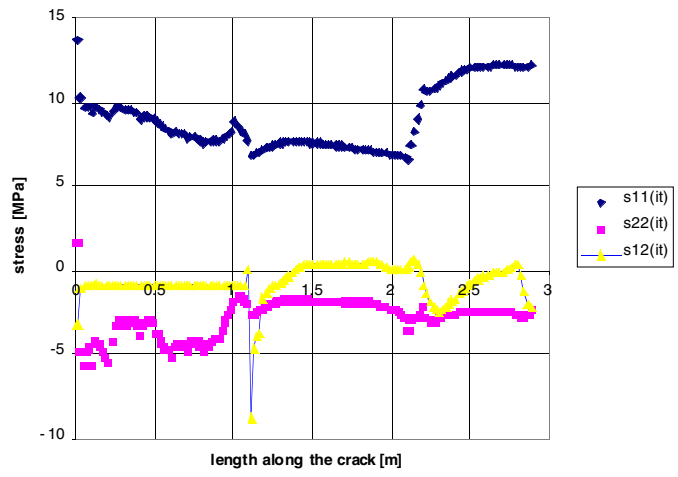
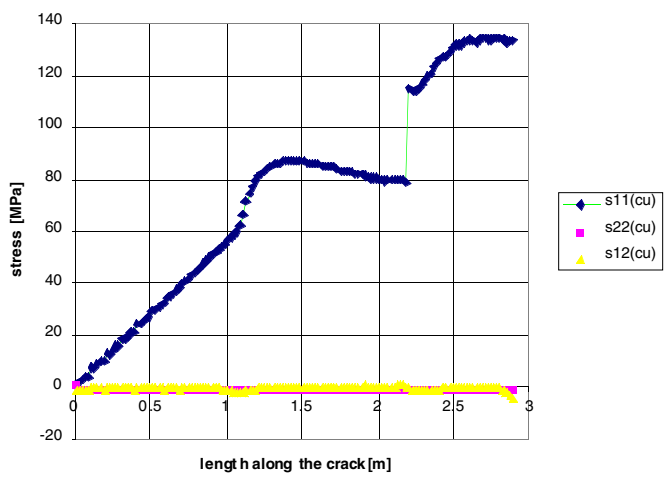


Fig. #18 Slice average copper axial stresses (612 mm long delamination)



(a)



(b)

Fig. #19 (a) 1st inter-turn stresses; (b) 1st turn stresses (1122 mm long delamination)

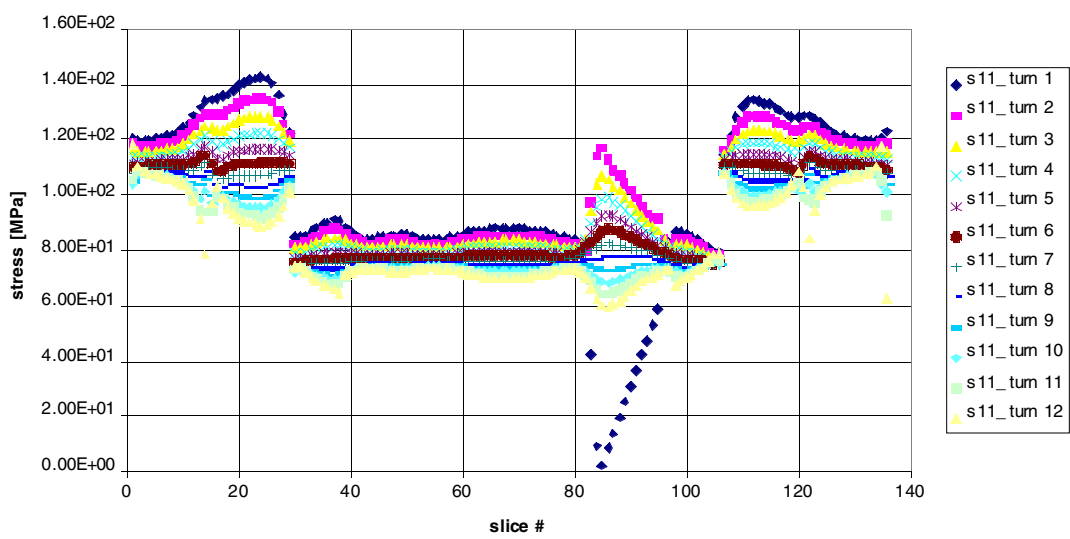
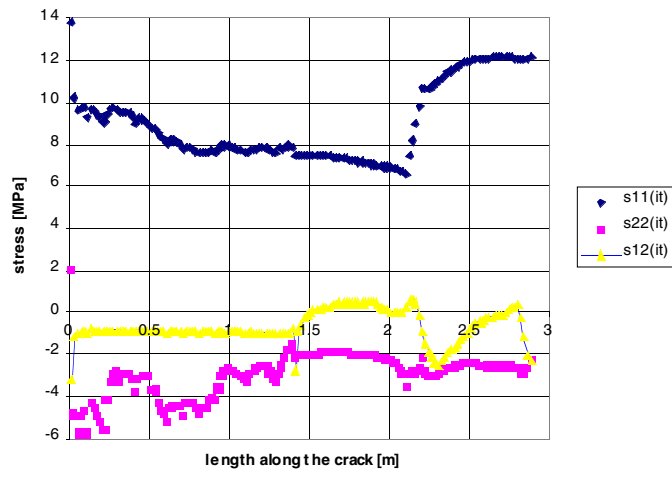
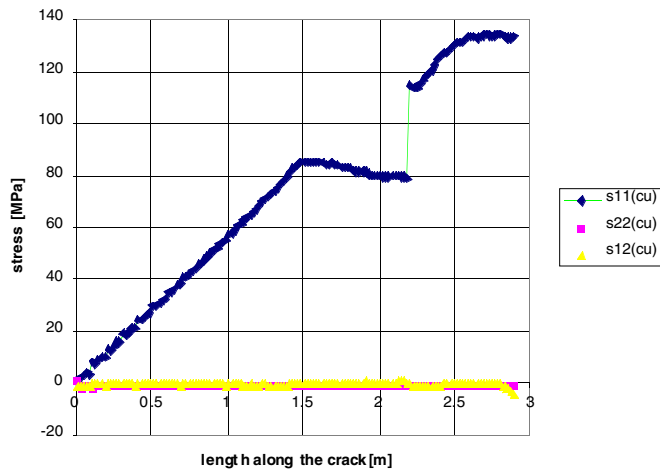


Fig. #20 Slice average copper axial stresses (1122 mm long delamination)



(a)



(b)

Fig. #21 (a) 1st inter-turn stresses; (b) 1st turn stresses (1428 mm long delamination)

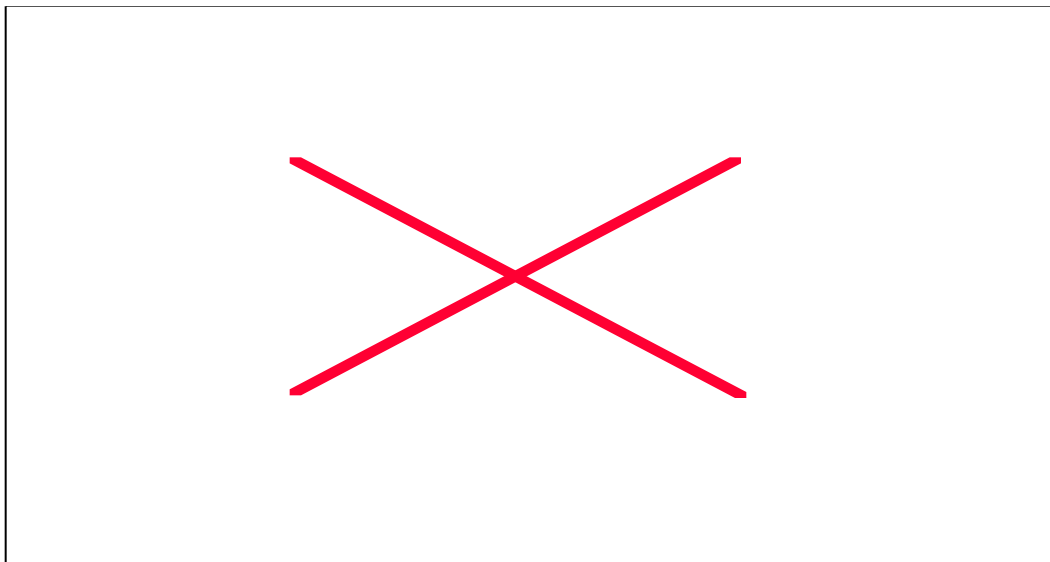


Fig. #22 Slice average copper axial stresses (1428 mm long delamination)

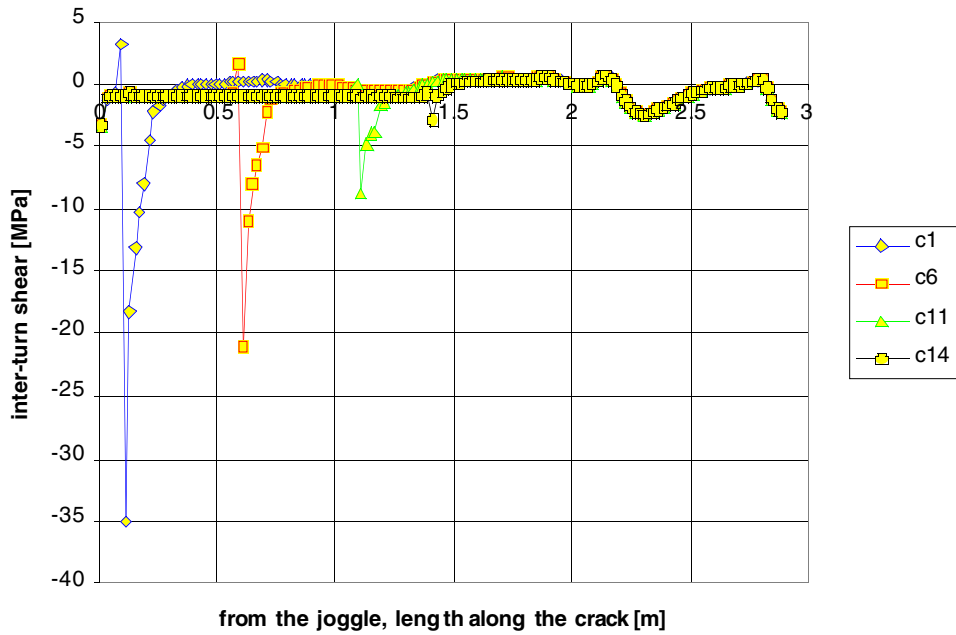


Fig. #23 1st inter-turn shear stress with delamination of different length: (c1) 102 mm, (c6) 612 mm, (c11) 1122 mm and (c14) 1428 mm.

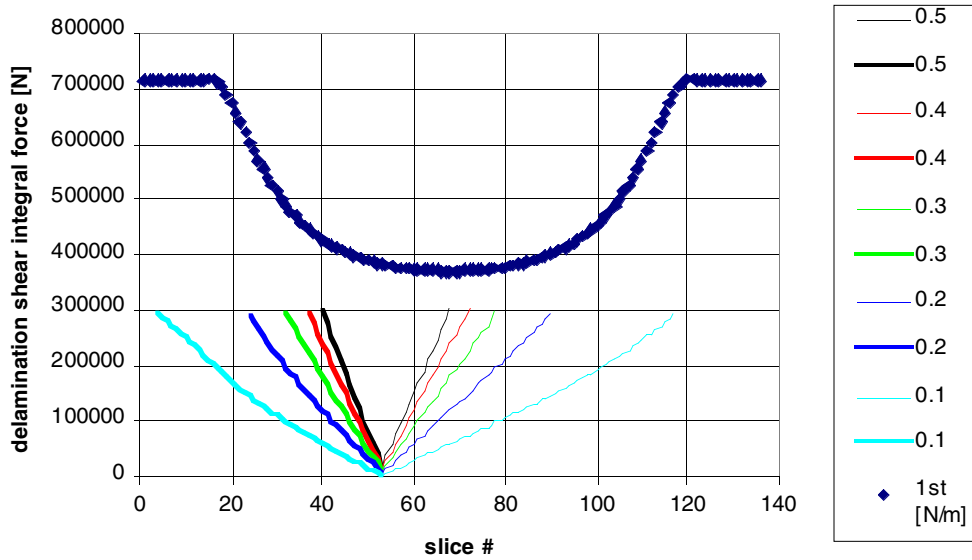


Fig. #24 Integral of the shear flow along the delamination for a range of friction coefficients

An analytical estimation of the crack growth can be carried out knowing the compression applied on the first turn, as this is transferred to shear by friction and the delamination stops when the shear force in the direction of the winding has built up to match the tension force in the conductor:

$$T = \int \sigma_c \mu dlw$$

where T is constant (289 kN) along the coil, w is the conductor thickness ($\sigma_c w$ for the 1st turn is plotted in Fig. #24) and μ is the friction coefficient. Depending on its value, the crack length changes (smaller with higher friction): in a very pessimistic case ($\mu=0.1$ and towards the low field region, the crack could develop up to 6 m); however for these kind of facing materials values between 0.25 and 0.5 are suggested for the friction

coefficient. A side effect of a long crack could be a different distribution of copper stresses with regions more loaded than with an even distribution.

Thermal Analysis for TF Coil

J. R. Last
09 November 1999

Contents

1	Introduction.....	2
2	Thermal Analysis Models.....	3
2.1	1 D model.....	3
2.2	2D Model.....	4
2.3	3D model.....	6
2.4	Comparison of 1D, 2D and 3D calculation.....	8
3	Electrical and coolant connection region.....	10
3.1	Temperature gradient at coolant inlet and outlet.....	11
3.2	Temperature difference at tail.....	13
4	Summary of key temperatures.....	16
5	Effect of change from water to Freon coolant.....	17
5.1	Design Report.....	17
5.2	Freon coolant.....	18
5.3	Water coolant.....	19
5.4	Summary of transverse gradient effects.....	20
6	Thermal stresses in connection region.....	22
6.1	Analytic calculation.....	22
6.2	Stresses at inlet outlet.....	22
6.3	Stress at TF coil tail.....	24
7	List of figures.....	27

1 Introduction

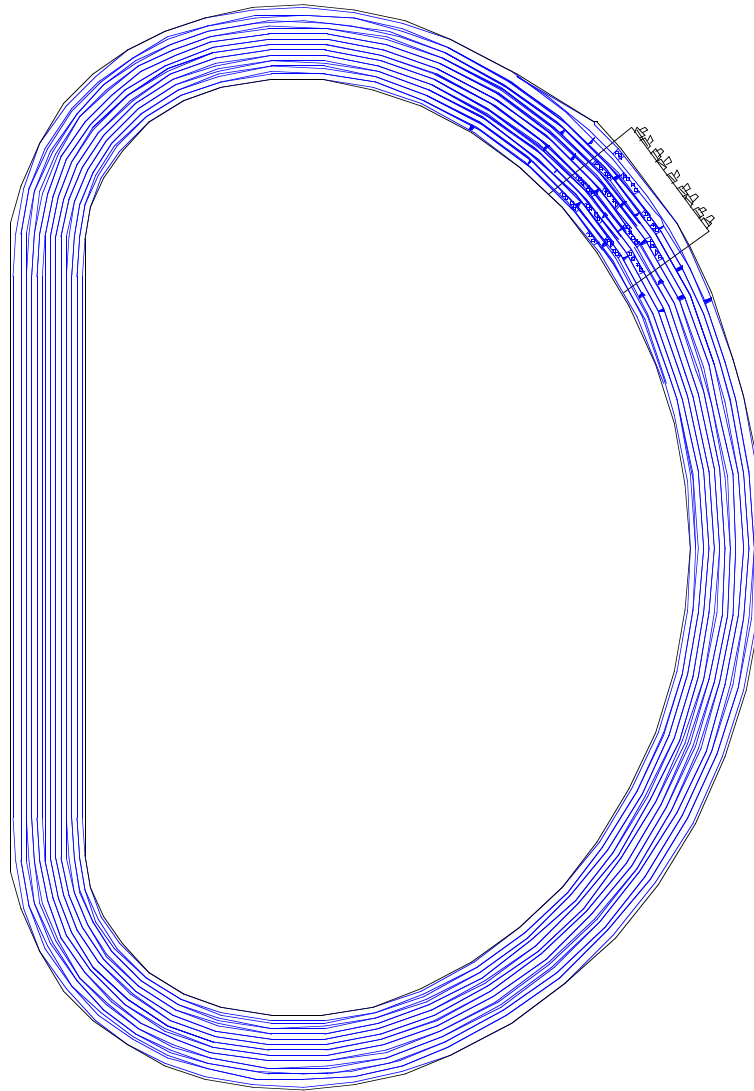


Figure 1 Coil showing connection region

This paper describes cooling calculations on the TF coil. The temperatures are used in FE models for thermal stress calculations. Also described are analytic thermal stress calculations for two points in the coil connection region.

Current and coolant enter and leave the coil at the terminal region. The current makes 24 turns but the coolant only makes a single turn. Thus all turns are cooled in parallel and temperature gradients across the coil cross-section are avoided.

2 Thermal Analysis Models

Dim. of model	Chronological order	Type	Portion of coil considered	Advantage	Used for
1 D	2	solves differential equations (JET programme)	up to 4 turns + tails	flexible	temp grad at connection region coil tails
2 D	1	finite element (JET programme.)	1 turn	shows longitudinal & perpendicular temperature distribution.	JET design modifications (e.g. change to Freon)
3 D	3	finite element (Abaqus)	1 turn	accurate potentially good interface to stress calculation.	checking 1 D model

2.1 1 D model

2.1.1 1D model equations

As turns all turns are similar, a calculation can be made for one turn considering only one dimension - the distance along the conductor.

Temperature is determined by solving the following differential equations.

For the copper conductor (note A_c (area of copper) is function of x)

$$\frac{dT_c}{dx} = \frac{j^2 \rho_e}{\rho_c C_c} - \frac{hs}{\rho_c C_c A_c} (T_c - T_f) + \frac{k_c}{\rho_c C_c} \frac{d^2 T_c}{dx^2}$$

rate of change of temp. electrical heating heat transfer to fluid longitudinal conduction

Note that A_c (area of copper) is a function of x .

For the cooling fluid

$$\frac{dT_f}{dx} = -v \frac{dT_f}{dx} + \frac{hs}{\rho_f C_f A_f} (T_c - T_f) + \frac{k_f}{\rho_f C_f} \frac{d^2 T_f}{dx^2}$$

rate of change of temp. heat transport by flow heat transfer from conductor longitudinal conduction

This type of calculation can be extended to several turns in series with conduction links between turns if required.

2.1.2 1D temperature calculations

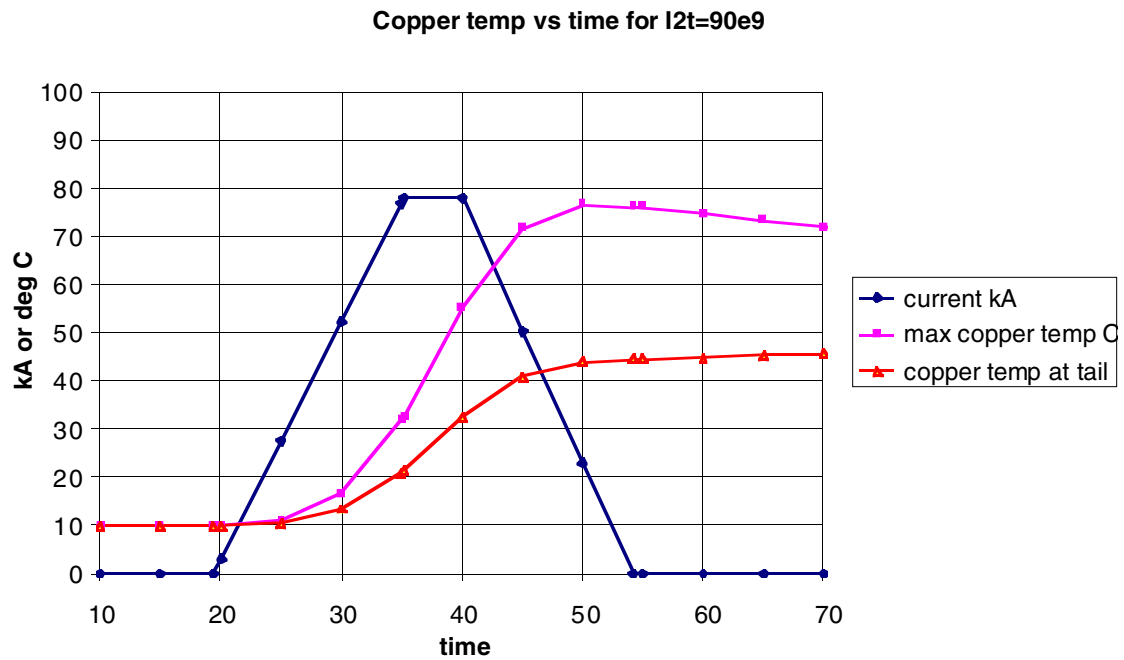


Figure 2 Current and temperature vs time for medium energy pulse

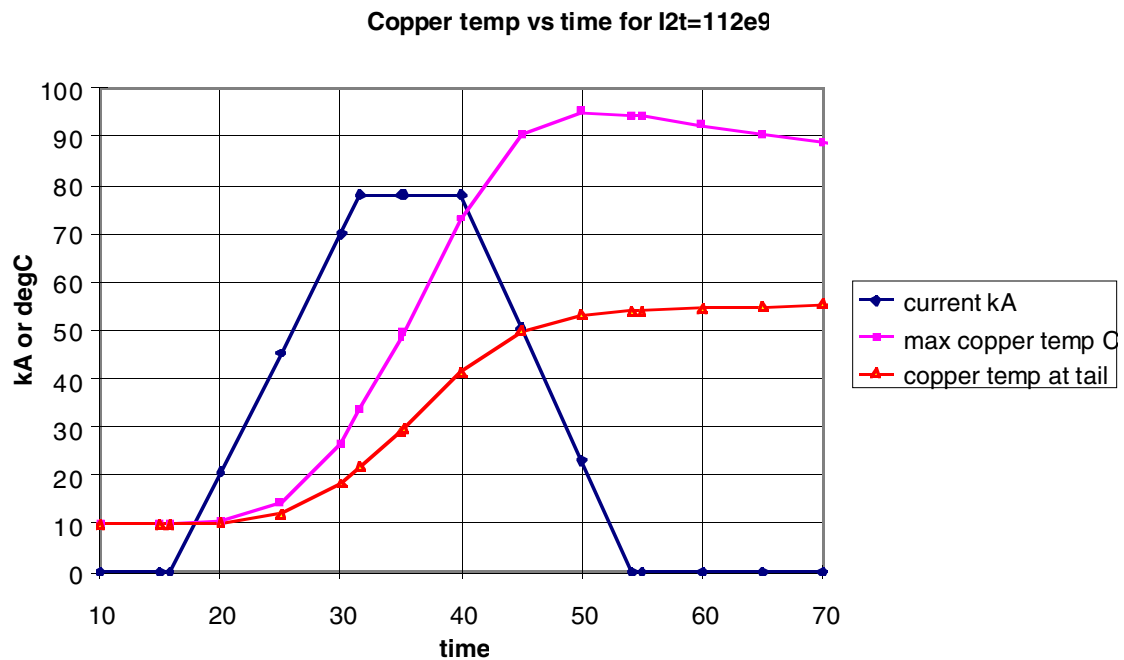


Figure 3 Current and temperature vs time for maximum energy pulse

2.2 2D Model

In this model the conductor of 1 turn is represented by a 2D mesh. The 2 dimensions are the length and width of the conductor. The thickness is represented by applying appropriate properties to the cells. The cooling hole is represented by a longitudinal array of cells.

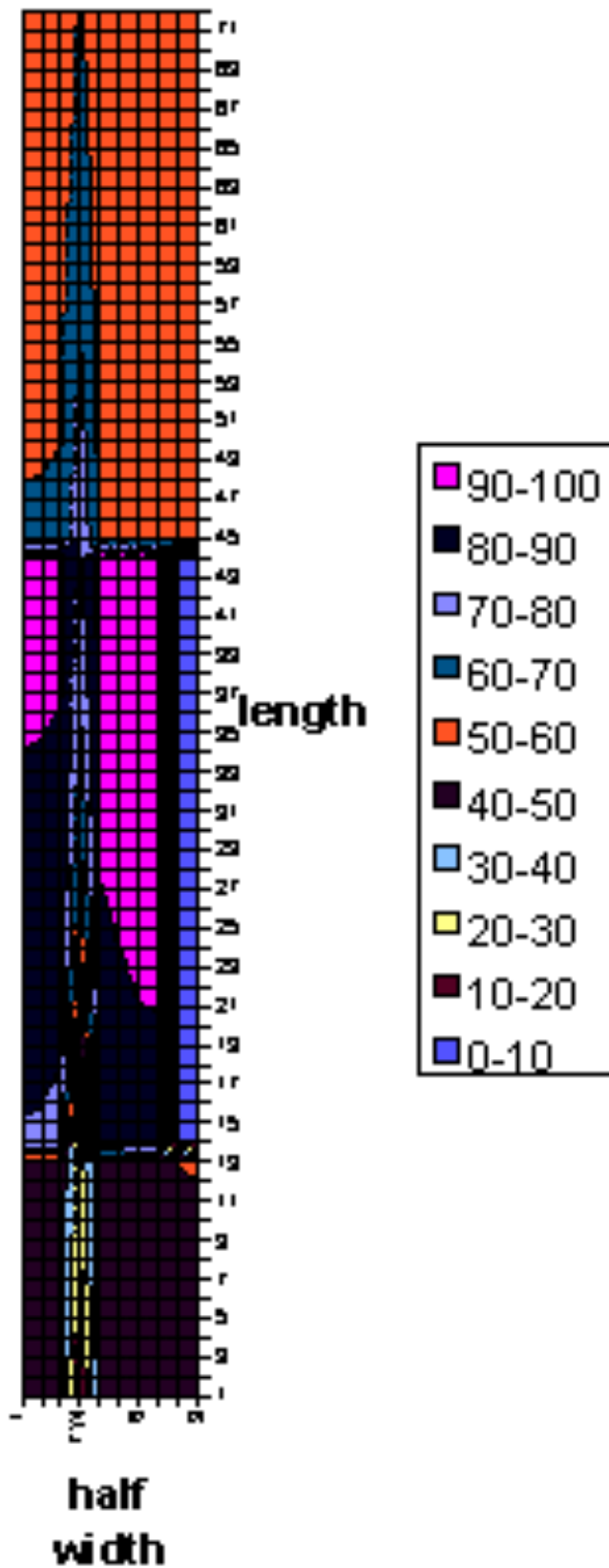


Figure 4 Temperature distribution across conductor at end of pulse. Only half the conductor width with one cooling hole is shown. The same data is plotted in a different way in Figure 18

Max. temp. and temp. diff. across width vs distance along conductor at end of pulse (~50s)

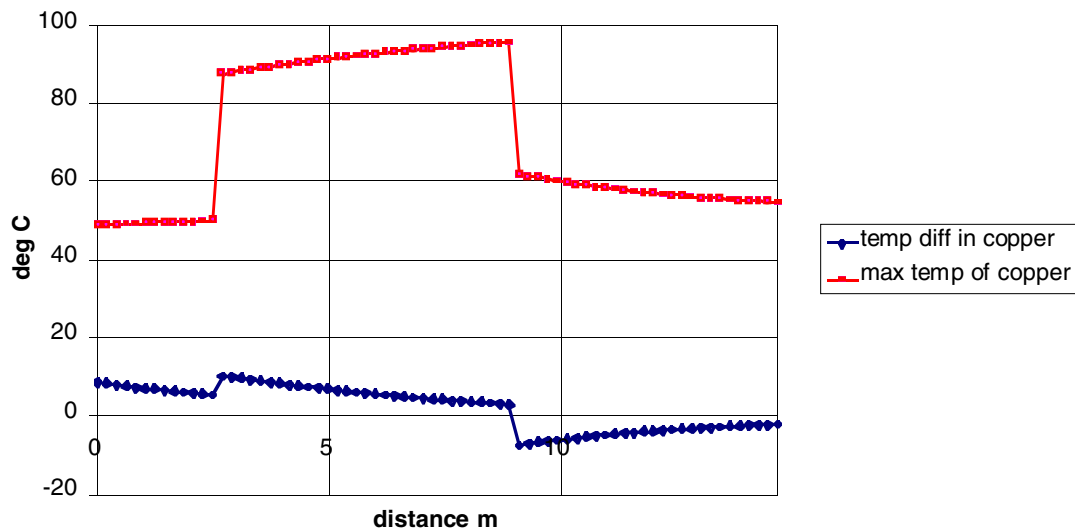


Figure 5 Temperature vs time for maximum energy pulse. The temperature difference across the conductor is the difference between the temperature adjacent to the cooling hole and the temperature at the edge of the conductor

Note that 3D analysis shows that temperature difference across width of conductor is less than shown above.

2.3 3D model

The 3D model is implemented in Abaqus. The conductor of a single turn is accurately modelled complete with cooling holes.

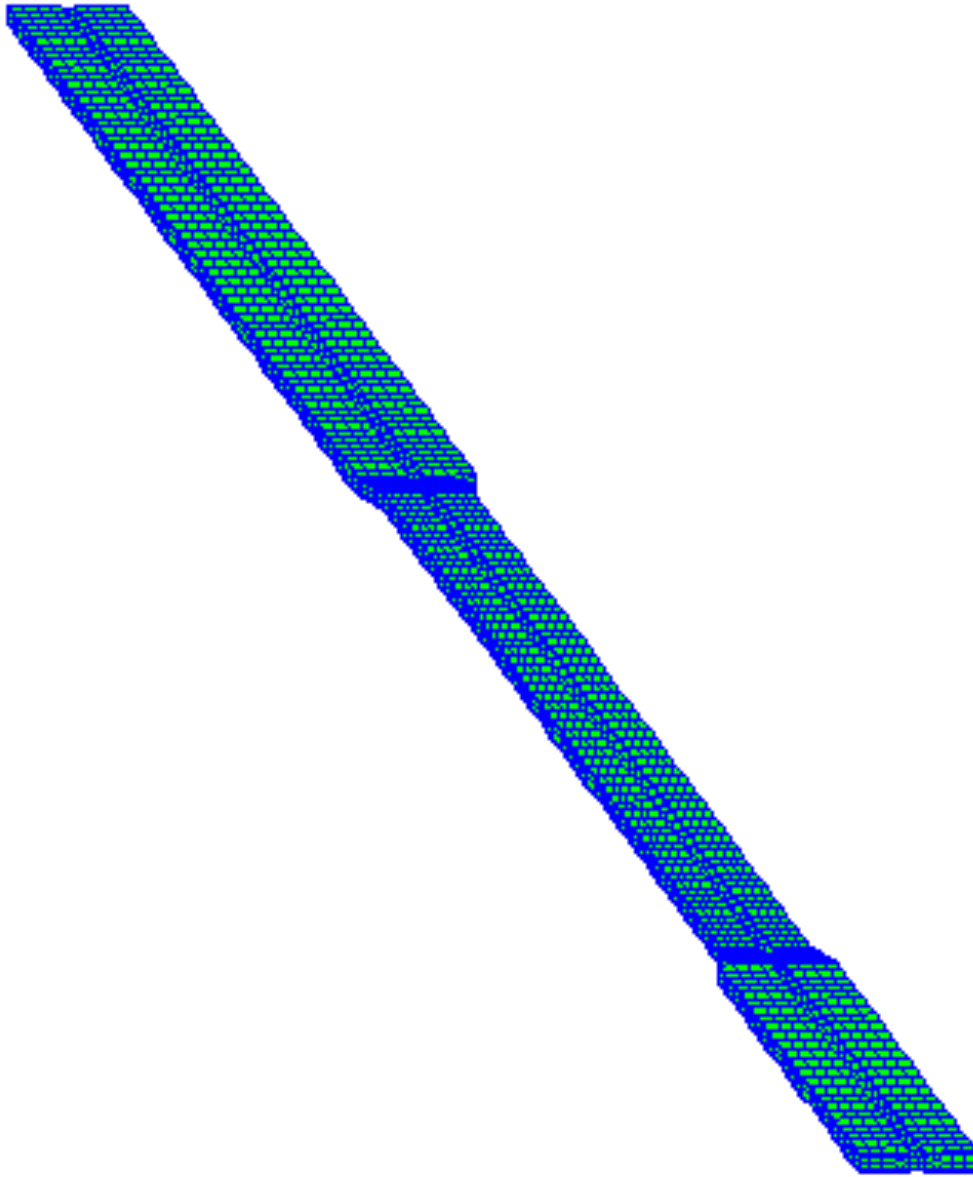


Figure 6 3D model of single turn

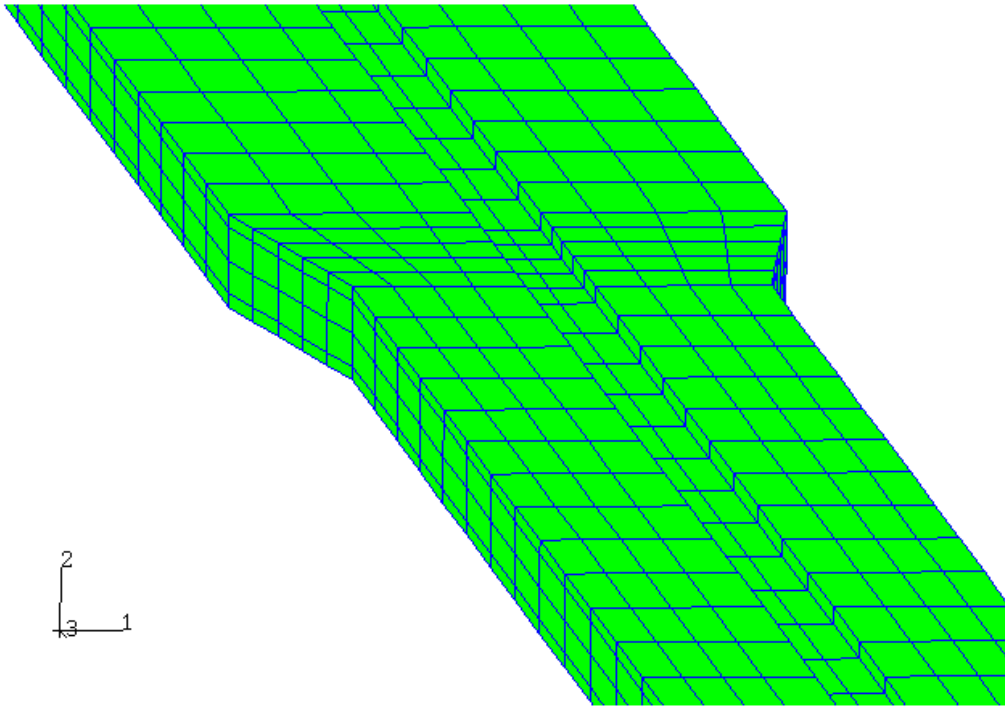


Figure 7 Detail of 3D model

2.4 Comparison of 1D, 2D and 3D calculation

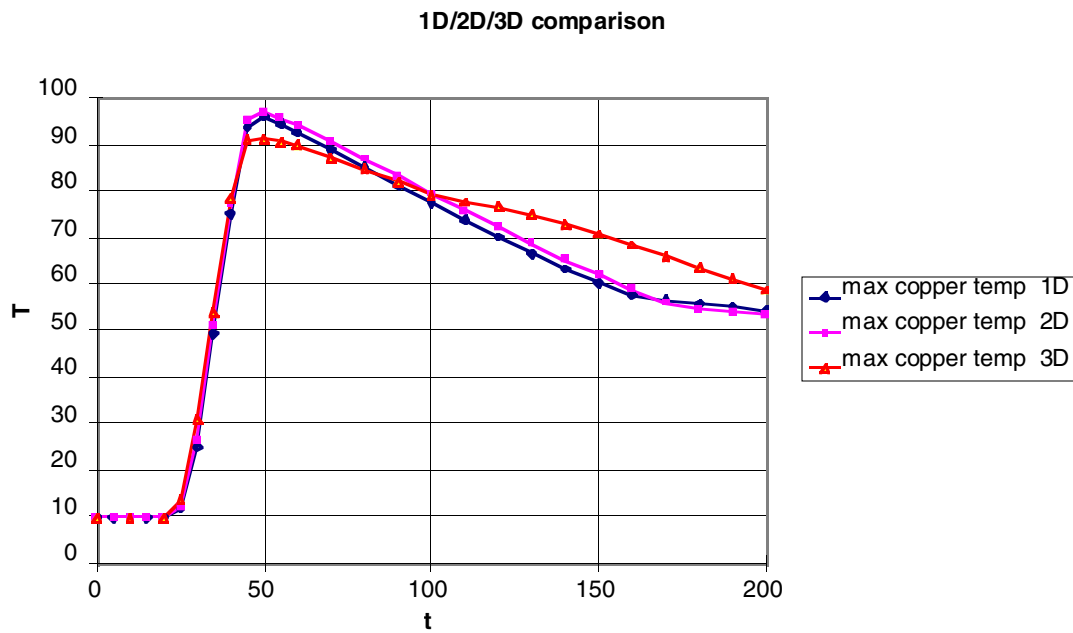


Figure 8 Maximum copper temperature vs time - comparison of 1D, 2D and 3D models

Difference in 3D calculation is due to

- insulation on surface of 3D conductor gives increase heat capacity

- different copper properties (specific heat, conductivity)
- slightly wrong copper and hole cross sectional area

3 Electrical and coolant connection region

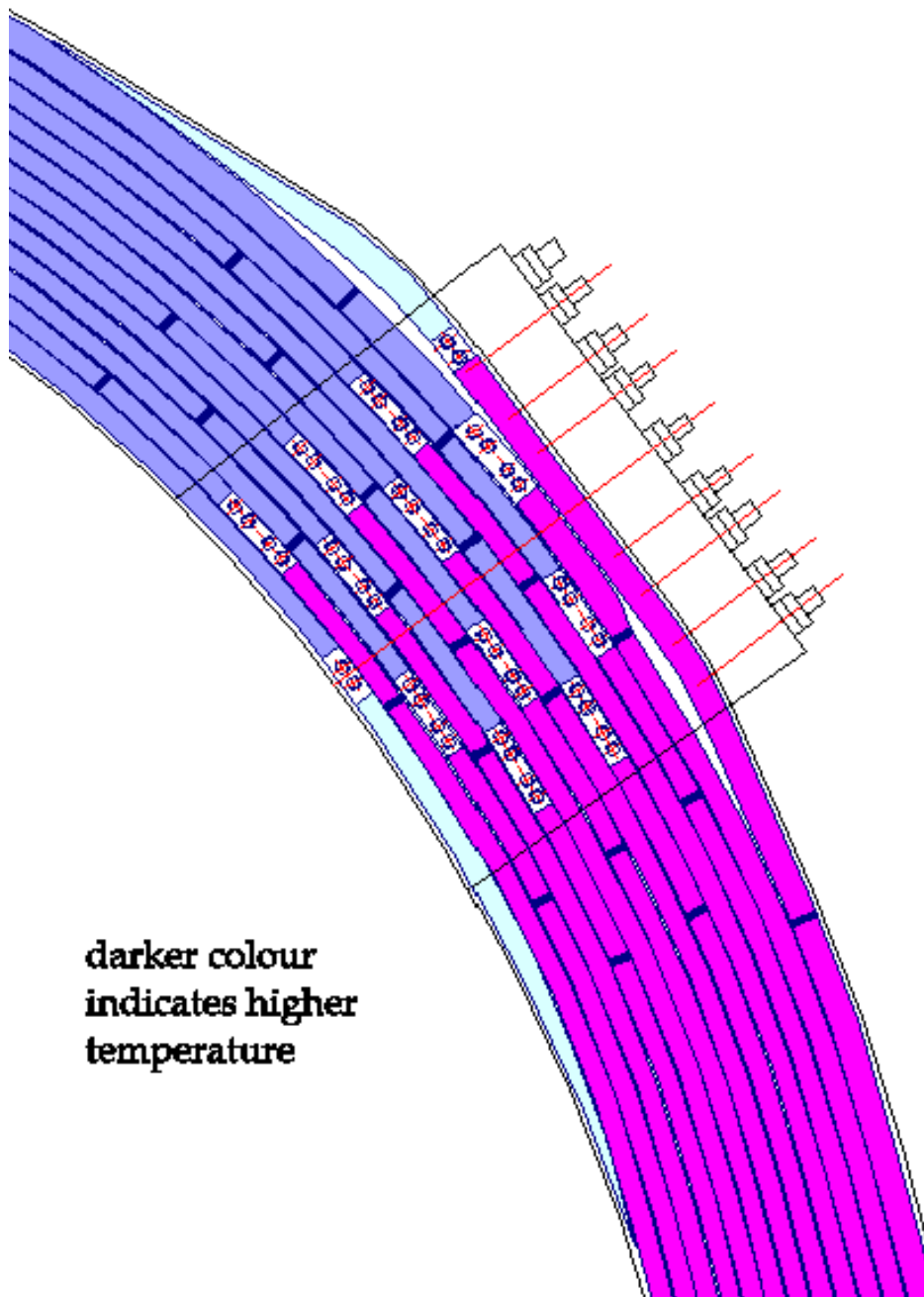


Figure 9 Electrical and coolant connection region

The inlet and outlet coolant connections are adjacent on each conductor. This means a step change in coolant temperature but the copper temperature is smoothed out by thermal conduction.

The tails are heated and cooled only by conduction (through copper or insulation). Their thermal time constant is ~300 seconds. Thus large temperature differences develop between the tail and the rest of the coil.

3.1 Temperature gradient at coolant inlet and outlet

As the cooling rate is much less than the electrical heating rate, the coil heats adiabatically and temperature difference across the coolant inlet/outlet connections is small. After the end of the pulse temperature differences develop, as shown in Fig. 10 .

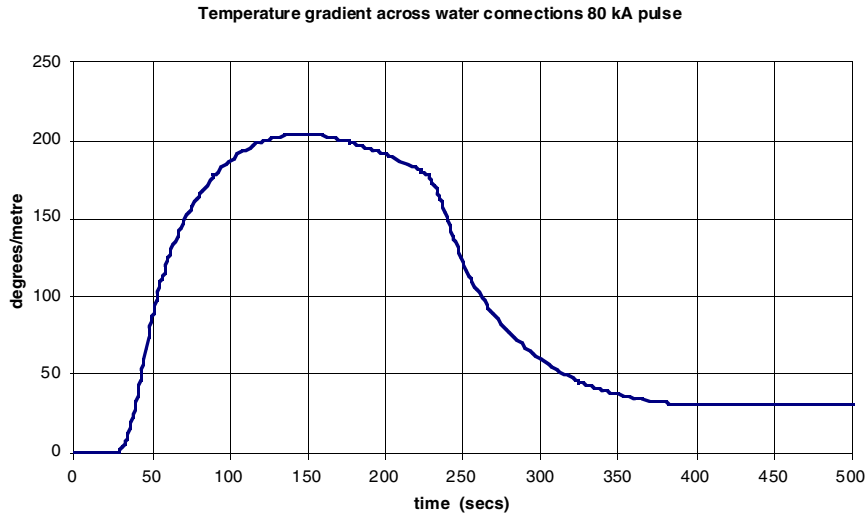


Figure 10 Electrical and coolant connection region

It will be seen that maximum temperature gradient at coolant inlet/outlet occurs at 150 seconds (long after pulse). This is further illustrated by Figs. 11 and 12.

Temperature distribution at time of maximum copper temperature, 80 kA pulse

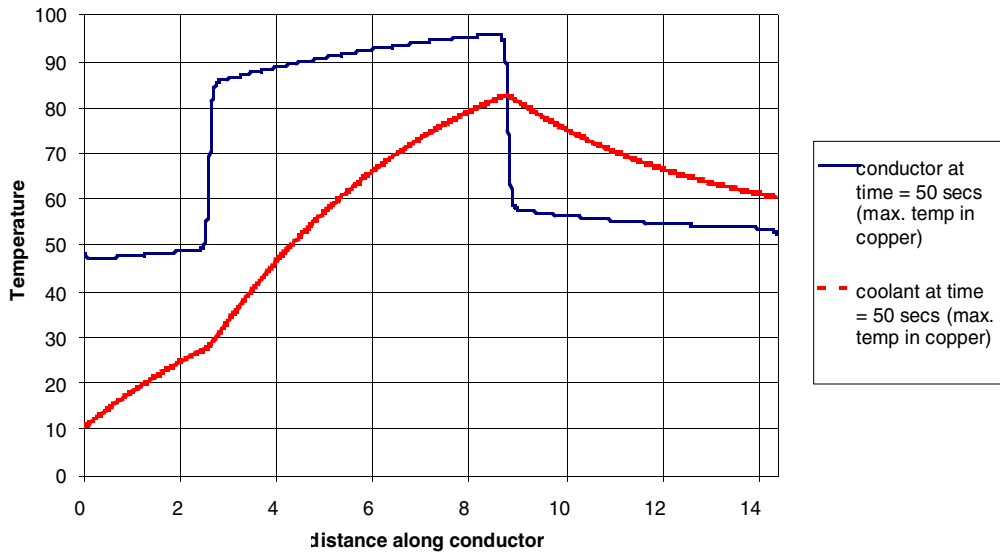


Figure 11 Temperature distribution at end of pulse. Temperature is maximum at the end of pulse. Highest temperature is reached in reduced cross-section. Note that copper temperature at inlet and outlet are approximately equal

Temperature distribution at time of max. temp. gradient at water connections

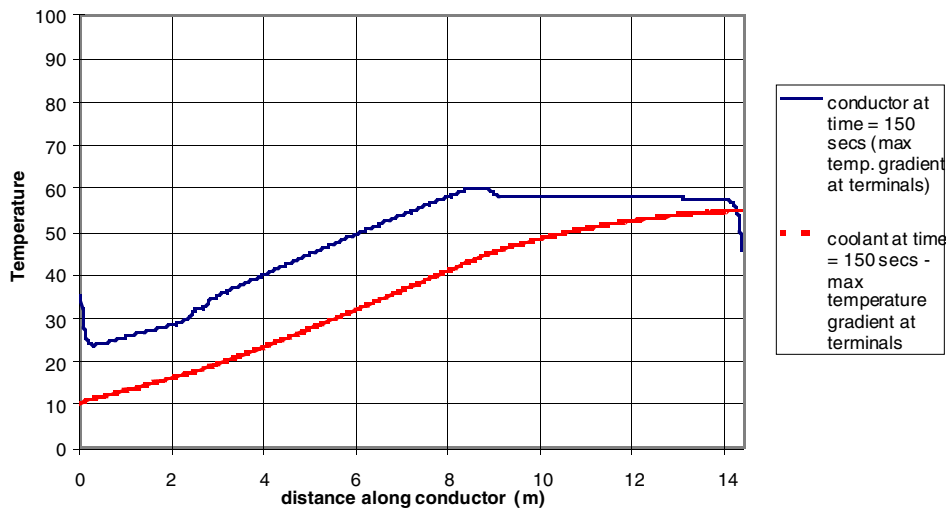


Figure 12 Temperature distribution 150 seconds after start of pulse. Copper temperature at inlet and outlet differ by about 30 degrees.

Temperature distribution near coolant connections at 150 secs, 80 kA pulse

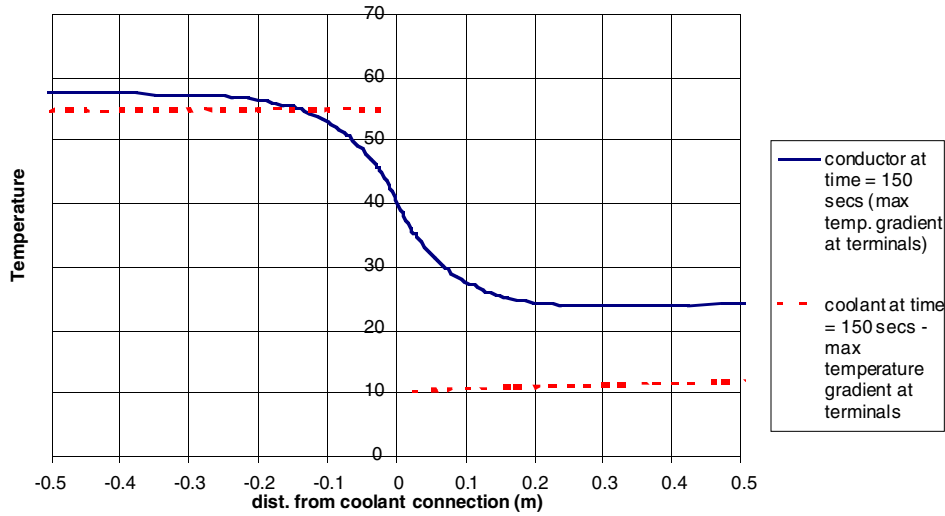


Figure 13 Detail of temperature distribution 150 seconds after start of pulse. Note that coolant temperature is discontinuous but copper temperature is smoothed

3.2 Temperature difference at tail

3.2.1 Thermal equations for several turns

To find the temperature of the tails we have to consider several turns. The previous 1D equations apply if conduction between turns is ignored.

If conduction between turns is included the equation for the conductor is modified.

$$\frac{fT_c}{ft} = \frac{j^2 \rho_e}{\rho_c C_c} - \frac{hs}{\rho_c C_c A_c} (T_c - T_f) + \frac{k_c}{\rho_c C_c} \frac{f^2 T_c}{fx^2} + \frac{k_i s_i}{h_i \rho_c C_c A_c} (T_{c(x+p)} + T_{c(x-p)} - 2T_c)$$

Rate of change of temp.	elect. heat	heat transfer to fluid	longitudinal conduction in copper	inter-turn conduction
-------------------------	-------------	------------------------	-----------------------------------	-----------------------

3.2.2 Temperature calculation for 4 turns

Using this approach a calculation of 4 turns with tails at either end has been made. This is sufficient to simulate the 12 turns of a pancake, as the connection pattern repeats across the pancake.

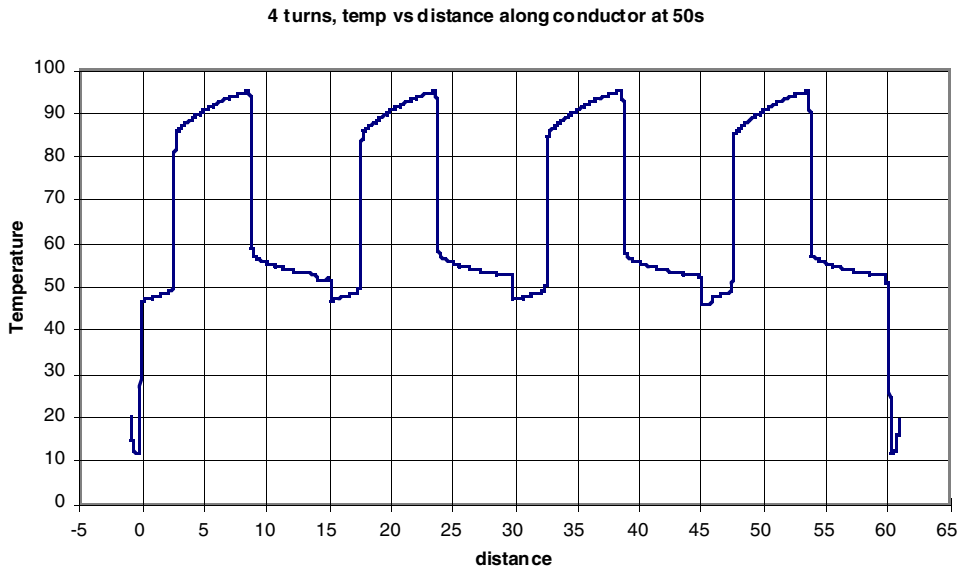


Figure 14 Temperature distribution at end of pulse for 4 turns. Note that 4 turns are similar but tails do not heat up. Temp. difference. at tails is largest at end of pulse (50s).

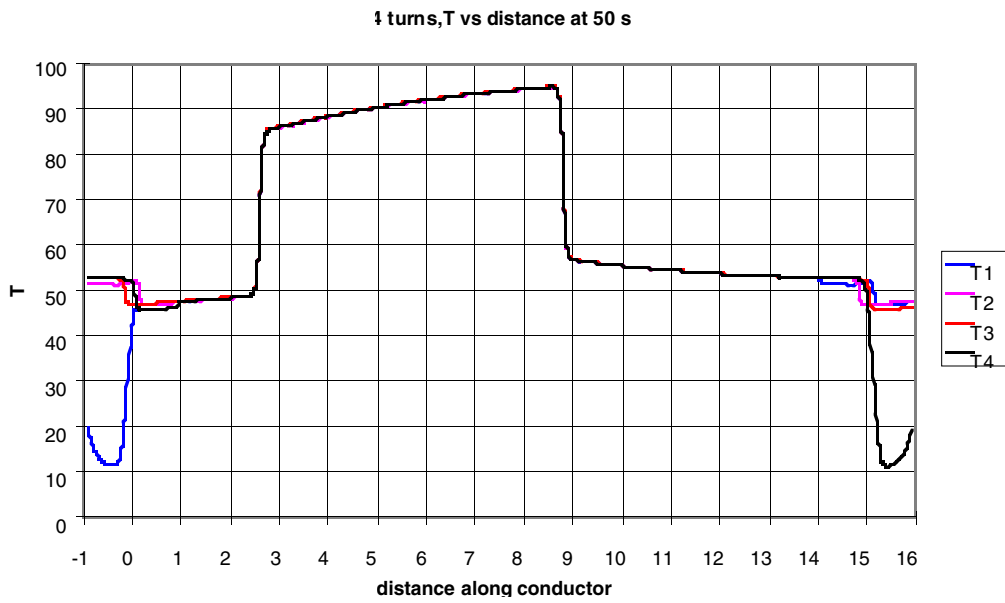


Figure 15 Temperature distribution at end of pulse for 4 turns (as previous graph) with 4 turns superimposed to show differences. The tails do not heat up. .

4 turns, T vs distance at 50s, detail at terminal region

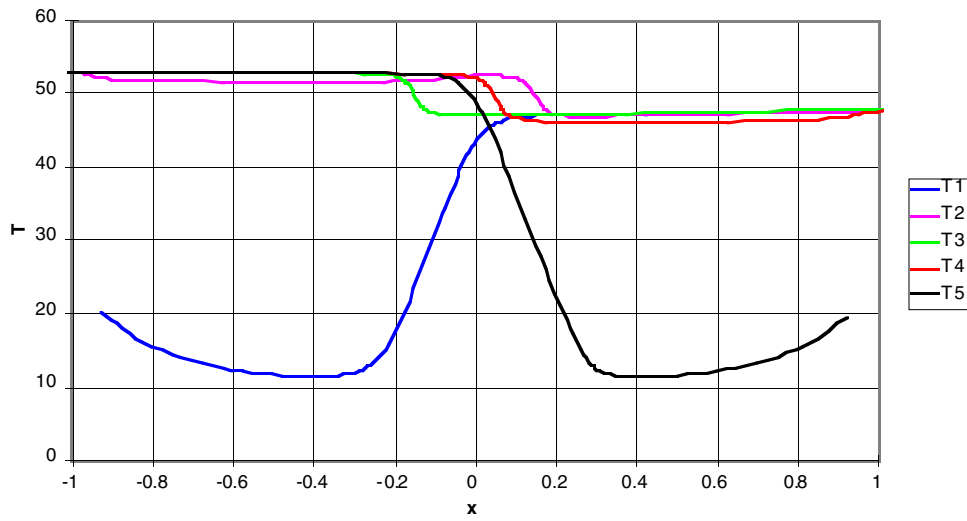


Figure 16 Detail of temperature distribution at terminal region. Turn up at ends is due to conduction through insulation. Graph shown for $I^2t=112e9$. Temp difference $\sim 10C$ less for $I^2t=90e9$

4 Summary of key temperatures

Condition	Region of coil	time	Temperature for $I^2t = 90.10^9 \text{ A}^2\text{s}$	Temperature for $I^2t = 112.10^9 \text{ A}^2\text{s}$
Max. temp in copper	end of reduced section -	end of flat top	55°C	73°C
Max. temp in copper	end of reduced section -	end of pulse	78°C	95°C
Max. temp. difference. across width of copper	beginning of reduced section ~collar (cold end)	end of pulse	<8°C	<10°C
Temp. difference. across width of copper at max. temp.	end of reduced section - ~collar	end of pulse	<2°C	<3°C
Max. longitudinal. temp. gradient in copper	at the coolant connections	at 150 secs (100 secs after end of pulse)	114°C/m	140°C/m
Max. temp. difference. between turns	at pancake ends (tails)	end of pulse	32°C	40°C

5 Effect of change from water to Freon coolant

Freon coolant affects the cooling rate and also the transverse temperature distribution across conductor. Non uniform temperature across the conductor width has an adverse effect because it causes inter-laminar tensile stresses.

5.1 Design Report

The problem of temperature gradients across the coil conductor was recognised in the original JET design report (R5), as illustrated in Fig.16.

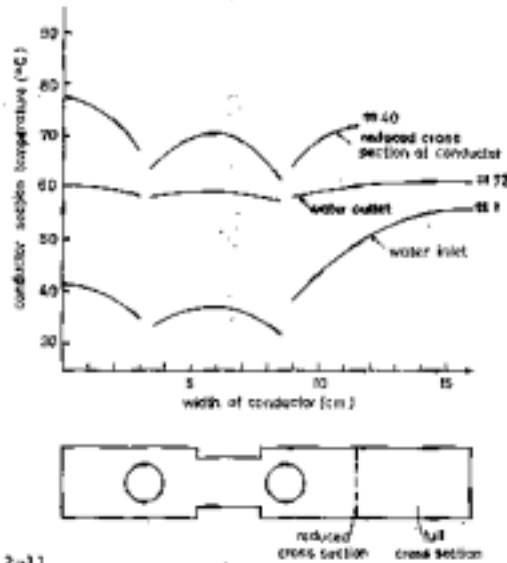


Fig. IV.2-11 Transverse Temperature Distributions in a TF Copper Conductor $I = 66.4 \text{ kA}$ for 20 s.

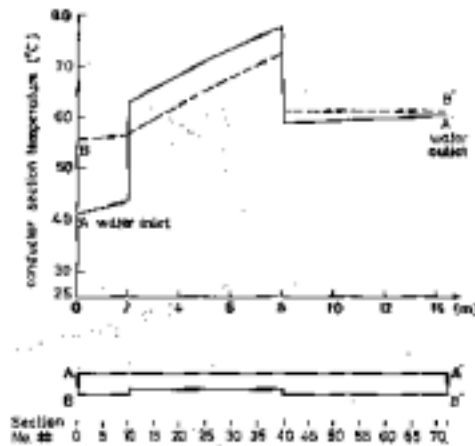


Fig. IV.2-12 Longitudinal Temperature Distributions in a TF Copper Conductor. $I = 66.4 \text{ kA}$ for 20 s. AA' is the inner edge, BB' is the outer edge of a turn.

[IV.2]-23

Figure 17 Temperatures and temperature gradients as described in the JET design report (R5).

5.2 Freon coolant

Since changing to Freon coolant the gradients are less as shown in the graphs below.

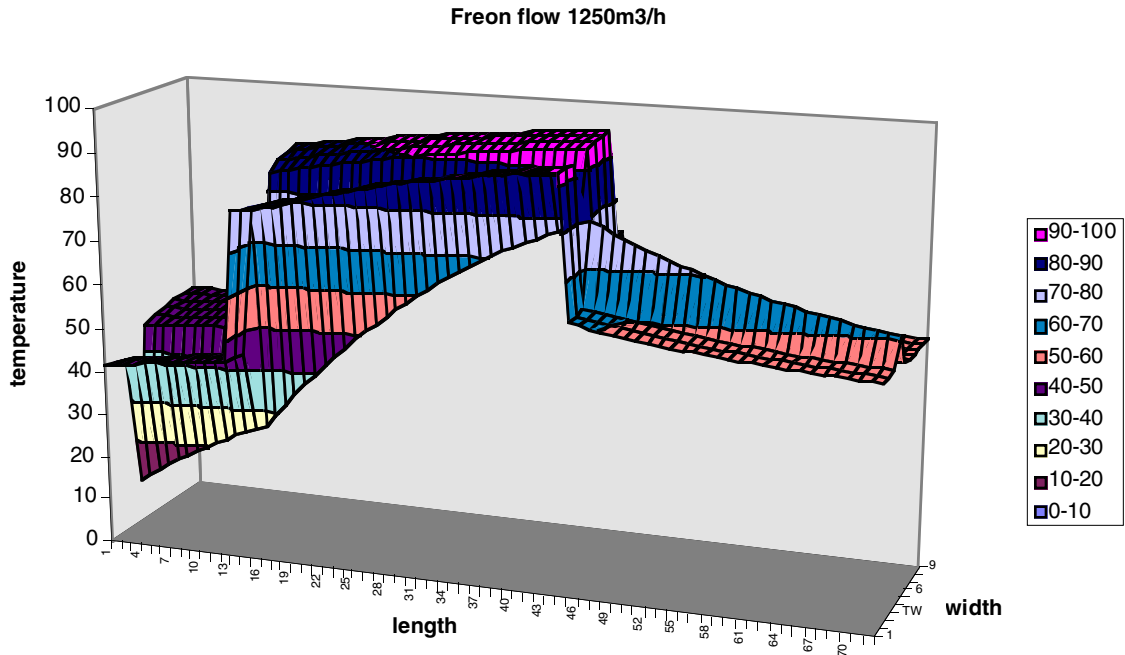


Figure 18 Freon cooling. Temperature distribution at the end of a pulse in one turn. “Length” represents the length of one turn and goes from coolant inlet to outlet. “Width” is the half the width of the conductor and includes one cooling hole. The groove or spine in the temperature profile represents the temperature of the coolant.

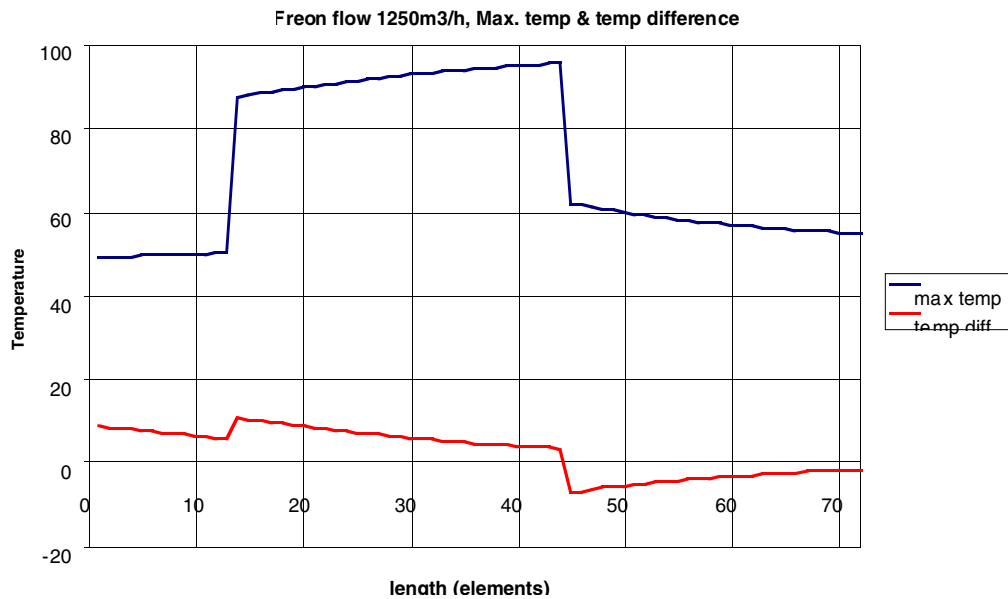


Figure 19 Freon cooling. Maximum temperature and temperature difference across width of conductor (=max. temp. in copper - min. temp. in copper at a given position along the length). Note that the temperature difference in the critical collar region, where the temperature is highest is less than 5°C.

5.3 Water coolant

Originally water was used at a higher flow rate. Heat transfer to water is better even at the same flow rate. This means that the temperature difference copper/coolant is less but the temperature difference inside the copper is higher because of the higher heat flux. Two flow rates with water cooling are shown below.

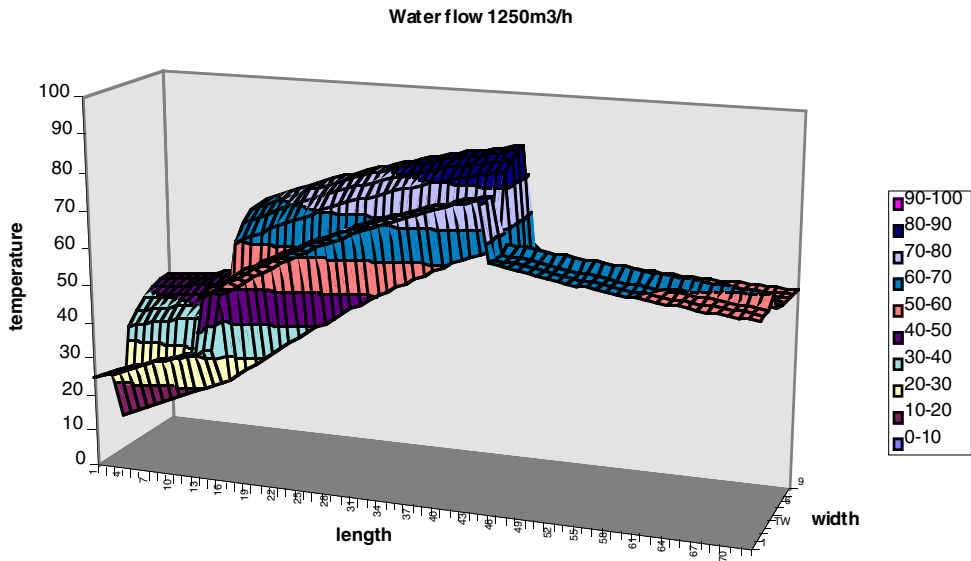


Figure 20 Water cooling 1250m³/h. Temperature distribution at the end of a pulse in one turn. “Length” represents the length of one turn and goes from coolant inlet to outlet. “Width” is the half the width of the conductor and includes one cooling hole. The groove or spine in the temperature profile represents the temperature of the coolant.

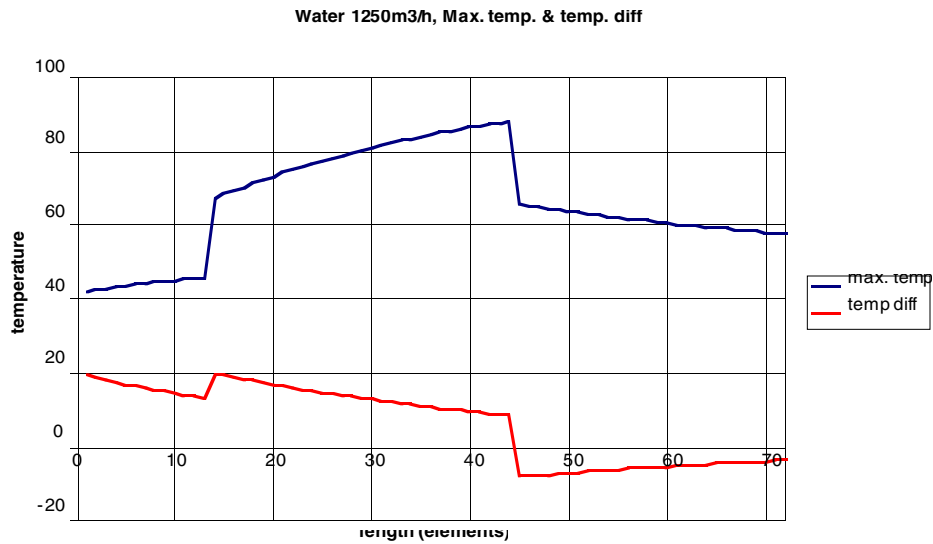


Figure 21 Water cooling 1250m³/h. Maximum temperature and temperature difference across width of conductor (=max. temp. in copper - min. temp. in copper at a given position along the length). Note that the temperature difference in the critical collar region, where the temperature is highest is 10 °C.

Water flow 2500m³/hr

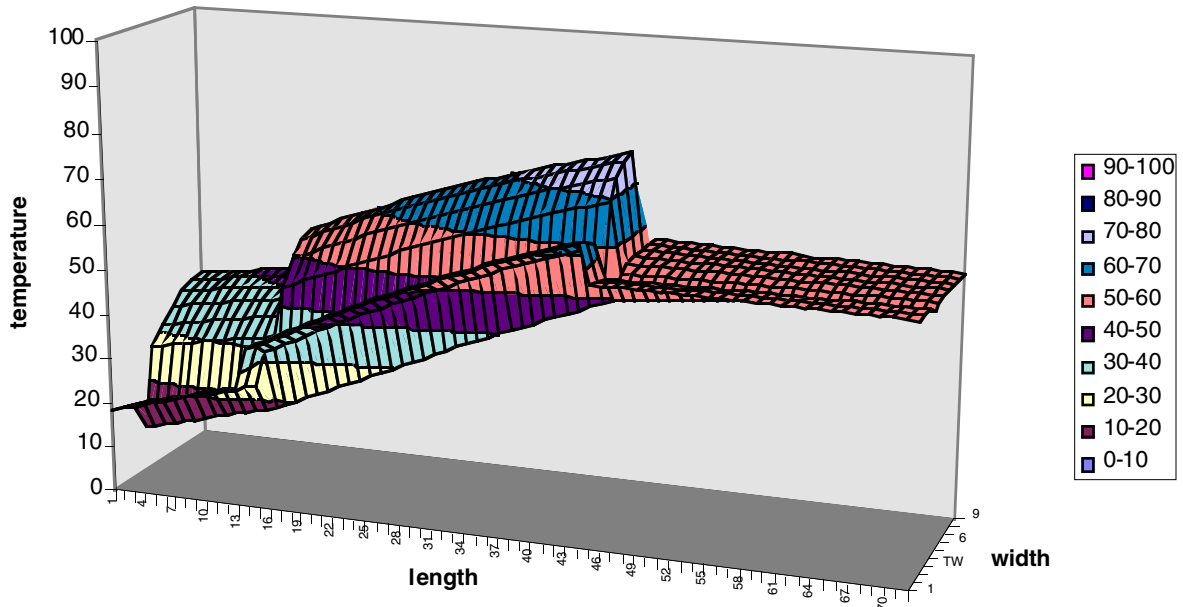


Figure 22 Water cooling 2500m³/h. Temperature distribution at the end of a pulse in one turn. “Length” represents the length of one turn and goes from coolant inlet to outlet. “Width” is the half the width of the conductor and includes one cooling hole. The groove in the temperature profile represents the temperature of the coolant.

Water flow 2500m³/hr, Max temp & temp. diff.

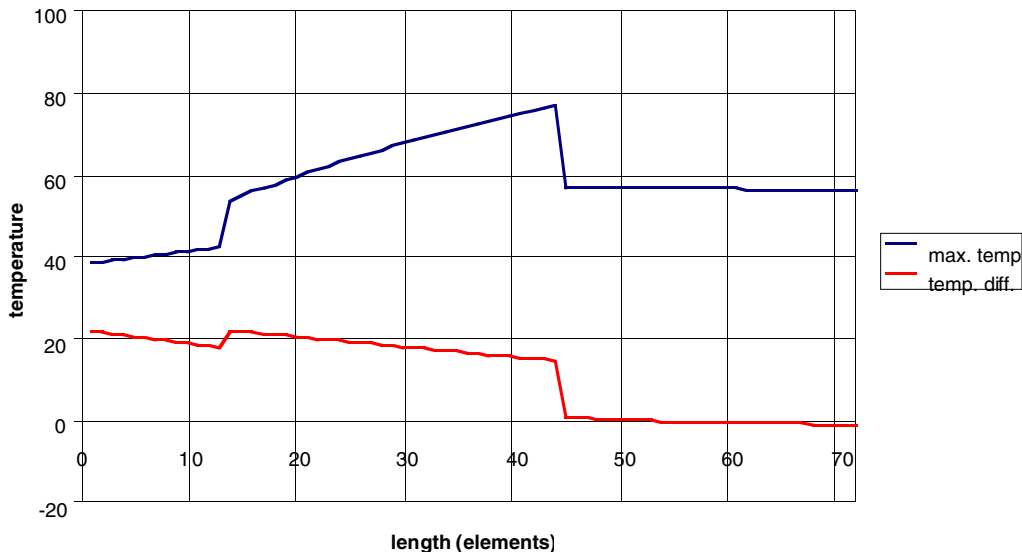


Figure 23 Water cooling 2500m³/h. Maximum temperature and temperature difference across width of conductor (=max. temp. in copper - min. temp. in copper at a given position along the length). Note that the temperature difference in the critical collar region, where the temperature is highest is 15 °C.

5.4 Summary of transverse gradient effects

When water cooled the temperature difference across the copper conductor at critical regions was 10 or 15°C depending on the flow rate. It has been reduced to 5°C by the use of Freon at a lower flow rate. This gives an inter-laminar tensile stress of about 2.5MPa.

6 Thermal stresses in connection region

6.1 Analytic calculation

The following are analytic calculations of stresses near the TF water connections. They are intended as an independent check and aid to understanding for the finite element calculation.

The temperature distribution near the TF coil water connections is approximately as shown below.

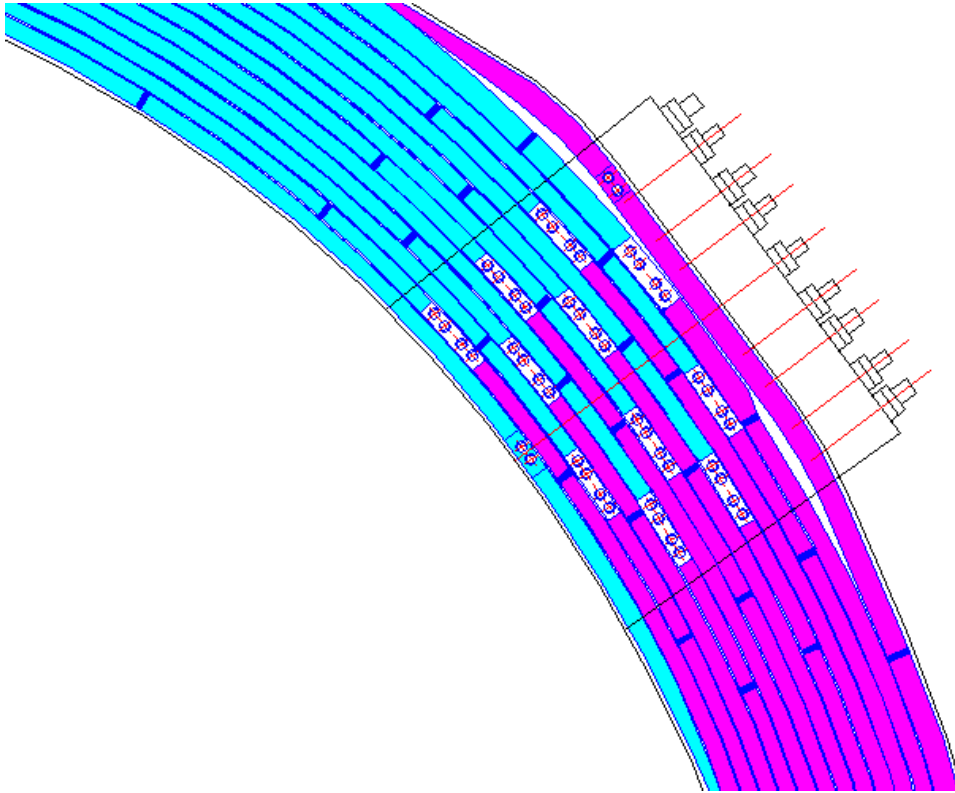


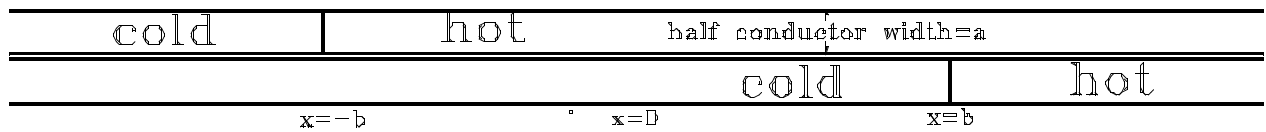
Figure 24 Connection region coloured to show hot and cold conductor.

6.2 Stresses at inlet outlet

This can be simplified to make an analytic model feasible.

		cold	hot
cold	hot		
		cold	hot
cold	hot		
		cold	hot

This is a periodic structure so we can cut along the centre of two adjacent conductors to make a solvable problem.



The differential equations are

$$\frac{d\sigma_1}{dx} = -\frac{\tau}{a}$$

$$\frac{d\sigma_2}{dx} = \frac{\tau}{a}$$

$$\tau = (y_2 - y_1) \frac{G}{h}$$

$$\frac{dy_1}{dx} = \frac{\sigma_1}{E} + \alpha T_1$$

$$\frac{dy_2}{dx} = \frac{\sigma_2}{E} + \alpha T_2$$

where σ is tensile stress in copper, τ is shear stress in insulation, x is distance along conductor, y is longitudinal displacement, T is temperature, E is tensile modulus of copper, G is shear modulus of insulation, a is thickness of copper, h is thickness of insulation and suffices 1 and 2 refer to upper and lower conductors.

The temperature is assumed to make a step change at each of the interfaces from T_c (cold) to T_h (hot). The problem divides into three regions; $-x$ to $-b$, $-b$ to b and b to x .

The solution is of the form

$$\sigma_1 = Ae^{-\frac{x}{L}} + Be^{\frac{x}{L}} + \frac{G\alpha L^2}{a_1 h} (T_2 - T_1)$$

where $L = \sqrt{\frac{hEa}{2G}}$

Applying boundary conditions and inserting numerical data ($E= 120000$, $G= 4000$, $\alpha = 1.70E-05$, $a= 14$, $b= 100$, $h= 2$, $L= 29$, $T_c= 10$, $T_h= 50$) we get the following distorted shape and stresses.

C	C	C	C	H	H	H	H	H	H	H	H	H	H	H	H	H
C	C	C	C	C	C	C	C	C	C	C	C	C	H	H	H	H

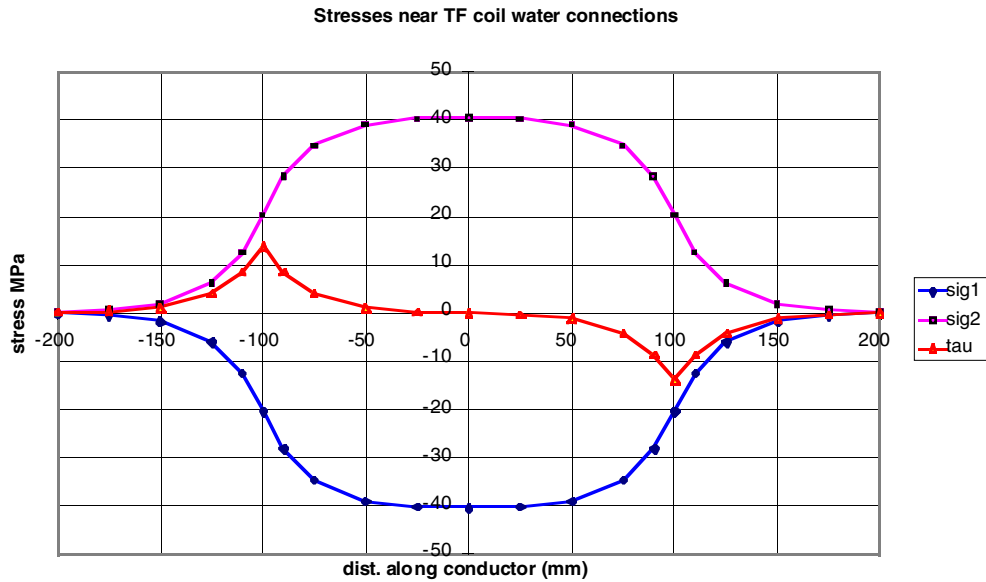


Figure 25 Stresses near water connections. (sig=tensile stress, tau=shear stress)

It will be seen that the maximum shear stress (14 MPa) occurs at the cold/hot interface. If we change 'a' to 28 mm (= full thickness of conductor) we get a maximum shear stress of 20 MPa.

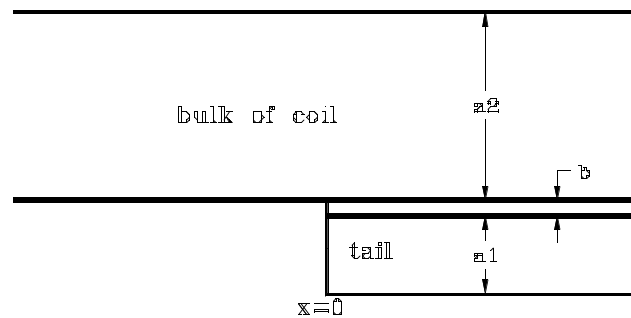
The hot conductor is compressed and the adjacent cold conductor is stretched. The tensile or compressive stress in the conductor is given by $\alpha E(T_h - T_c)/2 = 40$ MPa.

In reality the temperature change at the inlet/outlet has a gradient over about 200mm which should reduce the stress considerably.

6.3 Stress at TF coil tail

6.3.1 Model

The coil tail tip can be represented as shown below.



The differential equations for this are:

$$a_1 \frac{d\sigma_1}{dx} = \tau$$

$$a_2 \frac{d\sigma_2}{dx} = -\tau$$

$$\tau = (y_1 - y_2) \frac{G}{b}$$

$$\frac{dy_1}{dx} = \frac{\sigma_1}{E} + \alpha T_1$$

$$\frac{dy_2}{dx} = \frac{\sigma_2}{E} + \alpha T_2$$

where σ_1 and σ_2 are tensile stresses, τ is shear stress, y_1 and y_2 are the deflections of the two copper pieces, G is the shear modulus of the insulation and E the tensile modulus of the copper. These equations can be solved and an important characteristic length is revealed.

$$L = \sqrt{\frac{Eb}{\left(\frac{1}{a_1} + \frac{1}{a_2}\right)G}}$$

This length controls the exponential rate of decay of stress from the end of the tail. Mechanical and thermal stresses have different boundary conditions so are best solved separately.

6.3.2 Mechanical stresses

If σ_0 is the tensile stress as $x \rightarrow \infty$, then the solutions for $x > 0$ are

$$\sigma_1 = \sigma_0(1 - e^{-x/L})$$

$$\sigma_2 = \sigma_0\left(1 + \frac{a_1}{a_2}e^{-x/L}\right)$$

$$\tau = \frac{\sigma_0 a_1}{L} e^{-x/L}$$

If $E = 120\text{GPa}$, $G = 4\text{GPa}$, $b = 2$, $a_1 = 3$, $a_2 = 300$ and $\sigma_0 = 60\text{MPa}$, then $L = 13.4$ and $\tau_{\text{mech max}} = 13.4 \text{ MPa}$

6.3.3 Thermal stresses

Solutions for thermal stress ($x > 0$) are

$$\sigma_1 = \frac{G\alpha L^2(T_2 - T_1)}{a_1 b} (1 - e^{-x/L})$$

$$\sigma_2 = -\frac{G\alpha L^2(T_2 - T_1)}{a_2 b} (1 - e^{-x/L})$$

$$\tau = \frac{G\alpha L(T_2 - T_1)}{b} e^{-\frac{x}{L}}$$

If $T_2 - T_1 = 30$, $\alpha = 17e-6$ and other parameters are as above then $\tau_{th \max} = 13.7 \text{ MPa}$

6.3.4 Total shear stress

This is **27 MPa** which agrees quite well with FE calculations.

This agreement should not be taken as too significant because of the geometrical errors in the analytic model. These can be reduced if a_1 is made a function of x .

7 List of figures

Figure 1	Coil showing connection region	2
Figure 2	Current and temperature vs time for medium energy pulse	4
Figure 3	Current and temperature vs time for maximum energy pulse	4
Figure 4	Temperature distribution across conductor at end of pulse	5
Figure 5	Temperature vs time for maximum energy pulse. The temperature difference across the conductor is the difference between the temperature adjacent to the cooling hole and the temperature at the edge of the conductor	6
Figure 6	3D model of single turn	7
Figure 7	Detail of 3D model	8
Figure 8	Maximum copper temperature vs time - comparison of 1D, 2D and 3D models	8
Figure 9	Electrical and coolant connection region	10
Figure 10	Electrical and coolant connection region	11
Figure 11	Temperature distribution at end of pulse. Temperature is maximum at the end of pulse. Highest temperature is reached in reduced cross-section. Note that copper temperature at inlet and outlet are approximately equal	12
Figure 12	Temperature distribution 150 seconds after start of pulse. Copper temperature at inlet and outlet differ by about 30 degrees.	12
Figure 13	Detail of temperature distribution 150 seconds after start of pulse. Note that coolant temperature is discontinuous but copper temperature is smoothed	13
Figure 14	Temperature distribution at end of pulse for 4 turns. Note that 4 turns are similar but tails do not heat up. Temp. difference. at tails is largest at end of pulse (50s).	14
Figure 15	Temperature distribution at end of pulse for 4 turns (as previous graph) with 4 turns superimposed to show differences. The tails do not heat up. .	14
Figure 16	Detail of temperature distribution at terminal region. Turn up at ends is due to conduction through insulation. Graph shown for $I_2t=112e9$. Temp difference $\sim 10C$ less for $I_2t=90e9$	15
Figure 17	Temperatures and temperature gradients as described in the JET design report (R5).	17
Figure 18	Freon cooling. Temperature distribution at the end of a pulse in one turn. "Length" represents the length of one turn and goes from coolant inlet to outlet. "Width" is the half the width of the conductor and includes one cooling hole. The groove or spine in the temperature profile represents the temperature of the coolant.	18
Figure 19	Freon cooling. Maximum temperature and temperature difference across width of conductor (=max. temp. in copper - min. temp. in copper at a given position along the length). Note that the temperature difference in the critical collar region, where the temperature is highest is less than $5^{\circ}C$.	18
Figure 20	Water cooling $1250m^3/h$. Temperature distribution at the end of a pulse in one turn. "Length" represents the length of one turn and goes from coolant inlet to outlet. "Width" is the half the width of the conductor and includes one cooling	

hole. The groove or spine in the temperature profile represents the temperature of the coolant. 19

Figure 21 Water cooling 1250m³/h. Maximum temperature and temperature difference across width of conductor (=max. temp. in copper - min. temp. in copper at a given position along the length). Note that the temperature difference in the critical collar region, where the temperature is highest is 10°C. 19

Figure 22 Water cooling 2500m³/h. Temperature distribution at the end of a pulse in one turn. "Length" represents the length of one turn and goes from coolant inlet to outlet. "Width" is the half the width of the conductor and includes one cooling hole. The groove in the temperature profile represents the temperature of the coolant. 20

Figure 23 Water cooling 2500m³/h. Maximum temperature and temperature difference across width of conductor (=max. temp. in copper - min. temp. in copper at a given position along the length). Note that the temperature difference in the critical collar region, where the temperature is highest is 15°C. 20

Figure 24 Connection region coloured to show hot and cold conductor. 22

Figure 25 Stresses near water connections. (sig=tensile stress, tau=shear stress) 24

Thermal stresses at the coolant connections

P Miele
09 November 1999

Contents:

1.	2D Partial Model of a TF Coil	2
1.1.	Objectives:.....	3
1.2.	Model:.....	3
1.2.1.		Input 3
1.2.2.		Output 3
2.	Transient Analysis:.....	4
2.1.	Analysis:.....	5
3.	Results	10
3.1.	Confidence in the result:.....	10
4.	Conclusions	11

1. 2D Partial Model of a TF Coil

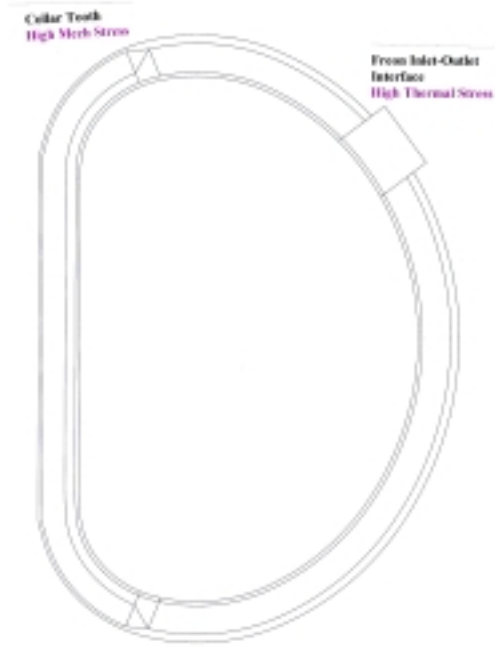


Figure 1 Coil showing connection region

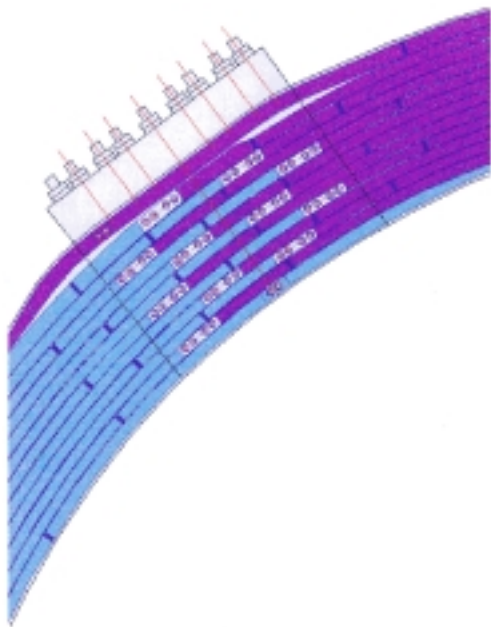


Figure 2. Detail of connection region

Mechanical Structure Model: Inter-Octant Keys and Coil Support Stiffness

V. Riccardo, G. Sannazzaro,

10 November 1999

Contents

1.	General description.....	1
2.	Description of the FE model of the MS	2
3.	Analytical and numerical calculation of the key and bolt forces....	5
4.	Stiffness of the mechanical structure.....	9
5.	Conclusions	14

1. General description

The MS (fig. 1) forms a shell enclosing and supporting the TF coils. It consists of 8 identical octants. The outer shell can be removed from the inner part of the MS. It includes one vessel octant and 4 TF coils.

Each of the TF coils is subject to a net radial centripetal force and to a twisting torque. The MS has been designed to take up these forces and at the same time to let the coils expand (because of their hoop loads and increase in temperature during pulsing).

The centripetal force is taken by the central solenoid (P1). Reinforcing steel rings are located inside this coil to decrease its compressive stress. P1 expands homogeneously during a pulse, so it provides a straight inner support to the TF coils.

The free vertical expansion of both the TF coils and P1 is made possible by means of thin layers of a low-friction material. The weight of each coil is taken by a spring jack at the bottom of the machine. This jack provides an elastic support allowing vertical expansion while the TF coil is pressed against P1. The TF coils can also slide freely

inside the shell structure. A small centripetal force is provided by the pre-loaded push-pull-jacks to ensure the TF coil is always in contact with P1.

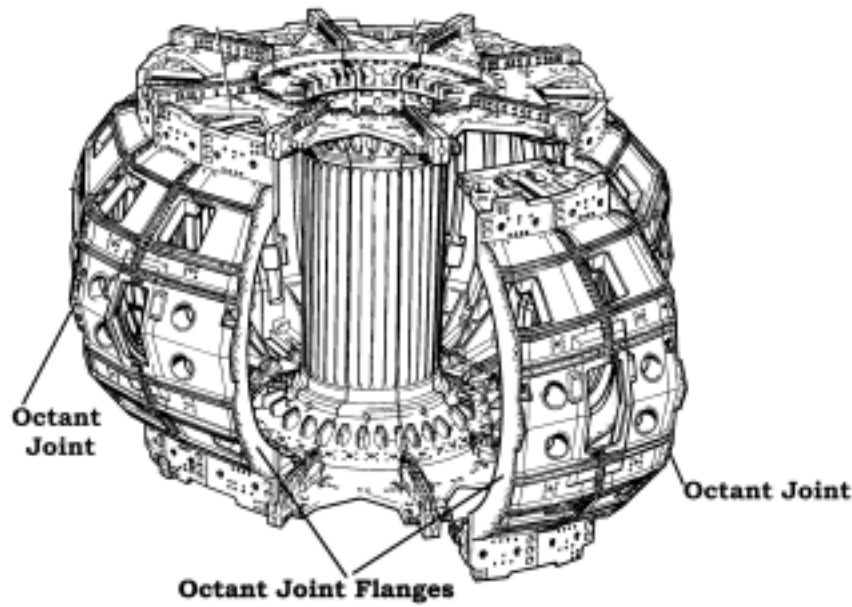


Fig. 1 Geometry and basic principle of assembly of the mechanical structure

The TF coils out-of-plane forces generated by the interaction of the coil current with the poloidal field are reacted where they arise, so avoiding large deflections due to bending moments. Because of the great variety of force distributions, the structure must provide a good support all around the coils. The structure is a thin metallic shell which completely surround the TF coils. Electrical breaks are provided to withstand the voltage induced by the PF coils. Between the TF coils and the structure are adjustable wedges which define the location of each coil and transmit the forces to the shell structure. Due to these twisting forces the shell is subject to shear stresses along the meridian and parallel lines.

The stiff part of the structure which actually reacts the torque is the outer shell. This is made by castings which contain grooves for the TF coils (except where some access to the vessel is required). The octant castings are split at the mid plane.

The upper and lower part of the shell is made of sections of a torsional ring which includes the ring teeth between the coils and which are mechanically connected to the outer part of the shell. The conically-shaped inner part of the structure is called the collar, contains the collar teeth and is connected to the inner cylinder with steel dowels.

The inner part of the MS is a thin cylinder split into 8 sectors. The aim of this inner cylinder is to prevent any lateral deflection of the TF coil because of the out-of-plane loads. For this purpose the nose of each coil rests in a vertical groove machined in the sectors of the cylinder. The inner cylinder does not resist any torque by itself, it only keeps the coil straight. The twisting forces applied by the coil to each sector are taken by the outer shell through the bottom and top dowel connections. Each of the sectors can slide along the dowels in order to allow for the thermal expansion of P1.

2. Description of the FE model of the MS

A FE models of the MS was generated to

- analyse the general behaviour of the component under different load conditions
- estimate the general stress and the stress concentrations in the structure
- estimate the load on the octant-to-octant and intra-octant joints (loads on bolts and keys)
- evaluate the structure stiffness

The FE model of the MS consist of one half of one octant of the structure; it comprises the outer shell, the ring, the collar, the inner cylinder and the TF coils.

The shell is the most complex component of the whole model of the MS (fig. 2). The shell has been modelled as a solid of revolution, by rotating a typical vertical section around the vertical axis through the centre of the machine. Such a kind of simplification was considered necessary to avoid over-complications in the modelling. The most significant departure from this generalisation is around the main port and at the circular openings (fig. 3).

The shape of the vertical section (fig. 4) was defined using the JET drawings and its initial definition only referred to the points where the slope changes and to the points in contact with the TF coils. These points were not enough to model the inter-octant and octant-octant keys. Moreover, the resulting mesh size would have been too coarse. In order to model the keys and simultaneously refine the mesh size, the previously defined points were inter-spaced with additional points.

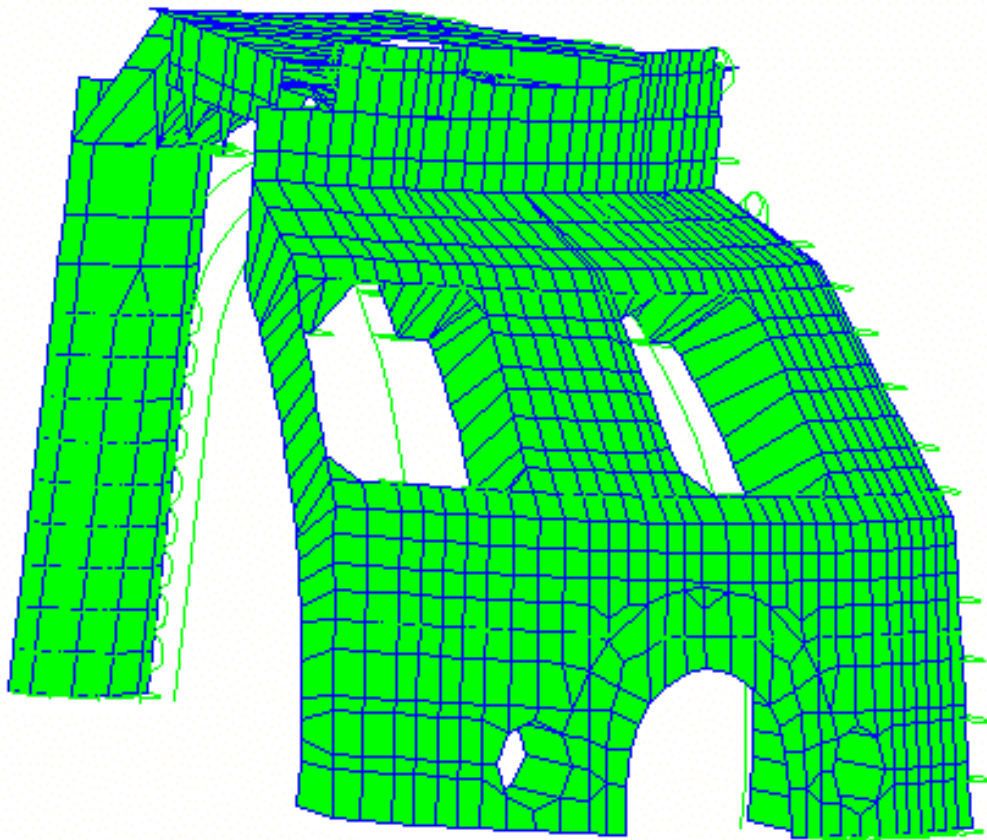


Fig. 2 The FE model of the MS (including the 4 TF coils)

The majority of the points is defined in two sets of co-ordinate systems:

- the large convex part of the shell is described by a set of spherical co-ordinate systems: in order to define properly the plane tilted at 2.5° it was not possible to use cylindrical co-ordinate systems, which would be otherwise easier to handle
- the tray and the flat vertical ports attached are defined in sets of cylindrical co-ordinate systems, all sharing a common horizontal plane and the z-axis: this simplifies the definition of the shell-tray connections, all of which are radial.

In each half octant there are two circular openings, two TF ports and half a main port.

The two circular opening have their own co-ordinate systems. For the purpose of this model, a radius of 200 mm has been used. This is not the radius at the mid-thickness, but it is more representative of the stiffness, since modelling the circle by an octagon of the same radius would have effectively strengthened the area around the hole.

The main port is defined as the interception surface between a horizontal cylinder and the skew planes that form the front of the shell. The axis of the cylinder is parallel to the x-axis at $z=200$ m, the inside radius is 500 mm and the outside radius is 850 mm. To define the mesh a grid has been drawn across the skew planes and the trace of the port has been taken on this grid.

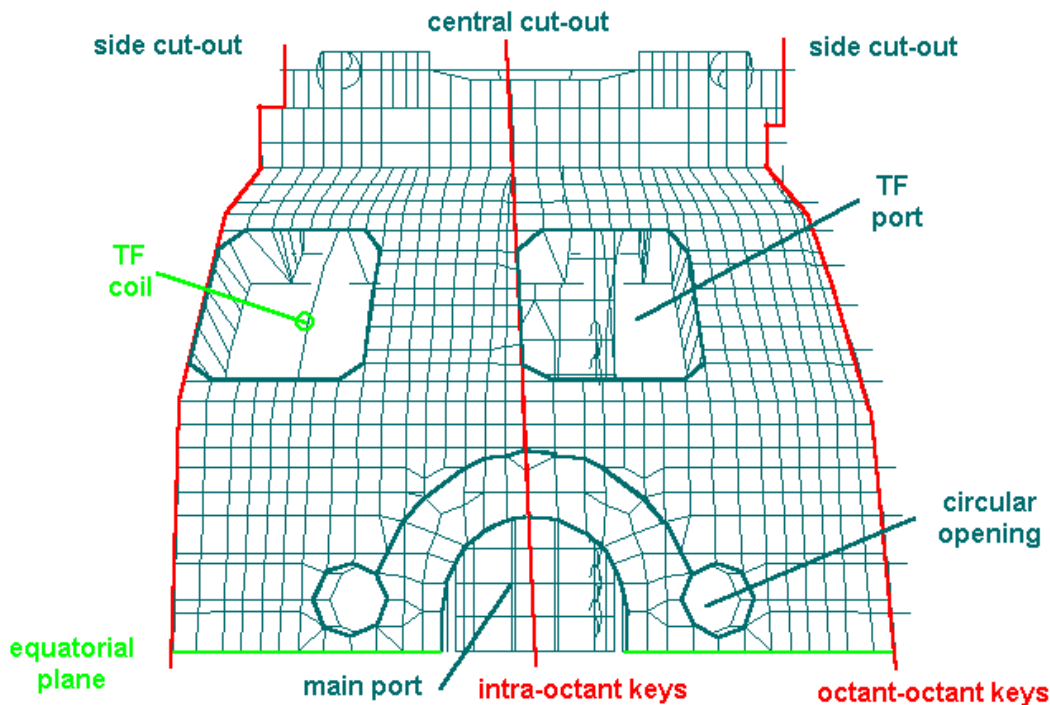


Fig. 3 View from outside of the MS mesh

Finally an attempt has been made to use different material definitions for functionally different areas of the shell: even if their thickness are known to be the same. This choice

has been done so that it is easier to change the material properties to adjust the model characteristics to the actual structure characteristics.

The model has cyclic symmetry (with springs between the octants, octant-to-octant keys, and in the middle of the octant, intra-octant keys, to represent the flexibility of the connection) applied to the nodes at the meridian boundary planes and at the equatorial plane. This boundary condition is in theory correct only if the load is antisymmetric with respect to the equatorial plane. In divertor configurations this is not true, but an assessment of the effect of the departure from the top/bottom antisymmetry has shown that this approximation introduced an error small enough to be acceptable.

Initially the loads were applied directly at the TF coil supports, the TF coils have been added later to the model. The aim of this upgrade was to apply the load in a self-consistent way. The TF coils have been modelled using beam elements. Spring elements have been used to represent the local flexibility of the contact points between the coil and the MS.

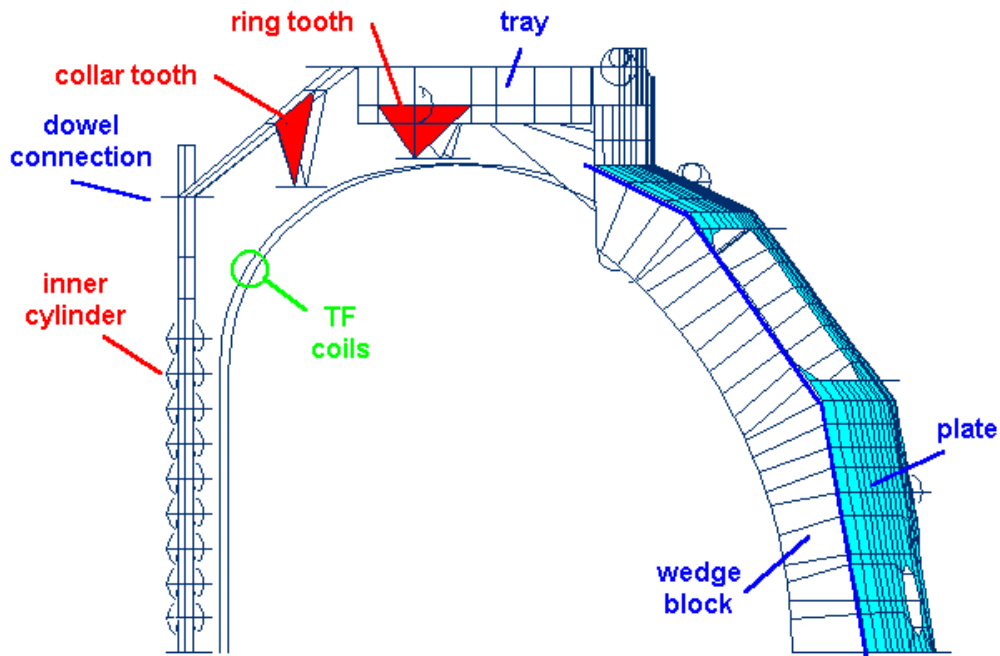


Fig. 4 View from the side of the MS mesh

3. Analytical and numerical calculation of the key and bolt forces

The out-of-plane forces acting on the TF coils are computed with equilibrium code. As an example with MaxFEA it is possible to write the poloidal field normal to the TF coil in a file suitable to be converted and added as load to the FE model of the MS. Once loaded the FE model computes, among other things, the poloidal force on the octant-to-octant keys (shear) and the toroidal force on the pair of bolts close to each key. These forces were of particular interest when the opportunity to re-tighten the inter-octant bolts was discussed in the autumn 1998 and are discussed in the following. Similarly the same out-of-plane force distribution can be used to analytically calculate machine torque (fig. 5) and the MS key forces. The machine torque is defined as the resulting moment calculated with respect to the central axis due to out-of-plane forces on the 32 upper and

lower halves of the TF coils (the torque on the upper half has to be of similar magnitude and opposite to the torque on the lower half, as the full machine torque is zero).

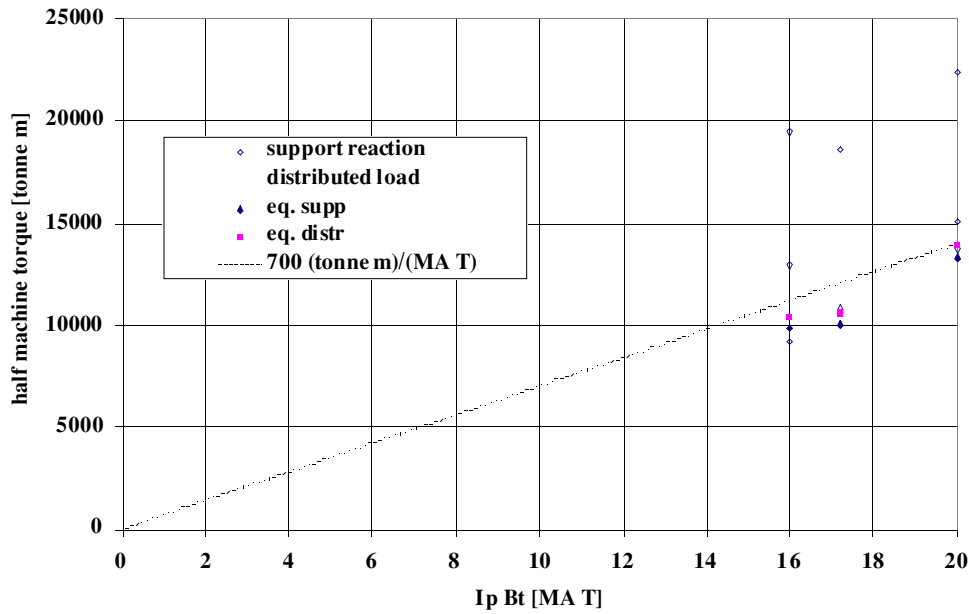
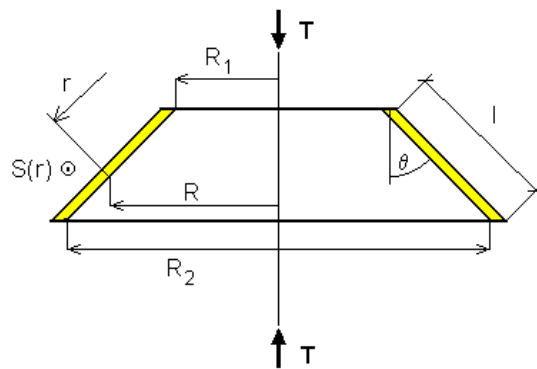


Fig. 5 The upper envelope for the equilibrium scaling of the torque [tonne m] is $700 I_p B_t$ [MA] Bt [T].

The torque at each of the conical shells making up the MS can be computed from the out of plane support reaction forces. Once the torque on the conical shell is known, it is possible to **analytically** evaluate the key forces.



The shear flow at a position r along the shell is

$$S(r) = \frac{T}{2\pi R^2}.$$

The average force acting on that shell is

$$F_{1,2} = \int S(r) dr = \int \frac{T}{2\pi R^2} dr.$$

Since

$$\sin \theta = \frac{dr}{R} = \frac{R_2 - R_1}{l}$$

the integration variable can be changed from r into R , being

$$dr = dR \frac{l}{R_2 - R_1}.$$

Therefore the average force on the conic shell is

$$F_{1,2} = \frac{Tl}{2\pi(R_2 - R_1)} \int_{R_1}^{R_2} \frac{dR}{R^2} = \frac{Tl}{2\pi R_1 R_2}.$$

This calculation can be done using a spreadsheet.

The force on the key and bolts of the MS for the three high performance scenarios at 4T have been computed with the FE model. The maximum key shear force has been compared with the analytical one (Fig. 6) and the two are in good agreement (the analytical one is a bit more conservative because it assumes infinite stiffness). The maximum key forces are summarised in Table 1 and the maximum bolt forces in Table 2.

The poloidal distribution of key and bolt forces has been calculated in equilibrium and disruption for each of the approved 4 T scenarios. The load distribution on the inter-octant keys and bolts are very similar in the three scenarios. This is because the geometry of the in-vessel components limits the shape (and hence the distribution of the poloidal field normal to the TF coils which is the actual load applied to the model) of the high performance plasmas that can be run. The highest forces are generated by the ELM-free H-mode plasma so results for this plasma are plotted.

Fig. 7 and 8 show the poloidal distribution of key and bolt forces respectively. Fig 9 and 10 compare the analytical and the FE key force along the MS.

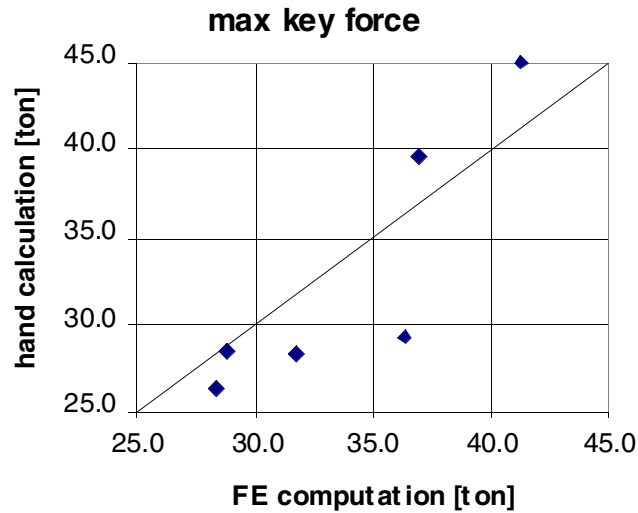


Fig. 6 Comparison between analytical and numerical calculation of the maximum shear force on the MS keys

	FE computation	hand calculation	unit
Optimised Shear (eq) 4 MA 4 T	28.6	26.3	ton
Optimised Shear (dis) 4 MA 4 T	36.4	29.2	ton
ELM-free H-mode (eq) 4.3 MA 4 T	28.8	28.4	ton
ELM-free H-mode (dis)4.3 MA 4 T	37.0	39.6	ton
ELMy H-mode (eq) 5 MA 4 T	31.7	28.3	ton
ELMy H-mode (dis) 5 MA 4 T	41.3	44.9	ton

Table 1 MS octant joint key forces

	bolt force [ton]
Optimised Shear (eq) 4 MA 4 T	1.8
Optimised Shear (dis) 4 MA 4 T	2.4
ELM-free H-mode (eq) 4.3 MA 4 T	2.0
ELM-free H-mode (dis)4.3 MA 4 T	2.5
ELMy H-mode (eq) 5 MA 4 T	2.0
ELMy H-mode (dis) 5 MA 4 T	2.6

Table 2 MS octant joint bolt force variation

The maximum force on any single bolt is 2.6 ton for a 5 MA disruption and 2.0 ton in equilibrium. For these M27 bolts >100,000 cycles with an amplitude of 1 ton are allowable, so fatigue is not an issue.

The maximum key force, 41.3 ton, is for a 5 MA disruption and the maximum equilibrium force is 31.7 ton, again for a 5 MA plasma. The maximum key forces are below their respective allowable values: 56 ton in disruption and 35 ton in equilibrium. These values are based on the tests done at Imperial College in 1982 and on the linear dependence of the allowable on the bolt pre-tension. In these tests the pre-tension was 20 ton and 12,000 cycles were done at 50 ton and a few cycles at 80 ton without damaging the key which was later installed.

4. Stiffness of the mechanical structure

The FE model of the MS has been used to estimate the flexibility of the structure. Several runs have been done with forces applied to each single support point. The flexibility was then calculated from the MS deflection. These spring constant can be used to estimate more accurately the out-of-plane forces on the TF coil at the MS supports using the beam model (Appendix B).

Stress and fatigue life assessment at the mechanical structure critical points

G Sannazzaro, T Raimondi

09 November 1999

Contents

1.	Stresses in collar and ring teeth and dowel connection	2
2.	Statistic load in previous operation and assessment of the fatigue damage..	4
3.	Fatigue life of the bolts	5
4.	Stress in the divertor configuration.....	6
5.	Annex I.....	16

1. Stresses in collar and ring teeth and dowel connection

Stresses in the collar tooth, ring tooth and the dowel connection of the inner cylinder to the collar have been recalculated to evaluate the limit values for operation and the fatigue life.

Fig.1 shows a cross section of the MS with the indication of the position of the collar and ring teeth and the inner cylinder dowel.

Figs.2-5 show drawings of the three components.

In table 1 the materials with their properties are reported

Component	Material type	Yield stress (MPa)	UTS (MPa)
Collar tooth	AISI 434 (or UNI 40 NCD 7)	620	810
Ring tooth (octant joint)	AISI 304N	335	645
Inner cylinder dowel	AISI 434 (or UNI 40 NCD 7)	620	810
BOLT (M27)	ISO 10.9	900	1030

Figs 5,6 and 7 report the fatigue curves for the materials.

In table 2 the maximum allowable force for each component are reported. The limit are based on the onset of yield in the teeth and dowel and on the proof load of the connecting bolts. Stresses in the teeth and dowel is due to bending, therefore ASME III (NB 3221.3) allows to reach the yield ($P1 + Pb < 1.5Sm - Sm = 2/3Sy$)

Component	Limit load (tons)	Notes
Collar (F1)	85	Onset of yield in the tooth
Ring (F2)	75	Proof load (35 tonnes) on the bolts
Inner cylinder dowel (Fd)	320	Onset of yield in the dowel

There is a stress concentration in the teeth and dowel that has to be considered for the fatigue life. The stress concentration in the teeth is due to the holes for the fixing bolts

(Stress concentration factor $K_t = 3$), while in the dowel is due to the variation of the cross section of the dowel from squared to cylindrical ($K_t = 2.2$). For the dowel teeth it has been assumed conservatively that the stress concentration is in the section where the stress is maximum. In table 3 the maximum stress in the components are reported for a reference load.

Table 3: Maximum stress for fatigue assessment in critical points of the MS for a reference load of 50 t

	Total stress (MPa)	Notes
Collar tooth	1094	Ref. load $F_1 = 50$ t; $K_t = 3$ at the bolt holes
Ring tooth	533	Ref. load $F_2 = 50$ t; $K_t = 3$ at the bolt holes
Inner cylinder dowel	213	Ref. load $F_d = 50$ t; $K_t = 2.2$

2. Statistic load in previous operation and assessment of the fatigue damage

In agreement with the statistic used for the fatigue assessment of the MS, JET pulses have been grouped as reported in table 4. The force distribution along the TF coil is very dependent on the plasma configuration. The values reported are based on maximum estimated or measured (maximum force on collar and ring teeth never exceeded 60 t corresponding to the alarm set in the machine protection system).

Plasma current (MA)	Force on collar tooth (tons)	Force on ring tooth (tons)	Force on cylinder dowel (tons)	N. of pulses
DISR.4.5 to 7 MA	60	60	150	90
DISR. 2.5 to 4.5 MA	39	39	100	1363
PULSE 4.5 to 7 MA	50	50	120	980
PULSE 2.5 to 4.5 MA	32	32	80	9355

Table 5 reports the maximum alternate stress in the component obtained from data reported in table 3 and 4. It also reports the total cumulative fatigue damage on each component obtained using the curves reported in fig.s 5a and 6. Note that the stress value in the figures is the alternate. The load from the TF coils is pulsed from 0 to the maximum, therefore values in table 3 have to be divided by 2. Fig.6 have already been adjusted to include the effects of a mean stress larger than zero (ASME III NB 3222.2). Fig 5b shows that the material resistance to pulsed load decreases by a factor 1.25 compared to alternate load. To take into account that effect, the calculated stress value entered in the curve of fig.5a for inner cylinder dowel and collar tooth has been multiplied by a factor 1.3.

Plasma current (MA)	Collar tooth stress (MPa)	Ring tooth stress (MPa)	Cylinder dowel stress (MPa)	N. of pulses
DISR.4.5 to 7 MA	656	320	320	90
DISR. 2.5 to 4.5 MA	426	208	213	1363
PULSE 4.5 to 7 MA	547	267	256	980
PULSE 2.5 to 4.5 MA	350	2.4	0.0	
Total damage (%)	2.2	2.4	0.0	

3. Fatigue life of the bolts

The bolts of the collar and ring teeth have been tightened with a torque that is giving a preload larger than 200 KN per bolt.

If the applied force on the support tooth doesn't give any increase in the bolt force there is no problem of fatigue.

The forces on the support teeth that give a load on the bolt of 200 KN are 56 tonnes and 80 tonnes for the ring and collar respectively. That means that for the collar teeth bolts there is no cycling load and that for the ring the cycling load has an amplitude of 4/2 tonnes only for high performance pulse that disrupted (90 pulses).

The nominal stress amplitude for an M27 bolt for that load is 40 MPa.

Assuming a stress intensification factor equal to 4, the maximum stress amplitude becomes 160 MPa. Using the fatigue curve in fig.7 this stress level corresponds to a fatigue life of 20000 pulses. The percentage of life used for the ring tooth bolts is then $100 \cdot 90 / 20000 = 0.45\%$

4. Stress in the divertor configuration

The load on the MS in the new divertor configuration has been calculated using FE simulation. From experimental comparison it appears that the calculations might have an error of 20% as a maximum.

Therefore the values previously calculated (and presented) have been increased by a factor 1.2 accordingly.

Table 6 reports the total torque and the loads on the critical points of the MS in the extreme divertor configurations (FAT 6MA and SLIM 5MA) in equilibrium and plasma disruption.

Table 6: Summary of loads in the divertor configurations (factor = 1.2 on calculated from FE program)				
Load case	Torque (tons*m)	F collar (tons)	F ring (tons)	F dowel (tons)
FAT 6MA Equilibrium	13600	56	29	121
SLIM 5MA Equilibrium	16800	53	31	142
FAT 6MA Disruption	18000	66	34	180
SLIM 5MA Disruption	21400	50	37	181

In table 7 the summary of the stress in the different parts (including the outer shell of the MS) is reported with the limits.

Limits are based on ASME III NB 3221.3 that refers to the membrane + bending primary stress for equilibrium conditions and on ASME III NB 3224.1 for disruption conditions (Level C Service) that allows an increase of 20%. There is no secondary stress. Conservatively, the stress value reported for the mechanical structure shell refers to the peak stress at the opening for the TF coil cooling pipes.

Table 7: Stress and limits in the critical points of the MS for divertor configuration (Calculated loads from FE model increased by 20%)						
Location	σ_y /UTS (MPa)	Criteria	Design stress limit (MPa)	Loading condition	Calculated stress (MPa)	Safety factor
MS outer shell	270/470	P1+Pb<Sy(NB 3221.3)	270	SLIM 5MA EQUIL	127	2.1
MS outer shell		P1+Pb<1.2Sy (NB 3224.1)	324	SLIM 5MA DISR.	160	2.0
Collar tooth	620/810	P1+Pb<Sy(NB 3221.3)	620	FAT 6MA EQUIL.	408	1.5
Collar tooth		P1+Pb<1.2Sy (NB 3224.1)	744	FAT 6MA DISR	481	1.5
Ring tooth bolts	900/1030	Pm<Sy/1.5 (NB3232.1)	600	SLIM 5MA EQUIL	319	1.9
Ring tooth bolts		Pm<Sy/1.5 (NB3221.3)	600	SLIM 5MA DISR.	376	1.6
Inner cylinder dowel	620/810	P1+Pb<Sy(NB 3221.3)	620	SLIM 5MA EQUIL	275	2.3
Inner cylinder dowel		P1+Pb<1.2Sy (NB 3224.1)	744	SLIM 5MA DISR.	351	2.1

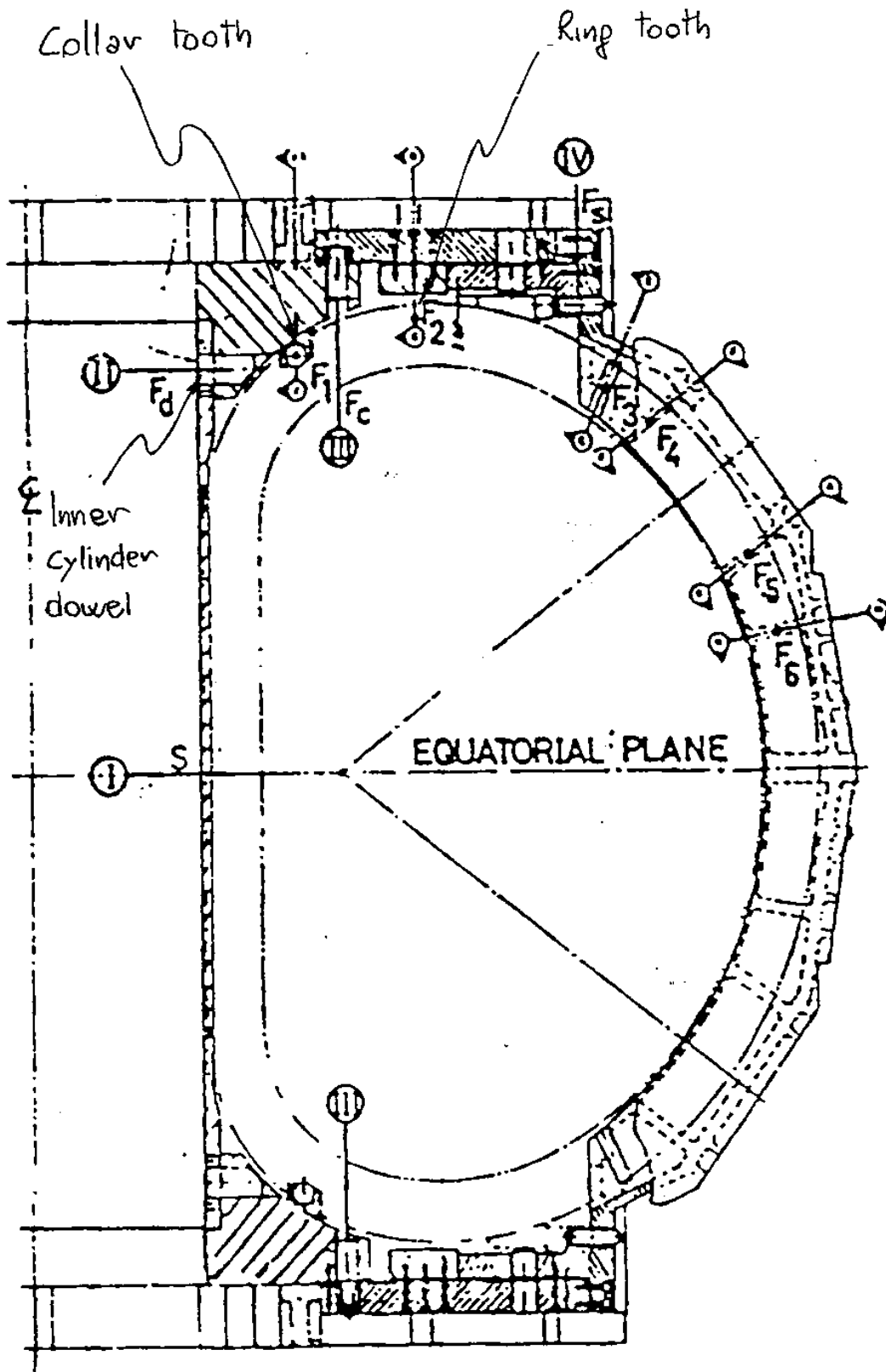


Fig. 1 Cross section

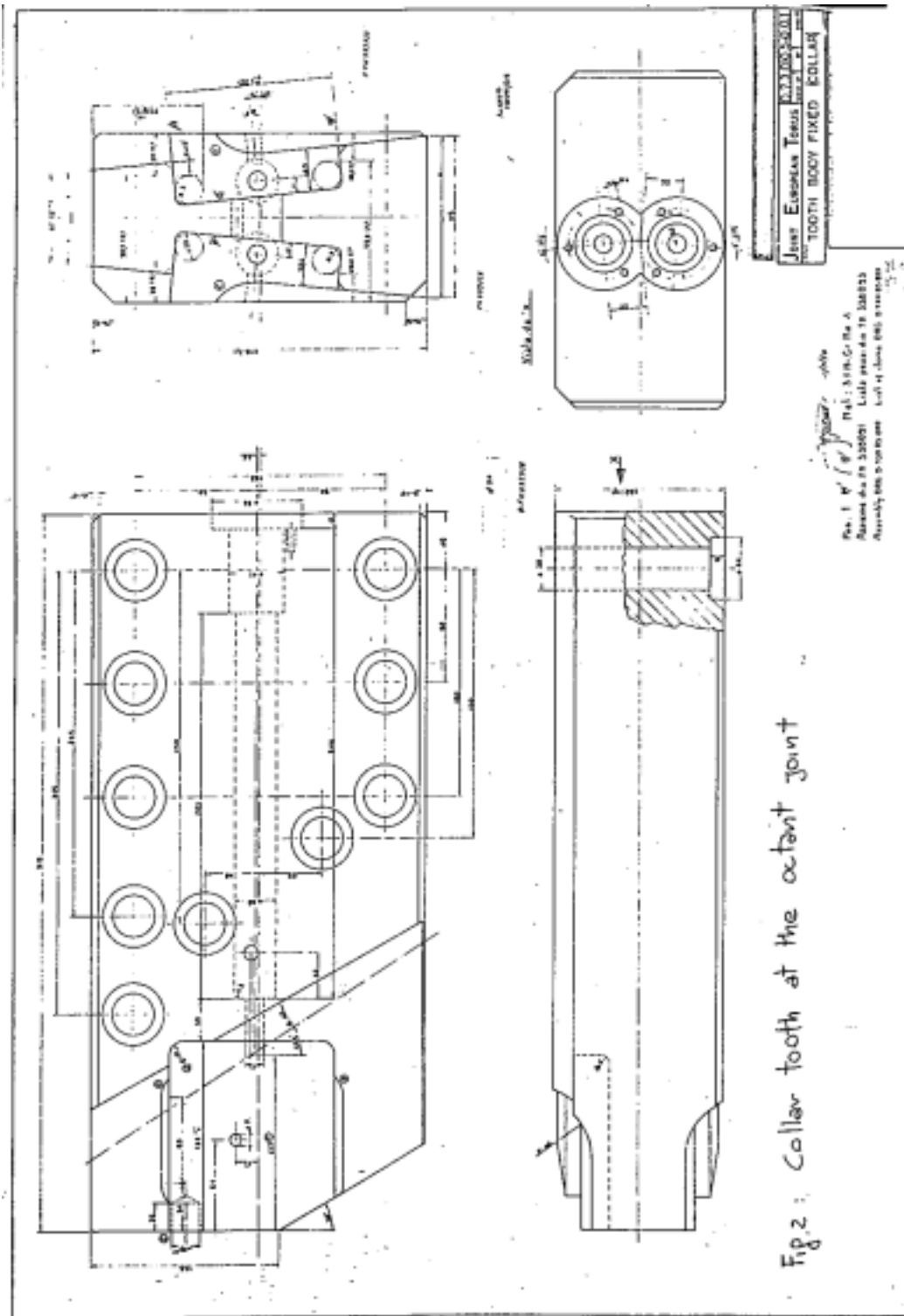


Fig. 2 Collar tooth at the octant joint

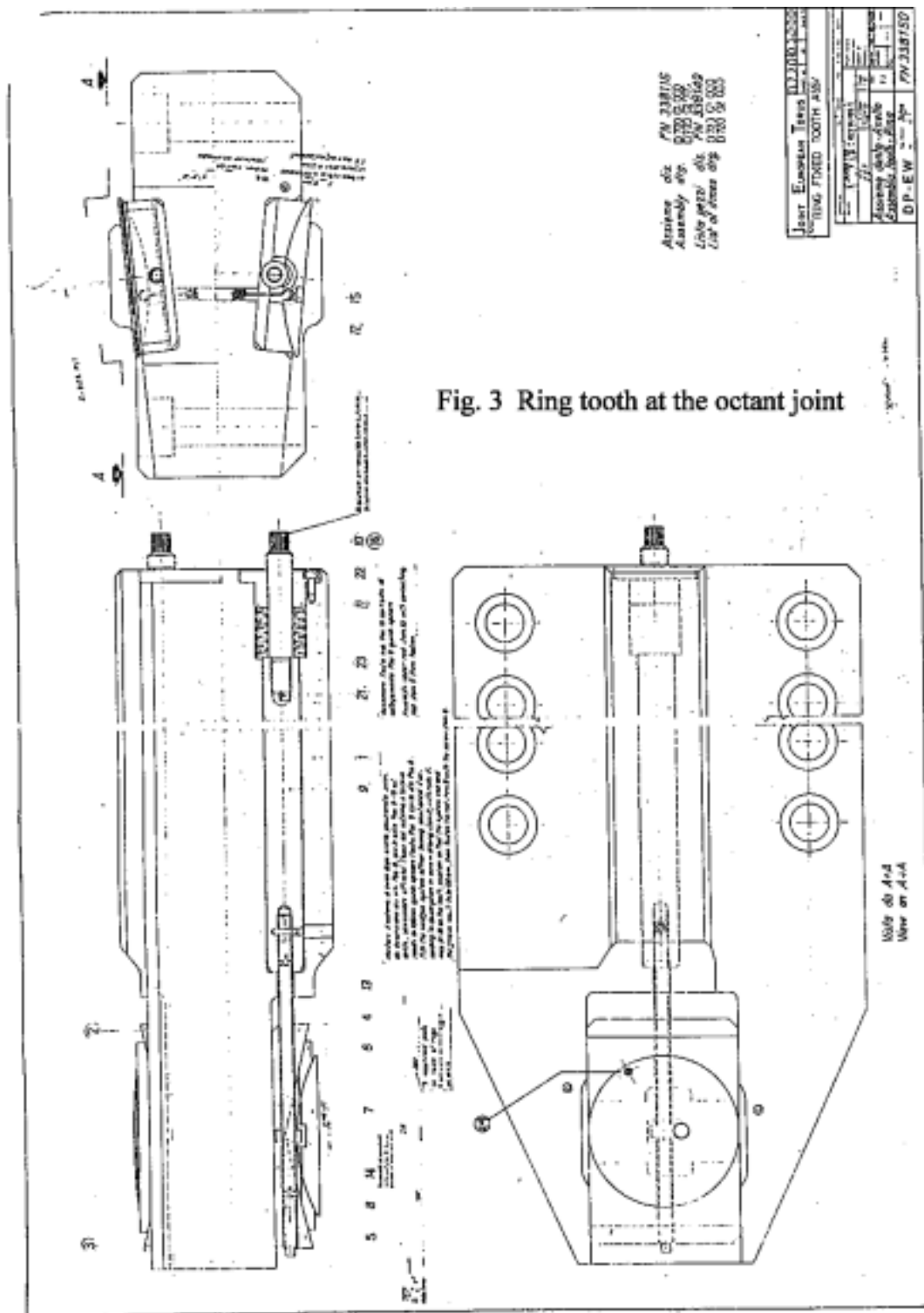


Fig. 3 Ring tooth at the octant joint

Fig. 3 Ring tooth at the octant joint

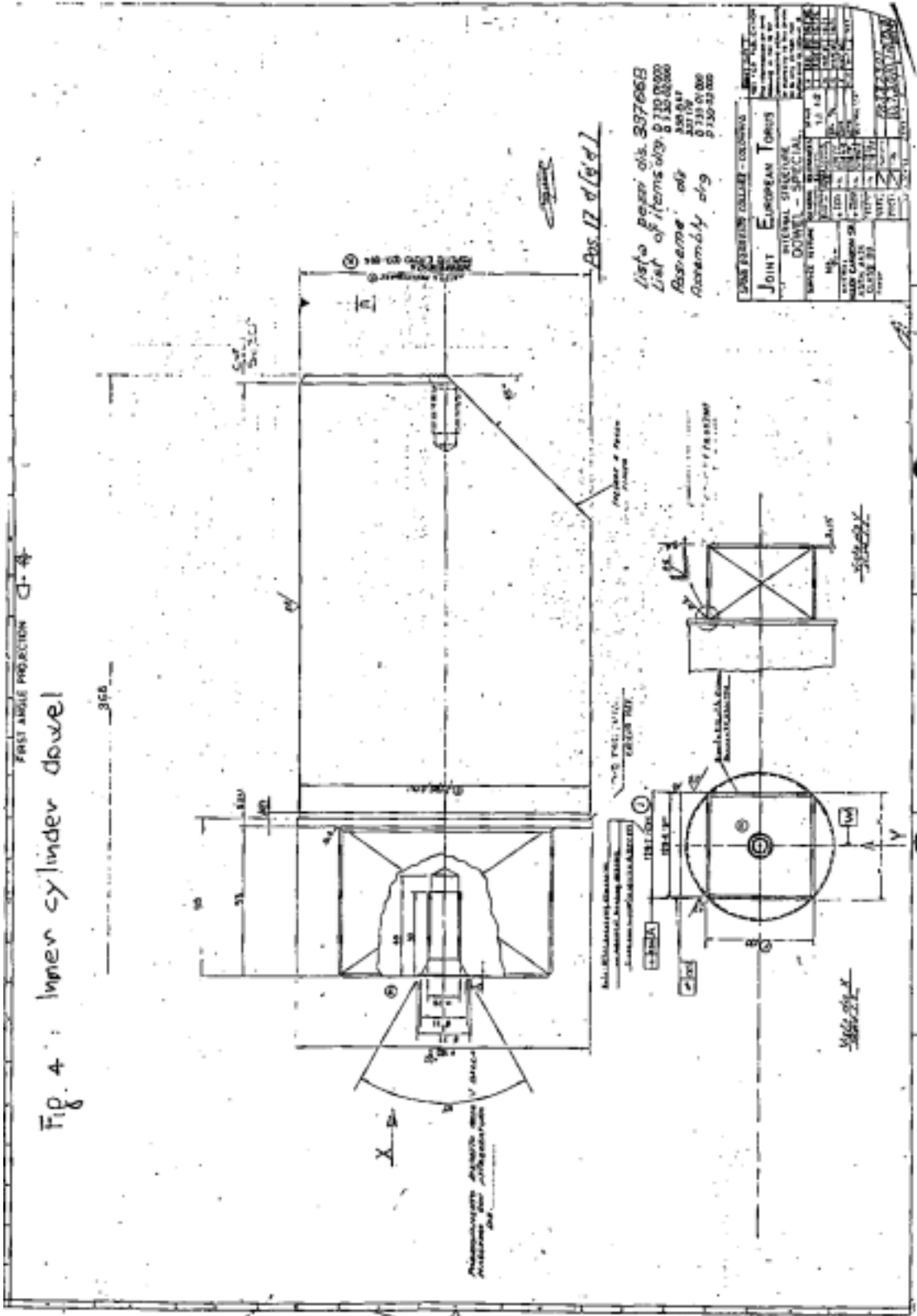


Fig. 4 Inner cylinder dowel

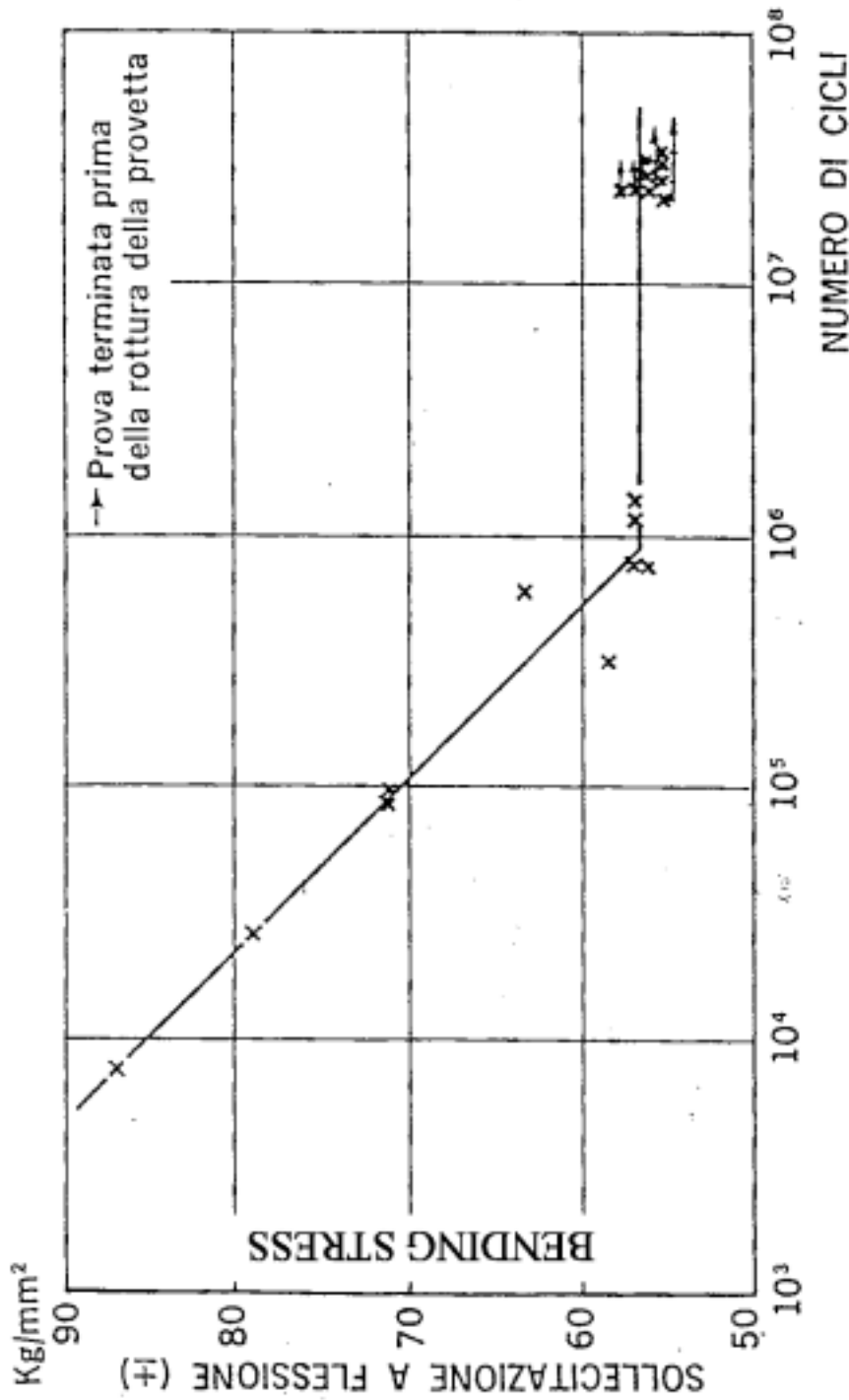


Fig. 118 - Relazione tra sollecitazione a flessione rotante e numero di cicli (curva di Wöhler) dell'acciaio UNI 40 NCD 7, temprato e rinvenuto a $R = 107 \text{ kg/mm}^2$, per $2 \cdot 10^7$ cicli. Il limite di fatica (valore dell'ordinata del tratto orizzontale del diagramma) è stato determinato con l'analisi statistica dei risultati al 50% di sopravvivenza. I dettagli delle prove sono indicati nel testo precedente.

Ref.: "ACCIAI TIPIEZATI" - Associazione industrie siderurgiche Italiane "ASSIDER" 1962

Fig. 5a fatigue curve for UNI 40 NCD7 equivalent to AISI 434 in rotating bending test - collar tooth and inner cylinder dowel

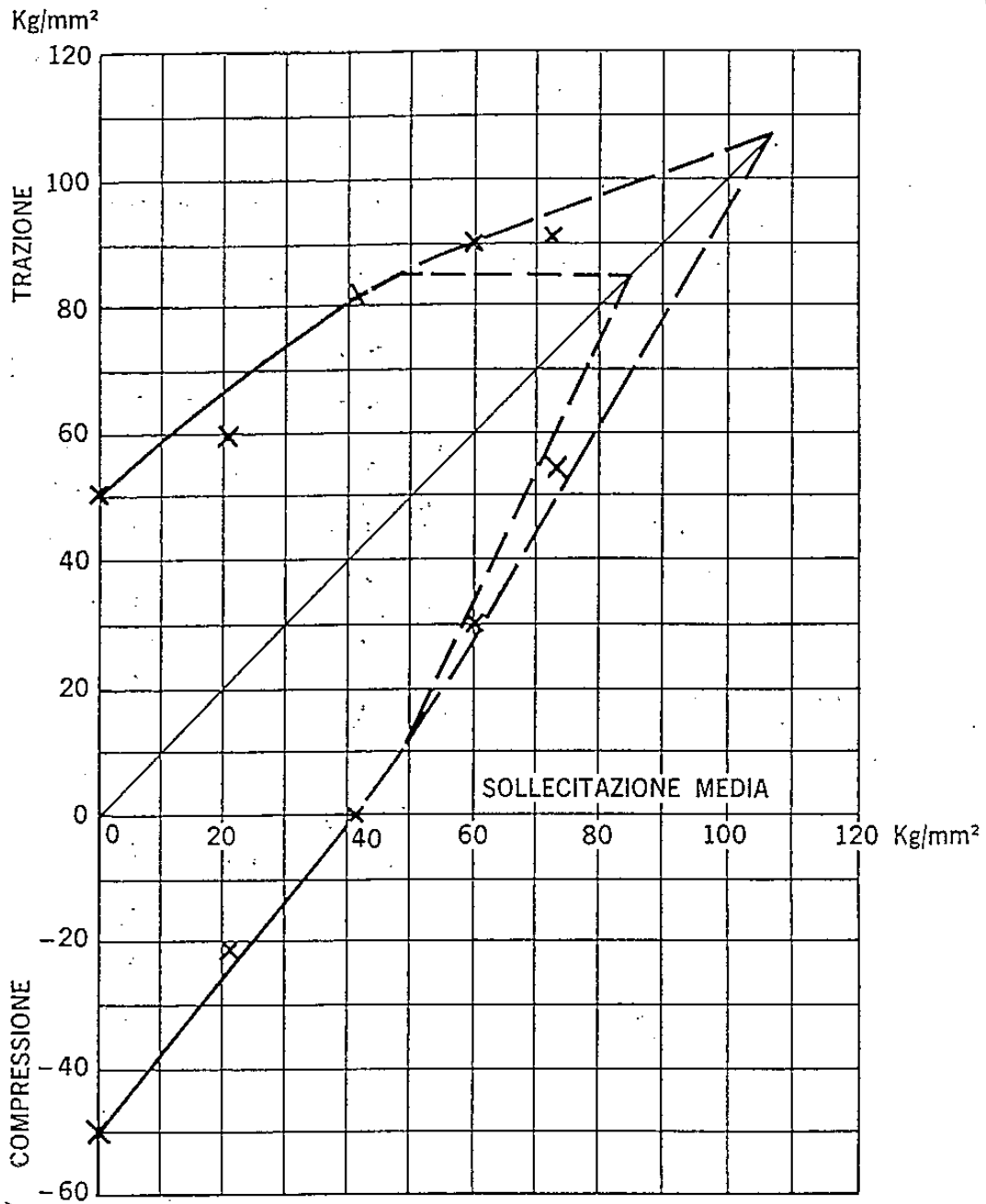
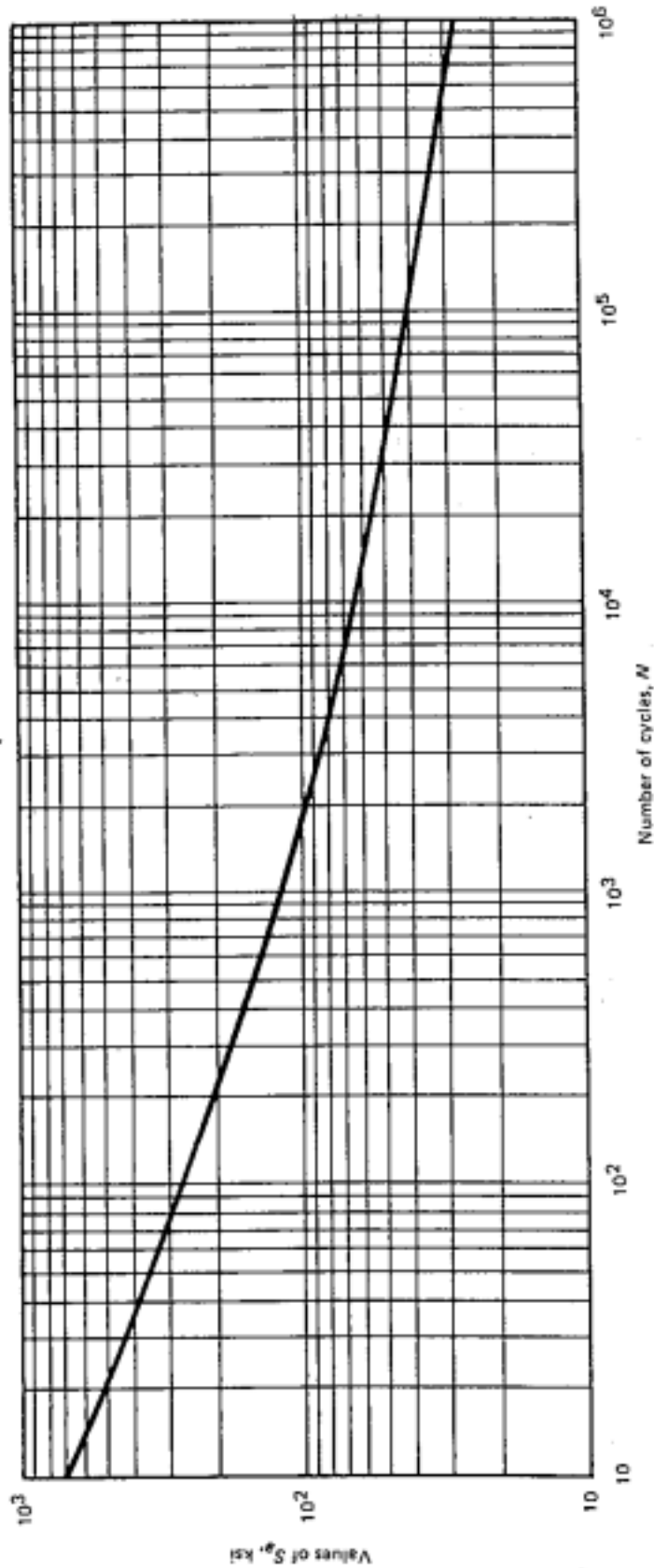


Fig. 121 - Area di sicurezza a trazione-compressione (diagramma di Goodman-Smith) dell'acciaio UNI 40 NCD 7, temprato e rinvenuto a $R = 107 \text{ kg/mm}^2$, per $2 \cdot 10^7$ cicli, al 50% di sopravvivenza. Limite di snervamento dinamico: 85 kg/mm^2 . I dettagli delle prove sono indicati nel testo precedente.

Ref.: "ACCIAI TIPIEZATI" - Associazione industrie siderurgiche Italiane "ASSIDER" 1962

Fig. 5b Goodman Smith diagram for UNI 40 NCD7



NOTE:
 $E = 28.3 \times 10^6$ psi

FIG. I-9.2.1 DESIGN FATIGUE CURVE FOR AUSTENITIC STEELS, NICKEL-CHROMIUM-IRON ALLOY, NICKEL-IRON-CHROMIUM ALLOY, AND NICKEL-COPPER ALLOY FOR $S_a > 28.2$ ksi, FOR TEMPERATURES NOT EXCEEDING 800°F

1 ksi = 6.8 MPa

(For $S_a \leq 28.2$ ksi, use Fig. I-9.2.2.)

Table I-9.1 Contains Tabulated Values and a Formula for Accurate Interpolation of This Curve

Fig. 6 Fatigue curve for material of the ring tooth

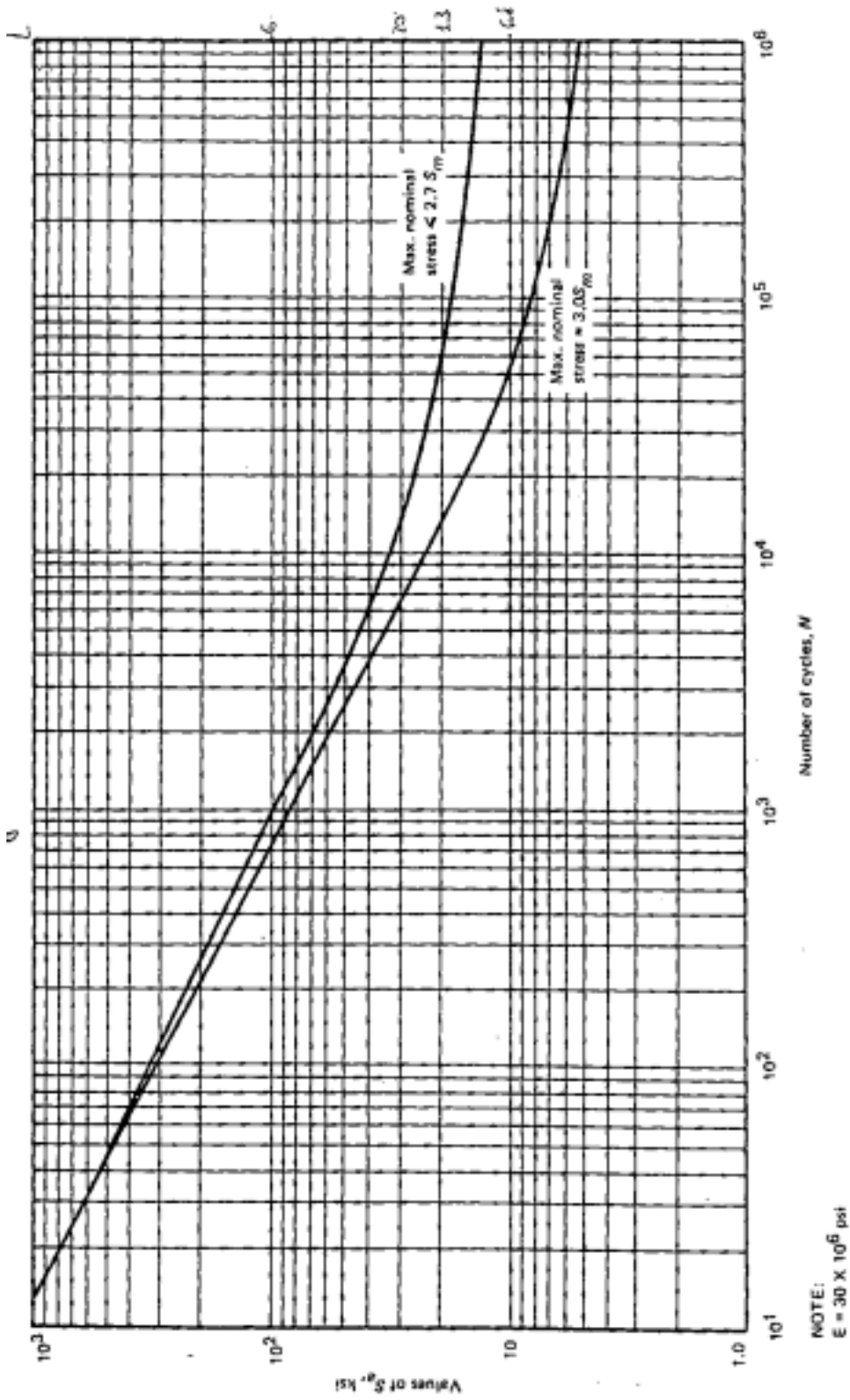
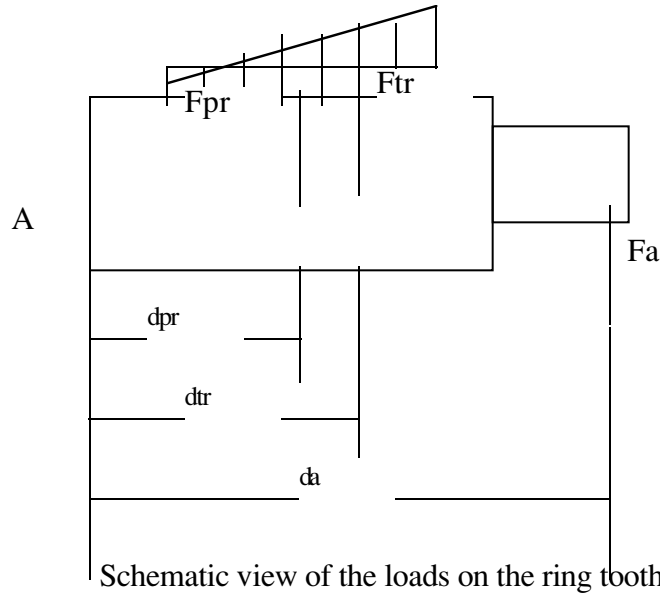


FIG. 1-9.4 DESIGN FATIGUE CURVE FOR HIGH STRENGTH STEEL BOLTING
 FOR TEMPERATURES NOT EXCEEDING 700°F
 Table 1-9.1 Contains Tabulated Values and a Formula for Accurate
 Interpolation of These Curves

Fig. 7 Fatigue curve for bolts

5. Annex I

I.1.1. Estimate of the limit load on the ring tooth bolts



The load on the ring tooth bolts has been estimated following 3 different assumptions.

Assumptions A :

- 1) All the flexibility of the joint connection tooth- ring is concentrated in the bolts (tooth is considered infinitely rigid)
- 2) Bolts have a preload of 20 t.

Following assumption 1) any applied load does not cause any increase of load in the bolts provided that :

$$Fa \cdot da < Fpr \cdot dpr$$

Where :

Fa = applied force on the ring tooth from the TF coil

da = distance of the applied force Fa from the assumed pivoting point (extremity of the tooth - Point A in previous sketch) = 566 mm

Fpr = total preload on the 10 bolts M27 = 200 t

dpr = distance of the baricenter of the force Fpr from the assumed pivoting point A = 160 mm

$$Fa_0 = Fpr \cdot dpr / da = 56 \text{ t}$$

As the applied force Fa exceeds Fa_0 the loads on the bolts increases. It is assumed that the increase is proportional to the distance from the pivoting point.

$$Fa \cdot da = Fpr \cdot dpr + Ftr \cdot dtr$$

Where :

Ftr = incremental tensile force on the bolts when Fa exceeds Fa₀

dtr = distance of the baricenter of the force Ftr from the assumed pivoting point = 203 mm

$$F_a = F_{a_0} + F_{tr} \cdot d_{tr} / d_a$$

The maximum tensile force in a bolt is $F_{pr}/10 + 2 \cdot F_{tr}/10$.

This force reaches the proof load (35 t) when this additional force Ftr reaches the value :

$$F_{tr} = (350 - 200)/2 = 75 \text{ t}$$

The force Fa that gives a maximum load on a bolt equal to the proof load is :

$$F_{a\text{-proof load-A}} = F_{a_0} + F_{tr} \cdot d_{tr} / d_a = 83 \text{ t}$$

To be more conservative, assuming that the force on the bolt is not linearly distributed, but there is a concentration factor of 1.1, the limit loads becomes :

$$F_{a\text{-proof load-A}} = \mathbf{75 \text{ t}}$$

Assumptions B :

- 1) All the flexibility of the joint connection tooth- ring is concentrated in the bolts
- 2) The bolts are not preloaded

In this case the relation between the applied load Fa and the maximum tensile load on a bolt Fb-max is given by :

$$F_a \cdot d_a = F_{b\text{-max}} \cdot d_{tr} \cdot 10/2$$

Assuming that the maximum tensile load on a bolt is 35 t (proof load) ->

$$F_{a\text{-proof load-B}} = \mathbf{63 \text{ t}}$$

Assumption C :

- 1) The bolt ductility allow a redistribution of the load on the bolts, therefore the bolts have the same load

$$F_a \cdot d_a = F_{pr} \cdot d_{pr}$$

Limit value of Fpr is 350 t (proof load 35 on 10 bolts), therefore

$$F_{a\text{-proof load-C}} = \mathbf{99 \text{ t}}$$

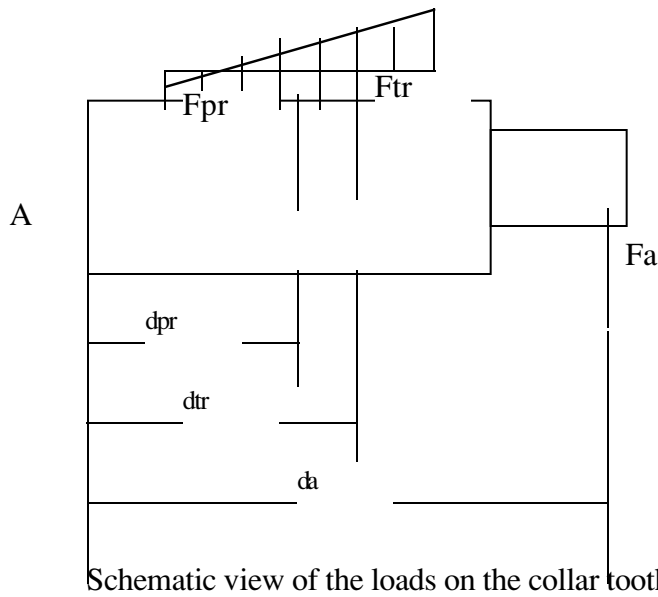
Summary :

Force on the ring tooth that gives a load on bolts equal to the proof load for different calculation assumption	
Assumption	Fa
A	75 t

B	63 t
C	99 t

The assumption A seems to be the most accurate.

I.1.2. Estimate of the limit load on the collar tooth bolts



The load on the ring tooth bolts has been estimated following 3 different assumptions.

As for the ring tooth bolts, the load on the collar tooth bolts has been estimated following 3 different assumptions.

Assumptions A :

- 1) All the flexibility of the joint connection tooth-collar is concentrated in the bolts (the collar tooth is considered infinitely rigid)
- 2) Bolts have a preload of 20 t.

Following assumption 1) any applied load does not cause any increase of load in the bolts provided that :

$$Fa \cdot da < Fpr \cdot dpr$$

Where :

Fa = applied force on the collar tooth from the TF coil

da = distance of the applied force Fa from the assumed pivoting point (extremity of the tooth – Point A in previous sketch) = 450 mm

Fpr = total preload on the 10 bolts M27 = 200 t

dpr = distance of the baricenter of the force Fpr from the assumed pivoting point A = 180 mm

$$Fa_0 = Fpr \cdot dpr / da = 80 \text{ t}$$

As the applied force Fa exceeds Fa₀ the loads on the bolts increases. It is assumed that the increase is proportional to the distance from the pivoting point.

$$Fa \cdot da = Fpr \cdot dpr + Ftr \cdot dtr$$

Where :

Ftr = incremental tensile force on the bolts when Fa exceeds Fa₀

dtr = distance of the baricenter of the force Ftr from the assumed pivoting point = 240 mm

$$F_a = F_{a_0} + F_{tr} \cdot dtr/da$$

The maximum tensile force in a bolt is $F_{pr}/10 + 2 \cdot F_{tr}/10$.

This force reaches the proof load (35 t) when this additional force Ftr reaches the value :

$$F_{tr} = (350 - 200)/2 = 75 \text{ t}$$

The force Fa that gives a maximum load on a bolt equal to the proof load is :

$$F_{a\text{-proof load-A}} = F_{a_0} + F_{tr} \cdot dtr/da = \mathbf{120 \text{ t}}$$

To be more conservative, assuming that the force on the bolt is not linearly distributed, but there is a concentration factor of 1.1, the limit loads becomes :

$$F_{a\text{-proof load-A}} = \mathbf{109 \text{ t}}$$

Assumptions B :

- 1) All the flexibility of the joint connection tooth- collar is concentrated in the bolts
- 2) The bolts are not preloaded

In this case the relation between the applied load Fa and the maximum tensile load on a bolt Fb-max is given by :

$$F_a \cdot da = F_{b\text{-max}} \cdot dtr \cdot 10/2$$

Assuming that the maximum tensile load on a bolt is 35 t (proof load) ->

$$F_{a\text{-proof load-B}} = \mathbf{93 \text{ t}}$$

Assumption C :

- 1) The bolt ductility allow a redistribution of the load on the bolts, therefore the bolts have the same load

$$F_a \cdot da = F_{pr} \cdot dpr$$

Limit value of Fpr is 350 t (proof load 35 on 10 bolts), therefore

$$F_{a\text{-proof load-C}} = \mathbf{140 \text{ t}}$$

Summary :

Force on the collar tooth that gives a load on bolts equal to the proof load for different calculation assumption	
Assumption	Fa
A	109 t
B	93 t
C	140 t

Even the most pessimistic assumption (assumption B) gives a limit force for the bolts that is larger than the limit force (85 t) that causes a stress in the tooth equal to the yield value (620 MPa).

I.1.3. Summary of the limit loads on the TF coil supports

The next table reports a summary of the limit loads on the TF coils supports at the ring and collar to avoid excessive stress in the support teeth and in the bolts connecting the teeth to the mechanical structure.

Limit value of force on the TF coil supports at the collar and ring		
	Onset of yield in the tooth	Limit on tensile load on the bolts
Ring	90	75
Collar	85	109

Inter-octant joints

J.R. Last
26 October 1999

Contents

1.	Introduction.....	1
2.	Measured bolt relaxation	3
3.	Strength of Inter-Octant Keys	4
4.	Forces on octant joints.....	5
5.	Operational Experience.....	6
6.	Tightening the octant joint bolts.....	7
7.	Conclusions	7

1. Introduction

The out of plane forces on the toroidal coils are resisted by the mechanical structure. The total effect of these forces is to apply a torque to the upper half of the structure which is resisted by an equal and opposite torque applied to the lower half of the structure. This torque causes shear stresses in the structure and shear forces at the octant joints of the structure.

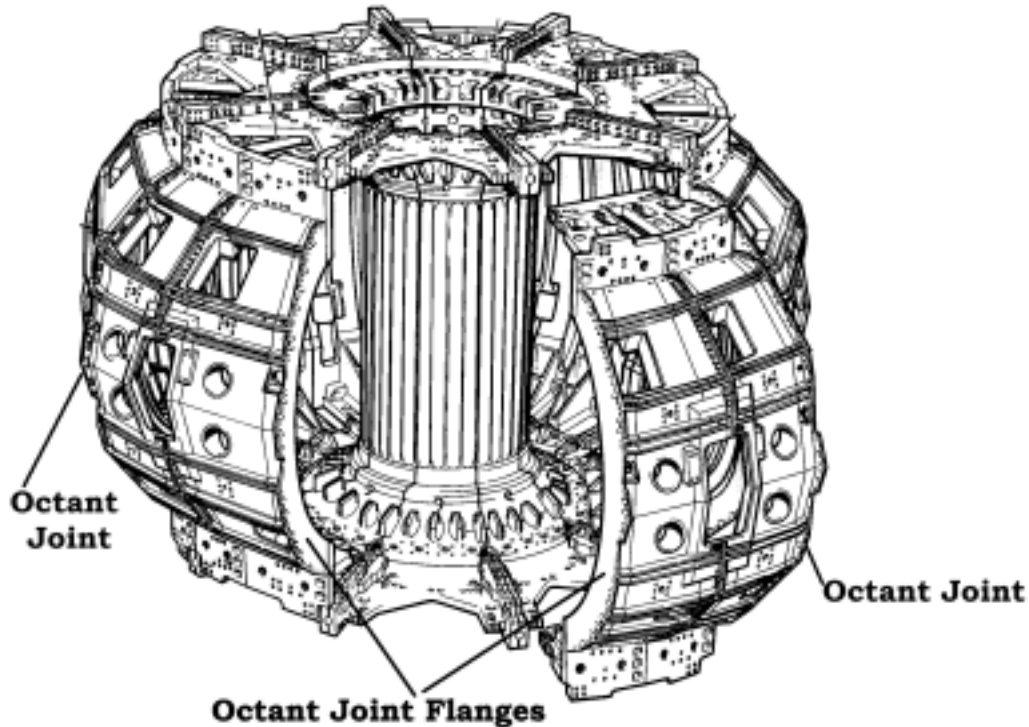


Fig. 1. Mechanical structure showing octant joints

The shear at the octant joints is resisted by a series of keys. The keys are circular and contain adjustment wedges. The key and wedge assembly are held in compression by the octant joint bolts. The bolts play no direct role in resisting the shear but are important in holding the key in compression and also carry a proportion of loads normal to the octant joint.

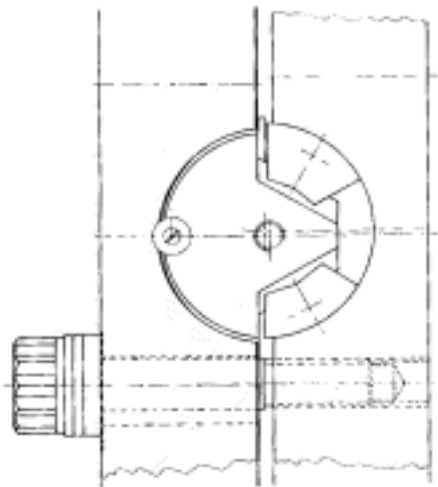


Fig. 2. Octant joint key showing wedges and octant joint bolt (1 of 2 per key)

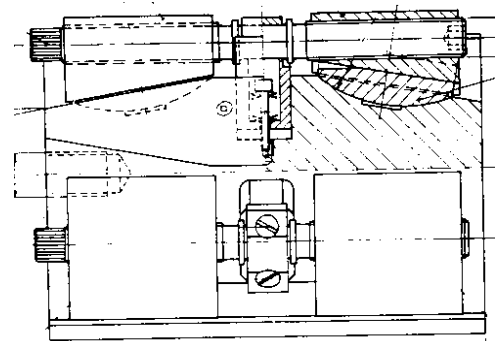


Fig. 3. Section through octant joint key showing wedges and drive mechanisms

The bolts were accurately tightened when the machine was initially assembled and again in 1990 when an octant was removed. The tension in the bolts is found by measuring their length and comparing it with their original un-tensioned length. Measurements made during shutdowns show that the bolt tension has relaxed by about 25% since 1990.

This relaxation is to be expected, as this joint is clearly less rigid than a normal bolted flanged joint. The flanges are not in contact but are separated by the key assembly. In operation the joint deflects in shear by about 0.05 mm for a high performance pulse. This shear movement has some effect on the bolt seating and on the key itself and allows the bolt tension to relax slightly.

2. Measured bolt relaxation

The octant joint bolts were tightened in 1990, when the P3 and P4 coils were moved. The procedure is to tighten the bolts to a predetermined torque and then measure the extension of the bolt to determine the stress. The tension in the bolt should be found more accurately by extension measurement than by torque measurement. The accuracy of the method depends on the accuracy and stability of the measuring device and on maintaining records of the original lengths. The (ultrasonic) measuring device is set up and calibrated before use.

When the bolts were first tightened the average extension was 0.35 mm. This equates to a bolt tension of 280 kN. Since 1990 the bolt extension has been measured 3 times, in 1996, 1998 and in 1999. The following graphs show how the tension has relaxed.

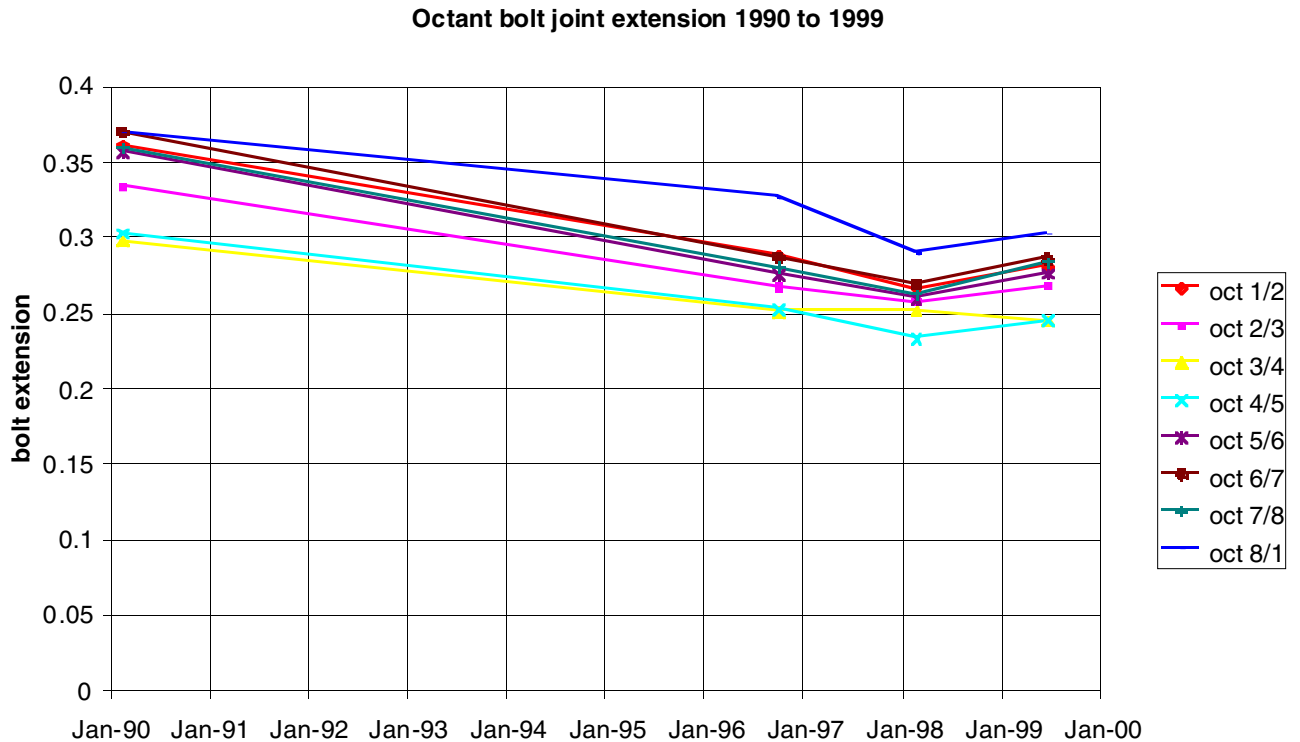


Fig.4. Change of bolt extension since 1990

Alternatively the relaxation can be presented relative to the status in 1990.

Relaxation of bolt tension 1990 to 1999

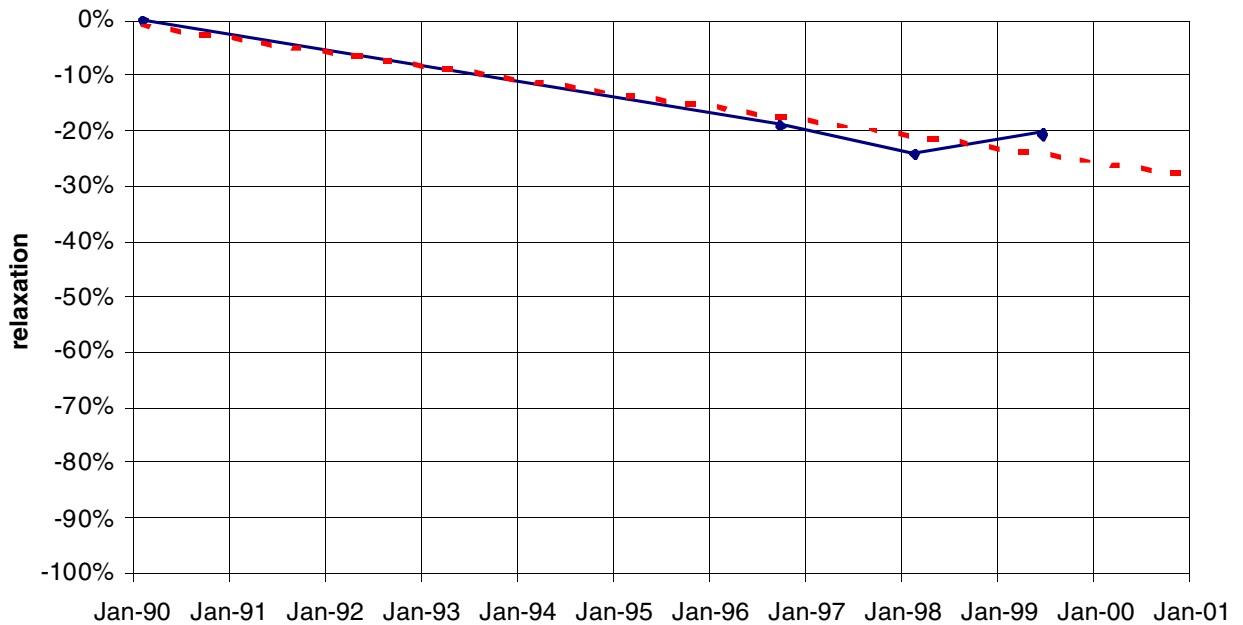


Fig.5. Bolt relaxation since 1990 (averaged over all octants)

The graphs show that the uniform rate fall in bolt tension seen until 1998 has not been maintained. There appears to be an upward trend in the last year.

The above graphs are based on the average of each octant. Differences between individual bolts and octants appear to be random. No significant trends could be found in terms of groups of bolts within an octant (upper, middle, lower), position of bolt or relaxation relative to initial tension.

In 1998 we said “the bolts seem to be relaxing in a predictable way at about 3% per year. One would therefore expect an average tension of about 70% of the original at the end of '99.” The new trend suggests that 70% of original tension will not be reached until January 2001.

3. Strength of Inter-Octant Keys

A key was tested at Imperial College in 1982 with the bolts pre-tensioned at 220 kN. A shear load of 500 kN was applied for 12,000 cycles. The key was also subjected to a few cycles at 800 kN. The behaviour was elastic and stable. No higher loads were attempted because the key was required for assembly in the JET machine. The key may be stronger than these tests indicate.

The tests also showed that the bolt tension is substantially unaffected by shear forces. A shear force of 500 kN gave a variation in bolt force of 15 kN, corresponding to a stress of 26 MPa, which is well below the fatigue limit (life > 10^6 cycles) of the bolt material. This means that there is no problem of bolt fatigue as long as the key operates within its allowable force.

We can therefore take 500 kN as an allowable repetitive shear load with the inter octant bolts pre-tensioned at 220 kN. A simple analysis shows that the allowable force is proportional to the bolt tension. The average pre-tension in the bolts was 280 kN in

1990 and at the end of 1999 it will be about 196 kN (280x0.7). This is 89% of the bolt tension in the test. However, to allow for variations between bolts, we can pessimistically take new allowable forces at 70% of the original.

Therefore the new allowable shear forces are;

- 350 kN per key for repetitive operation and
- 560 kN per key for occasional events.

4. Forces on octant joints

The shear at the octant joints is proportional to the torque applied to the TF coils and to a first order the torque is proportional to $I_p B_T$ as shown in the graph below. Therefore the effect of machine operation can be assessed in terms of $I_p B_T$.

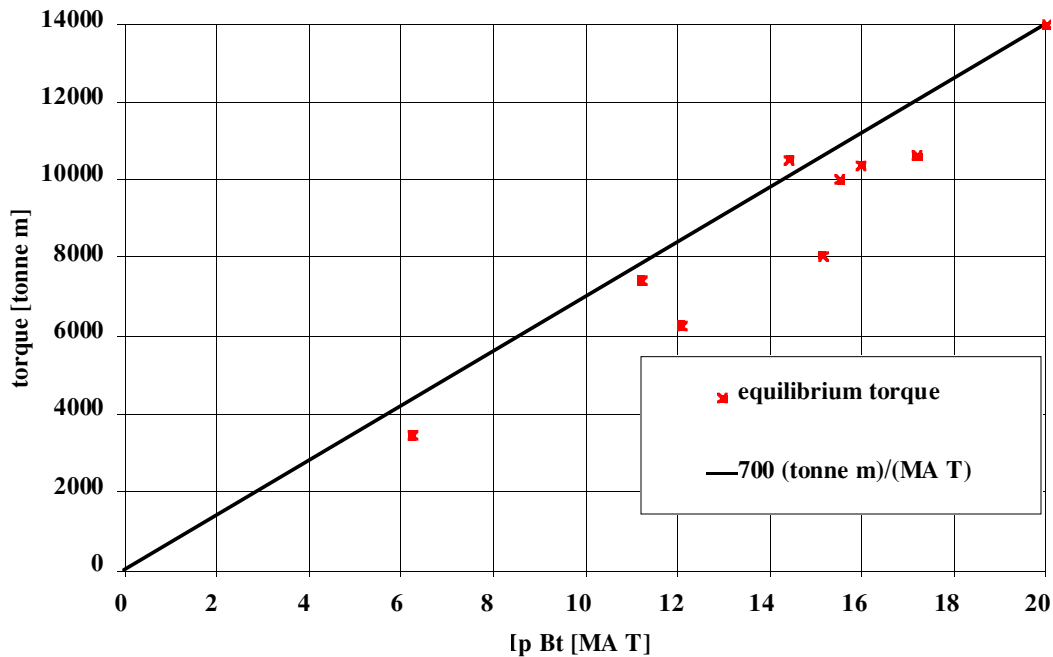


Fig. 6. Machine torque vs $I_p B_T$

Note that the constant of proportionality has changed since the divertor was installed. It was previously 400 Tm/MAT and is now 700 Tm/MAT. This is because the smaller plasma does not fit the TF coils so well and gives more perpendicular field.

Although the machine torque gives a good indication of the average shear at the octant joints, the distribution of forces between keys depends on the distribution of poloidal field around the toroidal coil, i.e. on the plasma shape. Therefore different scenarios have to be assessed to determine the maximum force on a key, as shown below.

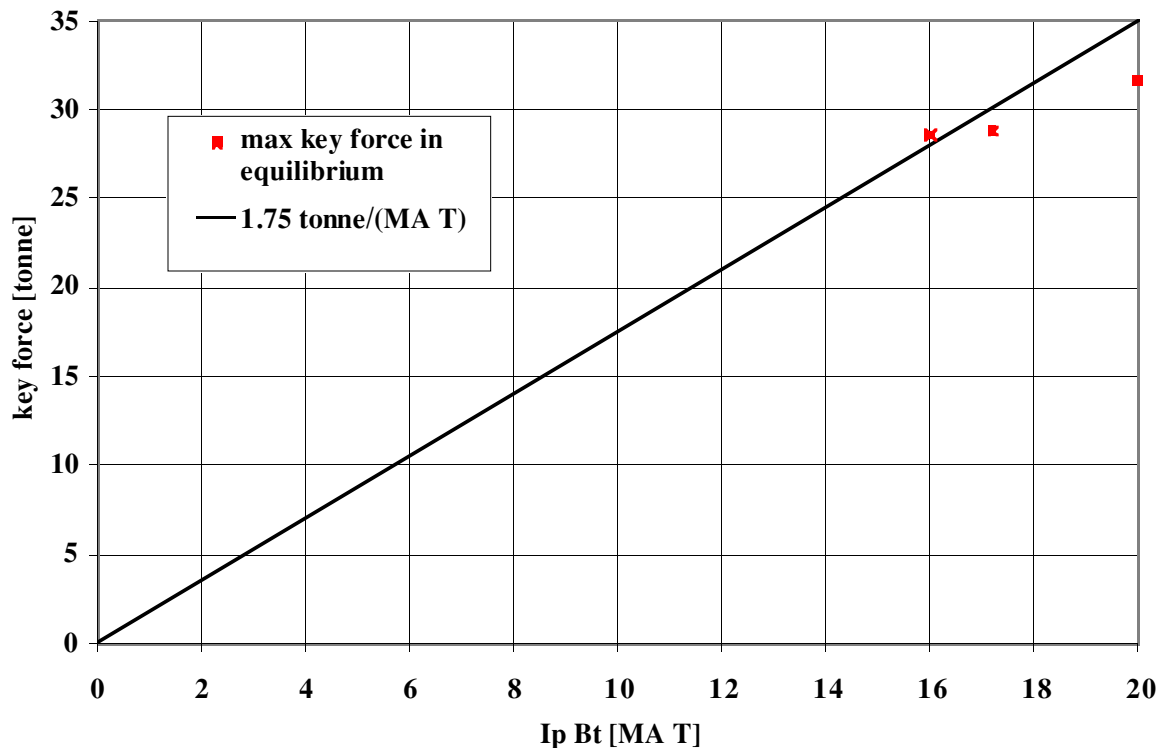


Fig. 7. Maximum key force vs $I_p B_T$ for Elmy H mode (5MA), Elm free H mode (4.3MA) and Optimised Shear (4MA) plasmas

If disruptions or v.d.e's occur, the torque can increase by up to 100% and the maximum force on a key by 60%. However in this case different force limits apply.

Normal forces at the octant joints causes the tension in the bolts to vary slightly. The maximum variation in bolt tension was 26 kN, corresponding to a stress of 45 MPa, which is below the fatigue limit for the bolt material.

5. Operational Experience

As stated above, the force on the keys is proportional to $I_p B_T$. As operation is expected to continue with similar values of I_p and B_T it seems clear that bolt relaxation will continue at the same rate and the simple time extrapolation given in section 2 will be correct.

However we have also looked at the history of operation in terms of machine torque. This shows that since 1990 the machine has experienced 73.10^6 ton.metre.pulses. This can be expressed as an equivalent number of any particular type of pulse. For example, it is equivalent to 5200 pulses at 14000 tonne-metres (the highest proposed torque in the coming year produced at 5 MA, 4T).

In the period remaining until the end of 1999 we might expect to make the equivalent of 1000 high performance pulses giving a 5% further relaxation of bolt tension (to about 70%)

6. Tightening the octant joint bolts

Some bolts are accessible and some need coils P3 and P4 to be moved. To avoid stress concentrations, all or none of the bolts should be tightened. Therefore moving P3 and P4 is necessary for any of the bolts to be tightened.

To access the octant joint bolts P3 and P4 upper have to be lifted and hung from the upper limbs and P3 and P4 lower have to be lowered and rested on the lower limbs. This involves considerable dismantling work on the machine including items such as TF Freon feed pipes, upper walkway, P3 & P4 cooling manifolds, P2 busbars, in vessel cooling pipes, some vacuum vessel brakes and supports, IVIS pipes, cryogenic lines and diagnostics (KS3, KL1, KT6, Oct. 6 equipment). The lifting operation itself involves a special mode of operation of the main crane using 4 ropes.

Estimated times are as follows

Dismantle equipment as necessary and move P3 and P4 coils	10 weeks
Octant Joint bolt tightening	3 weeks
Reassemble P3 and P4 coils and other equipment	12 weeks

Thus the total time required is about 6 months. This time might be reduced by optimised planning but some diagnostic and vacuum group work has not been fully defined.

The effects of radiation were considered in the context of the RTE shutdown and the work could have been done by a the normal shutdown work force without additional rotation. At the start of the RTE shutdown (3 months after DTE1) general radiation levels on the machine (e.g. P4 walkway) were of the order of 15 $\mu\text{Sv/hr}$ rising to 300 $\mu\text{Sv/hr}$ near main horizontal ports. This radiation decays with a half life of 70 days, so if the work was done 70 days earlier (i.e. about 1 month after a DT experiment) the radiation levels would be doubled. Some rotation of the workforce might then be required.

7. Conclusions

Reduced allowable forces for the keys have been assessed on a pessimistic basis but the table below shows a good factor of safety for the three high performance plasmas of interest in the coming year.

Description	Torque in equilibrium (tonne-metres)	Maximum key force	
		in equilibrium (tonne)	in disruption (tonne)
Allowable key force with expected bolt relaxation (see para. 3)		35	56
4 MA optimised shear	10400	29	36
4.3 MA ELM free H mode	10600	29	37
5 MA ELMy H mode	14000	32	41

Radiation (at the levels expected in JET, e.g. from DT experiments) has no effect on the mechanical performance of these components so no problems are expected up to the end of 1999.

In 1998 we recommended “to ensure that the machine is in good condition, the octant bolts should be checked and tightened at the end of 1999. If this is not done, the bolts will continue to relax and eventually the performance of the machine will have to be limited.” These latest results are surprising and do not show a continuing trend of degradation.

However, we must assume that there is a continuing trend of loss of tension with some variation about the mean due to the state of the machine at the last pulse before the shutdown. This variation was not picked up in the period 1990 to 1997 when no measurements were made. Extrapolating the new trend line give 2001 instead of 1999 for reaching a tension of 70% of the original but this prediction is very uncertain. The recommendation therefore remains that the work should be done but one can draw two alternative conclusions about the urgency;

- either that the new trend indicates the tightening is not so urgent or
- that the uncertainty in the joint behaviour means that the joints should be serviced as soon as possible.

When the bolts are tightened, the total operation will take about six months. This work should be done in parallel with other shutdown work (although it will delay other ex-vessel activities) and should not follow too closely after a DT experiment.

Pulse statistics

V. Riccardo
26 October 1999

Contents

1.	Basic	1
2.	Forces at the collar and ring supports	3
3.	Shear stress at the tip of the tail	5
4.	Axial stress in the copper conductor	7
5.	MS torque	8

1. Basic

The maximum TF current, the I_t^2 at the end of the flat top and at the end of the pulse have been collected. These quantities are plotted in bar charts and summarised in tables in the following (Fig. 1-2 and Tables 1-2). These data are useful to estimate the life consumption of various components such as the TF coil tails or the copper conductor.

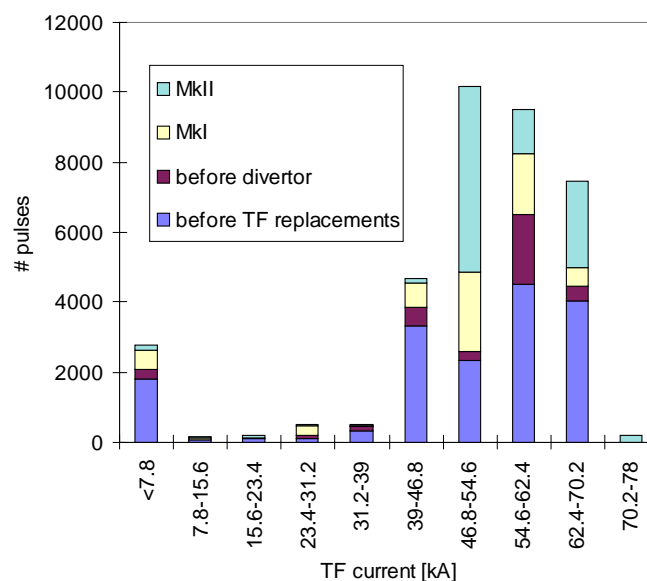


Fig. 1 TF current brackets sorted according to the pulse number.

TF current between [A]	# pulses
<7.8	2791
7.8-15.6	168
15.6-23.4	185
23.4-31.2	504
31.2-39	512
39-46.8	4669
46.8-54.6	10174
54.6-62.4	9502
62.4-70.2	7461
70.2-78	184

Table 2.3.1.1 Distribution in TF current for JET life (up to pulse 47200)

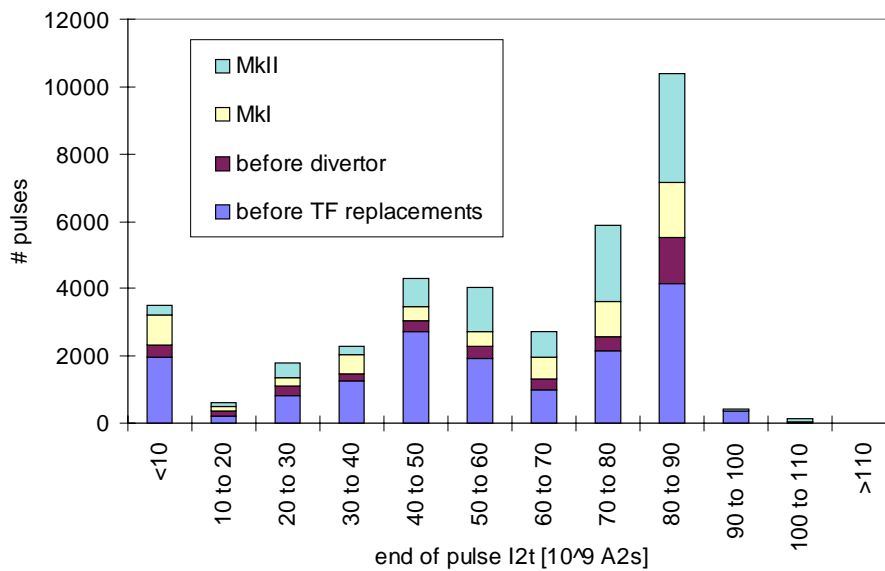


Fig. 2 I^2t at the end of the pulse brackets sorted according to the pulse number.

I^2t [$10^9 A^2s$]	# pulses (end of flat top)	# pulses (end of pulse)
<10	3499	3814
10 to 20	592	1982
20 to 30	1802	3261
30 to 40	2298	4474
40 to 50	4315	4034
50 to 60	4056	2802
60 to 70	2732	7781
70 to 80	5879	7606
80 to 90	10396	301
90 to 100	445	93
100 to 110	128	2
>110	8	0

Table 2 Distribution in I^2t (end of flat top and end of pulse) up to pulse 47200

2. Forces at the collar and ring supports

The out of plane reaction force at the collar tooth depends strongly on the shaping current, so to find pulses with high peak inter-turn shear stress (proportional in first instance to the collar reaction) the pre-divertor campaigns pulses have been sorted according to the shaping current and the TF current. The worst loads for the collar have to be at high shaping with high toroidal field. High load on the collar support mean high peak shear stress in the 3rd inter-turn, which has to be monitored for the integrity of the machine. Among the “boundary” pulses those which have been found with the maximum out of plane collar reaction are those with full field and full (50 kA) shaping current (4 pulses). In Fig. 3 there is the scatter of JET pre-divertor pulses in the Sh,TF current space. From the same data, the product Shaping current time TF current is sorted in brackets in Fig. 4.

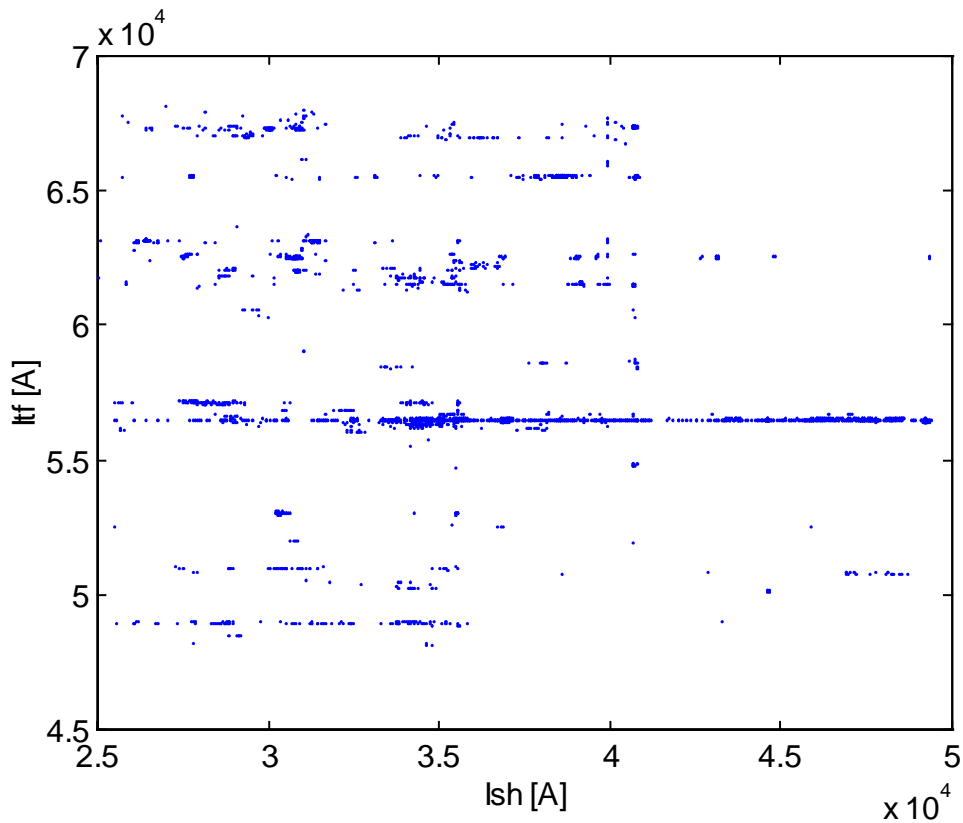


Fig. 3 JET pulses (up to ~28000) scattered according to the shaping current and the TF current.

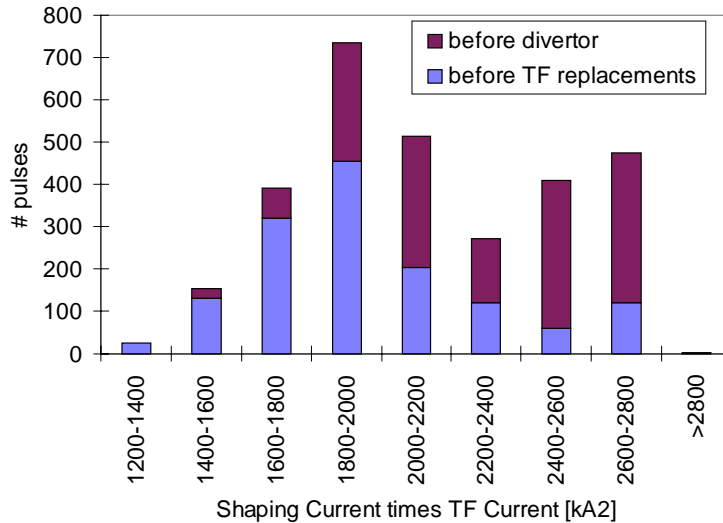


Fig. 4 Shaping current time TF current sorted brackets and divided according to the pulse number. Only 4 pulses have this product larger than $280 \cdot 10^6 \text{ kA}^2$, and these are the pulses with the highest out of plane force at the top collar (pulse 26805 and 3 similar pulses, with 50 kA shaping current)

The ring out of plane reaction is approximately proportional to the transverse flux at the TF FL 2 and 7 times the TF current. This quantity has been collected for JET pulses between ~ 3000 and ~ 47000 at the top ring (TF FL 2) and plotted in Fig. 5. This quantity never exceeded 15 kA Wb, corresponding to ~ 560 kN (ring bolts' endurance limit from a conservative standpoint on the pre-load), so the ring bolts should not have consumed any life.

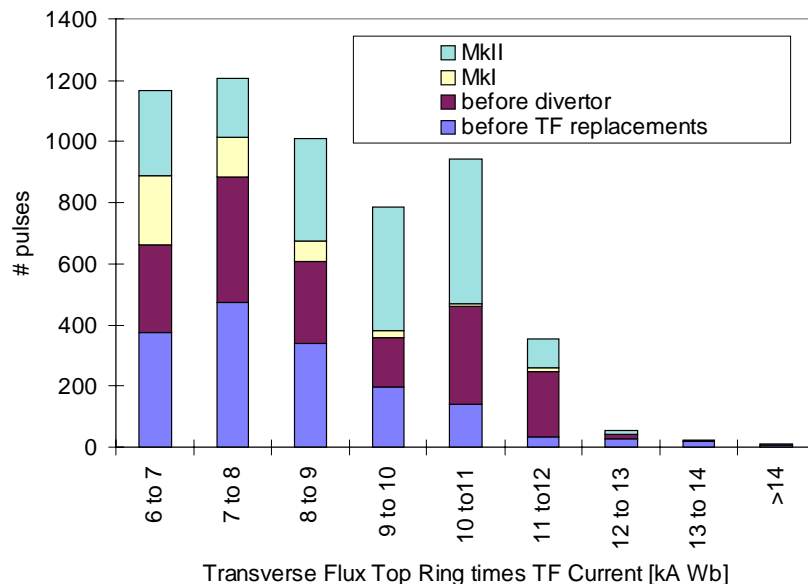


Fig. 5 TF transverse flux times TF current at the top ring flux loop sorted brackets and divided according to the pulse number.

3. Shear stress at the tip of the tail

The TF current has been collected primarily to estimate the life consumption at the TF coil tail tip, where the shear stress scales with the square of the TF current and the I^2t at the end of the flat top. A scatter plot of all the pulses of JET (from ~3000 to ~47000) on the B_T, I^2t space is in Fig. 6, assuming that the shear stress varies as $13 (B_T/4 \text{ T})^2 + 12 (I^2t/80 \cdot 10^9 \text{ A}^2\text{s})$. In Fig. 7 the maximum shear stress at the tail tip is sorted in shear brackets and then divided amongst periods of operation (the first going up to the replacement of the faulty TF coils, the second covering the high performance empty vessel campaign, the third being MkI operation and the fourth being MkII operation). The number of pulse for each shear bracket is summarised in Table 3a and the equivalent number of pulses for some relevant stress levels is listed in table 3b.

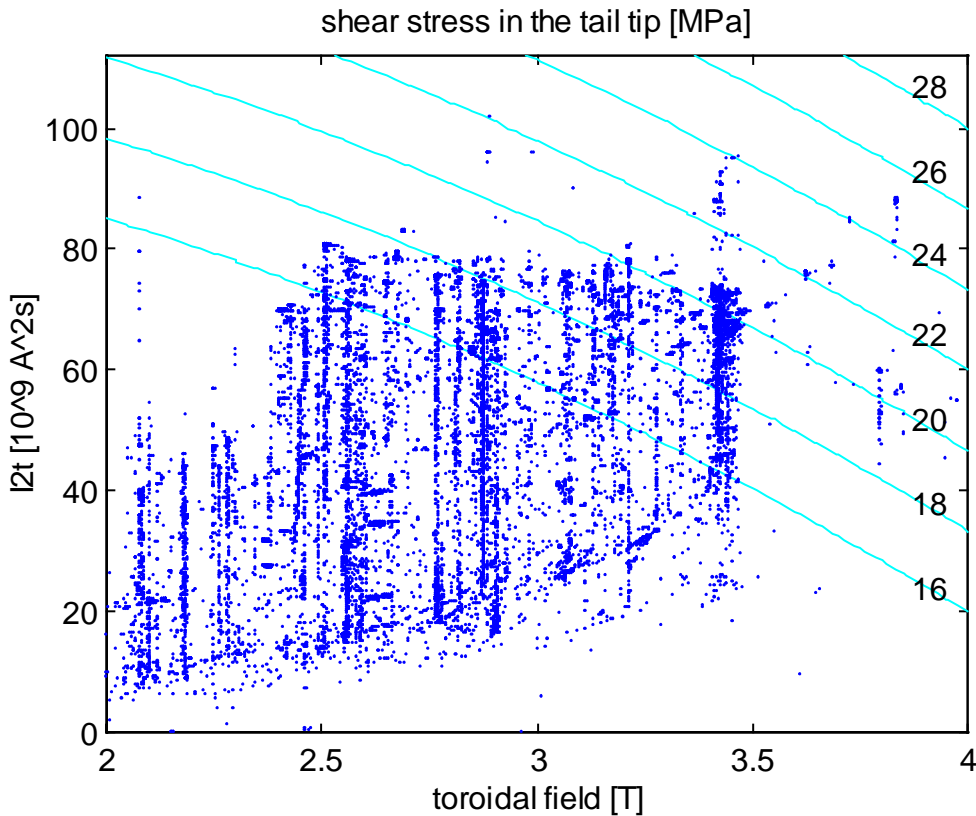


Fig. 6 Scatter plot on the I^2t , B_T space of JET pulses. The contours between 16 MPa and 28 MPa (2 MPa each line). A few points have an overestimated value of the I^2t , since the time integral is carried out until the TF current has gone below 91% of its maximum value.

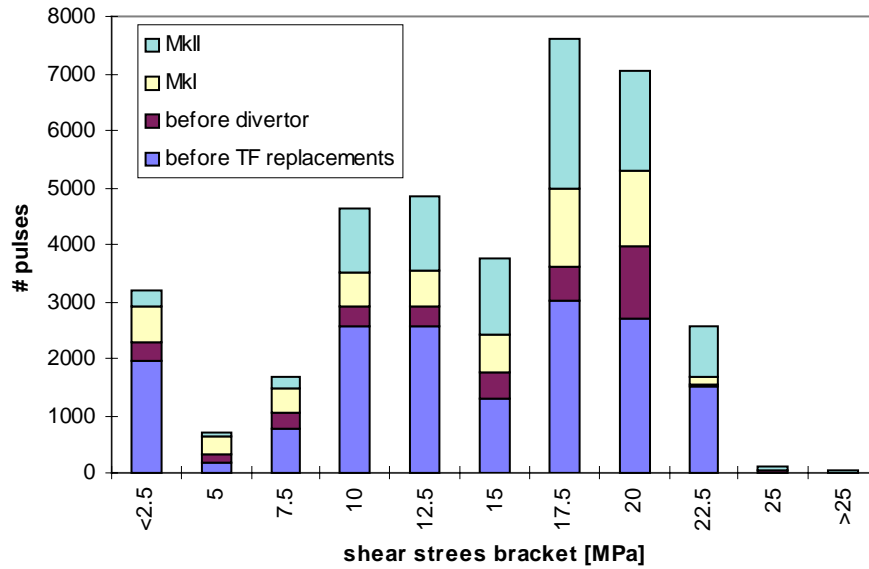


Fig. 7 Shear stress at the tip of the tail sorted in shear brackets and divided according to the pulse number. Most of the pulses producing more the 22.5 MPa are MkII pulses.

shear stress between [MPa]	# pulses
0÷2.5	3157
2.5÷5	712
5÷7.5	1685
7.5÷10	4694
10÷12.5	4842
12.5÷15	3757
15÷17.5	7989
17.5÷20	6788
20÷22.5	2341
22.5÷25	113
25÷27.5	30

Table 3a Distribution in shear stress at the tip of the tail up to pulse 47200

reference stress level [MPa]	equivalent # of pulses
17.5	125790
20	12729
22.5	1288
25	130
27.5	13
30	1.33

Table 3b Equivalent number of pulses at various reference stress levels with respect to the peak shear stress at the tip of the tail.

4. Axial stress in the copper conductor

The TF current collected primarily to estimate the life consumption at the TF coil tail tip can also be used to produce a guess of the life consumption in the high-stressed spots of the copper conductors (inboard at the end of the straight leg, opposite to the end of the inner cylinder support, where the membrane stress is summed with the tensile in-plane bending due to the constraint discontinuity). This estimate is even less accurate than the one done for the tail, as the peak load does not depend only on the toroidal field but also on the plasma scenario. It has been chosen to scale the pulses as if they were done at constant $I_p \cdot B_T$, so that the out-of-plane loads could be assumed proportional to the in-plane load. This simplification does not account for the shape of these loads in any case. To be conservative the scaling with the square of the toroidal field has been fixed to 170 MPa at 4 T, which is the highest stress computed during the 4 T assessment and which includes the effect of the compliance of the out-of-plane supports. Another source of error is that dry-runs are counted as plasma pulses. In Fig. 8 the maximum axial stress in the copper is sorted in brackets and then divided amongst periods of operation (the first going up to the replacement of the faulty TF coils, the second covering the high performance empty vessel campaign, the third being MkI operation and the fourth being MkII operation). The number of pulse for each axial stress bracket is summarised in Tables 4a and 4b.

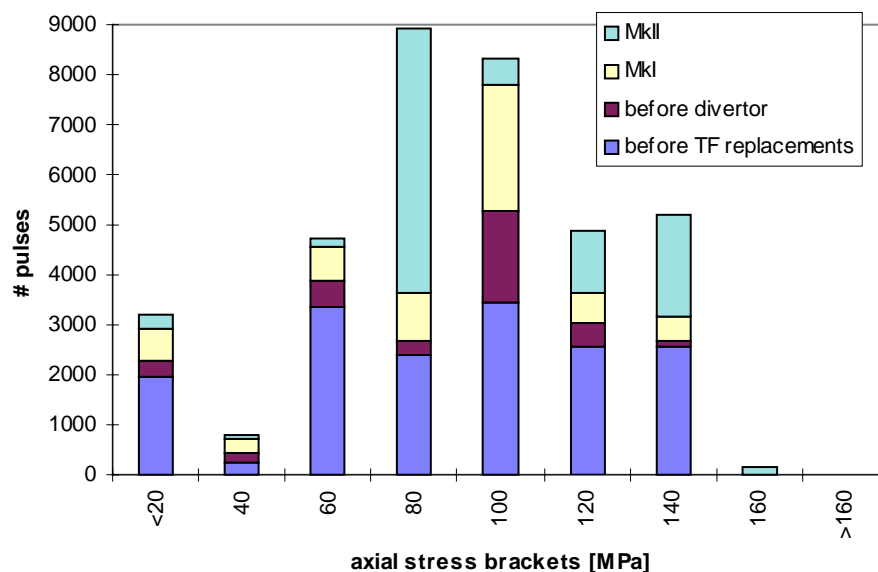


Fig. 8 Axial stress in the copper conductor (small section, inner leg) sorted in brackets and divided according to the pulse number. Most of the pulses producing more the 140 MPa are MkII pulses.

axial stress between [MPa]	# pulses
0÷20	3145
20÷40	789
40÷60	4749
60÷80	8895
80÷100	8786
100÷120	4397
120÷140	5205
140÷160	133
160÷180	9

Table 4a Distribution in copper axial stress in the reduced section up to pulse 47200

reference stress level [MPa]	equivalent # of pulses
80	52530
100	26126
120	14765
140	9114
160	6001

Table 4b Equivalent number of pulses at various reference stress levels with respect to the total axial stress in the reduced cross-section copper conductor (at 4 T or 170 MPa it would be 4960)

5. MS torque

Statistical analysis of the torque applied to the JET machine after 1990 has been carried out following some concerns about the loosening of the bolts at the octant joints. The bolts have been tightened at the beginning of 1990. Their length has been measured then, at the end of 1996 and at the beginning of 1998. These investigations showed a bolt loosening of ~30%. If the experienced torque and the loosening of the bolts are correlated it is worth examining the loads applied to the MS in the past seven years: between their tightening (before pulse 21071) and their last inspection (after pulse 44414).

Overall the torque scales with the product plasma current toroidal field for “similar” plasma configurations and that the disruption torque is usually larger (by a factor of ~1.8) than the equilibrium one, since the PF coils field is not compensated by the plasma field at the TF coils: for a plasma shaped as the coil the poloidal field normal to the coils themselves would be zero. The before-divertor-coil-installation equilibrium torque scales approximately (tested only on a few plasmas, like 7.2 MA 27864 and 27902, 50 kA-shaping 26805 and high shaping/plasma ratio 24497) as 400 (ton m)/(MA T), while the after-divertor-coil-installation equilibrium torque scales approximately as 700 (ton m)/(MA T). The different scaling is due the shape of the plasma being more similar to the shape of the TF coils before the divertor installation, so that the poloidal field normal to them was smaller.

CPF data base has been used to obtain the maximum plasma current and the toroidal field at the time of the maximum plasma current; the disruption data base has been

used to obtain the plasma current at the disruption. In total 15,291 pulses with plasma current larger than 1 MA have been found, among these 3,012 disrupted with a plasma current larger than 1 MA, between pulse 21071 and 44414. To each pulse a tag with the maximum torque has been associated

$$T = \max(B_T I_{p,eq}, 1.8 B_T I_{p,dis}) * C,$$

where C is a scaling factor: 400 (ton m)/(MA T) no-D-coil; 700 (ton m)/(MA T) with-D-coil . Then all the tags have been summed up. This sum ($75.6 \cdot 10^6$ ton m pulse) can be used to guess the equivalent number of pulses for a given product plasma current times toroidal field with the present machine configuration; an example is given in Table 5a. The worst equilibrium and disruptions between 1990 and 1998 are listed respectively in table 5b and 5c. The number of normal pulses and disruptions at different levels of torque is plotted in Fig. 9, while the torque versus pulse number is plotted in Fig. 10.

	Eq. # without disruption	Eq. # with disruption
5 MA, 4 T	5,400	3,000
3.5 MA, 3.45 T	7,500	4,200

Table 5a Equivalent-torque pulses between early 1990 and early 1998

pulse	Bt [T]	Ip [MA]	torque [ton]
35706	3.41	6.05	14429
35707	3.39	5.93	14068
35718	3.39	5.86	13932
35705	3.39	5.83	13848
35696	3.38	5.54	13116
35689	3.40	5.38	12796
35714	3.40	5.13	12186
35717	3.39	5.13	12172
35703	3.39	5.12	12166
35695	3.39	5.13	12156

Table 5b Equilibrium worst torque between 1990 and 1998

pulse	Bt [T]	Ip [MA]	torque [ton]
34486	3.14	5.63	22254
32762	2.79	6.18	21692
32824	3.39	4.99	21316
32280	3.39	4.83	20635
34221	3.14	5.15	20344
32799	3.39	4.63	19781
33082	3.39	4.62	19740
33644	3.39	4.52	19302
32690	3.39	4.35	18598
34211	3.14	4.70	18554

Table 5c Disruption worst torque between 1990 and 1998

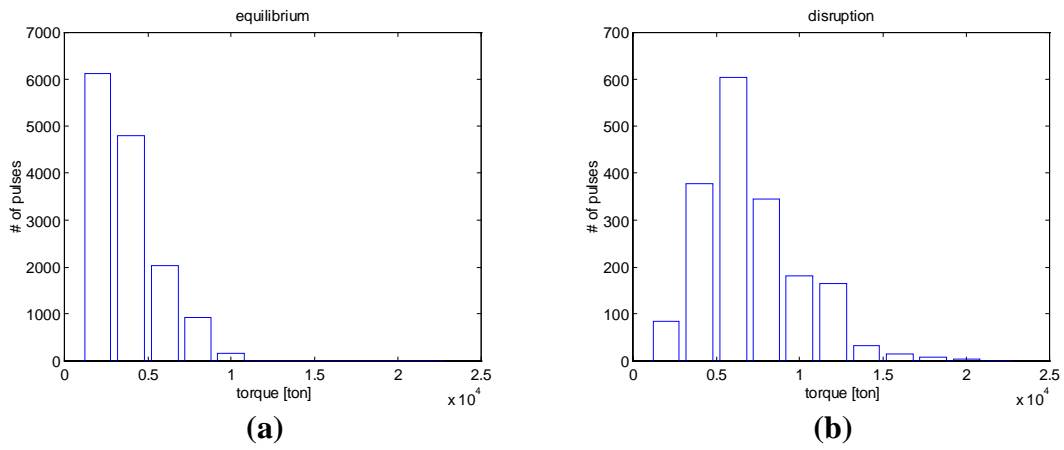


Fig. 9 Number of pulses at different torque level between 1990 and 1998

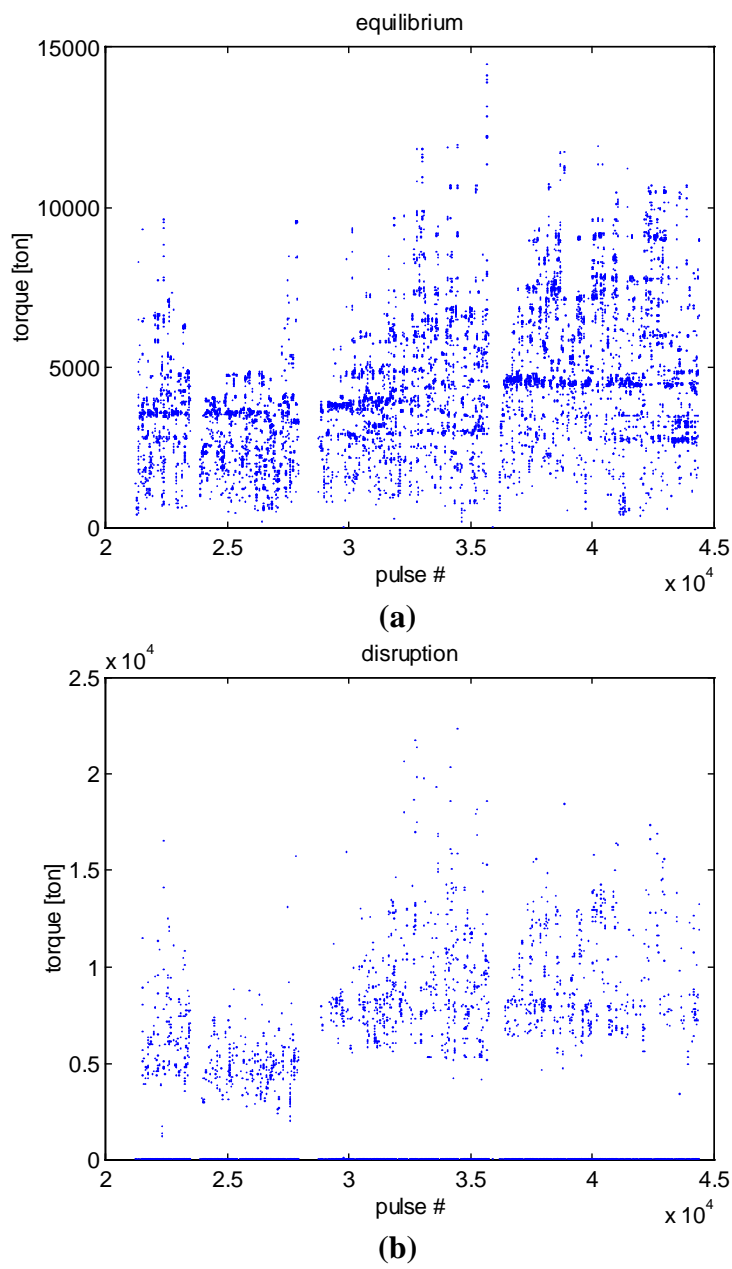


Fig. 10 Torque versus pulse number in equilibrium (a) and in disruption (b)

Analysis of signals: TF coil and structure

V. Riccardo
10 November 1999

Contents

1.	Signals analysed	1
2.	Flux loop measurements.....	3
2.1.	PF coil to Flux Loop contributions.....	3
2.2.	Comparison with maxfea (before the changes).....	4
2.3.	Changes in the simulation to minimise the errors	7
2.4.	Comparison with maxfea (after the changes).....	10
2.5.	Comparison of calculated force and measured transverse fluxes	12
2.6.	Reason for the remaining error.....	13
2.7.	Variable permeability and plasma equilibrium.....	14
2.8.	Plasma disruption and TF flux loop overshoots	25
3.	TF coil Radial Displacements at Push-pull Jacks and Midplane .	30
4.	Octant Joints shear and separation measuements	39

1. Signals analysed

Two coils (2.4 and 6.4) have 10 flux loops attached (8 double and 2 single, these in the inner leg). A sketch of the lay-out of these diagnostics is in Fig. 1. The TF flux loops are used to estimate the out of plane force acting on various parts of the coil. The force is scaled from the flux with the TF current; there is no other measure of the out of plane force on these coils as that. The most important flux loops are 3&6 (top and bottom collar supports) and 2&7 (top and bottom ring supports), as they are located in two critical regions of the coil: inter-turn shear at the collar, limited strength of the ring bolt assembly. These products of flux and current are always monitored during operations and safety limits are applied on them: a pulse can be stopped, more or less quickly (soft

stop or voltage off) depending on how much the trip level has been exceeded. The trip levels are set according to the stress/force level allowed on the coil in the specific region. These are investigated using Maxfea to get the poloidal field map on the coil and Abaqus to compute the support reaction forces. These two ways of exploiting the flux loops are summarised in Fig. 2.

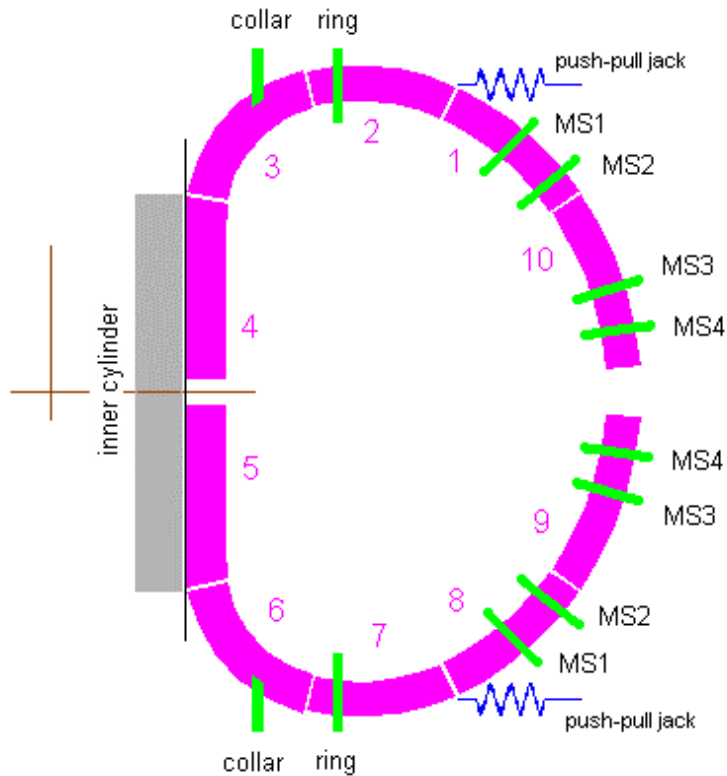


Fig. 1 Lay out of the TF coil supports and flux loops.

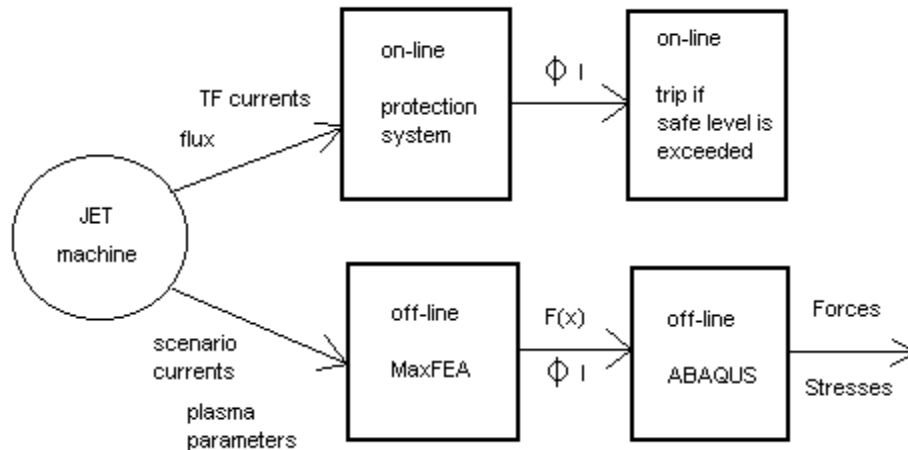


Fig. 2 On-line and off-line use of the TF flux loops.

The radial displacement of the TF coil is monitored using 16 transducers at the midplane (coils .1 and .4 of each octant) and 8 at the push-pull jacks (octant 3, all coils top and bottom). During any pulse, the TF coils move radially outwards both because of the magnetic hoop force and because of thermal expansion. Their movement is carefully monitored during high field pulses to check whether it is in agreement with expectations: these displacements are an indirect measure of the in-plane stiffness of

the coil, therefore unforeseen changes of behaviour could mean a variation in the mechanical strength of the system.

There are 16 octant joint force transducers (two in each octant, left and right), 8 octant joint shear and 8 octant joint separation transducers.

In addition, there are two pressure gauge instrumented ring wedges (one top and one bottom, producing 4 signals: left and right at each location). They should measure directly the out of plane force acting on the ring supports and provide a good cross-check for the computed (Maxfea+Abaqus) reaction force. However these diagnostic are still being commissioned and their behaviour has not been fully understood yet.

2. Flux loop measurements

It is important that the poloidal field computer by Maxfea and used as an input for the stress analysis is reliable. Therefore thorough investigations have been carried out the consistency between the flux normal to the TF coils as computed by Maxfea and the measured one. To this end the accuracy of the geometry of the mock flux loops in Maxfea is determinant. A very small change in it used to produce quite large flux errors, even if the poloidal field was basically correct. Also the assumption done on the status of the iron may be relevant, especially when the inner core and the shoes (ends of the torsion ring) cannot be taken as saturated. To get reasonably good agreement between maxfea and the measurements two major changes have been done: the detailed geometry of the loops has been modelled (including gaps between them, reductions of area...) and field dependent permeability (first for dry runs only, later also for plasma equilibrium calculations) has been added.

2.1. PF coil to Flux Loop contributions

The simplest pulse to check the consistency between computed and measured fluxes is a dry run (when only a PF coil at a time is energised). Dry runs have been used to compute the contribution of each circuit to the flux in any loop. Since the signals are affected by some TF pick-up and some drifting, the influence coefficients have been worked out using a min-squared error routine.

Assume the flux measured by a flux loop can be written as

$$\varphi(t) \approx \sum_i a_i I_i(t)$$

where the $I_i(t)$ are the PF and D coil currents, but also the TF coil current, a drift and a step function.

The coefficients a_i can be found minimising the square of the error between the flux loop signal and its linear approximation. For each flux loop measurement the error is

$$\varepsilon(t) = \sum_i a_i I_i(t) - \varphi(t)$$

and it is sampled in a number of points. The function to be minimised is

$$S(t) = \sum_i \left[\sum_j a_i I_i(t_j) - \varphi(t_j) \right]^2$$

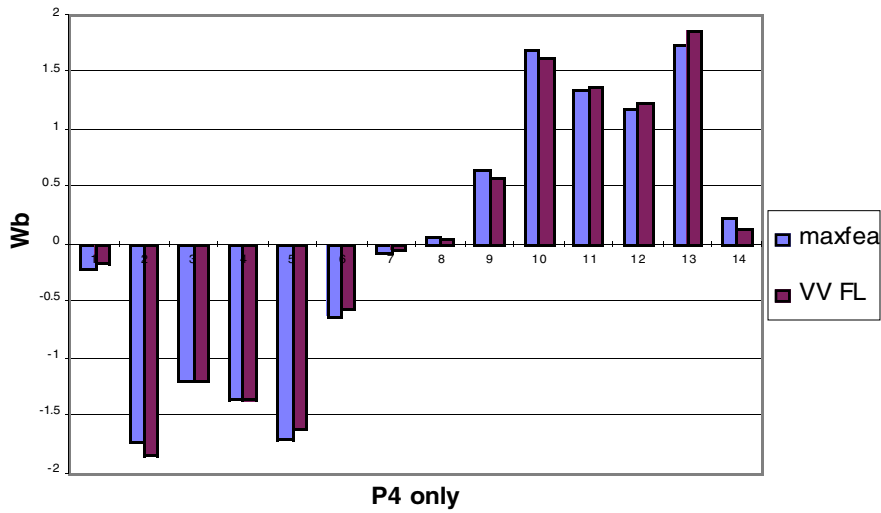
so there are as many linear equation to be solved as the number of coefficients a_i , since

for each of them $\frac{dS}{da_i} = 0$.

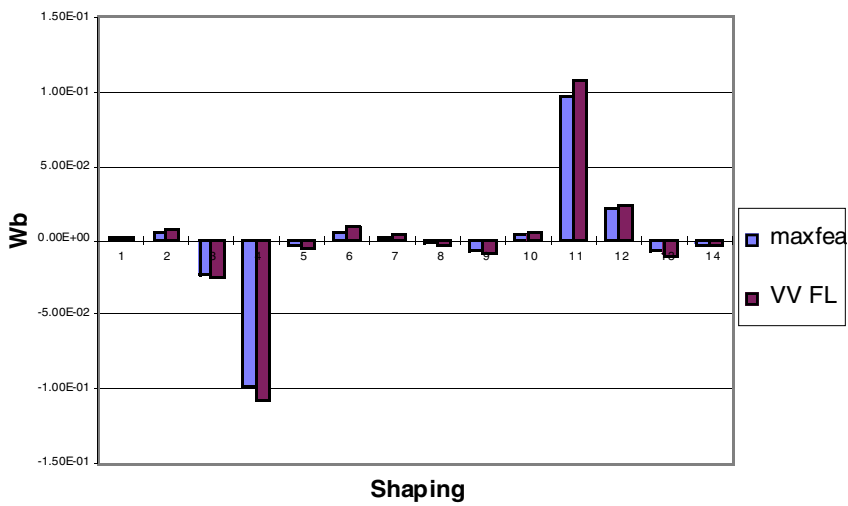
For the comparison with maxfea calculation only the coefficients for the PF and D coil currents are important, the other are "noise" to be cleaned.

22. Comparison with maxfea (before the changes)

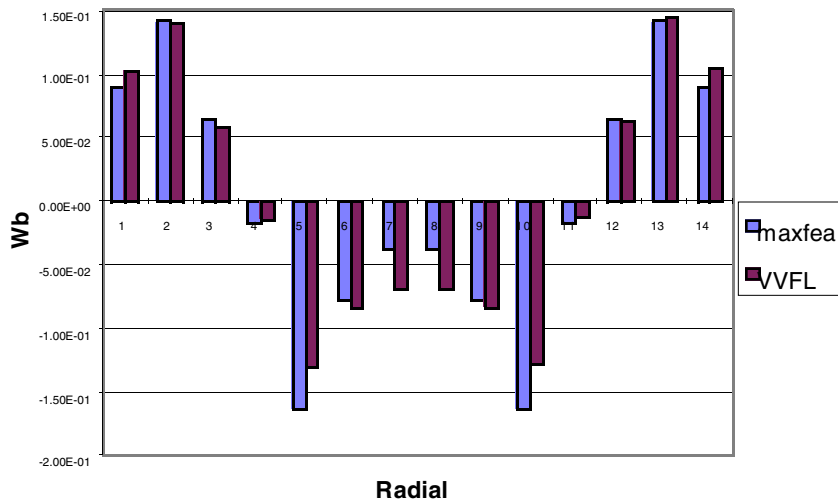
Influence coefficients of PF and D coils for the TF (Fig. 3a-b-c) and the VV (Fig. 4a-b-c) flux loops, calculated with Maxfea, have been compared to those coming from the measurements.



(a) P4 only

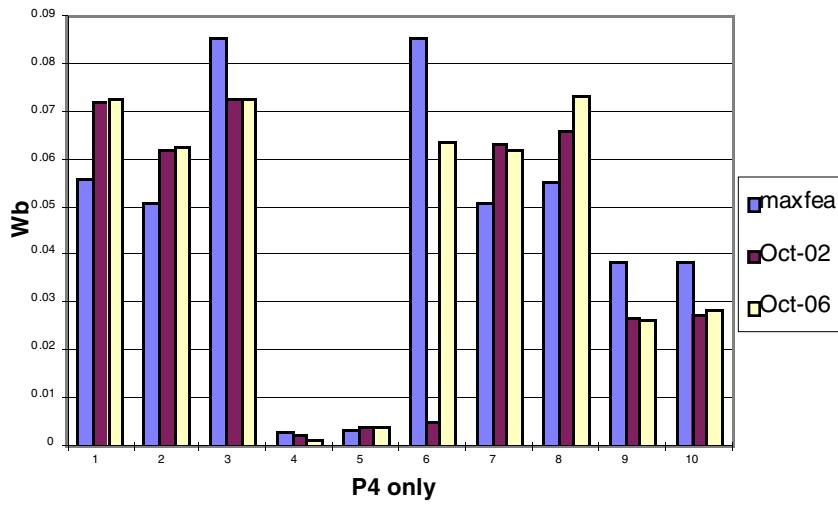


(b) Shaping only

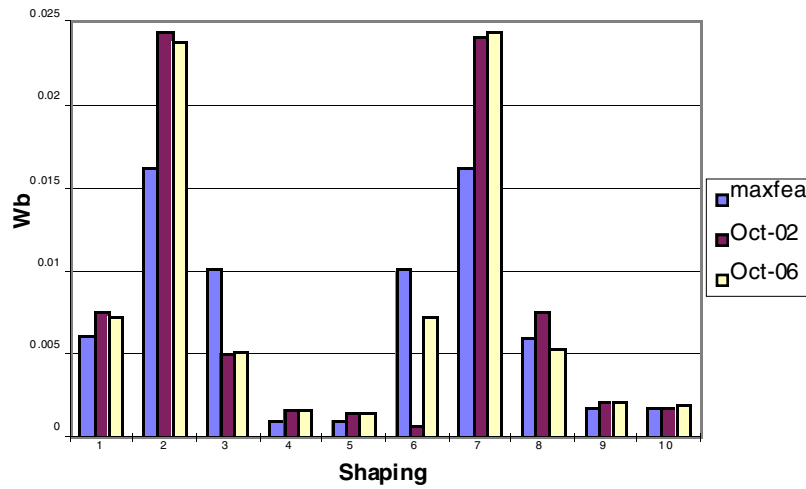


(c) Radial only

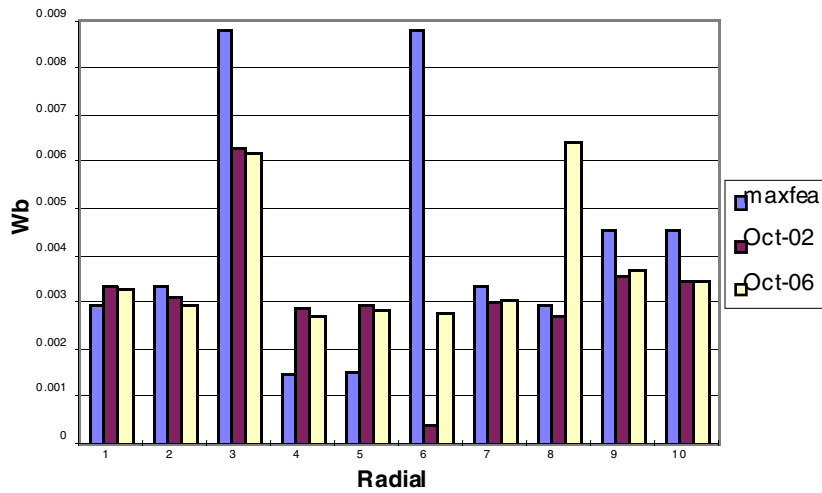
Fig. 3 Vessel flux measurements and maxfea calculations.



(a) P4 only



(b) Shaping only



(c) Radial only

Fig. 4 TF coil flux measurements and maxfea calculations -absolute values-

The vessel comparison for the P4 only case is far better than the same case for the TF coil flux loops, while for the Radial field the simulation results are poor in both cases. Since these coefficients have been evaluated from the dry runs, permeability plays an important role and the errors in the VV flux loops depend on it.

23. Changes in the simulation to minimise the errors

The first change made was to let the permeability adjust according to the magnetic field in the iron region (no plasma, PF&D currents only). Having done this, the Radial field case for the VV flux loop showed a good agreement with the experiment (Fig. 5).

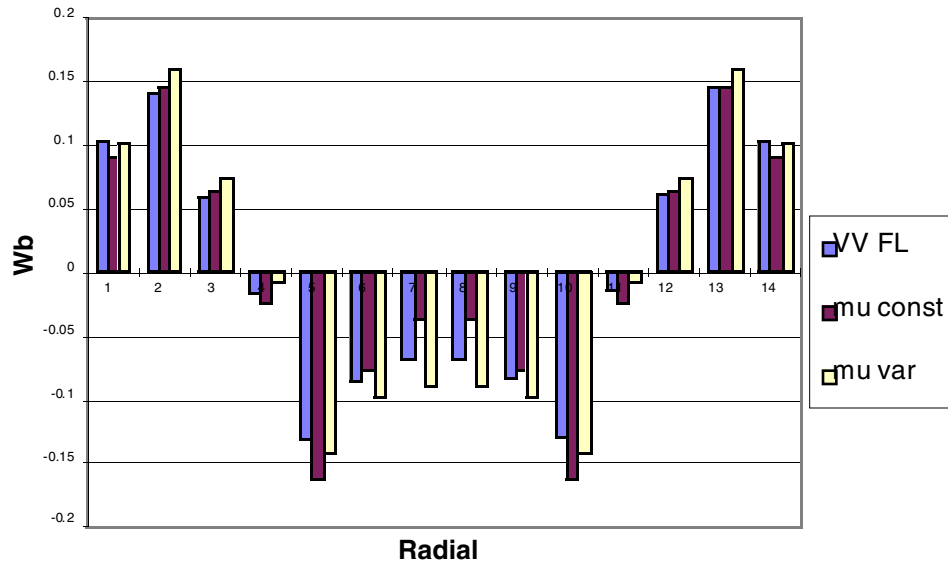
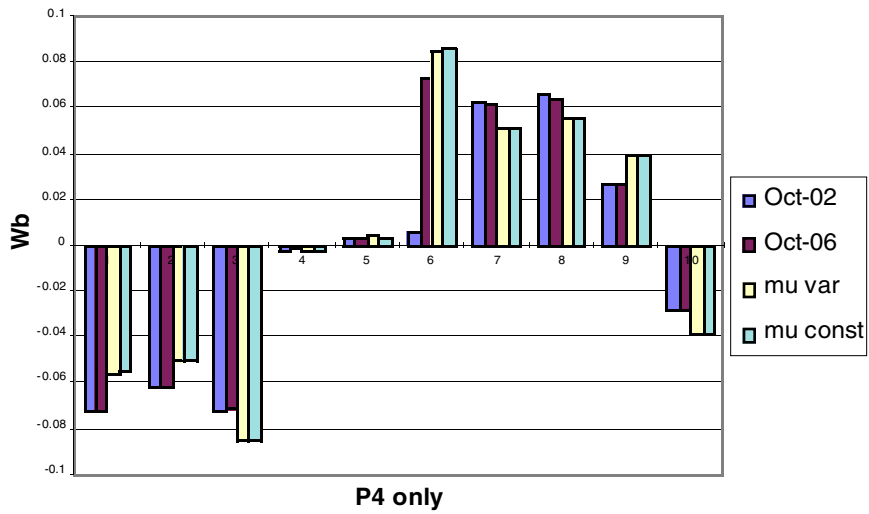


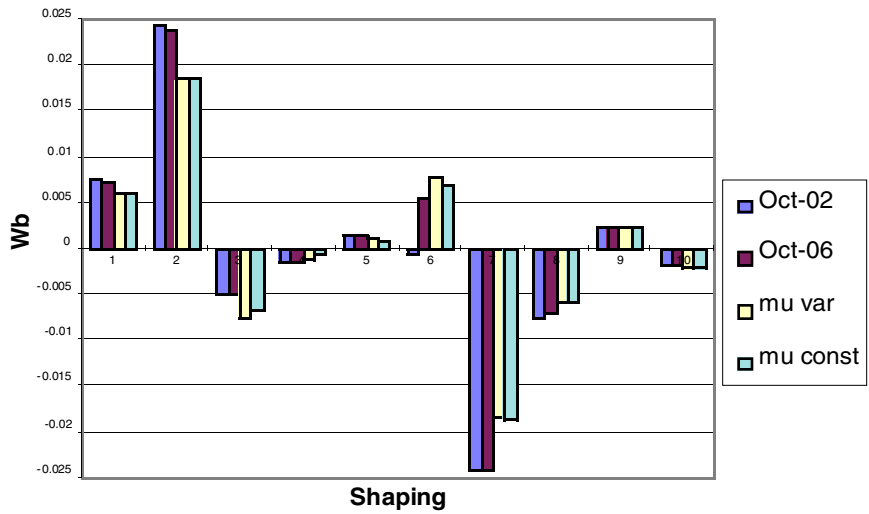
Fig. 5 Radial field case for the VV flux loops with and without variable permeability.

However, the errors for TF flux loop simulated coefficients did not decreased very much because of the variable permeability, except for the Radial field case (Fig. 6).

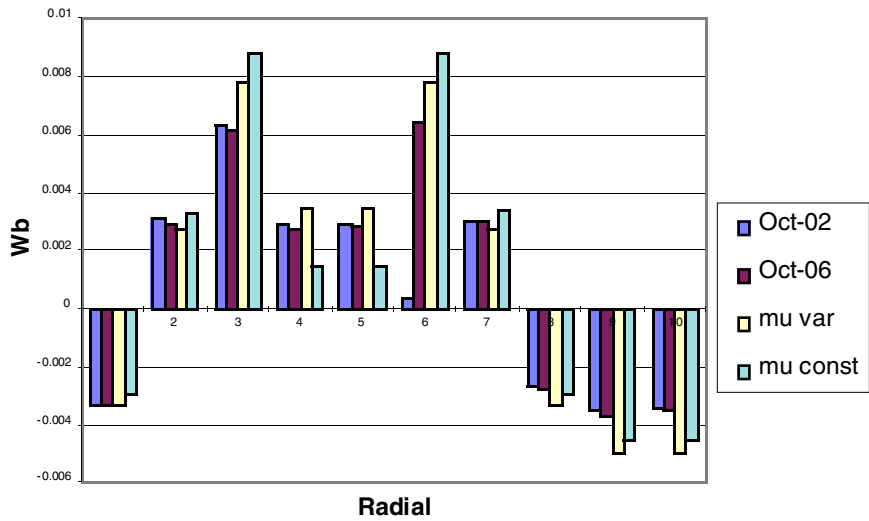
The second change has been made in the geometry of the TF flux loops to have then as similar as possible to those present on the machine. After the modification in their geometry the computed influence coefficients improved substantially (Fig. 7).



(a) P4 only

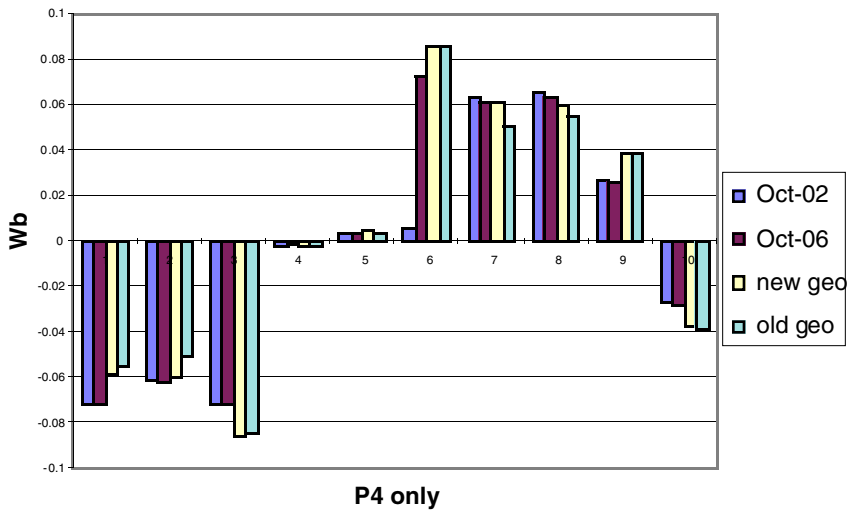


(b) Shaping only

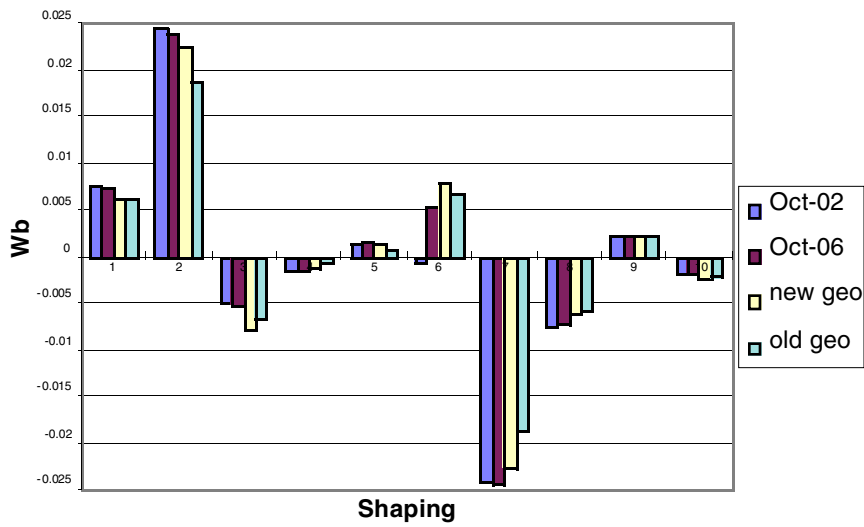


(c) Radial only

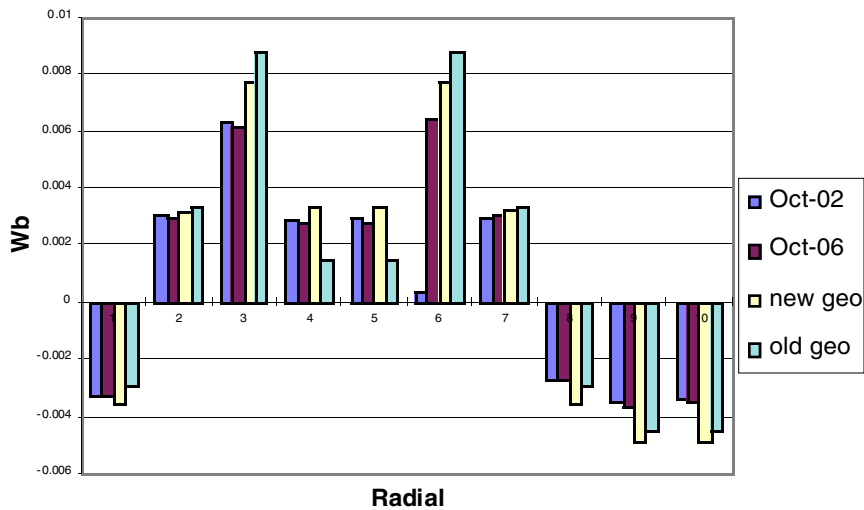
Fig. 6 TF flux loops, with and without variable permeability.



(a) P4 only



(b) Shaping only



(c) Radial only

Fig. 7 TF flux loops with the old and the new geometry.

24. Comparison with maxfea (after the changes)

The comparison of the measurements with the simulated fluxes in the TF flux loops for an equilibrium shows how the accuracy has changed. For cases when the plasma is included the permeability has to be fixed on each material, anyway the fields are high enough to define region where the iron is saturated and where it is not. The improvement is substantial on all the flux loops except 3 and 6 (Fig. 8).

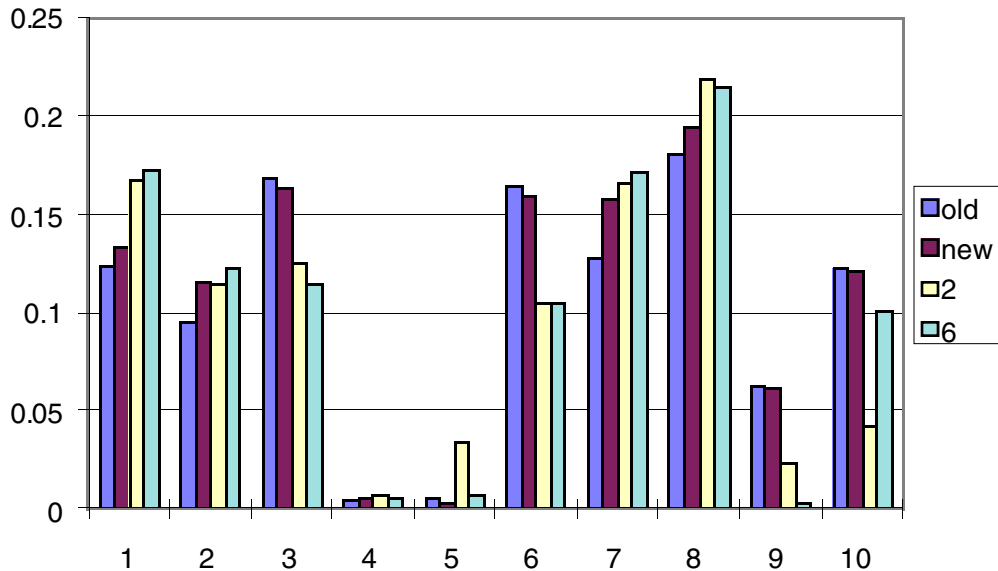
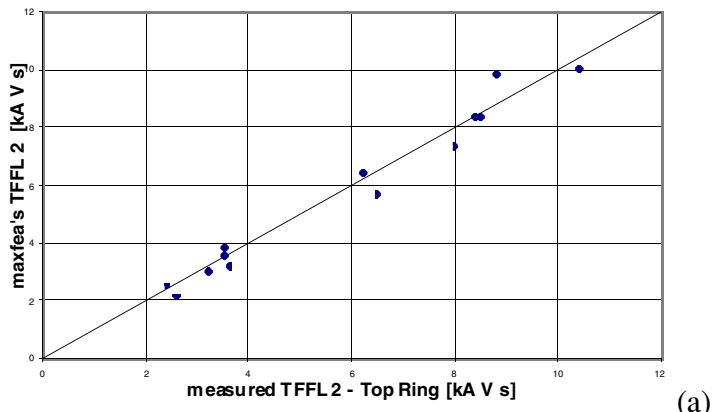
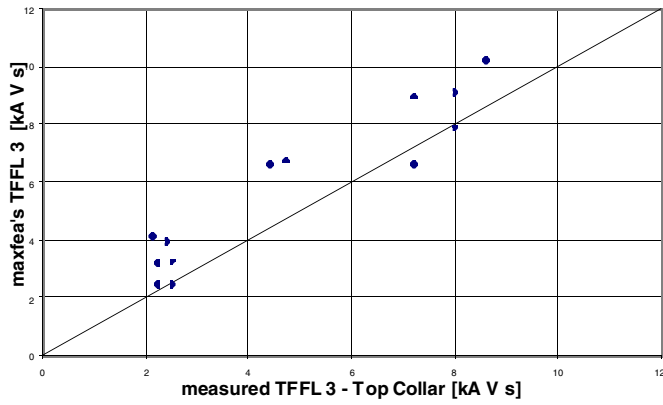


Fig. 8 TF flux measurements and maxfea calculations (with the old and the new TF flux loop geometry) for the equilibrium of pulse 38265.

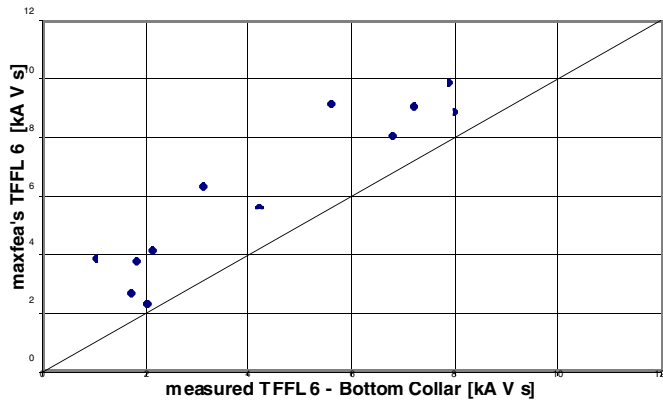
For 13 different plasma configurations the values of the Transverse Flux at the TF Flux Loops 2, 3, 6 and 7 (those close, respectively, to the Top Ring, Top Collar, Bottom Collar and Bottom Ring Teeth) has been retrieved and compared with the values evaluated by maxfea. The agreement is very good for Flux Loops 2 and 7, and not so good for 3 and 6 (Fig. 9).



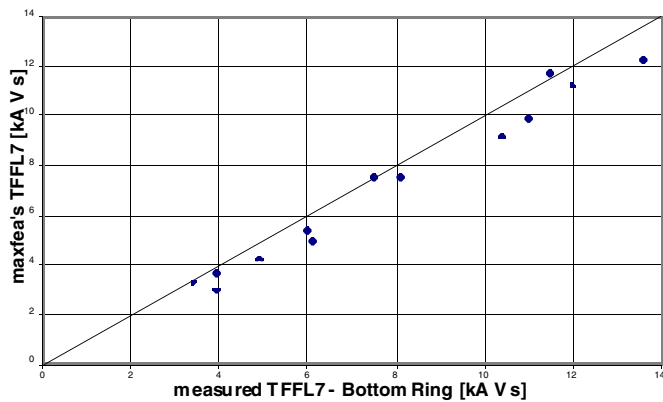
(a)



(b)



(c)

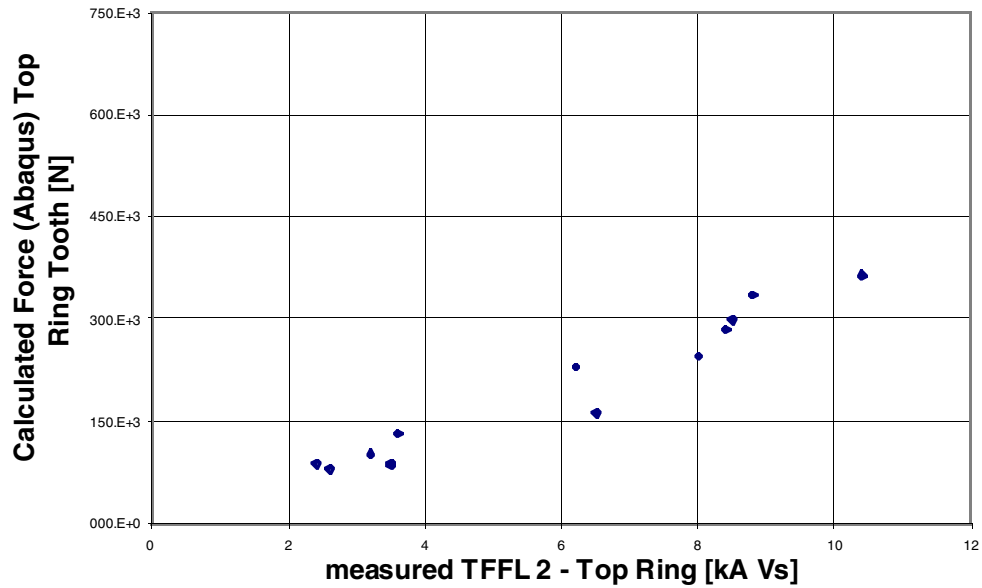


(d)

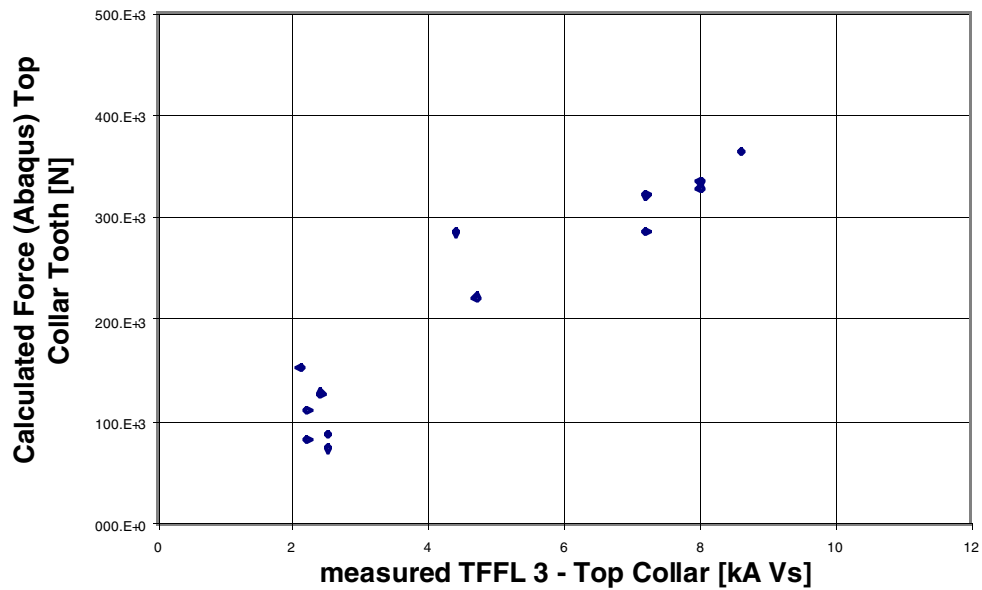
Fig. 9 TF flux measurements and maxfea calculations at the TF Flux Loop 2 (Top Ring, a), TF Flux Loop 3 (Top Collar, b), TF Flux Loop 6 (Bottom Collar, c) and TF Flux Loop 7 (Bottom Ring, d).

25. Comparison of calculated force and measured transverse fluxes

In addition the proportionality between the transverse flux and the force on the teeth (calculated using a beam model with Abaqus) has been investigated, results are plotted in Fig. 9a-b-c-d.

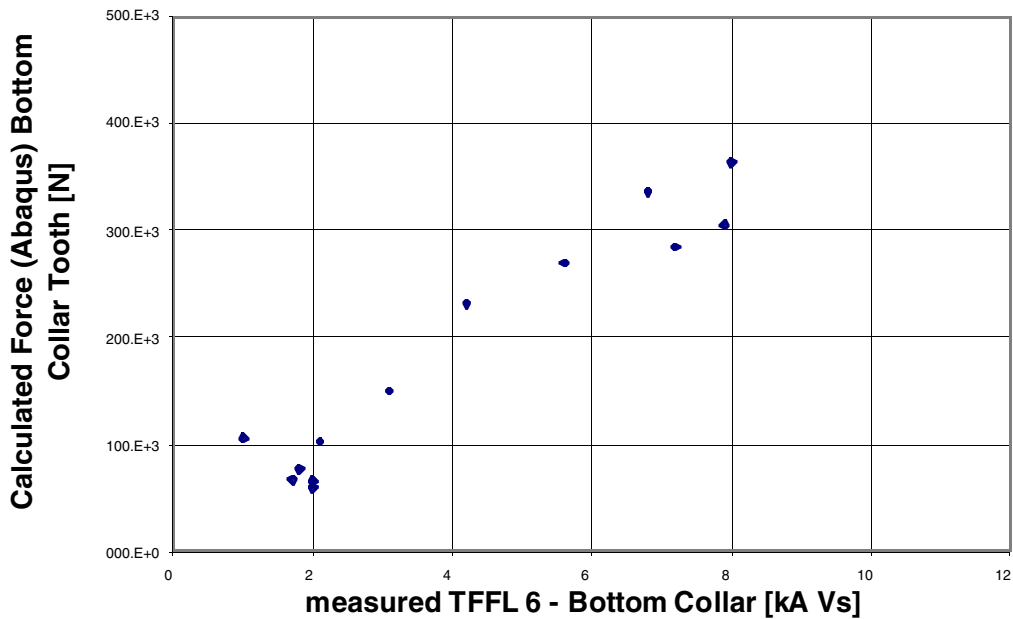


(a)

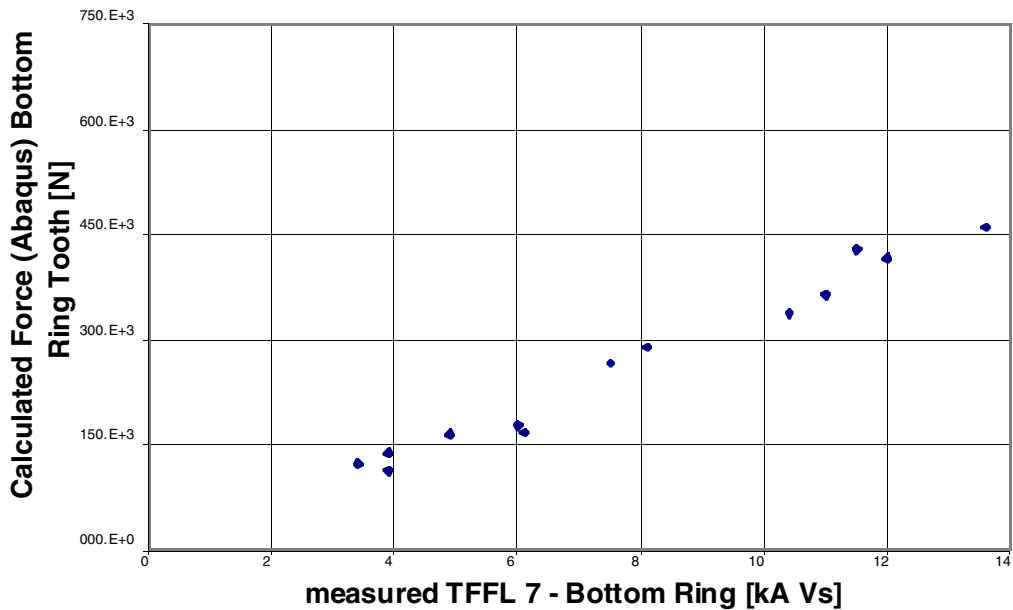


(b)

Fig. 10a & 10b Proportionality between the flux at the TF Flux Loops and the force at the supports: Ring lower than 75 t / 12 kA V s, Collar lower than 50 t / 12 kA V s.



(c)



(d)

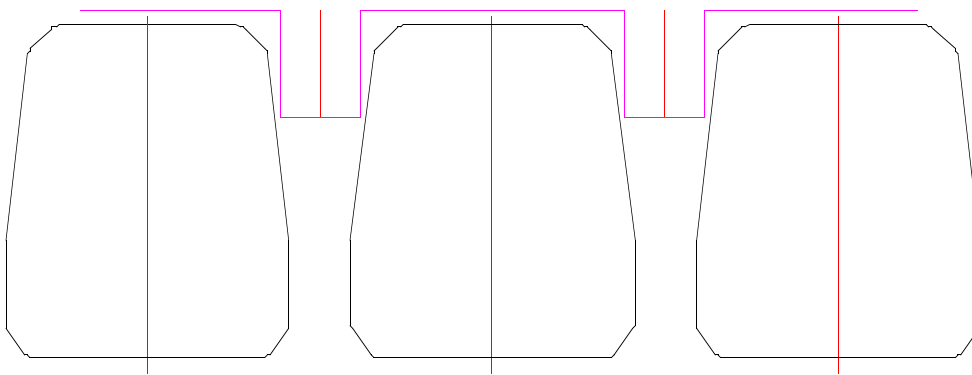
Fig. 10c & 10d Proportionality between the flux at the TF Flux Loops and the force at the supports: Ring lower than 75 t / 12 kA V s, Collar lower than 50 t / 12 kA V s.

26. Reason for the remaining error

Flux loops 3 and 6 are those close to the Collar Teeth and for them Maxfea gives a higher flux than the measurement. These loops are the closest to the iron core and the error could be due to non-axisymmetry of the poloidal field because of:

- the effect of the Collar Teeth which are ferromagnetic
- non symmetric permeability in the Collar due to the external toroidal ripple field

In either case the effect would be to divert flux away from the TF coils into the gap between the coils.



This effect can be estimated as follows: the typical value of the flux through this loop is 0.1 Wb, the area of the loop is 0.29 m² the poloidal field in the loop is then about 0.34 T; the area of the tooth is 0.016 m² so the tooth could carry 0.03 Wb (30% of the total flux) without saturating. accepting this explanation as the cause of the error, the flux loops can be taken as correct. The flux loops also give a correct indication of the force, since flux diverted away from the coil does not cause force. The flux in the Collar Teeth flux loops given by maxfea could be adjusted to the measured using ad hoc coefficients, but will give a pessimistic value of force.

Since the difference between calculated and measured flux is believed to be due to the shaping field passing through the teeth, the difference should be a function of the shaping field. The calculated flux is therefore fitted to a linear function of measured flux and P2 ampere-turns, the standard deviation decreases from more than 1 kA Wb to 0.55 kA Wb (Fig. 11). In addition, diversion of flux should also reduce the force, so the "measured" gradient is too conservative.

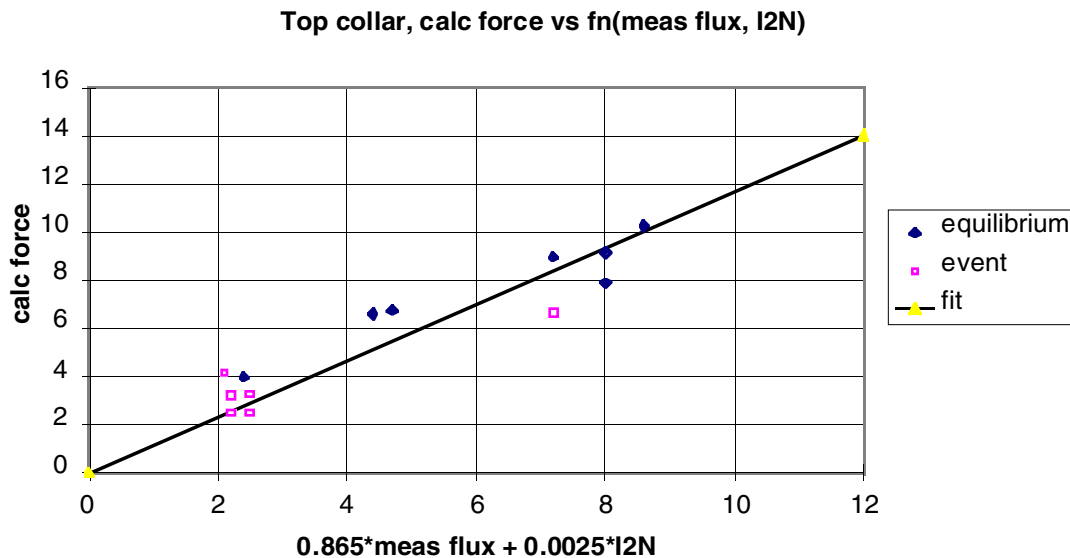


Fig. 11 The Top Collar calculated flux is in better agreement with the measured flux adjusted to compensate the non-toroidally symmetric effect of the teeth that cannot be taken into account in maxfea. A similar adjustment can be done at the Bottom Collar.

27. Variable permeability and plasma equilibrium

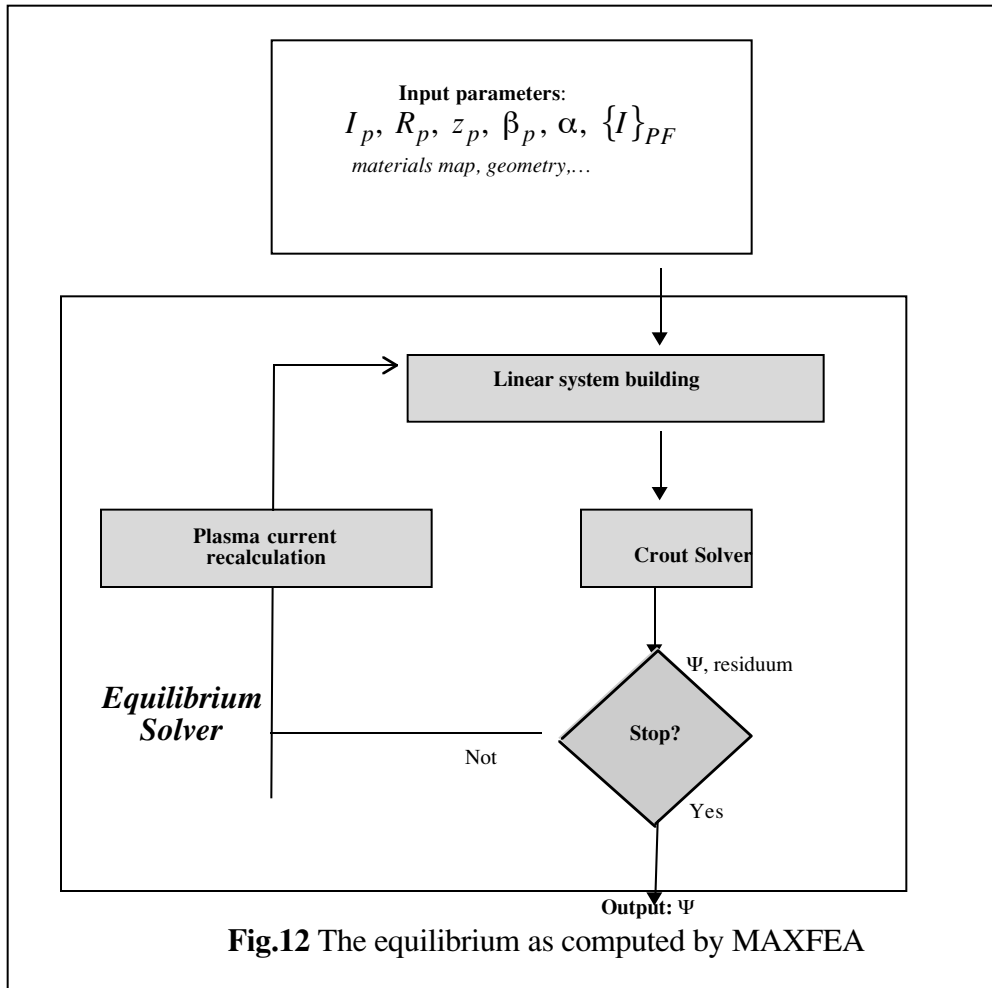
In order to introduce the permeability as a function of the field for the iron, the main structure of the solver had to be changed, so that it could still obtain the achieved reliability. Therefore, the non-linearity has been introduced by means of recursive computing of the permeability in the iron regions.

The Maxfea equilibrium routine continues to search for an improved resolution until interrupted. In the modified version, immediately after the convergence test an additional test is carried out only if iron is present in the system, so that the test on the convergence of the permeability starts only when the poloidal flux resolution is satisfactory. This loop continues if the resolution of permeability is unsatisfactory and the number of attempts in adjusting the permeability is less than the maximum allowed. At each non linear step the permeability is recalculated on each triangle of the iron regions by interpolating the adopted curve. Consequently the stiffness matrix of system is modified, so the program starts computing a new equilibrium. Fig. 12 shows the flow chart. This procedure, besides exploiting all the old equilibrium features, minimises the modifications in the subroutine so that time evolution can be run after the non linear analysis (keeping the permeability as during the equilibrium). In this way the user can choose the accuracy of the analysis and the computational effort to invest.

The upgrade of the permeability is performed by using a relaxation method. Therefore the current value of μ on each triangles in the iron regions is given by

$$\mu_{new} = (1 - x)\mu_{cal} + x\mu_{old}$$

where μ_{old} is the value used in the last step, μ_{cal} the computed new value, μ_{new} the value to be used in the next step. The method is implicit and hence intrinsically stable.



In order to check the convergence of the solution a residuum has been defined by introducing the l_1 norm of the relative errors:

$$res = \frac{2}{N_T} \sum_{i=1}^{N_T} \frac{|u_{new} - u_{old}|}{u_{new} + u_{old}}$$

where N_T is the number of the mesh triangles in the iron regions. Note that the value x only affects the speed of convergence and not the accuracy: a more rapid convergence is achieved choosing x to be between 0.4 and 0.5 (see Fig. 13, referring to pulse 38265 with the residuum set to 0.005). In addition the residuum is an average quantity in the whole field and therefore some considerable errors locally cannot be excluded.

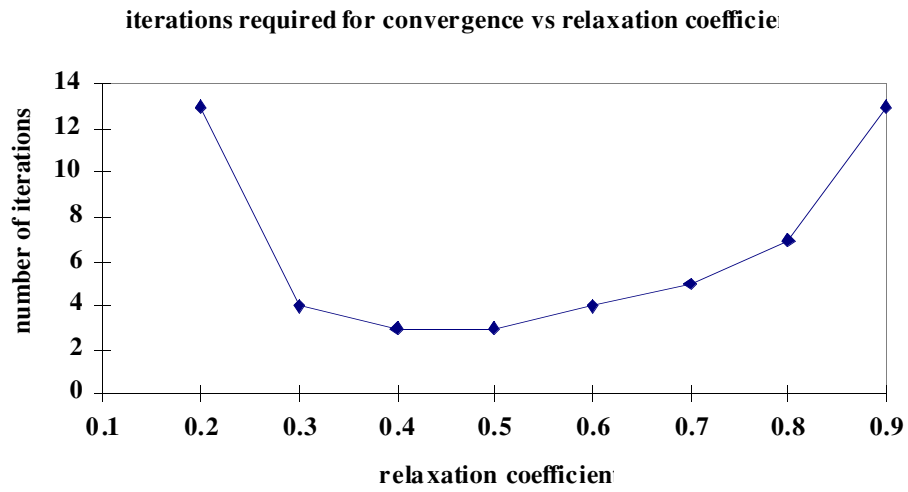


Fig.13 The influence of the relaxation coefficient on the velocity of convergence

To ensure that the modified code works correctly or not, a test session has been carried out. The results are shown in fig. 14 and 15 both for TFFL and VVFL, for the case of dry runs. It can be seen that the modified code predictions agree with the expected values (which have been calculated by means of the previously developed non linear routine available only without plasma).

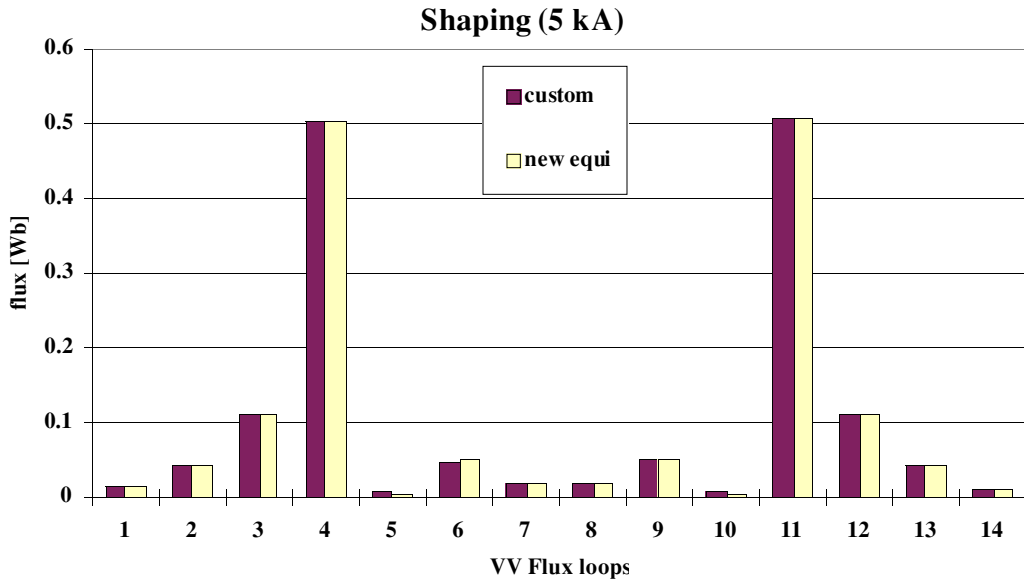
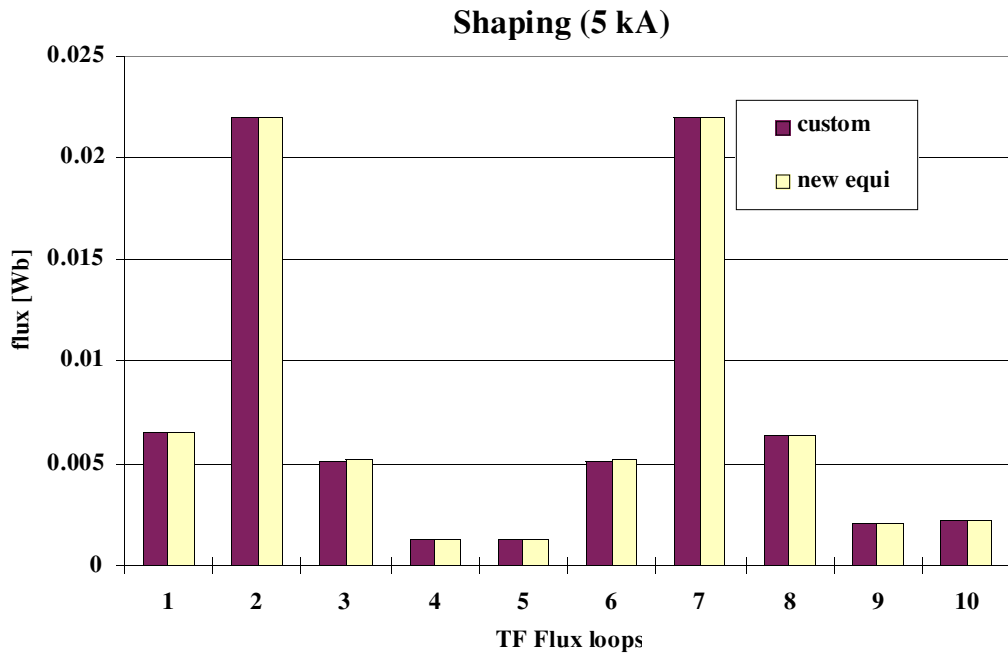


Fig. 14 Code validation using a shaping dry run

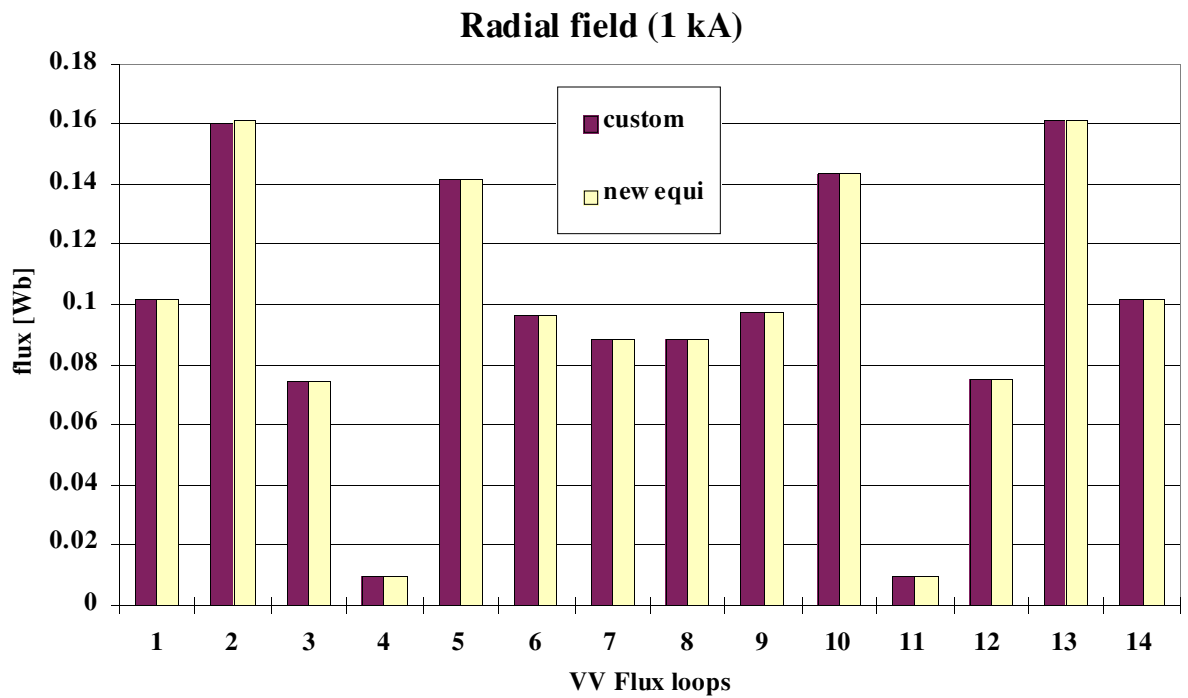
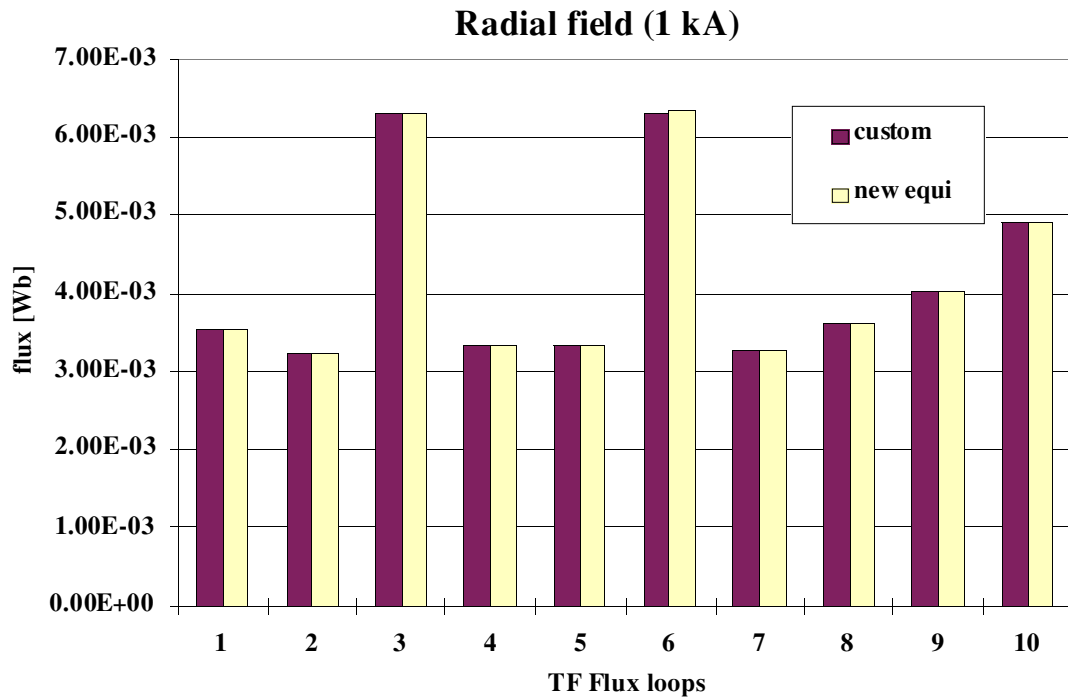
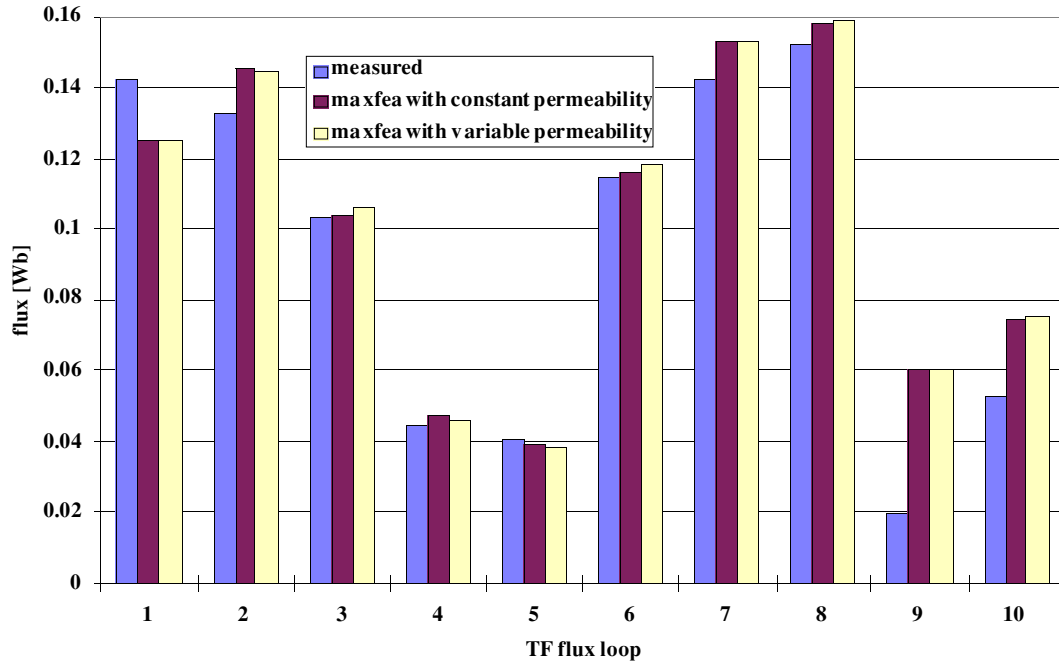


Fig. 15 Code validation using a radial field dry run

In the following, Fig. 16-17-18, results for three typical plasma scenarios (reverse shear, pulse 42221; hot ion, pulse 42976, and an ELMy H-mode scenario, pulse 42982).

Reverse shear (# 42221, $I_p = 3.6$ MA)



Reverse shear (# 42221, $I_p = 3.6$ MA)

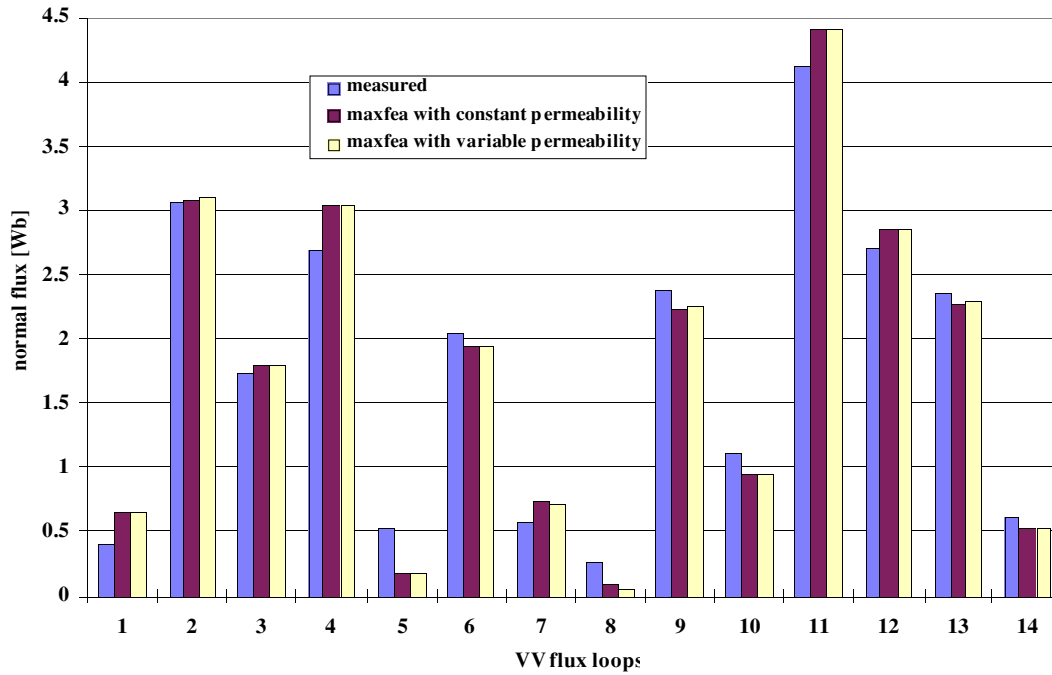
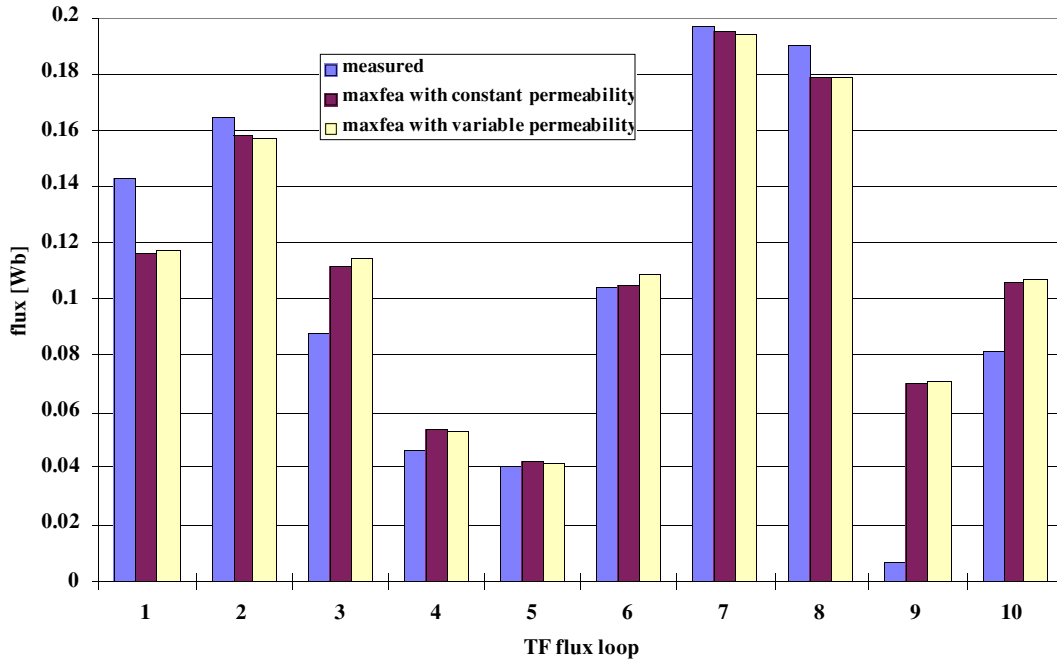


Fig.16 Results for a reverse shear scenario

Hot ion (# 42976, $I_p = 3.8$ MA)



Hot ion (# 42976, $I_p = 3.8$ MA)

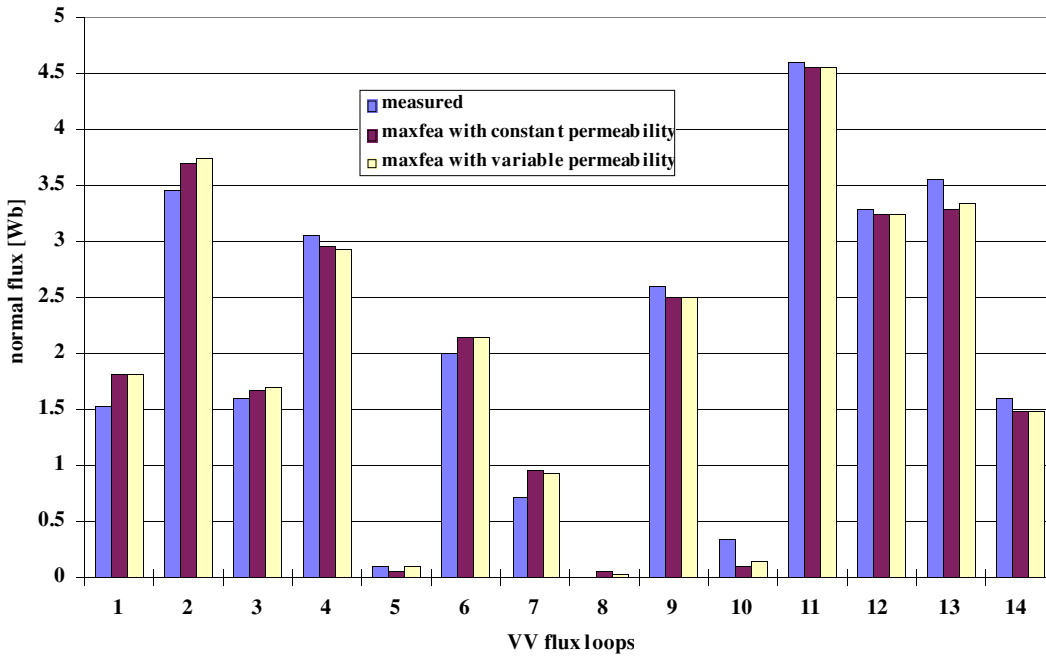
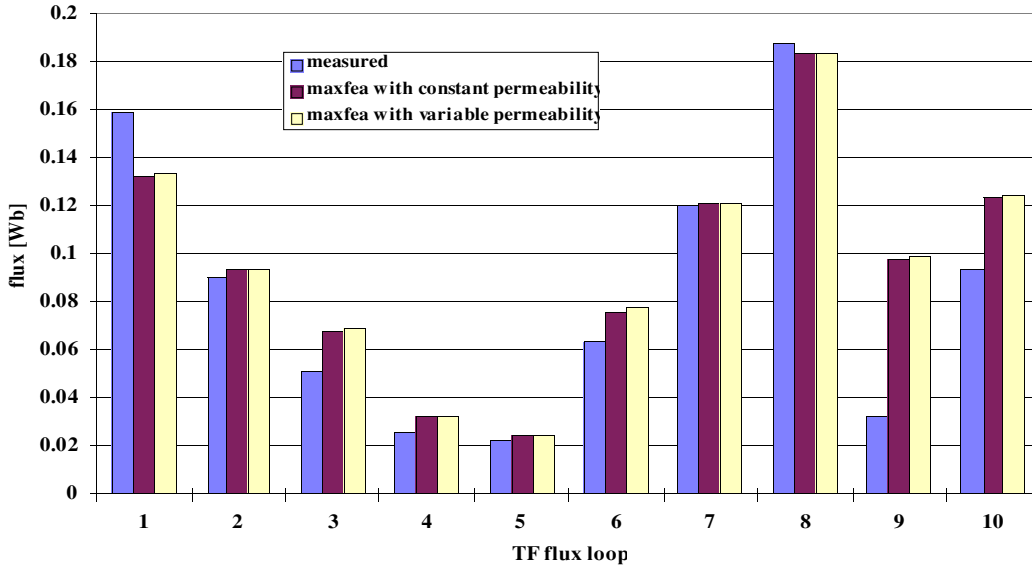


Fig.17 Results for a hot-ion scenario

ELMy H-mode (# 42982, $I_p = 3.8$ MA)



ELMy H-mode (# 42982, $I_p = 3.8$ MA)

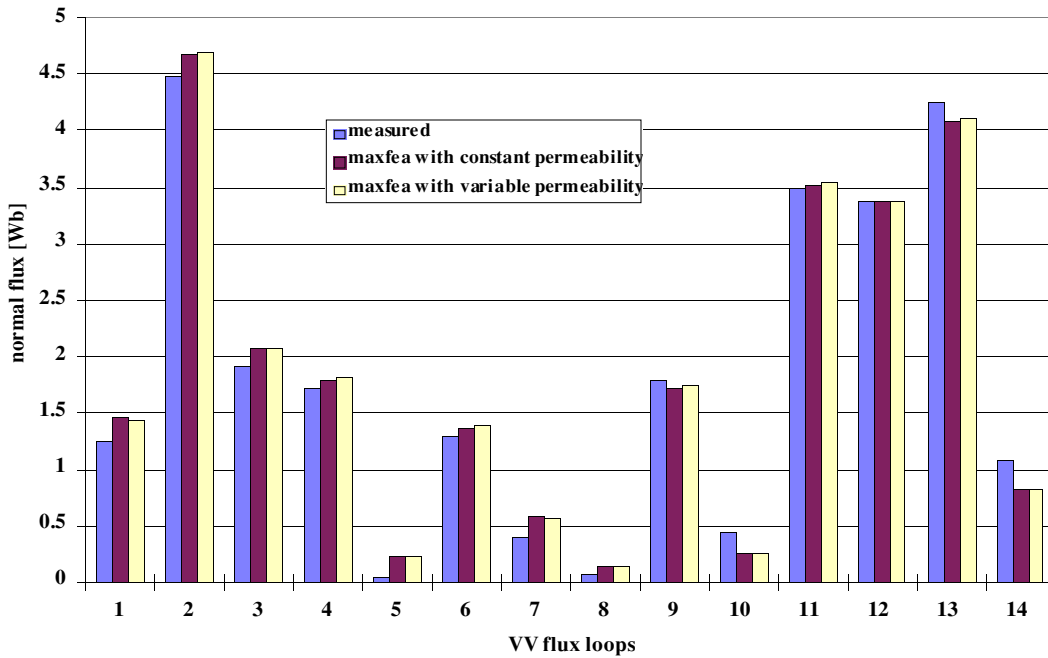


Fig.18 Results for a ELMy H-mode scenario

An accurate analysis of the above results allows us to conclude that when dealing with such plasma scenarios, no significant changes in the numerically computed flux are introduced by taking in account a variable rather than a constant permeability in the iron regions.

In order to provide an explanation for this result, the magnetic field in the iron regions as it results both using constant and variable permeability (with reference to an ELMy H-mode scenario) has to be examined. Fig. 19 shows the values in the core (close to the P1 coil) while fig. 20 shows the values in the limb (at the edge of the shoes).

ELMy H-mode (# 38265, $I_p = 4.7$ MA)

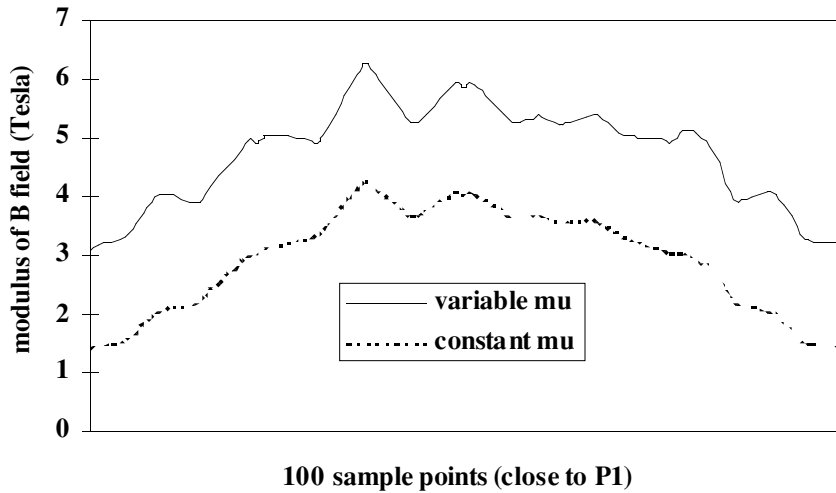


Fig.19 Magnetic field in the core for an ELMy H-mode scenario

ELMy H-mode (# 38265, $I_p = 4.7$ MA)

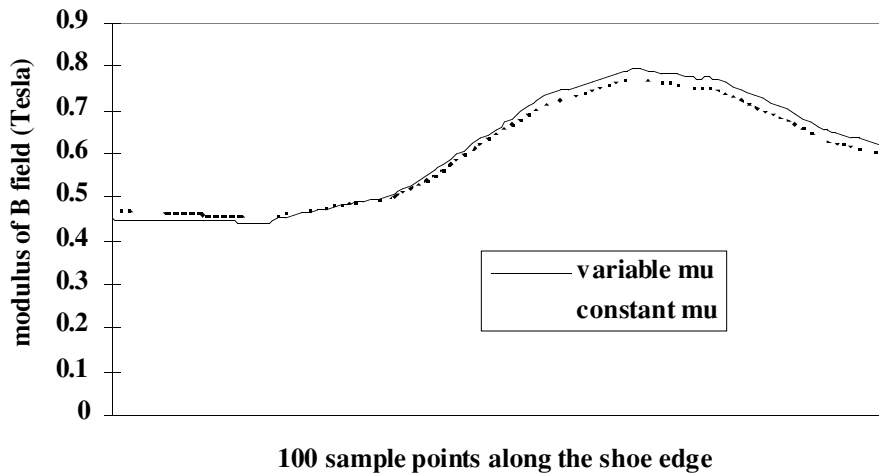


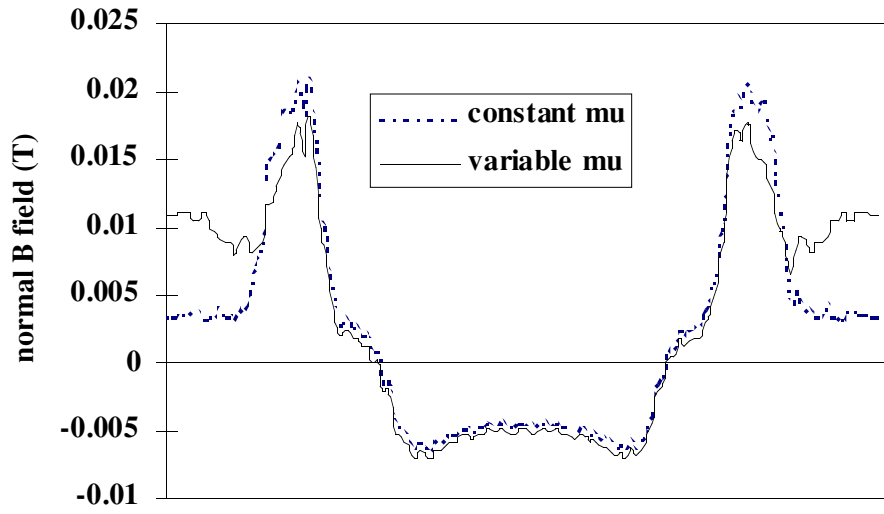
Fig.20 Magnetic field in the limb for a ELMy H-mode scenario

As expected, in the core the magnetic field is higher when computed with a variable rather than a constant permeability (although the profile shape is the same). Figures 19 and 20 show that the values of the magnetic field are such that the assumption made by the unmodified Maxfea code can be considered satisfactory. Therefore, when high current and high field plasma scenarios are considered, the introduction of a variable magnetic permeability in the iron regions does not introduce any relevant difference outside these regions.

Since there are no variations of the field and the flux outside the core, there are no changes to the values of the forces acting on the ring, the collar and the mechanical structure, as far as high current and high field scenarios are concerned. This statement holds not only when plasma scenarios are considered, but also for scenarios without plasma, when they are still characterised by high current and high field.

Instead, differences can be found when dealing with dry runs, as it can be seen in figure 21, where the poloidal field normal to the coil is plotted along its trace (strating at the inner midplane).

Radial Field (1 KA)



136 sample points along a TF coil

Fig.21 Magnetic field along a TF coil for a radial field dry run

In addition, Fig. 22 shows the comparison between the values of the normal component of the magnetic field along a TF coil (for an ELMy H-mode scenario), calculated both by MaxFEA and by the PROTEUS code (whose variable permeability is detailed described): as it can be seen the two sets of data agree quite well.

ELMy H-mode ($I_p = 3.0$ MA)

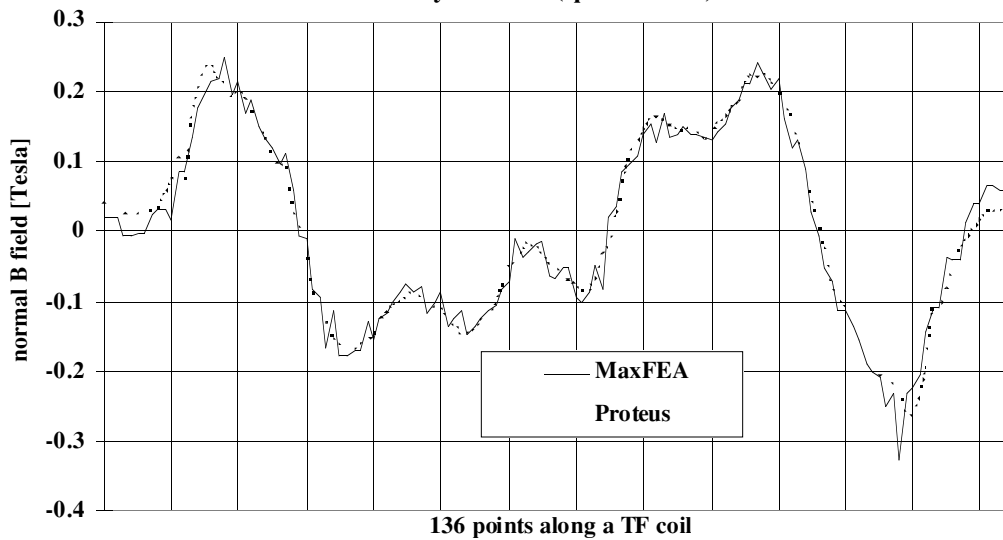


Fig.22 Magnetic field along a TF coil calculated both by MaxFEA and PROTEUS

It is now useful to summarise the findings of this paper in the following statements.

- Taking into account the correct value of the iron magnetic permeability leads to results which are in better agreement with the measurements when dry runs are considered, that is to say when low currents and weak field scenarios are considered.
- At high current and high field (plasma scenarios), the Maxfea results show no significant change in the TFFL and VVFL and outside the core, when a constant rather than a variable iron permeability is taken into account.
- As regards to the magnetic field in the core, one should refer to the values computed by Maxfea using variable permeability, both for high and low current cases.

The unmodified Maxfea code can still be used to estimate the forces acting on collar, ring and mechanical structure, without any significant error introduced by the iron modelling, as far as plasma scenarios and disruptions are concerned.

28. Plasma disruption and TF flux loop overshoots

After a disruption the transverse flux at the TF flux loop can be higher than when the plasma was present. This overshoot can happen at two different times of the disruptive event: during the plasma displacement in case of a VDE or some seconds after the plasma disappeared in any disruption (but not in all). The reason of the first kind of overshoot is trivial: the plasma current changes the field map when moving. The second kind of overshoot is due to residual current in the PF coils and could be avoided (as it used to be in the past) by applying an opposite voltage to the coils after the event has occurred to fasten their current decay.

During DTE1 these spikes had been cause of some concern as they exceeded the trip level in some occasion. In the following (Fig. 23a-b-c-d) the measured flux before and after the disruption is plotted for the collar and the ring flux loops for pulses of the MarkII-A campaign.

The collar trip level at high field during that campaign was 8.4 kA Wb, which is equivalent to ≈ 350 kN; spikes can produce overshoots of ≈ 2.5 kA Wb, hence an additional force of about 100 kN. The maximum equilibrium force on the collar was ≈ 300 kN therefore the maximum disruption force has been, ≈ 400 kN: less than the 420 kN allowed at the time for low field operation. At the ring support spikes can produce overshoots of ≈ 4 kA Wb, hence an additional force of about 130 kN. The maximum equilibrium force on the ring was ≈ 500 kN therefore the maximum disruption force has been, ≈ 630 kN.

TF FL 6 - Bottom Collar

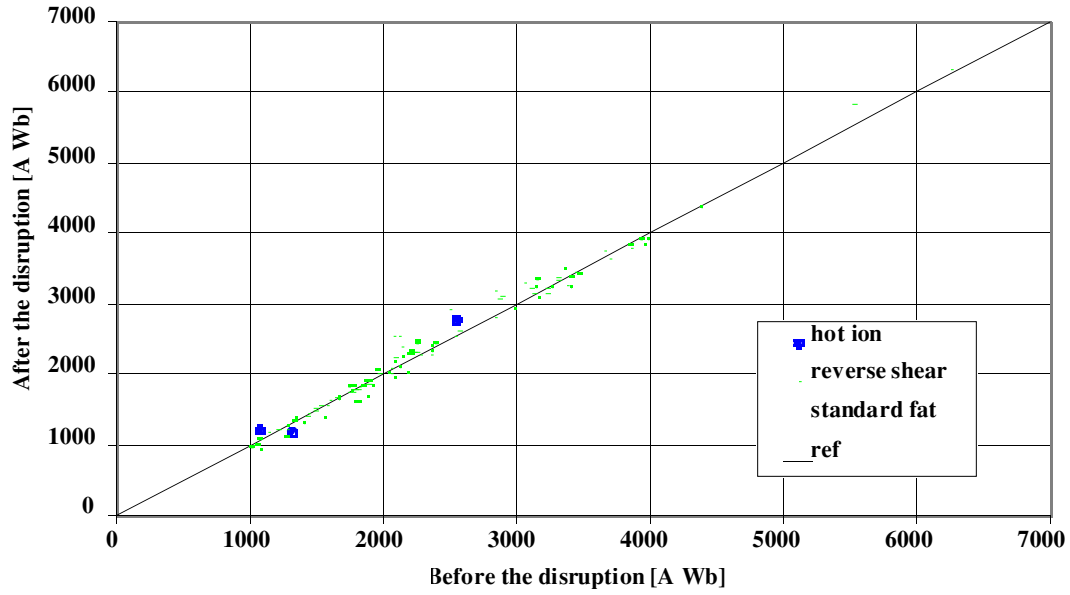


Fig. 23a Transverse flux time TF current at the TF bottom collar flux loops during severe MarkII-A disruptions

TF FL 3 - Top Collar

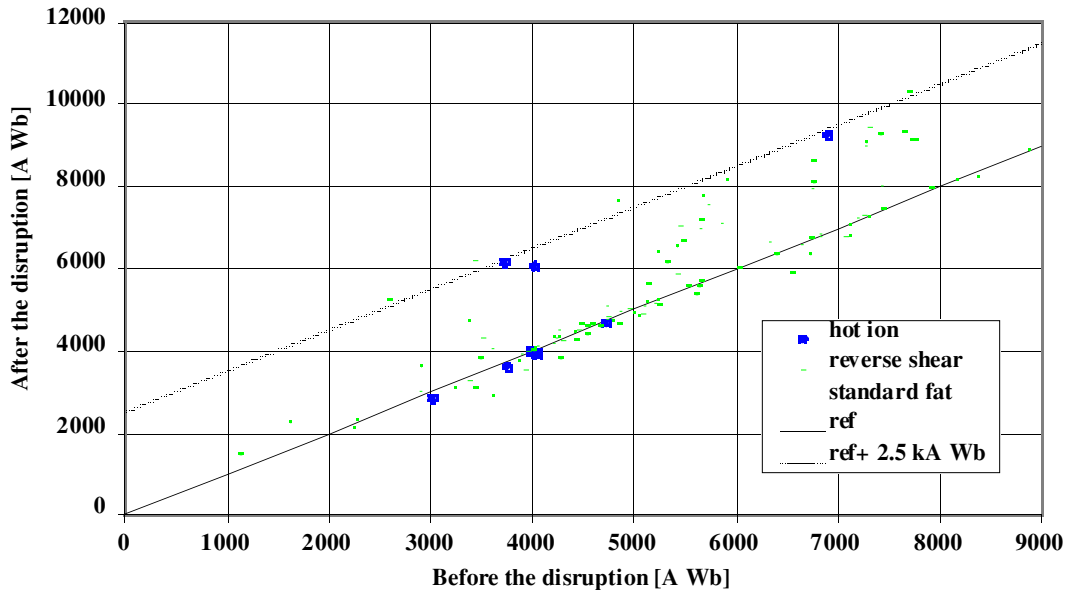


Fig. 23b Transverse flux time TF current at the TF top collar flux loops during severe MarkII-A disruptions

TF FL 7 - Bottom Ring

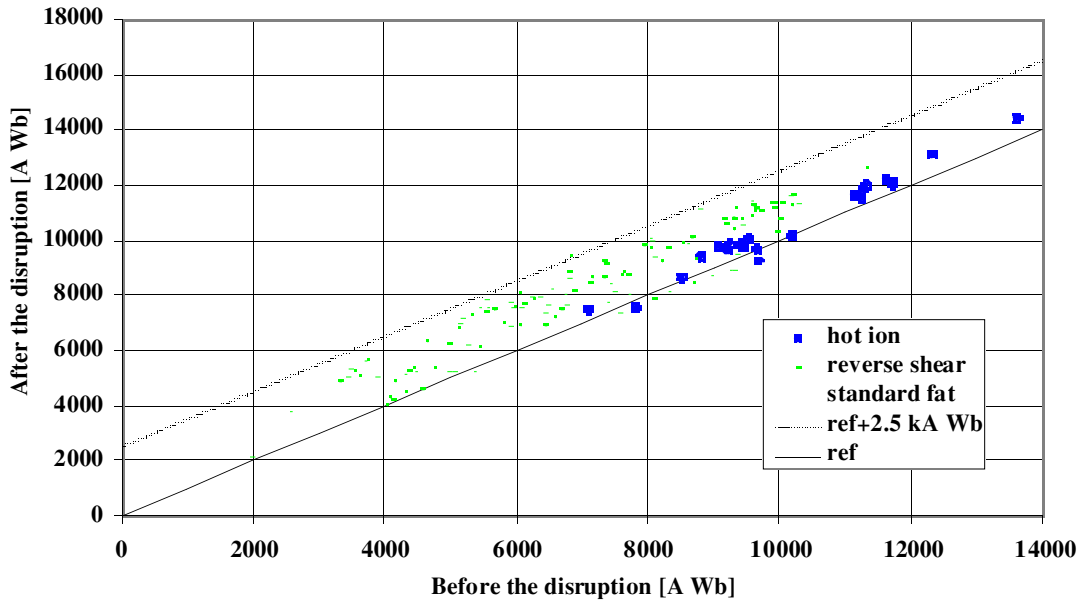


Fig. 23c Transverse flux time TF current at the TF bottom ring flux loops during severe MarkII-A disruptions

TF FL 2 - Top Ring

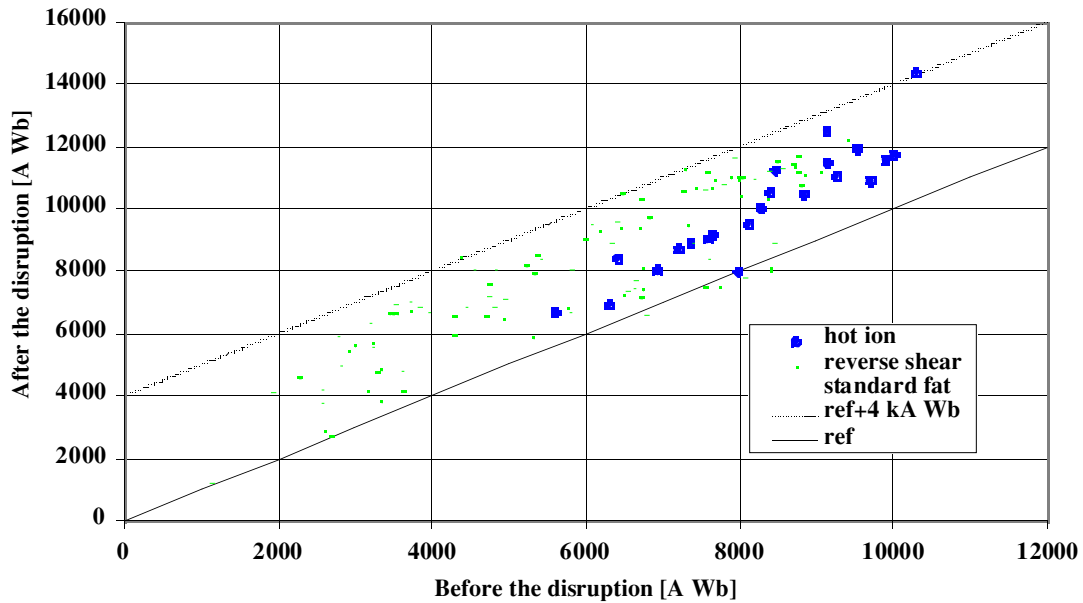


Fig. 23d Transverse flux time TF current at the TF top ring flux loops during severe MarkII-A disruptions

The overshoot events (as well as the less important delayed maxima) have been successfully simulated using Maxfea. The plasma is replaced by a current ring with elliptic cross section and peaked current distribution; the plasma position and current are prescribed. The PF current may be prescribed or PF circuits are kept in flux conservation. The mock TF FLs (and the poloidal field normal to the TF coil in 136 points) have been saved every N time steps. To gain confidence in the procedure a spiky disruption (42868) has been reproduced (Fig. 24a-b-c), then the same procedure has been applied to forecast worst case loading conditions for the scenarios proposed for the

4 T operation. To have realistic VDE plasma behaviour past plasma current and position waveforms have been fed in Maxfea. The results of the mechanical analysis are summarised in Table 1a-b-c (for these analyses the poloidal field normal to the TF coil is taken at the time the spike in TF FL 3 is maximum).

Forces at the MS teeth	Equilibrium	VDE Spike	allowable	unit
$F_{\text{COLLAR TOOTH}^2 \text{ top}}$	-277	-427	350/420	kN
$F_{\text{COLLAR TOOTH}^2 \text{ bottom}}$	250	272	350/420	kN
$F_{\text{RING TOOTH}^2 \text{ top}}$	443	675	675	kN
$F_{\text{RING TOOTH}^2 \text{ bottom}}$	-498	-477	675	kN

Table 1a ELM-free H-mode 4.3 MA 4 T support reactions

Forces at the MS teeth	Equilibrium	VDE Spike	allowable	unit
$F_{\text{COLLAR TOOTH}^2 \text{ top}}$	-222	-405	350/420	kN
$F_{\text{COLLAR TOOTH}^2 \text{ bottom}}$	245	270	350/420	kN
$F_{\text{RING TOOTH}^2 \text{ top}}$	313	549	675	kN
$F_{\text{RING TOOTH}^2 \text{ bottom}}$	-364	-337	675	kN

Table 1b Optimised Shear 4 MA 4 T support reactions

Forces at the MS teeth	Equilibrium	VDE Spike	allowable	unit
$F_{\text{COLLAR TOOTH}^2 \text{ top}}$	-298	-450	350/420	kN
$F_{\text{COLLAR TOOTH}^2 \text{ bottom}}$	332	334	350/420	kN
$F_{\text{RING TOOTH}^2 \text{ top}}$	297	489	675	kN
$F_{\text{RING TOOTH}^2 \text{ bottom}}$	-389	-375	675	kN

Table 1c ELMy H-mode 5 MA 4 T support reactions

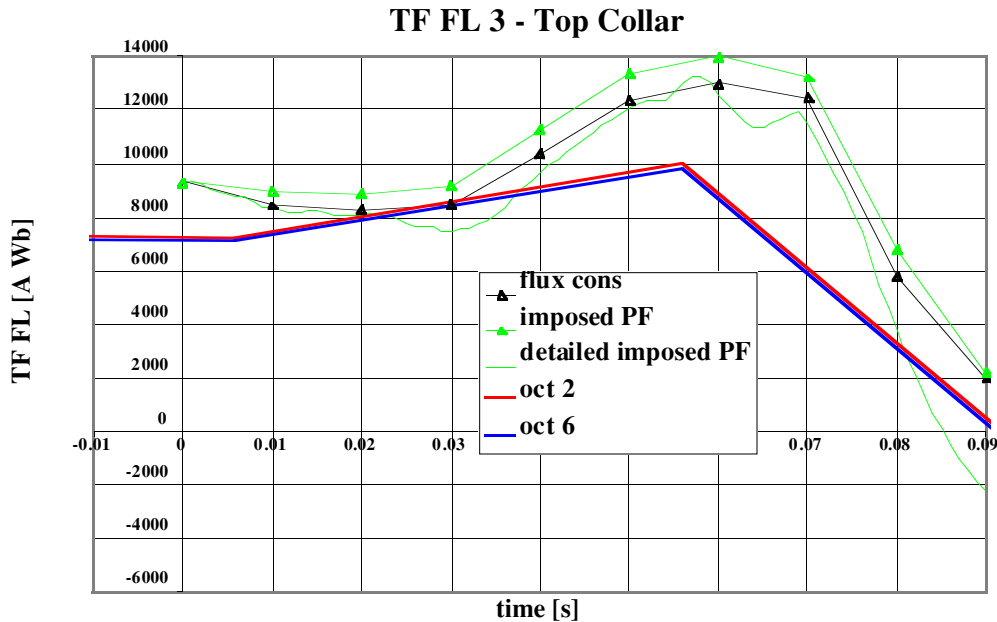


Fig. 24a Computed and measured flux at the top collar TF flux loops for the VDE of pulse 42686

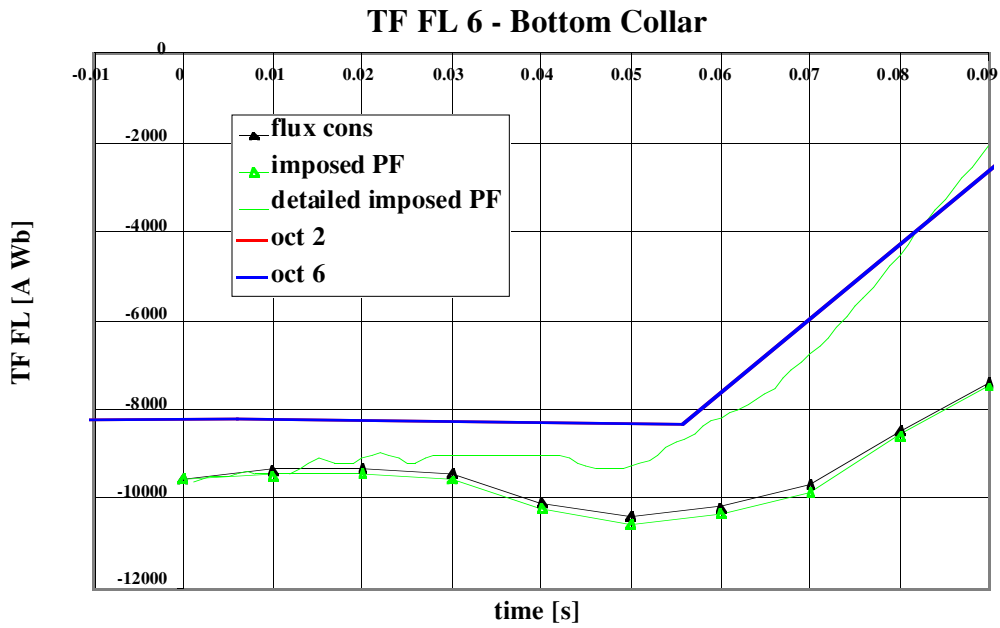


Fig. 24b Computed and measured flux at the bottom collar TF flux loops for the VDE of pulse 42686

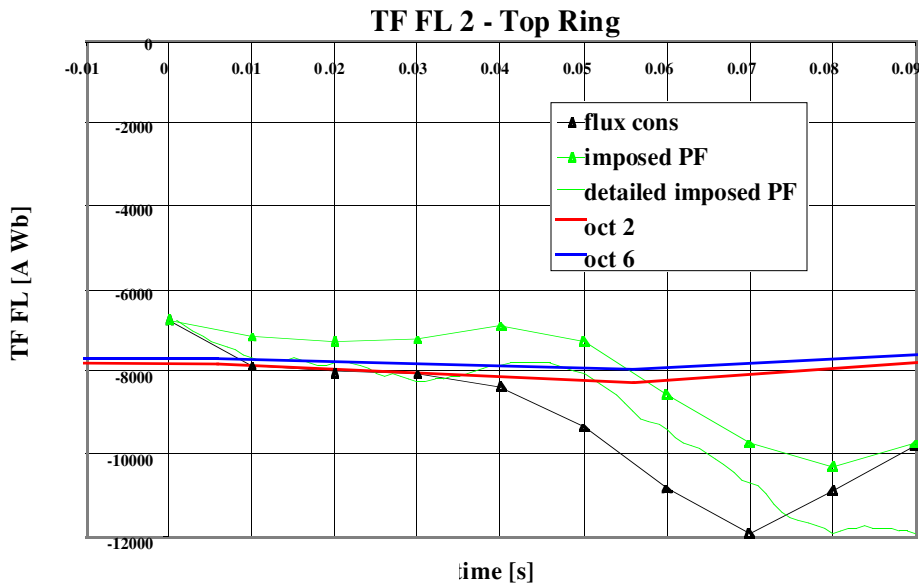


Fig. 24c Computed and measured flux at the top ring TF flux loops for the VDE of pulse 42686

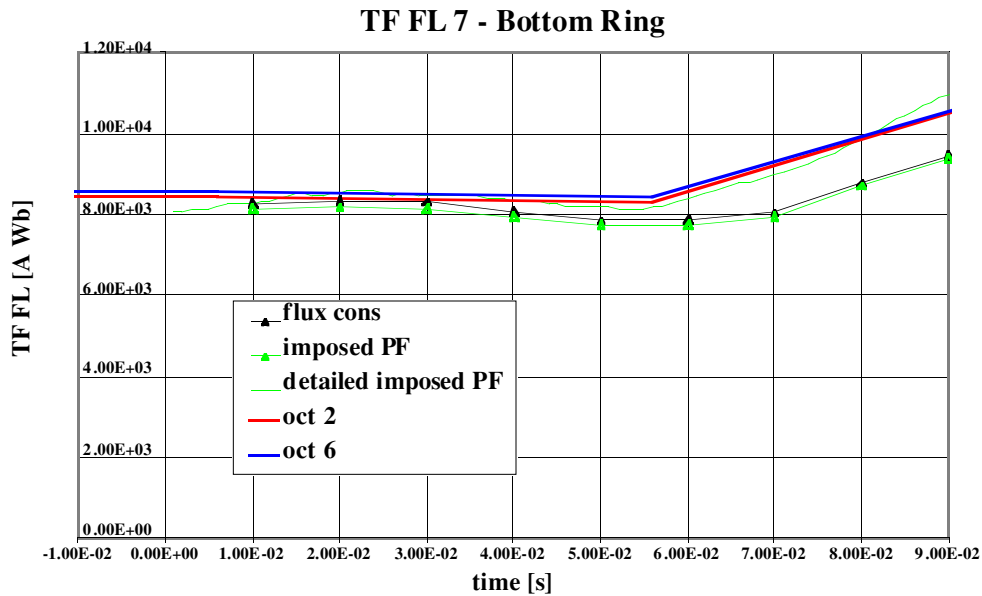


Fig. 24d Computed and measured flux at the bottom ring TF flux loops for the VDE of pulse 42686.

3. TF coil Radial Displacements at Push-pull Jacks and Midplane

The radial displacement of the TF coil are measured at the midplane (16 diagnostics: all octants coils 1's and 4's) and at the push-pull-jacks (8 diagnostics: one octant only, octant 3, all its coils top and bottom).

The radial displacement of the TF coil can be modelled as a function of the TF current wave form. The model is summarised in Box 1, where R_c is the resistance of the TF coil, τ is the cooling system time (400÷600 s) and I is the TF current pulse length (typically 20÷30 s); K_m [m/A²] is the magnetic coefficient and K_{th} [m/A²s] is the thermal coefficient.

$$\begin{aligned}
 u &= I_{TF}^2 \\
 y &= \delta R \\
 x &= P \quad \text{energy} \quad \& \quad \text{power} \\
 \& &= -\frac{1}{\tau}x + R_c u \quad ? \quad s \& + \frac{1}{\tau} \& = R_c u \& \\
 \& &= \frac{K_c}{s + \frac{1}{\tau}} \& \quad ? \quad \& = \frac{K_c}{s} \& \\
 x &= R_c \int_0^T u(t) dt \quad ? \quad \delta R = K_m I^2 + K_{th} \int_0^T I^2(t) dt
 \end{aligned}$$

Box 1 Analytical model of the TF coil radial displacement

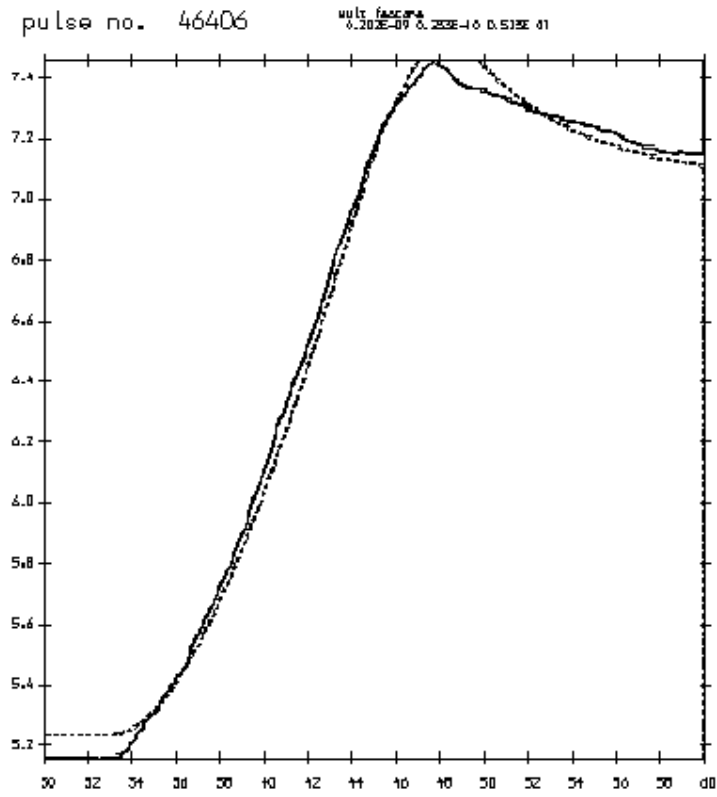


Fig. 25b Typical example of least square fit of the midplane radial displacement of the TF coil @ 4 T at to the I_{TF}^2 and $I_{TF}^2 t$

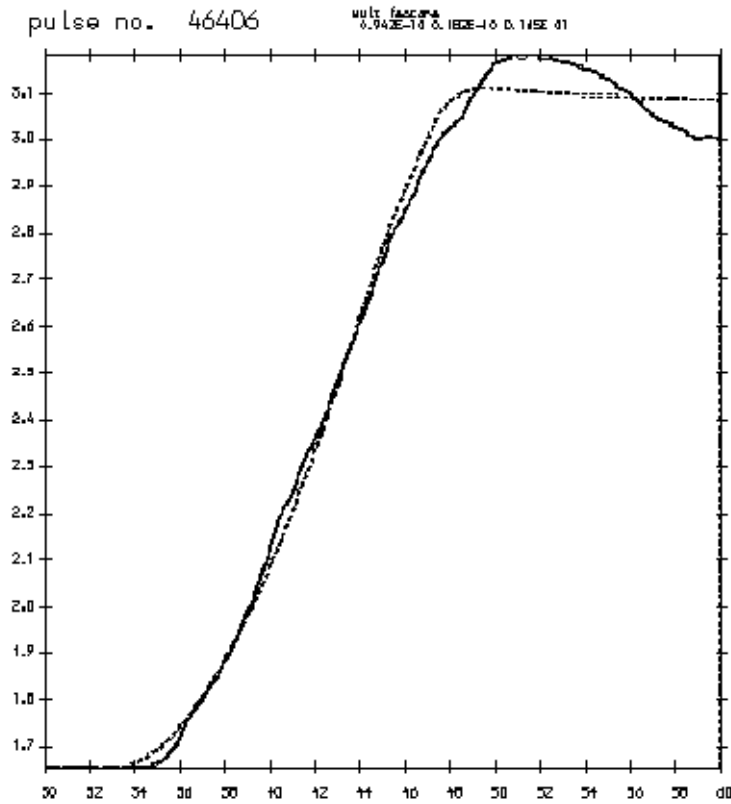


Fig. 25b Typical example of least square fit of the radial displacement of the push-pull jack of the TF coil @ 4 T at to the I_{TF}^2 and $I_{TF}^2 t$

To show that the behaviour of the TF coils during high current pulses is not different from it's useful to check their radial displacement. This has been done routinely during the 3.8 T commissioning (April 1997) and during the 4.0 T commissioning (27th November 1998). After the 4.0 T commissioning a small set of pulses have been chosen to estimate the hoop and thermal coefficients and then a larger set of pulses to check that the measurements kept consistent with that models before and after the high current pulses. The hoop and thermal coefficients were computed using a least-square fit algorithm: to find the K_m , the K_{th} and the offset (Fig. 25). The coefficient valid for the calibration during the 4 T commissioning are listed in Table 2 and plotted in Fig. 26. The expansion coefficients are not exactly the same for all the diagnostics of the same kind, but they do not change when the TF current changes (i.e. the push-pulls jacks coefficients in Fig. 27 as a function of the pulse number, the TF current in these pulses is plotted in Fig. 28). This means that the coil behaves consistently at any current level. In Fig. 29 and 30 the models are compared with the measurements. The measurement of the midplane and push-pull-jacks radial displacement during the first 4.0 T pulse with plasma (46406) are plotted in Fig. 31 and 32.

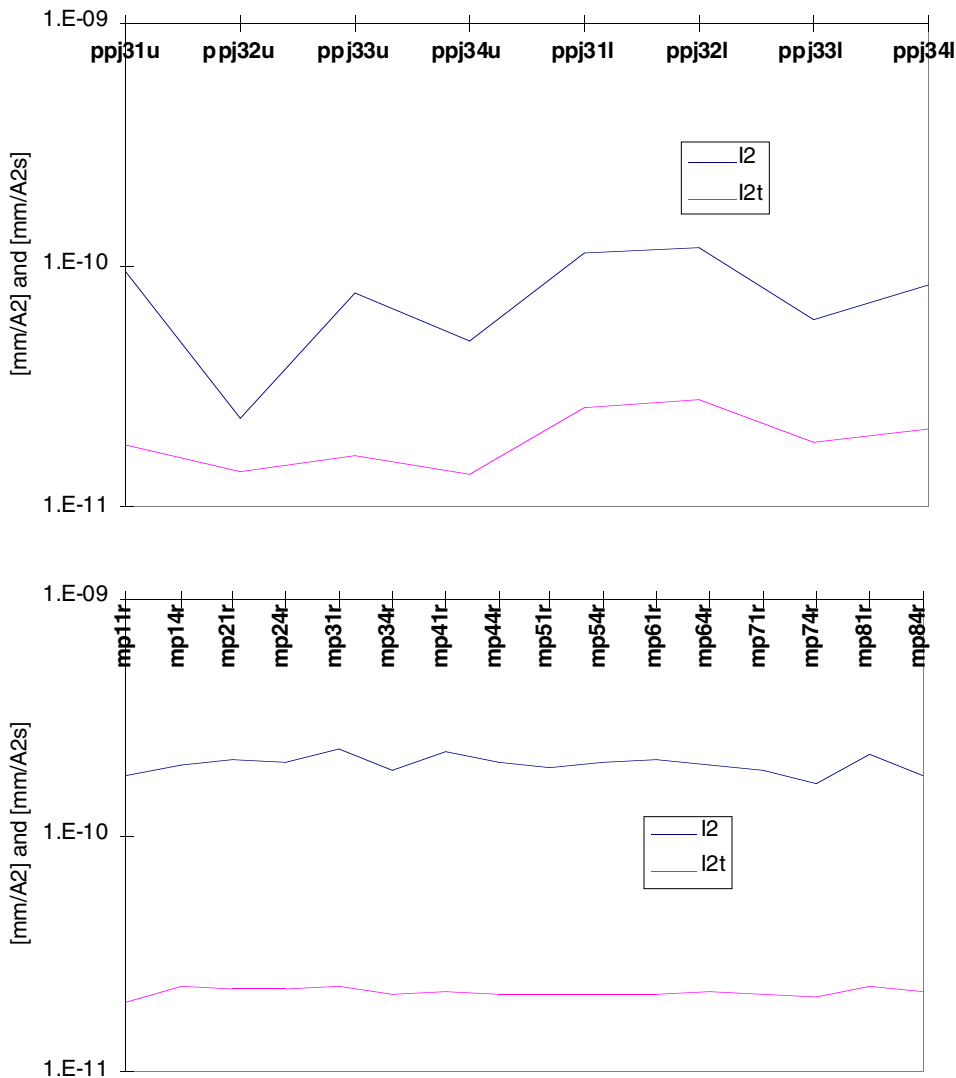
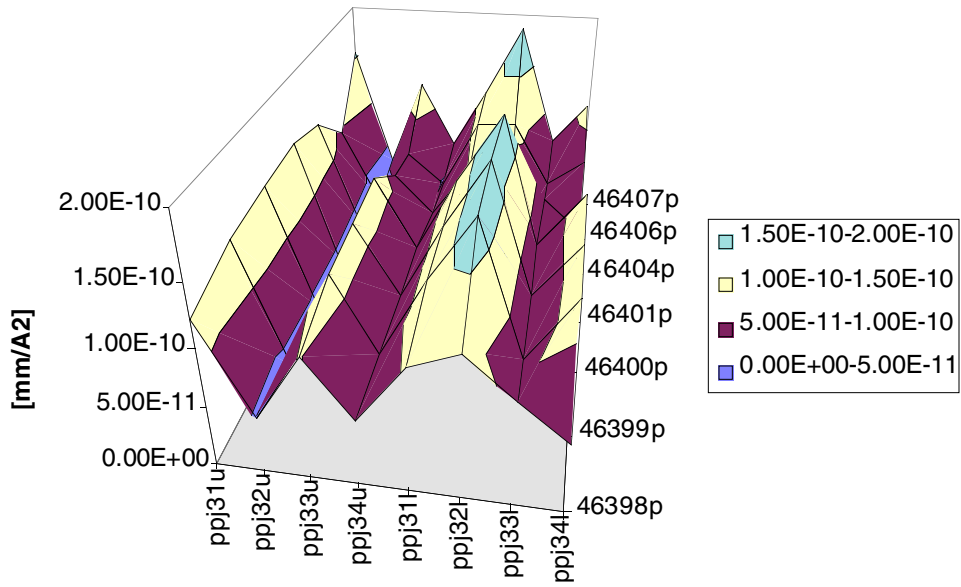
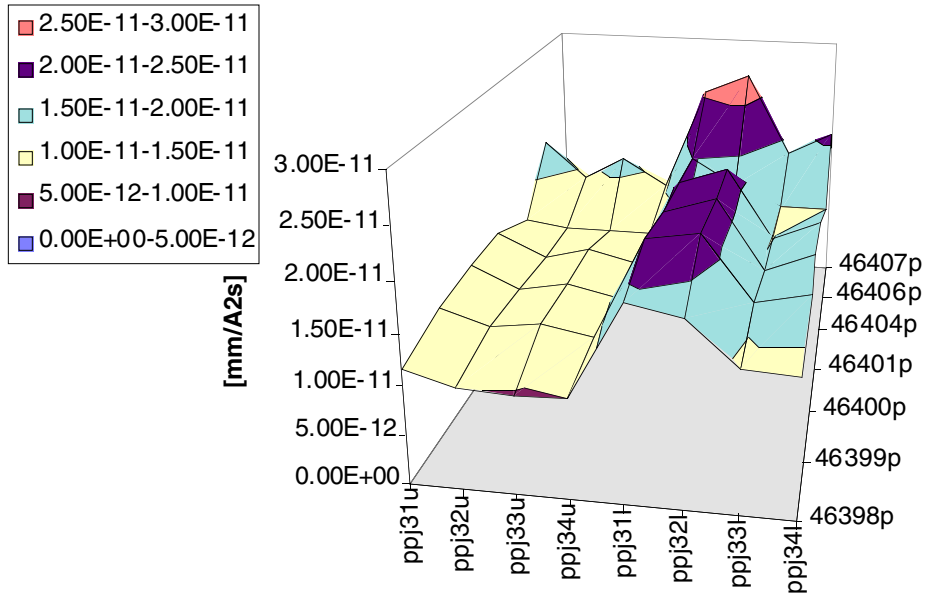


Fig. 26 Push-pull-jacks (left) and midplane (right) hoop and thermal expansion coefficients



(a)



(b)

Fig. 27 Push-pull jacks hoop (a) and thermal (b) coefficients as a function of the pulse number during the 4.0 T commissioning

	K_m [mm/A ²]	K_{th} [mm/A ² s]	off [mm]
ppj31u	9.42E-11	1.82E-11	1.65
ppj32u	2.35E-11	1.40E-11	0.39
ppj33u	7.73E-11	1.65E-11	0.25
ppj34u	4.84E-11	1.37E-11	3.28
ppj31l	1.14E-10	2.57E-11	3.85
ppj32l	1.16E-10	2.79E-11	2.80
ppj33l	5.90E-11	1.84E-11	0.76
ppj34l	8.22E-11	2.11E-11	3.02
mean	7.68E-11	1.94E-11	
st. dev.	3.00E-11	4.83E-12	

Table 2a Push-pulls jack hoop and thermal expansion coefficients

	K_m [mm/A ²]	K_{th} [mm/A ² s]	off [mm]
mp11r	1.78E-10	2.00E-11	6.40
mp14r	2.02E-10	2.33E-11	5.23
mp21r	2.10E-10	2.29E-11	3.84
mp24r	2.05E-10	2.28E-11	4.37
mp31r	2.34E-10	2.31E-11	4.41
mp34r	1.87E-10	2.14E-11	4.21
mp41r	2.27E-10	2.20E-11	6.31
mp44r	2.05E-10	2.17E-11	3.06
mp51r	1.96E-10	2.12E-11	3.34
mp54r	2.05E-10	2.15E-11	3.69
mp61r	2.08E-10	2.16E-11	2.88
mp64r	2.02E-10	2.19E-11	3.91
mp71r	1.89E-10	2.16E-11	3.96
mp74r	1.68E-10	2.11E-11	4.21
mp81r	2.18E-10	2.34E-11	3.57
mp84r	1.82E-10	2.20E-11	3.97
mean	2.01E-10	2.20E-11	
st. dev.	1.69E-11	8.90E-13	

Table 2b Midplane hoop and thermal expansion coefficients

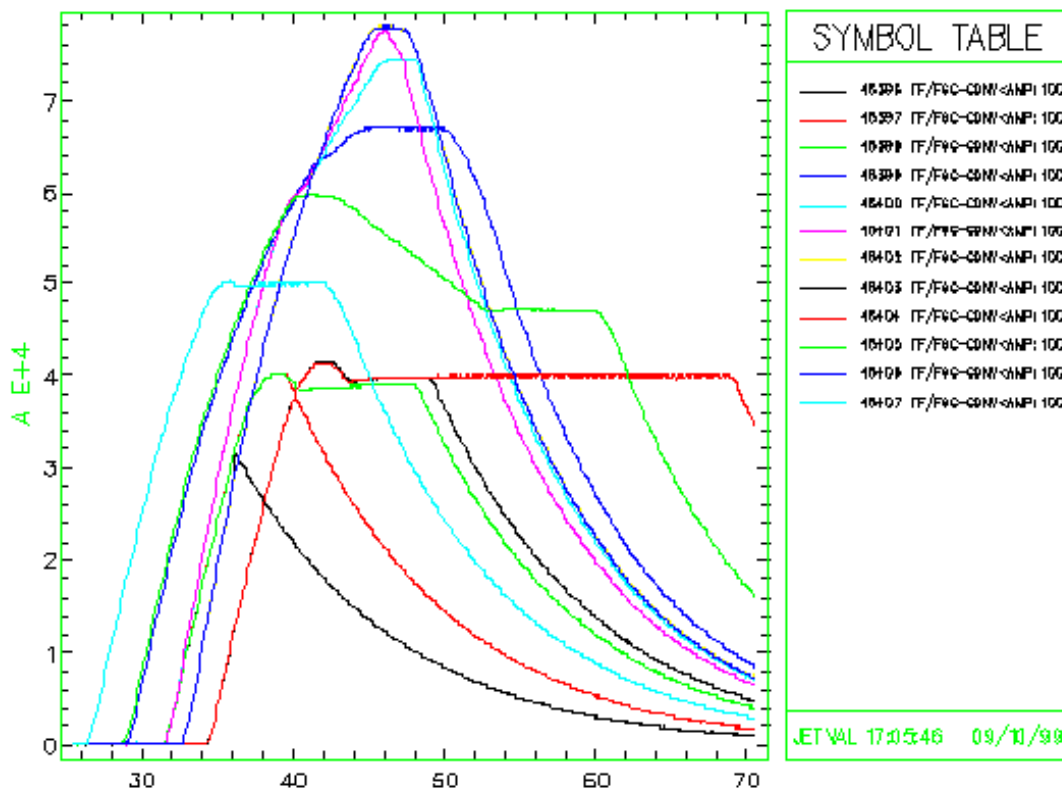
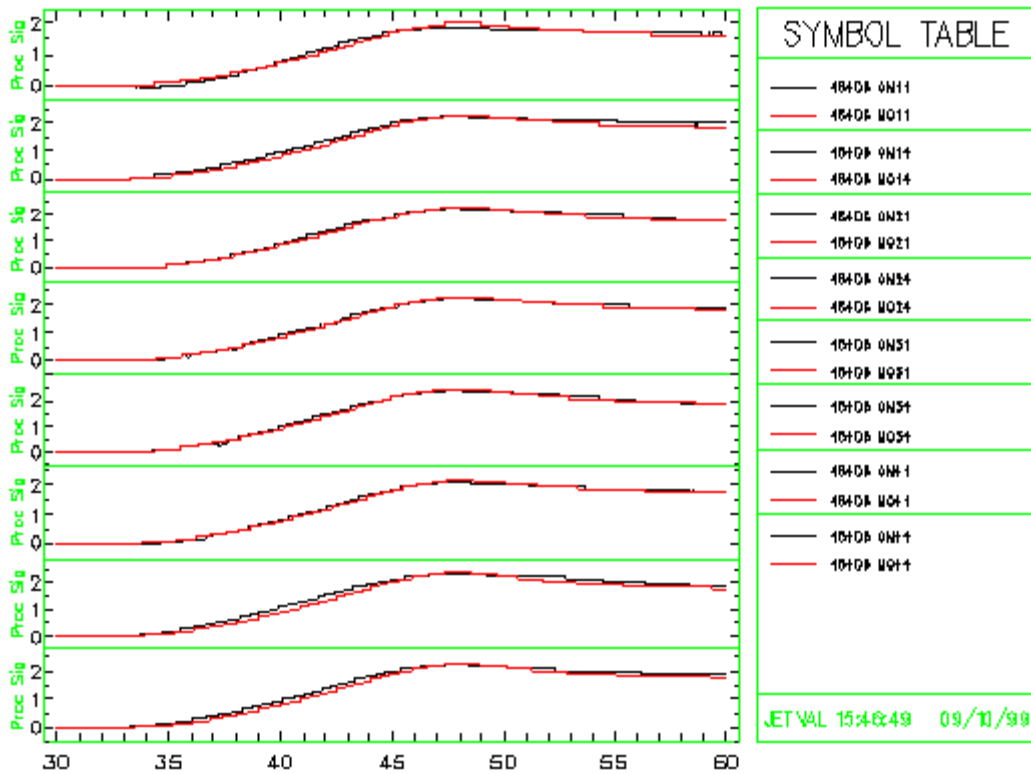
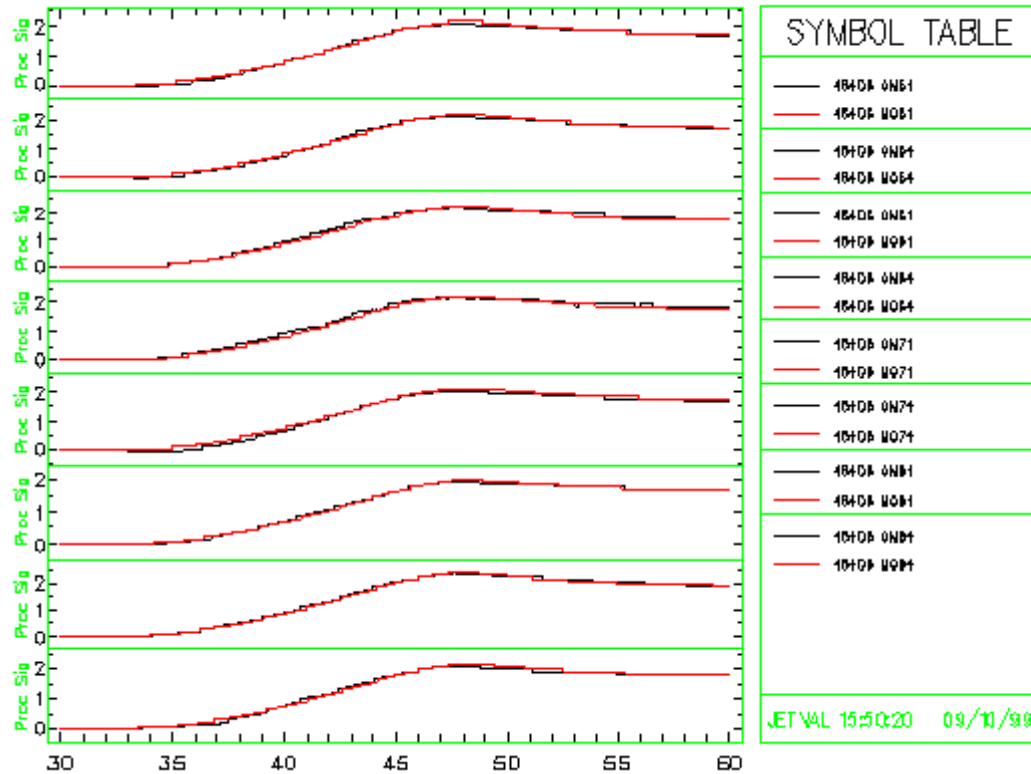


Fig. 28 TF current of the 4.0 T commissioning section (46407 is the dry run of the following session)



(a)



(b)

Fig. 29 Measurement (O#) and model (M#) of the radial displacement of the TF coil at the midplane radial displacements for the 3.3 MA 4 T pulse 46406: octants 1 to 4 (a) and 5 to 8 (b)

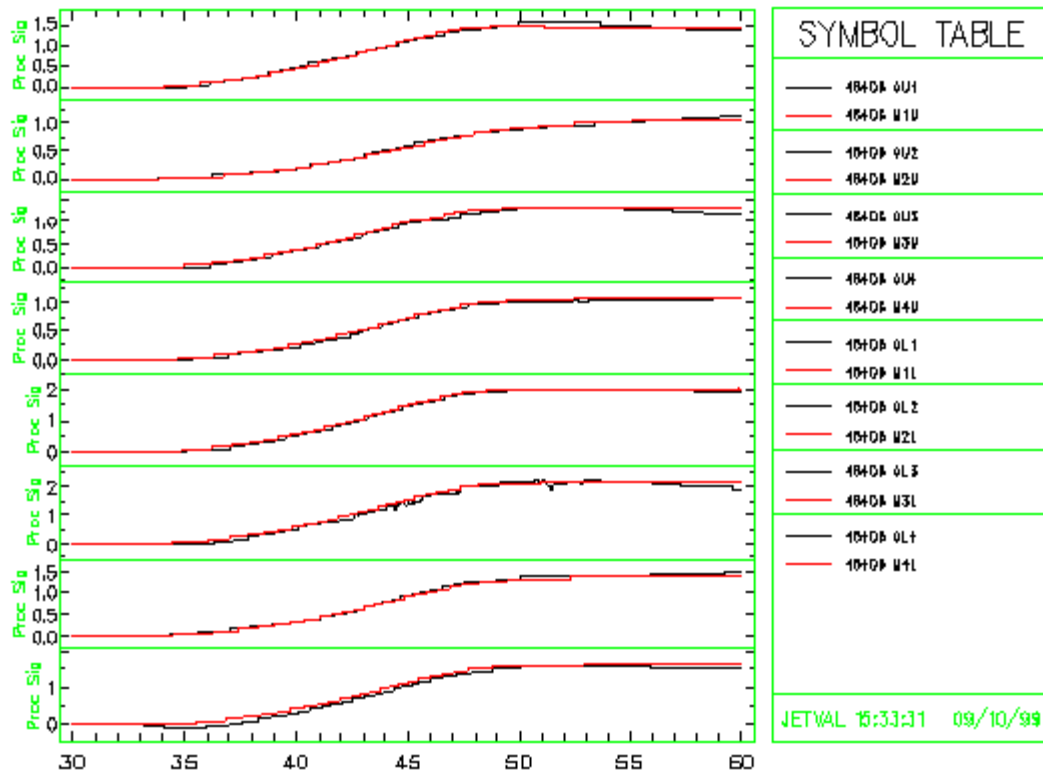


Fig. 30 Measurement (O#) and model (M#) of the radial displacements of the TF coil at the push-pull-jacks for the 3.3 MA 4 T pulse 46406

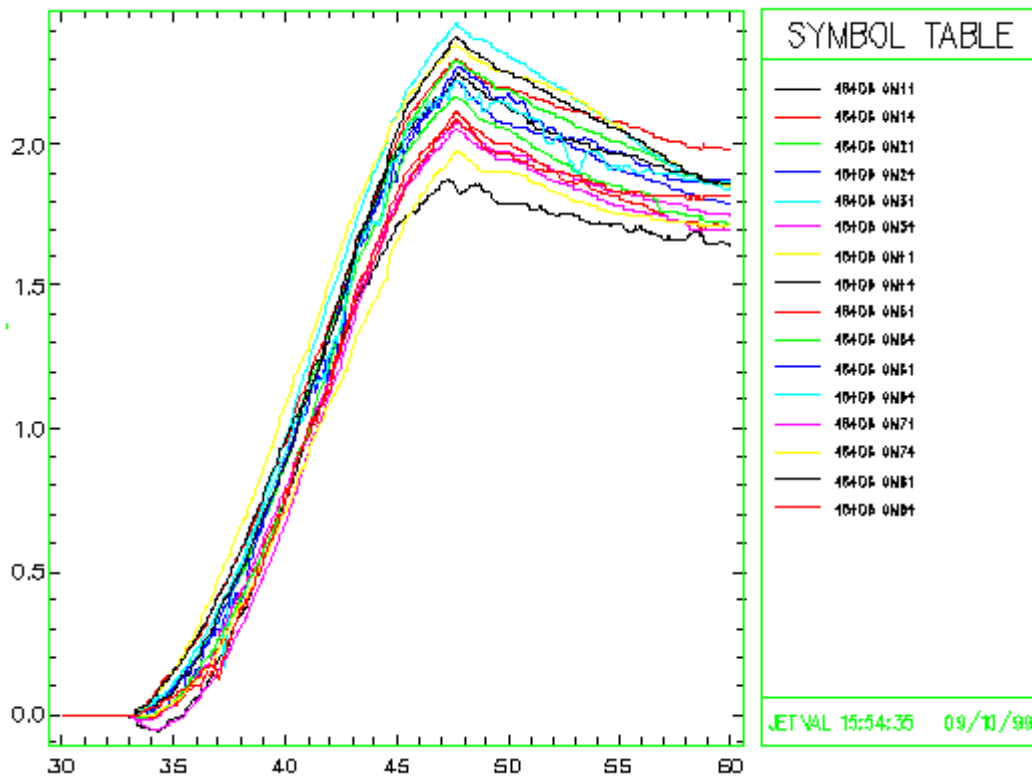


Fig. 31 TF coil radial displacement at the midplane measured during the first 4.0 T pulse with plasma

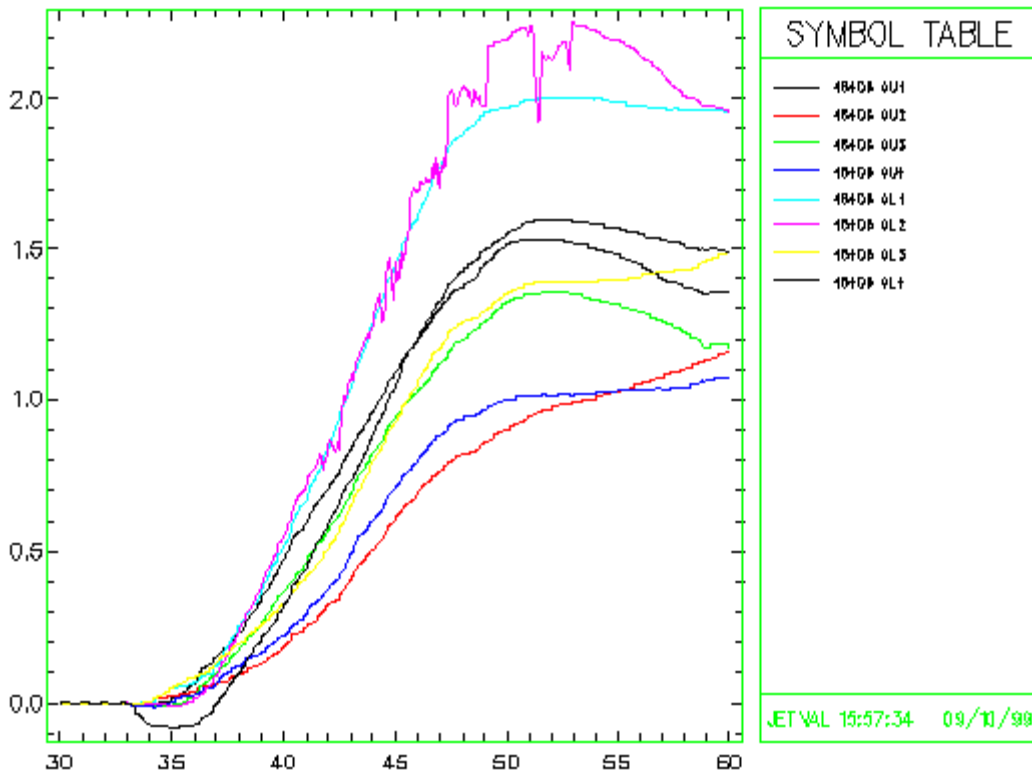


Fig. 32 Push-pull-jack radial displacement during pulse 46406: not all the push-pull-jacks behave the same, but their own characteristic behaviour is preserved at different TF current levels

The peak radial displacements at the midplane during the 4.0 T commissioning is plotted in Fig. 33. These diagnostics behave all very similarly, so one model is enough to reproduce them all and their peak can be simply derived from the max TF current and the I^2t at the end of the flat top. This regression procedure has been applied to look for changes in behaviour after the high current pulses on a set of ~400 pulses (46000-46430) and the result (no difference in their trend) is shown in Fig. 34.

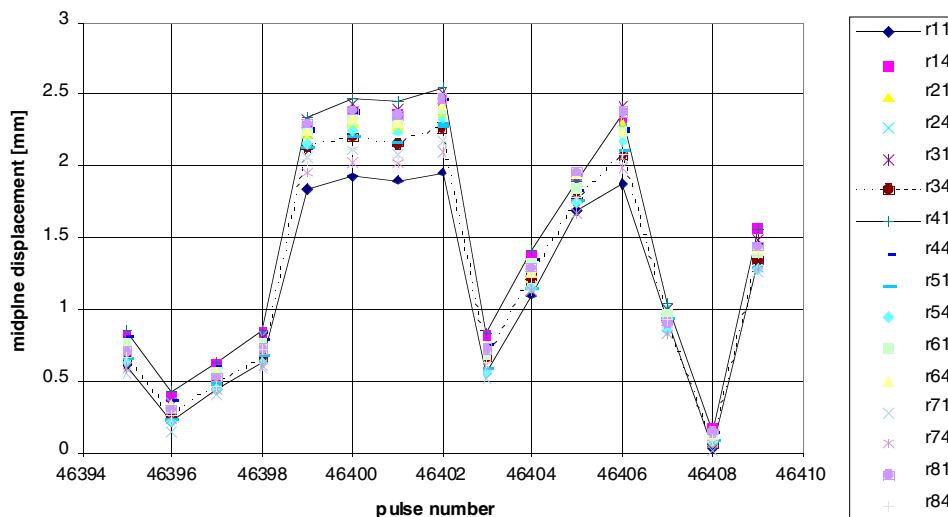


Fig. 33 Peak radial displacements at the midplane during the 4 T commissioning (RMD11 is the smallest and RMD41 the largest)

Comparison of used and unused coils

J.R. Last, V. Riccardo
26 October 1999

Contents

1.	Aim and conclusion	1
2.	Data of Object and Equipment	2
3.	Processing of the tests	2
4.	Results of the tests	3
5.	Tentative interpretation of the coil stiffness from test data	4

1. Aim and conclusion

Tests on the full coil were made in 1979 (at BBC on the prototype coil, using the same facility as the one used in the more recent tests at Noell), in 1988 (in view of the 7 MA campaigns) and repeated in 1997 (in the contest of the upgrade to 4 T).

Two types of tests were made in 1988. Test 1 simulated typical magnetic loading of the coil in the region of the collar support. Test 2 examined the behaviour of the coil at the entry of the flute of the inner cylinder. Forces and stresses of more than twice the present allowable values were applied with no detectable effects. As the hybrid model calculations (App. D) show that stress concentrations such as those occurring at the collar teeth are mainly determined by locally applied forces rather than the remote boundary conditions, these tests are a valid representation of the coil under local operation stress condition.

The Noell tests (1997) were made in order to compare the mechanical stiffness of used and unused coils to see whether it had been affected by operation. The coils were subject to in-plane and out-of-plane bending. Stress and deflection calculations were made to determine the forces required to give suitable stress levels (significant but not excessive). The comparison of the load/deflection diagrams of the two coils does not give significant evidence for a damage of the used coil: the used coil had stiffness within 8% of the stiffness of the unused coil. The deflection were also compared with a finite element brick model and attempts to best-fit the insulation shear modulus were carried out.

2. Data of Object and Equipment

The object are two TF coils: the spare coil is No. 4 of the series production sequence and the used (for 7 years) coil is No. 23 of the series production sequence.

The equipment is a hydraulic testing facility at Noell, which was already used for production-accompanying tests for various contracts. In particular, it was used for previous tests on the TF coils at BBC in 1979. The design of the testing arrangement was adapted each time to the different boundary conditions. The equipment is made up of a double acting hydraulic cylinder capable of a maximum operational pressure of 300 bar and a maximum operational force of 1700 kN, electronically controlled for tension, compression and oscillation.

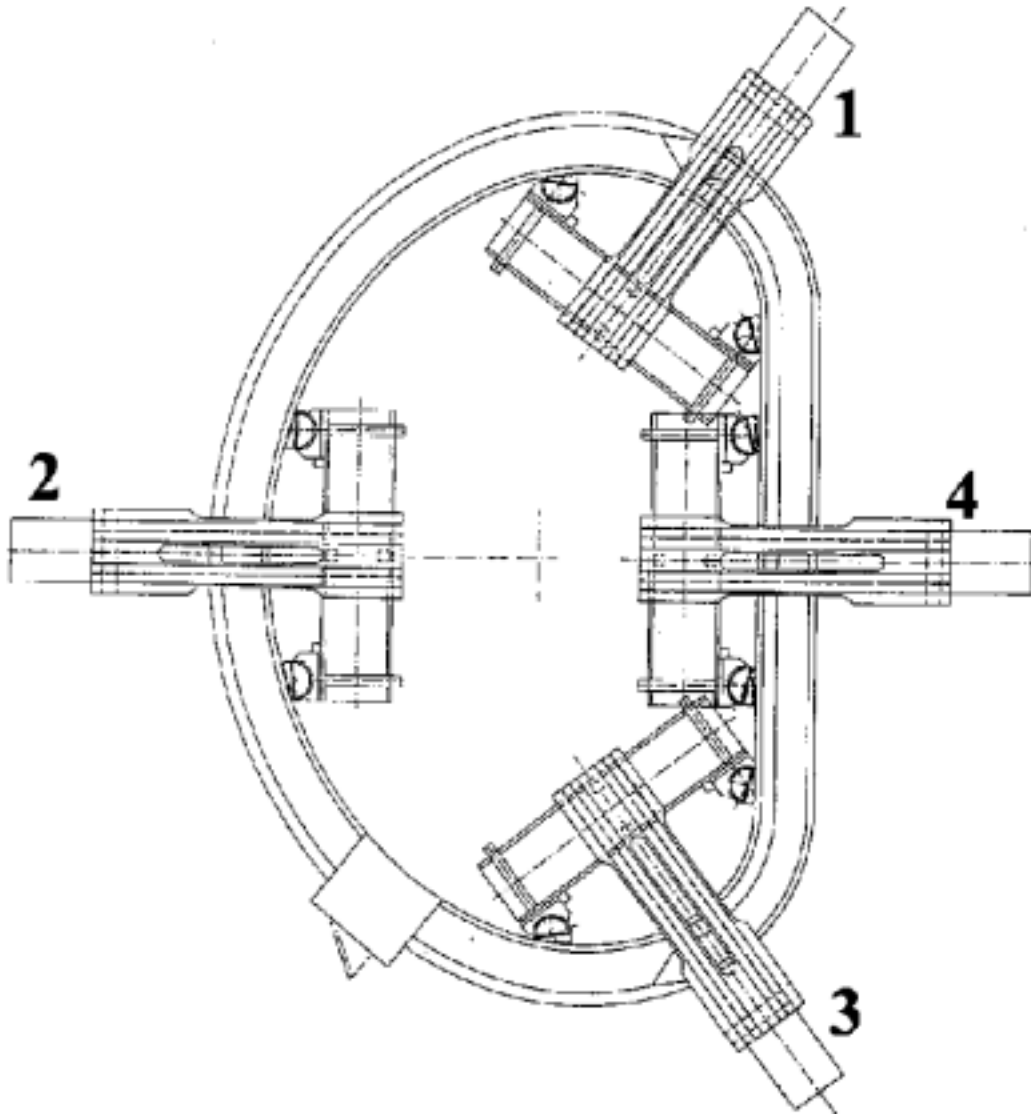


Fig. 1 Testing machine positions (machine shown as for in-plane loading).
The machine applies a central load which is reacted on either sides.

3. Processing of the tests

The testing sequence was the same as the one applied in the tests performed in 1979 on the prototype coil at BBC, in order to have the opportunity to compare the test results. The testing positions are shown in Fig. 1. Both coils were tested in positions 1, 2, 3 and 4 in-plane, and in position 6 out-of-plane (not shown in Fig. 1, but close to position 3 there).

As in the BBC tests frictional effects were not taken into account. In order to quantify for friction, tests were repeated in position 1 and done in position 3 adding low-friction material (Glycodur-sheets, by SKF) in the contact surface.

The consolidation of the glassfibre/resin compound, used as a cushion between the contact surfaces of the coil and the testing equipment, was measured using dial gauges attached to the reaction pads.

Each test was performed 5 times. The deflections were measured at discrete values of the loading force up to an upper deflection limit (which depended on the position and direction of testing) and the measured values were manually recorded.

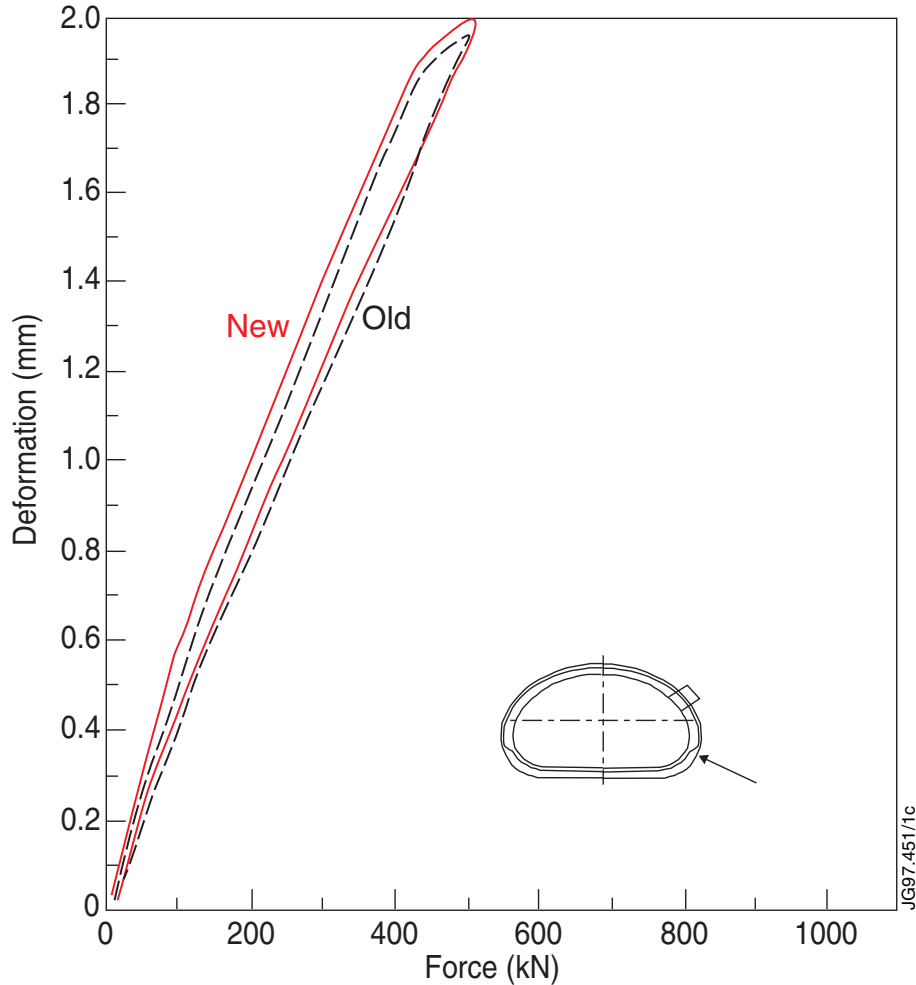


Fig. 2 Comparison of force/deformation diagram between an used and an unused coil, showing a difference in in-plane stiffness of ~8%

4. Results of the tests

For all testing positions the deflection limit originally set was 1 mm. However, as the forces were very small at the positions 1 and 4, it was decided together with JET to increase the deflection limit to 2 mm or 600 kN (whatever occurs first). A typical diagram of the load/deflection is plotted in Fig. 2 for the in-plane load at position 4. The decrease of the used coil with respect to the stiffness of the unused coil is reported in Table 1, where additional anti-friction procedures are also listed.

Test position	% decrease	anti-friction procedure
---------------	------------	-------------------------

4 (in)	6.4	n.a.
2 (in)	3.5	n.a.
1 (in)	13.0	n.a.
1 (in)	7.7	with Glycodur sheets
3 (in)	-1.5	with Glycodur sheets
6 (out)	5.3	with Teflon spray

Table 1 Percentual decrease of the used coil stiffness with respect to the unused coil stiffness

The mean value of the decrease in stiffness neglecting the results of position 1 without Glycour is 4.3%. Taking into account the various accuracy errors (like the exact positioning of the coil in the testing facility or the variations in the ground supports), this value is within the measurement tolerances.

The coil stiffness at the various test positions is reported in Table 2 for the tests done in 1979 and in 1997.

Test position	prototype (1979) [kN/mm]	used coil (1997) [kN/mm]	spare coil (1997) [kN/mm]	used/spare [#]
1 (in@collar)	223 to 527	236 to 250	248 to 265	0.95
2 (in@outer)	900 to 1000	1000	1000 to 1050	0.97
4 (in@inner)	590 to 850	690 to 705	750 to 770	0.92
6 (out@collar)	399 to 416	452	478	0.95

Table 2 Comparison of measured stiffness in the various full coil tests

5. Tentative interpretation of the coil stiffness from test data

Using the finite element model described in App. C and pictured in Fig. 3, the results from the stiffness have been used to attempt to fit the insulation shear modulus. Modelled and measured displacements at the testing positions are listed in Table 3. The deflection depended on the value of the shear modulus far less than expected and no conclusive estimate of the insulation shear modulus can be obtained by such an exercise.

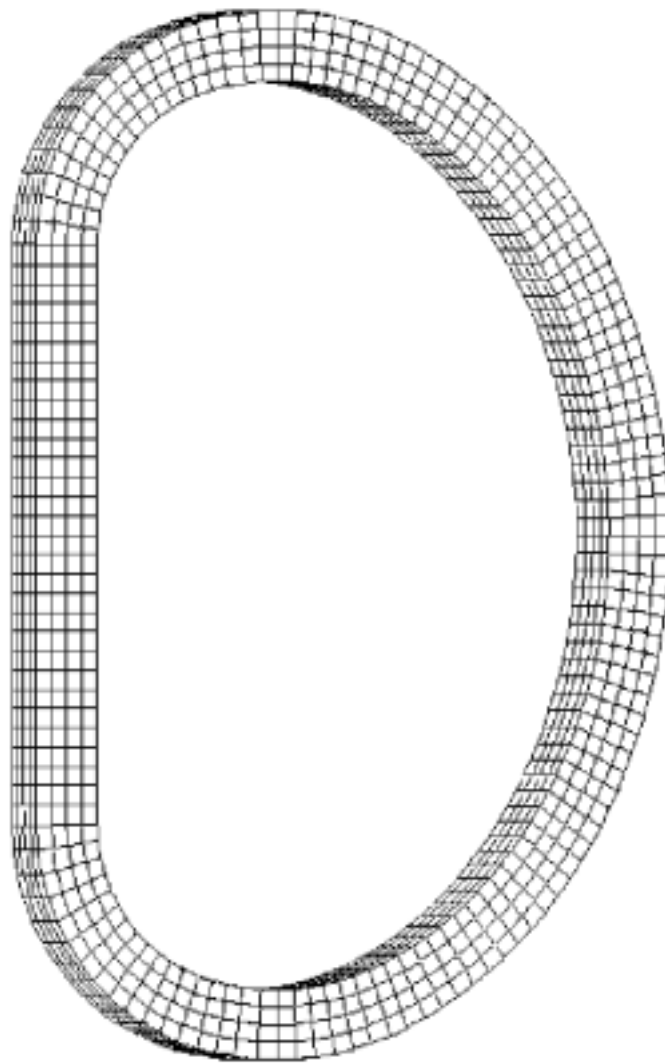


Fig. 3 Crude brick model of a full TF coil

Test position	computed (4 GPa) [mm]	computed (3 GPa) [mm]	computed (2 GPa) [mm]	measured [mm]
1 (in@collar)	1.36	1.42	1.42	1.62
2 (in@outer)	0.29	0.30	0.31	0.36
4 (in@inner)	0.41	0.43	0.45	0.53
6 (out@collar)	0.97	1.02	1.03	1.04

Table 3 Computed and equivalent to measured displacements for a 500 kN load

Tensile and Fatigue Tests on Copper Conductor and Brazed Joints

J. R. Last
09 November 1999

Contents

1	Introduction.....	2
2	X ray measurements on brazed joints	3
3	Static tensile tests on brazed joints.....	9
	3.1 Tests on complete joints.....	9
	3.2 Tests on machined samples from brazed joints.....	10
4	Fatigue tests on brazed joints.....	11
	4.1 Fatigue tests on complete joints.....	11
	4.2 Fatigue tests on machined samples.....	15
5	Tests on coil conductor.....	17
	5.1. Static tests	17
	5.2. Fatigue tests.....	17
	5.3. Conversion from $R = -1$ to $R = 0$	19
6	List of Figures	21
7	List of Tables.....	22

1 Introduction

Static and fatigue tests were made on both the copper conductor material and the brazed joints. All this material was taken from a TF coil formerly at position 3.1 and removed from the machine because of inter-turn faults.

For the brazed joint tests all 48 joints in the coil were first leak tested and X rayed. There were no leaks. Joints were selected for tensile and fatigue testing on the basis of the X ray measurements. The object was to include a range of defect sizes in each test. Four types of test were made on the brazed joints.

1. Tensile tests on whole joints
2. Stress controlled fatigue tests on whole joints
3. Tensile tests on samples machined from the brazed joint region
4. Strain controlled fatigue tests on samples machined from the brazed joint region

For the copper conductor tensile and fatigue samples were machined from randomly selected coil conductors.

Tests of TF Magnet Insulation Samples for the JET Upgrade to 4 Tesla

P. Miele
09 November 1999

Contents

1. Abstract.....	1
2. Introduction.....	2
3. Tests and Analysis on the Coil Insulation.....	3
3.1. Measurement of G with Iosipescu Method.....	3
3.2. Shear Strength with Iosipescu Method.....	4
3.3. Fatigue Tests.....	6
3.4. Micrographic Examination.....	7
3.5. Second Order Glass Transition Temperature (GTT).....	8
4. Conclusions	8
5. Acknowledgments	8
6. References.....	8

1. Abstract

The JET Toroidal Field (TF) coils were originally designed for operation at 3.4 tesla. In order to upgrade the field to 4 tesla and thus improve the performance of the JET machine, new mechanical tests and analysis were carried out on the insulation of TF coil samples. They are aimed at investigating the mechanical properties and the status of the insulation in order to set allowable stresses and force limits.

In particular since the shear stress in the insulation is strongly affected by the shear modulus of elasticity G, it is important to measure this parameter. A method for the

measurement of G in glass–resin fibres, the V-notched beam method (Iosipescu method), was applied. The particular shape of the rectangular Iosipescu V-notched sample and the particular modality of force application produce pure shear stress for a reliable measurement of the G value and of the shear strength of the insulation. The effect of temperature on these mechanical properties was also investigated. Results show higher average shear strength with lower scatter compared with previous tests on conventional rectangular samples, thus confirming the reliability of the method. Micrographic analysis of the insulation and comparison between the straight and curved regions of the magnet, where the highest stress occurs, confirm the good quality of the impregnation of the coil. Glass–resin content, void content, micros and TG measurements have been performed on different samples and correlation between the different properties of the insulation investigated. Moreover fatigue tests at different temperatures were performed and data analyzed with the cumulative damage technique, which allows for an extrapolation of the fatigue curve with less samples than the standard method.

2. Introduction

The JET toroidal field (TF) magnet system, Fig. 1, comprises 32 D-shaped coils originally designed to produce a field of 3.45 T at 2.96 m radius. Water-cooled and lately freon-cooled copper conductors and glass fibres-epoxy resin insulation are the main components of the coils. In-plane and out-of-plane forces created by the electromagnetic effect increase with the toroidal magnetic field B . In order to assess the condition of the TF magnet system for the implementation of the upgrade of the JET machine to 4 T operation, new analyses and tests have been made. The obtained data give the basis for the review of allowable stress and force limits.

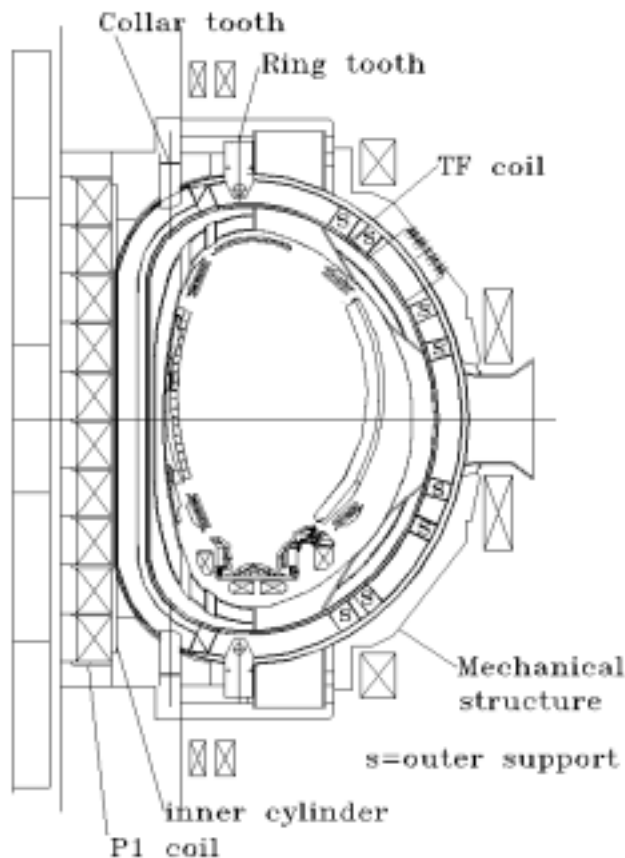


Fig. 1. A cross section of the JET machine showing a TF coil with its supports.

3. Tests and Analysis on the Coil Insulation

Optical examination and mechanical tests were carried out to investigate the mechanical properties and condition of the coil insulation, in particular the interturn insulation. Its constituents are glass fibres vacuum impregnated with epoxy resin. The resin composition is Araldite CY205 – Hardener HY906 – Flexibilizer DY040. Samples were cut from slices of the first faulty coil at various positions, so as to increase the statistics of the results.

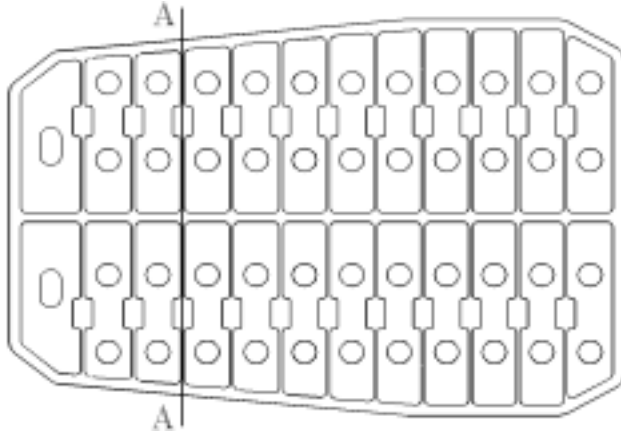


Fig. 3. A cross section of the TF coil.

3.1. Measurement of G with Iosipescu Method

The shear stress in the insulation is strongly affected by G, therefore it is of the utmost interest to measure this parameter. Since cylindrical samples for standard measurement of shear properties could not be machined out of the available material of the coil, the Iosipescu method for the measurement of G on rectangular samples was implemented [3]. This is a standard method designed to produce shear property data of composite materials. A rectangular sample with symmetrical centrally located V-notches is loaded in a mechanical testing machine by a special fixture designed to produce pure shear stress. The notches improve uniformity of the shear strain distribution along the loading direction. Any twisting of the sample is corrected through the readings from strain gauges on both sides of the sample. 18 samples were tested according to the standard and the τ - γ curve recorded up to failure. The effect of temperature was also investigated. For our measured ultimate shear strain capability the G value is derived from the chord in the shear strain range $1000 \div 6000 \mu\epsilon$.

$$G = \frac{\Delta\tau}{\Delta\gamma}$$

Preload test up to maximum 5 MPa at the 3 different temperatures $T=20^{\circ}\text{C}$, $T=70^{\circ}\text{C}$ and $T=90^{\circ}\text{C}$ and failure test at the chosen temperature were performed on each sample. The averaged G drastically decreases with temperature from 3700 MPa at room temperature down to about 2600 MPa at 70°C and 1400 MPa at 90°C , Fig. 4. The preload test gives the possibility to compare the G value of the same sample at the 3 different temperatures. Results from these tests give a constant G at low temperature, while G drastically decreases with the shear load increase at high temperature.

Preliminary calibration was carried out on a sample with well known G, which confirm reliability of the method within few percent.

Moreover finite elements analysis was carried out to check the stress field and sensitivity of G with the glass-resin content. A maximum 15% uncertainty was found between the computed and the measured G for the same glass-resin composition. This gave confidence for computing the G value of the key insulation, knowing its composition.

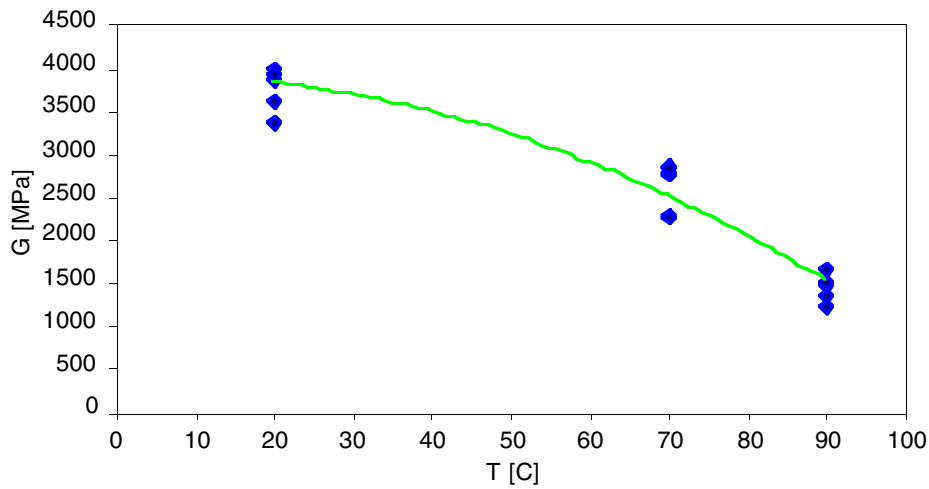


Fig. 4. Variability of G with temperature (Iosipescu samples).

3.2 Shear Strength with Iosipescu Method

The obtained data allow also for investigation of the shear strength capability of the insulation and its sensitivity with temperature, Fig. 5. Results show higher average with lower scatter compared with previous tests on conventional small rectangular samples, Fig. 6, and on double shear samples [1], thus improving confidence of the result. Fig. 7 shows the geometry of the different samples.

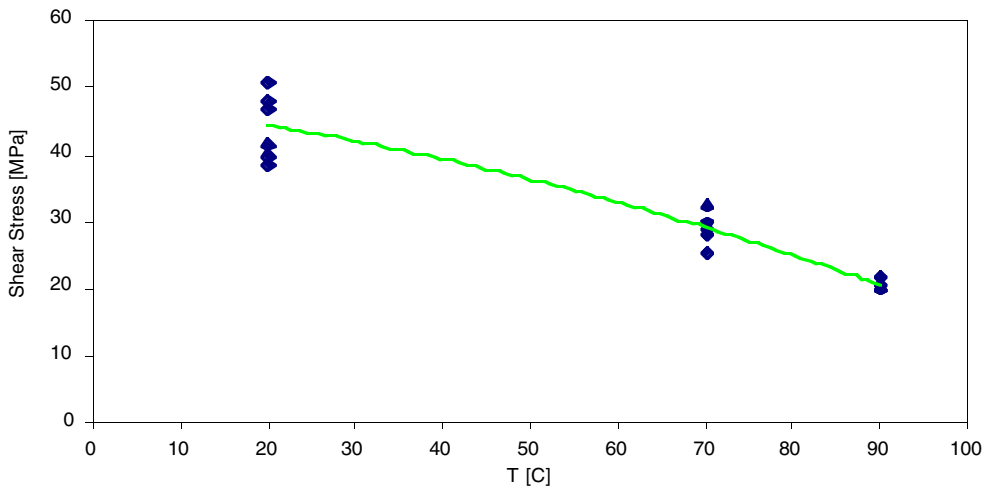


Fig. 5. Shear strength versus temperature (Iosipescu samples).

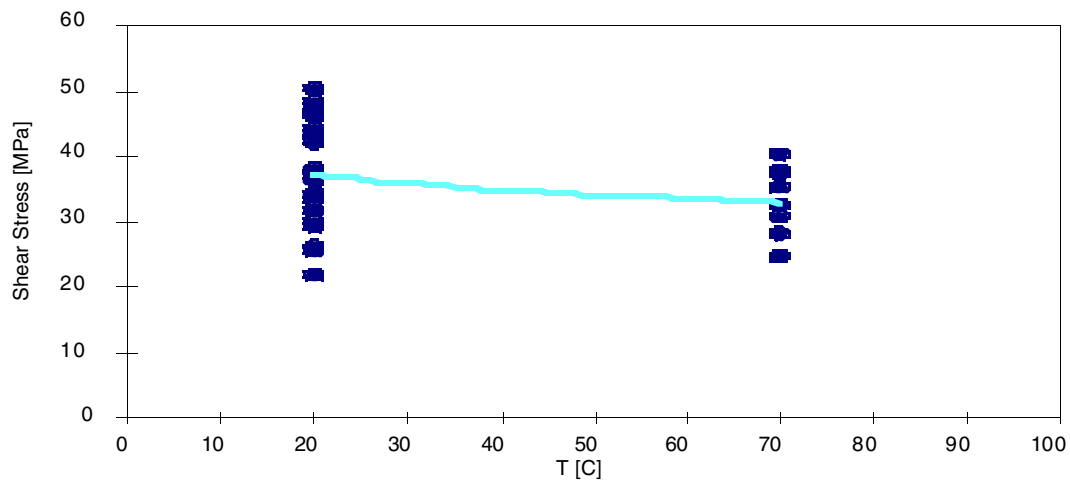


Fig. 6. Shear strength versus temperature (small samples).

The contact failure is defined as the percentage lack of resin over the total area. The void content is a volumetric measurement of voids, therefore it is a quantitative measurement of the percentage lack of resin in the sample volume. The qualitative information on the shape, concentration and topology of the voids is given by the contact failure. The contact failure is then the property which may explain the spread of shear strength in the measurements. Fig. 8 shows the correlation between contact failure and shear strength obtained by microscopic analysis in the failed area of the broken sample at room temperature for both Iosipescu and small samples. From the failure mode analysis 2 main failure mechanisms were observed, at the pre-preg layer in the center of the insulation and at the copper/insulation interface. The number of samples which break at the pre-preg layer is higher, thus confirming that the weakest point of the coil is related to the technological choices of the manufacturing cycle more than on the quality of the impregnation.

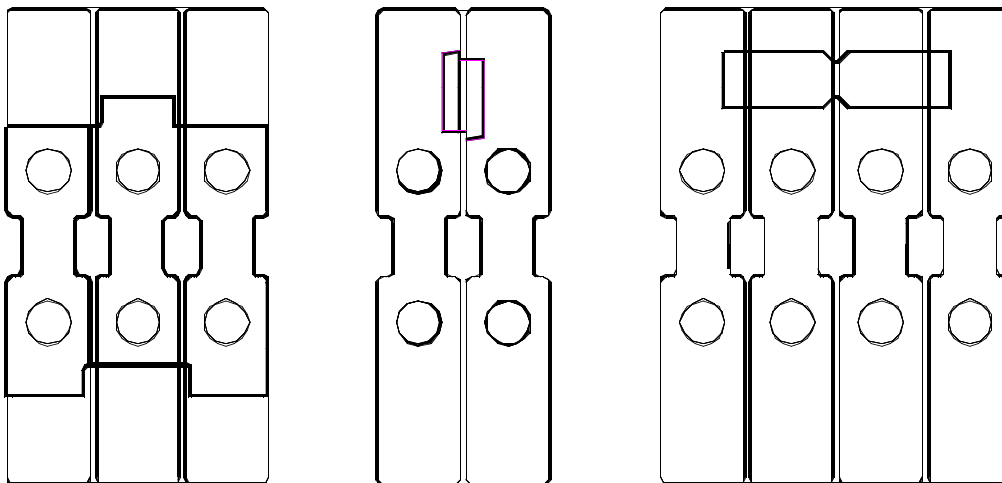


Fig. 7. Double, small and Iosipescu shear samples cut from coil cross section.

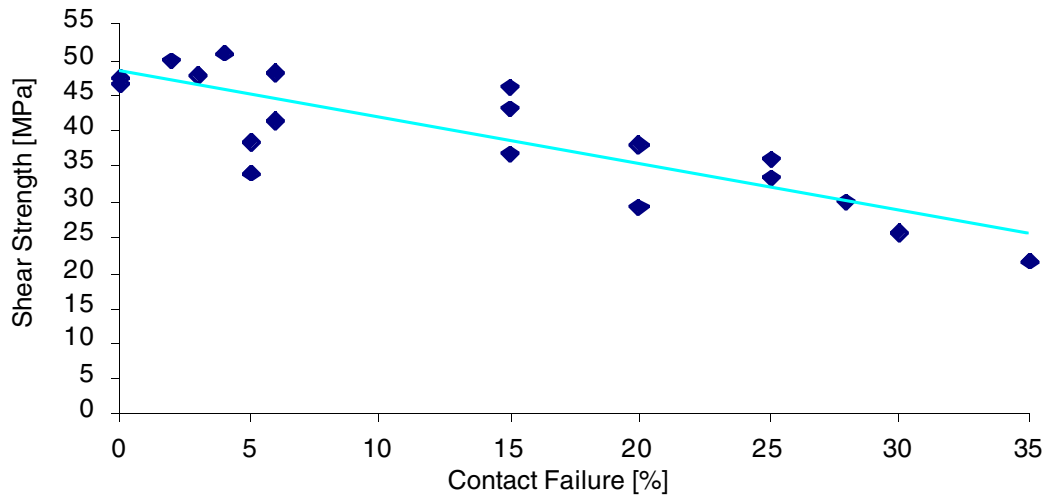


Fig. 8. Shear strength against contact failure at room temperature (Iosipescu and small samples).

3.3. Fatigue Tests

Fatigue tests were performed on conventional small samples with the cumulative damage technique. This allows for the determination of the S-N curve using less samples than the standard fatigue test method. The same sample is cycled for a chosen number of cycles, i.e. 20000 as it demonstrates double the required life, with a frequency $F=0.83$ Hz, at different stress levels with constant stress steps up to failure. The effect of the previous cycling is allowed for by cumulative damage calculations. 7 samples were tested at $T=20^{\circ}\text{C}$ and 6 at $T=90^{\circ}\text{C}$, Fig. 9.

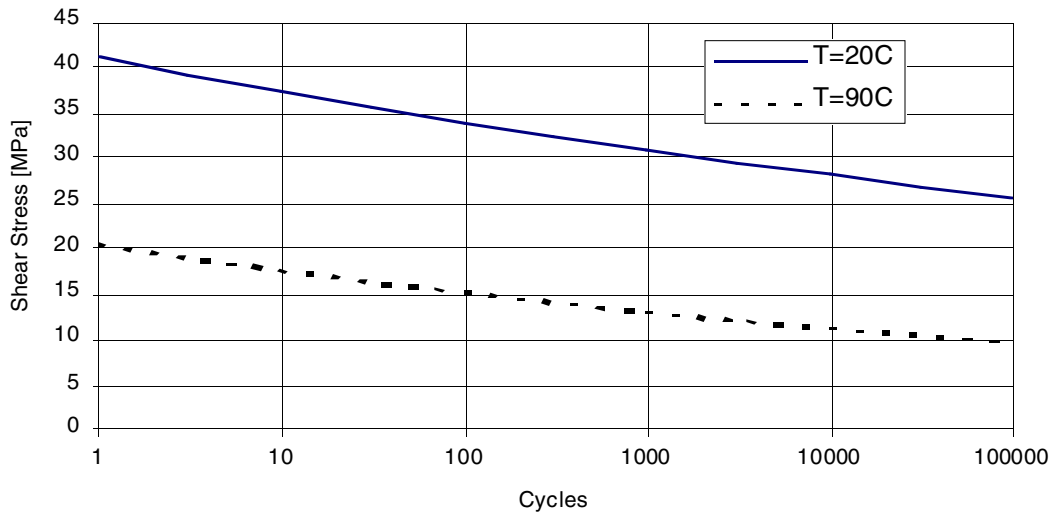


Fig. 9. Fatigue curves at temperature 20 and 90°C (small samples).

Other fatigue tests were performed on double shear samples at the different temperatures $T=20^{\circ}\text{C}$, $T=70^{\circ}\text{C}$ and $T=90^{\circ}\text{C}$, Fig. 10. The curves at room temperature are very similar, while they are different at high temperature. In particular the double shear samples give better result at high temperature: this is mainly due to the test frequency which is a factor 10 higher. Preliminary creep tests show a clear creep effect already at temperature $T=70^{\circ}\text{C}$, which implies that the total time at maximum load affects the fatigue behavior at temperature. Fig. 11 shows the fatigue curve at room temperature

obtained with Iosipescu samples and the standard fatigue method. The 3 curves at room temperature are very similar, thus increasing confidence on the result.

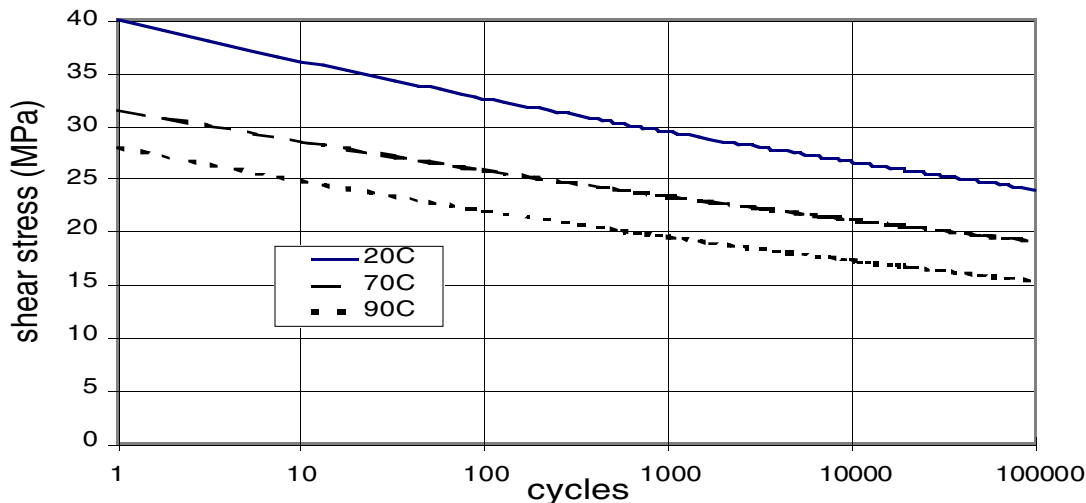


Fig. 10. Fatigue curves at 20, 70 and 90°C (double shear samples).

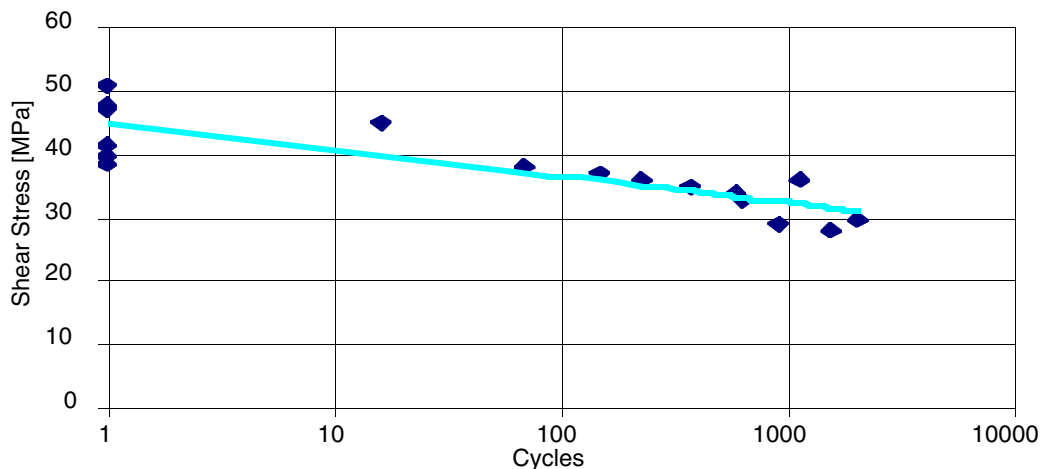


Fig. 11. Fatigue curve at temperature 20°C (Iosipescu samples).

3.4. Micrographic Examination

To investigate the condition of the insulation, micrographic analysis of samples taken at different positions in the section of the coil and comparison between the straight and curved region were carried out.

7 plus 7 interturn samples at correspondent positions in the 2 sections were chosen for the analysis taking into account also the sample position of the previous tests, in order to study possible correlation between the different parameters.

Void content [4] and glass-resin content [5] was performed through calcination of a sample. Moreover micrographic analysis of the 2 sections adjacent to the sample was carried out to study the morphology of the defects.

The average void content is 0.66%, in particular 0.64% in the straight region and 0.68% in the curved one. This confirms the good quality of the impregnation, since the limit reported in the standard is 1%. These voids are mainly due to the resin shrinkage, during the polymerization process and their main shape resembles a flattened sphere, which gives a lower overall weakening. The average glass content is 63.6% and the resin

content 35.7% and are not significantly different in the 2 analyzed regions. The lowest measured G does not correspond to a sample with the lowest glass and void content as expected, which implies that the glass content and void content have no correlation with the G values. This confirms that within the observed variability of the measurements, the mechanical properties of the insulation are not affected from region to region. The voids observed by micros show the same pattern and comparable concentration in the 2 regions and are mainly due to little air bubbles trapped during the manufacturing cycle in the 2 layers of pre-preg positioned in the middle of the inter-turn insulation. The shape of these voids suggests that they kept their shape and dimension since then. As already mentioned no correlation was found between void content and shear strength, while a correlation exists between contact failure and shear strength, Fig. 8.

3.5. Second Order Glass Transition Temperature (GTT)

GTT measurement was performed on different samples by both the Differential Scanning Calorimetry and the Differential Thermal Analysis [6]. The averaged GTT is 109°C, ranging from 105°C to 115°C. This level of temperatures explains the drastic fall of shear resistance observed in both static and fatigue tests performed at T=90°C. From correlation analysis on correspondent samples, GTT increases with G at the same glass content.

4. Conclusions

The results achieved confirm the good status of the coil insulation. It must be emphasized that the samples are cut from a real coil which has been operational in the JET machine for years, while normally new laboratory made samples are used for the tests. This increases our confidence on the results. The Iosipescu method for the G measurement was extended to determine also the shear strength and the fatigue behavior and gives results that are remarkably good.

The results obtained allow for definition of allowables and fatigue limits. Fatigue tests with different samples give approximately the same fatigue curve at room temperature, which is the basis for the fatigue assessment of the TF coils. The result from this work is the basis for the reliability assessment of the JET machine and acceptance of its upgrade to 4 tesla operation for improved performance.

5. Acknowledgments

Thanks are due to M Gasparotto, S Tosti and L Verdini for their contribution to this work.

6. References

[1] J Last et al, 'Analysis and Tests in support of Upgrading the JET Toroidal Field to 4 Tesla', MT-15, 1997.

[2] P Miele et al, 'Mechanical Assessment of the JET TF Coils for 4T Upgrade: the New 3D Hybrid Model', SOFT-20, 1998.

[3] ASTM D 5379/D 5379M – 93.

[4] ASTM D 2734 – 91.

[5] ASTM D 2584 – 85.

[6] ASTM E 1356 – 91.

Shear tests of insulation at Oxford Brookes

J. R. Last
09 November 1999

Contents

1.	Introduction.....	1
2.	Samples and tests.....	3
3.	Static tests	4
	3.1. Load deflection curve.....	4
	3.2. Summary of results.....	4
4.	Fatigue tests.....	6
	4.1. Procedure.....	6
	4.2. Fatigue test results.....	8
5.	Further details of static tests.....	10
	5.1. Graphical data	11
	5.2. Tabulated data	15
6.	Further details of fatigue tests.....	20
	6.1. Room temperature.....	20
	6.2. 70C.....	21
	6.3. 90C.....	21

1. Introduction

Cross sectional slices were cut from former coil 3.1 as shown in Fig. 1. Shear test samples were cut from these slices and were tested at Oxford Brookes University.

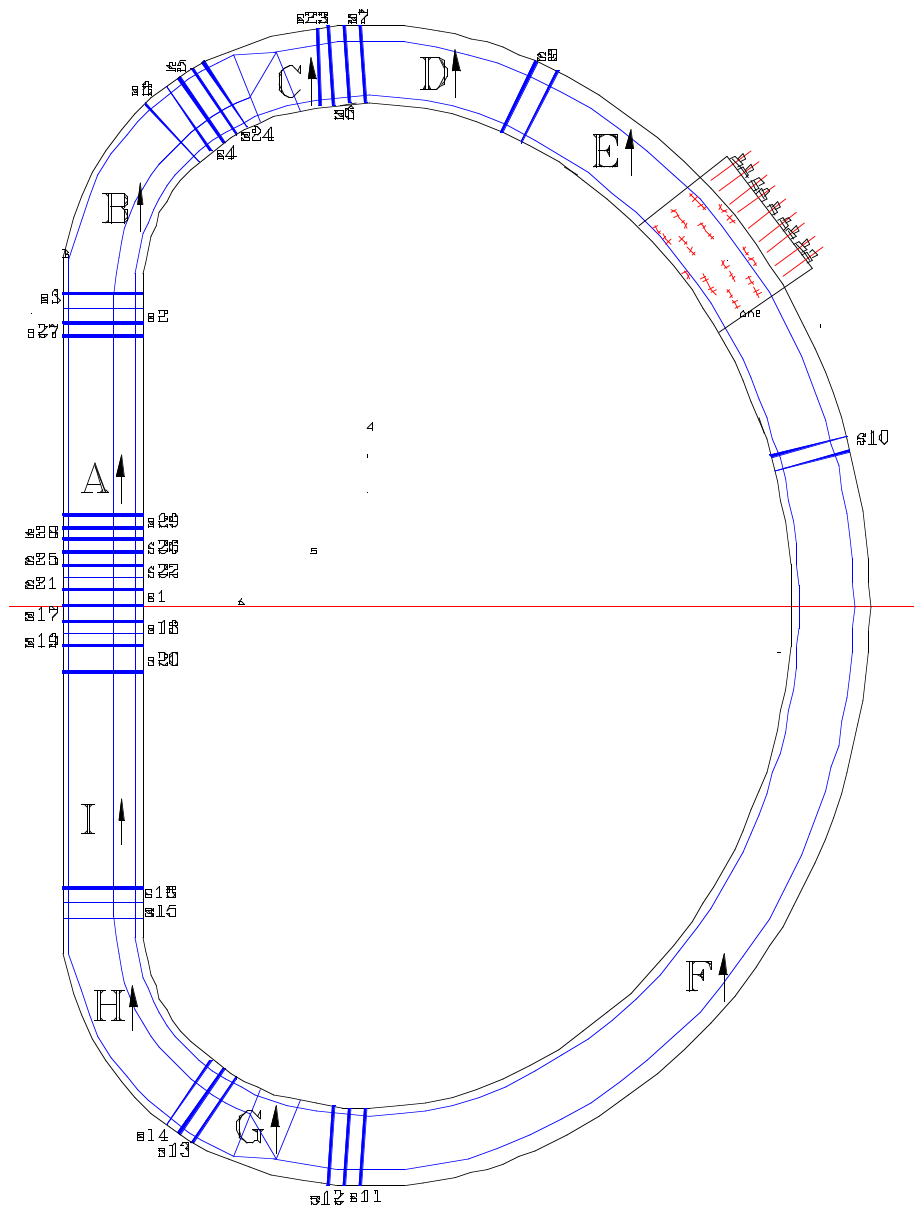


Figure 1. Position of slices for shear test and other samples

The design of sample allowed the key to be tested, as shown in Figs. 2 and 3. The double shear test piece is supported at the sides. The elasticity of the side supports is adjusted to ensure that the sample fails in shear rather than combined shear and tension.

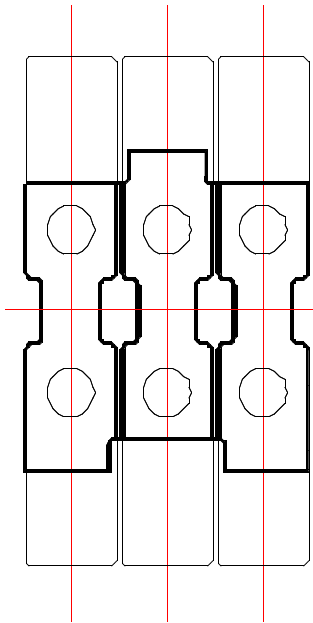


Figure 2. Double shear sample cut from coil cross-section

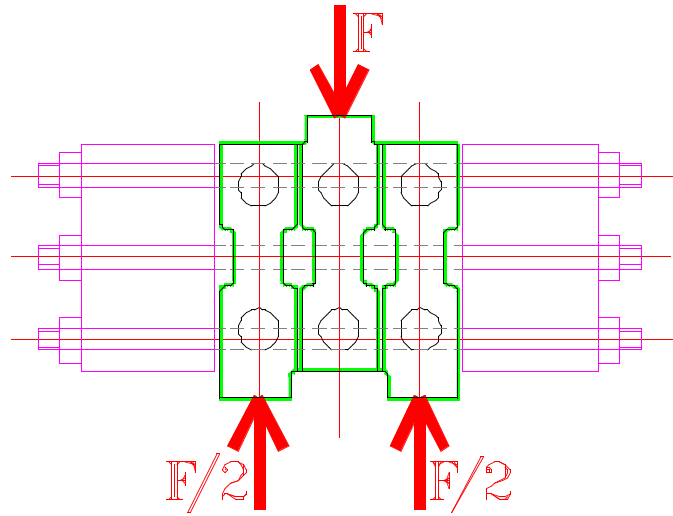


Figure 3. Sample with side supports

2. Samples and tests

All samples were taken from the part of the coil without built in stresses (middle of the straight), except where we investigated the effect of position on the coil. The variables investigated are listed in the table below.

Variable	Sample taken from	Test temperature	No samples
position on coil	mid straight	20(RT)	9
	end straight	“	6
	collar tooth	“	3
	ring tooth	“	4
sample size	mid straight	20(RT)	6*
temperature	mid straight	45	6
	“	70	6
fatigue	mid straight	20	6
	“	45	6
	“	70	6
	“	90	6
* double thickness (60 mm) samples			

Samples were tested in a Dennison Mays 500 kN, static and cyclic testing machine (accuracy 0.5%) at Oxford Brookes University.

3. Static tests

3.1. Load deflection curve

A typical static load/deflection graph is shown in Fig. 4. The first two steps in the graph occur when the two sides of inter-turn insulation fail. The load then transfers to the key. Further deflection is due to deflection of the key and finally to plastic flow of the copper adjacent to the key.

The first break is taken to calculate the shear stress in the insulation, as the stress conditions are not well defined after the first break.

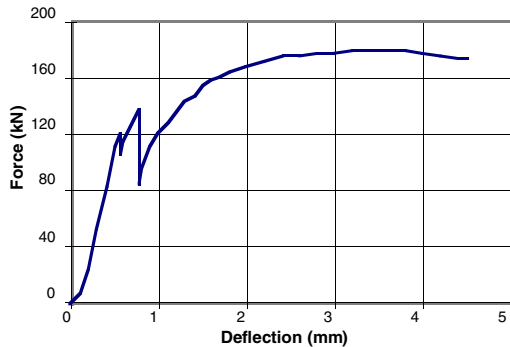


Figure 4. Typical force/deflection graph for sample in Figure 2.

3.2. Summary of results

3.2.1. Inter-turn shear

Two breaks are observed. The first is taken as the effective strength because conditions are less well defined after the first side is broken.

Variable	Sample taken from	Test temperature	Slice	Average shear stress MPa	Standard deviation MPa
position on coil	mid straight	20(RT)	18	35	16
	mid straight	20(RT)	25	44	12
	end straight	“	27	39	8
	collar tooth	“	24	16	14
	ring tooth	“	23	21	19
sample size	mid straight	20(RT)	20	40	6
temperature	mid straight	45	18	32	6
	mid straight	45	26	43	6
	“	70	29	33	3
	“	90	29	29	3

Examination of the above table allows the following conclusions to be drawn

Variable	Detail	Effect
----------	--------	--------

Position on coil	mid or end straight	no significant effect
Position on coil	collar or ring	erratic results with reduced average
Size of sample	30 mm or 60 mm thick	no significant effect
Temperature	RT, 45 & 70C	see graph

These conclusions enable all the results at room temperature (except at ring and collar) to be taken together to produce the summary histogram below.

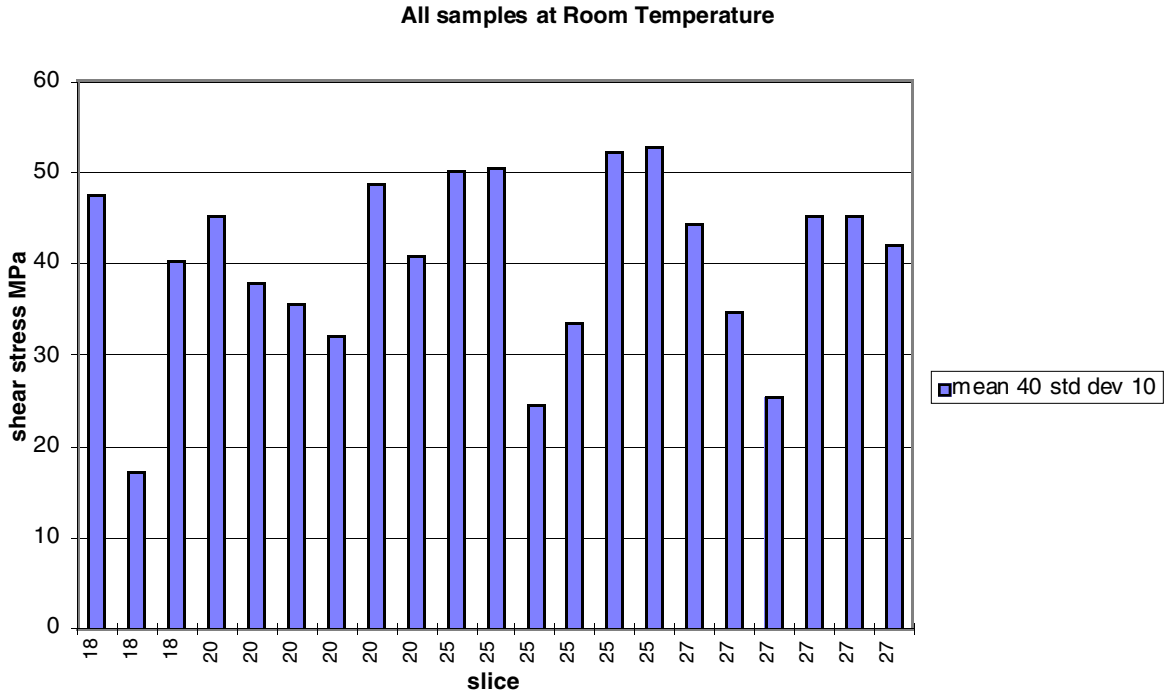


Figure 5. All samples at room temperature

The mean static strength at room temperature is 40 MPa. The results have a larger scatter than is normally seen in laboratory samples.

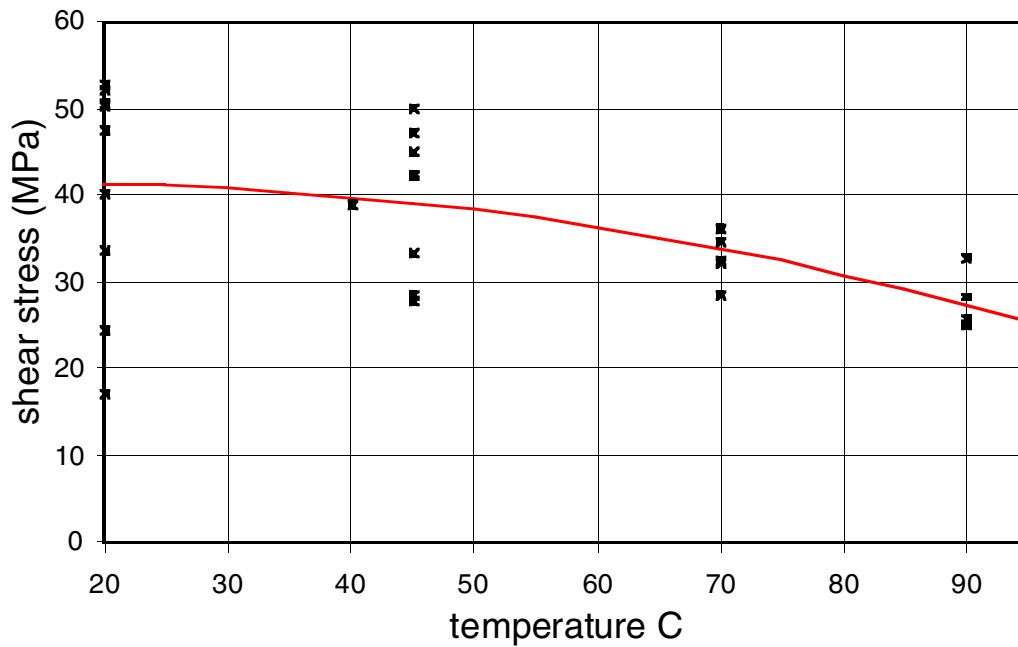


Figure 6. Effect of temperature

3.2.2. Strength of key

Variable	Sample taken from	Test temperature	Slice	Average strength kN/mm	Standard deviation kN/mm
position on coil	mid straight	20(RT)	18	7	0.7
	collar tooth	"	24	7	0.4
	ring tooth	"	23	6	1.2
sample size	mid straight	20(RT)	20	8	0.5
temperature	mid straight	45	18	7	0.5
	mid straight	45	26	not measured	not measured
	"	70	29	6	0.4

It will be seen that the strength of the key is constant regardless of position or sample size at about 7 kN/mm. (This is the total force divided by the sample width, i.e. double shear. For analysis, half this value would be appropriate.)

4. Fatigue tests

4.1. Procedure

4.1.1. Introduction

The fatigue tests were carried out in a way that is economical in samples and testing time. When making fatigue tests on a material that is not well known, it is difficult to determine suitable test stress levels.

- If the stress is set too low the sample will not fail and gives no useful information. To cause failure at a low stress the number of cycles has to be extended by orders of

magnitude which is expensive in time and money. In Magnet Group contracts we have often made a static test on samples that do not fail but this gives no usable information.

- If the stress level is set too high the sample fails at a low number of cycles. This may not be useful if one has an acceptance level in mind.

4.1.2. Test sequence

The method is based on testing samples for a limited number of cycles at a series of rising test stress levels until failure occurs. A calculation of cumulative damage is made to give a σ -N fatigue curve. The procedure for all samples is the same and is as follows;

1. Test at acceptance stress (say 15 MPa) level for twice the required life (say 20,000).
2. If the sample does not fail, test at higher level (20 MPa) for twice the required life.
3. If the sample does not fail, test at higher level (25 MPa) for twice the required life.
4. Continue this process until the sample fails.
5. When all the samples are tested analyse the results to determine an effective number of cycles at the failure stress for each sample.

4.1.3. Analysis

1. Assume an analytical form for the σ -N curve, such as $\sigma = \sigma_0 N^{-\alpha}$. This expression has two free parameters (σ_0 and α) to be determined.
2. Consider a sample which survives N_1 cycles at σ_1 , N_2 cycles at σ_2 , N_3 cycles at σ_3 ,..... and fails after N_f cycles at σ_f .

3. At σ_1 the expected life is $N_{1e} = \left(\frac{\sigma_0}{\sigma_1}\right)^{\frac{1}{\alpha}}$ and the cumulative damage is $\frac{N_1}{N_{1e}}$ and similarly for σ_2 , σ_3 , etc..

4. The total damage is given by $C_s = \frac{N_1}{N_{1e}} + \frac{N_2}{N_{2e}} + \frac{N_3}{N_{3e}} + \dots + \frac{N_f}{N_{fe}}$.

5. The effective number of cycles at σ_f is $N_f + N_{fe} \left(\frac{N_1}{N_{1e}} + \frac{N_2}{N_{2e}} + \frac{N_3}{N_{3e}} \right)$

6. The unknown parameters (σ_0 and α) are determined by setting the (geometric) average cumulative damage at failure for all the samples at 1. That is $(C_1 C_2 C_3 C_4 \dots)^{(1/n)} = 1$ for n samples. The geometric average was taken because it gave a better fit to our widely scattered results.

7. Starting with assumed values this type of optimisation can easily be done by for example "Solver" in Excel.

8. σ_f is plotted against the effective number of cycles $N_f + N_{fe} \left(\frac{N_1}{N_{1e}} + \frac{N_2}{N_{2e}} + \frac{N_3}{N_{3e}} \right)$ to give an σ -N curve.

The static results can be included as failures with a single cycle.

4.2. Fatigue test results

The samples were cycled at 8 Hz, the limit of the test machine. The test frequency for non metallic samples is sometimes limited by internal heating. In our samples the epoxy glass was relatively thin and well cooled by the adjacent copper.

As in the static tests failure of the inter-turn bond could be detected by an increase in flexibility of the sample. In some cases the test was continued until the key failed.

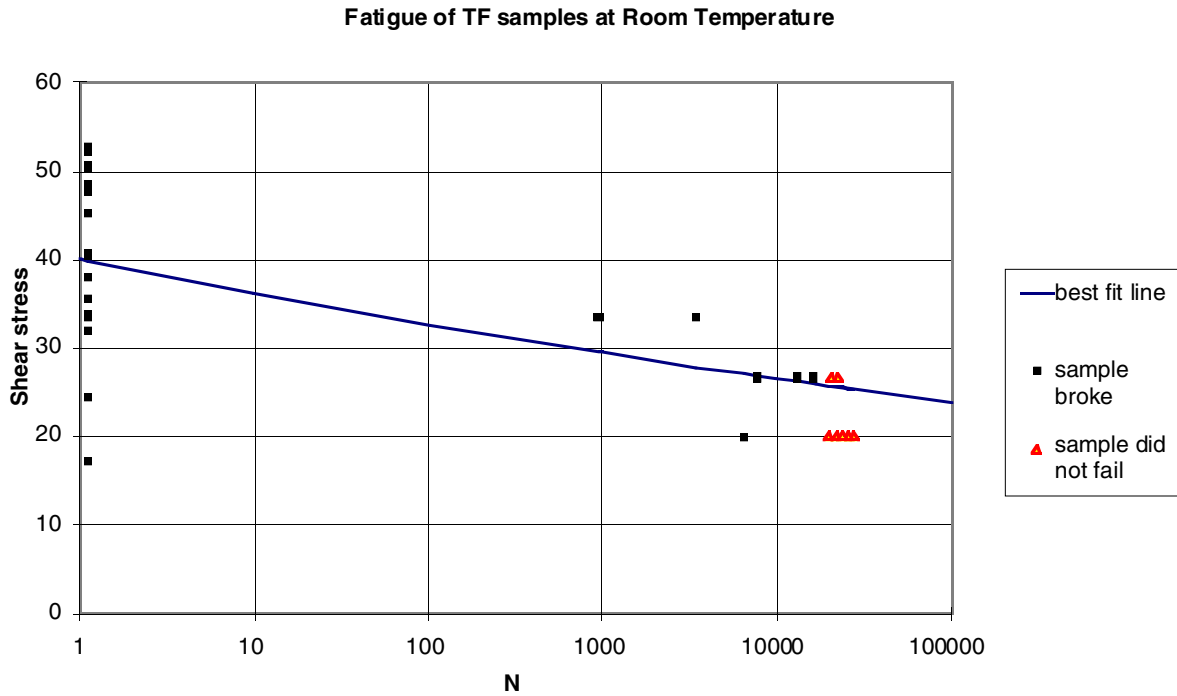


Figure 7. Fatigue at room temperature (slice 19)

Fatigue of TF samples at 70C

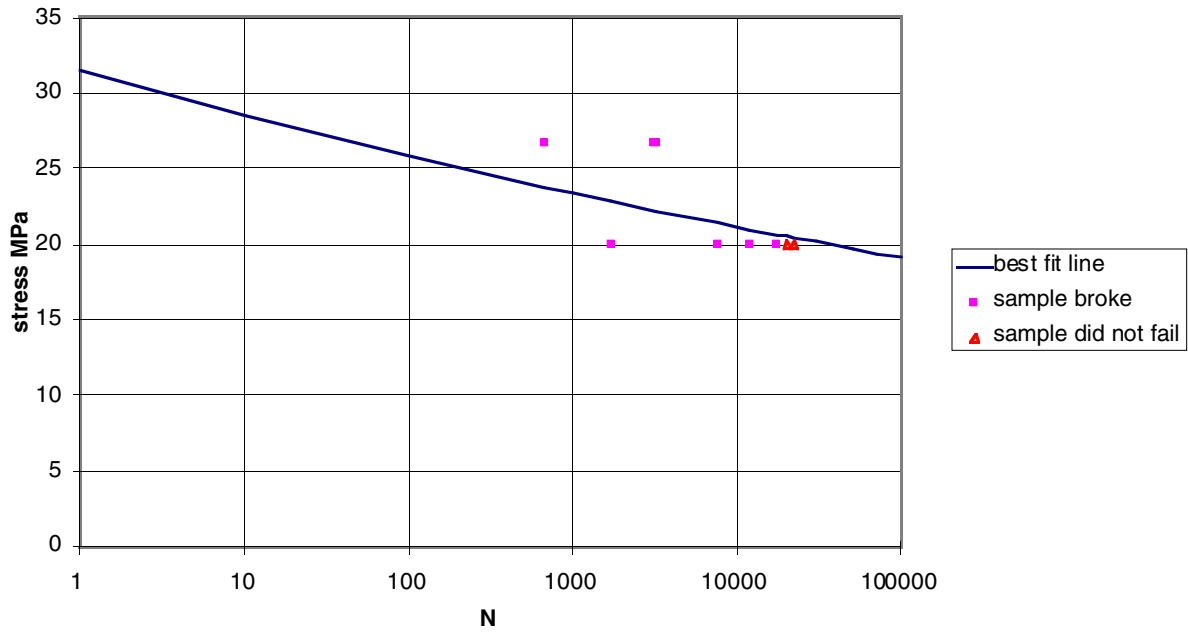


Figure 8. Fatigue at 70C (slice 22)

Fatigue at 90C, Oxford Brookes

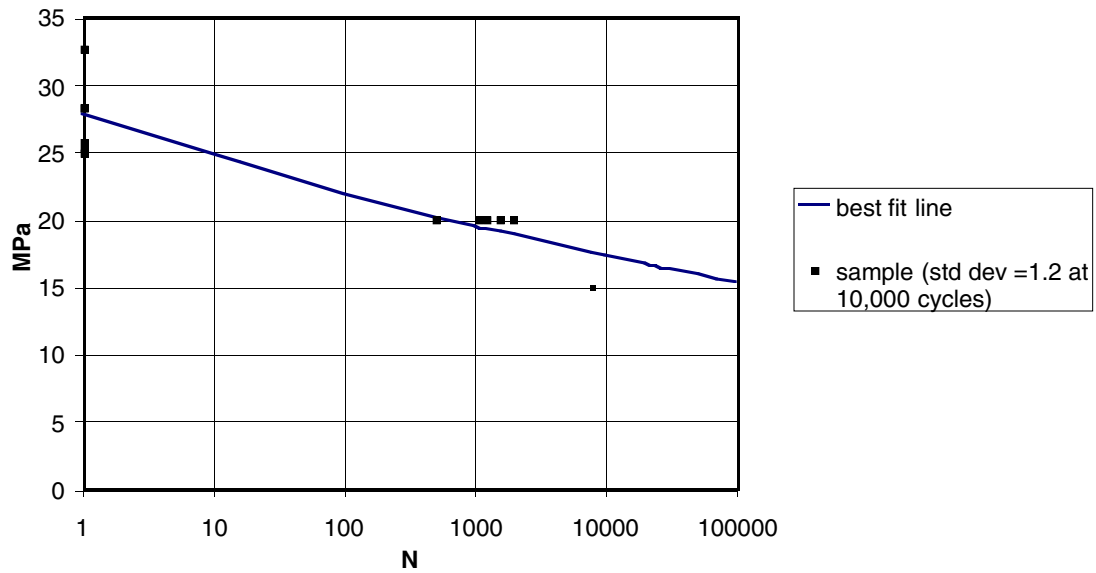


Figure 9. Fatigue at 90C (slice 31)

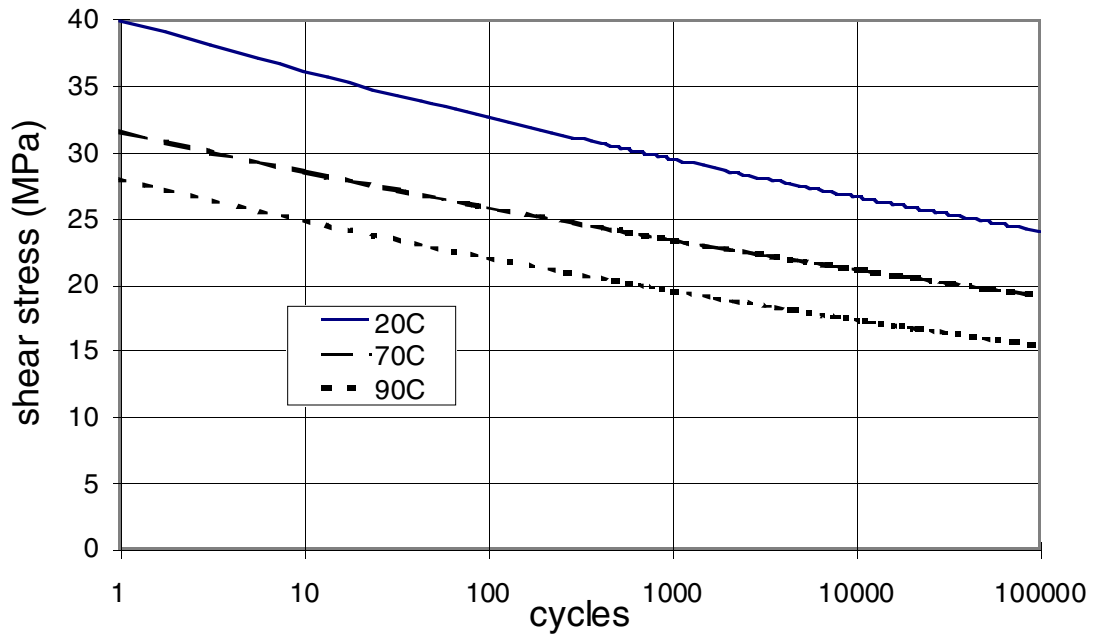


Figure 10. Comparison of fatigue at room temperature, 70 and 90C

5. Further details of static tests

Test results are given below for all slices in numerical order. The key strength is given in terms of average shear strength (total force/total shear area). The force per unit length is more relevant for design and analysis. The ultimate strength of the key was not found for all samples as the test involves large deflections which are not realistic in the coil environment.

5.1. Graphical data

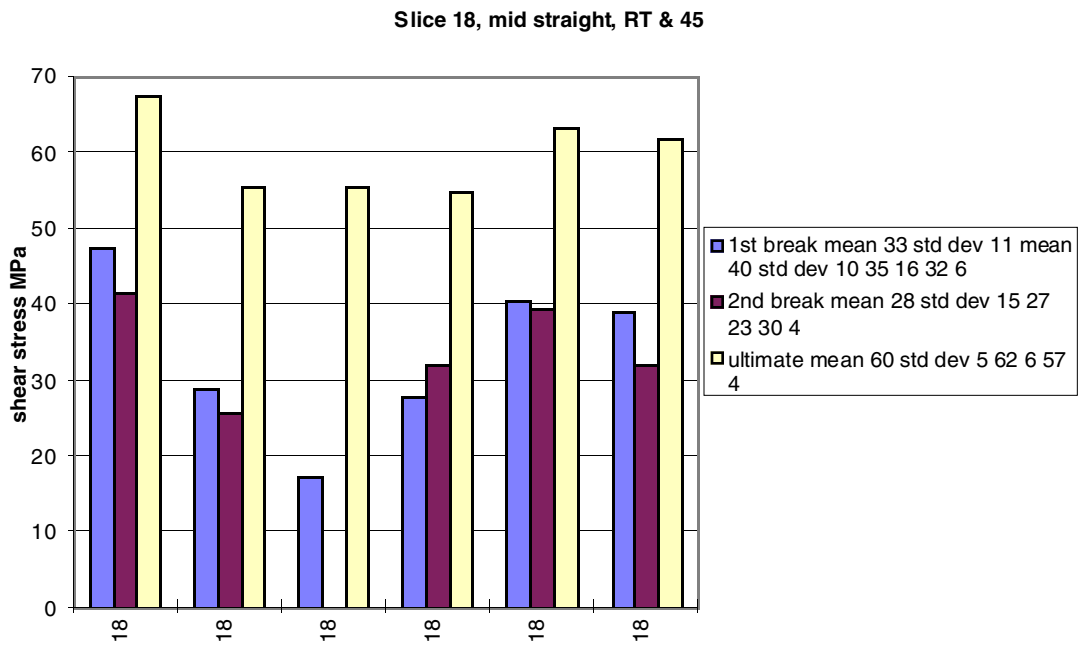


Figure 11. Slice 18, static test

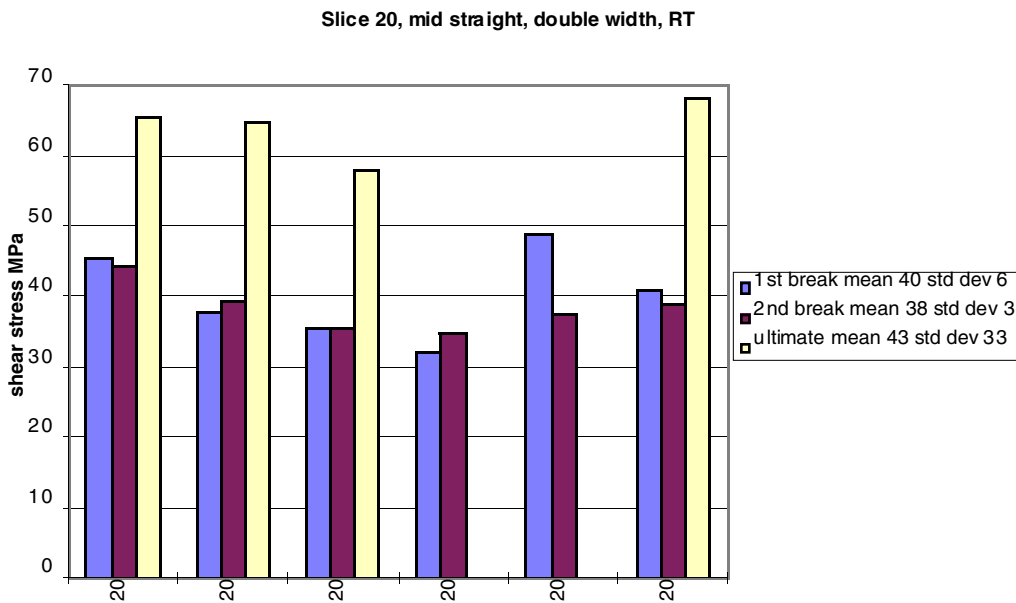


Figure 12. Slice 20, static test

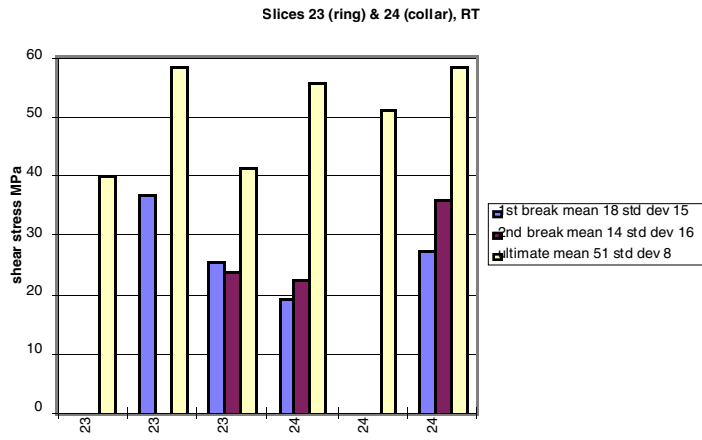


Figure 13. Slices 23 and 24, static test

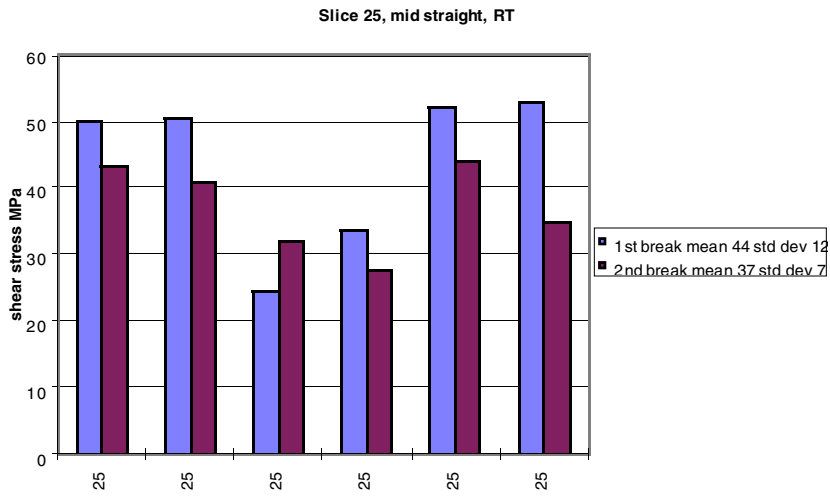


Figure 14. Slices 25, static test

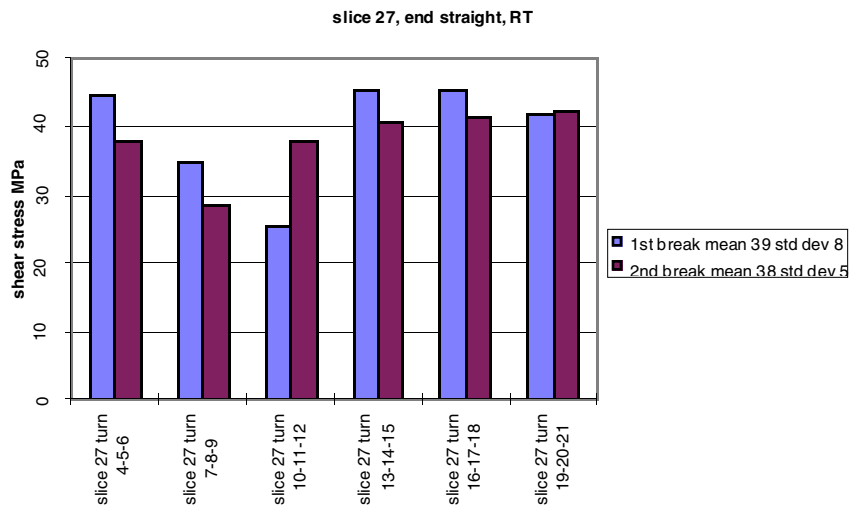


Figure 15. Slices 27, static test

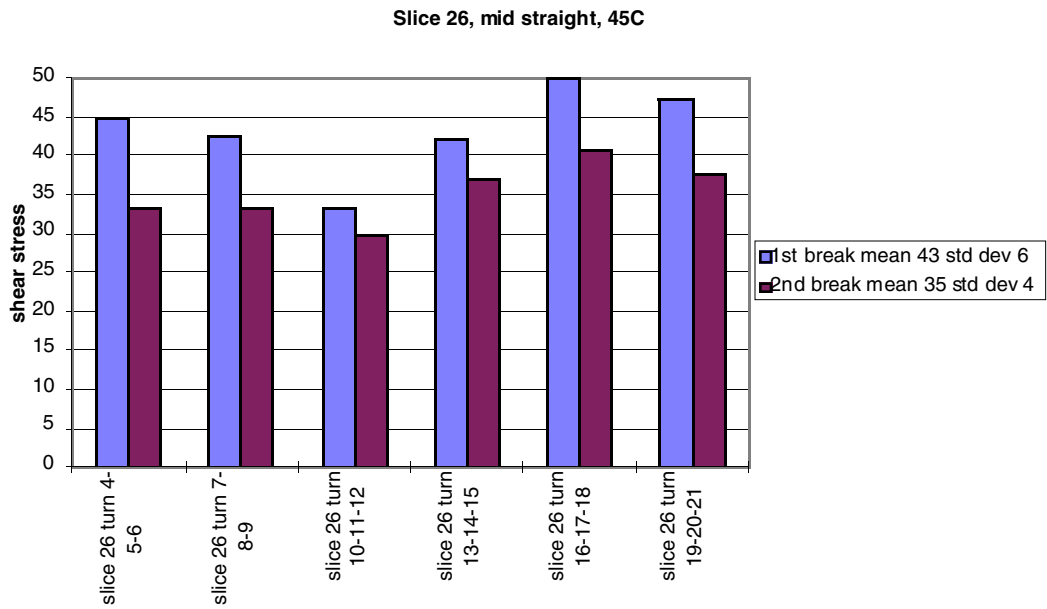


Figure 16 Slice 26

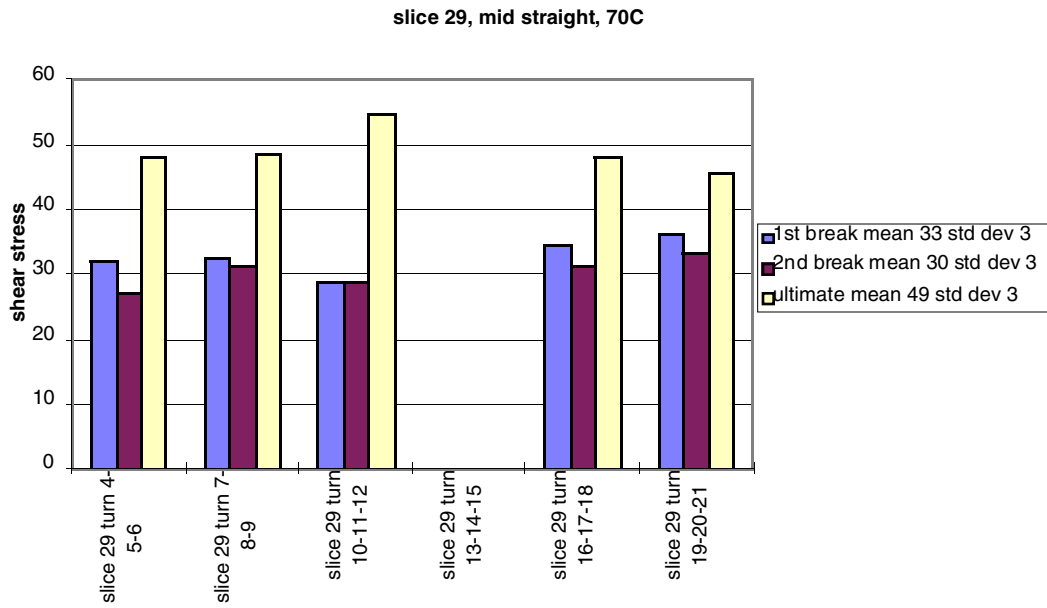


Figure 17 Slice 29

Slice 32, Static tests at 90C

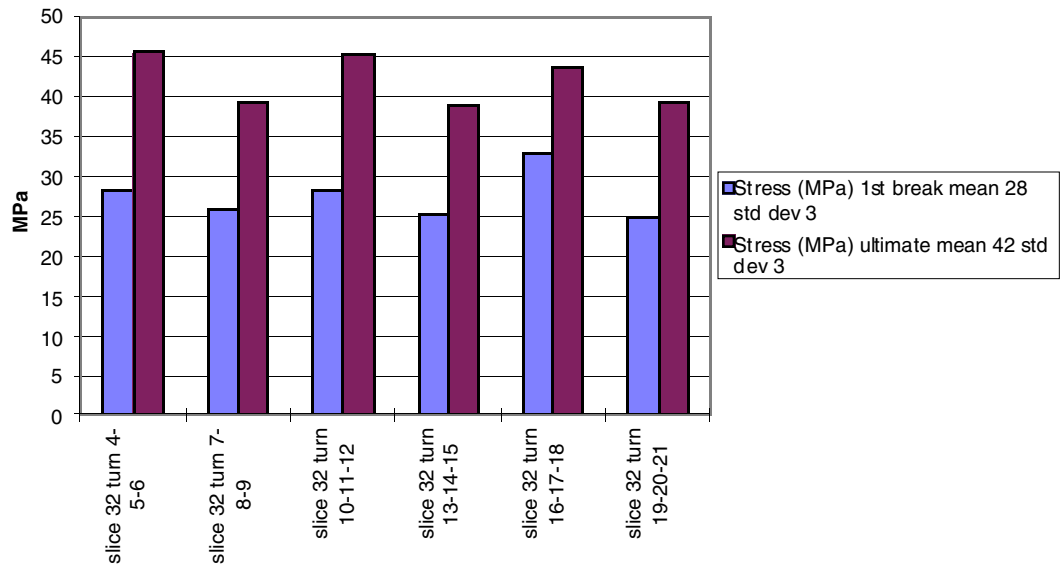


Figure 18 Slice 32

FE analysis of test samples

V. Riccardo
10 November 1999

Contents

1. TF coil insulation simple shear test samples.....	1
2. TF coil insulation losipescu shear test samples.....	4
3. TF coil insulation double shear test samples	5
4. TF coil insulation mode II crack growth test samples	7
4.1. FE computation of the J-integral value.....	8

1. TF coil insulation simple shear test samples

The mesh and boundary conditions for the single shear tests are plotted in figure 1a. The displaced mesh is in Fig. 1b. Contour plots of the shear stress are in Fig. 2. The stresses in the mid-plane of the insulation are rather uniform. Figure 4, where the insulation sub-model results are plotted along two lines of elements, shows that the model has converged: the mid-plane stresses go to zero at the free surface and have a glitch just before that, they are top/bottom symmetric as they should because of the applied boundary conditions. There is a small compressive stress in the mid-plane, while the interface, away from the ends, is in pure shear. The shear magnitude is about the same in all the insulation. On the bottom right (and top left) corner(s) of the insulation there is a stress concentration due to the geometry of the sample: this piece of insulation does not end in a proper free surface as it is rather close to the copper layer through which the load is applied.

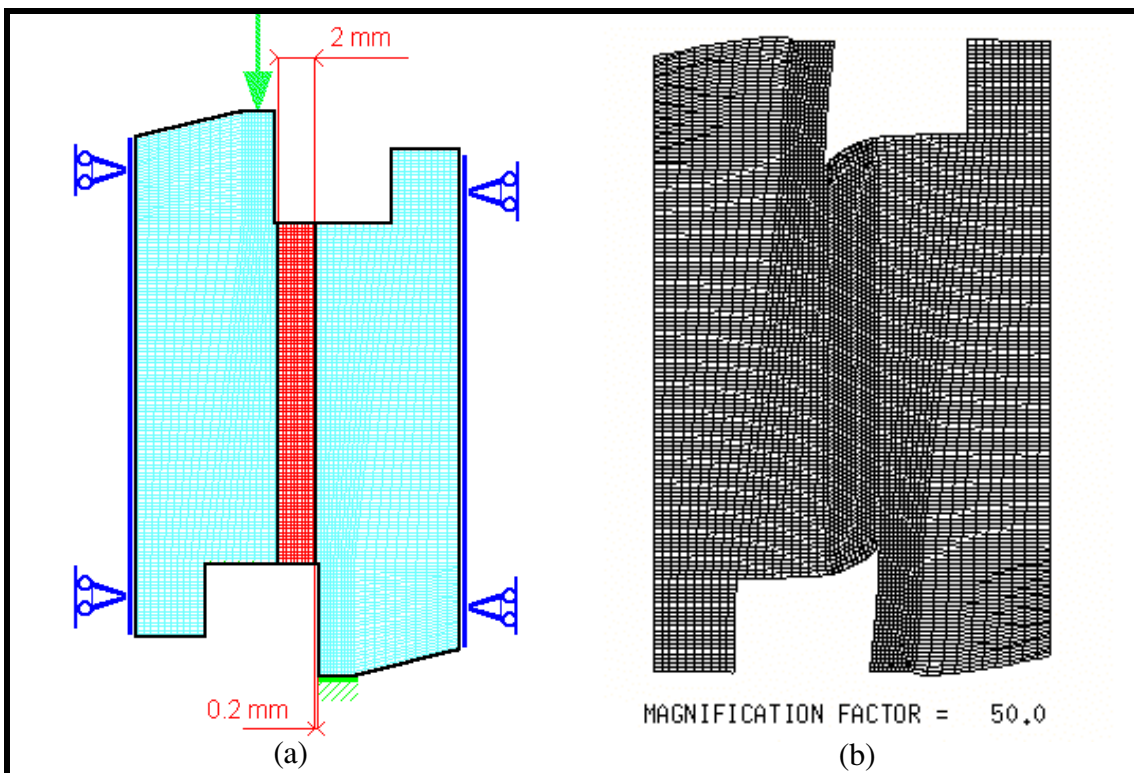


Fig. 1 Single shear sample: (a) mesh with dimensions and (b) displaced mesh

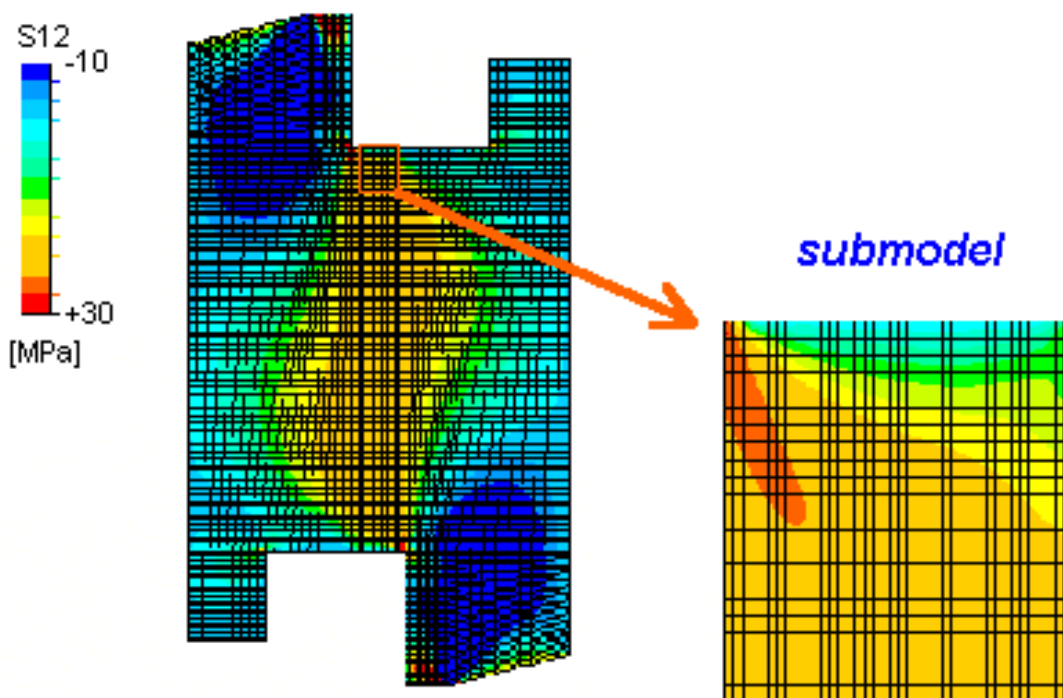


Fig. 2 Shear stress plots in the full model and in the submodel of the single shear test sample

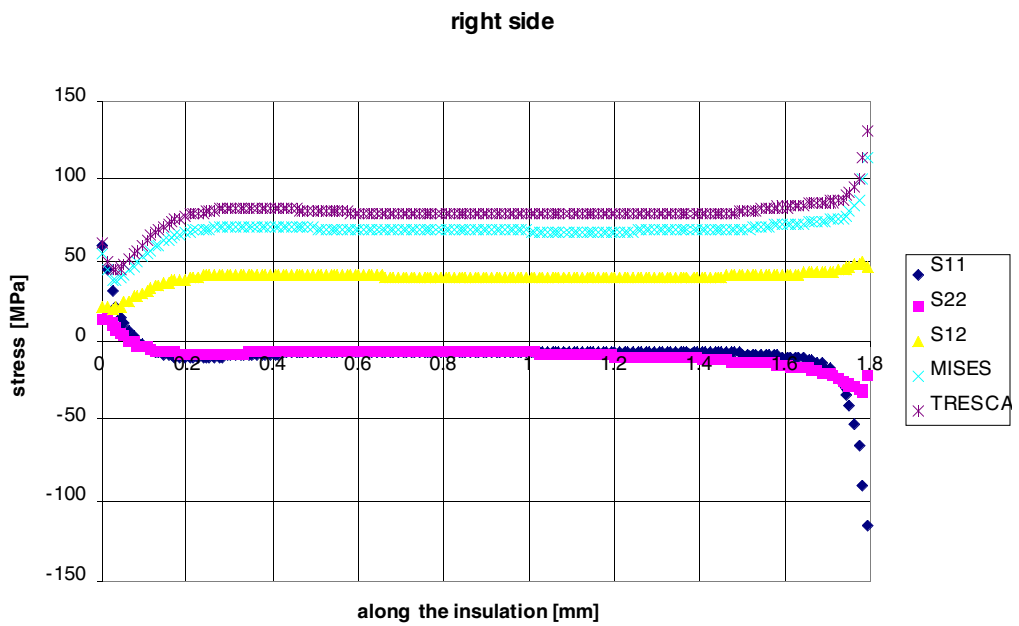
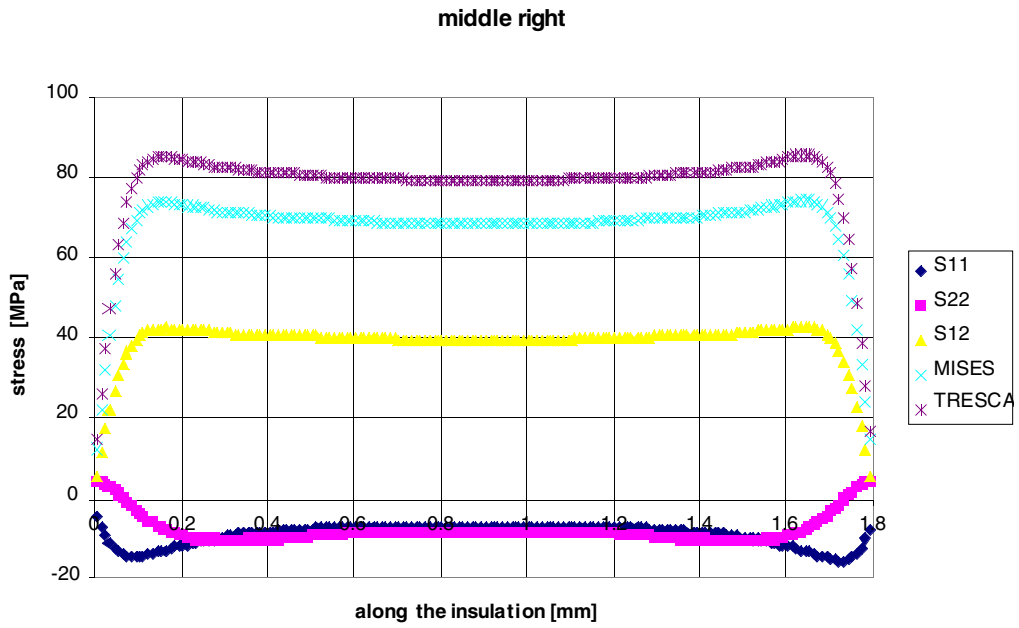


Fig. 3 Stresses along the middle of the insulation (a) and on the insulation facing the copper interface (b)

2. TF coil insulation Iosipescu shear test samples

The Iosipescu shear tests is done using a 4-point bending arrangement. The particularity of this specimen is the shape of the sample: this is V-notched at 45° so that there is pure shear also on the end portion of the sample. The geometry of the sample, with the dimensions of the one used for the TF coil insulation tests is reported in Fig. 4. As the single shear arrangement also this one is top/bottom and left/right anti-symmetric, as shown in Fig. 5.

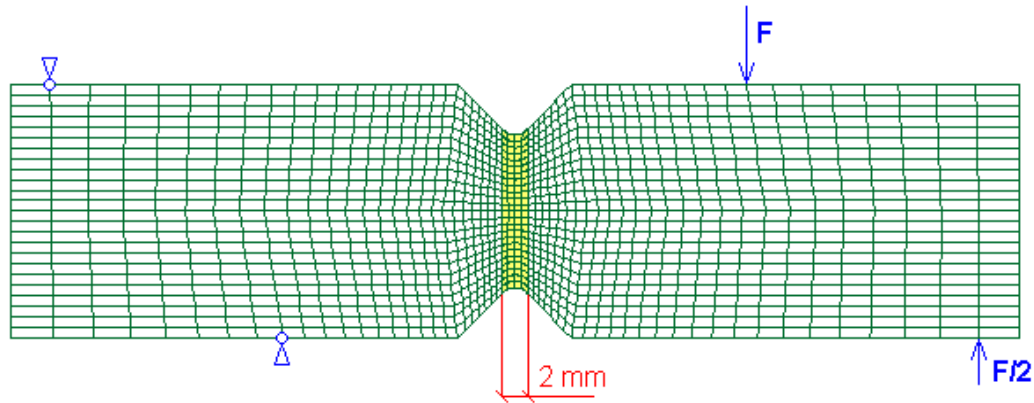


Fig. 4 Geometry, dimension, boundary conditions and loads of the Iosipescu shear sample

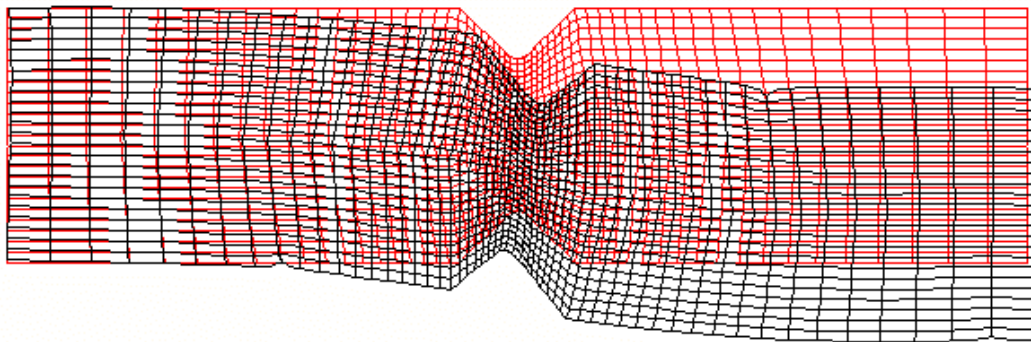


Fig. 5 Original and displaced mesh of the Iosipescu shear sample: this is the full sample model, from which the displacements are taken for the detailed insulation-only sub-model

The contour plots of the shear stress for the full sample model and for the insulation-only sub-model are reported in Fig. 6. In Fig. 7 the stresses, as computed with the detailed insulation-only sub-model, are plotted along the middle of the insulation.

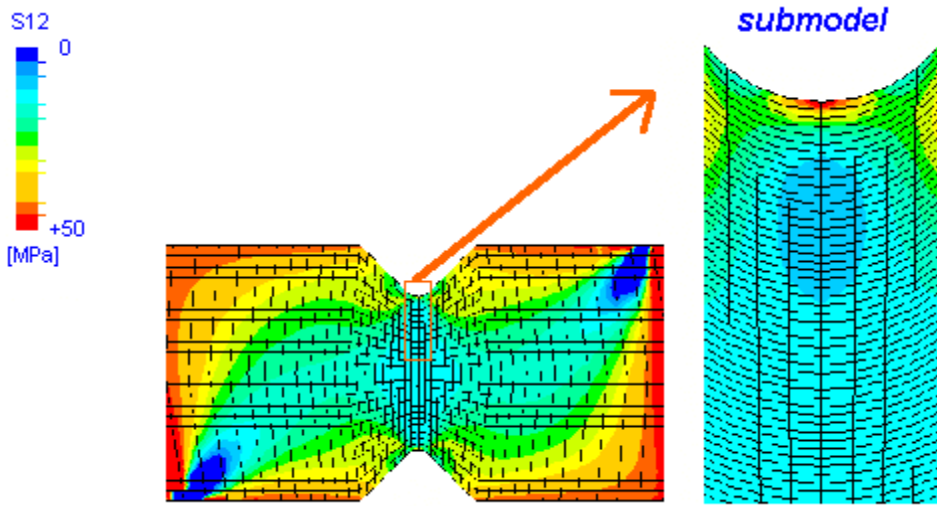


Fig. 6 Shear stress contour plots in the global model and in the sub-model of the Iosipescu sample

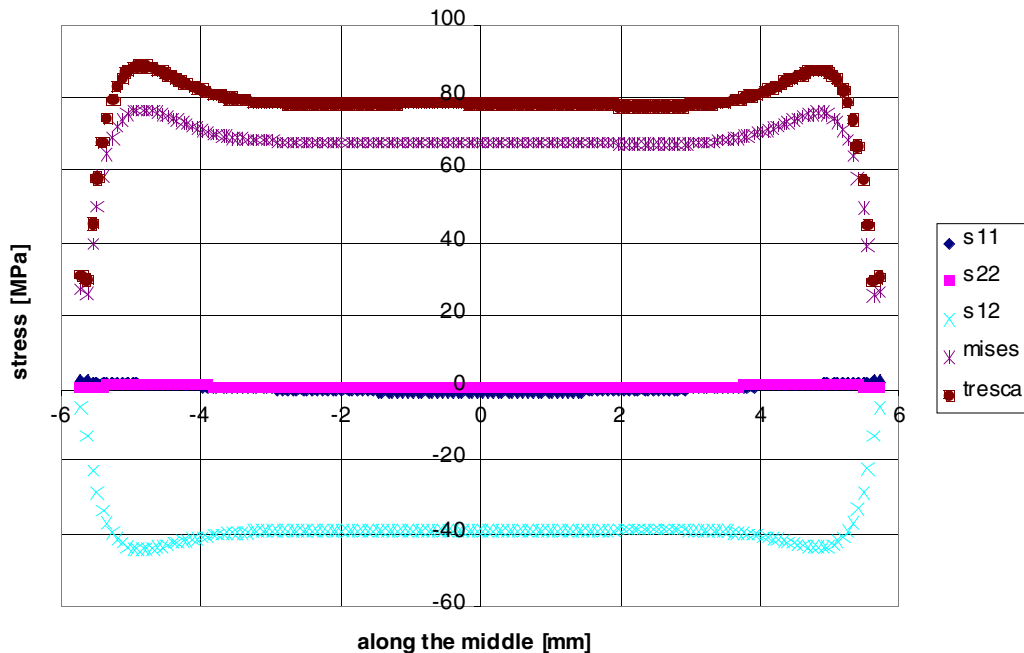


Fig. 7 Stresses along the middle of the insulation (from the detailed insulation-only sub-model)

The Iosipescu shear test gives a cleaner stress distribution on the insulation: here are no normal or tangential stresses in the middle of the insulation and the shear stress is uniform for the best part of the high of the sample.

3. TF coil insulation double shear test samples

The double shear test samples are the most complex (and complete) samples used to investigate the TF coil insulation properties: they comprise three pieces of turn and two inter-turn pieces, including 4 keys (Fig. 8). They have been used also to study the role played by the keys under shear load conditions. When the sample (mirror symmetric with respect to the vertical plane) is loaded as in Fig. 8, it displaces as in Fig. 9.

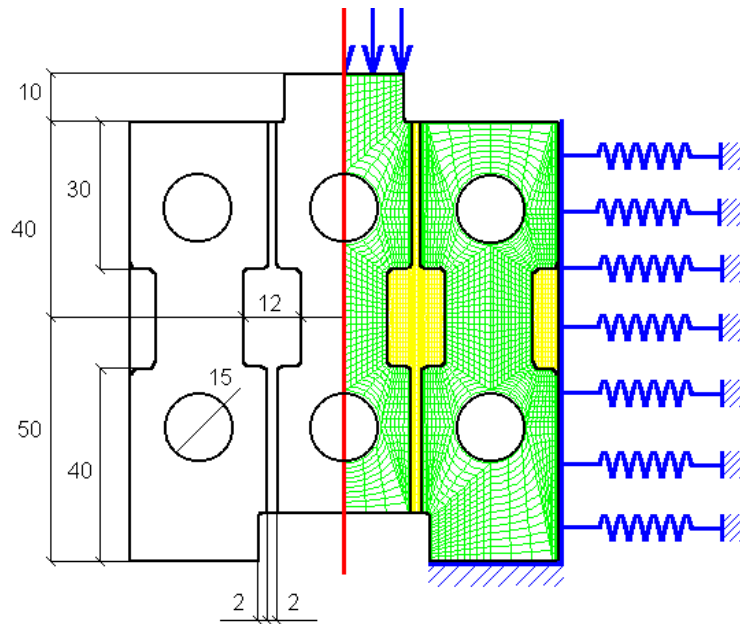
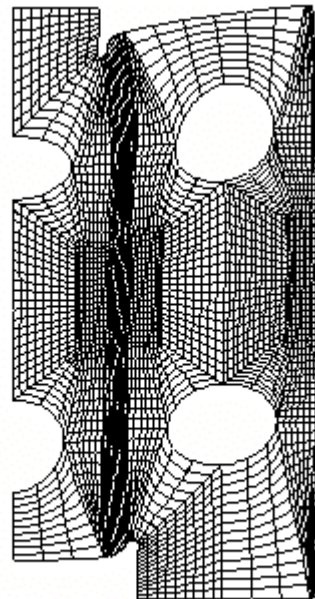


Fig. 8 Double shear sample: they are 30 mm thick, so that the stiffness at the side support is about 5.76 GN/m



DISPLACEMENT MAGNIFICATION FACTOR = 100.

Fig. 9 Displaced mesh for the TF coil insulation double shear test

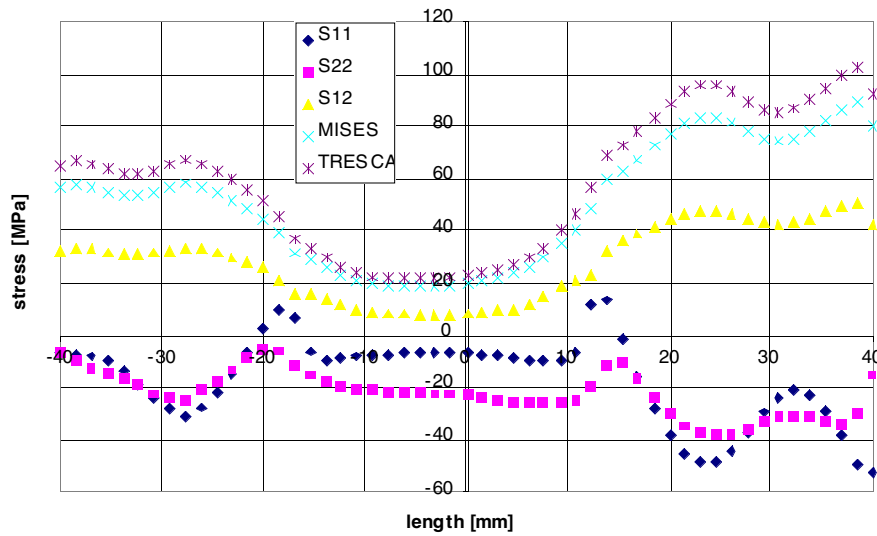


Fig. 10 Stress along the insulation of the double shear sample

In this sample the shear distribution is far from being uniform (Fig. 10) and there is a substantial normal compression in the high shear region.

4. TF coil insulation mode II crack growth test samples

The mode II crack tests are usually done using ENF (end notched flexure) specimens made only of the material that has to be tested and manufactured on purpose (i.e. with the crack in). To perform these tests on the TF coil insulation, it was necessary to start the crack first. This task has proven to be more difficult than previously thought: many samples failed before the test, when the crack was initiated. In order to limit the number of lost specimens, the sample had to be re-designed with thinner copper layers at the sides of the insulation. The samples used in the tests are 5 mm copper + 2 mm insulation + 5 mm copper, while originally the copper thickness was 10 mm (or more, in case the samples deformed excessively during the tests).

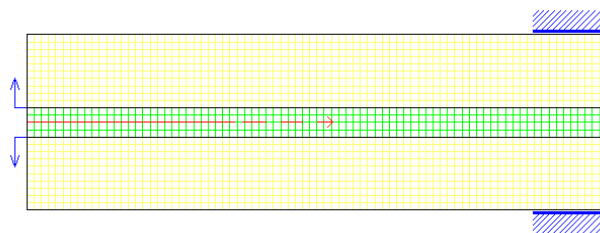


Fig. 11 5-2-5 sandwich to model the crack initiation procedure

The crack is initiated in mode I by inserting a razor blade in the insulation. This procedure has been modelled for sandwiches of different thickness: 5-2-5 mm (Fig. 11), 8-2-8 mm and 10-2-10 mm, to identify the reason for the copper/insulation frequent failures. The nodes at the razor blade have been displaced by 0.05 mm and the nodes at the clamp (35 mm down) built in. For each case the tension normal to the interface is plotted in Fig. 12. It is clear that a thicker copper layer may help in limiting the specimen deformation during the test, but results in high tension across the insulation during the sample preparation.

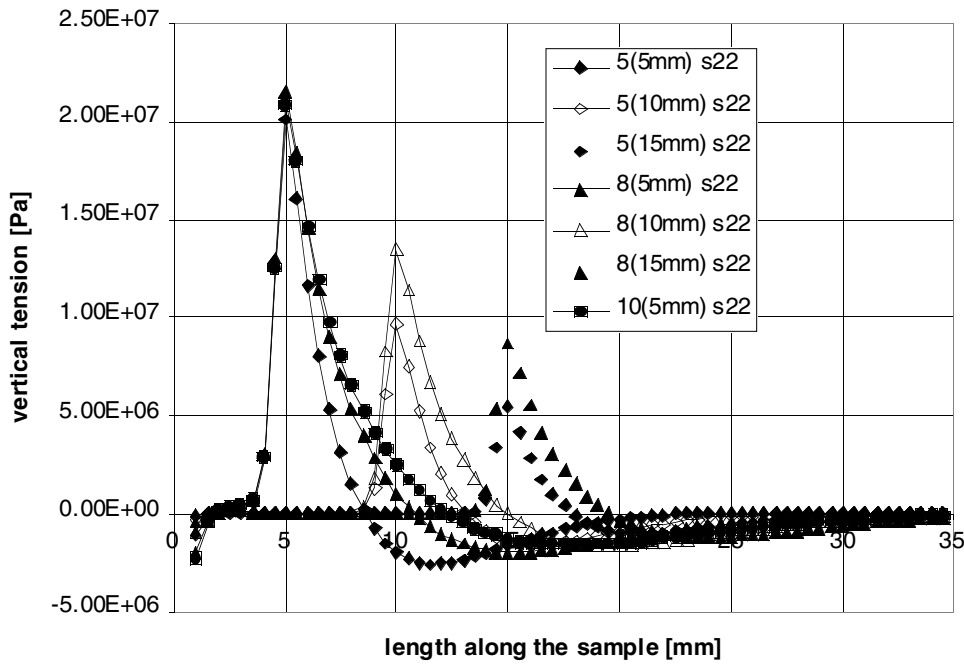


Fig. 12 Normal tension stress for different thickness/crack length combinations

4.1. FE computation of the J-integral value

The intensity of the stress field at the tip of a crack can be described by a path-independent contour integral. The definition of the integral is

$$J = \int_{\Gamma} W(\epsilon) dy - T \frac{f u}{f_x} ds$$

where

$W(\epsilon)$ is the strain energy per unit volume

T is the resultant traction force normal to the path

u is the corresponding displacement normal to the path

This formula can be evaluated directly from the stresses and the displacements on a path in a FE model, and ABAQUS has a dedicate subroutine, whose only requirement is a properly defined set of paths (usually nested rings of elements, with a singularity at the centre of the innermost ring). The value of J , for linear elastic material properties is equal to the strain energy release rate or crack extension force, G , which is linked to the stress intensity factor K : $G=\Gamma K^2$, with $\Gamma=1/E$ for plane strain and $\Gamma=(1-\nu^2)/E$ for plain stress.

This feature of ABAQUS has been used to compute the J -value of the 3-point ENF bending tests. The geometry of the model is reported in Fig. 13, the model is also plotted with the shear contour on the displaced mesh (for a load of 4228 N) in Fig. 14.

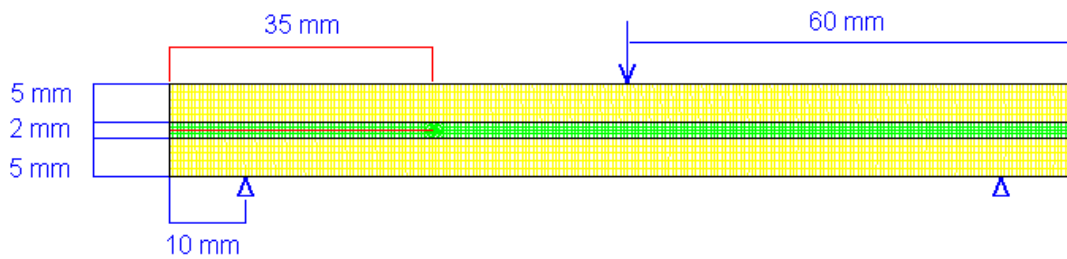


Fig. 13 Geometry, dimensions, boundary conditions and loads of the 3-point bending ENF TF coil insulation sample used in the test for the critical crack realise energy and the crack growth test

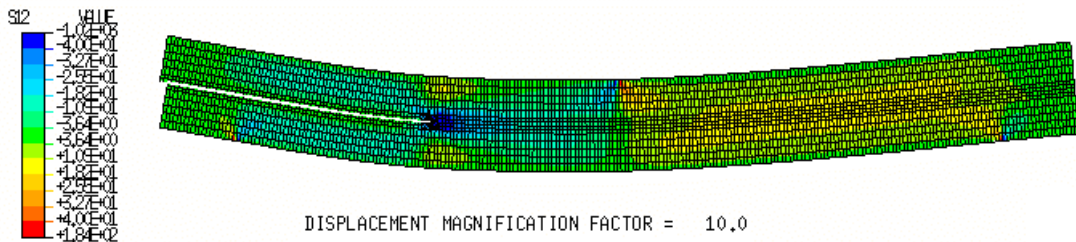


Fig. 14 Displaced mesh (with shear contours) for the 3-point bending test

The J-values computed using linear elastic properties are considered accurate as long as the plastic zone is less than 10% of the crack length, but for a load as the test load used to reproduce the preliminary NPL results (4228 N), almost half of the crack length is in plastic regime. In order to find a more accurate J-value a fully plastic (both for the copper and the insulation material properties) analysis has been carried out. The computed J-values are listed in Table 1 and the plot of the crack tip in the two cases is reported in Fig. 15.

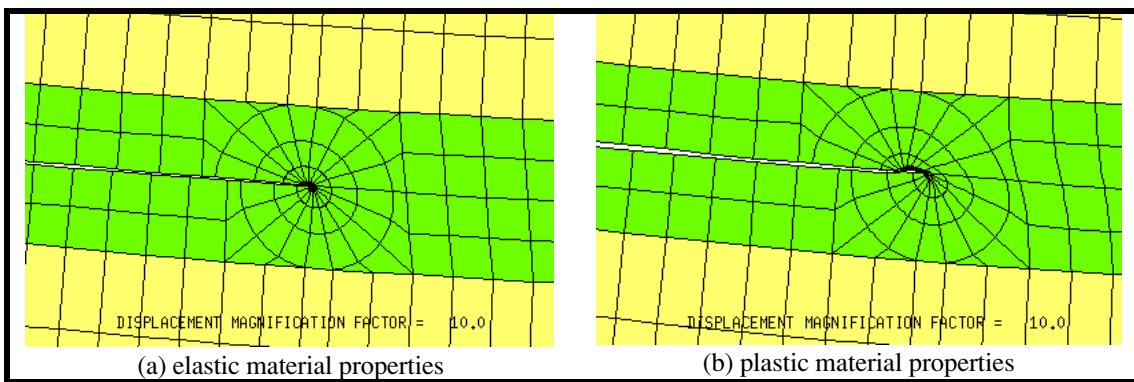


Fig. 15 Displaced mesh of the J-integral contour region

	Average J-value on contours 2-4 [N/m]
elastic material properties	1348
plastic material properties	1425

Table 1 J-integrals at the tip of the 35-mm long crack for a load of 4228 N

Stress in P1 coils

J.R. Last

26 October 1999

Contents

1. Description	
2	
2. Forces and stresses	
3	
3. Allowables	
4	
4. Analysis	
5	
4.1. Axi-symmetric 1D analysis	5
4.2. Current Scenarios	6
4.3. Summary of stresses at 4T	9
4.4. FE models	9
5. Conclusions	
11	

List of Figures

Figure 1. P1 coil assembly, showing 10 coils, upper ring and lifting ring	2
Figure 2. Von Mises stress in the copper as a function of toroidal and poloidal current for zero temperature rise	5
Figure 3. Von Mises stress in the copper as a function of toroidal and poloidal current for temperature rise of 30 C	6
Figure 4. Current waveforms & von Mises stress for 4T, 4MA pulse	6
Figure 5. Current waveforms & von Mises stress for 4T, 5MA pulse	7
Figure 6. Current waveforms & von Mises stress for 4T, 5MA pulse with disruption	7
Figure 7. Current waveforms & von Mises stress for 4T, 6MA pulse	8
Figure 8. Safe operating region for P1 coil. The P1 current has to be below the upper limit and above the temperature limit when the coil is hot. The pulse trajectory crosses the temperature limit in the early part of the pulse but this is acceptable because the coil is cool at this time.	8
Figure 9. Global finite element model of P1 coil	9

1. Description

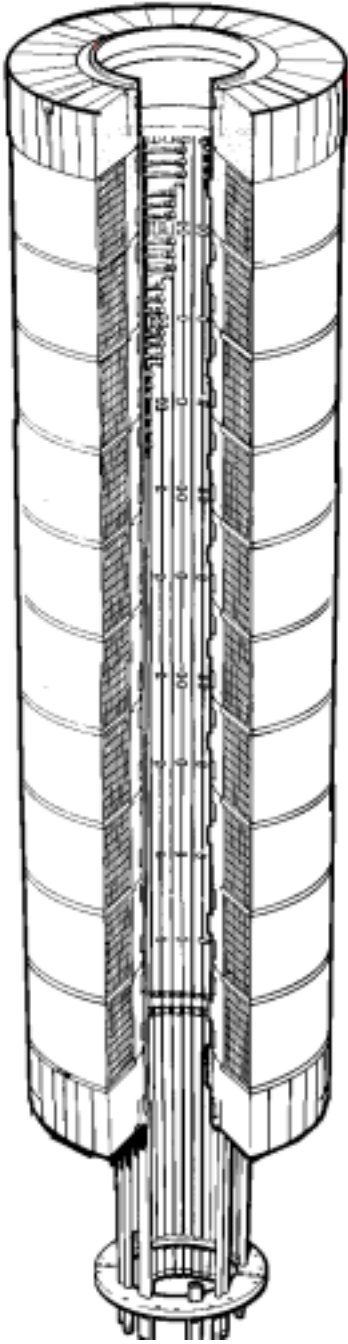


Figure 1. P1 coil assembly, showing 10 coils, upper ring and lifting ring

The P1 coils carry the magnetising current for the JET magnetic circuit (). As the central core is highly saturated at maximum field (8 T), the coils carry high current and are stressed in tension. The P1 coils also support the inward force of the TF coils, which stresses them in compression. To limit the compressive stress the coils are wound on steel support rings, which share the inward force.

The coils are made from hollow water cooled copper conductor and are insulated with epoxy impregnated glass and Kapton tapes. The insulation system is basically the same as the TF coil insulation but the Kapton improves the electrical insulation properties.

The ten P1 coils are stacked at the centre of the machine and carry the weight and magnetic loads due to the upper magnetic circuit elements. This causes compressive stresses in the coils.

Only the centre six coils support the TF inward load. As the PF and TF forces acting on the coils tend to balance each other, the centre six coils are allowed to carry a larger poloidal current than the end coils (60 kA instead of 40 kA). The JET PPCC control system limits the central coil current as a function of toroidal current and a protection system checks for unsafe operation.

EM forces on VV

V. Riccardo
26 October 1999

Contents

1. Plasma scenarios and EM forces (VV-eq).....	1
2. Plasma scenarios and EM forces (VV-dis).....	1
3. Scaling with the toroidal field.....	4
4. Modelling of the magnetic force during AVDEs	5
4.1. Description of the analytical model.....	5
4.2. Experimental observations.....	6
4.3. Validation of the magnetic model using a lumped parameter mechanical model 7	
4.4. Data analysis using the magnetic model.....	13

1. Plasma scenarios and EM forces (VV-eq)

The vacuum vessel experience the largest loads during disruption, the only load present in equilibrium is a relatively small vertical force due to the divertor coil currents (proportional to $I_p I_d$, where I_d is the signed sum of the current in the divertor coils and I_p is the plasma current), which produces a static small roll of the vessel cross section: top outwards and bottom inwards, at the Main Vertical Ports (MVPs). This produces negligible stresses on any structural component.

2. Plasma scenarios and EM forces (VV-dis)

Disruption induced loads are characterised by vertical and radial components of the order of MN, with typical time scales ranging from 20 to 60 ms. Since the installation of additional restraint rings (1989) the vessel has become quite rigid with respect to radial axisymmetric forces and, in the present configuration, the most conspicuous mechanical effects are due essentially to the vertical and the asymmetric loads. Because of the particular arrangement of the supports which block the vertical movement of the MVPs, the highest stress values in the vessel during disruption occur at the root of the MVPs in case of both vertical forces generated by Vertical Displacement Events (VDEs) and of sideways forces generated by Asymmetric VDEs (AVDEs). The stresses and movements of the vessel depend on the response of the structure to both vertical and

sideways forces, which has been analysed in a considerable number of disruptions. The analysis of the disruptive events is done, from the point of view of the acting force, using measured plasma parameters: plasma current and position, halo current, induced currents, etc.

Plasma parameters are computed using poloidal field gauges (18 pick-up coils for the poloidal field component parallel to the vessel wall and 14 saddle loops for the poloidal field component normal to the vessel; these are recorded in 4 toroidal locations at 90° apart: octants 1, 3, 5 and 7): the plasma current is the 0-moment, the vertical position is the ratio of the z -moment to the 0-moment, the radial position is the ratio approximated with the ratio of a $(R-r)$ -moment to the 0-moment, etc.

Halo current were measured with toroidal field pick-up coils at the bottom and the top of the vessel, in 2 toroidal locations (octants 3 and 7), many of which had broken during the Mk II campaigns and could not be replaced, and by instrumented mushroom tiles at the outer top of the vessel (2 in each octant).

Addition currents flowing in the vessel are measured at the restraint rings and at the divertor support structure.

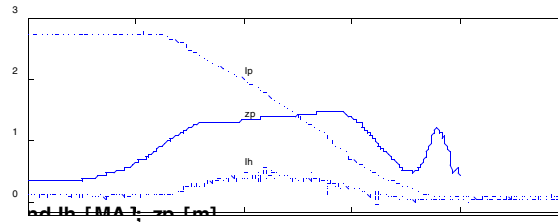


Fig. 1 (top) plasma current and vertical position and halo current and (bottom) loop voltages during the disruption of pulse 38070, $t_0=60$ s.

A typical (pulse 38070) VDE is plotted in Fig. 1. The plasma has lost its equilibrium vertical position and it has displaced upwards, while maintaining most of its current. As the plasma goes up with constant current, stabilising eddy currents are induced in the upper half of the vessel (V_{top} is positive), but as soon as the plasma current starts to decrease the vessel eddy currents invert their polarity (V_{top} negative) and they attract the plasma even more strongly. However, the plasma does not go further up, since its boundary has started intercepting the wall and part of its current has a mixed path (a fraction in the plasma and a fraction in the vessel); this is the halo current, which has always a stabilising effect: it pushes the plasma away from the wall. Meanwhile the vertical force on the vessel supports increases from the constant equilibrium value (due to the interaction of the plasma current with the divertor coil currents) to reach its maximum more or less at the time when the product $I_p \Delta z_p$ is maximum, then it quickly reverses to the now negative divertor coil force and slowly goes to zero.

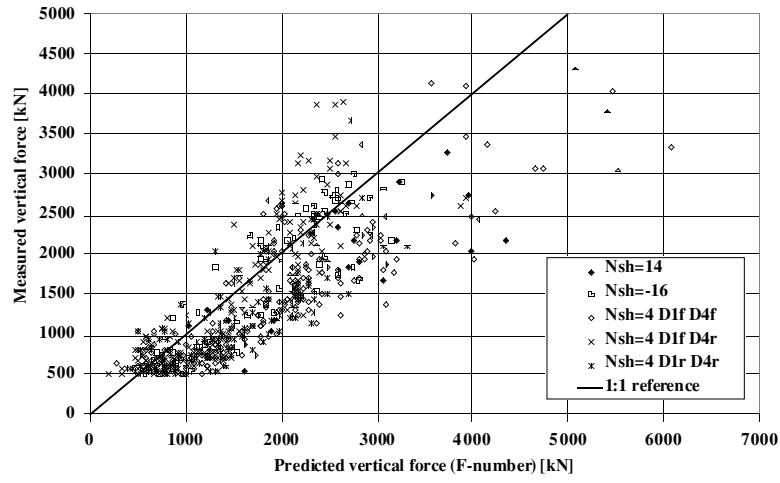


Fig. 2 Predicted (F_{number}) and measured vertical force swings during Mk IIa campaign

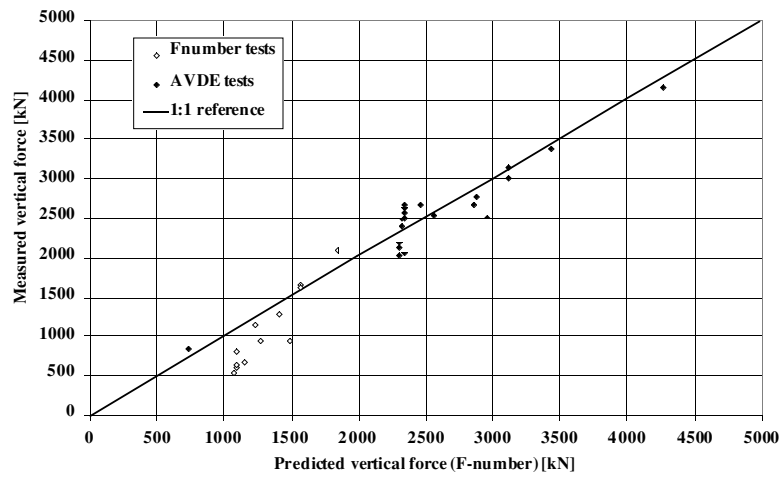


Fig. 3 Predicted (F_{number}) and measured vertical force swings during Mk IIa campaign, only for disruption tests

The vertical force acting on the vessel is due both to the poloidal component of the halo current with the toroidal field and to the change of current and radial field at the divertor coils. The vertical force depends on the change of the vertical moment during the disruption and it scales roughly with the square of the plasma current. More accurate scalings have been attempted ($F_{\text{number}}: I_p (\alpha I_p + \beta I_d + \gamma I_{EX} + \delta I_{sh})$), but their weak point is the same as the one of the simple I_p^2 -scaling: they overestimate the vertical force at high plasma current (Fig. 2). These scaling are correct in theory: high plasma current kicked VDEs fit the worst scaling (Fig. 3), but they are over-pessimistic for controlled events, when ameliorating actions are taken on the PF currents at the beginning of the VDE.

During some of the VDEs the plasma parameter measured are toroidally non-uniform, these events are AVDEs (Fig. 4 shows a typical event). They occur when the boundary safety factor decreases to a critical value, about 1, and let a mode $m=1/n=1$ start. The plasma centre of current shifts along an axis and it tilts about the same axis (Fig. 5). Because of the tilt, the plasma current is no longer parallel to the toroidal field and a net horizontal force is transmitted to the vessel via induced and intercepted currents. This force is proportional to the amplitude of asymmetry in the vertical current moment times the toroidal field. Since there is a geometrical limit to the vertical position asymmetry and a physical limit on the duration of the disruption, the worst AVDEs produce net

horizontal impulses proportional to the product of the initial plasma current times the toroidal field. For the same reason, the upper limit for the vessel sideways displacements is $I_p B_T$.

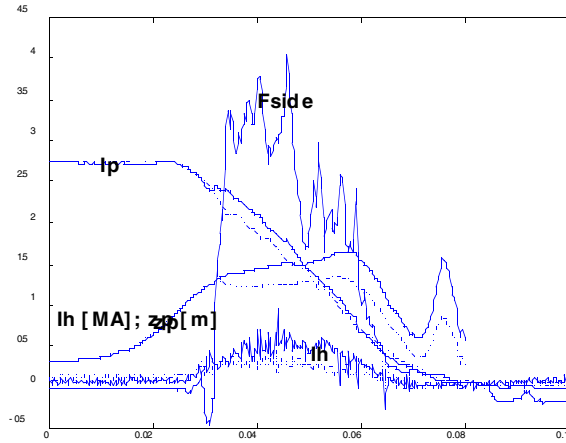


Fig. 4 plasma current and vertical position and halo current in octants 3 and 7 and the asymmetric horizontal force during the disruption of pulse 38070, $t_0=60$ s.

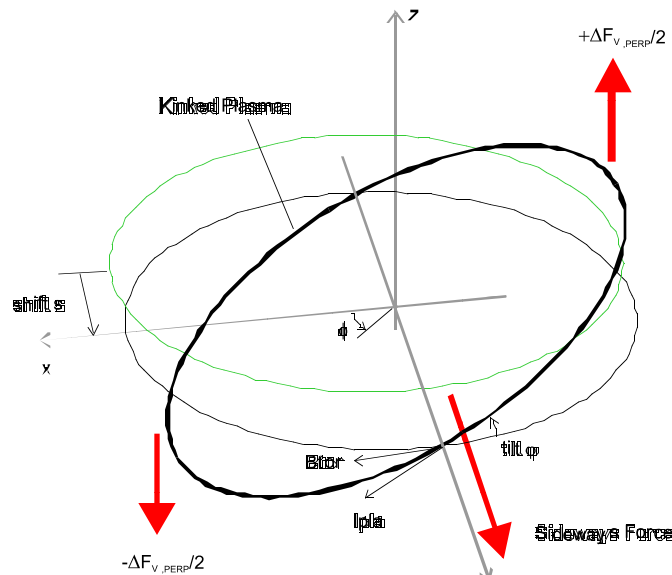


Fig. 5 Kink model for the sideways forces

3. Scaling with the toroidal field

Sideways vessel displacements are, in the worst cases, proportional to the product plasma current times toroidal field, so they scale linearly (at constant I_p) with the toroidal field.

Less clear is the effect on the rolling motion. Assuming the plasma stops displacing vertically when its boundary safety factor has decreased to 1, the maximum vertical displacement is

$$\Delta z_{p,max} \sim h - (I_p R_p^2 / (5 B_{T0} R_0))^{1/2},$$

where $h \sim 1.75$ m. Consequently an increase of the toroidal field from 3.4 T to 4. T should produce an increase of 8% in the vertical force. However there is no experimental evidence to support this thesis.

4. Modelling of the magnetic force during AVDEs

In this section a more detailed description of the model used in Section 2 is given. This is a simple model which allows the lateral forces generated during such a disruption to be estimated as a function of relatively easily obtained electromagnetic parameters: the asymmetries in the vertical current moment. This model is validated by using it to predict the displacement history of the JET Tokamak caused by a number of major AVDEs. It is shown that the predicted forces and displacements agree well with quantities measured during these disruptions. One conclusion from the model is that the maximum sideways displacement scales with the product of the plasma current and the toroidal field, and this recipe is now used at JET to assess a priori the hazards of performing high current and high field pulses when they are known to be likely to disrupt.

4.1. Description of the analytical model

The plasma is represented by a rigid current carrying ring with major radius R_0 , minor radius a and toroidal current I_0 . As suggested by measurements of the current centroid position, the current ring is assumed to be shifted by Δx along the x -axis and tilted about that axis by a small angle $\alpha = \Delta z / R_0$. The toroidal field gives rise to a force at the current ring in the x -direction and to a torque about the x -axis with the same polarity as the assumed tilt α . The force can be calculated as follows.

In the frame moving with the current ring the component of the magnetic field can be expressed as a function of R , φ and z . To the first order in the small quantities α and Δx one finds

$$\begin{aligned} B_R &\cup B_0 R_0 (\Delta x \sin \varphi - \alpha z \cos \varphi) / R^2 \\ B_\varphi &\cup B_0 R_0 (R - \Delta x \cos \varphi - \alpha z \sin \varphi) / R^2 \\ B_z &\cup B_0 R_0 \alpha \cos \varphi / R \end{aligned}$$

where B_0 is the original toroidal magnetic field at the radius R_0 , and the location of a current ring element δI_0 inside the cross section πa^2 is defined by R, z . The force in x -direction acting on the current element becomes

$$\delta F_x = \oint \delta I_0 B_z(R, \varphi) \cos \varphi R d\varphi \cup \pi \delta I_0 B_0 R_0 \alpha .$$

This is independent of R, z to the first order. The total force acting on the current I_0 through the toroidal magnetic field is therefore

$$F_x \cup \pi I_0 B_0 R_0 \alpha = \pi I_0 B_0 \Delta z .$$

Poloidal currents inside the current ring have no external stray field and give therefore no interaction forces with external magnetic fields.

The external equilibrium magnetic field causes a much smaller lateral force than the toroidal magnetic field. Before the onset of the asymmetry of the VDE the equilibrium field in the vicinity of the vertically displaced current ring can be represented by

$$\begin{aligned} B_R &\cup B_{R0} + (R - R_0) \frac{f B_R}{f R} + z \frac{f B_R}{z} \\ B_\varphi &= 0 \end{aligned}$$

$$B_z \cup B_{z0} + (R - R_0) \frac{f B_z}{f R} + z \frac{f B_z}{f z}$$

where $B_{R0} = -R_0 \left[\frac{f B_R}{f R} + \frac{f B_z}{f z} \right]$ is the radial magnetic field, which produces the global

vertical force at the plasma. This force is balanced essentially by the repelling force between the plasma and the vessel caused by the axi-symmetric part of the halo current.

When the current ring is shifted sideways by Δx and tilted about the x -axis by the angle α , the magnetic fields becomes toroidally non-uniform in the frame of the current ring. For the estimate of the lateral forces one needs only the asymmetric part of B_z :

$$\tilde{B}_z \cup \Delta x \frac{f B_z}{f R} \cos \varphi + \alpha \overline{B}_{R0} - R_0 \frac{f B_z}{f z} \sin \varphi .$$

The lateral forces acting on the current ring are

$$F_x \cup \pi I_0 R_0 \frac{f B_z}{f R} \Delta x$$

$$F_y \cup \pi I_0 \overline{B}_{R0} - R_0 \frac{f B_z}{f z} R_0 \alpha = -\pi I_0 R_0 \frac{f B_R}{f R} + 2 \frac{f B_z}{f z} \Delta z$$

The gradient $f B_z / f R$ is due to the quadrupolar component of the equilibrium magnetic field required to obtain a vertically elongated plasma shape as used in JET. If I_0 is taken as positive in the $+\varphi$ direction, $f B_z / f R$ must be negative. The force F_x therefore is opposite to the assumed lateral shift Δx . However, $|f B_z / f R|$ is less than 0.1 T/m for JET plasmas with plasma currents of the order of 3 MA, while the toroidal magnetic field at the plasma axis for the relevant radius during a disruption (2.5 m) is more than 3 T. Furthermore, the measured lateral shift is smaller than the asymmetric vertical displacement amplitude. Consequently the force F_x due to the equilibrium magnetic field is more than one order of magnitude smaller than the force F_x caused by the tilted current ring interacting with the toroidal magnetic field. The lateral force F_y caused by the tilt in the equilibrium field is of a similar magnitude as F_x caused by $f B_z / f R$ and Δx and causes a small deviation of the force direction from the tilt axis. Bearing in mind that the model is supposed to give only a coarse estimate of sideways forces it is justified to retain only the contribution due to the interaction with the toroidal magnetic field; this force can also be written as

$$F_x \cup \frac{\pi}{2} \Delta M_z B_0$$

where ΔM_z is the difference between the vertical current moment at $\varphi = -\pi/2$ and $\varphi = +\pi/2$.

4.2. Experimental observations

Use of the magnetic force model requires that the quantity ΔM_z , the difference between the vertical current moment at opposite locations, be measured. The difference in the vertical current moments is usually close to zero because the plasma is nearly always symmetric. It is substantially different from zero only during AVDEs and goes back to zero when the plasma current disappears.

Vertical current moments are obtained by processing the signals of pick-up coils (18) and saddle loops (14) measuring the poloidal magnetic field parallel and normal to the vessel surface. These instruments are present in four toroidal locations 90° apart from each other (in octants 1, 3, 5 and 7). The set of diagnostics in octant 3 and 7 is better (new electronics) than the set in octants 1 and 5, and in practice for only a few pulses reliable data have been collected in the old set of magnetic diagnostics.

Vessel displacements are recorded using Linear Variable Resistors (LVRs) in 8 toroidal locations, both at the top and bottom MVPs, and on the MHPs. Displacements quoted in magnetic model validation will be restricted to those obtained from measurements at the MVPs, as these measurements have been made from the beginning of JET operation, and provide a reliable and consistent set of data.

Each of the displacement transducers has an accuracy of ~ 0.2 mm, excluding spurious signals. The average radial displacement is measured in 8 toroidal locations, therefore the accuracy of the sideways vessel displacement measurements is at least as good as the accuracy of a single transducer, while typical displacements of interest are ~ 3 -7 mm.

The uncertainty in the sideways force measurement is significantly greater, as it relies on the measurement of the asymmetry of the vertical current moment. This is estimated using a composition of many poloidal field and current measurements. The poloidal

field parallel to the vessel wall is measured via pick-up coils, which have an accuracy of ~ 0.0015 T, while the normal component is measured via saddle loops, which have an accuracy of ~ 0.003 T.

The plasma vertical current moment, at each toroidal location of the magnetic diagnostics, is estimated as

$$\left(z_p - z_{ref} \right) \mathbf{I}_p = M_{z,p} \cup \frac{1}{\mu_0} \sum_{i=1}^{18} B_{\theta,i} z_i l_i + \frac{1}{\mu_0} \sum_{j=1}^{14} R_j B_{r,j} l_j \ln \frac{R_j}{R_{ref}} + \text{axi-symmetric terms}$$

where z_i are the vertical locations and l_i the mean distance to the two neighbours of the pick-up coils, R_j are the average radial locations and l_j the poloidal widths of the flux-loops and R_{ref} the reference radius and z_{ref} the reference vertical position ($z_{ref} = 0$). The uncertainty of the vertical current moment measurement at one toroidal position caused by the above mentioned uncertainties of poloidal magnetic field measurements is then obtained by adding up the absolute values of all the 18+14 contributions as weighted according to the formula for the vertical current moment and this is ~ 40 kAm. The same uncertainty applies for the measurements at the opposite cross section. The resulting uncertainty of the vertical current moment asymmetry, taken from the difference in opposite cross sections, could be as high as ~ 80 kAm. In addition, the effect of other currents, such as those in the restraint rings and the divertor structure, taken as axis-symmetric without being sure they are so, has to be taken into account while making estimates of the uncertainty in the computation of the vertical current moment asymmetry. However, because the locations of greatest interest here are far away from those continuous conductors, these contributions to the error are smaller than those coming from the accuracy of the poloidal field measurements. Combining these, the total the plasma current moment asymmetry uncertainty is unlikely to be larger than 100 kA·m, and with the toroidal field at the plasma centroid being about 3 T we have a resulting uncertainty of about 300 kN in the sideways force which the magnetic model predicts.

4.3. Validation of the magnetic model using a lumped parameter mechanical model

The objective is to validate the model of plasma and vessel forces by comparing observed vessel displacement histories with those which our magnetic force model would predict. This naturally requires some mechanical response model, to predict displacement dynamics as a function of magnetic force histories, and this mechanical model is outlined in the following sections. The lumped parameter model used, a combination of inertias, stiffnesses and damping elements can be assembled a set of equations (1) the solution of which predicts a radial displacement history as a function of an applied lateral magnetic force.

The first equation of the set refers to the Vacuum Vessel (VV), which is linked to the Neutral Injector Boxes (NIB), is mechanically restrained via the MVP dampers (acting both tangentially and radially) and via the MHP, and is magnetically restrained by the toroidal field; in this equation F_{sw} is the sideways force acting on the vessel because of the plasma asymmetry and $F_{friction}$ is the friction force at the supports.

The second equation describes the behaviour of the NIB.

The third and the fourth equations are for the hydraulic dampers, respectively at the MVPs and at the MHPs. The last equation describes the magnetic restraint of the vessel.

$$\begin{aligned}
& \overline{M}_{vv} \frac{d^2}{dt^2} x + k_{MVP(tg)} \downarrow x + \overline{M}_{NIB} \frac{d^2}{dt^2} x + \beta_{NIB} \frac{d}{dt} \downarrow x_{NIB} + k_{MHP} x_{MHP} + \\
& + \beta_{MVP(rad)} \frac{d}{dt} x_{MVP(rad)} + \beta_{mg} \frac{d}{dt} x_{mg} = F_{SW} + F_{Friction} \\
& - k_{NIB} x + \overline{M}_{NIB} \frac{d^2}{dt^2} x + \beta_{NIB} \frac{d}{dt} \downarrow x_{NIB} = 0 \\
& - k_{MVP(rad)} x + \overline{\beta}_{MVP(rad)} \frac{d}{dt} \downarrow x_{MVP(rad)} + k_{MVP(rad)} \downarrow x_{MVP(rad)} = 0 \\
& \overline{k}_{HH} + \beta_{HH} \frac{d}{dt} \downarrow x + \frac{\overline{k}_{HH}}{k_{MHP}} + 1 \downarrow \beta_{HH} \frac{d}{dt} \downarrow x_{MHP} + k_{HH} \downarrow x_{MHP} = 0 \\
& - \beta_{mg} \frac{d}{dt} x + \overline{\beta}_{mg} \frac{d}{dt} \downarrow x_{mg} + k_{mg} \downarrow x_{mg} = 0
\end{aligned} \tag{1}$$

definition	base value		scan values	line #
vessel mass [10 ³ kg]	M_{vv}	140	+22%, +44%	1; 2
friction force [kN]	$F_{Friction}$	250	+22%, +44%	1; 2
MVP tangential stiffness [MN/m]	$k_{MVP(tg)}$	50	+22%, +44%	1; 2
MVP radial stiffness [MN/m]	$k_{MVP(rad)}$	1000	fixed	/
MVP radial damping [MN/(m/s)]	$\beta_{MVP(rad)}$	100	fixed	/
magnetic stiffness/ B_T^2 [(MN/m)/T ²]	k_{mg}	49	-33%, +33%	3; 4
magnetic damping/ B_T^2 [(MN/(m/s))/T ²]	β_{mg}	0.41	-33%, +33%	3; 4
NIB mass [10 ³ kg]	M_{NIB}	80	-50%, +50%	5; 6
NIB stiffness [MN/m]	k_{NIB}	100	-50%	7
NIB damping [MN/(m/s)]	β_{NIB}	2	fixed	/
MHP stiffness [MN/m]	k_{MHP}	600	fixed	/
stiffness MHP hydraulic dampers [MN/m]	k_{HH}	200	fixed	/
damping MHP hydraulic dampers [MN/(m/s)]	β_{HH}	20	-50%, +50%	8; 9

Table 1 Base parameter and their scan brackets for the mechanical model

Clearly, any such few-element lumped parameter mechanical model of a structure as complex as JET can only represent its behaviour approximately. In particular, even once a qualitatively correct model has been established, comprising the right assemblage of elements, there must remain considerable uncertainty over what numerical values of parameters to employ. Based on the history of the use of the such models table 1 lists base values of parameters (masses, damping coefficients, stiffness constants and friction force).

The uncertainty on the vessel mass, and consequently on the MVP tangential stiffness and friction are mainly due to the presence of heavy diagnostics attached on the top of the vessel ports. The radial supports at the MVP have been recently refurbished and they seem to behave according to the design parameters, so no uncertainty has been placed on them. The uncertainty on the magnetic damping coefficient and stiffness constant are linked to the simplifications made to the vessel geometry and material properties in computing them. The resistance to motion of the NIB depends on the direction of the vessel displacement, so its value is uncertain. Both the structural stiffness of the MHP and the stiffness of the attached hydraulic belt are known well, while the efficiency of the dampers is less so.

There are unhelpfully many parameters to vary in the actual comparisons of measured displacements and those predicted using the magnetic model, so in the next few paragraphs we will discuss and demonstrate sensitivities. We will now compute the

vessel displacement histories caused by the predicted magnetic forces, using both these base values (in table 1), and a range values around them which reflects their uncertainties.

A typical force history, predicted by the magnetic model, is shown in figure 6, along with the corresponding displacement history predicted by the mechanical model with the base parameter set. We will now investigate how this predicted displacement history is modified by plausible variations in the values of the principal parameters of the mechanical model. What is ‘plausible’ is necessarily subjective and in itself uncertain; we have attempted to select by engineering judgement perturbations which are of similar probability for each of the various parameters.

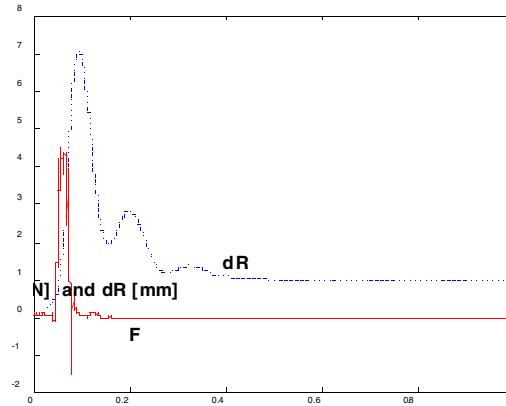


Fig. 6 The sideways force input in the lumped base-parameter mechanical model (solid line, representative of pulse 38705), which then predicts the sideways displacement (dashed line).

For a given impulsive force, the **vessel mass and support system stiffness** together are the principal determinants of the amplitude of the first oscillation. From many analyses, the natural frequency of tangential oscillations of the MVP is known with some confidence (to be 3 Hz), so we need to investigate the variation in response only as the effective mass and stiffness are changed in tandem, keeping their ratio constant. Further, in order to keep the end-offset correct, which is a function of the frictional forces between the vessel and its supports, the friction force also has to be changed with the vessel mass, in effect keeping the coefficient of friction constant.

The lines 2 and 3 in figure 7 show the response with the effective mass and stiffness changed simultaneously by 22% and 44%, with corresponding adjustment also of the frictional force. The peak amplitude changes by less than 5% and the time at which peak displacement is reached alters similarly little. These results provide some confidence that even quite a wide uncertainty in the mass has little effect on the predictions of the model, and consequently on the suitability of using the lumped parameter mechanical model in assessing the validity of the analytic magnetic model in predicting the magnetic force.

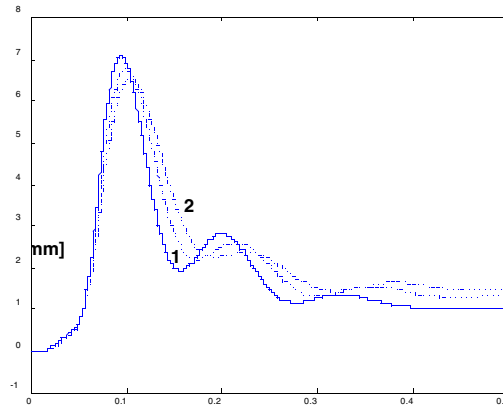


Fig. 7 Effect of the vessel mass on the displacement amplitude. The sets of parameters used are: (solid) $M_{vv}=140 \cdot 10^3$ kg, $k_{MVP(tg)}=50$ MN/m and $F_{Friction}=250$ kN; (1) $M_{vv}=180 \cdot 10^3$ kg, $k_{MVP(tg)}=64.3$ MN/m and $F_{Friction}=332$ kN; (2) $M_{vv}=220 \cdot 10^3$ kg, $k_{MVP(tg)}=78.6$ MN/m and $F_{Friction}=392$ kN.

As the vessel moves sideways, it finds itself in a different toroidal field, but the conductive walls try to screen the field variation inside, therefore asymmetric currents are induced. These interact with the toroidal magnetic field and give a force which opposes the sideways displacement. These magnetic forces scale as the square of the toroidal field and can be represented by a viscous damping coefficient and by a stiffness constant. The **normalised magnetic stiffness and damping** have been computed using a shell eddy current model to be 49 (MN/m)/T² and 0.41 (MN/(m/s))/T². Even changing them up and down by a third does not make a significant difference in the mechanical model response (figure 8).

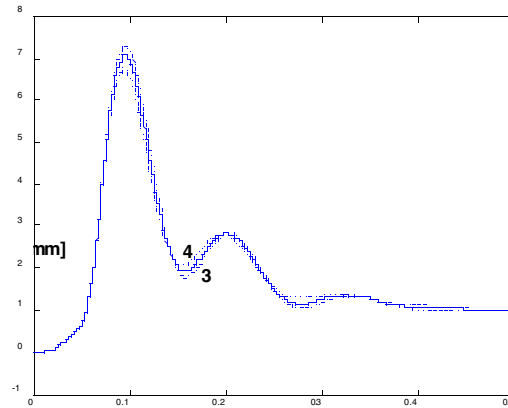


Fig. 8 Small changes are introduced by a $\pm 33\%$ variation in magnetic restraint strength. The set of parameter used are: (3) $k'_{mg}=36$ (MN/m)/T² and $\beta'_{mb}=0.29$ (MN/(m/s))/T²; (solid) $k'_{mg}=49$ (MN/m)/T² and $\beta'_{mb}=0.41$ (MN/(m/s))/T²; (4) $k'_{mg}=67$ (MN/m)/T² and $\beta'_{mb}=0.53$ (MN/(m/s))/T²

The principal influence of the **NIB mass and stiffness** is in determining the shape of second peak: the mass is linked to its height and the stiffness to the depth of the valley between the two peaks (figure 9). As is seen, the effect on the amplitude of the first peak is negligible.

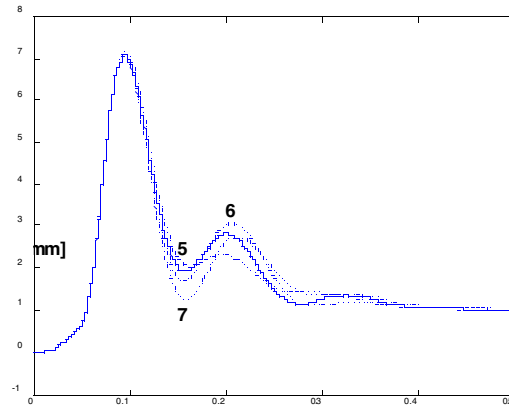


Fig. 9 NIB mass and stiffness influence on the shape of the second peak: (5) $M_{NIB}=40 \cdot 10^3$ kg and $k_{NIB}=100$ MN/m; (solid) $M_{NIB}=80 \cdot 10^3$ kg and $k_{NIB}=100$ MN/m; (6) $M_{NIB}=120 \cdot 10^3$ kg and $k_{NIB}=100$ MN/m; (7) $M_{NIB}=80 \cdot 10^3$ kg and $k_{NIB}=50$ MN/m.

The effect on the response is rather stronger for the MHP damping coefficient (figure 10), especially when β_{HH} is decreased by 50% (this produces a 13% increase in the peak of the sideways displacement), while the peak amplitude changes by less than 4% if β_{HH} is increased by 50%. Such a large variation used for the MHP damping is due to the doubts on the closeness of the system to design parameters.

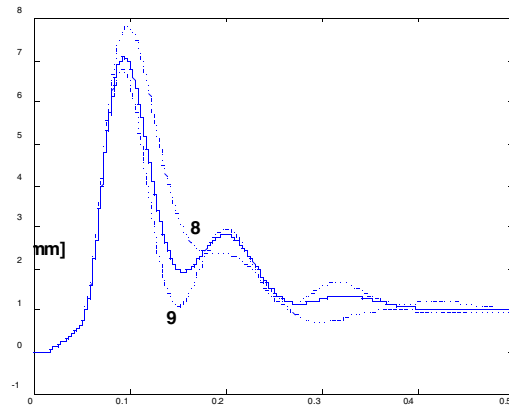


Fig. 10 Effects of varying the MHP damping by $\pm 50\%$: (8) $\beta_{HH}=10$ MN/(m/s); (solid) $\beta_{HH}=20$ MN/(m/s); (9) $\beta_{HH}=30$ MN/(m/s)

It is naturally the magnitudes of the peak displacement which are of greatest interest in assessing the threat to vessel integrity posed by AVDEs. These seem to be robustly predicted by the mechanical model, regardless of which physically plausible set of model parameters are adopted. This observation provides considerable confidence in the suitability of our subsequent use of the mechanical model in the investigation of the validity of the magnetic force model.

To perform the following stage of the validation process the same sets of parameters used in the above sensitivity analysis are used to compute displacements histories, and these histories are those compared with displacement histories as measured at the

MVPs. The input to the magnetic model is the measurement of vertical current moment differences at opposite locations, and its output a predicted lateral force history.

In figures 11a-b-c-d the force predicted by the magnetic model is shown, along with the measured displacement history, for the AVDEs of JET pulses 38705, 38070, 39207 and 39055. Our objective now is to see if the mechanical model discussed above predicts displacement histories consistent with these when given our magnetic model force history as input. For each of the magnetic force histories in figures 11a-b-c-d a set of predicted displacement histories has been computed and plotted together with the measured ones in figures 12a-b-c-d (where labels refer to the numbered parameter groups in table 1). In all cases the measured displacement histories lie fairly consistently within the range of displacement histories which the combined magnetic force and mechanical model predicts as the set of mechanical parameter values is scanned.

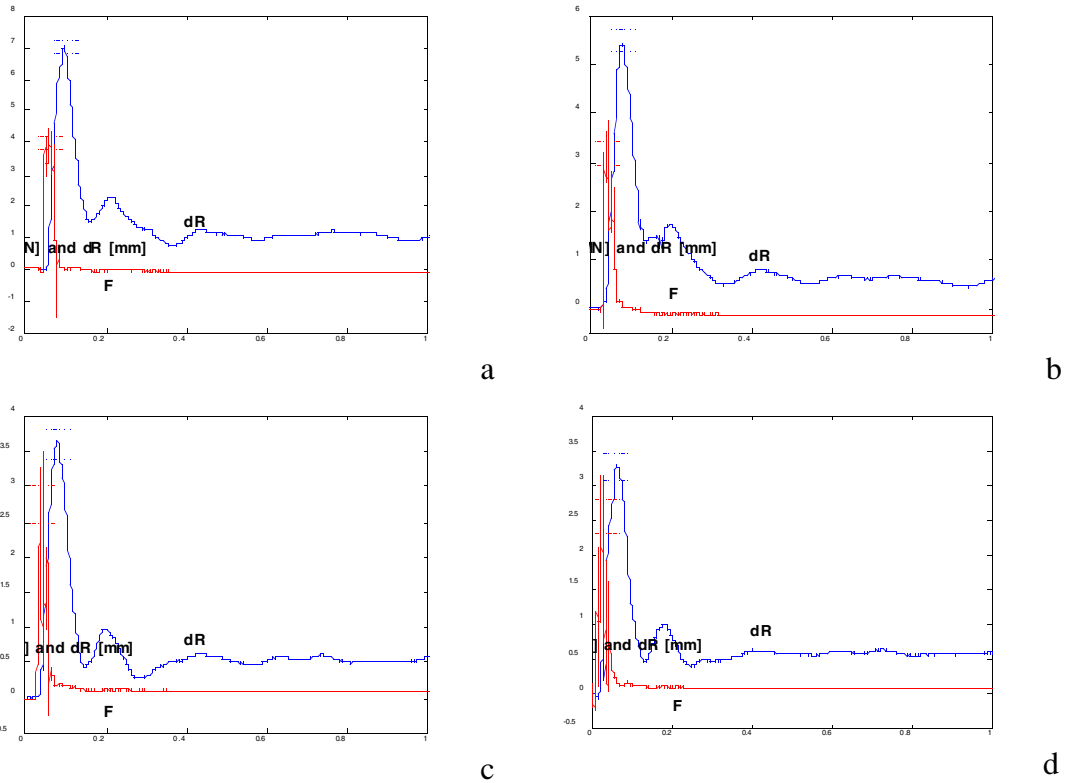
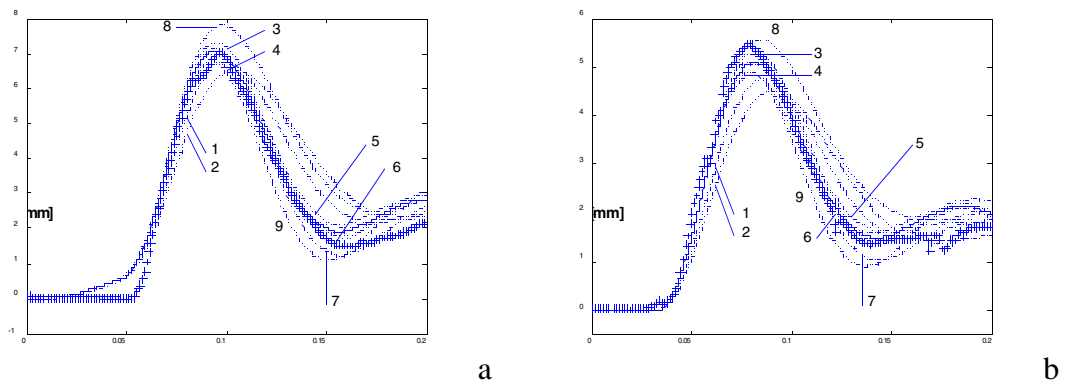


Fig. 11 Sideways force and vessel displacement for pulse 38705(a), 38070(b), 39209(c) and 39055(d), the dashed lines indicate the uncertainty bracket on the peak of the smoothed measured displacement and magnetic force



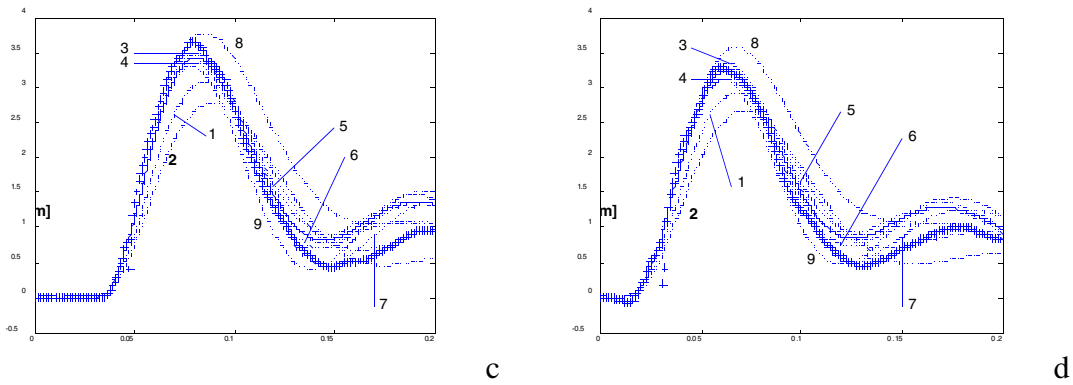


Fig. 12 Displacement history, measured (cross- points) and with parameter sets as described above for pulses 38705(a), 38070(b), 39209(c) and 39055(d)

4.4. Data analysis using the magnetic model

Time integration of the sideways force, computed from the difference between the vertical current moment at opposite locations, allows the magnetic model to be used to predict the **direction** of the impulse imparted to the vessel. This validation exercise has been done only for the few pulses where the data collected from the magnetic signals in octants 1 and 5 (the old set of magnetic diagnostics) were of acceptable quality.

Figure 13 shows the results of this comparison between analytical model and measurement. Once the predicted direction of the impulse has been computed, the co-ordinates have been rotated so that the sideways impulse vector points towards $\phi=0$. The measured sideways displacements, in this rotated co-ordinate system, are reasonably consistent with the direction of the impulse predicted by the simple model. The model's use of the difference between the vertical current moments in opposite cross sections is thus a valid predictor of the force direction.

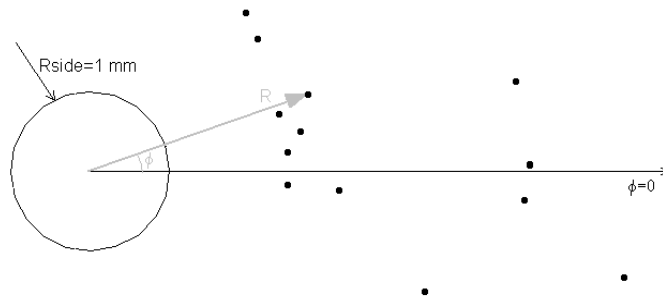


Fig. 13 Sideways displacements in a frame system rotated so that the vector force impulse points along $\phi=0$

The component of the impulse predicted by the magnetic model in a given direction (from octant 5 towards octant 1, using the magnetic data from octants 3 and 7) has been compared with the component of the (peak) vessel displacement in the same direction for a set of 40 AVDEs. The results, shown in figure 14, confirm that the two quantities are **proportional**, indicating the model is also a valid predictor of the displacement amplitude.

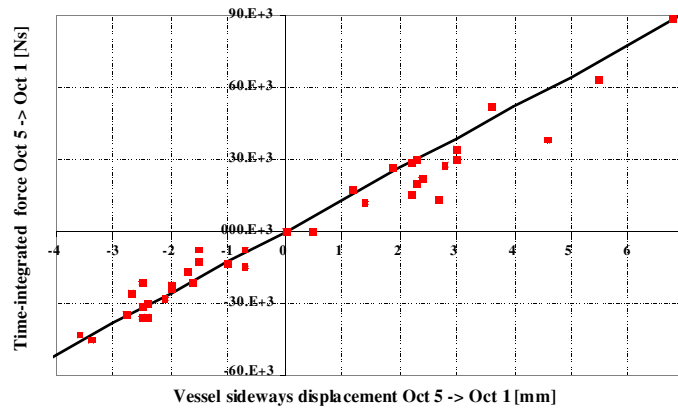


Fig. 14 Vessel sideways displacement component in direction octant 5 to octant 1 as measured at the MVPs plotted versus the sideways force impulse in the same direction as computed using the simplified magnetic model.

Modelling of the vessel movement

V. Riccardo, M. Buzio

26 October 1999

Contents

1.	Modelling of the vessel movement (Rolling)	1
2.	Modelling of the vessel movement (Sideways)	4

A number of mechanical models are used to assess critical stresses in the VV and in the associated components due to observed or anticipated events. These models are of two basic kinds:

- 1) Finite Element (FE) models, which have hundreds of thousands of degrees-of-freedom (d.o.f.) and give detailed 3D stress and deformation distributions;
- 2) simplified lumped-parameter models with three or four d.o.f., which are used to run quickly and efficiently transient simulations, including where necessary complicated non-linear effects.

These two kind of tools complement each other very effectively: for instance, FE provide accurate values of stiffness which are then used for the spring constants in the simplified models; on the other hand, lumped parameters provide for example dynamic amplification factors that can be used to assess dynamic effects on stresses and displacements obtained from the FE.

1. Modelling of the vessel movement (Rolling)

This kind of oscillation is induced by the vertical force impulse generated by the vertical displacement of the plasma and subsequent current quench. Due to the off-set of the vertical force (Fig. 1) from the vertical supports of the MVPs and the additional restraints, the inboard side of the vessel starts oscillating vertically. The vessel cross section is deformed, causing a radial oscillation of the MVPs. Inertia effects of the attached masses and radial dampers connected to the MVPs give rise to radial forces on the MVPs and peak strains at their root.

The rolling motion response of the vessel to vertical forces has been analysed statically and dynamically with the help of FE models and lumped-parameter models. A NASTRAN axis-symmetric FE model for half-octant (Fig. 1) has been used to investigate the basic behaviour of the vessel under static and dynamic axi-symmetric loads and as the basis to refine the lumped-parameter model of the rolling motion. In addition, an extensive range of static and dynamic simulations has been carried out with

the lumped-parameter model to assess preliminarily the effects of possible modifications to the support system in order to reduce peak stresses due to vertical vessel forces.

The NASTRAN model includes approx. 3500 shell and beam elements and it is able, with the appropriate symmetry boundary conditions, to represent axi-symmetric deformations of the vessel. Results indicate that vertical forces are the main cause of the rolling motion and that the actual position of the force matters little on the global deformation pattern. In particular, local stresses where loads are applied tend to be smaller compared with the concentration peak at the root of the MVP. The NASTRAN eigenvalue decomposition capability has been used to calculate the vessel natural frequencies. As usual in the study of free, lightly damped vibrations, linearity of the structure is assumed and dissipative effects are neglected (in particular the non-linear nature of the hydraulic dampers is not taken into account). Most of the first modal shapes are related to local deformations of the IVPs and the bellows (the more compliant parts). The second mode, however, represents exactly a rotation of the vessel about the major axis and it is very similar to the deformed shape obtained from static loading cases. The natural frequency matches precisely the experimental values, varying in the range from 14 to 17 Hz depending on the presence of the diverter and of the MVP supports. For these reasons, the single d.o.f. represented by the second natural frequency is usually associated to the rolling motion. The participation of this mode in the response of the vessel has been quantified by means of a comparative series of dynamic NASTRAN runs. These have been carried out with reference loads representative of the typical disruption conditions, characterised by a frequency content not exceeding 100 Hz, using both available methods of dynamic analysis (i.e. the modal superposition, where a specified number of eigenmodes is used to set up a reduced-order set of uncoupled dynamic equations; and the direct transient, which integrates the full matrix system and is therefore equivalent to use all the modes at once). Assuming that the direct integration gives the “true” response, the superposition of a small number of modes will result in a relative error both in the peak-to-peak displacement and in the support vertical force; using only the rolling mode these errors are respectively 0.5% and 30%, while using 20 modes they become 0.1% and 0.5%. These results confirm that the rolling motion can be approximated to a very good degree of accuracy by a single d.o.f. system like the one used in the lumped-parameter model. The less satisfactory approximation of the support force indicates that a more accurate model, possibly including additional d.o.f.s, would be appropriate.

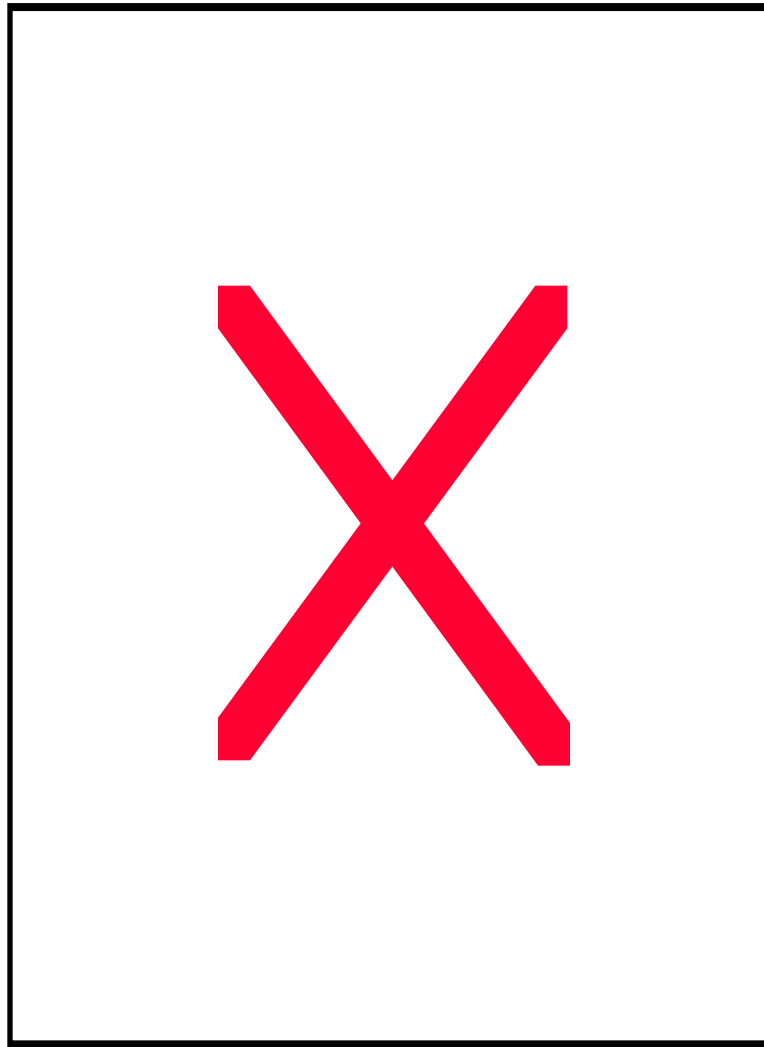


Fig. 1 FE model showing the rolling motion, some of the supports and of the available mechanical diagnostics

Static and dynamic FE calculations show that:

- as all the main ports are prevented from moving vertically, the bulk of the vessel appears to rotate around a pivot point (midplane on the vertical passing through the MVP supports)
- the rotation is due to a torque about this pivot point which, in turn, can be thought of as generated by a vertical force at a given distance from the pivot itself.
- the vertical load is reacted mainly by the MVP supports: the OJ and MHP supports, being relatively soft and close to the pivot, take only a small part (~3%) of the force.

On the basis of these considerations, it is possible to lump the structural mass into three rigid bodies able to translate and rotate in the poloidal plane. This arrangement is the simplest to be kinematically consistent with the deformed shape, as obtained from the FE model, and the external restraints. Note that relative movements between vessel bulk and MHPs are constrained, so that the pair behaves effectively as a single d.o.f., and being the movement of the MHP small the dynamic of the system can be approximated by just two equations. The use of a second d.o.f. seems to contradict the statement that the rolling motion is dynamically equivalent to a single d.o.f., but in practice the port stiffness is so high that its deflection is less than 5% of the total port displacement and corresponding to a eigenfrequency of 90 Hz, which is undetectable from the experimental data.

All the spring stiffnesses used in this model have been computed using the NASTRAN FE model, and according to the results of sensitivity analysis, these calculations have a nominal accuracy of 5%. The non-linear damping at the MVP hydraulic dampers is modelled representing the force with an hyperbolic tangent, to smoothen the transition from parabolic medium-velocity response and constant high-velocity response. This model for the rolling motion has been used extensively to analyse the dynamics of the radial oscillations of the MVPs during disruptions. Forces, displacements and peak plastic strains have been extrapolated to future scenarios, including 4T/5MA.

The base of the MVPs is the most critical area for stress concentration due to port bending, because of the presence of a 90° re-entrant corner. A separate detailed non-linear FE ABAQUS model has been used to determine peak plastic strains due mainly to dynamic loads during radial oscillations. This model has been further refined with volume elements in the critical area and the interface with the larger overall model, defining the boundary conditions, is being enhanced. Results indicate that, for the same load conditions, previous results were conservative. This detailed analysis of local stress concentration is used, in conjunction with new experimental fatigue tests, to assess with more precision the amount of fatigue life consumed in the component.

Radial displacements and forces at the MVPs given by these models have been compared with the real values given by experimental data. The electromagnetic force on the vessel has been derived from the MaxFEA code using measured vertical displacement of the plasma and current decay and extrapolated to higher currents. The maximum vertical force computed at 5 MA / 4 T is 10 MN (peak to peak).

The response of the vessel to asymmetric loads has also been addressed, by using a 180° FE model (Fig. 2) and a Simulink model. It has been shown that the torsional stiffness of the vessel has a great beneficial effect in equalising the response. For instance a non-uniform vertical force with peaking factor 2 (where the peaking factor is defined as the ratio of the maximum value over all octants to the average value) would produce port displacements, and hence stresses at the root of the ports, with a peaking factor of about 1.2.

In no case observed to date has the maximum rolling motion of an octant exceeded the predicted value obtained using MaxFEA in conjunction with the FE mechanical models.

2. Modelling of the vessel movement (Sideways)

Considerable sideways horizontal movements have been observed in the past, also after new horizontal restraints on the MHPs have been installed (1996), even if analysis shows that these restraints are working as expected from design, supporting up to 800 kN sideways force. With these new restraint in place the horizontal movement is much more damped than it was with the MVP dampers alone. Magnetic damping has been found as one of the restraining forces, especially in the beginning of the displacement. In addition, the vessel shows a residual displacement up to 1.5 mm after a large sideways event. This indicates friction of the order of 150 kN. It follows from these findings that the horizontal forces applied to the vessel by the disruption are about double than those originally assumed.

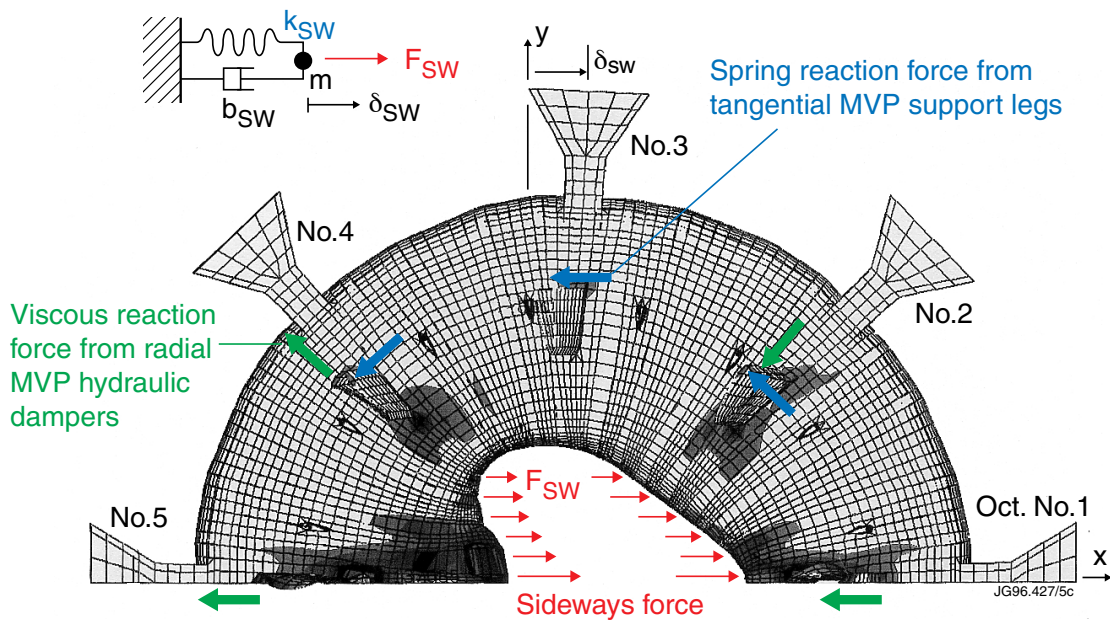


Fig. 2 FE model of 180° of the VV showing the sideways deformations.

A NASTRAN FE model covering 180° of the vessel (Fig. 2) has been used to further investigate the effects of non-axis-symmetric loads giving rise to sideways movements. Several load conditions have been analysed, each characterised by different degrees of concentration of the sideways force determined on the basis of different assumptions on the toroidal and poloidal distribution of halo currents, taking into account dynamic factors determined on the basis of the modal response of the structure. Concentrated loads give rise to additional stresses in the bellows, which are bridged by short beams working only in compression which may be opened up by magnetic load exceeding locally atmospheric pressure. These stresses have been accurately calculated and have been found to be in the elastic range for all considered cases up to the worst-case reference 8 MN×20 ms @ 5MA/4T.

Lumped parameter models for the sideways motion have been used to provide detailed information on the dynamics of the vessel during sideways events, highlighting in particular the predominant role of magnetic effects in the observed damping. Simplified models have been developed, taking into account the MVP radial hydraulic dampers, the MHP tangential hydraulic restraints, the magnetic damping and friction effects.

The models have also masses representing the Neutral Beam Injector (NBI) units, which are free to move along radial rails and which follow partially the movement of the vessel in the horizontal plane. This refinement has allowed to predict the dynamic forces transmitted between vessel and NBIs during the oscillations, also including backlash and friction effects.

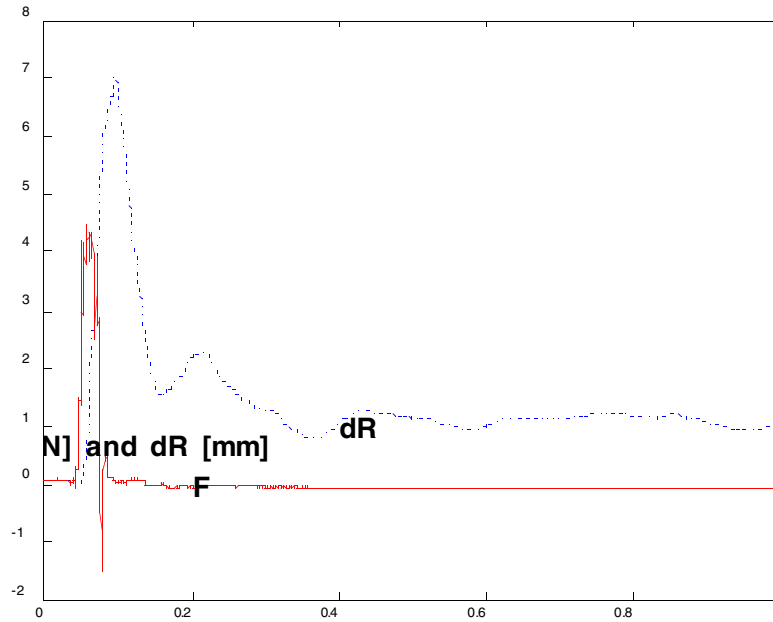


Fig. 3 Sideways force computed using the current ring model and measured vessel displacement for pulse 38705 (starting time 56.8 s)

Assuming a typical disruption pulse of 20 ms, the model indicates that a horizontal acting force applied to the vessel has to be of the order of 4 MN to produce the record displacement of 7 mm observed in pulse 38705 (which gave 7 mm at the MVPs and 6 mm at the NIBs and a global sideways reacting force of 15 MN), this force is in good agreement with the sideways force computed from experimental magnetic data according to a simple current ring model (Fig. 3). Assuming a rigid plasma ring kinked ($m=1/n=1$) it is in fact possible to calculate the plasma tilt angle from the magnetic measurements and the corresponding horizontal forces applied to the vessel. The force impulse has been found to correlate satisfactory with the sideways motion in a number of disruptions, both in direction (Fig. 4) and in amplitude (Fig. 5). According to this model, the maximum sideways displacement is anticipated to scale at worst with the product of plasma current and toroidal field. The present data best supports this scaling, however the kink mode, which causes the horizontal forces may be more stable at high fields and a more favourable scaling would apply. Extrapolating from the present data base to high current and high field operation gives 15.6 mm vessel side movement at 5 MA 4 T, but none of the high field high current pulses run so far has gone any close to this scaling: it has to be reminded that disruptions leading to substantial sideways displacements are very rare and that they need a series of conditions (initially slow current quench, large vertical displacement of the plasma, critical safety factor at the boundary, long locked kink...) to be satisfied before hand to free their potential danger.

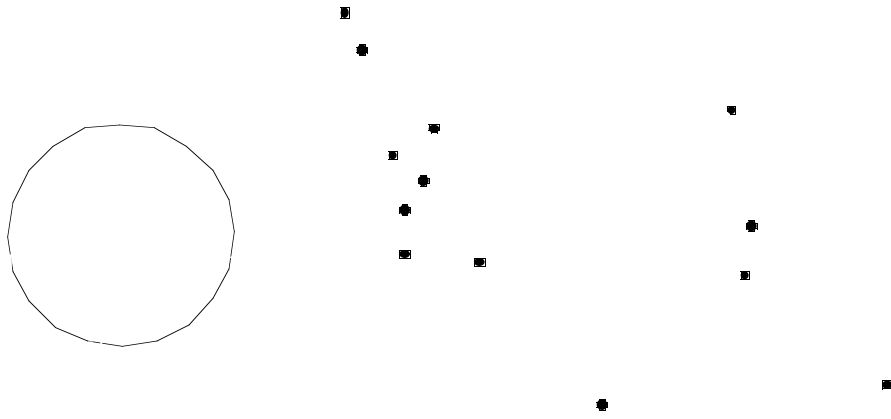


Fig. 4 Sideways displacements (the reference radius is set at 1 mm) in a frame system rotated so that the vector force impulse points towards $\phi=0$

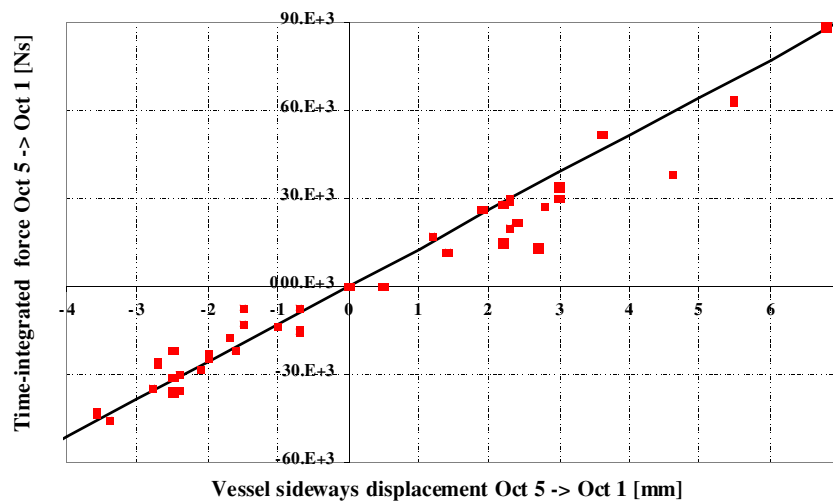


Fig. 5 Vessel sideways displacement in direction octant 5 to octant 1 as measure at the MVPs plotted versus the sideways force impulse in the same direction as computed using the simplified model, the straight line is the one which fits the largest vessel sideways in that direction (pulse 380705, 6.9 mm)

The damping effect due to the magnetic field has been evaluated analytically in a simple configuration, then used to benchmark a FE code, which was subsequently exploited to compute the effects of the magnetic damping on the actual vessel geometry and lumped material properties. This code/model gives a normalised magnetic stiffness constant of 50 MN/m/T^2 and a normalised magnetic damping coefficient of $0.4 \text{ MN}/(\text{m/s})/\text{T}^2$. A new procedure for systematic matching of the simulated response with measurements has shown, in particular, that the values of 4.9 MNs/m for the magnetic damping and 70 MN/m for the magnetic stiffness (both of them at $B_T=3.5 \text{ T}$) are in good agreement with both independent electromagnetic calculations and observations.

A final remark should be done on the superposition of rolling motion and sideways displacement: combining the sideways and the rolling, the latter is decrease by a factor of about 0.5 to take into account its larger frequency (14 Hz vs. 3 Hz) which prevents the maximum values of the two movements from occurring at the same time. The worst possible combination of rolling motion and sideways displacements for a 5 MA 4 T pulse would produce a local strain at the MVP root of 0.3%, leading to a fatigue life of about 800 disruptions (Table 1).

	Ip [MA]	max. ampl. rolling [mm]	max. sideways [mm]	rad. Force VDE only [kN]	rad. force AVDE only [kN]	rad. force comb. cycle [kN]	$\epsilon\%$	cycles
Opt. Shear	4.0	4.2	12.5	67	62	+129/-95	0.18	3000
ELM free	4.3	4.8	13.4	77	67	+144/-105	0.20	2400
ELMy-H	5.0	6.5	15.6	104	78	+181/-130	0.29	800

Table 1 Estimated number of life equivalent to worst case disruptions for the three scenarios selected for 4 T operation, with combined VDE+AVDE including a stress concentration factor of 1.5; for a VDE only the strain is about 60% of the stated value

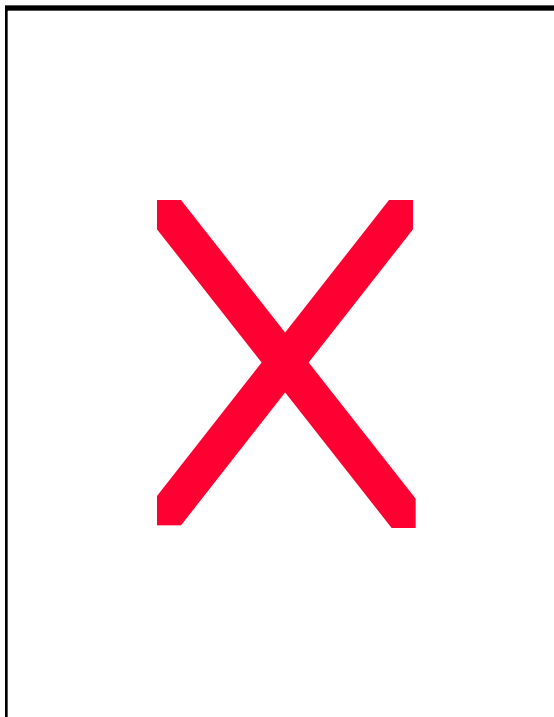
Machine measurements during plasma instabilities

V. Riccardo

26 October 1999

Contents

1. Machine measurements during plasma instabilities (Rolling)	2
2. Machine measurements during plasma instabilities (Sideways)	3
3. Correlations between plasma parameters and vessel sideways displacements	4
3.1. Pre-disruption parameters.....	4
3.2. Disruption parameters.....	6



The reacting force is measured at the MVPs by 8X4X2 strain gauges (4 double at each octant, each pair is set on the dampers, left and right of the ports) and at the Main

Horizontal Ports (MHPs) with 8X2 pressure gauges (a pair each hydraulic damper). The vessel movements are monitored using 8X2 Linear Variable Resistors (LVRs) at the MVPs in radial direction and 8X2 LVRs at the MHPs in radial and tangential direction.

1. Machine measurements during plasma instabilities (Rolling)

The rolling motion is the difference between the radial displacement of the top and the bottom MVPs. It usually axis-symmetric (toroidal peaking factor <1.2).

The rolling motion signal usually looks like a damped sine wave, typical of a single d.o.f. oscillator. This is confirmed by the Fourier analysis, which shows a marked peak at the frequency of 14 Hz; in addition the spectral energy content vanishes rapidly for frequencies higher than 30 Hz. The rolling motion frequency has changed during the years in the range 9-18 Hz, following changes of the support stiffness and mass distribution inside and outside the vessel.

The vertical force at the MVPs show the same pattern as the rolling motion, with a clearly pronounced peak at 14 Hz and no contributions above 30 Hz. In some cases, however, a much smaller peak at 25 Hz can be detected. This seems to suggest that a high frequency mode, related to the vertical deformation of the vessel, may contribute to the vertical support force even if it does not appear in the rolling motion. As the MVP stresses depend essentially on the radial movement of the port and not on the vertical force, this contribution is usually disregarded.

This motion is proportional to the vertical force (Fig. 1), with a proportionality coefficient depending on the MVP-dampers characteristics (Fig. 2). Consequently the rolling motion is roughly proportional to the square of the disruption plasma current (Fig. 3).

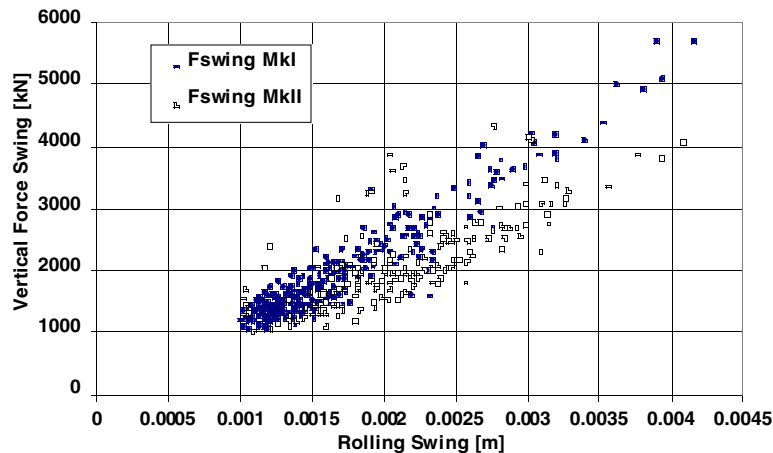


Fig. 1 Vertical force swing versus rolling motion: there are two slopes (MkI and MkII) depending on the characteristics of the MVP-dampers

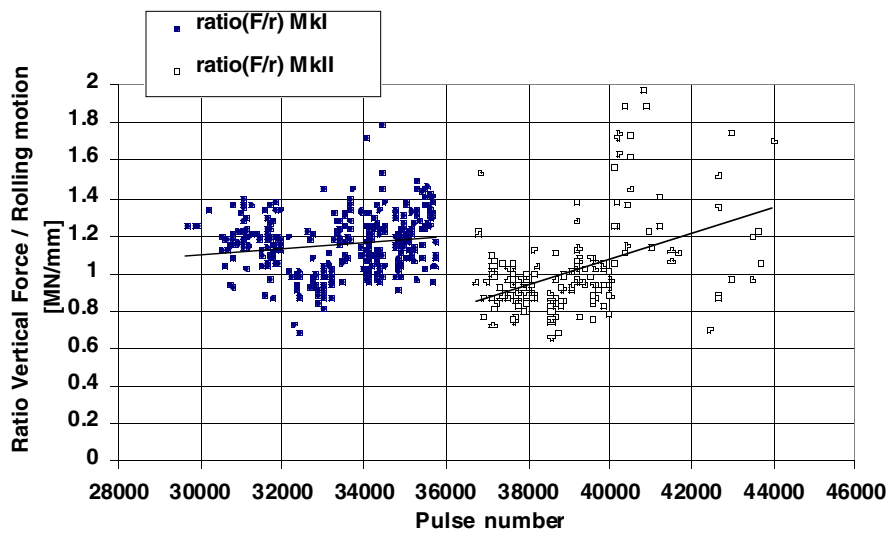


Fig. 2 Ratio rolling motion to vertical force in MkI and MkII campaigns

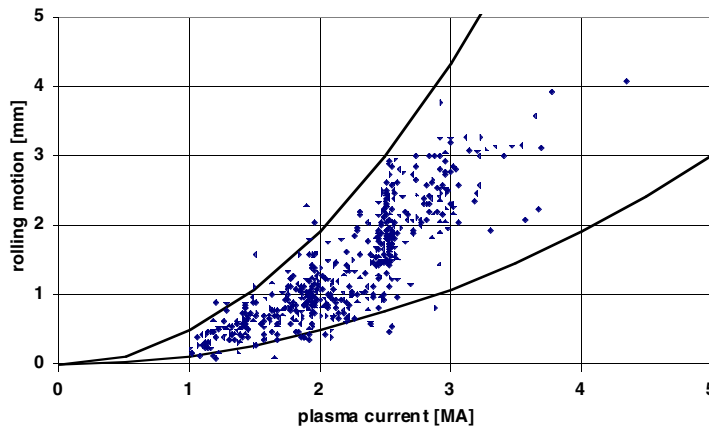


Fig. 3 Rolling motion versus plasma current, reference lines $0.12 I_p^2$ and $0.48 I_p^2$

2. Machine measurements during plasma instabilities (Sideways)

The sideways displacement can be measured at the MVPs, by composition of the radial average (top plus bottom half) octant displacement, and at the MHPs, by composition of the radial displacements. When the vessel moves sideways, also the tangential MHPs displacements show asymmetries, but they are smaller than those measured in the radial direction, as effect of the horizontal hydraulic belt: the vessel at the MHPs has a drop shape when it goes sideways.

In case of sideways events, individual measurements taken at each port show clearly the superposition of a slower oscillation on the top of the rolling motion pattern. The composed sideways motion signal is usually characterised by a single, heavily damped low-frequency half-cycle followed by smaller fluctuations. The identification of the fundamental frequencies is complicated by the fact that, theoretically, the Fourier spectrum of a critically damped sine is a uniformly decreasing function of the frequency without clearly defined peaks. In real cases, the Fourier spectra of the sideways displacement and of the support horizontal force show a small peak in the region around 5 Hz, revealing that the underlying frequency component has a damping slightly below the critical level. This peak can be artificially enhanced by removing the “trend” from the signal (i.e. by subtracting the line going from the start to the end point). Doing so, additional small peaks appear in the spectrum, this correspond to the oscillation in the

last part of the signal, which may be interpreted as due to the dynamic of NIB units or higher order structural eigenmodes. As in the case of the rolling motion, the energy content becomes negligible above 30 Hz.

The sideways displacement has an upper limit in the product of the toroidal field times the plasma current prior to the disruption (Fig. 4): only locked AVDEs lay on this upper envelope.

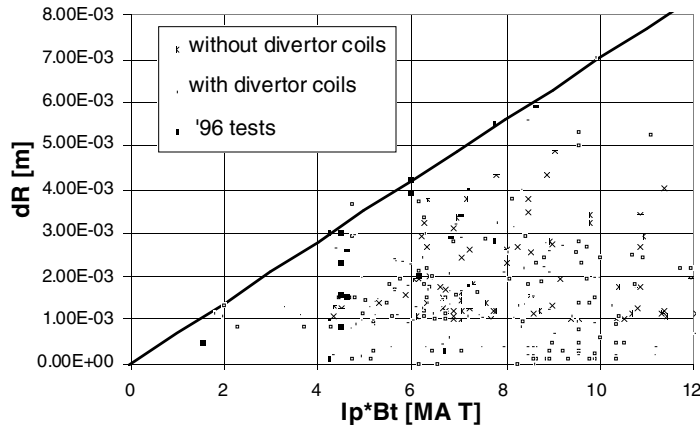


Fig. 4 Sideways displacement versus plasma current times toroidal field, reference line $0.7 I_p B_T$

3. Correlations between plasma parameters and vessel sideways displacements

Attempts have been made to identify associations between plasma parameters and large asymmetric vessel displacements, by analysis of data from some hundreds of disruptive JET pulses. In particular some days of operations have been devoted to this study in the autumn of 1996.

As far as the pre-disruption parameters are concerned, the amplitude of vessel sideways displacements shows a trend with the boundary safety factor and the poloidal beta. No link has been identified with the plasma triangularity or elongation.

With regard to plasma parameters during the disruption, the data show a trend with the amplitude of the instability mode $n=1$, and a trend with the plasma current quench rate and the minimum value of the boundary safety factor.

Hardly any practical operational space has been found to be wholly safe from triggering such vessel sideways displacements.

3.1. Pre-disruption parameters

The analysis results presented in the following will show that amongst the pre-disruption plasma parameters, the amplitude of the sideways displacement at the end of the plasma instability shows a clear trend with the boundary safety factor and the poloidal beta. Initial links with plasma upper triangularity could not be confirmed, probably because the data set used in the first analysis was biased by the fact that high triangularity plasmas were also high poloidal beta plasmas (as the increase of the plasma pressure, roughly proportional to the poloidal beta, has this shaping effect). Indeed high poloidal beta, as it will be shown later, is linked to the amplitude of the vessel sideways displacements. In addition no significant correlation between pre-disruption plasma elongation and amplitude of the sideways displacement has been found.

The data collected on the **boundary safety factor** are measurements of the cylindrical approximation of q_{05} (i.e. safety factors computed on the plasma surface where the

normalised poloidal flux is 0.95), since the presence of the X-point makes inaccurate the computation of the actual boundary factors.

A reduction of the boundary safety factor can occur during VDEs when the plasma cross section shrinks faster than the plasma current falls, due to the plasma being pushed to the wall. For any given plasma current, when the safety factor prior to the disruption is large it seems plausible that the VDEs will produce only small vessel displacements, because there is a large margin in the safety factor before it reaches a small enough value to trigger the first poloidal mode. This trend is shown in Fig. 5, where the normalised (to the product of the plasma current times the toroidal field) sideways displacement is small when the boundary safety factor prior to the disruption is larger than 3.5. In addition, the amplitude of the normalised sideways displacements seems not to depend on the pre-disruption safety factor (when this is in the range 1.5 to 3.5) and among the many disruptions analysed only a few give rise to a large vessel asymmetric motion.

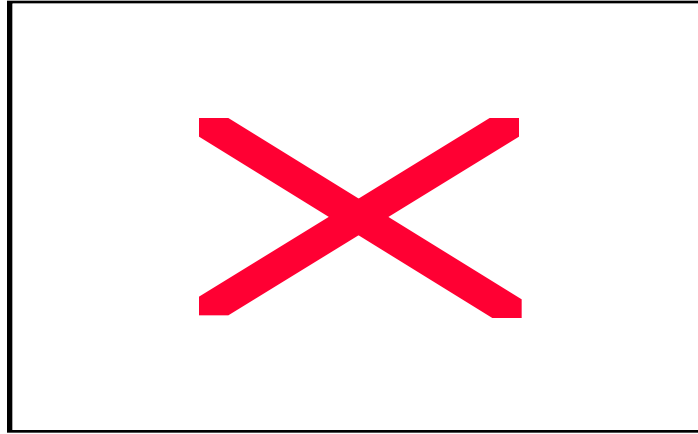


Fig. 5 Normalised sideways displacement versus the boundary safety factor before the disruption

The definition of the **poloidal beta**, β_p , retrieved in the statistical analysis is the following

$$\beta_p = \frac{\int p \, dS / \int dS}{B_{\theta a}^2 / 2\mu_0},$$

where the integrals are surface integrals over the poloidal cross section and $B_{\theta a}$ is the poloidal magnetic field at the plasma boundary (taken as $\mu_0 I / l$, if l is the length of the poloidal perimeter of the plasma).

The value of β_p determines the displacement of the plasma when the control of its position is lost: it is usually observed that the larger is the β_p the bigger is the inward jump the plasma will make. When moving away from the equilibrium position the plasma finds a frozen externally imposed poloidal field different from the one at the equilibrium position. Depending on this field the plasma may be pushed upwards or downwards. The first consequence of a large β_p is an immediate strong interaction with the inner wall due to the inward jump. This produces impurities which cause a faster current quench because of the increased resistance. That high poloidal beta plasma do not produce slow disruptions is clear in Fig. 6, where the plasma energy, proportional to $\beta_p I_p^2$, is plotted versus the plasma current time derivative. The second consequence is a larger push away from the vertical equilibrium position. Of the two effects the predominant is the fast current decay, which prevents the critical boundary safety factor being reached.

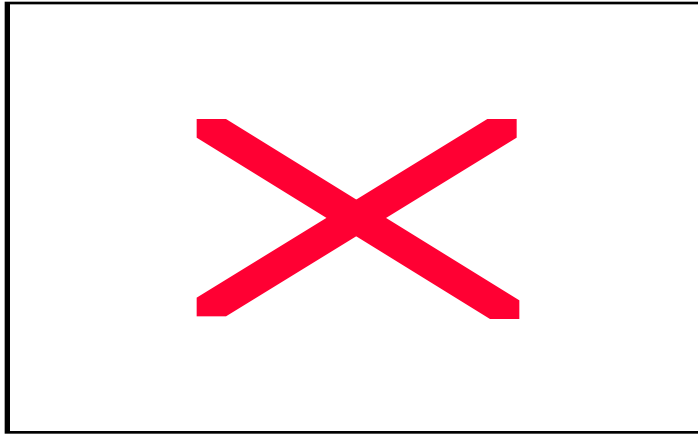


Fig. 6 Plasma energy versus plasma current quench rate

A plasma with a small β_p has better chances to survive the energy quench jump, because its inward jump is smaller and unlikely to cause a substantial production of impurities. Consequently the plasma starting the disruption with a small β_p has a higher probability of producing an AVDE and then to cause the vessel sideways motion. This is supported in Fig. 7.

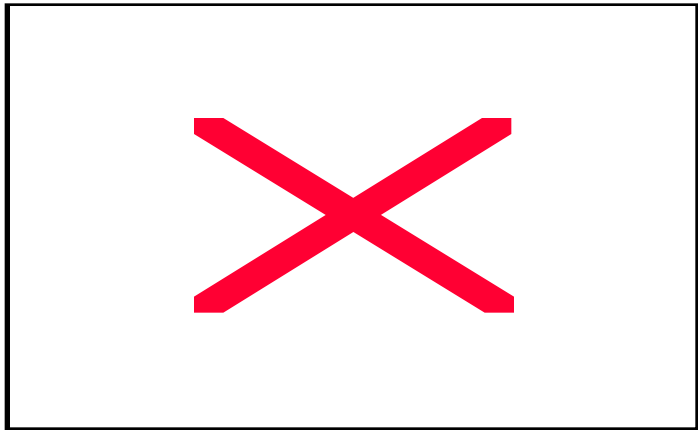


Fig. 7 Normalised vessel sideways displacement versus poloidal beta

3.2. Disruption parameters

In the following the link between the minimum safety factor at the boundary, the current quench rate and the amplitude of the localised n=1 instability during the disruption and the amplitude of the subsequent vessel sideways displacement will be presented.

The **minimum safety factor** during the disruption is not available as processed data, so it has been evaluated, using a cylindrical approximation, as

$$q_c = 5 \frac{B_0 a^2}{I_p R_p},$$

where a is the plasma minor radius, B_0 is the vacuum toroidal magnetic field at the magnetic axis, and R_p and I_p are the radial position of the plasma centroid and the plasma current. The plasma minor radius has been taken, from plasma position measurements, as the shortest distance between the plasma centroid and the wall.

In the estimate of this reference minimum boundary safety factor the residual plasma elongation is not accounted for. A circular plasma with minor radius a has a larger safety factor than a plasma with the same current and with the same vertical dimension but smaller horizontal dimension. The q_c value is therefore an overestimate of the actual boundary safety factor. This overestimate is moderate, typically <20% according to a

simple analysis, because the reduction of the plasma size during the VDE leads to a substantial reduction of the original elongation. On the other end, the measured current flows partly as halo current outside the confined cross-section area, so the safety factor at a minor radius a is larger than the one given by the expression used for q_c . For a typical instantaneous ratio of the poloidal halo current to the total toroidal current of ~ 0.25 , the q_c value is underestimated by $<25\%$. Both effects cancel each other to some extent. The adopted expression for the boundary safety factor gives therefore a reasonable reference value.

If the plasma current density prior to the disruption preserve its profile during the event, the elongation has to decrease because of the change in the external quadrupolar field is changing at a slower rate or staying constant. This leads to smaller (by $\sim 20\%$) value of the boundary safety factor than the one computed, since this is based on the change of the plasma section major axis. If the current profile changes (from a peaked one to a more flat one) the reduction, both on the elongation and on the actual safety factor is diminished ($\sim 10\%$). An opposite effect is due to the presence of the halo current: the plasma centroid position computed from the boundary magnetic field measurements is displaced as it does not discriminate between confined current and halo current producing an overestimate of the actual centre to wall distance, this leads to an underestimate ($\sim 20\%$) of the confined boundary safety factor. At this stage the asymmetry of the plasma position does not matter: due to all the uncertainties this computation has (i.e. elongation is neglected and toroidal halo current is not discriminated from the confined toroidal current, so that the actual safety factor is between 0.8 and 1.2 times the cylindrical-approximation one), the position asymmetry is simply included in the inaccuracy of the calculation. In addition, the search for the minimum boundary safety factor stops when the plasma current has decreased below a third of its starting value. This simplifies the analysis, by eliminating any spurious extremely small q_{min} , and does not miss plasmas which could become asymmetric when their current is still high.

The analysis of the collected data confirmed that vessel sideways displacements, if not AVDEs, are strongly dependent on the minimum value the safety factor can reach during a VDE. A displacement larger than $\sim 0.4 \text{ mm}/(\text{MA T})$ (normalised by the product plasma current times toroidal field) has never been recorded for disruptions whose minimum safety factor at the boundary (q_{min}) has been above 1.2 (Fig. 8), as if a q_{min} of about 1 is needed to trigger the instability.

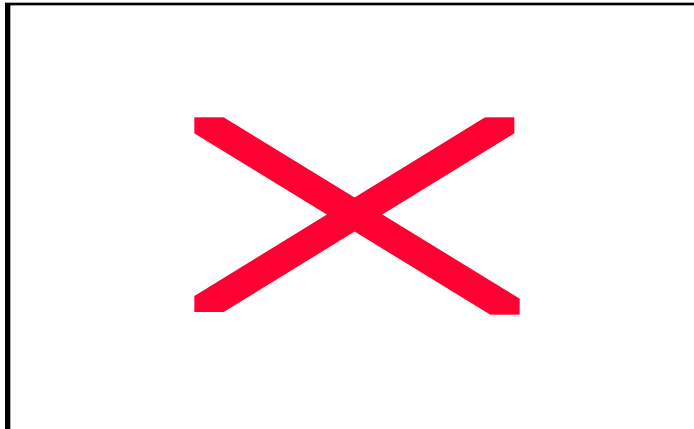


Fig. 8 Minimum safety factor during the disruption versus the normalised amplitude of the vessel sideways displacement

The **plasma current decay rate** is defined as the ratio of the current change to the time during which this change occurs ($\Delta I_p / \Delta t \cdot 1/I_{p0}$). The interval chosen is the one between the time of the plasma current maximum (the temporary increase of plasma current due to the flattening of the current profile, if present, the starting value, otherwise) and the time when the plasma current has decreased to 40% of that maximum. In other words, the normalised decay rate is 0.6 divided by the time taken for the plasma current to decrease by 60%. A threshold behaviour is even more clear for the normalised initial rate

of decay of the plasma current: when the quench rate is more than 30 s^{-1} all normalised sideways displacements are smaller than $0.4 \text{ mm}/(\text{MA T})$ (Fig. 9). Figures 8 and 9 together show that large sideways displacements occur only when the plasma current falls sufficiently slowly so that the plasma has time to shrink enough for the minimum safety factor at the boundary to reach an instability-trigger value of about 1. The fact that fast disruptions do not show significant sideways vessel displacements suggests that the use of killer pellets, or other means of fast plasma termination, could be a way to limit disruption electromechanical loads on the vessel.

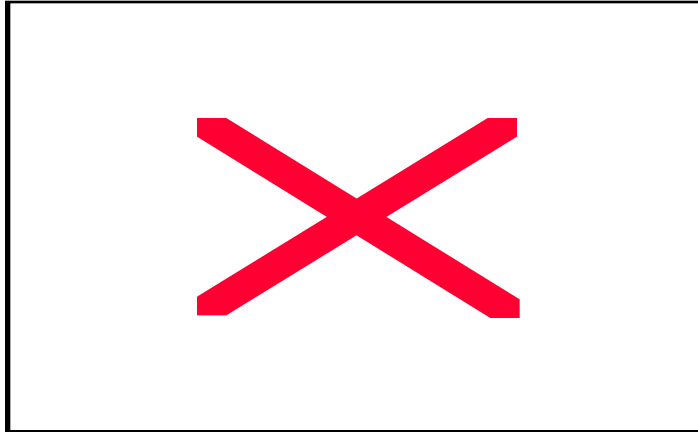


Fig. 9 Plasma current quench rate versus the normalised amplitude of the vessel sideways displacement

The **amplitude of the toroidal mode $n=1$** is computed using a combination of poloidal magnetic fields normal to the vessel wall at the midplane (one pair of flux loops per cross section in four toroidal locations, one pair every 90°). Basically, this quantity is proportional to the amplitude of the asymmetry of the plasma vertical current moment, but it does not carry any information on the toroidal phase angle of the asymmetry and of its possible change of phase angle during the AVDE. The amplitude of the vessel sideways displacement can be therefore small even when the amplitude of the toroidal mode $n=1$ is high, but if the mode amplitude is small sideways displacements can never be large. This is shown in Fig. 10. Using the same raw magnetic data it is possible to identify the location of the peak of the instability. Information on the amplitude and phase of the toroidal mode $n=1$ and of the vessel sideways displacement has been collected and analysed only for a selected set of disruptions. In this subset of data a correlation between the two amplitudes and the two phases has been found. This exercise is too complex to check on a large number of pulses.

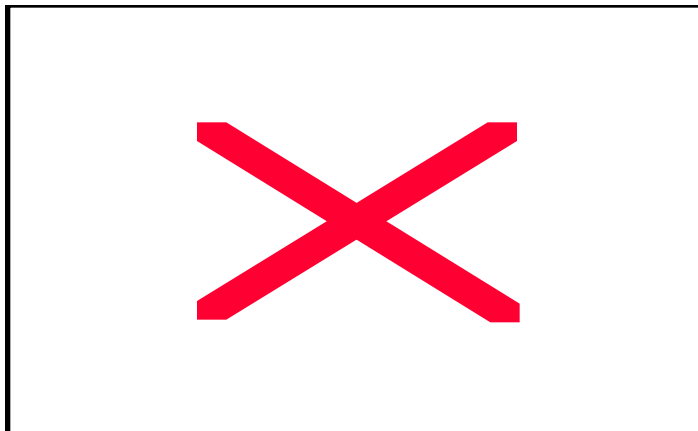


Fig. 10 Amplitude of the toroidal mode $n=1$ versus the normalised amplitude of the vessel sideways displacement

Summary of the Vacuum Vessel Stresses and Fatigue Life in 4 Tesla Operation.

R. Walton

10 November 1999

Contents

1. Introduction.....	1
2. Material Tests and Documented Fatigue Life Data.....	2
2.1. Results.....	4
2.2. Note.....	5
3. Finite Element Models.....	5
3.1. Results.....	6
4. Disruptions.....	10
5. Assessment of Results	10
5.1. Plastic Fatigue Assessment	11
5.2. ASME VIII Div. 2 Assessment.....	11
5.3. Discussion.....	11
6. Summary.....	12
7. List of figures.....	13

1. Introduction

During disruptions, the vacuum vessel exhibits a lateral movement, and also a ‘rolling’ motion. Dampers fitted to the main vertical ports (MVP) are used to control this motion. Forces generated within the dampers are reacted by the MVPs producing cyclical stresses particularly at the base of the port. This occurs in the outer skin of the vessel at a welded joint in 12mm plate, and would be extremely difficult to repair should a leak

develop. This area has been examined in detail to establish whether the fatigue life here could limit the machine performance.

2. Material Tests and Documented Fatigue Life Data.

Fatigue life data based on ASME VIII Division 2 S/N curve for Nickel Alloys, and fatigue test results produced by L Sonnerup are shown in figures 1 & 2. These curves show the variation of strain against the number of cycles at that strain. The ASME curve has been transposed onto figure 2 by multiplication of the stress values given in figure 1 by the Young's Modulus of the material to give strain. It should be noted that the levels of stress calculated in this way are sometimes fictitious because the material would actually be plastic at the higher stress levels.

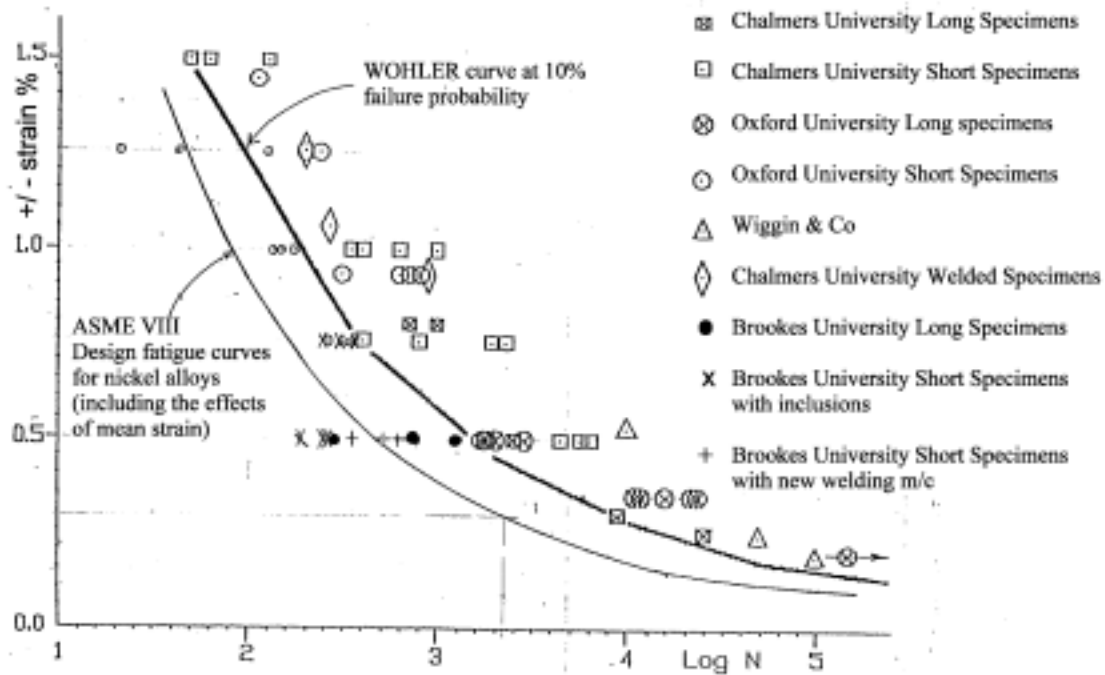


Figure 1. Low cycle fatigue data based on JET results and those listed above

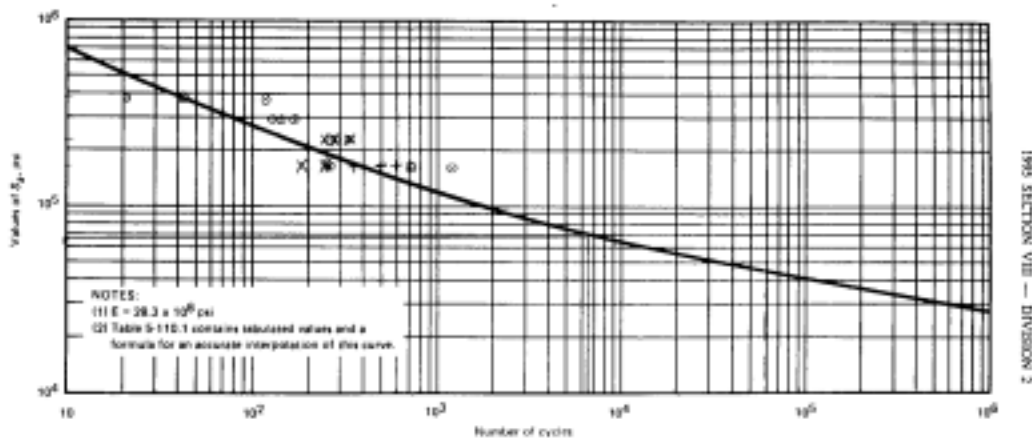


FIG. 5-110.2.1 DESIGN FATIGUE CURVE FOR SERIES 30X HIGH ALLOY STEELS, NICKEL-CHROMIUM-IRON ALLOY, NICKEL-IRON-CHROMIUM ALLOY, AND NICKEL-COPPER ALLOY FOR TEMPERATURES NOT EXCEEDING 800F AND $S_u > 28.2$ ksi (USE FIG. 5-110.2.2 FOR $S_u \leq 28.2$ ksi)

- Original long test pieces
- X Short test pieces - linear inclusion found in post mortem
- + Short test pieces with new welding machine

Figure 2. ASME VIII Division II S/N Curve

Recent fatigue test results obtained from welded samples have been compared with the above criteria. These tests were performed at Brookes University on an initial 12 welded samples at 300 C. It was observed that some of the high strain (1.25%) samples were repeatedly buckling under the compressive load cycle, undermining those results. One poor result at 0.5% strain is attributed to a weld defect. A further six shorter specimens were then tested to eliminate the buckling effect. All of the test data has been entered onto the above curves.

Laminar defects were found in many of the fatigue specimens used subsequent to failure. See figures 3, 4 and 5. These are the result of inclusions generated during rolling/cooling during the material manufacturing process. The test samples, came from the original batch of 19mm inconel 600 plate from which the vessel was manufactured. The inclusions were known to exist in the 19mm plate at the time of manufacture, but were accepted in order to avoid a reduction in yield strength associated with a particular heat treatment which would have removed them. These inclusions are not present in plate 16 mm thick or less, such as those used in the most highly stressed area of the port. During the manufacture of the vacuum vessel many stress strain tests were performed on the materials used in order to check the material properties.



Figure 3. Broken face of sample



Figure 4. Broken face of sample